fractal and fractional

Special Issue Reprint

Application of Fractal Processes and Fractional Derivatives in Finance

Edited by
Leung Lung Chan

mdpi.com/journal/fractalfract

MDPI

Application of Fractal Processes and Fractional Derivatives in Finance

Application of Fractal Processes and Fractional Derivatives in Finance

Editor

Leung Lung Chan

MDPI

Basel • Beijing • Wuhan • Barcelona • Belgrade • Novi Sad • Cluj • Manchester

Editor
Leung Lung Chan
University of New South
Wales
Sydney, NSW
Australia

Editorial Office
MDPI
St. Alban-Anlage 66
4052 Basel, Switzerland

This is a reprint of articles from the Special Issue published online in the open access journal *Fractal and Fractional* (ISSN 2504-3110) (available at: https://www.mdpi.com/journal/fractalfract/special_issues/Fractional_Derivatives_in_Finance).

For citation purposes, cite each article independently as indicated on the article page online and as indicated below:

Lastname, A.A.; Lastname, B.B. Article Title. *Journal Name* **Year**, *Volume Number*, Page Range.

ISBN 978-3-7258-1091-8 (Hbk)
ISBN 978-3-7258-1092-5 (PDF)
doi.org/10.3390/books978-3-7258-1092-5

Contents

fractal and fractional

Article

Comparing Market Efficiency in Developed, Emerging, and Frontier Equity Markets: A Multifractal Detrended Fluctuation Analysis

Min-Jae Lee [1] and Sun-Yong Choi [2,*]

[1] Department of Applied Statistics, Gachon University, Seongnam 13120, Republic of Korea
[2] Department of Financial Mathematics, Gachon University, Seongnam 13120, Republic of Korea
* Correspondence: sunyongchoi@gachon.ac.kr; Tel.: +82-31-750-5387

Abstract: In this article, we investigate the market efficiency of global stock markets using the multifractal detrended fluctuation analysis methodology and analyze the results by dividing them into developed, emerging, and frontier groups. The static analysis results reveal that financially advanced countries, such as Switzerland, the UK, and the US, have more efficient stock markets than other countries. Rolling window analysis shows that global issues dominate the developed country group, while emerging markets are vulnerable to foreign capital movements and political risks. In the frontier group, intensive domestic market issues vary, making it difficult to distinguish similar dynamics. Our findings have important implications for international investors and policymakers. International investors can establish investment strategies based on the degree of market efficiency of individual stock markets. Policymakers in countries with significant fluctuations in market efficiency should consider implementing new regulations to enhance market efficiency. Overall, this study provides valuable insights into the market efficiency of global stock markets and highlights the need for careful consideration by international investors and policymakers.

Keywords: global market efficiency; multifractal detrended fluctuation analysis; developed markets; emerging markets; frontier markets

Citation: Lee, M.-J.; Choi, S.-Y. Comparing Market Efficiency in Developed, Emerging, and Frontier Equity Markets: A Multifractal Detrended Fluctuation Analysis. *Fractal Fract.* **2023**, *7*, 478. https://doi.org/10.3390/fractalfract7060478

Academic Editor: Leung Lung Chan

Received: 21 April 2023
Revised: 7 June 2023
Accepted: 13 June 2023
Published: 15 June 2023

1. Introduction

The efficient market hypothesis (EMH) posits that information in the stock market is promptly incorporated into stock prices. According to this theory, current stock prices already encompass all available information. Consequently, stock prices are subject to random movements and cannot be deemed undervalued or overvalued. Fama divides the efficient market hypothesis into three hypotheses based on the range of related information. A weak-form efficient market is a market that reflects historical information in the current price, and excess profits can be obtained if current or future information is used. The semi-strong-form efficient market reflects current information in addition to past information and can generate excess profits if future information is obtained. The strong-form efficient market hypothesis states that all market participants know all information, including future undisclosed information, and that no information analysis can generate excess profits.

Determining the specific efficient market hypothesis that governs the stock market holds significant implications for comprehending the information reflected in current stock prices. This understanding plays a vital role in effective risk management by facilitating the prediction of future stock price fluctuations. Furthermore, it facilitates effective resource allocation, leveraging the prevailing market prices for efficient growth. In cases where the market does not strictly adhere to a strong-form efficient market, valuable insights can be gained to guide decision making concerning the specific information and information analysis methods necessary for obtaining excess profits.

As market efficiency is important, many studies have been conducted on this topic. For example, Horta et al. [1] showed that financial crises significantly influenced most stock markets, and that markets lost efficiency during the subprime crisis. Hull and McGroarty [2] investigated the relationship between efficiency and market development. Rizvi et al. [3] revealed a relatively high efficiency ranking in developed markets in the short term and a medium efficiency ranking in the long term. Charfeddine and Khediri [4] researched the weak-form efficiency of the Gulf Cooperation Council stock markets, and concluded that while the GCC market has different degrees of efficiency over time, it is also improving over time. Ali et al. [5] compared the efficiency of conventional stock markets and their Islamic counterparts, and the result was that developed markets were relatively more efficient.

Two main methodologies have been employed to investigate the EMH. The first approach utilizes the Hurst–Mandelbrot–Walis R/S statistics, a statistical methodology. Based on this method, Horta et al. [1] discovered that stock price increments in the pre-crisis era align more closely with the random walk paradigm compared to the post-crisis period. Similarly, Hull and McGroarty [2] noted that more advanced emerging markets display lower levels of long-term persistence. The second methodology employed is the multifractal detrended fluctuation analysis (MF-DFA). By using the MF-DFA approach, Rizvi et al. [3] emphasized the efficient performance of Islamic markets during crises, while Horta et al. [1] suggested deviations that are indicative of long memory and reverting patterns. Charfeddine and Khediri [4] ranked Qatar as the most efficient market, while Bahrain and Oman were considered less efficient. Furthermore, Ali et al. [5] provided rankings of the efficiency of stock markets in non-Islamic, BRICS, and developed countries, as well as their corresponding Islamic counterparts.

This study investigated the efficiency of the stock markets of several countries around the world. Market efficiency was calculated using stock indices from 60 countries, and the results were analyzed by dividing them into developed, emergent, and frontier groups (MSCI market classification, https://https://www.msci.com/our-solutions/indexes/acwi accessed on 1 May 2023). We describe the stock index data in Section 3.

We employed the MF-DFA method to calculate market efficiency. Recently, this method has been widely used in research on the market efficiency hypothesis and multifractality of financial assets (e.g., Miloş et al. [6], Choi [7], Yin and Wang [8], Pak and Choi [9], Gaio et al. [10]). Furthermore, we performed both static and rolling window analyses in order to assess the market efficiency of global stock markets. Through this method, we analyzed market efficiency for the entire sample period and time-varying market efficiency.

This study contributes to the financial literature in two ways. First, the market efficiency of various countries around the world shows some differences between the developed, emerging, and frontier groups. Rather than focusing on individual countries, this research adopted a group perspective to analyze stock market efficiency. While studies on market efficiency in developed countries have been extensively reported, the attention given to emerging and frontier countries has been relatively limited. Previous research on emerging or frontier countries has primarily compared and analyzed market efficiencies among individual countries or a small number of countries (e.g., Caraiani [11], Arshad et al. [12], Aslam et al. [13], and Nargunam and Lahiri [14]). In contrast, this study aims to overcome these limitations by incorporating as many stock markets as possible, spanning developed, emerging, and frontier countries. This approach provides a comparative advantage in terms of the number of stock markets considered compared to previous studies (e.g., Rizvi et al. [3], Ali et al. [5], Lee et al. [15], and Aslam et al. [16]).

Second, we methodologically investigated how market efficiency in individual countries changes over time using rolling window analysis. In particular, we analyzed and compared the degree of response of individual markets to systematic risks, such as the 2008 global financial crisis and COVID-19 pandemic, while several studies have examined the impact of the COVID-19 pandemic on stock market efficiency (e.g., Aslam et al. [17], Mensi et al. [18], and Saâdaoui [19]), the range of stock markets considered in these studies was narrower than that of our research. By employing rolling window analysis, this study provides valuable insights into the evolving nature of market efficiency in individual countries over time.

Overall, this study contributes to the financial literature by examining stock market efficiency from a group perspective and incorporating a wide range of stock markets from developed, emerging, and frontier countries. Furthermore, it enhances the understanding of how market efficiency changes within individual countries over time by investigating their responsiveness to systematic risks. The findings of this study have implications for investors, policymakers, and researchers seeking to comprehend and navigate the dynamics of global financial markets.

The remainder of this paper is organized as follows. In the following section, we introduce previous studies on market efficiency. Section 3 describes global stock market data and provides a preliminary statistical analysis. In Section 4, we briefly review the MF-DFA method. Section 5 presents the results of static and rolling window analyses. Section 6 presents the summary and concluding remarks.

2. Literature Review

2.1. Global Stock Markets

Many studies have compared national stock market efficiencies. Studies on efficiency suggest that most developed markets are more efficient than emerging markets. Lim [20] defined the sequence of efficiency of the US, Korea, Taiwan, Japan, Thailand, Philippines, Brazil, Mexico, India, Indonesia, Malaysia, Chile, and Argentina, with emerging and developed markets using H-statistic. The relationship between market efficiency and market development was investigated by Hull and McGroarty [2]. Their study employed the Hurst–Mandelbrot–Walis R/S statistic and the Jarque–Bera test to analyze markets categorized as either advanced or secondary. The findings indicated that advanced markets demonstrate higher levels of efficiency in comparison to secondary markets. Using MF-DFA, Rizvi et al. [3] showed that developed markets (e.g., the US, Japan, and Hong Kong) are more efficient, excluding Malaysia, Indonesia, and Turkey, which have Islamic and developed markets (e.g., Bahrain, Bangladesh, and Egypt). Further, Ali et al. [5] revealed that developed markets are the most efficient, followed by BRICS markets. In addition, every Islamic stock market, except Russia, Jordan, and Pakistan, is more efficient than its conventional counterparts, such as Turkey, the USA, and China. Anagnostidis et al. [21] investigated the effects of the 2008 financial crisis on Eurozone stock markets, using GHE (generalized Hurst exponent). They classified them into three groups according to how adversely they were affected by the crisis.

2.2. Time-Varying Market Efficiency

Several studies have investigated the evolution of market efficiency over time. For example, Rizvi and Arshad [22], using MF-DFA, examined the efficiency of East Asian stock markets during booms and busts. The study concluded that economic booms affected each market differently, with a decrease in efficiency during recession periods and an increase during boom periods. Interestingly, only Singapore’s market efficiency increased during these events. In another comprehensive examination of financial crises, Horta et al. [1] studied the impact of the 2008 and 2010 crises on stock markets. Their findings indicated the presence of market efficiency dynamics and financial contagion during these periods. Moreover, the study observed that developed markets were minimally affected by financial crises, while less-developed markets experienced significant impact.

Many studies have been conducted to examine the fluctuations in market efficiency levels. Smith [23] studied European emerging and developed stock markets and used variance ratio tests of the martingale hypothesis. They revealed that each country has different levels of efficiency; the most efficient market is Turkey and the least efficient markets are Malta and Ukraine. They also suggested that the global financial crisis had little effect on weak-form efficiency markets, such as Greece and Russia. Furthermore, according to the changing efficiency over time, the relative efficiency also changes. While the market with the largest improvement is Romania, that with the smallest improvement is Croatia. Sensoy [24] showed that the MENA stock markets have different levels of long-term dependence by using the rolling window technique. They also suggested that the most efficient markets, such as Turkey and Israel, reduce the capital costs of less-efficient markets, such as Iran and the UAE.

3. Data Description

In our analysis, we utilized a range of global stock indices to capture market performance. Specifically, we considered stock price indices from 23 developed markets, 22 emerging markets, and 15 frontier markets. The data for these indices were sourced from Reuters, providing a comprehensive view of market trends and movements. Our analysis covered the period from January 2007 to June 2022, allowing us to examine the performance of these markets over a substantial time period. We display the log returns of the global stock indices in three groups in Figures 1–3. Furthermore, Table 1 shows the summary statistics for the log returns of global stock indices. Based on the information provided in the above table, it can be observed that all three groups exhibit a bias towards the left side of the distribution. This indicates that the data do not follow a normal distribution. However, Vietnam is biased toward the right, showing lower-than-average profits. The average kurtosis is 19, 76, 84 (rounded from the first decimal place) for each group, and the emerging and frontier groups are greatly affected by extreme values, showing relatively unstable returns. In particular, Turkey has a value of 1239.4757 in the emerging group and Iceland has a value of 838.6851 among the frontier group, which is extreme within the group.

Table 1. Descriptive statistics of global stock indices in three groups. ‡ indicates rejection of the null hypothesis at the 1% significance level. Note: Skew., Kurt., and J.-B. refer to skewness, kurtosis, and Jarque–Bera statistics, respectively.

Group	Country	Mean	Std.Dev.	Skew.	Kurt.	J.-B.
Developed	Austria	−0.0003	0.0286	−2.23	23.97	34,312.3 ‡
	Australia	0.0001	0.0181	−1.37	14.29	12,225.4 ‡
	Belgium	−0.0001	0.0227	−2.49	33.61	66,593.6 ‡
	Canada	0.0003	0.0186	−3.59	54.18	172,326.9 ‡
	Switzerland	0.0001	0.0178	−0.89	8.43	4291.6 ‡
	Germany	0.0005	0.0236	−1.46	13.40	10,865.4 ‡
	Denmark	0.0008	0.0207	−1.45	17.40	17,969.6 ‡
	Spain	−0.0004	0.0243	−0.64	5.78	2030.5 ‡
	Finland	0.0001	0.0229	−1.01	8.93	4844.8 ‡
	France	0.0001	0.0228	−1.2	10.69	6959.5 ‡
	United Kingdom	0.0001	0.0193	−1.54	19.23	21,893.2 ‡
	Hong Kong	0.0001	0.0250	−0.33	7.19	3015.5 ‡
	Ireland	−0.0002	0.0267	−1.98	19.56	23,003.4 ‡
	Israel	0.0005	0.0182	−1.35	11.96	8688.4 ‡
	Italy	−0.0005	0.0262	−0.99	7.53	3508.5 ‡
	Japan	0.0003	0.0234	−1.13	11.26	7612.8 ‡
	Netherlands	0.0002	0.0223	−2.58	33.46	66,148.6 ‡
	Norway	0.0004	0.0254	−2.58	36.18	77,071.1 ‡
	New Zealand	0.0007	0.0135	−1.35	17.00	17,098.1 ‡
	Portugal	−0.0004	0.0230	−0.90	7.33	3295.8 ‡
	Sweden	0.0005	0.0212	−1.45	12.99	10,230.5 ‡
	Singapore	0.0001	0.0197	−1.36	26.08	39,688.4 ‡
	United States	0.0007	0.0195	−2.44	30.52	55,108.3 ‡
Emerging	Brazil	0.0006	0.0275	−1.35	16.90	16,904.2 ‡
	Chile	0.0005	0.0208	−1.51	21.89	28,191.9 ‡
	China	0.0010	0.0381	−0.84	6.52	2622.6 ‡

Table 1. *Cont.*

Group	Country	Mean	Std.Dev.	Skew.	Kurt.	J.-B.
	Czech Republic	−0.0001	0.0225	−2.11	24.99	37,082.7 ‡
	Egypt	0.0002	0.0285	−0.85	9.12	4970.4 ‡
	Greece	−0.0012	0.0352	−0.56	5.68	1941.4 ‡
	Indonesia	0.0010	0.0225	−1.31	19.56	22,467.4 ‡
	India	0.0010	0.0243	−1.46	19.31	22,025.8 ‡
	South Korea	0.0004	0.0216	−2.00	23.92	33,942.8 ‡
	Mexico	0.0004	0.0191	−0.62	9.94	5792.5 ‡
	Malaysia	0.0002	0.0144	−1.60	19.73	23,069.1 ‡
	Peru	0.0003	0.0277	−1.07	20.70	25,000.7 ‡
	Philippines	0.0005	0.0231	−1.83	30.66	55,014.2 ‡
	Poland	−0.0004	0.0251	−1.33	11.32	7812.2 ‡
	Qatar	0.0004	0.0229	−0.10	12.68	9282.7 ‡
	Saudi Arabia	0.0003	0.0219	−1.30	11.51	8030.4 ‡
	Thailand	0.0007	0.0209	−1.87	24.35	35,040.5 ‡
	Turkey	−0.0020	0.1294	−34.34	1239.47	88,866,224 ‡
	Taiwan	0.0005	0.0219	−1.00	13.11	10,152.5 ‡
	U.A.E.	−0.0002	0.0286	−0.91	19.27	21,636.1 ‡
	South Africa	−0.0002	0.0371	−1.29	24.93	36,242.1 ‡
Frontier	Bahrain	−0.0001	0.0103	−1.06	9.22	5171.3 ‡
	Estonia	0.0005	0.0196	−1.32	18.41	19,949.7 ‡
	Croatia	−0.0003	0.0196	−1.19	23.81	33,047.3 ‡
	Iceland	−0.0007	0.0433	−25.71	818.68	38,803,863 ‡
	Jordan	−0.0009	0.0236	−4.71	103.63	624,502.1 ‡
	Kenya	−0.0010	0.0181	−1.39	17.91	18,944.9 ‡
	Lithuania	0.0004	0.0185	−1.55	36.21	76,200.1 ‡
	Morocco	0.0001	0.0151	−2.14	34.50	69,721.5 ‡
	Mauritius	0.0004	0.0149	−2.33	66.04	252,860.5 ‡
	Oman	−0.0002	0.0164	−0.41	14.93	12,911.4 ‡
	Romania	0.0003	0.0254	−1.41	14.45	12,514.1 ‡
	Serbia	−0.0005	0.0234	−0.92	28.09	45,734.8 ‡
	Slovenia	−0.0002	0.0250	−0.45	101.78	597,553.8 ‡
	Tunisia	0.0008	0.0102	−1.82	22.05	28,837.1 ‡
	Vietnam	0.0002	0.0269	0.01	7.56	3302.1 ‡

Larger kurtosis values tend to increase J-B statistics. The following are the top five countries in each group: Canada, Norway, Belgium, the Netherlands, and the US in the developed group; Turkey, the Philippines, the Czech Republic, South Africa, and Thailand in the emerging group; and Iceland, Jordan, Slovenia, Mauritius, and Lithuania in the frontier group.

Comparing the Jarque–Bera statistics for each group, there are very large outliers such as Turkey, where the median is 1225.4, emerging is 22,025.8, and frontier is 30,942.2, showing that developed countries are relatively trying to follow the normal distribution, making the most stable return. Spain has the smallest value which can be considered stable, followed by Hong Kong.

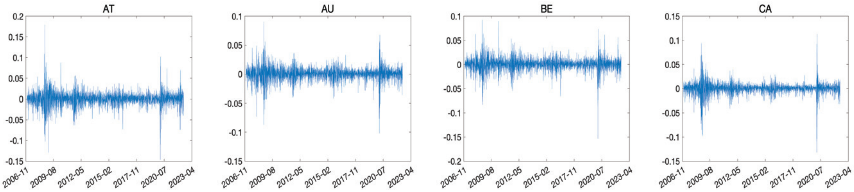

(**a**) Austria (**b**) Australia (**c**)Belgium (**d**) Canada

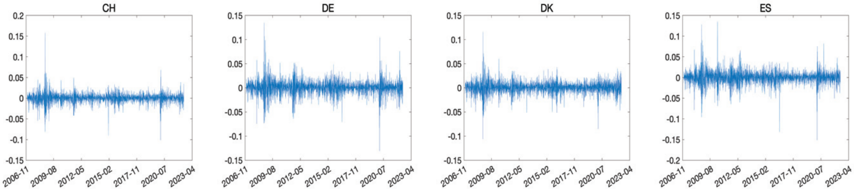

(**e**) Switzerland (**f**) Germany (**g**) Denmark (**h**) Spain

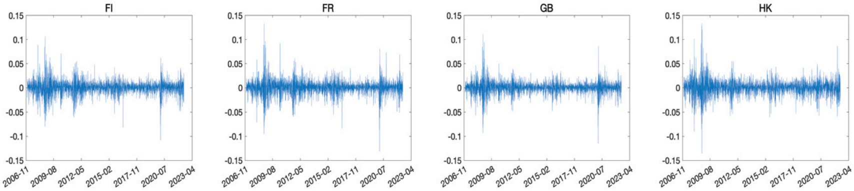

(**i**) Finland (**j**) France (**k**) United Kingdom (**l**) Hong Kong

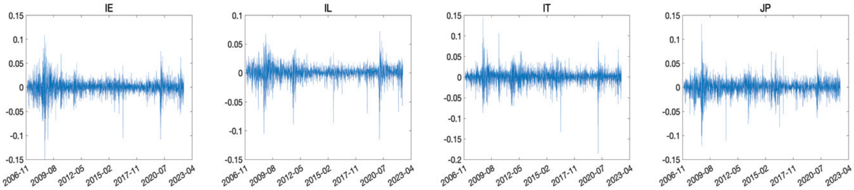

(**m**) Ireland (**n**) Israel (**o**) Italy (**p**) Japan

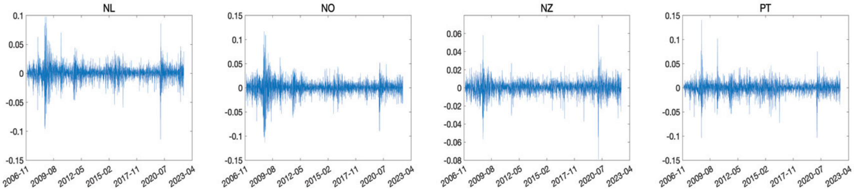

(**q**) Netherlands (**r**) Norway (**s**) New Zealand (**t**) Portugal

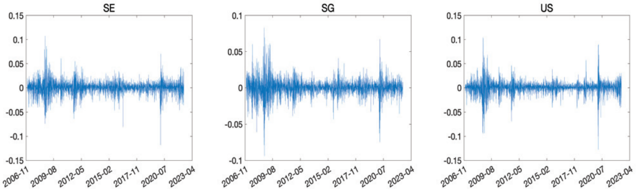

(**u**) Sweden (**v**) Singapore (**w**) United States

Figure 1. The log return time series for all the indices in developed countries.

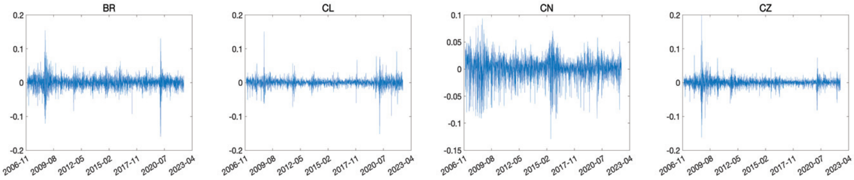

(**a**) Brazil (**b**) Chile (**c**) China (**d**) Czech Republic

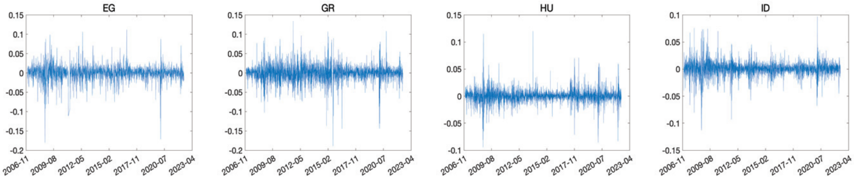

(**e**) Egypt (**f**) Greece (**g**)Hungary (**h**) Indonesia

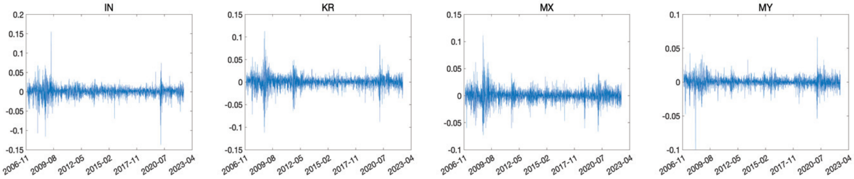

(**i**) India (**j**) Korea (**k**) Mexico (**l**) Malaysia

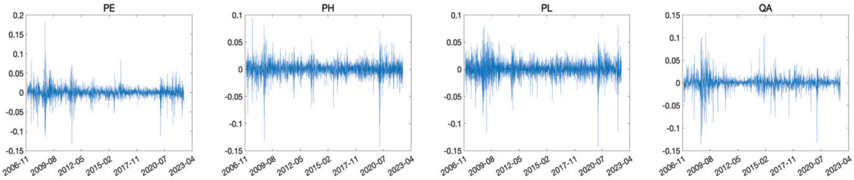

(**m**) Peru (**n**) Philippines (**o**) Poland (**p**) Qatar

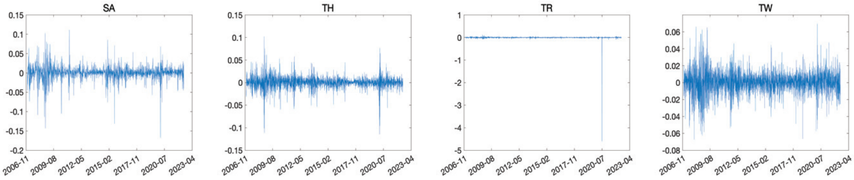

(**q**) Saudi Arabia (**r**) Thailand (**s**) Turkey (**t**) Taiwan

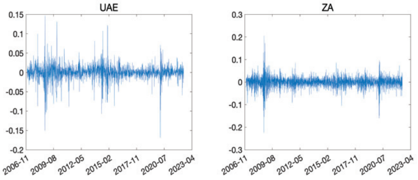

(**u**) United Arab Emirates (**v**) South Africa

Figure 2. The log return time series for all the indices in emerging countries.

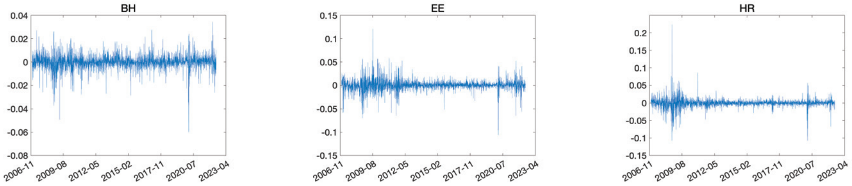

(**a**) Bahrain (**b**) Estonia (**c**) Croatia

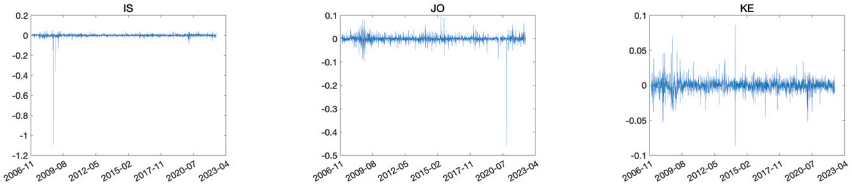

(**d**) Iceland (**e**) Jordan (**f**) Kenya

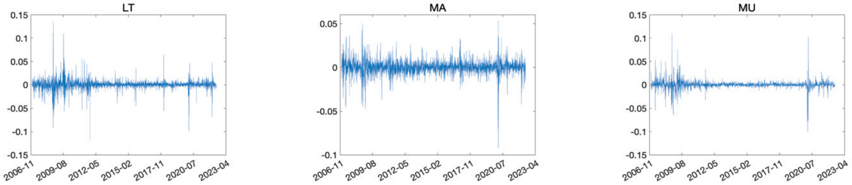

(**g**) Lithuania (**h**) Morocco (**i**) Mauritius

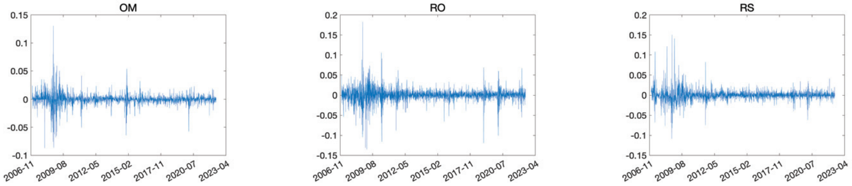

(**j**) Oman (**k**) Romania (**l**) Serbia

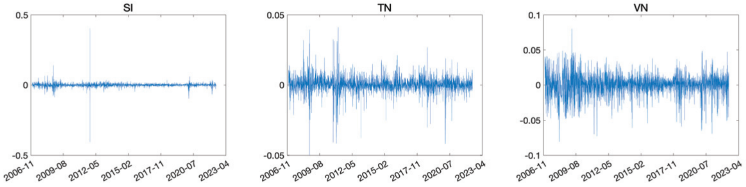

(**m**) Slovenia (**n**) Tunisia (**o**) Vietnam

Figure 3. The log return time series for all the indices in frontier countries.

4. Multifractal Detrended Fluctuation Analysis

The multifractal detrended fluctuation analysis (MF-DFA) method was used to assess the multifractal characteristics of the financial time series and rank market efficiency. It can be executed in five steps, as outlined by [25] and summarized by [26].

Let $\{x_k, k = 1, \cdots, N\}$ be a time series, where N is its length.

- Step 1. Determine the profile $Y(i)(i = 1, 2, \cdots, N)$

$$Y(i) = \sum_{k=1}^{i} (x(k) - \bar{x}), \tag{1}$$

where

$$\bar{x} = \sum_{k=1}^{N} x(k)/N. \tag{2}$$

- Step 2. Divide the profile $\{Y(i)\}(i = 1, 2, \cdots, N)$ into $N_s \equiv int(N/s)$ non-overlapping segments of equal length s. To ensure that the entire sample is covered, the same procedure is repeated starting from the end of the sample. By doing so, a total of $2N_s$ segments are obtained:

$$\{Y[(\nu - 1)s + i]\}_{i=1}^{s},\ \nu = 1, 2, \ldots, N_s \tag{3}$$

$$\{Y[N - (\nu - N_s)s + i]\}_{i=1}^{s},\ \nu = N_s + 1, N_s + 2, \ldots, 2N_s. \tag{4}$$

- Step 3. Calculate the local trend for each of the $2N_s$ segments. To estimate the local trend in each segment, a least-squares fitting polynomial is used. Once the local trend has been determined, the variance is calculated accordingly.

$$F^2(s,\nu) = \begin{cases} \frac{1}{s}\sum_{i=1}^{s}\left\{Y[(\nu-1)s+i] - \hat{Y}_\nu^m(i)\right\}^2, & \nu = 1, 2, \ldots, N_s \\ \frac{1}{s}\sum_{i=1}^{s}\left\{Y[N-(\nu-N_s)s+i] - \hat{Y}_\nu^m(i)\right\}^2, & \nu = N_s+1, N_s+2, \ldots, 2N_s. \end{cases} \tag{5}$$

The fitting polynomial with order m in segment ν is denoted as $\hat{Y}_\nu^m(i)$. Typically, a linear ($m = 1$), quadratic ($m = 2$), or cubic ($m = 3$) polynomial is used to estimate the local trend in each segment, as reported in previous studies ([27–29]). However, in this study, in order to avoid overfitting and simplify the calculation process, a linear polynomial ($m = 1$) is employed, as suggested in [30,31].

- Step 4. Average over all the segments. Then, we obtain the q-th order fluctuation function:

$$F_q(s) = \begin{cases} \left[\frac{1}{2N_s}\sum_{\nu=1}^{2N_s}\left(F^2(s,\nu)\right)^{q/2}\right]^{1/q}, & q \neq 0 \\ \exp\left[\frac{1}{4N_s}\sum_{\nu=1}^{2N_s}\ln\left(F^2(s,\nu)\right)\right] & q = 0. \end{cases} \tag{6}$$

- Step 5. Determine the scaling behavior of the fluctuation functions. To determine if a long-range power law correlation exists, the log–log plots of $F_q(s)$ are compared for each value of q. If the series exhibits long-range power law correlation, $F_q(s)$ will increase as s becomes large. The power law relationship can be expressed in the following form.

$$F_q(s) \propto s^{h(q)}, \tag{7}$$

where $h(q)$ represents the generalized Hurst exponent. Equation (7) can be written as $F_q(s) = a \cdot s^{h(q)} + b$. After taking the logarithms of both sides,

$$\log\left(F_q(s)\right) = h(q) \cdot \log(s) + c, \tag{8}$$

where c is a constant.

The value of the exponent $h(q)$ depends on q. If $h(q)$ is independent of q, then the time series is monofractal; otherwise, it is multifractal. When $q = 2$, $h(2)$ is equivalent to the Hurst exponent ([32]); thus, $h(q)$ is referred to as the generalized Hurst exponent. $h(2) = 0.5$ indicates that the time series are uncorrelated and follow a random walk process, suggesting that the market is weakly efficient ([32,33]). If $0.5 < h(2)$, the time series is long-range dependent, meaning that an increase (decrease) is more likely to be followed by another increase (decrease). By contrast, $h(2) < 0.5$ indicates a non-persistent series, where an increase (decrease) is more likely to be followed by a decrease (increase).

According to Reference [25], the relationship between $h(q)$ and multifractal scaling exponent $\tau(q)$ can be expressed as follows:

$$\tau(q) = qh(q) - 1. \tag{9}$$

To estimate multifractality, a Legendre transform was used to convert q and $\tau(q)$ into α and $f(\alpha)$, respectively, using the following equations:

$$\alpha = \frac{d}{dq}\tau(q), \;\; f(\alpha) = \alpha(q)q - \tau(q), \tag{10}$$

where $f(\alpha)$ is the multifractal or singularity spectrum and α is the singularity strength.

In addition, a definition of the width of the multifractal spectrum $\Delta\alpha$ is provided in References [34–36].

$$\Delta\alpha = \max(\alpha) - \min(\alpha). \tag{11}$$

A wider multifractal spectrum implies a higher degree of multifractality. The next section presents the empirical results pertaining to the multifractality of the average return series for all sectors.

5. Empirical Results

This section provides a static and rolling window analysis of the market efficiencies of the three groups.

5.1. Static Analysis

Figures 4–6 show the log−log plots of $F_q(s)$ compared with s for all average sector return series during the GFC and COVID-19 pandemic for $q = -10, -9, \ldots, 9, 10$ corresponding to the curve from the bottom to the top when the polynomial order $m = 1$.

The Hurst exponent $H(q)$ for developed, emerging, and frontier countries is shown in Figures 7–9. As shown, the generalized Hurst exponent of the index return series decreases as q increases from -10 to 10, indicating that the return series of all markets have clear multifractal characteristics. For $q = 2$, the generalized Hurst exponent $h(q)$ is equal to the Hurst exponent. Most Hurst exponents differed from 0.5, providing evidence against the presence of the random-walk behavior. Furthermore, the Hurst exponents of all markets in the frontier group are greater than 0.5. In other words, the average return series for all the markets in the frontier group are persistent. In particular, the stock markets of Switzerland, the United Kingdom, and the United States have Hurst exponents close to 0.5, indicating that their stock markets are close to the efficiency market.

We rank the efficiency of each stock market using the measure $\Delta\alpha$ in Table 2. Table 2 lists the efficiency rankings of the three groups. Although the rankings changed according to these two criteria, the higher and lower ranks remained the same. Furthermore, Figures 10–12 plot the multifractal spectra of all the index returns. In several subfigures, a phenomenon called knotting phenomena occurs, in which the curve is twisted near the peak of the curve. This phenomenon can be attributed to several factors, including the scaling range, irregular fluctuation functions observed at large scales, and the non-monotonic behavior exhibited by the estimated generalized Hurst index function according to previous studies (Jiang et al. [27], Zhou et al. [37], Gao et al. [38]).

According to Table 2, within the developed group, the stock market of Hong Kong is the most efficient, while the stock market of Italy is the least efficient. Within the emerging group, Taiwan and Turkey have the most- and least-efficient stock markets, respectively. Within the emerging group, Oman and Jordan have the most- and least-efficient stock markets, respectively, in the frontier group. Among all countries, Taiwan and Turkey have the highest and lowest stock market efficiencies, respectively.

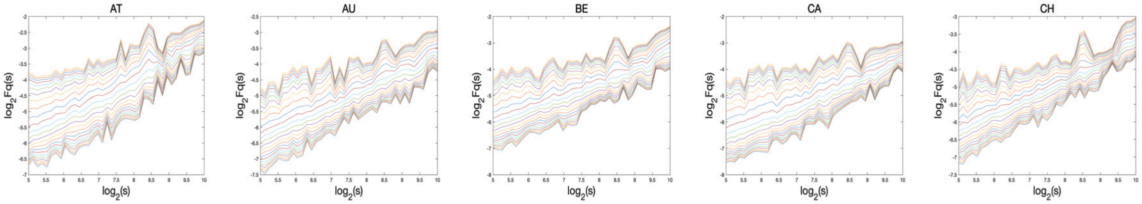

(**a**) Austria (**b**) Australia (**c**) Belgium (**d**) Canada (**e**) Switzerland

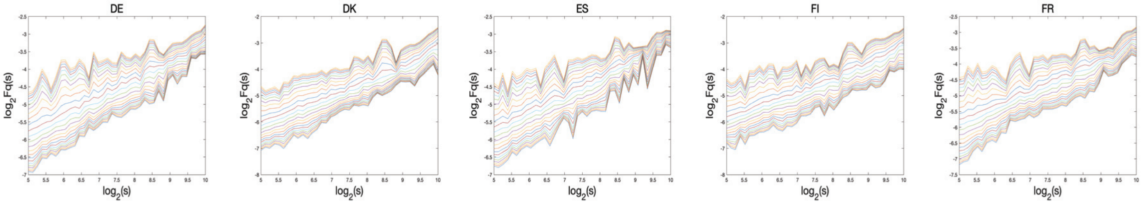

(**f**) Germany (**g**) Denmark (**h**) Spain (**i**) Finland (**j**) France

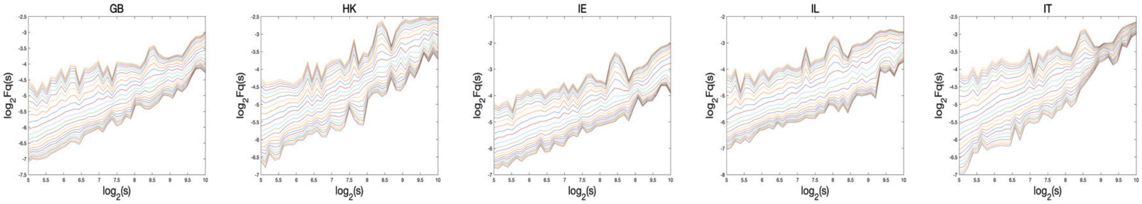

(**k**) United Kingdom (**l**) Hong Kong (**m**) Ireland (**n**) Israel (**o**) Italy

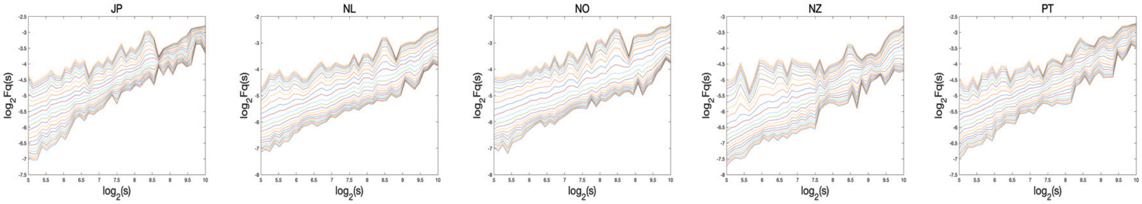

(**p**) Japan (**q**) Netherlands (**r**) Norway (**s**) New Zealand (**t**) Portugal

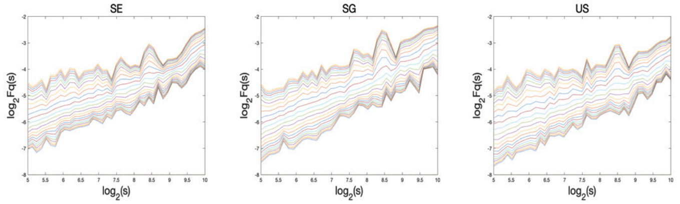

(**u**) Sweden (**v**) Singapore (**w**) United States

Figure 4. The curve of the multifractal fluctuation function $Fq(s)$ compared to s in a log–log plot of the average return for all the indices in developed countries.

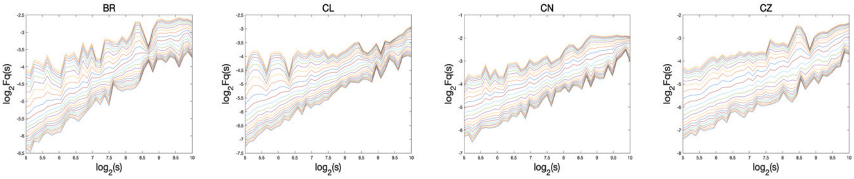

(**a**) Brazil (**b**) Chile (**c**) China (**d**) Czech Republic

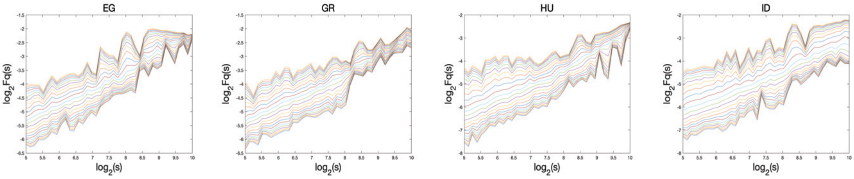

(**e**) Egypt (**f**) Greece (**g**) Hungary (**h**) Indonesia

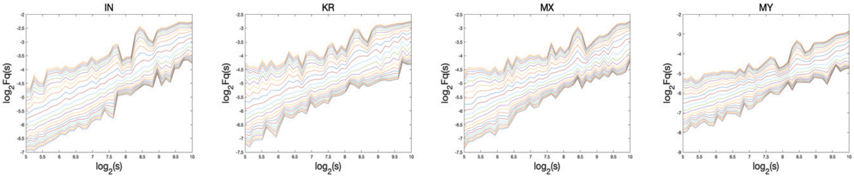

(**i**) India (**j**) Korea (**k**) Mexico (**l**) Malaysia

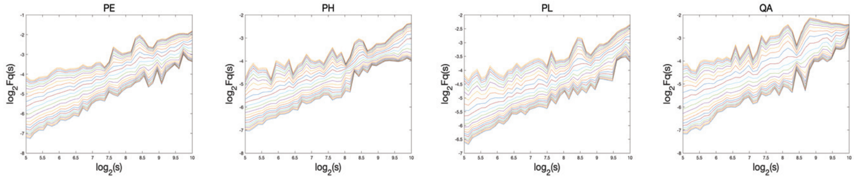

(**m**) Peru (**n**) Philippines (**o**) Poland (**p**) Qatar

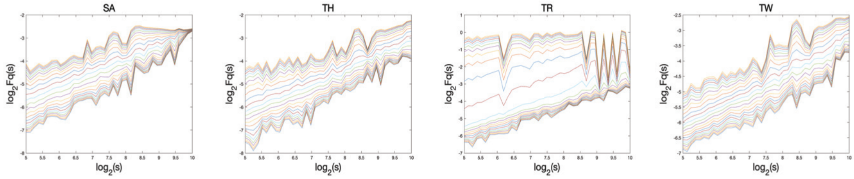

(**q**) Saudi Arabia (**r**) Thailand (**s**) Turkey (**t**) Taiwan

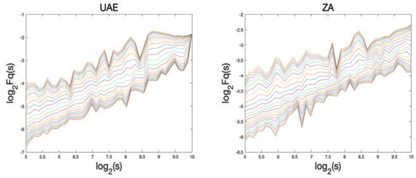

(**u**) United Arab Emirates (**v**) South Africa

Figure 5. The curve of the multifractal fluctuation function $Fq(s)$ compared to s in a log–log plot of the average return for all the indices in emerging countries.

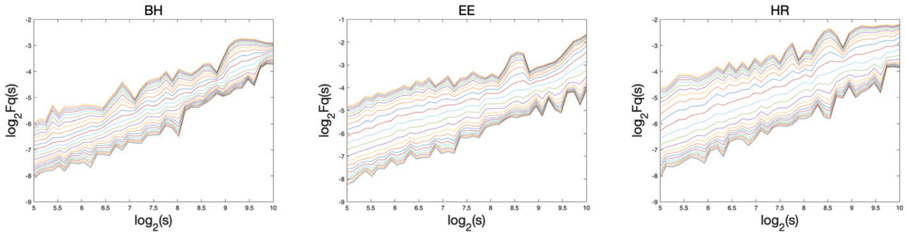

(**a**) Bahrain (**b**) Estonia (**c**) Croatia

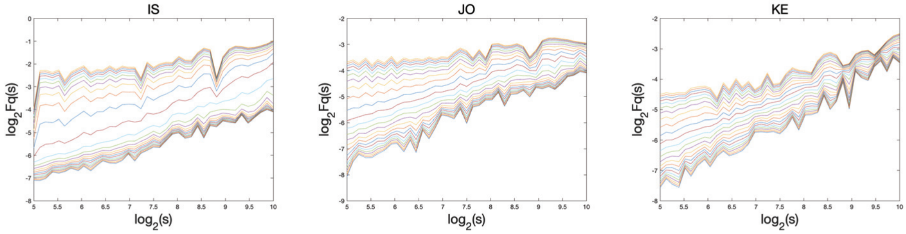

(**d**) Iceland (**e**) Jordan (**f**) Kenya

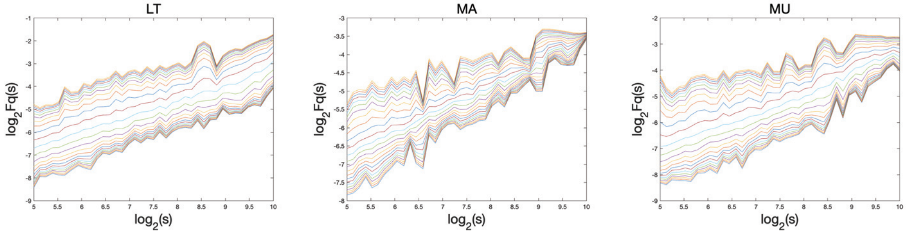

(**g**) Lithuania (**h**) Morocco (**i**) Mauritius

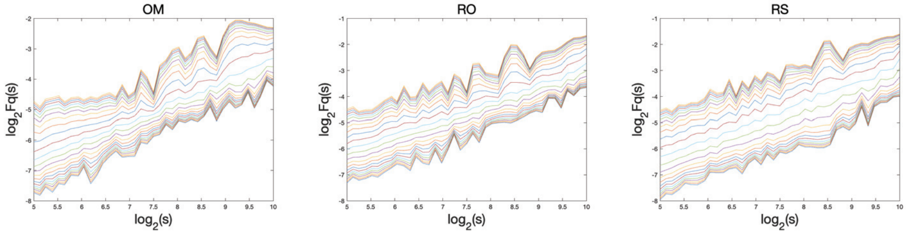

(**j**) Oman (**k**) Romania (**l**) Serbia

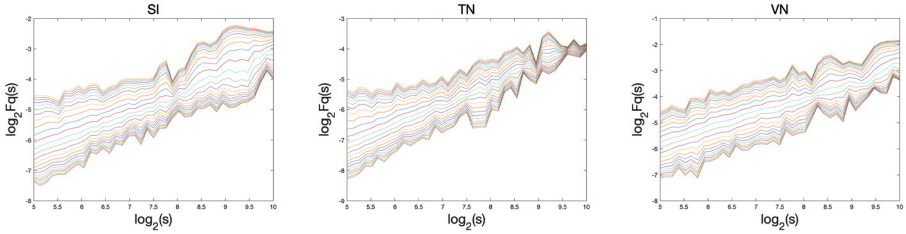

(**m**) Slovenia (**n**) Tunisia (**o**) Vietnam

Figure 6. The curve of the multifractal fluctuation function $Fq(s)$ compared to s in a log–log plot of the average return for all the indices in frontier countries.

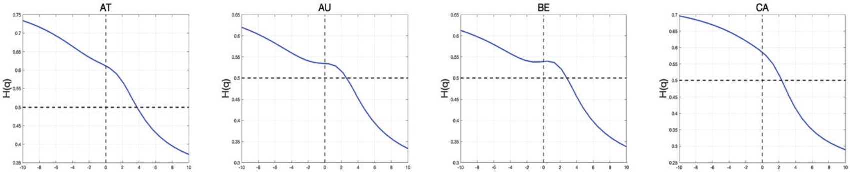

(**a**) Austria (**b**) Australia (**c**) Belgium (**d**) Canada

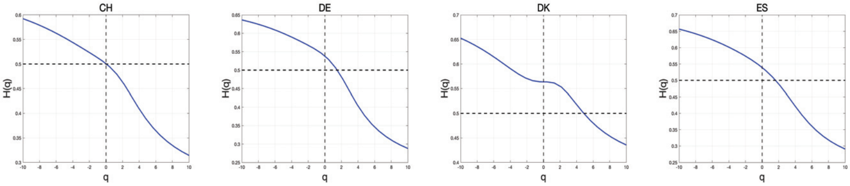

(**e**) Switzerland (**f**) Germany (**g**) Denmark (**h**) Spain

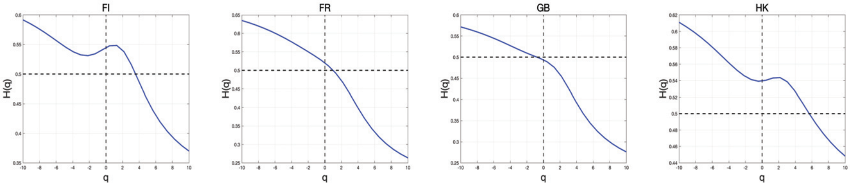

(**i**) Finland (**j**) France (**k**) United Kingdom (**l**) Hong Kong

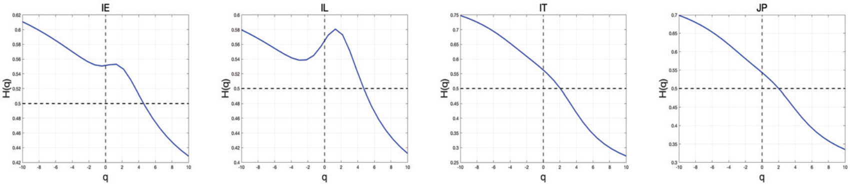

(**m**) Ireland (**n**) Israel (**o**) Italy (**p**) Japan

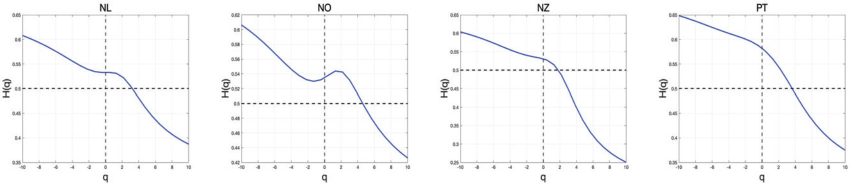

(**q**) Netherlands (**r**) Norway (**s**) New Zealand (**t**) Portugal

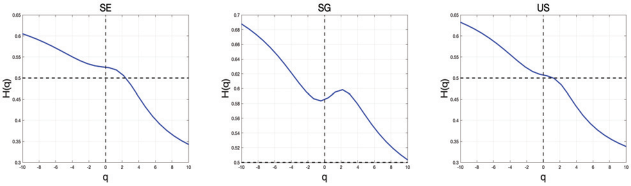

(**u**) Sweden (**v**) Singapore (**w**) United States

Figure 7. Generalized Hurst exponents $h(q)$ of the index return in developed countries.

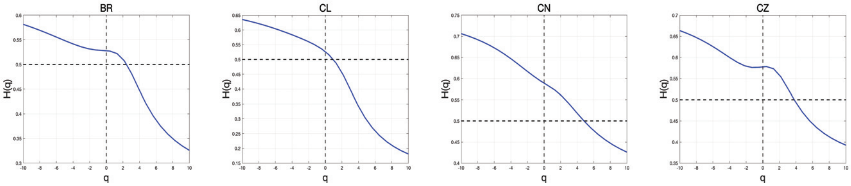

(**a**) Brazil (**b**) Chile (**c**) China (**d**) Czech Republic

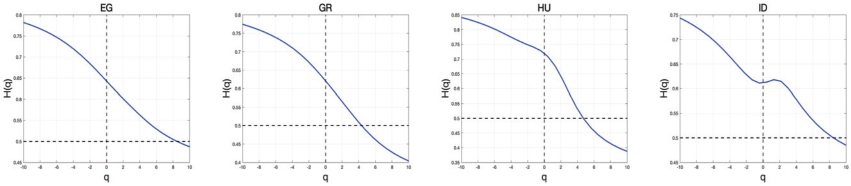

(**e**) Egypt (**f**) Greece (**g**) Hungary (**h**) Indonesia

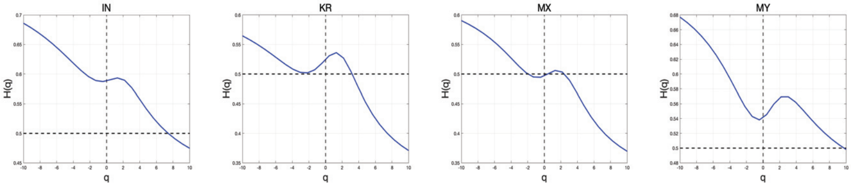

(**i**) India (**j**) Korea (**k**) Mexico (**l**) Malaysia

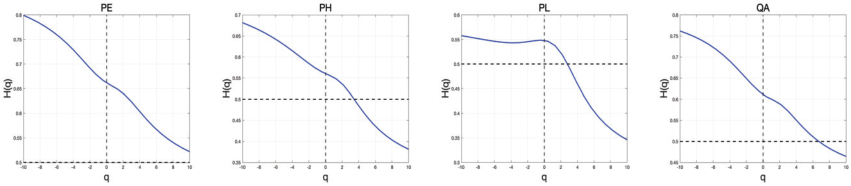

(**m**) Peru (**n**) Philippines (**o**) Poland (**p**) Qatar

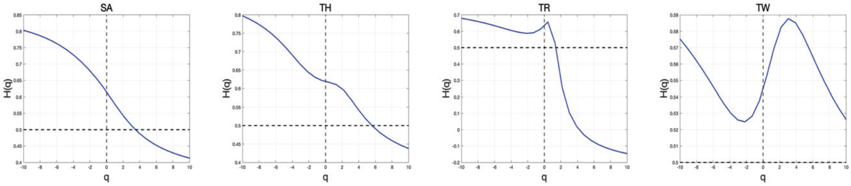

(**q**) Saudi Arabia (**r**) Thailand (**s**) Turkey (**t**) Taiwan

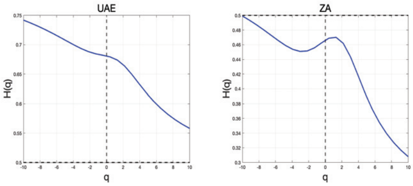

(**u**) United Arab Emirates (**v**) South Africa

Figure 8. Generalized Hurst exponents $h(q)$ of the index return in emerging countries.

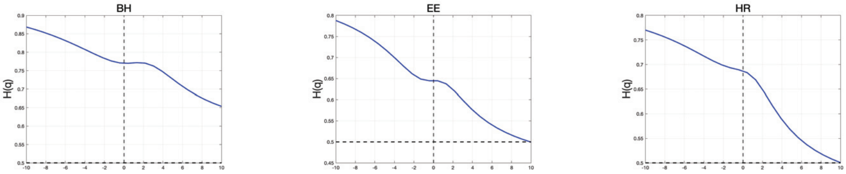

(**a**) Bahrain (**b**) Estonia (**c**) Croatia

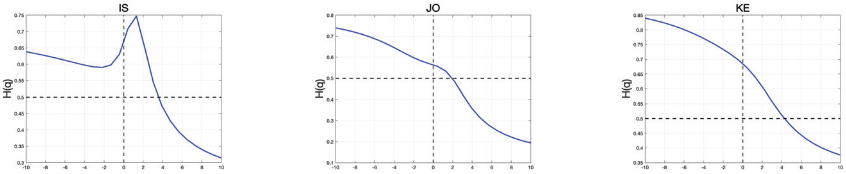

(**d**) Iceland (**e**) Jordan (**f**) Kenya

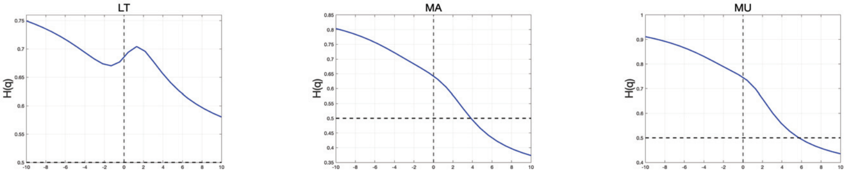

(**g**) Lithuania (**h**) Morocco (**i**) Mauritius

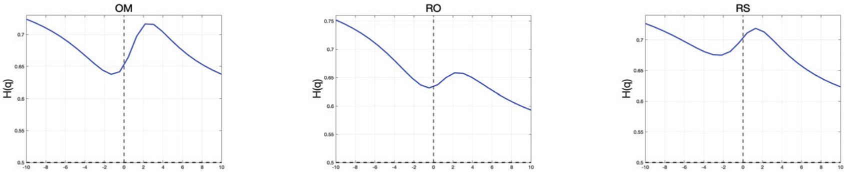

(**j**) Oman (**k**) Romania (**l**) Serbia

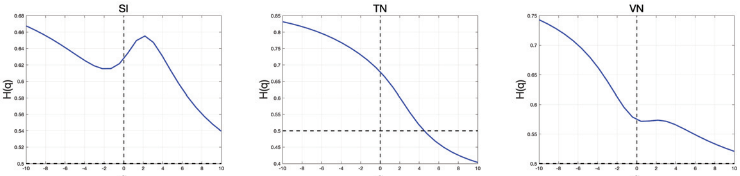

(**m**) Slovenia (**n**) Tunisia (**o**) Vietnam

Figure 9. Generalized Hurst exponents $h(q)$ of the index return in frontier countries.

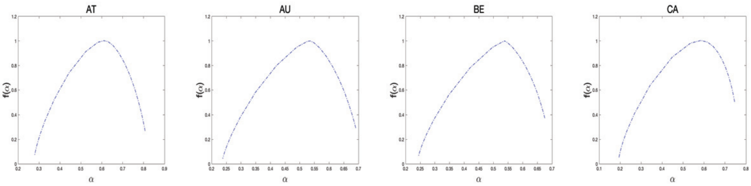

(**a**) Austria (**b**) Australia (**c**) Belgium (**d**) Canada

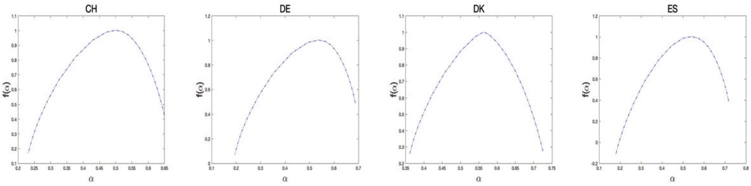

(**e**) Switzerland (**f**) Germany (**g**) Denmark (**h**) Spain

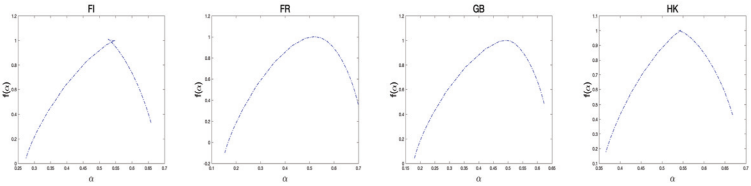

(**i**) Finland (**j**) France (**k**) United Kingdom (**l**) Hong Kong

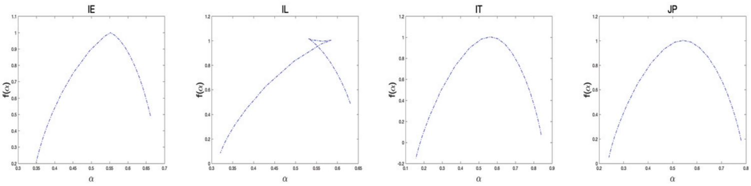

(**m**) Ireland (**n**) Israel (**o**) Italy (**p**) Japan

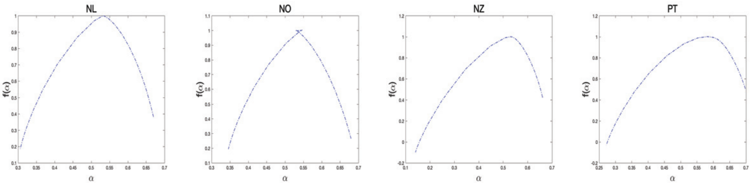

(**q**) Netherlands (**r**) Norway (**s**) New Zealand (**t**) Portugal

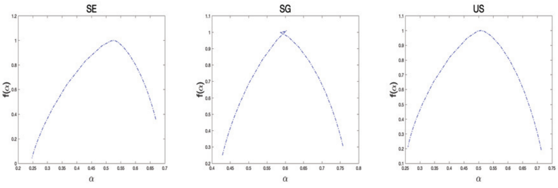

(**u**) Sweden (**v**) Singapore (**w**) United States

Figure 10. The multifractal spectra of each index return in developed countries.

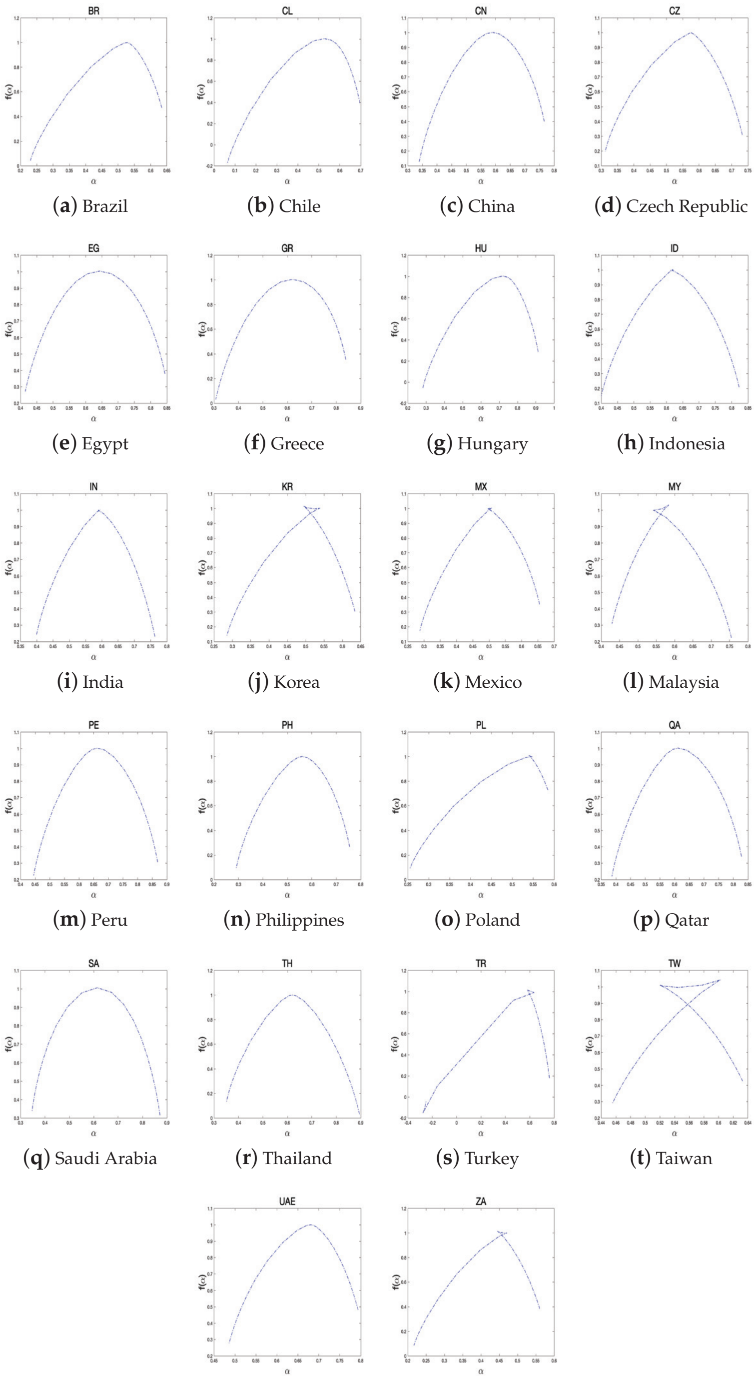

(**a**) Brazil (**b**) Chile (**c**) China (**d**) Czech Republic

(**e**) Egypt (**f**) Greece (**g**) Hungary (**h**) Indonesia

(**i**) India (**j**) Korea (**k**) Mexico (**l**) Malaysia

(**m**) Peru (**n**) Philippines (**o**) Poland (**p**) Qatar

(**q**) Saudi Arabia (**r**) Thailand (**s**) Turkey (**t**) Taiwan

(**u**) United Arab Emirates (**v**) South Africa

Figure 11. The multifractal spectra of each index return in emerging countries.

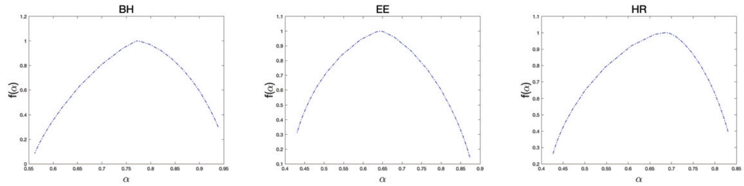

(**a**) Bahrain (**b**) Estonia (**c**) Croatia

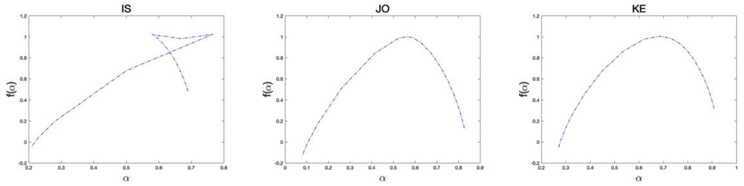

(**d**) Iceland (**e**) Jordan (**f**) Kenya

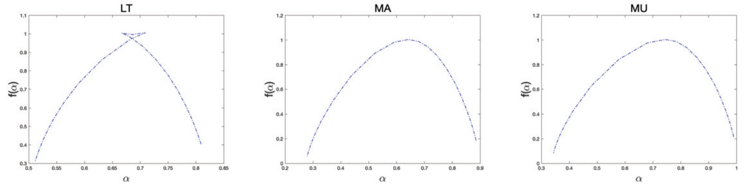

(**g**) Lithuania (**h**) Morocco (**i**) Mauritius

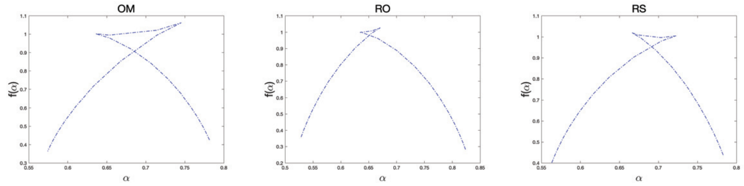

(**j**) Oman (**k**) Romania (**l**) Serbia

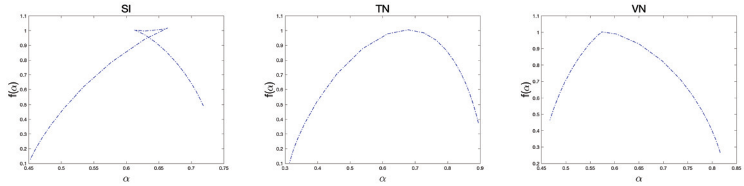

(**m**) Slovenia (**n**) Tunisia (**o**) Vietnam

Figure 12. The multifractal spectra of each index return in frontier countries.

Since the static analysis does not reflect changes in the market efficiency of a stock market over time, we investigate the dynamics of market efficiency using the rolling window analysis in the following section.

Table 2. The width of the multifractal spectrum $\Delta\alpha$ for the developed, emerging, and frontier groups.

Developed		**Emerging**		**Frontier**	
Country	**$\Delta\alpha$**	**Country**	**$\Delta\alpha$**	**Country**	**$\Delta\alpha$**
Austria	0.5278	Brazil	0.404	Bahrain	0.3762
Australia	0.4531	Chile	0.6333	Estoina	0.4434
Belgium	0.4315	China	0.4274	Croatia	0.4039
Canada	0.5514	Czech Republic	0.4204	Iceland	0.5567
Switzerland	0.4183	Egypt	0.4296	Jordan	0.7454
Germany	0.4921	Greece	0.5321	Kenya	0.6379
Denmark	0.3635	Hungary	0.6306	Lithuania	0.2978
Spain	0.5384	Indonesia	0.4228	Morocco	0.6059
Finland	0.3852	India	0.3645	Mauritius	0.6464
France	0.5453	Korea	0.3497	Oman	0.2073
United Kingdom	0.443	Mexico	0.3681	Romania	0.2951
Hong Kong	0.3024	Malaysia	0.3257	Serbia	0.2197
Ireland	0.3125	Peru	0.4241	Slovenia	0.2665
Israel	0.3101	Philippines	0.4638	Tunisia	0.5804
Italy	0.684	Poland	0.3303	Vietnam	0.3494
Japan	0.5402	Qatar	0.4415		
Netherlands	0.3639	Saudi Arabia	0.5248		
Norway	0.3343	Thailand	0.5434		
New Zealand	0.5209	Turkey	1.0386		
Portugal	0.4261	Taiwan	0.1773		
Sweden	0.4222	United Arab Emirates	0.3078		
Singapore	0.3291	South Africa	0.3442		
United States	0.4544				

5.2. Rolling Window Analysis

In this section, we provide the dynamics of $\Delta\alpha$ for each stock-index return using rolling window analysis. This approach has been used in several studies on MF-DFA methods (Wang et al. [39], Sensoy and Tabak [40], Gajardo and Kristjanpoller [41], and Aloui et al. [42]). In this study, we chose a window length of 400 days to include the GFC period in our calculation and avoid severe fluctuations. In particular, we test the robustness of our spillover analysis results by comparing different rolling window sizes (300, 400, and 500 days). Figures A1–A3 display the $\Delta\alpha$ time series for each rolling window length. In the subfigure, the $\Delta\alpha$ shows a similar fluctuation pattern under each variation of rolling window length. Therefore, our choice of widow size is reasonable for our investigation.

Figures 13–15 illustrate the dynamics of $\Delta\alpha$ for the three groups. We summarize the key features by developed, emerging, and frontier groups as follows.

The fluctuations in the efficiencies of developed markets differ from country to country; however, they generally exhibit similar patterns. The key characteristics of these markets can be summarized as follows:

First, developed markets are highly sensitive to global issues. The dynamics of market efficiency often change rapidly, as observed during significant events such as the 2008 global financial crisis and the 2020 COVID-19 pandemic. The United States, with its large stock market and diverse range of market participants, is particularly susceptible to various issues. Notable changes in market efficiency were observed during events such as the 2010 European fiscal crisis and the 2018 US–China trade dispute. The United Kingdom, on the other hand, is influenced by changes in the energy industry and the financial sector (“15 February: Energy Firms Furthermore, Banks Lead Buoyant Market”, Forbes; “UK stocks close higher following Truss energy plan”, “Miners and energy stocks help FTSE 100 end volatile week higher”, Reuters).

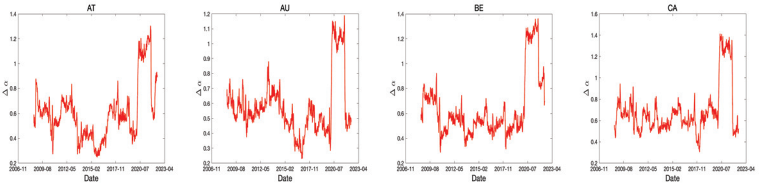

(a) Austria **(b)** Australia **(c)** Belgium **(d)** Canada

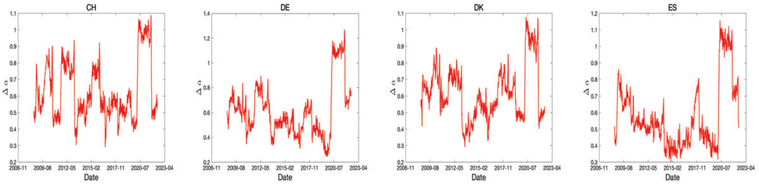

(e) Switzerland **(f)** Germany **(g)** Denmark **(h)** Spain

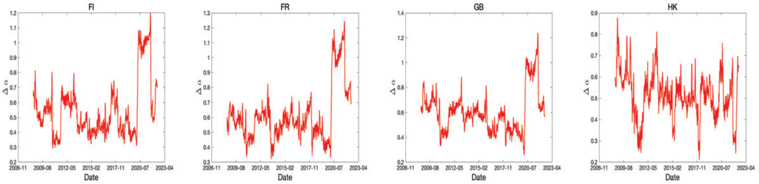

(i) Finland **(j)** France **(k)** United Kingdom **(l)** Hong Kong

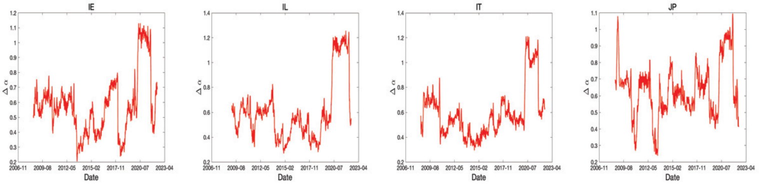

(m) Ireland **(n)** Israel **(o)** Italy **(p)** Japan

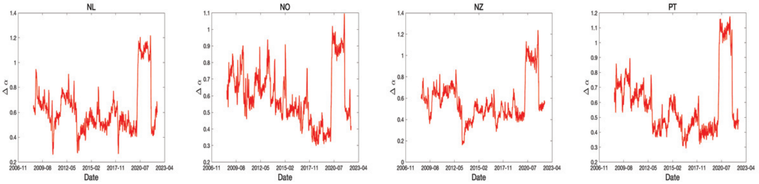

(q) Netherlands **(r)** Norway **(s)** New Zealand **(t)** Portugal

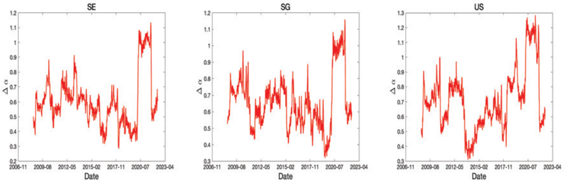

(u) Sweden **(v)** Singapore **(w)** United States

Figure 13. The dynamics of $\Delta\alpha$ using a rolling window for developed countries. The window length is 400 days.

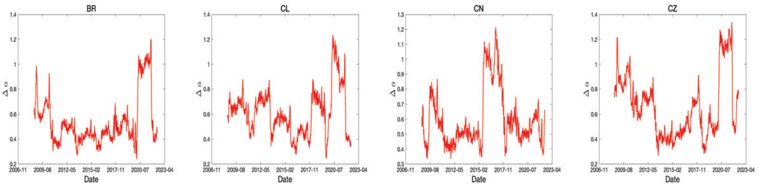

(**a**) Brazil (**b**) Chile (**c**) China (**d**) Czech Republic

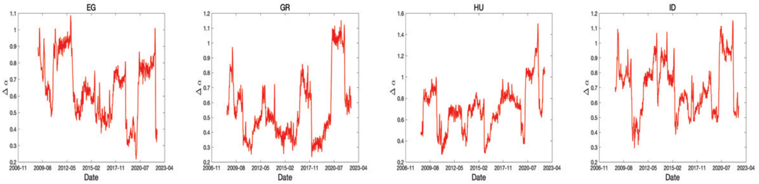

(**e**) Egypt (**f**) Greece (**g**) Hungary (**h**) Indonesia

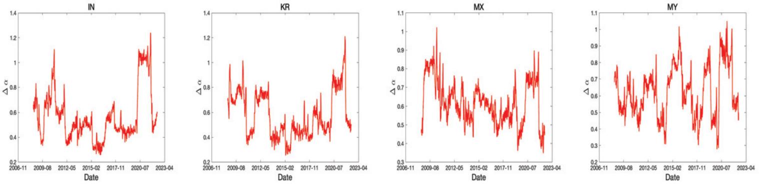

(**i**) India (**j**) Korea (**k**) Mexico (**l**) Malaysia

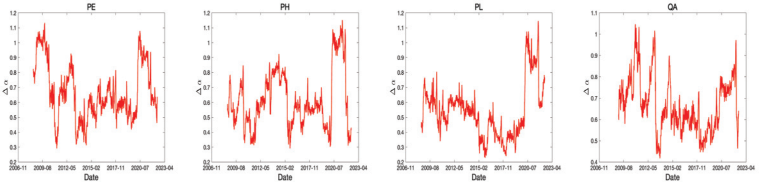

(**m**) Peru (**n**) Philippines (**o**) Poland (**p**) Qatar

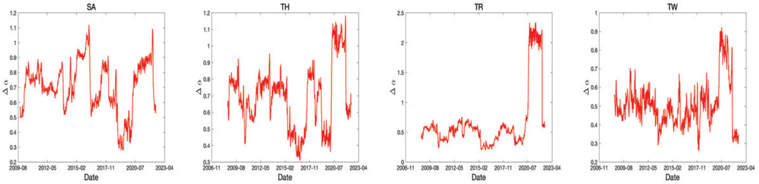

(**q**) Saudi Arabia (**r**) Thailand (**s**) Turkey (**t**) Taiwan

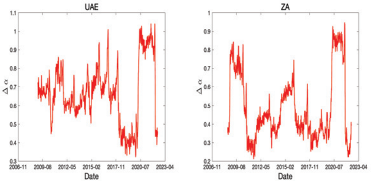

(**u**) United Arab Emirates (**v**) South Africa

Figure 14. The dynamics of $\Delta\alpha$ using a rolling window for emerging countries. The window length is 400 days.

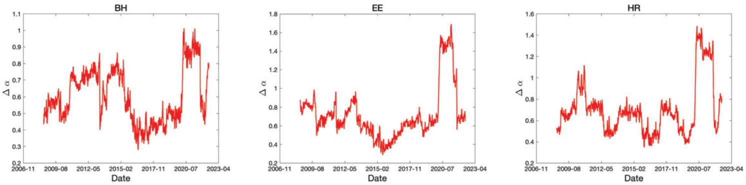

(**a**) Bahrain (**b**) Estonia (**c**) Croatia

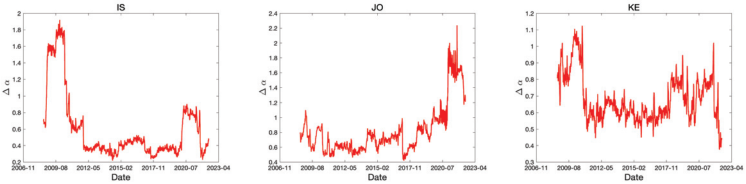

(**d**) Iceland (**e**) Jordan (**f**) Kenya

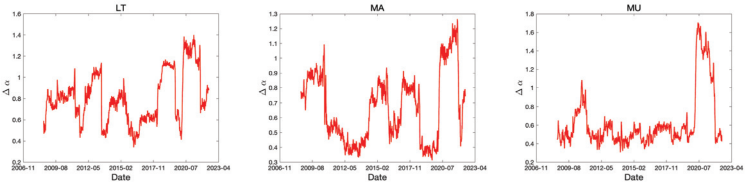

(**g**) Lithuania (**h**) Morocco (**i**) Mauritius

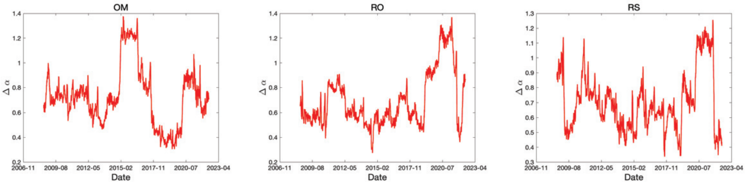

(**j**) Oman (**k**) Romania (**l**) Serbia

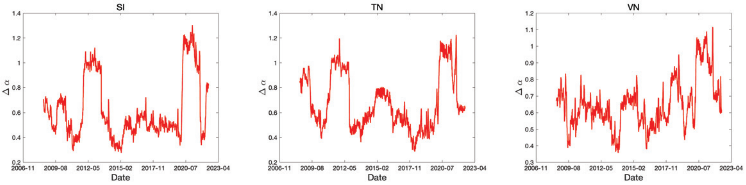

(**m**) Slovenia (**n**) Tunisia (**o**) Vietnam

Figure 15. The dynamics of $\Delta\alpha$ using a rolling window for frontier countries. The window length is 400 days.

Second, each developed country has its own unique factors that strongly influence its stock market dynamics. For instance, Japan is greatly affected by exchange rate and interest rate fluctuations due to its economic policy, as demonstrated during the 2013 Abenomics (Fukuda [43]) and the 2016 Negative Interest Rate and Yield Curve Control initiatives (Kawamoto et al. [44]).

Third, similar dynamics can be observed based on trade relations between countries, governance, and institutions. For example, countries within the North American Free Trade Agreement (NAFTA) such as Canada and the United States exhibit comparable patterns. Similarly, European countries within the EU share certain dynamics, and countries like

England, Australia, and New Zealand, belonging to the Commonwealth of Nations, may display similar market behavior. Emerging markets exhibit similar trends to developed markets, but the dynamics of market efficiency within individual countries in this group show significant variations. Several factors contribute to these variations:

First, financial policies play a crucial role in shaping market efficiency dynamics. China, for example, has strict trading regulations and limited foreign investment, resulting in relatively low fluctuations in market dynamics during events such as the COVID-19 pandemic. Previous studies have also highlighted these observations (Hu et al. [45], Petry [46]). Similarly, in Egypt, stock returns are significantly influenced by EGP/USD exchange rates, which are impacted by various exchange rate systems (Ahmed [47]).

Second, compared to developed markets, emerging markets are more influenced by foreign capital. For instance, South Korea tends to follow foreign investment trends (Kim and Jo [48]), which greatly affect corporate dividend policies to attract foreign institutional investors (Kang et al. [49]). In Taiwan, stocks with high foreign ownership outperform those with low foreign ownership (Huang and Shiu [50]). In India, there is a positive relationship between foreign direct investment, foreign institutional investment, and stock market indices (Nagpal [51]).

Third, geopolitical and political risks are prevalent in this group. The risk of war exists in several regions, including South Korea, North Korea, Taiwan, and China. Conflicts also frequently occur in the Middle East and South America. Furthermore, significant fluctuations in market dynamics were observed during events such as the 2011 Egyptian Revolution and the 2013 military coup in Egypt.

Frontier markets often exhibit unique characteristics compared to developed and emerging markets, making it challenging to identify similar dynamics within the group. These distinctions arise due to the following factors:

First, frontier markets tend to experience significant impacts from crises, resulting in high levels of risk compared to other markets. Although it is difficult to pinpoint specific periods of rapid fluctuations beyond the 2008 financial crisis and the 2020 COVID-19 pandemic, it is worth noting that Iceland was greatly affected by the crisis (Reuters, "Iceland's biggest taken over and all shares halted").

Second, frontier markets are heavily influenced by specific industrial and regional issues. The key factors that affect their stock markets and subsequent dynamic fluctuations vary widely, largely due to their reliance on domestic markets. (Meziani [52]).

6. Discussion and Concluding Remarks

We investigated the market efficiency of each stock market using global stock market index data. To this end, we used the MF-DFA methodology and conducted static and rolling window analyses. We analyzed the results by categorizing them under developed, emerging, and frontier groups.

According to the static analysis results, Switzerland, the UK, and the US, known as financially advanced countries, have more efficient stock markets than other countries. Based on the several previous studies (Lim and Brooks [53], Ali et al. [5], and Bouoiyour et al. [54]), it has been observed that stock markets in developed countries demonstrate a higher degree of efficiency when compared to their emerging counterparts. This efficiency gap can be attributed to the incomplete nature of financial systems in emerging economies (Mookerjee and Yu [55], Islam et al. [56]), in contrast to the more advanced counterparts. On the other hand, advanced countries have relatively efficient stock markets, which can be explained by factors such as robust economic growth rates, larger market sizes, and the presence of open financial markets (Zunino et al. [57], Tongurai and Vithessonthi [58]). In order to minimize the disparity in stock market efficiency between developed and emerging countries, scholars have put forth proposals for laws pertaining to foreign investment, financial liberalization, and de-politicization (Vo [59], Rejeb and Boughrara [60], Goodell et al. [61]).

The notable findings of the rolling window analysis are as follows: First, markets cannot be insulated from global issues such as the 2008 financial crisis and the COVID-19 pandemic. These issues dominate, particularly in the developed country group, including the United States and the United Kingdom. Asian countries in this group, such as Japan, are impacted differently due to their strong domestic markets. Similar dynamics are also found in countries that are part of international trade blocs, such as NAFTA, the EU, and the Commonwealth. Second, emerging markets are vulnerable to foreign capital movement, and financial policies related to foreign investment heavily influence them. This is evident in the cases of China and Egypt, for example. Emerging markets also tend to follow foreign investment trends, as observed in South Korea, Taiwan, and India. Additionally, geopolitical risk is a critical issue, including the risk of war in South Korea, North Korea, Taiwan, and China, as well as frequent conflicts in the Middle East, South America, and Egypt. Third, distinguishing similar dynamics within the frontier group is difficult due to the varying intensive domestic market issues. Some frontier markets have been significantly affected by global issues, as was the case in Iceland during the 2008 financial crisis. Therefore, investment in frontier group markets should be approached with careful consideration compared to the other groups.

These findings have important implications for international investors and policymakers. First, international investors can establish investment strategies based on the degree of efficiency of individual stock markets. In other words, data on long-term memory and the degree of persistence over time can be utilized by global investors to gain an edge in the market and achieve above-average returns. However, the efficient nature of stock markets implies that consistently outperforming it through individual stock selection or timing is challenging. Therefore, investors may opt for a passive investment approach, such as investing in index funds that strive to match the market's performance. Second, while the efficient market hypothesis assumes that the market is self-regulating and does not require government intervention, discovering market inefficiencies may require more regulations to safeguard investors and preserve market stability. Consequently, policymakers in countries with significant variations in market efficiency should consider implementing new regulations to enhance market efficiency.

As an additional research topic, we propose to analyze the market efficiency of the three groups of countries from a behavioral finance perspective. The efficient market hypothesis assumes that all investors have access to the same information and make rational decisions based on this information. However, behavioral finance research has shown that investors often make irrational decisions based on emotions, biases, and heuristics. Therefore, the proposed research can help inform our understanding of how individual markets function and investors make decisions. Furthermore, we suggest employing clustering analysis for $\Delta\alpha$ time series data. This approach can help identify distinct patterns in $\Delta\alpha$ movements within each country or confirm the similarity of these patterns through cluster analysis. By conducting such future studies, we can enhance the robustness of our findings and gain further insights from this research.

Author Contributions: Conceptualization, S.-Y.C.; methodology, S.-Y.C.; software, S.-Y.C.; formal analysis, M.-J.L. and S.-Y.C.; investigation, M.-J.L. and S.-Y.C.; writing—original draft, M.-J.L. and S.-Y.C.; writing—review and editing, M.-J.L. and S.-Y.C.; funding acquisition S.-Y. All authors have read and agreed to the published version of the manuscript.

Funding: The work of S.-Y. Choi was supported by the National Research Foundation of Korea (NRF) grant funded by the Korean government (MSIT) (No. 2021R1F1A1046138).

Data Availability Statement: The data that support the findings of this study are available from the corresponding author upon reasonable request.

Acknowledgments: We thank the anonymous reviewers; their comments and suggestions helped improve and refine this manuscript.

Conflicts of Interest: The authors declare no conflicts of interest.

Appendix A

Table A1. The stock index for each country.

Developed		Emerging		Frontier	
Country	**Index**	**Country**	**Index**	**Country**	**Index**
Austria	Austrian Traded Index	Brazil	IBOVESPA	Bahrain	Bahrain BHSEASI
Australia	S&P/ASX 200	Chile	S&P/CLX	Estoina	Tallinn SE General
Belgium	BEL 20	China	CSI 300	Croatia	CROBEX
Canda	S&P/TSX	Czech Republic	PX	Iceland	OMX Iceland All-Share
Switzerland	SMI	Egypt	EGX 30	Jordan	MSCI JORDAN US
Germany	DAX	Greece	FTSE Athex Large Cap	Kenya	Kenya NSE 20
Denmark	OMX Copenhagen 25	Hungary	BUMIX	Lituania	Vilnius SE General
Spain	IBEX 35	Indonesia	IDX	Morocco	Morocco MASI
Finland	OMX Helsinki 25	India	NIFTY 50	Mauritius	Semdex
France	CAC 40	Korea	KOSPI	Oman	Oman MSM
United Kingdom	UK 100	Mexico	S&P/BMV IPC	Romania	BET
Hong Kong	Hang Senng	Malaysia	KLCI	Serbia	Belex 15
Ireland	ISEQ 20	Peru	S&P Lima General	Slovenia	SLOVENIAN BLUE CHIP
Israel	TA 125	Philippines	PSEi	Tunisia	Tunindex
Italy	Italy 40	Poland	WIG 20	Vietnam	VNI
Japan	Nikkei 225	Qatar	QE General		
Netherlands	AEX	Saudi Arabia	Tadawul All Share		
Norway	OBX Price	Thailand	SET		
New Zealand	S&P/NZX 50	Turkey	BIST 100		
Portugal	PSI	Taiwan	TSEC Taiwan 50		
Sweden	OMX Stockholm 30	United Arab Emirates	DFM General		
Singapore	FTSE Singapore	South Africa	iShares MSCI South Africa		
United States	S&P 500				

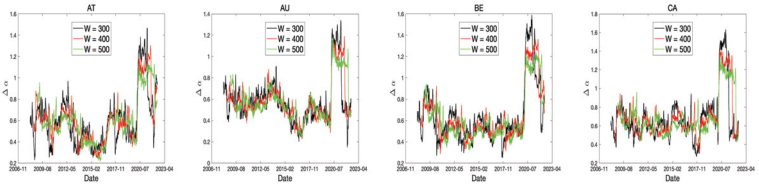

(**a**) Austria (**b**) Australia (**c**) Belgium (**d**) Canada

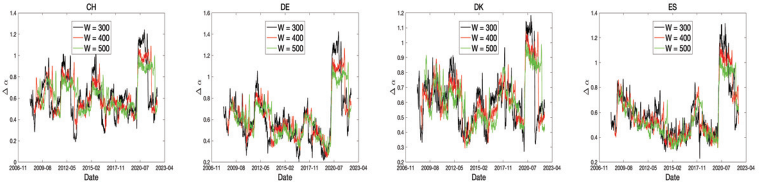

(**e**) Switzerland (**f**) Germany (**g**) Denmark (**h**) Spain

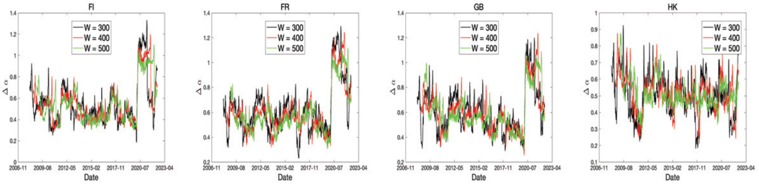

(**i**) Finland (**j**) France (**k**) United Kingdom (**l**) Hong Kong

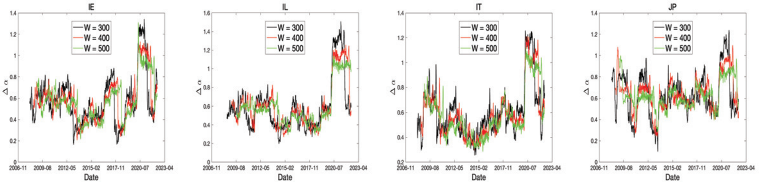

(**m**) Ireland (**n**) Israel (**o**) Italy (**p**) Japan

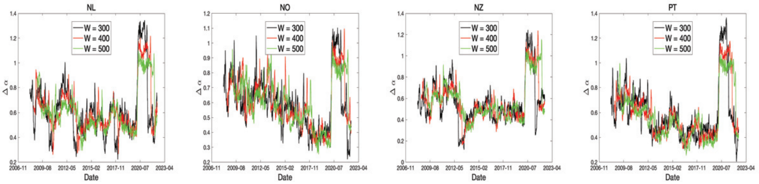

(**q**) Netherlands (**r**)Norway (**s**) New Zealand (**t**) Portugal

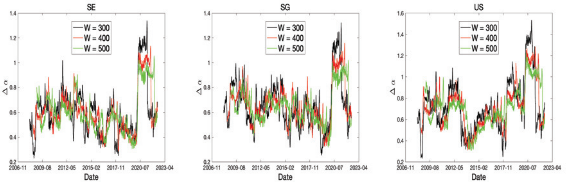

(**u**) Sweden (**v**) Singapore (**w**) United States

Figure A1. The dynamics of $\Delta\alpha$ using a rolling window for developed countries with the window length (300, 400, 500 days).

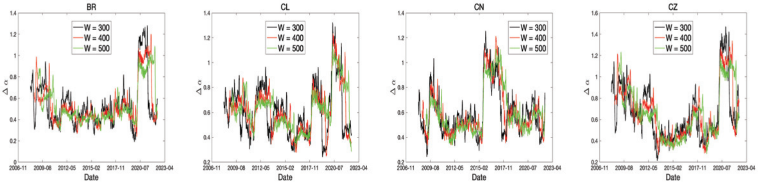

(**a**) Brazil (**b**) Chile (**c**) China (**d**) Czech Republic

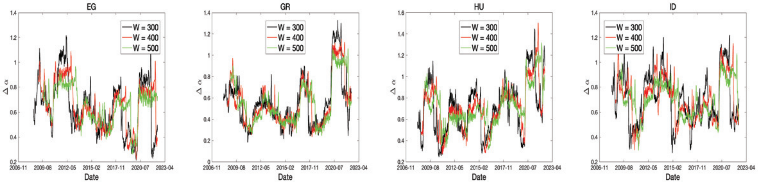

(**e**) Egypt (**f**) Greece (**g**) Hungary (**h**) Indonesia

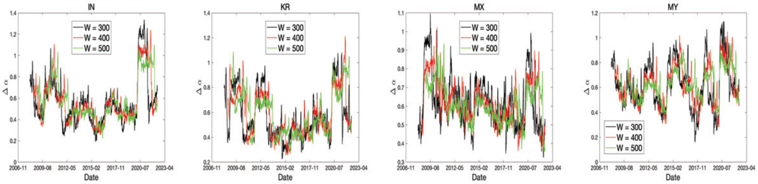

(**i**) India (**j**) Korea (**k**) Mexico (**l**) Malaysia

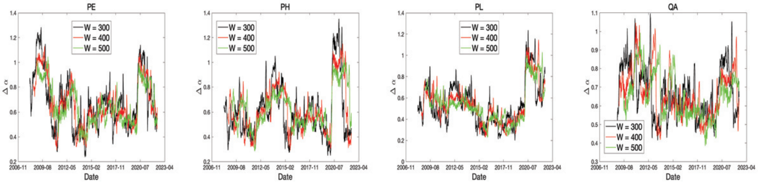

(**m**) Peru (**n**) Philippines (**o**) Poland (**p**) Qatar

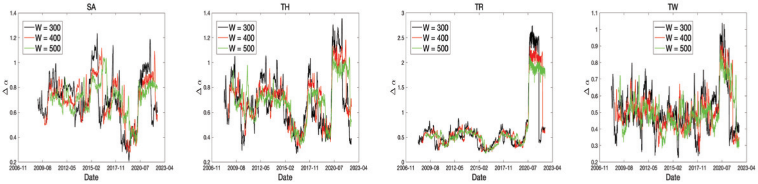

(**q**) Saudi Arabia (**r**) Thailand (**s**) Turkey (**t**) Taiwan

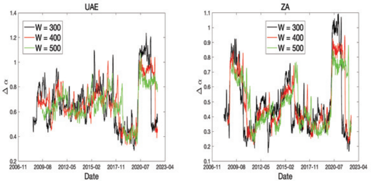

(**u**) United Arab Emirates (**v**) South Africa

Figure A2. The dynamics of $\Delta\alpha$ using a rolling window for emerging countries with the window length (300, 400, 500 days).

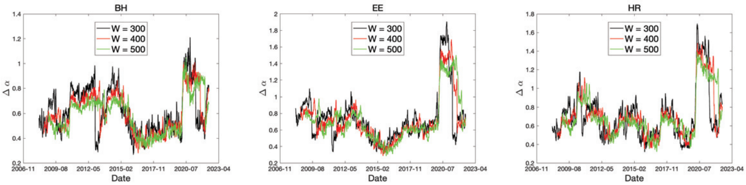

(**a**) Bahrain (**b**) Estonia (**c**) Croatia

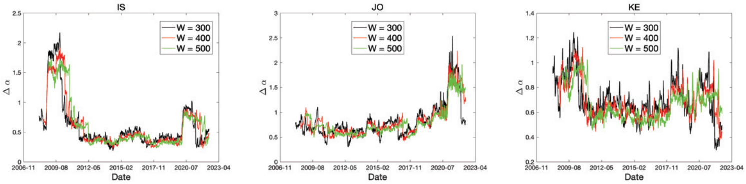

(**d**) Iceland (**e**) Jordan (**f**) Kenya

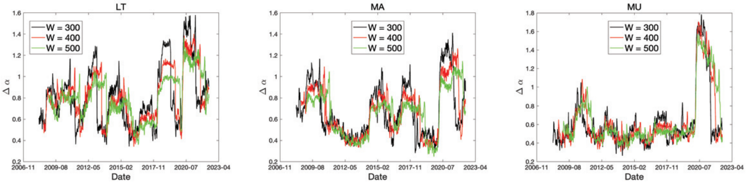

(**g**) Lithuania (**h**) Morocco (**i**) Mauritius

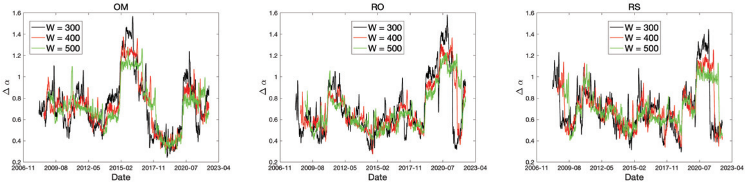

(**j**) Oman (**k**) Romania (**l**) Serbia

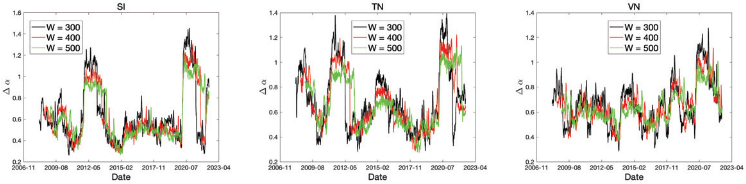

(**m**) Slovenia (**n**) Tunisia (**o**) Vietnam

Figure A3. The dynamics of $\Delta\alpha$ using a rolling window for frontier countries with the window length (300, 400, 500 days).

References

1. Horta, P.; Lagoa, S.; Martins, L. The impact of the 2008 and 2010 financial crises on the Hurst exponents of international stock markets: Implications for efficiency and contagion. *Int. Rev. Financ. Anal.* **2014**, *35*, 140–153. [CrossRef]
2. Hull, M.; McGroarty, F. Do emerging markets become more efficient as they develop? Long memory persistence in equity indices. *Emerg. Mark. Rev.* **2014**, *18*, 45–61. [CrossRef]
3. Rizvi, S.A.R.; Dewandaru, G.; Bacha, O.I.; Masih, M. An analysis of stock market efficiency: Developed vs. Islamic stock markets using MF-DFA. *Phys. A Stat. Mech. Its Appl.* **2014**, *407*, 86–99. [CrossRef]
4. Charfeddine, L.; Khediri, K.B. Time varying market efficiency of the GCC stock markets. *Phys. A Stat. Mech. Its Appl.* **2016**, *444*, 487–504. [CrossRef]

5. Ali, S.; Shahzad, S.J.H.; Raza, N.; Al-Yahyaee, K.H. Stock market efficiency: A comparative analysis of Islamic and conventional stock markets. *Phys. A Stat. Mech. Its Appl.* **2018**, *503*, 139–153. [CrossRef]
6. Miloş, L.R.; Haţiegan, C.; Miloş, M.C.; Barna, F.M.; Boțoc, C. Multifractal detrended fluctuation analysis (MF-DFA) of stock market indexes. Empirical evidence from seven central and eastern European markets. *Sustainability* **2020**, *12*, 535. [CrossRef]
7. Choi, S.Y. Analysis of stock market efficiency during crisis periods in the US stock market: Differences between the global financial crisis and COVID-19 pandemic. *Phys. A Stat. Mech. Its Appl.* **2021**, *574*, 125988. [CrossRef]
8. Yin, T.; Wang, Y. Market efficiency and nonlinear analysis of soybean futures. *Sustainability* **2021**, *13*, 518. [CrossRef]
9. Pak, D.; Choi, S.Y. Economic Policy Uncertainty and Sectoral Trading Volume in the US Stock Market: Evidence from the COVID-19 Crisis. *Complexity* **2022**, *2022*, 2248731 . [CrossRef]
10. Gaio, L.E.; Stefanelli, N.O.; Júnior, T.P.; Bonacim, C.A.G.; Gatsios, R.C. The impact of the Russia-Ukraine conflict on market efficiency: Evidence for the developed stock market. *Financ. Res. Lett.* **2022**, *50*, 103302. [CrossRef]
11. Caraiani, P. Evidence of multifractality from emerging European stock markets. *PLoS ONE* **2012**, *7*, e40693. [CrossRef] [PubMed]
12. Arshad, S.; Rizvi, S.A.R.; Ghani, G.M.; Duasa, J. Investigating stock market efficiency: A look at OIC member countries. *Res. Int. Bus. Financ.* **2016**, *36*, 402–413. [CrossRef]
13. Aslam, F.; Ferreira, P.; Mohti, W. Investigating efficiency of frontier stock markets using multifractal detrended fluctuation analysis. *Int. J. Emerg. Mark.* 2021, *ahead of print*.
14. Nargunam, R.; Lahiri, A. Persistence in daily returns of stocks with highest market capitalization in the Indian market. *Digit. Financ.* **2022**, *4*, 341–374. [CrossRef]
15. Lee, M.; Song, J.W.; Kim, S.; Chang, W. Asymmetric market efficiency using the index-based asymmetric-MFDFA. *Phys. A Stat. Mech. Its Appl.* **2018**, *512*, 1278–1294. [CrossRef]
16. Aslam, F.; Latif, S.; Ferreira, P. Investigating long-range dependence of emerging Asian stock markets using multifractal detrended fluctuation analysis. *Symmetry* **2020**, *12*, 1157. [CrossRef]
17. Aslam, F.; Ferreira, P.; Ali, H.; Kauser, S. Herding behavior during the COVID-19 pandemic: A comparison between Asian and European stock markets based on intraday multifractality. *Eurasian Econ. Rev.* **2021**, *12*, 333–359. [CrossRef]
18. Mensi, W.; Yousaf, I.; Vo, X.V.; Kang, S.H. Multifractality during upside/downside trends in the MENA stock markets: The effects of the global financial crisis, oil crash and COVID-19 pandemic. *Int. J. Emerg. Mark.* 2022, *ahead of print*.
19. Saâdaoui, F. Skewed multifractal scaling of stock markets during the COVID-19 pandemic. *Chaos Solitons Fractals* **2023**, *170*, 113372. [CrossRef]
20. Lim, K.P. Ranking market efficiency for stock markets: A nonlinear perspective. *Phys. A Stat. Mech. Its Appl.* **2007**, *376*, 445–454. [CrossRef]
21. Anagnostidis, P.; Varsakelis, C.; Emmanouilides, C.J. Has the 2008 financial crisis affected stock market efficiency? The case of Eurozone. *Phys. A Stat. Mech. Its Appl.* **2016**, *447*, 116–128. [CrossRef]
22. Rizvi, S.A.R.; Arshad, S. Investigating the efficiency of East Asian stock markets through booms and busts. *Pac. Sci. Rev.* **2014**, *16*, 275–279. [CrossRef]
23. Smith, G. The changing and relative efficiency of European emerging stock markets. *Eur. J. Financ.* **2012**, *18*, 689–708. [CrossRef]
24. Sensoy, A. Generalized Hurst exponent approach to efficiency in MENA markets. *Phys. A Stat. Mech. Its Appl.* **2013**, *392*, 5019–5026. [CrossRef]
25. Kantelhardt, J.W.; Zschiegner, S.A.; Koscielny-Bunde, E.; Havlin, S.; Bunde, A.; Stanley, H.E. Multifractal detrended fluctuation analysis of nonstationary time series. *Phys. A Stat. Mech. Its Appl.* **2002**, *316*, 87–114. [CrossRef]
26. Wang, F.; Ye, X.; Wu, C. Multifractal characteristics analysis of crude oil futures prices fluctuation in China. *Phys. A Stat. Mech. Its Appl.* **2019**, *533*, 122021. [CrossRef]
27. Jiang, Z.Q.; Chen, W.; Zhou, W.X. Detrended fluctuation analysis of intertrade durations. *Phys. A Stat. Mech. Its Appl.* **2009**, *388*, 433–440. [CrossRef]
28. Qian, X.Y.; Gu, G.F.; Zhou, W.X. Modified detrended fluctuation analysis based on empirical mode decomposition for the characterization of anti-persistent processes. *Phys. A Stat. Mech. Its Appl.* **2011**, *390*, 4388–4395. [CrossRef]
29. Han, C.; Wang, Y.; Xu, Y. Efficiency and multifractality analysis of the Chinese stock market: Evidence from stock indices before and after the 2015 stock market crash. *Sustainability* **2019**, *11*, 1699. [CrossRef]
30. Lashermes, B.; Abry, P.; Chainais, P. New insights into the estimation of scaling exponents. *Int. J. Wavelets Multiresolut. Inf. Process.* **2004**, *2*, 497–523. [CrossRef]
31. Ning, Y.; Wang, Y.; Su, C.w. How did China's foreign exchange reform affect the efficiency of foreign exchange market? *Phys. A Stat. Mech. Its Appl.* **2017**, *483*, 219–226. [CrossRef]
32. Calvet, L.; Fisher, A. Multifractality in asset returns: Theory and evidence. *Rev. Econ. Stat.* **2002**, *84*, 381–406. [CrossRef]
33. Alvarez-Ramirez, J.; Cisneros, M.; Ibarra-Valdez, C.; Soriano, A. Multifractal Hurst analysis of crude oil prices. *Phys. A Stat. Mech. Its Appl.* **2002**, *313*, 651–670. [CrossRef]
34. Wang, Y.; Wu, C.; Pan, Z. Multifractal detrending moving average analysis on the US Dollar exchange rates. *Phys. A Stat. Mech. Its Appl.* **2011**, *390*, 3512–3523. [CrossRef]
35. da Silva Filho, A.C.; Maganini, N.D.; de Almeida, E.F. Multifractal analysis of Bitcoin market. *Phys. A Stat. Mech. Its Appl.* **2018**, *512*, 954–967. [CrossRef]

36. Ruan, Q.; Zhang, S.; Lv, D.; Lu, X. Financial liberalization and stock market cross-correlation: MF-DCCA analysis based on Shanghai-Hong Kong Stock Connect. *Phys. A Stat. Mech. Its Appl.* **2018**, *491*, 779–791. [CrossRef]
37. Zhou, W.; Dang, Y.; Gu, R. Efficiency and multifractality analysis of CSI 300 based on multifractal detrending moving average algorithm. *Phys. A Stat. Mech. Its Appl.* **2013**, *392*, 1429–1438. [CrossRef]
38. Gao, X.L.; Shao, Y.H.; Yang, Y.H.; Zhou, W.X. Do the global grain spot markets exhibit multifractal nature? *Chaos Solitons Fractals* **2022**, *164*, 112663. [CrossRef]
39. Wang, Y.; Wei, Y.; Wu, C. Analysis of the efficiency and multifractality of gold markets based on multifractal detrended fluctuation analysis. *Phys. A Stat. Mech. Its Appl.* **2011**, *390*, 817–827. [CrossRef]
40. Sensoy, A.; Tabak, B.M. Time-varying long term memory in the European Union stock markets. *Phys. A Stat. Mech. Its Appl.* **2015**, *436*, 147–158. [CrossRef]
41. Gajardo, G.; Kristjanpoller, W. Asymmetric multifractal cross-correlations and time varying features between Latin-American stock market indices and crude oil market. *Chaos Solitons Fractals* **2017**, *104*, 121–128. [CrossRef]
42. Aloui, C.; Shahzad, S.J.H.; Jammazi, R. Dynamic efficiency of European credit sectors: A rolling-window multifractal detrended fluctuation analysis. *Phys. A Stat. Mech. Its Appl.* **2018**, *506*, 337–349. [CrossRef]
43. Fukuda, S.i. Abenomics: Why was it so successful in changing market expectations? *J. Jpn. Int. Econ.* **2015**, *37*, 1–20. [CrossRef]
44. Kawamoto, T.; Nakazawa, T.; Kishaba, Y.; Matsumura, K.; Nakajima, J. Estimating the macroeconomic effects of Japan's expansionary monetary policy under Quantitative and Qualitative Monetary Easing during 2013–2020. *Econ. Anal. Policy* **2023**, *78*, 208-224. [CrossRef]
45. Hu, G.X.; Pan, J.; Wang, J. *Chinese Capital Market: An Empirical Overview*; NBER: Cambridge, MA, USA, 2018.
46. Petry, J. Same same, but different: Varieties of capital markets, Chinese state capitalism and the global financial order. *Compet. Change* **2021**, *25*, 605–630. [CrossRef]
47. Ahmed, W.M. Asymmetric impact of exchange rate changes on stock returns: Evidence of two de facto regimes. *Rev. Account. Financ.* **2020**, *19*, 147–173. [CrossRef]
48. Kim, Y.; Jo, G.J. The impact of foreign investors on the stock price of Korean enterprises during the global financial crisis. *Sustainability* **2019**, *11*, 1576. [CrossRef]
49. Kang, S.; Sul, W.; Kim, S. Impact of foreign institutional investors on dividend policy in Korea: A stock market perspective. *J. Financ. Manag. Anal.* **2010**, *23*, 10–26.
50. Huang, R.D.; Shiu, C.Y. Local effects of foreign ownership in an emerging financial market: Evidence from qualified foreign institutional investors in Taiwan. *Financ. Manag.* **2009**, *38*, 567–602. [CrossRef]
51. Nagpal, P. An empirical study on impact of flow of FDI & FII on Indian stock market. *SSRN* **2016**, *3*, 19–25.
52. Meziani, A.S. Frontier Markets: Understanding the Risks. *J. Beta Invest. Strateg.* **2020**, *11*, 43–56. [CrossRef]
53. Lim, K.P.; Brooks, R.D. *The Evolving and Relative Efficiencies of Stock Markets: Empirical Evidence from Rolling Bicorrelation Test Statistics*; SSRN: Rochester, NY, USA, 2006.
54. Bouoiyour, J.; Selmi, R.; Wohar, M.E. Are Islamic stock markets efficient? A multifractal detrended fluctuation analysis. *Financ. Res. Lett.* **2018**, *26*, 100–105. [CrossRef]
55. Mookerjee, R.; Yu, Q. An empirical analysis of the equity markets in China. *Rev. Financ. Econ.* **1999**, *8*, 41–60. [CrossRef]
56. Islam, S.M.; Watanapalachaikul, S.; Clark, C. Some tests of the efficiency of the emerging financial markets: An analysis of the Thai stock market. *J. Emerg. Mark. Financ.* **2007**, *6*, 291–302. [CrossRef]
57. Zunino, L.; Bariviera, A.F.; Guercio, M.B.; Martinez, L.B.; Rosso, O.A. On the efficiency of sovereign bond markets. *Phys. A Stat. Mech. Its Appl.* **2012**, *391*, 4342–4349. [CrossRef]
58. Tongurai, J.; Vithessonthi, C. Financial Openness and Financial Market Development. *J. Multinatl. Financ. Manag.* **2023**, *67*, 100782. [CrossRef]
59. Vo, X.V. Do foreign investors promote stock price efficiency in emerging markets? *Int. Rev. Financ.* **2019**, *19*, 223–235. [CrossRef]
60. Rejeb, A.B.; Boughrara, A. Financial liberalization and stock markets efficiency: New evidence from emerging economies. *Emerg. Mark. Rev.* **2013**, *17*, 186–208. [CrossRef]
61. Goodell, J.W.; Li, M.; Liu, D.; Peng, H. Depoliticization and market efficiency: Evidence from China. *Financ. Res. Lett.* **2022**, *47*, 102712. [CrossRef]

fractal and fractional

Article

Stock Index Return Volatility Forecast via Excitatory and Inhibitory Neuronal Synapse Unit with Modified MF-ADCCA

Luochao Wang and Raymond S. T. Lee *

Department of Computer Science, Beijing Normal University-Hong Kong Baptist University United International College, Zhuhai 519000, China
* Correspondence: raymondshtlee@uic.edu.cn

Abstract: Financial prediction persists a strenuous task in Fintech research. This paper introduces a multifractal asymmetric detrended cross-correlation analysis (MF-ADCCA)-based deep learning forecasting model to predict a succeeding day log return via excitatory and inhibitory neuronal synapse unit (EINS) using asymmetric Hurst exponent as input features, with return and volatility increment of Shanghai Stock Exchanges Composite Index (SSECI) from 2014 to 2020 as proxies for analysis. Experimental results revealed that multifractal elements by MF-ADCCA method as input features are applicable to time series forecasting in deep learning than multifractal detrended fluctuation analysis (MF-DFA) method. Further, the proposed biologically inspired EINS model achieved satisfactory performances in effectiveness and reliability in time series prediction compared with prevalent recurrent neural networks (RNNs) such as LSTM and GRU. The contributions of this paper are to (1) introduce a moving-window MF-ADCCA method to obtain asymmetric Hurst exponent sequences used directly as an input feature for deep learning prediction and (2) evaluate performances of various asymmetric multifractal approaches for deep learning time series forecasting.

Keywords: stock prediction; asymmetry Hurst exponent; deep learning; multifractal; neural networks

Citation: Wang, L.; Lee, R.S.T. Stock Index Return Volatility Forecast via Excitatory and Inhibitory Neuronal Synapse Unit with Modified MF-ADCCA. *Fractal Fract.* **2023**, *7*, 292. https://doi.org/10.3390/fractalfract7040292

Academic Editors: Bruce Henry and Leung Lung Chan

Received: 9 March 2023
Revised: 21 March 2023
Accepted: 24 March 2023
Published: 28 March 2023

1. Introduction

Financial trends fluctuations have amassed complexities by rapid global markets development in the recent decades. Time series prediction is a strenuous task since it contains chaotic, fuzzy, and incomplete information [1]. The focus of this paper is to interpret the financial fluctuation patterns and to predict their future trends.

Financial researchers often used statistical and econometric methods to construct prediction models by studying the characteristics and operating rules to assess and forecast volatility before the advent of machine learning algorithms. They indicated that financial market is a synthetical object with nonlinear multifractal characteristics [2,3], where multiscale properties and nonlinear evolution can be quantitatively analyzed by self-similar behavior of multifractal theory. These multifractal analysis techniques include rescaled range analysis (R/S) [4], detrended fluctuation analysis (DFA) [5], and multifractal detrended fluctuation analysis (MF-DFA) [6]. To compare, DFA can eliminate estimates of long-term relationships and increase credibility than rescaled range analysis, whereas multifractal detrended cross-correlation analysis (MF-DCCA) [7] is proposed to combine MF-DFA and DCCA [8] identifying the cross-correlation between two non-stationary data to quantify multifractal characteristics of the correlation. MF-DCCA method has extended to numerous research [9,10] such as multifractal asymmetric detrended cross-correlation analysis (MF-ADCCA) [11] studying asymmetric cross-correlations of non-stationary time series by integrating MF-DCCA with asymmetric DFA [12] to address its predicting upward (or downward) trend of cross-correlation characteristic limitation in time series. It studied the scaling features of cross-correlation between finance market stability and real estate price changes [13], in cryptocurrency markets research [14], and in gold futures market's price-volume correlation [15] indicating that MF-ADCCA is effective to complex nonlinear dynamics.

The generalized Hurst exponent (H) is an econophysics concept to describe time series features and evaluate their complexities as a quantitative metric to study time series long-range dependence by various multifractal analysis approaches. A time series is characterized by anti-persistent behavior when $0 < H < 0.5$, which means that the data are uncorrelated temporally. In this case, the relative tendency shows the potential for an enormous reversal signal and continuity. When $0.5 < H < 1$, the relative tendency is characterized by persistent behavior, its current trend continuity is likely in time series contrary to the previous case. If $H = 0.5$, the time series is expected to be neither anti-persistent nor persistent but is characterized by a negatively correlated dataset with any definable behavior. Hence, the generalized Hurst exponent is valuable for quantifying time series tendency.

Although asymmetric Hurst exponents can provide probabilistic trend assessments to express the likelihood of a continuous trend, but cannot provide a precise forecast of future values as they are sensitive to non-stationary or precipitous data changes in time series behaviors [16–18]. Deep learning methods for financial prediction has gradually become the core direction of fintech research in recent years [19,20]. Recurrent neural networks (RNNs) are mostly used time series prediction models for long-range time series dependence with their unique memory mechanisms to generate the current state by using the hidden state of previous time step as input to store past information [21]. Nevertheless, vanishing and exploding gradients problems occurred when the network parameters are trained repetitively in model training process inducing RNNs inability to guarantee generality and reliability of the prediction model. A biologically motivated recurrent unit based on neuronal synaptic activity mechanism and chaotic behaviors called excitatory and inhibitory neural synapse unit (EINS) is proposed by the author's previous research to address these problems.

Additionally, a novel deep learning model is introduced to forecast absolute return of SXP500 Index by combining RNNs and asymmetric fractality exponent (A-MFDFA) to explore asymmetric multifractal elements [22]. Experimental results indicated that asymmetric Hurst exponents improved deep learning approaches for absolute return prediction accuracy and robustness in volatile financial markets, but A-MFDFA method only analyzed multifractal characteristics of single non-stationary time series inducing the loss of cross-correlation information in financial factors. MF-ADCCA is a comprehensive technique to consider asymmetric structure and multifractal scaling features between two time series to improve complex nonlinear financial dynamics understanding, which is more appropriate than A-MFDFA as an input feature in financial forecasting.

Hence, this paper focuses on predicting financial time series via EINS using asymmetric Hurst exponent based on MF-ADCCA. First, it used a moving-window method to modify MF-ADCCA so that times series of past T days can obtain asymmetric Hurst exponent of the day. Second, MF-ADCCA is to estimate asymmetric multifractal features of cross-correlations between price fluctuations and realized volatility of Shanghai Stock Exchanges Composite Index (SSECI). Third, the succeeding day log return is predicted by EINS using asymmetric Hurst exponent based on MF-ADCCA and log return of past T days as input. Then, the predictive capacities of MF-ADCCA are examined and compared with MF-DFA-based RNNs model (delete and to be mentioned in results section-Experimental results showed that MF-ADCCA predictive capacities outperformed MF-DFA in deep learning financial forecasting tasks, and EINS model achieved satisfactory performances for effectiveness and reliability in time series prediction compared to RNNs such as LSTM [23] and GRU [24]).

This paper is organized as follows: Section 2 introduces a moving-window MF-ADCCA method and EINS; Section 3 presents the financial time series analyzed by MF-ADCCA and deep learning forecasting experiment implementation; Section 4 discusses the experimental results followed by conclusion in Section 5.

2. Materials and Methods

2.1. Multifractal Asymmetric Detrended Cross-Correlation Analysis (MF-ADCCA)

This subsection introduces MF-ADCCA method used in time series prediction experiment to measure the asymmetric cross-correlations between two non-stationary time series $\{x_t : t = 1, \ldots, N\}$ and $\{y_t : t = 1, \ldots, N\}$, and examine the aggregated index to present a positive or a negative increment [11] summarized as follows:

Step 1: Construct profile of the original time series as

$$X(k) = \sum_{t=1}^{k} (x_t - \overline{x}), t = 1, \ldots, N, \tag{1}$$

$$Y(k) = \sum_{t=1}^{k} (y_t - \overline{y}), t = 1, \ldots, N, \tag{2}$$

where $\overline{x}$ and $\overline{y}$ are average values over the entire return series respectively. The index proxy series is calculated by $I(k) = I(k-1)\exp(x_k)$ for $k = 1, \ldots, N$ with $I(0) = 1$ to assess positive and negative trend of the index.

Step 2: Divide profiles $X(k)$, $Y(k)$, and index proxy $I(k)$ into $N_S = \lfloor N/s \rfloor$ non-overlapping segments of length s. Repeat the division from other end of the series to consider the whole profile for a total of $2N_S$ segments for each series.

Step 3: Calculate detrended covariance for each $2N_S$ segment as

$$f^2(s,v) = \frac{1}{s}\sum_{i=1}^{s}\left|X((v-1)s+i) - \widetilde{X_v}(i)\right|\left|Y((v-1)s+i) - \widetilde{Y}_v(i)\right| \tag{3}$$

for $v = 1, \ldots, N$, and

$$f^2(s,v) = \frac{1}{s}\sum_{i=1}^{s}\left|X(N-(v-N_s)s+i) - \widetilde{X}_v(i)\right|\left|Y(N-(v-N_s)s+i) - \widetilde{Y}_v(i)\right| \tag{4}$$

for $v = 1, \ldots, 2N_S$. By fitting a least-square degree-2 polynomial $\widetilde{X}_v$ and $\widetilde{Y}_v$, calculate profiles local trend and applied to detrend $X(k)$ and $Y(k)$ respectively. Further, the local asymmetric direction of the index is determined by assessing the least-square linear fit $\widetilde{I}_v(i) = a_{I_v} + b_{I_v} i (i = 1, \ldots, s)$ for each segment, where the sign of slope b_{I_v} is to discriminate the index trend. If $b_{I_v} > 0$, the index trend has a positive trend, or a negative trend if otherwise.

Step 4: Calculate directional q-order average fluctuation functions as

$$\left.\begin{aligned} F_q^{+}(s)| &= \left\{\frac{1}{M^{+}}\sum_{v=1}^{2N_s}\frac{1+\mathrm{sgn}(b_{I_v})}{2}\left[f^2(s,v)\right]^{q/2}\right\}^{1/q}, \\ F_q^{-}(s)| &= \left\{\frac{1}{M^{-}}\sum_{v=1}^{2N_s}\frac{1-\mathrm{sgn}(b_{I_v})}{2}\left[f^2(s,v)\right]^{q/2}\right\}^{1/q}, \end{aligned}\right. q \neq 0 \tag{5}$$

and

$$\left.\begin{aligned} F_0^{+}(s) &= \exp\left\{\frac{1}{2M^{+}}\sum_{v=1}^{2N_s}\frac{1+\mathrm{sgn}(b_{I_v})}{2}\mathrm{In}\left[f^2(s,v)\right]\right\}, \\ F_0^{-}(s) &= \exp\left\{\frac{1}{2M^{-}}\sum_{v=1}^{2N_s}\frac{1-\mathrm{sgn}(b_{I_v})}{2}\mathrm{In}\left[f^2(s,v)\right]\right\}, \end{aligned}\right. q = 0 \tag{6}$$

where $M^{+} = \sum_{v=1}^{2N_s}\frac{1+\mathrm{sgn}b_{(I_v)}}{2}$ and $M^{-} = \sum_{v=1}^{2N_s}\frac{1+\mathrm{sgn}b_{(I_v)}}{2}$ are subseries numbers with positive and negative tendencies in which $b_{I_v} \neq 0$ for $v = 1, \ldots, 2N_S$, thus $M^{+} + M^{-} = 2N_S$.

Step 5: Calculate q-order fluctuation functions for overall trend as

$$F_q(s) = \left\{ \frac{1}{2N_s} \sum_{v=1}^{2N_s} \left[f^2(s,v) \right]^{\frac{q}{2}} \right\}^{\frac{1}{q}}, q = 0 \tag{7}$$

and

$$F_0(s) = \exp\left\{ \frac{1}{4N_s} \sum_{v=1}^{2N_s} \mathrm{In}\left[f^2(s,v) \right] \right\}, q \neq 0 \tag{8}$$

Step 6: Calculate generalized Hurst exponents as

$$F_q^+(s) \sim s^{h_{xy}^+(q)}, F_q^-(s) \sim s^{h_{xy}^-(q)}, \text{ and } F_q(s) \sim s^{h_{xy}(q)} \tag{9}$$

when q-order fluctuation functions follow a power-law of forms $F_q^+(s) \sim s^{h_{xy}^+(q)}$, $F_q^-(s) \sim s^{h_{xy}^-(q)}$, and $F_q(s) \sim s^{h_{xy}(q)}$, the two non-stationary series present long-range power-law cross-correlated features. Scaling exponent $h_{xy}(q)$, known as generalized Hurst exponent, is used to express the long-range power-law correlation features that can be calculated by fitting a log-log linear regression, while $h_{xy}^+(q)$ and $h_{xy}^-(q)$ are used to measure the positive and negative increments. To avoid errors and preserve estimation validity, this paper used a scale range from $s_{min} = max(20, N/100)$ to $s_{max} = min(20s_{min}, N/10)$ and 100 points in the regression [14].

If $0 < h_{xy}(q) < 0.5$, the two series present an anti-persistent cross-correlation indicating that one series is likely to be followed by a fluctuation opposite to the current trend in the other series. If $0.5 < h_{xy}(q) < 1$, the two series present persistent cross-correlation indicating that one series is likely to be followed by a fluctuation similar to the current trend in the other series. When $h_{xy}(q) = 0.5$, the two series have neither obvious cross-correlations nor any correlation.

The order q represents to various volatility magnitudes degree assessed. If $0 < q$, scaling exponents present larger or smaller fluctuations behavior. Additionally, if $h_{xy}(q)$ is independent of q, a series is multifractal. It is noted that the Hurst exponent of target series can be calculated by setting $q = 2$. Since the generalized Hurst exponents series calculated by MF-ADCCA cannot be used directly as input feature for deep learning forecasting, a moving-window method is used to modify MF-ADCCA by calculating asymmetric Hurst exponent value of the day using past T days data depicted in Algorithm 1.

Algorithm 1. Algorithm to Moving-window MF-ADCCA Method.

```
Input:    Time Series: $X_t$;                              < Size ($w * l$) >
          Time Series: $Y_t$;                              < Size ($w * l$) >
          Days Scaling: $T$;
          Step: $t$;
Output:   Asymmetric generalized Hurst exponents;
          Function Moving-window MF-ADCCA ($X_t$, $Y_t$, $T$, $t$)
          Initialize Hurst ← Array[0, ... $N_{w-T+1}$], Hurst⁺ ← Array[0, ... $N_{w-T+1}$],
Hurst⁻ ← Array[0, ... $N_{w-T+1}$]
          for $i$ in range (0, $N_{w-T+1}$, step) do
             $Series\ A \leftarrow X_t[i, \ldots i + T]$
$Series\ B \leftarrow Y_t[i, \ldots i + T]$
             $Hurst, , Hurst^+, Hurst^- \leftarrow MF - ADCCA(Series\ A,\ Series\ B)$
             $Hurst_{[i]} \leftarrow Hurst$
             $Hurst^+_{[i]} \leftarrow Hurst^+$
             $Hurst^-_{[i]} \leftarrow Hurst^-$
             return Hurst, , Hurst⁺, Hurst⁻
          End function
```

2.2. Excitatory and Inhibitory Neuronal Synapse Unit (EINS)

This section explains an EINS illustrated in Figure 1. It is a biologically inspired neural network model with synaptic activity mechanism to simulate the neurodynamics of spike alternation and neurotransmitter transmission within neurons during memory behavior [25–27]. The design is based on memristive synapse-coupled bi-neuron networks structure enabling the model to have the same memory mechanisms as human brain [28–30]. A single EINS unit is expressed as follows:

$$D(t+1) = Tanh\ [x(t+1)Wd - Bd\ ] \tag{10}$$

$$E(t+1) = Sigmoid[A(t)\,Wea + E(t)Wee - I(t)Wei + D(t+1)Wed - B_e] \tag{11}$$

$$I(t+1) = Sigmoid[A(t)\,Wia - E(t)Wie + I(t)Wii + D(t+1)Wid - B_i] \tag{12}$$

$$A(t+1) = [E(t+1) - I(t+1)]e^{-kD^2(t+1)} + D(t+1) \tag{13}$$

where x(t+1) denotes the external stimulation at each time step; $D(t+1)$, $E(t+1)$, $I(t+1)$, $A(t+1)$ denote the neuronal dendrite layer, excitatory neurotransmitter state layer, inhibitory neurotransmitter state layer, and the neuronal axon layer, respectively; Wea, Wee, Wei, Wed, and B_e express weights and bias of neuronal axon, excitatory neurotransmitter state, inhibitory neurotransmitter state, neuronal dendrite, and excitatory state layer in the excitatory state layer $E(t+1)$ respectively; similarly, Wia, Wie, Wii, Wid, and B_i are weights and bias of corresponding terms in the inhibitory state layer, $I(t+1)$.

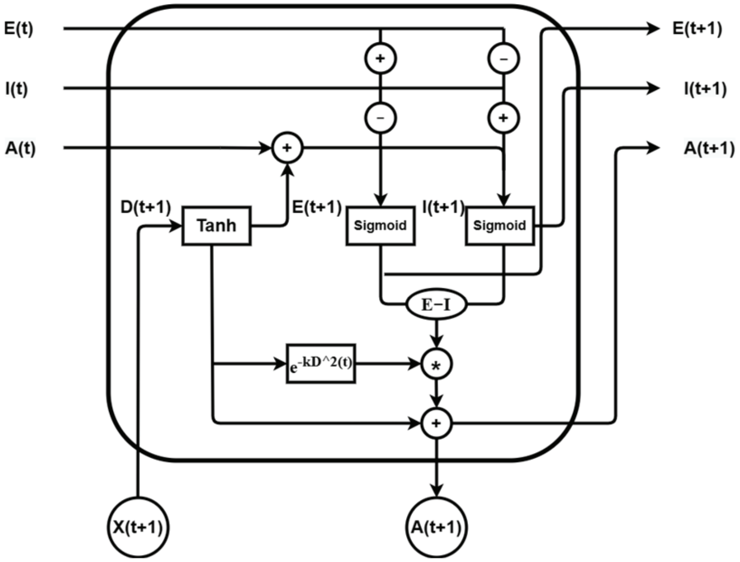

Figure 1. Diagram of EINS unit.

It showed that the dendrite layer receives external input and sends processed results to the hidden state with previous state values. The updated hidden state values are preserved in the hidden state to be learnt in subsequent time steps. Further, the proposed unit outputs the learnt result via an axon layer using the neurodynamic mechanism of memristive synapse-coupled bi-neuron networks and sends it to the next hidden state. Its model is depicted in Algorithm 2.

Algorithm 2. Algorithm to Excitatory and Inhibitory Neural Synapse Model.

```
Input:    Time Series: $T_t$;    < Size ($batch, time\ step,\ input\ size$) >
          Input Size: $I$; Hidden Size: $H$; Output Size: $O$;
          Step: $t$;
Output:   Prediction Result: $T_{t+1}$;
          Procedure EINS ($n,\ p,\ i,\ j, \theta_0$)
          Initialize $\boldsymbol{E_t} \leftarrow 0$; $\boldsymbol{I_t} \leftarrow 0$; $\boldsymbol{A_t} \leftarrow 0$; $\theta \leftarrow \theta_0$; $i \leftarrow 0$; $j \leftarrow 0$.
          for $X_i$ in $T_t$ do
            $\boldsymbol{D_t} \leftarrow tanh\left(X_i W_d^{I*H} - b_d^H\right)$
$\boldsymbol{E_t} \leftarrow \delta\left(A_{t-1} W_{ea}^{H*H} + E_{t-1} W_{ee}^{H*H} - I_{t-1} W_{ei}^{H*H} + D_t W_{ed}^{H*H} - b_e^H\right)$
            $\boldsymbol{I_t} \leftarrow \delta\left(A_{t-1} W_{ia}^{H*H} - E_{t-1} W_{ie}^{H*H} + I_{t-1} W_{ii}^{H*H} + D_t W_{id}^{H*H} - b_i^H\right)$
            $\boldsymbol{A_t} \leftarrow (E_t - I_t) \odot exp^{-k*D_t^2} + D_t$
$T_{t+1} \leftarrow \left(A_t W_O^{H*O} - b_O^O\right)$
return $T_{t+1}$
          End for
          While $j < p$ do
            Update $\theta$ by running training algorithm for $n$ steps
            $i \leftarrow i + n$
            $T_{t+1} \leftarrow ValidationSetError(\theta)$
            if $T_{t+1} < T_{valid}$ then
              $j \leftarrow 0$
              $\theta^* \leftarrow \theta$
              $i^* \leftarrow i$
            else
              $j \leftarrow j + 1$
            End if
          End while
          return $\theta^*$ and save the trained EINS model weights
          End Procedure
```

RNNs memory mechanisms rely on preserving past information in hidden layer, their training encounters vanishing and exploding gradients problems occurred due to these trainable parameters are repetitively applied to the hidden state. The proposed experimental model used chaotic property of memristive synapse-coupled bi-neuron networks to mitigate them and explore the feasibility of combining biologically inspired approach with deep learning algorithms.

3. Data and Experiments

3.1. Data Description

The data are a log return series extracted by Shanghai Stock Exchanges Composite Index (SSECI). The experiment introduced a deep learning forecasting model with asymmetric multifractal characteristics, using close prices from 2014 to 2020 for calculation as depicted in Figure 2. The log return r_t is calculated by:

$$r_t = \ln p_t - \ln p_{t-1} \tag{14}$$

where p_t is daily close price on day t; r_t is the log return on day t. The log return series of SSECI from 2014–2020 is illustrated in Figure 3. Additionally, the volatility increments from this period are another proxy for MF-ADCCA analysis given by:

$$v_t = \ln \hat{\sigma}_t - \ln \hat{\sigma}_{t-1} \tag{15}$$

where $\hat{\sigma}_t = \sqrt{\mathrm{BPV}_t}$, and BPV_t represent the realized bipower variation [31] given by:

$$\mathrm{BRV}_t = \sum_t |r_t||r_{t+1}| \tag{16}$$

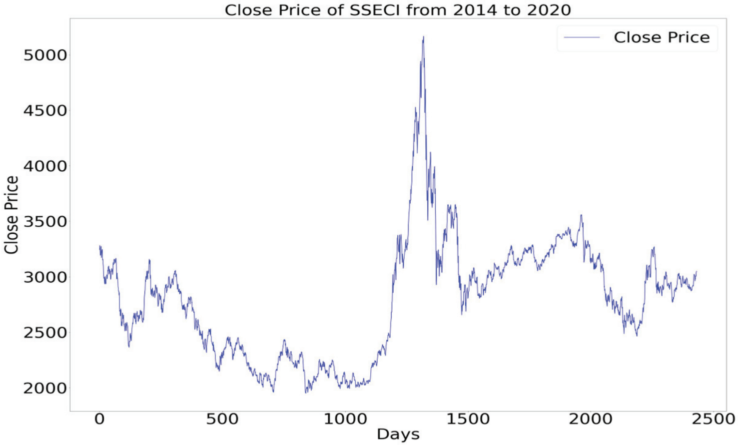

Figure 2. The graph of SSECI close price from 2014 to 2020.

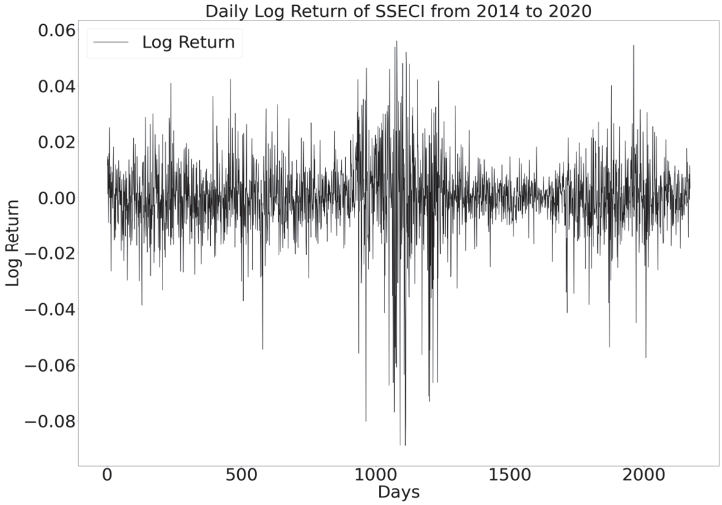

Figure 3. The graph of SSECI log return from 2014 to 2020.

Figure 4 illustrated the volatility increments (volatility changes) of SSECI. The data length of volatility increments series is 2177 similar to log return series. Augmented Dickey–Fuller (ADF) test [32], Kwiatkowski–Philips–Schmidt–Shin (KPSS) test [33], and Jarque-Bera statistic tests are implemented to examine statistical characteristics of two proxy series. The descriptive statistics information of the log return and volatility increments of SSECI are listed in Table 1. It showed that the mean values of return increments and volatility increments are close to 0 indicating that these series are self-regression equilibrium. The absolute value of return increments is larger than volatility increments indicating that the return increments have greater asymmetry. Further, Jarque-Bera statistic test result showed that all series are not null hypothesis of Gaussian distribution at 1% significance level. It is noted that the null hypothesis of unit root existence in ADF test is rejected at 1% significance level, and KPSS tests showed that the null hypothesis of stationarity is rejected at 1% significance level.

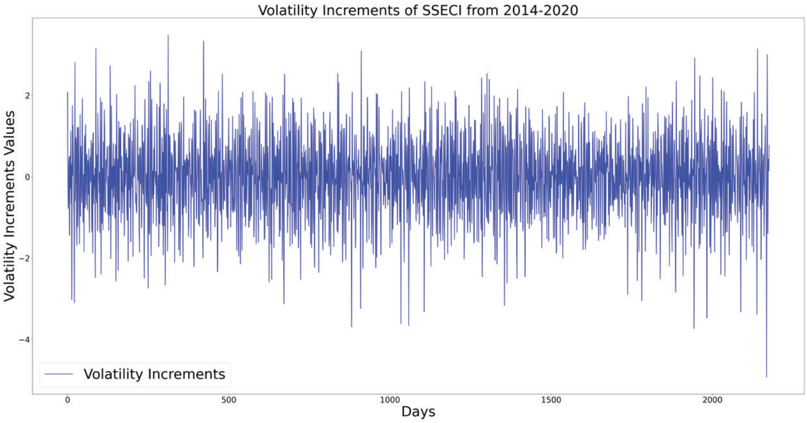

Figure 4. The graph of SSECI volatility increments from 2014 to 2020.

Table 1. Descriptive statistics for log return and volatility increments of SSECI.

	Mean	Max	Min	Std	Skew	Kurt	J-Bera [1]	ADF [2]	KPSS [3]
r_t	4.6×10^{-5}	5.6×10^{-3}	-8.9×10^{-2}	1.3×10^{-2}	−0.953	6.695	4372.8 *	−9.148 *	8.27×10^{-2} *
v_t	2.1×10^{-4}	3.7987	−3.7436	0.8384	7.8×10^{-3}	1.0185	93.18 *	−15.769 *	7.88×10^{-2} *

[1] denotes Jarque-Bera statistic tests; [2] denotes Augmented Dickey–Fuller test; [3] denotes Kwiatkowski–Philips–Schmidt–Shin (KPSS) test; * represents 1% significance level. Note: (1) The ADF test uses null to express the existence of a unit root; (2) the KPSS test uses the null to express stationary.

The log return series and volatility increment series are used as proxies for MF-ADCCA analysis. Figures 5 and 6 illustrated up-trend Hurst exponents $(h^{+}_{xy}(2))$ and up-trend Hurst exponents $(h^{-}_{xy}(2))$ of SSECI log returns based on the moving-window of MF-ADCCA analysis accordingly.

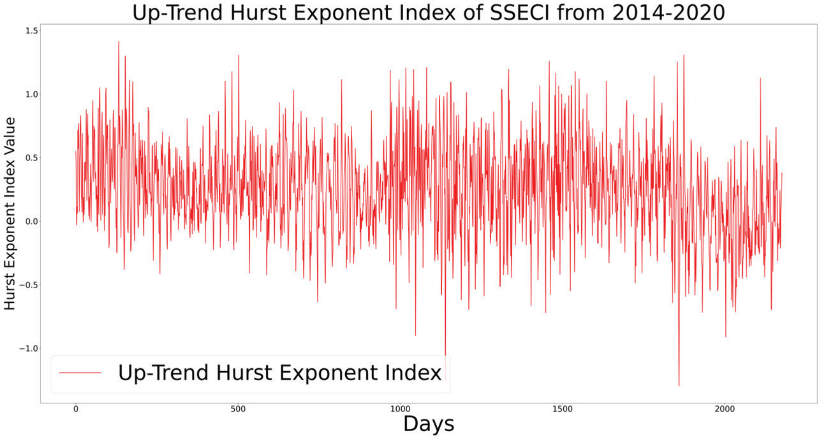

Figure 5. The graph of up-trend Hurst exponent index of SSECI.

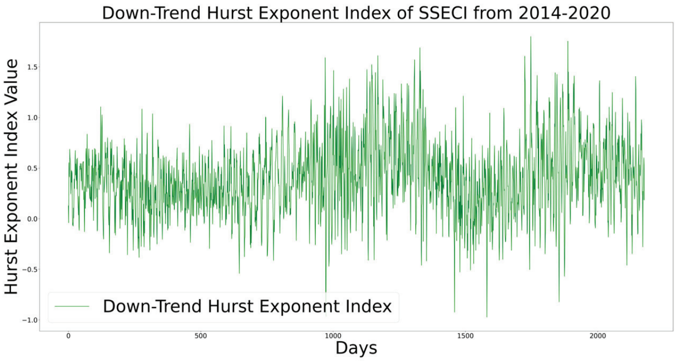

Figure 6. The graph of down-trend Hurst exponent index of SSECI.

3.2. Experiments

The succeeding day log return of SSECI using past days log return with asymmetric Hurst exponents for experiment implementation are illustrated in Figure 7. The implementation code is written in Python 3.9 using Pytorch library on a hardware environment with Intel CPU Xeon@2.00 GHz, GPU Tesla V100, 12 GB RAM, and Windows 11 operating system. First, a moving-window MF-ADCCA is used to estimate the asymmetric Hurst exponent of Shanghai Stock Exchanges Composite Index (SSECI) and log return series volatility increments series are used as proxies. Second, the succeeding day log return of SSECI is predicted by EINS using asymmetric Hurst exponent based on the moving-window MF-ADCCA. Third, RNNs predictive capacities with MF-ADCCA are examined and compared with MF-DFA-based RNNs model such as LSTM and GRU. All datasets are normalized to the range from -1 to 1 with Min-Max normalized method prior feeding into the network as expressed by:

$$y_i = \frac{x_i - x_{mean}}{\underset{1\le i\le n}{max}\left\{x_j\right\} - \underset{1\le i\le n}{min}\left\{x_j\right\}} \tag{17}$$

where y_i is the normalized value, x_i is a data in the dataset, x_{mean} is the mean value of sample set, $\underset{1\le i\le n}{max}\left\{x_j\right\}$ is the minimum data while $\underset{1\le i\le n}{min}\left\{x_j\right\}$ is the maximal data in the dataset. Each dataset is divided into three parts with the same train-valid-test split rate—80% is used for models' training, 10% for validation, and the remaining for performance testing.

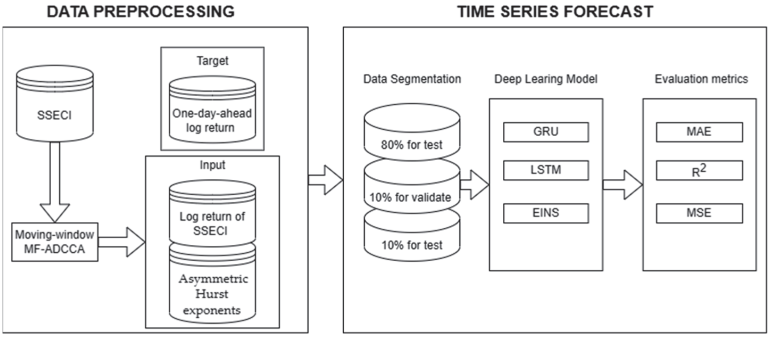

Figure 7. Flowchart of time series prediction implementation.

The experiment used a four-layer deep learning model structure for time series forecast two recurrent layers connected by two fully connected layers as illustrated in Figure 8, and used hyper-parameters to examine RNNs predictive capacities with MF-ADCCA as listed in Table 2. Further, three regression indicators including mean square error (MSE), mean absolute error (MAE), and coefficient of determination (R^2) are used to evaluate models' performances as given by:

$$MSE = \frac{1}{N}\sum_{i=1}^{N} \left(\widetilde{y}_t^i - y_t^i\right)^2 \tag{18}$$

$$MAE = \frac{1}{N}\sum_{i=1}^{N} \left|\widetilde{y}_t^i - \widetilde{y}_t^i\right| \tag{19}$$

$$R^2 = 1 - \frac{\sum_{i=1}^{N} \left(y_t^i - \widetilde{y}_t^i\right))}{\sum_{i=1}^{N} \left(\overline{y}_t^i - \widetilde{y}_t^i\right)} \tag{20}$$

where y_t^i, $\overline{y}_t^i$, and $\widetilde{y}_t^i$ represent the actual, the mean, and the predicted value of test set respectively; N is the total samples number indicating that the lower MSE and MAE values represent more accurate prediction results. Further, the closer R^2 value to 1 represent the model robustness to fit dataset and prediction performance.

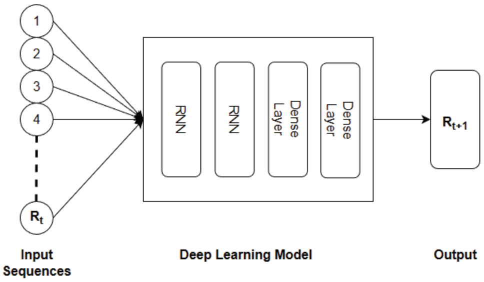

Figure 8. Model structure for time series prediction.

Table 2. Hyper-parameters setting list.

Hyper-Parameters	Settings
Hidden neurons	128,256
Time Horizons	32,128
Learning rate	1×10^{-3}
Dropout rate	0.2
Epochs	100
Optimizer	Adam
Error function	Mean squared error

4. Results and Discussion

The experimental forecast results are listed in Table 3. They showed that MF-DFA asymmetric Hurst exponents achieved predictive capacities for forecasting time series with RNNs [19]. In particular, the performance of up-trend Hurst exponents ($h_{xy}^{+}(2)$) and up-trend Hurst exponents ($h_{xy}^{-}(2)$) for deep learning forecasting outperformed the generalized Hurst exponent ($h_{xy}(2)$). They are used as benchmarks to compare with MF-ADCCA asymmetric Hurst exponents to examine predictive capacities of various asymmetric multifractal analysis approaches.

Table 3. Forecasting performance with various hyper-parameters (note: best results highlighted in **BOLD**).

Multifractal	Model	MSE	MAE	R^2
Hidden neurons $= 128$, Time horizons $= 32$, Learning rate $= 1 \times 10^{-3}$				
MF-DFA	EINS	0.02584	0.11069	−0.01746
	LSTM	0.02704	0.11351	−0.06485
	GRU	0.02769	0.11494	−0.09042
MF-ADCCA	EINS	**0.02549**	**0.10999**	**−0.00398**
	LSTM	0.02577	0.11091	−0.01469
	GRU	0.02580	0.11130	−0.01605
Hidden neurons $= 128$, Time Horizons $= 128$, Learning rate $= 1 \times 10^{-3}$				
MF-DFA	EINS	0.02324	0.10689	−0.00691
	LSTM	0.02337	0.10810	−0.01262
	GRU	0.02354	0.10885	−0.02011
MF-ADCCA	EINS	**0.02372**	**0.10770**	**−0.02798**
	LSTM	0.02507	0.11252	−0.08636
	GRU	0.02496	0.11118	−0.08178
Hidden neurons $= 256$, Time Horizons $= 32$, Learning rate $= 1 \times 10^{-3}$				
MF-DFA	EINS	0.02582	0.11069	−0.01666
	LSTM	0.02727	0.11501	−0.07390
	GRU	0.02699	0.11419	−0.06298
MF-ADCCA	EINS	**0.02532**	**0.11003**	**0.00296**
	LSTM	0.02704	0.11489	−0.06500
	GRU	0.02593	0.11145	−0.02102
Hidden neurons $= 256$, Time Horizons $= 128$, Learning rate $= 1 \times 10^{-3}$				
MF-DFA	EINS	0.02366	0.10756	−0.02516
	LSTM	0.02467	0.11103	−0.06923
	GRU	0.02774	0.11885	−0.20226
MF-ADCCA	EINS	**0.02335**	**0.10705**	**−0.01197**
	LSTM	0.02419	0.10989	−0.04810
	GRU	0.02418	0.11025	−0.04761

They also showed that three evaluation metrics values MSE, MAE, and R^2 of MF-ADCCA-based forecasting models outperformed MF-DFA under corresponding hyper-parameters. However, the multifractal elements obtained by MF-ADCCA method lacked stability when fitted into deep learning model due to proxy design diversities. Hence, it is recommended to use indicators related to financial technical analysis as proxies for MF-ADCCA method since prerequisite fintech knowledge is essential. It is noted that the improvement in MF-ADCCA performance to multiple proxies mechanism allowed to retain more time series' past information indicating that asymmetric multifractal elements by MF-ADCCA method as input features are applicable to time series forecasting in deep learning.

For deep neural network prediction performance, it examined the feasibility of combining neuroscience and brain science into deep learning algorithms. The results showed that EINS prediction error is lower than LSTM and GRU under corresponding hyper-parameters as its architecture and information flow are based on memristive synapse-coupled bi-neuron networks to simulate synapse activity mechanisms during electric signals exchange and chemical transmitters between neurons. It has a deep neural network model with neuro-dynamics of spike alternation and neuro-transmitter transmission within neurons during memory indicating that EINS is a significant comparison method for effectiveness and reliability in time series prediction.

5. Conclusions

This paper focused not only on predicting financial time series via EINS with asymmetric Hurst exponent based on MF-ADCCA, but also examined the predictive capacities of various asymmetric multifractal approaches in deep learning. The log return and volatility increment of Shanghai Stock Exchanges Composite Index (SSECI) from 2014 to 2020 are used as proxies for MF-ADCCA analysis. It used a moving-window MF-ADCCA to estimate the asymmetric Hurst exponent, and a succeeding day log return predicted by EINS using asymmetric Hurst exponent based on moving-window MF-ADCCA with log return of past T days as input to examine MF-ADCCA predictive capacity in deep learning to compare with MF-DFA-based RNNs model. A four-layer deep learning model structure is constructed for time series forecast where two recurrent layers are connected by two fully connected layers. Further, mean square error (MSE), mean absolute error (MAE), and coefficient of determination (R^2) are used to evaluate the models' performances. The results showed that MF-ADCCA outperformed MF-DFA in deep learning financial forecasting tasks. Further, the biologically inspired EINS model achieved satisfactory performances for effectiveness and reliability in time series prediction as compared with prevalent RNNs such as LSTM and GRU.

The contributions of this paper are to (1) introduce a moving-window MF-ADCCA method to calculate asymmetric Hurst exponent of the day using times series of the past T days by setting $q = 2$ to obtain asymmetric Hurst exponent sequences that can be directly used as an input feature for deep learning prediction and (2) evaluate various asymmetric multifractal approaches performances for deep learning time series forecasting.

Future research will focus on other financial markets such as cryptocurrency markets, gold markets, and other state-of-the-art multifractal methods as benchmarks.

Author Contributions: Conceptualization, R.S.T.L.; methodology, L.W.; software, L.W.; validation, L.W.; formal analysis, L.W.; investigation, L.W.; resources, L.W.; data curation, L.W.; writing—original draft preparation, L.W.; writing—review and editing, R.S.T.L.; visualization, L.W.; supervision, R.S.T.L.; project administration, R.S.T.L.; funding acquisition, R.S.T.L. All authors have read and agreed to the published version of the manuscript.

Funding: This paper was supported by Research Grant R202008 of Beijing Normal University-Hong Kong Baptist University United International College (UIC), Key Laboratory for Artificial Intelligence and Multi-Model Data Processing of Department of Education of Guangdong Province, Guangdong Province F1 project grant on Curriculum Development and Teaching Enhancement on Quantum Finance course UICR0400050-21CTL and by the Guangdong Provincial Key Laboratory of Interdisciplinary Research and Application for Data Science, BNU-HKBU United International College (2022B1212010006).

Informed Consent Statement: This research article describing a study do not involve humans.

Data Availability Statement: The program source and financial dataset can be accessed from https://github.com/JeffRody/MF-ADCCA-Deep-Learning-time-series-forecasting, accessed on 2 March 2023.

Conflicts of Interest: The authors declare no conflict of interest.

References

1. Zhang, L.; Wang, F.; Xu, B.; Chi, W.; Wang, Q.; Sun, T. Prediction of stock prices based on LM-BP neural network and the estimation of overfitting point by RDCI. *Neural Comput. Appl.* **2018**, *30*, 1425–1444. [CrossRef]
2. Liu, G.; Yu, C.P.; Shiu, S.N.; Shih, I.T. The Efficient Market Hypothesis and the Fractal Market Hypothesis: Interfluves, Fusions, and Evolutions. *Sage Open* **2022**, *12*, 21582440221082137. [CrossRef]
3. Arashi, M.; Rounaghi, M.M. Analysis of market efficiency and fractal feature of NASDAQ stock exchange: Time series modeling and forecasting of stock index using ARMA-GARCH model. *Futur. Bus. J.* **2022**, *8*, 14. [CrossRef]
4. Hurst, H.E. Long-term storage capacity of reservoirs. *Trans. Am. Soc. Civ. Eng.* **1951**, *116*, 770–799. [CrossRef]
5. Peters, E.E. *Fractal Market Analysis: Applying Chaos Theory to Investment and Economics*; John Wiley & Sons: Hoboken, NJ, USA, 1994; Volume 24.

6. Kantelhardt, J.W.; Zschiegner, S.A.; Koscielny-Bunde, E.; Havlin, S.; Bunde, A.; Stanley, H. Multifractal detrended fluctuation analysis of nonstationary time series. *Phys. A Stat. Mech. Its Appl.* **2002**, *316*, 87–114. [CrossRef]
7. Zhou, W.-X. Multifractal detrended cross-correlation analysis for two nonstationary signals. *Phys. Rev. E* **2008**, *77*, 066211. [CrossRef]
8. Podobnik, B.; Stanley, H.E. Detrended Cross-Correlation Analysis: A New Method for Analyzing Two Nonstationary Time Series. *Phys. Rev. Lett.* **2008**, *100*, 084102. [CrossRef]
9. Cao, G.; Zhang, M.; Li, Q. Volatility-constrained multifractal detrended cross-correlation analysis: Cross-correlation among Mainland China, US, and Hong Kong stock markets. *Phys. A Stat. Mech. Its Appl.* **2017**, *472*, 67–76. [CrossRef]
10. Yuan, X.; Sun, Y.; Lu, X. SHIBOR Fluctuations and Stock Market Liquidity: An MF-DCCA Approach. *Emerg. Mark. Financ. Trade* **2022**, *58*, 2050–2065. [CrossRef]
11. Cao, G.; Cao, J.; Xu, L.; He, L. Detrended cross-correlation analysis approach for assessing asymmetric multifractal detrended cross-correlations and their application to the Chinese financial market. *Phys. A Stat. Mech. Its Appl.* **2014**, *393*, 460–469. [CrossRef]
12. Alvarez-Ramirez, J.; Rodriguez, E.; Echeverria, J.C. A DFA approach for assessing asymmetric correlations. *Phys. A Stat. Mech. Its Appl.* **2009**, *388*, 2263–2270. [CrossRef]
13. Liu, C.; Zheng, Y.; Zhao, Q.; Wang, C. Financial stability and real estate price fluctuation in China. *Phys. A Stat. Mech. Its Appl.* **2020**, *540*, 122980. [CrossRef]
14. Kakinaka, S.; Umeno, K. Exploring asymmetric multifractal cross-correlations of price-volatility and asymmetric volatility dynamics in cryptocurrency markets. *Phys. A Stat. Mech. its Appl.* **2021**, *581*, 126237. [CrossRef]
15. Guo, Y.; Yu, Z.; Yu, C.; Cheng, H.; Chen, W.; Zhang, H. Asymmetric multifractal features of the price–volume correlation in China's gold futures market based on MF-ADCCA. *Res. Int. Bus. Financ.* **2021**, *58*, 101495. [CrossRef]
16. Yuan, Y.; Zhang, T. Forecasting stock market in high and low volatility periods: A modified multifractal volatility approach. *Chaos Solitons Fractals* **2020**, *140*, 110252. [CrossRef]
17. Hu, H.; Zhao, C.; Li, J.; Huang, Y. Stock Prediction Model Based on Mixed Fractional Brownian Motion and Improved Fractional-Order Particle Swarm Optimization Algorithm. *Fractal Fract.* **2022**, *6*, 560. [CrossRef]
18. Cao, G.; Han, Y.; Li, Q.; Xu, W. Asymmetric MF-DCCA method based on risk conduction and its application in the Chinese and foreign stock markets. *Phys. A Stat. Mech. Its Appl.* **2017**, *468*, 119–130. [CrossRef]
19. Jaiswal, R.; Jha, G.K.; Kumar, R.R.; Choudhary, K. Deep long short-term memory based model for agricultural price forecasting. *Neural Comput. Appl.* **2022**, *34*, 4661–4676. [CrossRef]
20. Lee, M.-C.; Chang, J.-W.; Yeh, S.-C.; Chia, T.-L.; Liao, J.-S.; Chen, X.-M. Applying attention-based BiLSTM and technical indicators in the design and performance analysis of stock trading strategies. *Neural Comput. Appl.* **2022**, *34*, 13267–13279. [CrossRef] [PubMed]
21. Chandar, S.; Sankar, C.; Vorontsov, E.; Kahou, S.E.; Bengio, Y. Towards non-saturating recurrent units for modelling long-term dependencies. *Proc. AAAI Conf. Artif. Intell.* **2019**, *33*, 3280–3287. [CrossRef]
22. Cho, P.; Lee, M. Forecasting the Volatility of the Stock Index with Deep Learning Using Asymmetric Hurst Exponents. *Fractal Fract.* **2022**, *6*, 394. [CrossRef]
23. Hochreiter, S.; Schmidhuber, J. Long short-term memory. *Neural Comput.* **1997**, *9*, 1735–1780. [CrossRef] [PubMed]
24. Chung, J.; Gulcehre, C.; Cho, K.; Bengio, Y. Empirical evaluation of gated recurrent neural networks on sequence modeling. *arXiv* **2014**, arXiv:1412.3555.
25. Cifelli, P.; Ruffolo, G.; De Felice, E.; Alfano, V.; van Vliet, E.A.; Aronica, E.; Palma, E. Phytocannabinoids in Neurological Diseases: Could They Restore a Physiological GABAergic Transmission? *Int. J. Mol. Sci.* **2020**, *21*, 723. [CrossRef] [PubMed]
26. Xu, Y.; Jia, Y.; Ma, J.; Alsaedi, A.; Ahmad, B. Synchronization between neurons coupled by memristor. *Chaos Solitons Fractals* **2017**, *104*, 435–442. [CrossRef]
27. Zhang, J.; Liao, X. Synchronization and chaos in coupled memristor-based FitzHugh-Nagumo circuits with memristor synapse. *Aeu-Int. J. Electron. Commun.* **2017**, *75*, 82–90. [CrossRef]
28. Lee, R.S.T. Chaotic Type-2 Transient-Fuzzy Deep Neuro-Oscillatory Network (CT2TFDNN) for Worldwide Financial Prediction. *IEEE Trans. Fuzzy Syst.* **2019**, *28*, 731–745. [CrossRef]
29. Njitacke, Z.T.; Doubla, I.S.; Kengne, J.; Cheukem, A. Coexistence of firing patterns and its control in two neurons coupled through an asymmetric electrical synapse. *Chaos: Interdiscip. J. Nonlinear Sci.* **2020**, *30*, 023101. [CrossRef]
30. Lee, R.S.T. Chaotic interval type-2 fuzzy neuro-oscillatory network (CIT2-FNON) for Worldwide 129 financial products prediction. *Int. J. Fuzzy Syst.* **2019**, *21*, 2223–2244. [CrossRef]
31. Barndorff-Nielsen, O.E.; Shephard, N. Power and bipower variation with stochastic volatility and jumps. *J. Financ. Econom.* **2004**, *2*, 1–37. [CrossRef]

32. Dickey, D.A.; Fuller, W.A. Distribution of the estimators for autoregressive time series with a unit root. *J. Am. Stat. Assoc.* **1979**, *74*, 427–431.
33. Kwiatkowski, D.; Phillips, P.C.B.; Schmidt, P.; Shin, Y. Testing the null hypothesis of stationarity against the alternative of a unit root: How sure are we that economic time series have a unit root? *J. Econom.* **1992**, *54*, 159–178. [CrossRef]

fractal and fractional

Article

Multifractal Characteristics of China's Stock Market and Slump's Fractal Prediction

Yong Li

Business School, China University of Political Science and Law, Beijing 100085, China; yongli@cupl.edu.cn

Abstract: It is necessary to quantitatively describe or illustrate the characteristics of abnormal stock price fluctuations in order to prevent and control financial risks. This paper studies the fractal structure of China's stock market by calculating the fractal dimension and scaling behavior on the timeline of its eight big slumps, the results show that the slumps have multifractal characteristics, which are correlated with the policy intervention, institutional arrangements, and investors' rationality. The empirical findings are a perfect match with the anomalous features of the stock prices. The fractal dimensions of the eight stock collapses are between 0.84 and 0.98. The fractal dimension distribution of the slumps is sensitive to market conditions and the active degree of speculative trading. The more mature market conditions and the more risk-averse investors correspond to the higher fractal dimension and the fall which is less deep. Therefore, the fractal characteristics could reflect the evolution characteristics of the stock market and investment philosophy. The parameter set calculated in this paper could be used as an effective tool to foresee the slumps on the horizon.

Keywords: China's stock market; stock market slump; multifractality

Citation: Li, Y. Multifractal Characteristics of China's Stock Market and Slump's Fractal Prediction. *Fractal Fract.* **2022**, *6*, 499. https://doi.org/10.3390/fractalfract6090499

Academic Editors: Carlo Cattani and Leung Lung Chan

Received: 10 June 2022
Accepted: 1 September 2022
Published: 5 September 2022

1. Introduction

An effective way to evaluate and predict financial stability on-time is by studying the characteristics of the stock market and its operation rules. Many empirical studies have proved that the stock market is a complex fractal object [1–4], its nonlinear evolution and multi-scale characteristics can be described quantitatively using the self-similar behavior analysis method of multi-fractal theory. Many valuable research results have been obtained on the fluctuations of various types of financial markets [5–9]. Many scholars verified that the Chinese stock market has nonlinear multifractal characteristics. Chen et al. constructed an indicator of extremes and predicted the financial extremes from the complex network perspective based on 12 kinds of worldwide stock indices [10]. Zhuang et al. used the Multifractal Detrended Fluctuation Analysis (MF-DFA) method and generalized Hurst exponents to evaluate ten important Chinese sectoral stock indices and revealed that they have different degrees of multifractality [11]. Du and Ning found that the Shanghai stock market has weak multifractal features and there are long-range power-law correlations between the index series [12]. Chen et al. verified the multifractal walk of the Chinese stock market, and established a stock price prediction model combining the wavelet, genetic algorithm, and neural network, according to the local scale characteristics and multi-scale correlation of the multifractal process [13]. Li proposed that the temporal spectrum of the dominant fractal dimension α_0 could be used to characterize stock market fluctuations, and that the spectrum parameter set $(\alpha_0, \Delta\alpha, -B)$ could distinguish the bubble from the normal fluctuation status well [14]. Li et al. found the degree of the marketization of the stock market has a significant impact on the multifractal spectrum of the bubbles of the Shanghai Stock Exchange Composite Index (SSECI) [15].

Although multifractality, as a nonlinear method, has been used by many scholars to study high-frequency financial time series to investigate the problems and phenomena which cannot be explained by traditional economic theory, so far, most of the related research remains in the stage of inspecting the multifractal characteristics of financial asset price volatility. To my knowledge, the dynamic mechanism of the formation of such fractal characteristics and scaling behavior has not been explored, and the relations between fractal structure and policy, the stock market institutional arrangement, and investors' rationality has not been dug into deeply. In recent years, the research on the stock market fractals has almost stopped, and the existing research results have not been effectively applied in the prediction of the stock market crash. The main reason is that the huge fluctuation of the stock market in China is a policy-induced plunge, and institutional arrangements and investors' rationality also affect stock market volatility, and in turn, affect its multifractal characteristics. Correctly understanding and analyzing the impact of them on stock market fractal characteristics is of great significance to the slump's early warning. However, as mentioned above, there is still a lack of research in this area, which is the focus of this paper.

The organization of the paper is as follows. Section 2 is devoted to identifying slump episodes and describing the trigger and market conditions of the slumps in China's stock market. Section 3 gives the calculation results of the multifractal spectrum of the Chinese stock market slumps. Section 4 reveals the correlation between multifractals and policies, market institutional surroundings, and investors' rationality. Section 5 illustrates the fractal prediction of the stock market slump. Section 6 summarizes the paper's conclusions.

2. The Eight Slumps of China's Stock Market and Their Direct Triggers

The Chinese stock market has experienced eight large ups and downs since its opening. Since the trading volume and stock market value of the Shanghai Stock Exchange are much larger than those of the Shenzhen Stock Exchange in the past, the SSECI is used in this paper to represent the trend of the Chinese stock market.

Although there is no numerically specific definition of a stock market slump, the term commonly applies to steep double-digit percentage losses in a stock market index over a period of several days. Here we define a stock market slump as an event when the SSECI declines relative to the historical maximum for more than 25 percent (the 25% was selected as the threshold value mainly because it could well distinguish the eight widely recognized major stock market crashes in China. We have also tried to use other values as the threshold, e.g. 20%, such that three more shocks are also eligible: 1999 (the SSECI index from 1756 points on 30 June 31999 down to 1361 on 4 January 2000), 2018 (from 3587 points on 30 January 2018 to 2440 on 4 January 2019), and 2021 (from 3708 on 21 December 2021 to 3023 on 16 March 2022). However, due to the low steepness of the decline of the three oscillations, the consistency of the variability of the calculated fractal parameters are not obvious, especially for $\Delta\alpha$. Therefore, only the results of the eight meltdowns selected using a 25% threshold value are reported here). The beginning of the slump is the date when the SSECI falls below this threshold level. The time of the trough is the date when the SSECI reaches its minimum level during the slump. The time of recovery is the first date when the SSECI reaches 25 percent of the pre-slump maximum level after the slump is triggered. To avoid counting the same slump twice, additional triggers occurring within a slump are considered part of the existing slump, instead of being an indicator of a new slump. The eight slump episodes are identified here by applying an operational version of this criterion to the data of the SSECI, and their specific time, the extent of the fall, and the direct triggers are shown in Table 1.

Table 1. Chinese stock market slump samples and their context.

No.	Beginning of Slump	Price Decline to Trough (%)	Month to Trough	Triggers	Investors' Feature	Market Institutional Conditions
1	26 May 1992	58.92	3	1. Stamp duty on stock trading increased from 1‰ to 3‰; 2. "August 10 incident" ①.	1. Most investors lacked professional knowledge; 2. Investors had weak risk awareness.	The authoritative approval system was based on quota control in the primary market, the issuing scale of listed companies' stocks was controlled by authority
2	16 February 1993	75.43	15	"Old eight shares" expansion ②.	1. Most investors lacked professional knowledge; 2. Investors had weak risk awareness.	1. The authoritative approval system was based on quota control in the primary market; 2. Financial consolidation for soft landing strategy.
3	13 September 1994	51.38	16	1. Chang T + 0 to T + 1; 2. "327 Treasury bond futures incident" ③.	The number of well-educated investors increased who had a certain risk awareness.	1. The authoritative approval system was based on quota control in the primary market; 2. The contractionary macroeconomic policies were used to alleviate the inflationary pressure.
4	12 May 1997	30.66	24	1. Stamp duty on stock trading increased from 3‰ to 5‰; 2. Limit the price rise and fall within 10%.	Investors' investment mentality became more and more rational and mature, and their risk tolerance increased.	1. The authoritative approval system was based on broker-dealer recommendation in the primary market; 2. The overall outbreak of southeast Asia economic crisis.
5	14 June 2001	52.18	42	1. The Reduction of State-owned Shares to Raise Social Security Fund in 2001 ④; 2. China officially launched the delisting system in 2001.	Investors' investment mentality became more and more rational and mature, and their risk tolerance increased.	1. The authoritative approval system was based on broker-dealer recommendation in the primary market; 2. The entire world economy has entered a depression cycle; 3.China's stock market is positioned to serve the financing of state-owned enterprises.

Table 1. *Cont.*

No.	Beginning of Slump	Price Decline to Trough (%)	Month to Trough	Triggers	Investors' Feature	Market Institutional Conditions
6	16 October 2007	70.97	11	1. Monetary policy gradually shifted from "prudent" to "moderately tight"; 2. Stock markets in major economies broke out; 3. Lifting the ban on Non-tradable Shares.	Ultra-sophisticated individualists ⑤.	1. The authoritative approval system was based on sponsor recommendation in the primary market; 2. The global financial crisis took place.
7	4 August 2009	28.12	19	The reserve requirement ratio was raised by 1 percentage point.	Ultra-sophisticated individualists.	1. The authoritative approval system was based on sponsor recommendation in the primary market; 2. The economy was overheating and inflation was rising.
8	12 June 2015	44.95	2	"Deleveraging" ⑥.	Ultra-sophisticated individualists.	1. The primary market adopted administrative ratification system; 2. Policy preferences focused on supporting high-tech equipment manufacturing Internet +, Industry 4.0, state-owned enterprise reform expectations.

Note: A crash is triggered when, relative to the historical maximum, the SSEI declined more than 25 per cent. The end of a trough is the date when the index reached 25 percent of pre-trigger maximum level the first instance after the trigger time. We exclude triggers occurring within six months of the initial trigger time. Source: The materials are collated by author according to the network publications of China Securities Regulatory Commission (CSRC). The annotation in the table could be found at the end of the article.

Table 1 tells us, firstly, that the eight slumps were triggered by different policies, the slumps in 1993, 2001, and 2007 are mainly due to the accelerated expansion of the secondary market, the other five slumps are initially due to the measures to alleviate the market overheating such as raising the deposit reserve ratio, enhancing stamp duty, imposing a limit on the rise and fall of prices, deleveraging, and so on. Secondly, traders' mentalities are gradually becoming more and more rational and mature from the lack of professional knowledge in the 1990s to the present, and their risk attitudes have changed a lot during this process. Thirdly, the institutional environment of the primary market has been marching on from a government-led to market-oriented system. The approval system for securities issuance has been gradually substituted by an examination registration system.

3. Fractal Characteristics of China's Stock Market Slumps

Multifractal is a method using a singularity spectrum to quantitatively describe the distribution of the probability on the whole set caused by different local conditions or different levels in the evolution process of the fractals, which is a measure of the degree of irregularity and inhomogeneity of the fractal structure. It can reproduce the financial transactions with drastic fluctuations in the financial market [2], obtain detailed information of the different degrees of volatility of financial asset prices on different time scales [5], provide the probability estimate of market movements, show the nature of market volatility [7], and thus gain a better understanding of the dynamics of the unpredictable financial market. The multifractal spectrum is composed of two relations. One is the power function relationship between the scale T and the subset composed of a series of probabilities $\mu(T)$: $\mu(T) \propto T \cdot \alpha$, α is called the singular exponent and reflects the singularity degree of the fractal object. The other is the power function relation between the number of boxes M(T) needed to cover the time series and the scale of T: $M(T) \propto T \cdot f(\alpha)$. Here, $f(\alpha)$ is the multifractal spectrum, which represents the fractal dimension of a subset of the same α value. There are many methods to calculate the fractal dimension, such as the box dimension [16], similarity dimension [17], capacity dimension [18], correlation dimension [19], information dimension [20], perimeter-area dimension [21], etc. The box-counting dimension is one of the most widely used fractal dimension algorithms. This paper will use this method to calculate the fractal dimension and multifractal spectrum.

In order to study the changes in the characteristics of the slumps and their evolution features of the multifractal dimension under different market conditions, we have divided the sample periods in terms of different trading day time scale, i.e., 132, 64, 32, 16, 8, 4, 2, and 1 days, for the eight slumps (in order to show the whole picture of the lnMq(T) and lnT relationship as much as possible, there must be a sufficiently long sample interval. It can be found that the multifractal spectrum calculated using more than 132 trading days has no change in the linear relationship between lnMq(T) and lnT. Therefore, here, the multifractal spectrum of 132 trading data before and after a sharp fall occurred is reported. In this case, T takes 1/132, 1/64, 1/32, 1/16, 1/8, 1/4, 1/2, and 1), and then calculated the multifractal dimension in terms of the distribution characteristics of each scale. The detailed calculation method is exhibited in Appendix A.

For the time series satisfying the multifractal feature, the logarithmic partition function lnMq(T) and the logarithmic time length lnT should have a good linear relationship. Figure 1 shows the lnMq(T) ~ lnT curve clusters with different values of q of the eight slumps. q, a weight factor, denotes the specific gravity of different probability measures for the partition function Mq(T).

It can be seen from Figure 1 that no matter what value q takes, lnMq(T) ~ lnT has a good linear relationship and shows scale invariance when $|\ln T| < 5$. This result is strong evidence of the existence of a multi-scale relationship in the SSECI time series, indicating that the price fluctuation of each scale obeys the multifractal random walk.

Figure 2 gives the generalized correlation dimensions Dq with different values of q.

Figure 2 illustrates that $D_0 > D_1 > D_2 > \ldots > D_\infty$ for all eight slumps. It is only if $D_0 = D_1 = D_2 = \ldots > D_\infty$ that the fractal is uniform, so the eight slumps all have a multifractal structure. As q increases, Dq decreases. When q > 180, Dq changes very little, so $D_\infty = D_{180}$ is a reasonable consideration.

Singular intensity α and the multifractal spectrum f(α) are calculated according to Formulas (A1)–(A3) in the Appendix A. Figure 3 shows the singular spectrum of each slump.

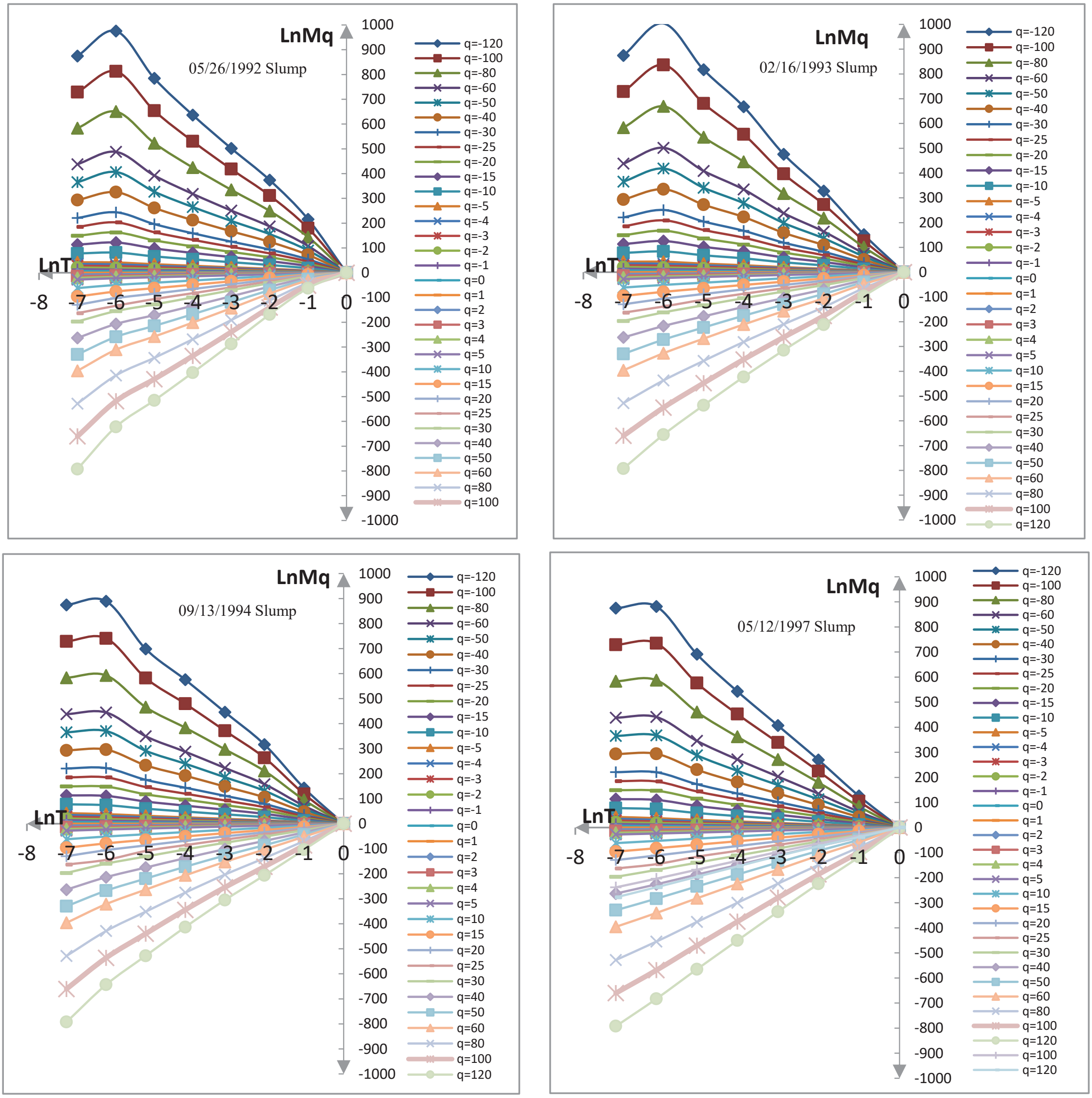

Figure 1. *Cont.*

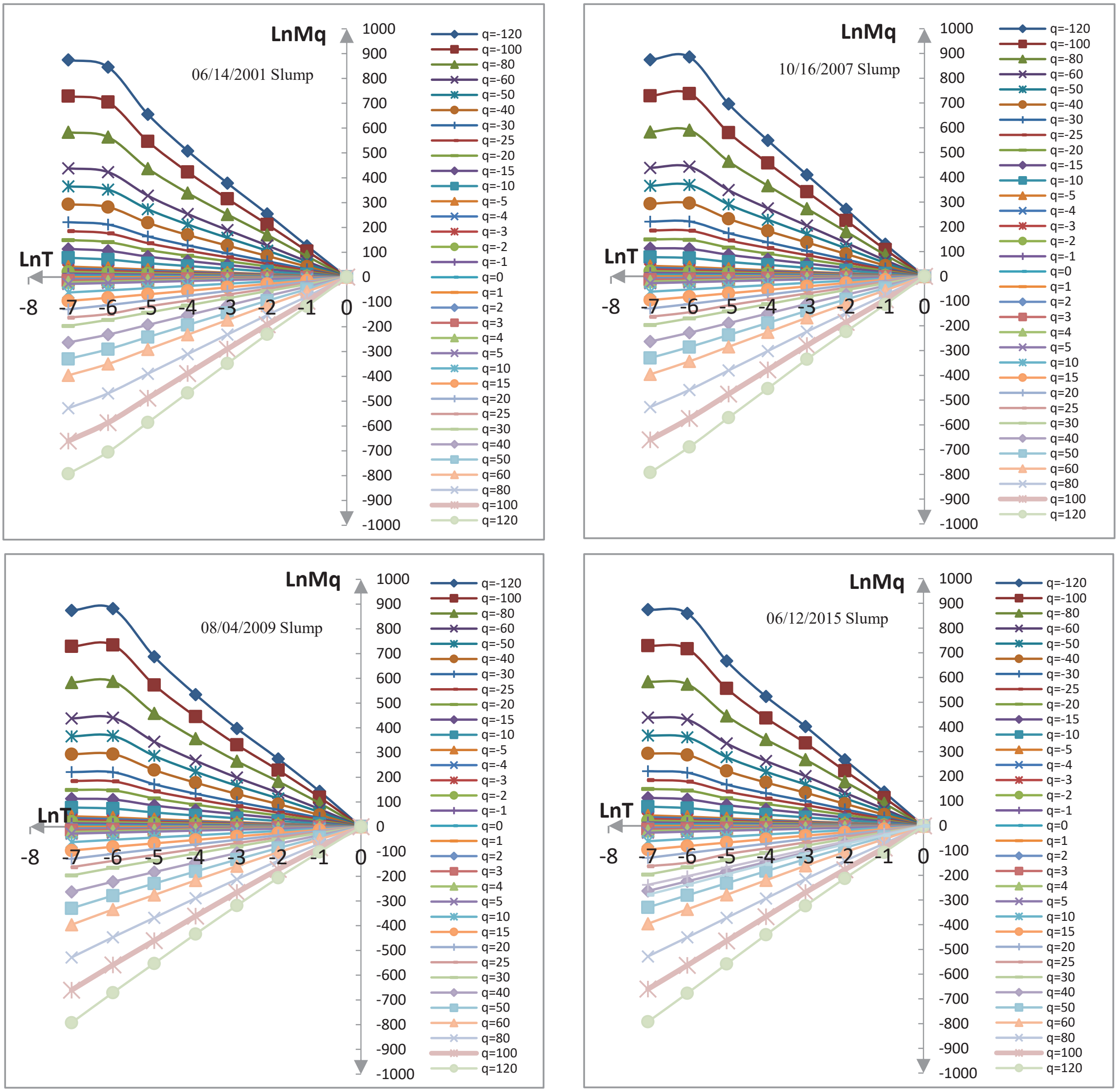

Figure 1. Curves of lnMq(T) vs. ln(T) with different values of q.

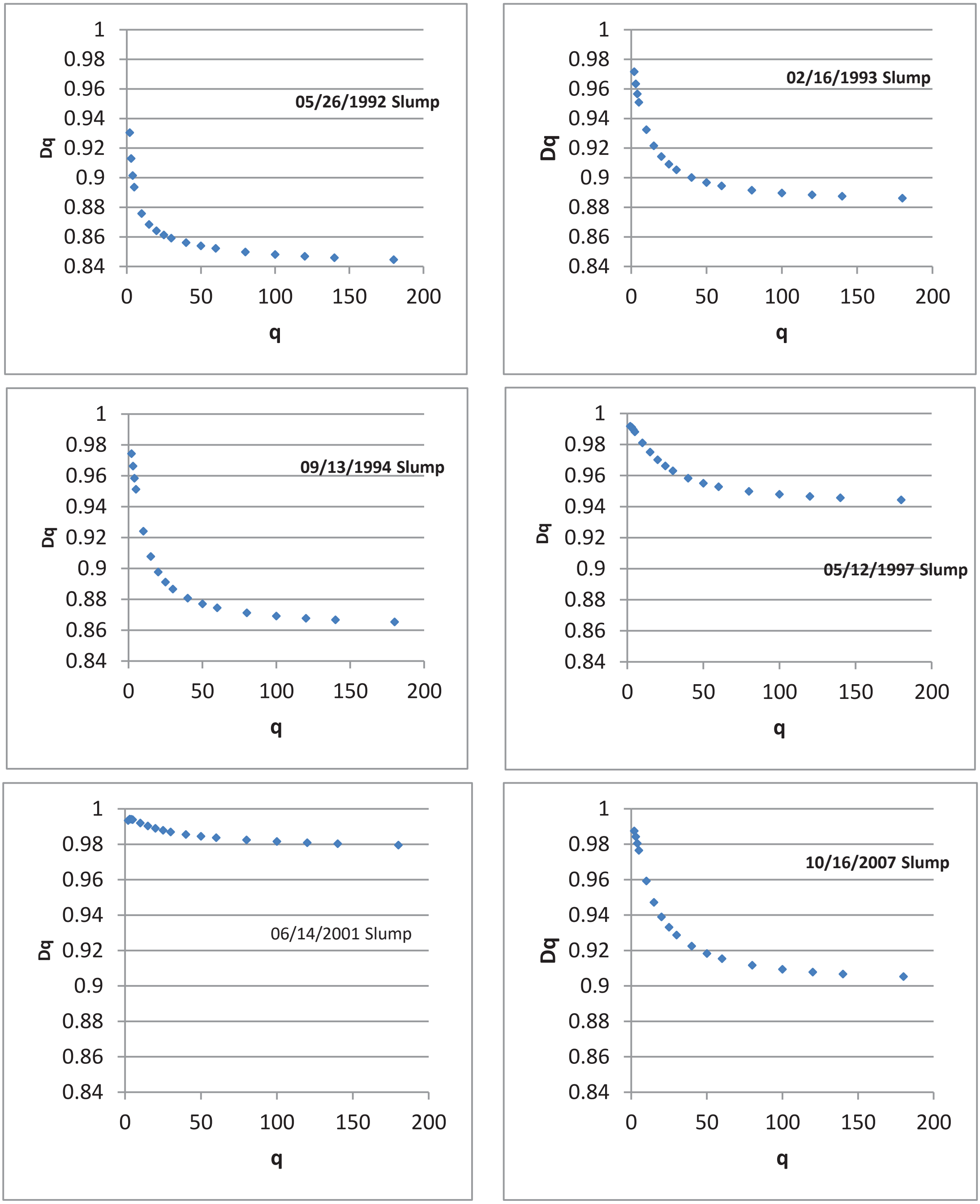

Figure 2. *Cont.*

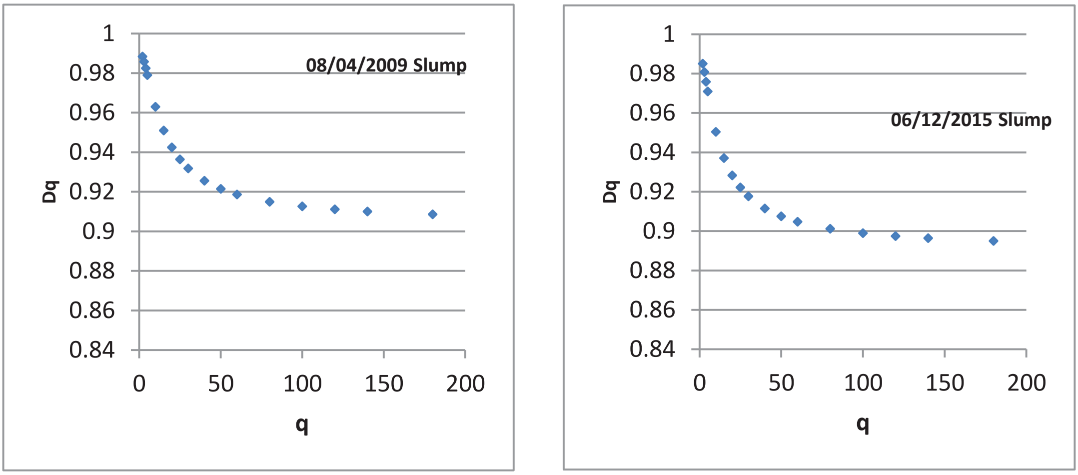

Figure 2. Generalized correlation dimensions Dq with different values of q.

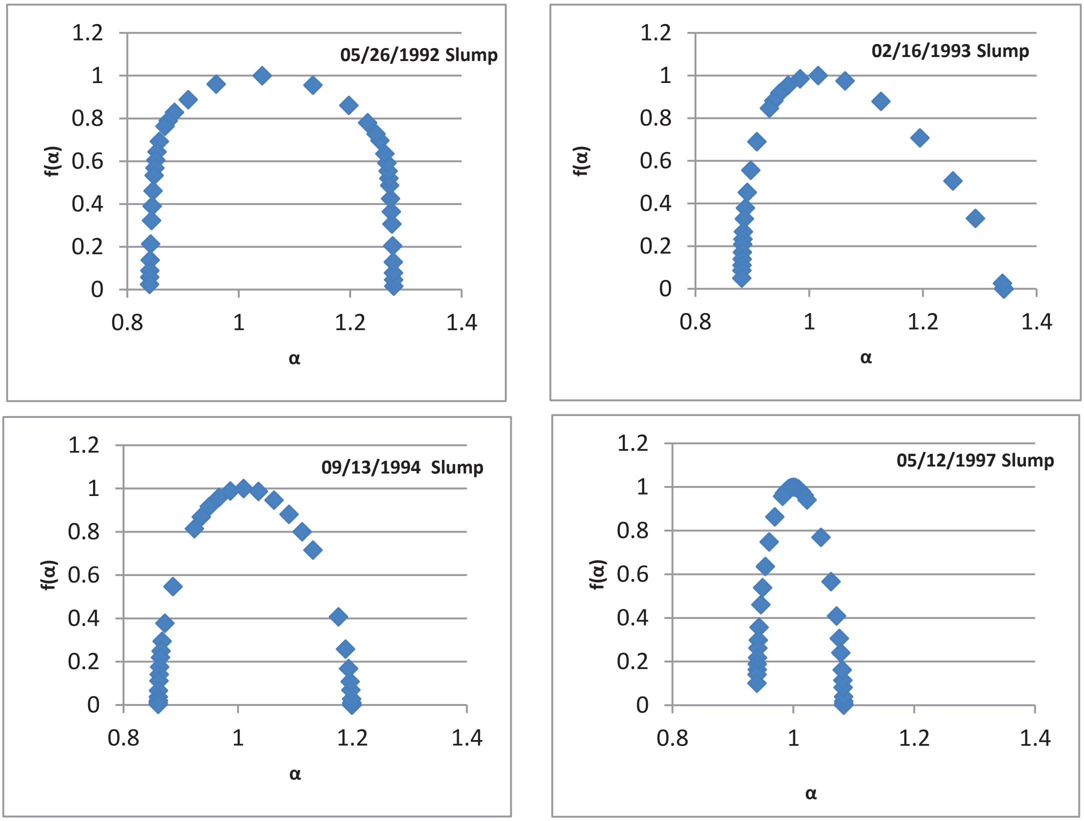

Figure 3. *Cont.*

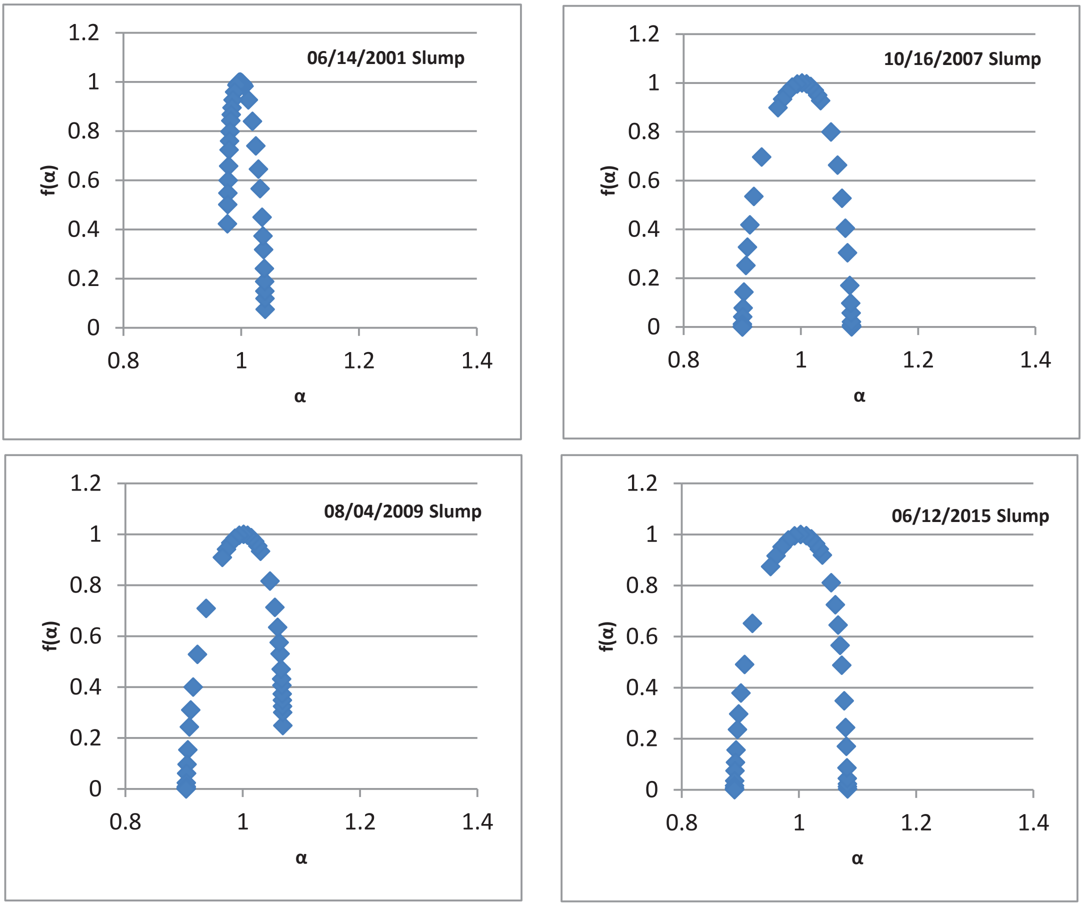

Figure 3. The multi-fractal spectra f(α) for the slump records of the SSECI.

The value of α is determined by the information radiated from the dynamic process of the normalized SSECI, and the range of its value indicates the size of the distribution range of a singular intensity. The spectrum span of the slumps in 1992, 1993, and 1994 are relatively large, indicating that the amplitude of the SSECI are relatively large at that time. Strong multifractal characteristics mean more obvious nonlinear fluctuations. In addition, the asymmetry of the singular spectrum reflects the variation range of the scale index caused by large or small fluctuations. It can be seen from Figure 3 that the singular spectra of the 1992 and 2007 slumps are symmetric, indicating that the scale range of the long range correlation caused by the small or large fluctuation of the SSECI is constant. For the 2009 and 2015 slumps, the peak of the fractal spectrum is right-biased, and its left end is significantly lower than the right end, so the α ~ f(α) spectrum belongs to the dense distribution of buying power dominated, which means higher normalized prices dominate the multifractal behavior of the SSECI change, and the stock collapse occurs at the time when the SSECI tends to rise. Apart from the 1993, 1994, 1997, and 2001 slumps, the peak of the fractal spectrum is left-biased and the right end is significantly lower than the left end, and the α ~ f(α) spectrum belongs to the sparse distribution of abnormal prices, which means the lower normalized prices dominate the multifractal behavior of the price change, and the stock collapse occurs at the time when the SSECI tends to decline.

For a certain scale, $\Delta\alpha$ reflects the inhomogeneity degree of the probability distribution measure on the whole fractal structure and the complexity of the process, and reflects the amplitude of fluctuation of the SSECI data. The greater $\Delta\alpha$ is, the more uneven the uncertainty distribution of the SSECI is, the more violent the data fluctuation is, and the greater vitality the stock market presents. Δf equals the ratio of the number of peak and trough positions of the SSECI under the condition that the scale remains unchanged. $\Delta f > 0$ indicates that for each group of data, the number of the SSECI reaching the highest point is more than what it reached at the lowest point. $\Delta f < 0$ means that the number of the SSECI that reached the highest point is less than that which it reached at the lowest point. $R = (\alpha_0 - \alpha_{\min})/(\alpha_{\max} - \alpha_0)$, which is called the deflection coefficient of the multifractal spectrum and reflects the asymmetry degree of the curves. If $R > 1$, the vertex of the spectrum is skewed to the right, and a larger R corresponds to a more right-oriented deviation. If $R < 1$, the vertex of the spectrum deviates to the left, and a smaller R corresponds to a more left-oriented deviation. If $R = 1$, the spectrum has a symmetric shape. So, the three parameters (R, $\Delta\alpha$, and $\Delta f(\alpha)$) of the multifractal spectrum can perfectly express the characteristic change of the multifractal spectrum of each stock collapse. Table 2 gives the $\Delta\alpha$, Δf, and R obtained from the multifractals of eight stock collapse processes; here, $\Delta\alpha$ and Δf are equal to the differences between α and $f(\alpha)$ when q is 2 and 180, individually.

Table 2. The value of $\Delta\alpha$, Δf, and R for the eight slumps.

No.	Slumps	$\alpha_{\max}$	$\alpha_{\min}$	$\Delta\alpha$	α_0	R	$f(\alpha_{\max})$	$f(\alpha_{\min})$	Δf
1	26 May 1992	1.2782	0.8401	0.4381	1.0422	0.8564	0.0158	0.0247	−0.0089
2	16 February 1993	1.3423	0.8815	0.4608	1.0159	0.4118	0	0.0501	−0.0501
3	13 September 1994	1.1991	0.8605	0.3386	1.0097	0.7878	0	0.0030	−0.003
4	12 May 1997	1.0834	0.9396	0.1438	0.9998	0.7205	0.0007	0.1013	−0.1006
5	14 June 2001	1.0406	0.9764	0.0642	0.9979	0.5030	0.0754	0.4233	−0.3479
6	16 October 2007	1.0865	0.9003	0.1862	1.0019	1.2022	0.0001	0.0002	−0.0001
7	4 August 2009	1.0683	0.9036	0.1647	1.0014	1.4618	0.2491	0.0002	0.2489
8	12 June 2015	1.0828	0.8900	0.1928	1.0029	1.4146	0.0033	0.0005	0.0028

Note: $\alpha_{\max}$ and $\alpha_{\min}$ are the corresponding values when $q = 2$ and $q = 180$. $\Delta\alpha = \alpha_{\max} - \alpha_{\min}$; $\Delta f = f(\alpha_{\max}) - f(\alpha_{\min})$.

As can be seen from Table 2, the values of $\Delta\alpha$ for the various slumps are different, which indicates that the heterogeneity degree of probability measure distribution on the whole fractal structure and the complexity of the process are also different. The different Δf represents that each slump occurs in a different upward or downward trend of the SSECI.

4. The Impact of Policies, Market Institutional Conditions, and Investors' Rationality on the Stock Market Multifractals

The ups and downs of China's stock market are affected seriously by policy intervention, investors' sentiment, and stock market institutional arrangements. Therefore, its fractal characteristics should also be correlated with them. It can be explored by the comparative analysis of the fractal dimension of the eight slumps which took place under different market conditions.

4.1. The "Stock Market Expansion" Policy Leads to a Smaller Fractal Dimension of the Stock Collapse

As can be seen from Figure 2, the values of fractal dimension D_∞ for the eight slumps are between 0.84–0.98. The smaller the D_∞ is, the greater the non-uniformity of the spatial distribution of speculative trading behavior is, the stronger the vulnerability of the stock market is, and the deeper the slump declines. The fractal dimension is negatively correlated with the depth of the slump. However, when the speculative trading activities have relatively weak non-uniformity in the market trading space, the D_∞ is larger. This is consistent with the eight slumps of the SSECI. For example, the 1992 slump had the smallest fractal dimension, $D_\infty = 0.8446$, and the slump lasted for 5 months, with a maximum decline of 72%; the 2001 slump had the highest fractal dimension, $D_\infty = 0.9795$, and the slump lasted for 48 months, with a maximum decline of 55%, reflecting the fact that the consistency of the former speculative transaction is greater than that of the latter. So, the fractal dimension D_∞ could represent the concentration degree of stock market bubbles and speculative trading activities and the consistency degree of stock market trading.

We further observed that the 1993 collapse triggered by the policy of "old eight shares expansion", the 2001 collapse triggered by the "reduction of state-owned shares", and the 2007 collapse triggered by the "lifting the ban of the non-tradable shares", all of which were meant to expand the stock market. However, the other five slumps were triggered by various policies aimed at alleviating the market frenzy, including raising the stamp duty, imposing limits on the rise or fall of stock price, raising the reserve requirement ratio, deleveraging, and so on. It can be found that the market expansion policy as a trigger could makes the collapse more serious under the same fractal dimension, or the fractal dimension value increases under the same crash intensity.

The reason why the market expansion policies as a trigger bring so strong a slump effect is that the price of the new expanded share is usually lower than that of the shares in circulation, but only a small part of the privileged people have the priority to buy it, which provides opportunity for them to cash out at a high margin. Legally speaking, such a share expansion is not in line with the spirit of contract. However, it was once considered to be a financial innovation to serve the state-owned companies' development in China. So, as soon as the share expansion is announced, the stock prices will go down, reflecting shareholders' resistance and rebellion to such "innovation".

4.2. The Mature Market Conditions Reduce the Width of the Fractal Spectrum of the Slump

Figure 3 shows that the $\Delta\alpha$ values of the collapses in 1993, 1994, and 1997 are larger than those of the last five collapses. The reason for this is because China's stock market was in the start-up period before 1997, and the stock market lacked unified laws and regulations for stock issuance examination and approval management. After 1997, especially with the promulgation of <the Procedures for Approval of Stock Issuance> by the China Securities Regulatory Commission (CSRC) on 6 March 2000, the institutional arrangement of the securities market gradually advanced from being "government-led" to "market-oriented".

It can be seen that, compared with immature market conditions, relatively mature market conditions will reduce the range of price fluctuations, and the span of the corresponding slump spectrum is narrower, that is, the $\Delta\alpha$ value is becoming smaller, indicating that the non-uniformity of the SSECI distribution decline, and the intensity of price fluctuations near the collapse is lower.

4.3. The Investors' Rationality Affects the Time of Stock Collapse

From Table 2 and Figure 3, for the 1992, 1993, 1994, 1997, and 2001 slumps, $R < 1$, and the α-$f(\alpha)$ spectra all belong to the sparse type, meaning the selling prices dominate the multifractal behavior of price change, meaning the price has a tendency to go down. Meanwhile, $\Delta f < 0$ indicates that the slumps occur at the position where the selling power dominates the stock price movement.

For the collapse in 2007, $R > 1$, and the $\alpha \sim f(\alpha)$ spectrum belongs to an intensive type, meaning the buying power dominates the multifractal behavior of price change. However, $\Delta f = -0.0001 < 0$, indicating that the rising trend of the SSECI is accompanied by local turbulence.

For the slumps in 2009 and 2015, $R > 1$, the $\alpha \sim f(\alpha)$ spectra belong to the intensive type, indicating that the collapses occur at the position where the buyer power dominates the multifractal behavior of price change, and the stock price tends to rise. $\Delta f > 0$ indicates that the slumps occur at the position where the buying power dominates the stock price movement. The larger Δf is, the nearer the SSECI is to peak.

The rationality of investors could be a good reason for explaining the above phenomenon. Stock traders in China exhibit different characteristics in different periods: the first generation of traders (who entered the stock market in the early 1990s) entered the new securities market with some certain blindness, and were attracted only by the myth of making money during the stock market boom. Most of them lacked professional knowledge, and had weak risk awareness. The second generation (who entered the stock market in the early 2000s) mastered some trading techniques, most of them were well-educated and had a certain risk awareness, but still were far from being rational traders. The 3rd generation (who entered the stock market in the second half of the 2000s) were more rational and matured in the investment mentality, and their risk tolerance tended to increase. The fourth generation (who entered the stock market around and after the 2010s), called ultra-sophisticated individualists by some scholars, were highly intelligent, unscrupulous, and manipulated different applications of stock speculation technology in the bull and bear market. Their risk traits: "Be greedy when others are fearful, and be fearful when others are greedy". They wanted to get high investment returns by leveraging up during the stock market boom, but at the first sign of trouble, they were quick and desperate to get out of the market, even at any cost. This inevitably led to a stampede on the stock market. Such traders would be bound to increase volatility in China's stock market, and could result in the slump which took place at the position where the buyers' power still dominated the price movement ($\Delta f > 0$).

5. Fractal Prediction of Stock Market Slump

According to the multifractal analysis in section IV, a percussive anomaly characteristic exists before and after the largest volatility of the SSECI: when the large volatility approaches, the opening of the bell-shaped spectrum is obviously widened, its top becomes round, the spectrum tends to be right (or left)-biased, and the right (or left) end of the spectrum is significantly lowed. Just after the biggest fluctuations, the opening of the spectrum will quickly become smaller, and the top of the spectrum will revert back to sharp from smooth.

In order to illustrate clearly how the desired multifractal parameter changes as it approaches the point of crisis, we calculated the eight slumps' multifractal parameters of crisis phenomena in the moving window mode, when the parameters are calculated for a part of the time series that slides along it with a certain step. Considering that $|\ln T| < 5$ is the fractal scale-free range, we here choose 16 trading days as the window width. Figure 4 shows the temporal spectrum of the multifractal spectrum for eight slumps in nine stages of the SSECI calculated using the method demonstrated in the Appendix A. Stage 5 is the crash period, Stage 4 and 6 are near the crash period, Stage 3 and 7 are before and after the large shock period, Stage 2 and 8 are at the beginning and end of the abnormal fluctuations, and Stage 1 and 9 are the normal periods far from the crash.

As can be seen from Figure 4, the multifractal spectrum curves of the SSECI time series at each stage of the eight slumps are different in shape, and the spectrum parameters change significantly, which indicates that the distribution structure of the SSECI fluctuations is very complex. Comparing the multifractal spectra of the eight slumps at different stages, it can be found that:

1. When the SSECI fluctuate in a normal state (corresponding to the stage 1 and 2 in Figure 4), the top of the bell-shaped spectrum is relatively sharp, the opening is narrow, and the curve is concentrated in a very small range, which indicates that the stock market is in disorder, and stock price fluctuation is relatively stable.
2. When the SSECI oscillation become larger (corresponding to the stage 3 and unit 4 in Figure 4), the opening of the $\alpha \sim f(\alpha)$ spectrum changes from narrow to wide, the top becomes round from sharp, the span widens significantly, and the left or right endpoints drop. The long-term correlation of the stock market system gradually accumulates under the effect of the cluster effect, and the system approaches the critical state.

3. At the biggest oscillation stage (corresponding to the stage 5 in Figure 4), the opening of the bell-shaped spectrum widens to the maximum and the top becomes the most round and flat. It shows that the stock price fluctuates very violently at this stage, which is caused by the turbulence inside the system.

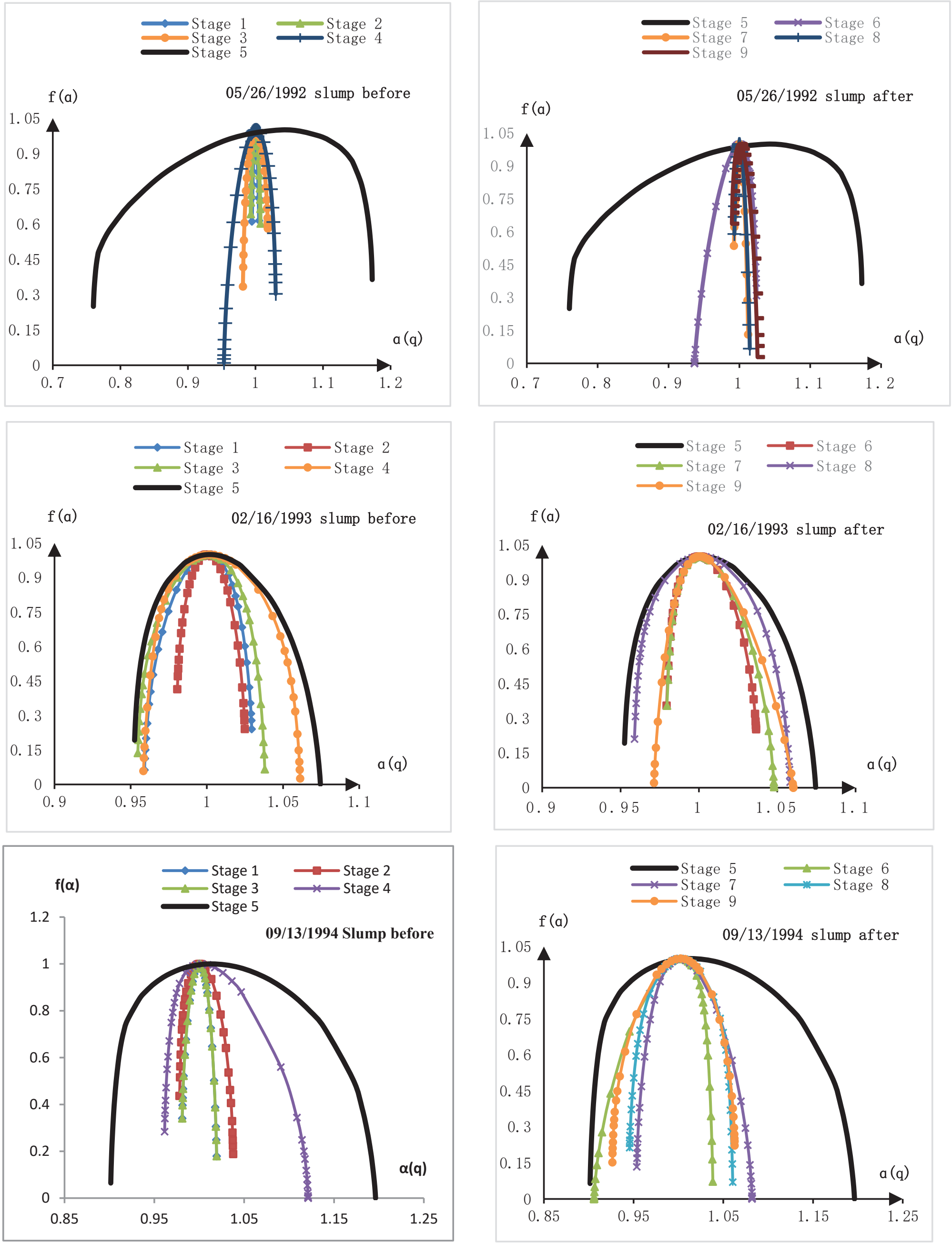

Figure 4. *Cont.*

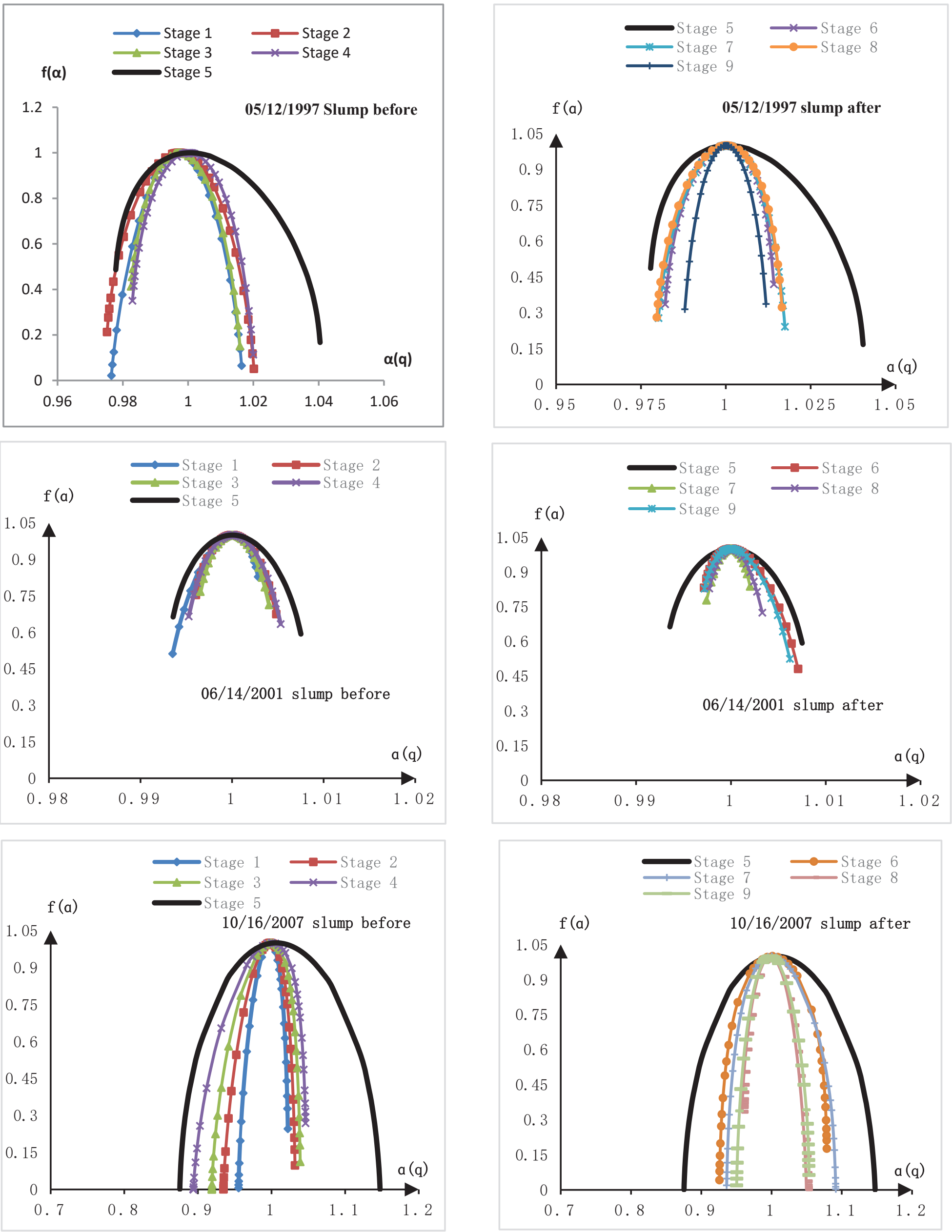

Figure 4. *Cont.*

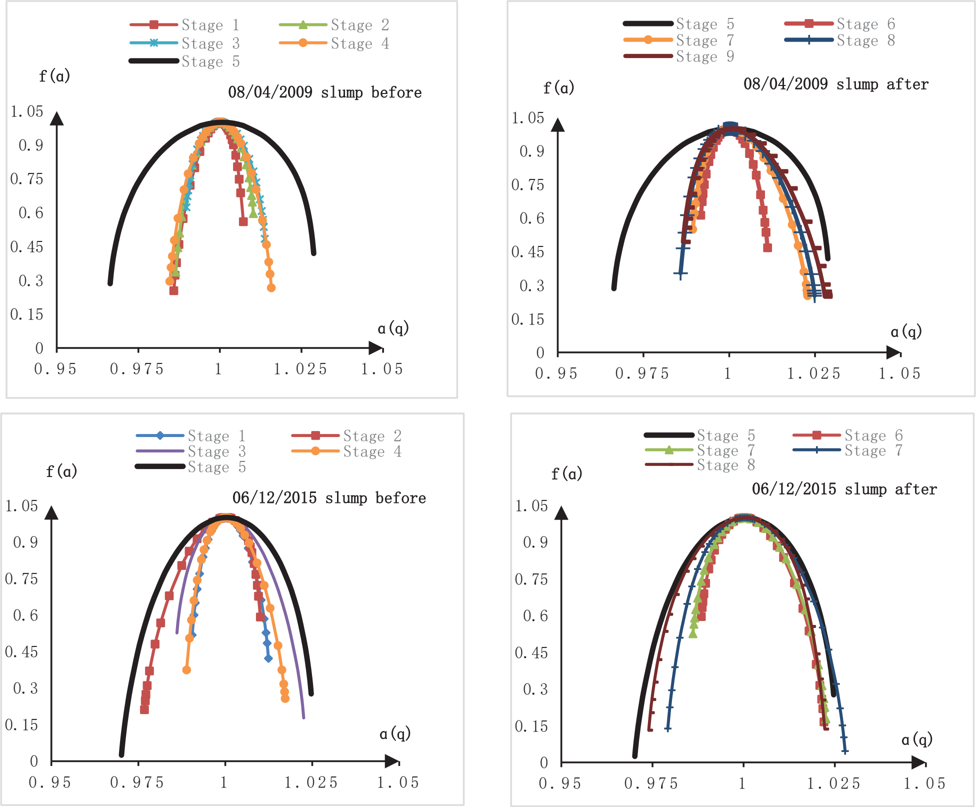

Figure 4. The temporal spectrum of the multifractal spectrum for eight slumps.

4. At stage 6 and 7 in Figure 4, the sharp swings tend to abate, the span of the $\alpha \sim f(\alpha)$ spectrum narrows rapidly, and the top becomes slightly round from round. These characteristics suggest that sustained declines have been followed by a rebound in stock prices, accompanied by partial declines.
5. At stage 8 and 9 in Figure 4, a certain period of time has passed after the sharp oscillation, the change of fractal spectra for each slump shows different features. The spectra of the slumps in 2001, 2007, and 2009 are dominated by the sparse type, indicating that stock prices mainly fall after a surge. For other slumps, the spectra have both a sparse and intensive type, indicating that stock prices will rebound to a certain extent after sustained sharp falls. These activities will evolve over time and will not end in a short time.

The alternating expansion and contraction of the multifractal spectrum just shows that the dynamic system of the stock trading is in an extremely unstable state before and after the sharpest fluctuations. As the slump approaches, the span of the $\alpha \sim f(\alpha)$ spectrum gradually widens, the top becomes slightly round from sharp, and the value of $f(\alpha_{min})$ (or $f(\alpha_{max})$) drops quickly. When the opening of the spectrum becomes narrower and the top becomes sharper, it indicates the end of abnormal stock price movements. These appearances reflect the changes in the complexity of the fractal structure of the SSECI series, which provide the precursory information with predictive significance for the beginning and end of the stock slump.

6. Conclusions

This paper uses the SSECI daily data to calculate China's stock market multifractal parameters, and explores the impact of the policy interventions, institutional conditions, and the investors' characteristics on the fractal parameters. We find that the shape of the multifractal spectrum and the changes of its parameters have certain rules; the policy interventions, market conditions, and investors' trading features can obviously influence the time and intensity of the collapse. The specific conclusions are as follows:

1. The stock market collapse process has self-similar characteristics in a limited scale, which can be studied and analyzed using multifractal theory;
2. The fractal dimension of stock slumps triggered by the "stock market expansion" policy is smaller than those of stock slumps triggered by measures to alleviate stock market overheating such as raising the reserve ratio and stamp duty, deleveraging, etc., and the non-uniformity of the fractal structure of the former is less than that of the latter.
3. The maturity of market conditions and the institutional arrangement of the stock market affect $\Delta\alpha$, which represents the intensity of stock price fluctuations. The larger $\Delta\alpha$ is, the speedier the stock price rises. The slumps in 1992, 1993, and 1997, with a relatively deeper drop, correspond to the higher $\Delta\alpha$ values, while the other five stock slumps with a relatively smaller drop correspond to the lower $\Delta\alpha$ values.
4. The rationality of the traders affects the time of stock collapse. The first five slumps occurred in the status where the seller power dominated the stock price, but the subsequent three slumps happened at the position where the buying power dominated the market prices, which suggests that traders possess "ultra-sophisticated individualists" characteristics. Their foreknowledge of impending risks brings forward the timing of stock crashes and enhances the $\Delta\alpha$.
5. The temporal spectrum of the $\alpha \sim f(\alpha)$ fractal spectrum has a good precursor property of collapse. The alternating relaxation and contraction of the multifractal spectrum just shows that the dynamic system of stock prices is in an extremely unstable state before and after the sharpest fluctuations. As it approaches the critical state, the span of the $\alpha \sim f(\alpha)$ spectrum widens quickly, the top becomes round from sharp, and the value of $f(\alpha_{\min})$ (or $f(\alpha_{\max})$) drops sharply. When the opening of the spectrum becomes narrower and the top becomes sharper, it indicates the end of the abnormal stock price movements.

Due to the parameters of the multifractal spectrum being subject to the influence of policy interventions, institutional arrangement, and investors' rationality, it is necessary to take into account their impact when fractal spectrum parameters are used to guide risk management or to construct risk measure indexes.

Funding: This research was funded by the Scientific Research and Innovation Project of China University of Political Science and Law, grant number 20ZFG79001, and the Humanities and Social Science Foundation of the Ministry of Education of China, grant number project 19YJA790046.

Informed Consent Statement: This research article describing a study do not involve humans.

Data Availability Statement: The SSECI data is at https://www.wind.com.cn/.

Conflicts of Interest: The authors declare no conflict of interest.

Appendix A. The Method of Calculating Multi-Fractal Parameters

Multi-fractal parameters are composed of fractal sets of several sub-fractal dimensions, which involve all of the non-integer fractal dimensions considered. Kantelhardt developed the multifractal detrended volatility analysis (MF-DFA) by extending the one-dimensional detrended volatility analysis (DFA) method [22]. Although some scholars used the MF-DFA method to analyze the financial time series and showed that the Chinese stock market had multifractal characteristics [10,23], Thomas Lux's research on the New York and German stock markets showed that the MF-DFA method could not diagnose whether multifractals really existed in the financial data [24]. Therefore, we apply the method of multifractal statistical physics here, which is a generalization of the box-counting method and has been used in some of the literature [5,14]. Compared with MF-DFA, the statistical physical method greatly reduces the computational complexity and has a larger scale invariant range for irregular multifractals. Applying the multifractal statistical physics to financial analysis, the steps to solve the multifractal spectrum are as follows:

(1) To cover the one-dimensional time series by the "box" with the scale of T, that is, divide it into non-overlapping intervals according to the unit time scale T.
(2) Normalize each data, let probability measures $\mu_i(T) = \frac{p_i}{\Sigma p_i}$ and $\Sigma\mu_i = 1$; μ_i is the sum of the i-th interval data with time scale T and p_i is the sum of the stock indices collected in the i-th interval with scale T.
(3) To calculate the partition function Mq(T) of a multi-fractal system which is defined as the weighted sum of the probability μ_i(T) to the q power:

$$M_q(T) \equiv \sum_{i=1}^{n} \mu_i^q(T) \tag{A1}$$

Here, n is the total number of time windows whose time length is T, and q is the real number in $(-\infty \sim +\infty)$.

Different q values denote the specific gravity of different probability measures of μ_i for the partition function Mq(T). When q is positive, the larger q is, the greater weight of the larger value of the probability measure of μ_i will be. It describes the dense areas. When q is negative, the greater the absolute value of q is, the greater the weight of the smaller value of the probability measure μ_i will be, which is the sparse area.

For the multi-fractal distribution, the partition function has the following scaling relationship with the time length T:

$$Mq(T) \propto T^{h(q)} \tag{A2}$$

(4) Formula (A2) gives the curve lnMq(T) ~ lnT, if there is a good linear relationship between lnMq(T) and lnT, the distribution belong to a multi-fractal distribution. The slope of the curve h(q) can be estimated by the least square regression of the lnM ~ lnT, fitting to the points in the scale-free interval (namely the linear interval), and lnA is the residual of the regression.

$$\ln(M_q(T)) = h(q)\ln T + \ln A \tag{A3}$$

(5) If the time series studied have multi-fractal properties, the following equation can be obtained by using the statistical physics method and Legendre transformation:

$$\tau\,(q) = qh(q) - 1 \tag{A4}$$

$$\alpha(q) = d\tau(q)/dq = h(q) + qdh(q)/dq \tag{A5}$$

$$\Delta\alpha = \alpha_{max} - \alpha_{min} \tag{A6}$$

$$f(\alpha) = \alpha q - \tau(q) = q(\alpha - h(q)) + 1 \tag{A7}$$

$$\Delta f = f(\alpha_{max}) - f(\alpha_{min}) \tag{A8}$$

$$D_q = \frac{\tau(q)}{q-1} \tag{A9}$$

Here, $\tau(q)$ stands for the mass index, $\alpha(q)$ is the singular index, $f(\alpha)$ is the multi-fractal spectrum, and Dq is the generalized fractal dimension.

Appendix B. Notes

1. "August 10 incident": On August 10, Shenzhen, in the fourth "1992 Stock Subscription Warrant" lottery. Five million application forms for the subscription of public offers were issued, and each person could buy 10 application forms with his/her ID card. All the application forms were sold out in less than half a day, but some people could not believe that and doubted about whether backdoor buying existed. That evening, thousands of people who failed to buy the form marched on Shennan Middle Road, carrying slogans of anti-corruption and justice, and sieged the Shenzhen municipal government and the People's Bank of China. The Shenzhen municipal government spent nearly the whole night coming up with a plan to issue an additional 0.5 million forms for the subscription of new shares, and the matter was put to rest gradually. That is called the "August 10 incident". It triggered a plunge in the Shanghai and Shenzhen stock markets.
2. "Old eight shares": From 1990 to 1992, in the initial "experimental phase", only eight stocks were listed in Shanghai, the so-called "old eight shares". They are Shanghai Shenhua electrician joint company, Shanghai Yuyuan tourist shopping mall CO, LTD, Shanghai Fila vacuum electronics CO, LTD, Shanghai CO, LTD, Zhejiang phoenix chemical CO, LTD Company, Shanghai Feile Audio CO, LTD, Shanghai Aiyang Electronic Equipment CO, LTD, and Shanghai Yanzhong Industrial CO, LTD.
3. The "327 Treasury bond": "327" is the code name of the Treasury bond futures contract. It is a 3-year Treasury bond which was issued in 1992 and matured in June 1995. The total amount of the bond issued was 24 billion Yuan. On 23 February 1995, Shanghai Wanguo Securities Company illegally traded 327 contracts, and in the last 8 min of the trading time, a total of 10.56 million selling orders were sold, with a face value of 211.2 billion Yuan of the Treasury bond. In the end, Wanguo lost 1.6 billion Yuan due to government intervention.
4. "The reduction of state-owned shares": This means that the state transfered the state-owned untradeable shares to other shareholders at the market price so that they could be circulated in the market. Since the number of shares held by the state was so large, even the state was to sell a small portion of its shares, meaning the market supply would suddenly increase and share prices would fall.
5. "Deleveraging": On 13 June 2015, the China Securities Regulatory Commission (CSRC) issued a statement on Sina Weibo, "Securities companies are prohibited to facilitate over-the-counter capital allocation activities" and strictly investigated the capital allocation, causing the stock market to plunge.
6. "Ultra-sophisticated individualists": The term "Ultra-sophisticated individualists", as well as the term "extreme refined individualists", was first put forward by Professor Qian Liqun of Peking University when he spoke about the talent cultivation of China's university education. He said "They are highly intelligent, secular, sophisticated, good at performance, know how to cooperate, and are better at using the system to achieve their goals". Once this concept was put forward, it not only spread widely in the Chinese scholar circle, but also became the truest portrayal for some personal behaviors in real life. Here, it refers to such market traders who make extreme use of all the modern technology, resources, and system defects to maximize their interests. It can be said that this is the root of the over-the-counter stock market allocation system which was played to the extreme in 2015, and also the social root of the slump of the Chinese stock market in 2015.

References

1. Mandelbrot, B.B. A multifractal walk down wall street. *Sci. Am.* **1999**, *5*, 20–23. [CrossRef]
2. Stosic, D.; Stosic, D.; Stosic, T.; Stanley, H.E. Multifractal properties of price change and volume change of stock market indices. *Phys. A Stat. Mech. Its Appl.* **2015**, *428*, 46–51. [CrossRef]
3. Andreadis, I.; Serletis, A. Evidence of a random multifractal turbulent structure in the Dow Jones industrial average. *Chaos Solitons Fractals* **2002**, *13*, 1309–1315. [CrossRef]

4. Fulco, U.L.; Lyra, M.L.; Petroni, F.; Serva, M.; Viswanathan, G.M. A stochastic model for multifractal behavior of stock prices. *Int. J. Mod. Phys. B* **2004**, *18*, 681–689. [CrossRef]
5. Ho, D.S.; Lee, C.K.; Wang, C.C.; Chuang, M. Scaling characteristics in the Taiwan stock market. *Phys. A* **2004**, *332*, 448–460. [CrossRef]
6. Cont, R.; Potters, M.; Bouchaud, J.P. *Scaling in Stock Market Data: Stable Laws and Beyond*; Springer: Berlin/Heidelberg, Germany, 1997; Volume 7, pp. 75–85.
7. Wang, B.H.; Hui, P.M. The distribution and scaling of fluctuations for Hang Seng index in Hong Kong stock market. *Eur. Phys. J. B* **2001**, *20*, 573–579.
8. Zhuang, X.T.; Huang, X.Y.; Sha, Y.L. Research on the fractal structure in the Chinese stock market. *Phys. A* **2004**, *333*, 293–305. [CrossRef]
9. Sun, X.; Chen, H.; Yuan, Y.; Wu, Z. Predictability of multifractal analysis of Hang Seng stock index in Hong Kong. *Phys. A* **2001**, *301*, 473–482. [CrossRef]
10. Chen, D.-R.; Liu, C.; Zhang, Y.-C.; Zhang, Z.-K. Predicting Financial Extremes Based on Weighted Visual Graph of Major Stock Indices. *Complexity* **2019**, *5320686*, 1–17. [CrossRef]
11. Zhuang, X.; Wei, Y.; Ma, F. Multifractality, efficiency analysis of Chinese stock market and its cross-correlation with WTI crude oil price. *Phys. A Stat. Mech. Its Appl.* **2015**, *430*, 101–113. [CrossRef]
12. Du, G.; Ning, X. Multifractal properties of Chinese stock market in Shanghai. *Phys. A Stat. Mech. Its Appl.* **2008**, *387*, 261–269. [CrossRef]
13. Chen, W.; Wei, Y.; Lang, Q.; Lin, Y.; Liu, M. Financial market volatility and contagion effect: A copula–multifractal volatility approach. *Phys. A Stat. Mech. Its Appl.* **2014**, *398*, 289–300. [CrossRef]
14. Li, Y.; Vilela, A.; Stanley, H.E. The institutional characteristics of multifractal spectrum of China's stock market. *Phys. A Stat. Mech. Its Appl.* **2020**, *550*, 124129. [CrossRef]
15. Li, Y. Multifractal view on China's stock market crashes. *Phys. A Stat. Mech. Its Appl.* **2019**, *536*, 122591. [CrossRef]
16. Olga, M.; Veronica, N. The use of fractal dimension calculation algorithm. *Agents Actions* **2007**, *25*, 234–236.
17. Zhang, H.; Wei, D.; Hu, Y.; Lan, X.; Deng, Y. Modeling the self-similarity in complex networks based on Coulomb's law. *Commun. Nonlinear Sci. Numer. Simul.* **2016**, *35*, 97–104. [CrossRef]
18. Gusso, A.; Mello, L.D. Fractal dimension of basin boundaries calculated using the basin entropy. *Chaos Solitons Fractals* **2021**, *153*, 2. [CrossRef]
19. Stelter, P.; Pfingsten, T. Calculation of the fractal dimension via the correlation integral. *Chaos Solitons Fractals* **1991**, *1*, 273–280. [CrossRef]
20. Liu, J.; Ding, W.; Dai, J.; Zhao, G.; Sun, Y.; Yang, H. Unreliable determination of fractal characteristics using the capacity dimension and a new method for computing the information dimension. *Chaos Solitons Fractals* **2018**, *113*, 16–24. [CrossRef]
21. Imre, A.R. Artificial fractal dimension obtained by using perimeter–area relationship on digitalized images. *Appl. Math. Comput.* **2006**, *173*, 443–449. [CrossRef]
22. Kantelhardt, J.W.; Zschiegner, S.A.; Koscielny-Bunde, E.; Havlin, S.; Bunde, A.; Stanley, H.E. Multifractal detrended fluctuation analysis of nonstationary time series. *Phys. A Stat. Mech. Its Appl.* **2002**, *316*, 87–114. [CrossRef]
23. Gu, R.; Shao, Y.; Wang, Q. Is the efficiency of stock market correlated with multifractality? An evidence from the Shanghai stock market. *Phys. A Stat. Mech. Its Appl.* **2013**, *392*, 361–370. [CrossRef]
24. Lux, T. Detecting multi-fractal properties in asset returns: The failure of the scaling estimator. *Econ. Work. Pap.* **2003**, *15*, 481–491.

fractal and fractional

Article

Cross-Correlation Multifractal Analysis of Technological Innovation, Financial Market and Real Economy Indices

Jinchuan Ke *, Yu Duan, Chao Xu and Yue Zhang

School of Economics & Management, Beijing Jiaotong University, Beijing 100044, China
* Correspondence: jchke@bjtu.edu.cn

Abstract: Technological innovation, the financial market, and the real economy are mutually promoting and restricting. Considering the interference of market-noise information, this paper applies the wavelet-denoising method of the soft- and hard-threshold compromise functions to process the original information so as to eliminate the noise information, and combines multifractal detrended cross-correlation analysis with the sliding-window approach, focusing on the change in the Hurst index and the parameter change in the multifractal spectrum to explore the interaction in between. The research results show that there is a certain cross-correlation among technological-innovation, financial-market, and real-economy indices. Firstly, the cross-correlation among them has significant multifractal characteristics rather than single-fractal characteristics. Secondly, the fractal characteristics reveal the long memory of the interaction among the three indices. Thirdly, there are also obvious differences in the degree of local chaos and volatility of the interaction. Fourthly, the cross-correlation among technological-innovation, financial-market, and real-economy indices has significant multifractal characteristics rather than single-fractal characteristics. In comparison, the cross-correlation multifractal characteristics among technological innovation, the financial market, and the real economy are time-varying, and the cross-correlation multifractal characteristics between the technological-innovation index and the real-economy index are the most obvious.

Keywords: technological innovation; finance; real economy; multifractal; denoising

Citation: Ke, J.; Duan, Y.; Xu, C.; Zhang, Y. Cross-Correlation Multifractal Analysis of Technological Innovation, Financial Market and Real Economy Indices. *Fractal Fract.* **2023**, *7*, 267. https://doi.org/10.3390/fractalfract7030267

Academic Editor: Leung Lung Chan

Received: 15 February 2023
Revised: 12 March 2023
Accepted: 15 March 2023
Published: 17 March 2023

1. Introduction

The financial market and the real economy have a mutually reinforcing relationship. The financial market provides the required financial support for the actual economy's development. The real economy serves as the tangible foundation for the growth of the financial market. Technological innovation empowers the traditional financial market and provides continuous vitality for the financial market's transformation and upgrading, whereas the financial market plays an indispensable role in accelerating entrepreneurial investment, technology realization, and production promotion. Technological innovation has stimulated innovative financial products and services to provide more efficient and convenient financing channels for the development of the real economy, fueled by cutting-edge technologies such as big data, artificial intelligence, cloud computing, blockchain, and mobile internet [1]. Technological innovation has increased the availability of financial services, raised the efficiency of capital distribution in the real economy, and played a key role in fostering the development of the real economy. Excessive integration and expansion of the financial market and technological innovation, on the other hand, can easily cause an imbalance in the financial-industry structure, separate the development of financial innovation from the real economy, and produce a risk-spillover effect, leading to a gradual decline in the financial market's and technological innovation's ability to serve the real economy [2].

Modern financial theory has transformed the analysis of this problem from qualitative to quantitative and has also produced a large number of scientific-analysis methods, such as financial-market microstructure theory, behavioral-finance theory, and fractal-market theory, in terms of the interrelationship between technological-innovation, financial-market, and real-economy indices. Because financial data frequently exhibit peak and thick tail features, self-similarity, long memory, and volatility concentration, the fractal-market theory based on nonlinear dynamic systems can accurately reflect the real condition of the financial market. Furthermore, fractal-market theory deviates from the original linear research paradigm by describing the price-fluctuation characteristics of financial markets in greater depth and detail [3]. Among these, the multifractal theory can express precise information about financial-asset values at diverse time scales and degrees of volatility [4,5], better capturing the financial market's complex nonlinear dynamic characteristics. Therefore, this research examines the relationship between technical-innovation, financial-market, and real-economy indices from a multifractal perspective.

2. Literature Review

The impact mechanism of technological innovation and the financial market on the development of the real economy is mainly manifested in that the financial market acts on technological innovation and the real economy from three aspects: provision of funds [6], innovation decentralization [7], and incentive supervision [8]. The financial market has gathered equity funds for technological innovation and provided financial support for the development of technological-innovation activities. Advanced technology promotes the development of the real economy and can effectively improve the innovation level and production efficiency of enterprises, make the industrial structure more reasonable, and then promote the development of the real economy. Technological innovation provides technical means for the development of financial markets, breaks through technical difficulties in financial markets, and enriches financial products. At the same time, the innovation-feedback effect brought by technological innovation also improves the financial system [9].

The interaction between technological innovation, the financial market, and the real economy has been a hot research topic in academic circles in recent years. Scholars have published papers about the impact of scientific and technological finance on economic development, and most of them believe that the use of industry-finance data or industry stock indices can roughly reflect the relevant performance between industries [10–12]. Dagar et al. constructed the technological-innovation-development index and used the GMM two-step test to draw the conclusion that technological innovation has a significant role in promoting the upgrading of industrial structure and can promote economic growth [13]. Qi and Li analyzed the stock-price data of listed companies in the manufacturing industry, summarized the dependency between the real economy and financial technology, and found that the various industries and technology companies in the real economy were greatly affected by the stock-price fluctuations of AI, blockchain, and large data-technology companies in financial technology, showing a positive correlation [14]. Peng and Ke employed the R-vine Copula approach to successfully examine the risk-spillover impact between financial technology and the real economy [15]. They chose stock-index samples to fit the residual tail features of the time series. Furthermore, some scholars use industry data to research and discover that there is a threshold effect in Fintech, which can support real-economy growth in the early stages of Fintech development and restrict real-economy growth in the later stages [16]. Some studies suggest that Fintech can improve the optimization and upgrading of industrial structure through basic technology innovation and development, hence encouraging economic growth [17]. The rise of financial technology has resulted in the pursuit of capital, with capital flowing to artificial intelligence, blockchain, and other underlying technologies, in combination with the industrial linkage effect, to drive the upgrading of industrial structure and thus promote high-quality economic development [18].

The concept of the fractal was first proposed by Mandelbrot, and the definition emphasizes the similarity between the whole and the part of the fractal [19]. Peters put forward the fractal-market hypothesis based on the fractal theory proposed by Mandelbrot. It is based on the nonlinear paradigm and believes that the capital market is a complex nonlinear dynamic system with the characteristics of interactivity and adaptability [20]. The market's information flow is frequently unstable, difficult to conform to conventional modeling assumptions, and frequently volatile. In contrast, the fractal statistical-analysis approach based on fractal and chaos theory can effectively explain the nonlinear fundamental features of the market. This makes it difficult for some standard statistical-analysis methods to characterize the volatility characteristics of the market.

Fractal-theory research techniques have seen constant innovation and development in recent years. The rescaled range analysis (R/S), put forth by the hydrologist Hurst, is particularly well liked in early fractal research [21]. Previous studies have confirmed that there is long-term autocorrelation in the capital market, which means that the capital market is not an efficient market [22,23]. However, the R/S analysis method is relatively sensitive to outliers and dependent on extreme values, so it is mostly used to analyze non-trending stationary time series, whereas the analysis of non-stationary time series is prone to errors. In order to study the non-stationary time series with trends, Peng et al. proposed the DFA analysis method [24]. This method introduces a long-term power–law relationship in time-series analysis to supplement short-term correlation conditions to avoid the occurrence of false correlation. The Hurst result calculated by the DFA method is more accurate than that estimated by the R/S analysis method. Subsequently, scholars introduced a multifractal on the basis of the DFA method and evolved it into a more applicable MF-DFA analysis method [25]. Gulich and Zunino conducted a comprehensive and systematic analysis of the algorithm to determine the parameters in the MF-DFA method and studied the natural time series to ensure the effectiveness of the algorithm [26]. Unfortunately, this method can only study the long-term correlation of a single time series. In view of this, the DFA method has been expanded into a DCCA method that can explore the cross-correlation between two non-stationary time series [27]. As a result, the DCCA approach has been steadily used to develop the MF-DCCA approach, which can accurately and quantitatively examine the multifractal properties of two cross-correlation time series [28]. This method can be used in the capital market to examine the cross-correlation [29].

The processing of economic or financial time series is the key to empirical analysis. If a large amount of noise data is directly used, it is very likely to bias the research results. The existing research results show that using special methods to denoise the time series can reduce the instability of the time series to a certain extent and ensure that the research results are more authentic and reliable [30]. In the early days, the moving average was one of the most widely used denoising methods. Although this method is simple, it is easy to remove much useful information when denoising [31]. The Fourier-transform filtering method is another traditional denoising method, but it can only be processed in the whole time domain and cannot give the change of the signal at the specific node. A small mutation of the signal is likely to affect the whole analysis result [32]. The wavelet-transform method is a relatively effective time-frequency denoising-analysis method that can overcome the shortcomings of the Fourier-transform method [33]. Common wavelet-denoising methods mainly include modulus maximum-reconstruction denoising and threshold denoising. Mallat proposed a denoising method based on modulus maxima. Its idea is to remove the amplitude extreme points that decrease with the increase in scale by observing the change rule of the modulus maxima of the wavelet transform at different scales and only retain the amplitude points that increase with the increase in scale so as to achieve the denoising effect [34]. This method is more suitable for the situation that the signal contains white noise and has many singular points and can effectively retain the information of singular points. The wavelet threshold denoising algorithm proposed by Donoho and Johnstone has been widely used because of its simple operation logic and good denoising effect [35]. In the wavelet-threshold denoising method, the selection of threshold function is also very important. The previously widely used hard-threshold function and soft-threshold function have some defects [36]. For example, the hard-threshold function preserves the points whose absolute value is greater than the threshold value and zeros the points whose absolute value is less than the threshold value. This processing causes sudden changes in the wavelet domain, resulting in local jitter of the results after denoising and discontinuity of the results. The defect of the soft-threshold function is that the derivative is discontinuous, and there is a constant deviation between the estimated wavelet coefficients and the wavelet coefficients of the processed signal. In addition, most de-noising processing has been successfully applied to various disciplines such as signal analysis, image processing, and seismic survey. The application of time series in the financial market or economic market is still in the exploration stage, but it can be expected that wavelet denoising has certain advantages in processing time-series data.

To sum up, the existing research on the interaction between scientific and technological innovation, the financial market, and the real economy is mainly focused on their impact, but few explore the multifractal characteristics between them from the perspective of cross-correlation. Moreover, most of the research is based on linear methods, and the sample data selected are based on the direct data of the market, ignoring the impact of noise information. Therefore, this paper firstly uses the wavelet-threshold denoising method to eliminate the noise impact in scientific- and technological-innovation, financial-market and real-economy indices; retain effective fluctuation information; and use the sliding-window segmentation method (SW) to optimize. Then, with the help of the MF-DCCA method in the nonlinear field, the cross-correlation fractal features are studied in terms of fractal multiplicity, long-term memory, similarity, and singularity of the fractal spectrum to better reveal the complex relationship.

3. Method

3.1. Wavelet-Threshold Denoising Method

The basic principle of wavelet-threshold denoising is to set a threshold to process high-frequency noise signals. Specifically, useful signals with wavelet coefficients greater than the threshold are shrunk and retained. The noise of the wavelet coefficient lower than the threshold value is eliminated. The one-dimensional signal model with noise can be expressed as [37]:

$$f(t) = s(t) + n(t) \tag{1}$$

where $f(t)$ is the signal with noise, $s(t)$ is the effective signal in the original signal, $n(t)$ is the noise signal, and t is the time variable.

Specifically, the denoising process of wavelet-threshold denoising can be divided into three steps. Firstly, the signal containing noise is decomposed by a wavelet. The appropriate wavelet-basis function and decomposition scale for wavelet decomposition is selected to obtain a set of wavelet coefficients. Secondly, the high-frequency coefficients of each layer of wavelet decomposition are processed by threshold quantization to obtain the estimated value of wavelet coefficients. Finally, the wavelet coefficients processed by threshold quantization are transformed by an inverse wavelet to reconstruct the signal and obtain the denoised signal.

The proper threshold function will affect the denoising effect. When the signal is decomposed, the wavelet coefficients need to be threshold processed. The commonly used threshold functions are divided into hard-threshold function and soft-threshold function [38]. The mathematical expression of the hard-threshold function is as follows:

$$\hat{\omega}_{j,k} = \begin{cases} \omega_{j,k} & \left|\omega_{j,k}\right| \geq \lambda \\ 0 & \left|\omega_{j,k}\right| < \lambda \end{cases} \tag{2}$$

where λ represents the threshold value, the estimated value of the wavelet coefficients is expressed by $\hat{\omega}_{j,k}$, and the wavelet coefficient of the j-th layer is represented by $\omega_{j,k}$.

The mathematical expression of the soft-threshold function is as follows:

$$\hat{\omega}_{j,k} = \begin{cases} sign\left(\omega_{j,k}\right)\left(\left|\omega_{j,k}\right| - \lambda\right) & \left|\omega_{j,k}\right| \geq \lambda \\ 0 & \left|\omega_{j,k}\right| < \lambda \end{cases} \tag{3}$$

However, the above threshold functions have certain limitations in practical applications. Therefore, the soft- and hard-threshold compromise function can be introduced to overcome the discontinuity problem in the hard-threshold function and reduce the constant deviation in the soft-threshold function. The expression is as follows:

$$\hat{\omega}_{j,k} = \begin{cases} (1-\mu)\omega_{j,k} + \mu sign\left(\omega_{j,k}\right)\left(\left|\omega_{j,k}\right| - \lambda\right) & \left|\omega_{j,k}\right| \geq \lambda \\ 0 & \left|\omega_{j,k}\right| < \lambda \end{cases} \tag{4}$$

where μ is the weighting factor, and is usually set to 0.5.

$$\lambda = \sigma\sqrt{2lnN} \tag{5}$$

$$\sigma = \frac{\sum_{k=1}^{n}\left|\hat{\omega}_{j,k}\right|}{0.6475n} \tag{6}$$

where σ is the mean square error of the j-th layer wavelet transform.

In the process of denoising, the selection of wavelet function is also very important. At present, there are dozens of wavelet functions that have been developed and applied. These wavelet functions are suitable for different situations due to their own characteristics. The most widely applied are Daubechies wavelet-basis function (dbN), Coiflet wavelet-basis function (coifN), and Symlets wavelet-basis function (symN). Different wavelet bases have different degrees of orthogonality, compact support, vanishing moment, and symmetry [39]. After the wavelet function with orthogonality is transformed, the correlation between wavelet coefficients will not be destroyed by the transformation, so it has high noise-reduction ability. The wavelet-basis function with compact support has better local noise resolution and denoising ability when the support width is small. The vanishing moment can smooth the high-order part of signals when analyzing and processing the time-series data with strong fluctuations. The symmetric-wavelet function can reduce the distortion of signal reconstruction to some extent. In addition, it is necessary to consider the appropriate number of decomposition layers in wavelet denoising.

3.2. Multifractal Detrended Cross-Correlation-Analysis Method

3.2.1. The DCCA Method

In order to study the cross-correlation between two variable sequences, detrended cross-correlation analysis (DCCA) can be used [27]. This method is based on the detrended covariance-analysis method, which can filter out the trend components of each order to eliminate non-stationary influence in the original sequence.

Suppose there are two time series $\{x(t)\}$ and $\{y(t)\}$ of length $N,\ t = 1, 2, \cdots, N$. The cumulative deviation series of the two original time series can be calculated by the following formulas:

$$X(t) = \sum_{k=1}^{t}(x(k) - \overline{x}),\ \ t = 1, 2, \cdots, N \tag{7}$$

$$Y(t) = \sum_{k=1}^{t}(y(k) - \overline{y}), \qquad t = 1, 2, \cdots, N \tag{8}$$

where $\overline{x}$ and $\overline{y}$ are the mean of the sequence, $\overline{x} = \frac{1}{N}\sum_{t=1}^{N} x(t), \overline{y} = \frac{1}{N}\sum_{t=1}^{N} y(t)$.

The cumulative-deviation sequence is divided into equal-length subsequences. The least-square fitting is performed for each subsequence, and the fitting curves $\widetilde{X}_v(i)$ and

$\widetilde{Y}_v(i)$ are obtained. Then, each subsequence is detrended, and the covariance function of the detrended subsequence is finally obtained.

For $v = 1, 2, \cdots, N_s$, the local covariance function is:

$$F^2(s,v) = \frac{1}{s}\sum_{i=1}^{s}\left\{X[(v-1)s+i] - \widetilde{X}_v(i)\right\} \times \left\{Y[(v-1)s+i] - \widetilde{Y}_v(i)\right\} \tag{9}$$

For $v = N_s + 1, \cdots, 2N_s$, the following formula is established:

$$F^2(s,v) = \frac{1}{s}\sum_{i=1}^{s}\left\{X[N-(v-N_s)s+i] - \widetilde{X}_v(i)\right\} \times \left\{Y[N-(v-N_s)s+i] - \widetilde{Y}_v(i)\right\} \tag{10}$$

where the preceding N_s subintervals represent the positive segmentation subsequence of the deviation sequence, and the following N_s subintervals represent the segmentation subsequence after the reversal of the deviation sequence.

The mean value of the local covariance function of all subintervals is determined to obtain the fluctuation function described in the following formula:

$$F_q(s) = \frac{1}{2N_s}\sum_{v=1}^{2N_s} F^2(s,v) \tag{11}$$

The calculation can be repeated to obtain the fluctuation function under different scales s. The limitation of the DCCA method is that it can only reveal the single-fractal characteristics of mutual correlation. However, the existence of multifractal characteristics has gradually become a consensus in the academic community. Therefore, it is not comprehensive to focus solely on the single-fractal characteristics.

3.2.2. The MF-DCCA Method

The modeling process of the MF-DCCA method and the DCCA method is similar, and the detrended covariance function of the subsequence is described in the same way. The difference between the two methods is that the MF-DCCA method takes into account the different fluctuation order q when calculating the fluctuation function, whereas the DCCA method only considers the single fluctuation order when calculating the fluctuation function [28].

The MF-DCCA method takes the mean of the local covariance of all subintervals, and the q-order fluctuation function can be obtained:

$$F_q(s) = \left\{\frac{1}{2N_s}\sum_{v=1}^{2N_s}\left[F^2(s,v)\right]^{q/2}\right\}^{1/q} \tag{12}$$

In general, q can be any real number that is non-zero. When the value of q is 0, the following formula can be obtained from L'Hospital's rule:

$$F_0(s) = exp\left\{\frac{1}{4N_s}\sum_{v=1}^{2N_s}\left[F^2(s,v)\right]\right\} \tag{13}$$

Then, the fluctuation function $F_q(s)$ corresponding to different scales s is calculated. If there is a long-range power-law cross-correlation between the two time series, then the fluctuation function $F_q(s)$ and the time scale s have the following relationship:

$$F_q(s) \sim s^{H_{xy}(q)} \tag{14}$$

Then, the following formula is established:

$$\log F_q(s) = H_{xy}(q)\log s + \log A \tag{15}$$

For each q value, the linear slope obtained by $\log F_q(s)$ and $\log s$ regression is $H_{xy}(q)$, which is called the generalized Hurst index. Whether $H_{xy}(q)$ changes with the change of fluctuation order q can be used to describe whether the cross-correlation fractal characteristic between two variables is multiplicity. The value of $H_{xy}(q)$ can reflect whether the interaction between variables has the characteristics of long memory. For the larger fluctuation order q, $H_{xy}(q)$ transmits the scaling behavior that the larger fluctuation dominates. On the contrary, for negative or small fluctuation order q, $H_{xy}(q)$ transmits the scaling behavior that small fluctuation dominates. It is worth mentioning that when q is 2, $H_{xy}(2)$ is the classical Hurst index.

The relation between the generalized Hurst index $H_{xy}(q)$ and the multifractal scale index $\tau(q)$ obtained by the MF-DCCA method is as follows:

$$\tau(q) = qH_{xy}(q) - 1 \tag{16}$$

If $\tau(q)$ and q are linear, then the two time series have the characteristics of a single fractal. Otherwise, they present the characteristics of a multifractal. Through Legendre transformation, a singular exponent and multifractal spectrum can be obtained.

$$\alpha = H_{xy}(q) + qH'_{xy}(q) \tag{17}$$

$$f(\alpha) = q\left[\alpha - H_{xy}(q)\right] + 1 \tag{18}$$

Among them, α is the singular index, which is used to describe the degree of singularity of sequence. $f(\alpha)$ is the multifractal spectrum whose value reflects the fractal dimension with singular index α. The multifractal spectrum transmits a lot of valuable fluctuation information. For example, the multifractal intensity can be measured by the width of the fractal spectrum. The wider the fractal spectrum, the stronger the multifractal intensity of the correlation between variables.

3.2.3. The Improved MF-DCCA Based on the OSW Method

The traditional MF-DCCA method will inevitably produce fluctuation errors in the fitting process due to the discontinuity when the cumulative deviation sequence is divided into subintervals, which may lead to a decline in the accuracy of the scale-index estimation. In order to minimize the negative impact of data-point discontinuity, it has been considered that the sliding-window approach can further reduce the generation of fluctuation error [40]. The specific steps of splitting the deviation sequence into subintervals are described below.

The deviation sequence of each original signal can be regarded as consisting of N_s non-overlapping equal sequences, namely, $N_s = int(N/s)$, and the length of the subsequences is s. In most cases, the length N of the deviation sequence of each original signal is not divisible by the length s of the subsequence. In order to make full use of all the data information, the data sequence is usually recalculated in the reverse direction, so $2N_s$ subintervals can be obtained.

In this study, the deviation sequence was divided into subintervals and the continuous overlapping-sliding-window (OSW) segmentation method was adopted to replace the original segmentation method. The idea of OSW is to set a fixed window length s, and then slide back in steps of unit length until the window reaches the end of the time series. The specific details are shown in Figure 1 below. In this way, the sequence information is continuous and none of redundant information is left.

The subsequence was divided by the continuous overlapping-sliding-window technique and the fluctuation analysis was carried out by the MF-DCCA method. The combination of these two can be called OSW-MF-DCCA, which reveals that the fractal discovery had certain robustness.

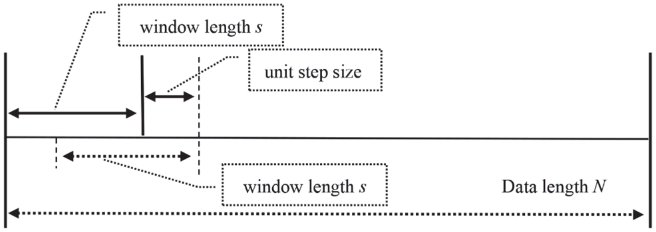

Figure 1. Details of sliding-window segmentation.

4. Empirical Analysis

4.1. Index Construction and Sample Selection

This study screened and weighted the data of different sectors in the stock market to construct comprehensive indices that can represent technological innovation, financial development, and the real economy. The main reason for starting from the original data in the stock market is that, first, the stock market is more sensitive to the perception of information, and fluctuations in any industry can be quickly reflected in the stock market. Second, stock-market data have the advantages of high integrity, strong continuity, and high frequency, whereas traditional economic data are often difficult to count. Therefore, the composite index constructed in the form of weighted stock data can largely reflect the actual situation of the industry.

This paper mainly selected and constructed the technological-innovation index (TI), financial-market index (FI), and real-economy index (RE) in the stock market to represent the overall situation of the technological-innovation industry, the financial industry, and the real-economy industry. In the actual selection of exponents, the TI selected the representative technology 100 index, which is mainly used to reflect the overall trend of company stocks with high-tech or independent innovation characteristics and has strong representation for the technology-innovation industry. The compilation of the FI and the RE refers to the compilation methods of S&P500 and CSI (China Securities Industry Index). The financial industry can be divided into the banking industry and the non-banking financial industry according to the classification basis of the Shenwan primary industry index. The FI was constructed by weighting the constituent stocks of the banking and non-banking financial industries. The RE is represented by the nine China securities-industry indices, which basically cover real-economy fields such as energy, information industry, industrial manufacturing, medical treatment, consumer goods, and agricultural products. Specifically, they are China Securities Energy, China Securities Material, China Securities Consumption, China Securities Optional Consumption, China Securities Information, China Securities Medicine, China Securities Telecom, China Securities Public Utility, and China Securities Industry. Through the weighted average of the constituent stocks of the real-economy industries, the RE was constructed. The data selected in this paper were daily data from January 2012 to December 2021, and the data were processed by logarithmic difference to improve the stability of the time series.

4.2. Descriptive Statistical Analysis

This study plotted the index time-series diagram of fluctuations of the TI, FI, and RE, as shown in Figure 2. In the figure, the horizontal axis represents the beginning of 2012 to the ending of 2021, and the vertical axis represents the fluctuation range of the data. The part above 0 represents the positive fluctuations, whereas the part below 0 represents the negative fluctuations caused by the adverse impact. It was found that the fluctuations of the TI, FI, and RE were more volatile, and their peaks were mainly concentrated during the stock-market crash in 2015 and the COVID-19 pandemic that started in 2019. It is worth noting that there were more obvious volatility aggregations during the two crises, which may have been caused by short-term noise interference, so the TI, FI, and RE were affected in a sustained way.

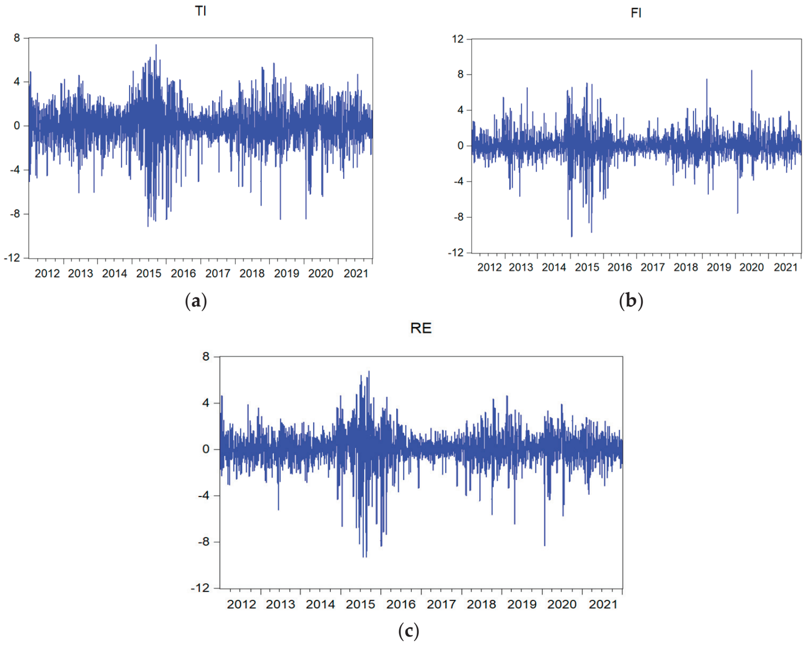

(**a**) (**b**) (**c**)

Figure 2. The fluctuation-sequence charts of the TI, FI, and RE. (**a**) TI. (**b**) FI. (**c**) RE.

The descriptive statistics of the indices for the fundamental characteristics are listed in Table 1.

Table 1. Descriptive statistical results.

Variable	Median	Mean	Std. Dev.	Skewness	Kurtosis	Jarque–Bera
TI	0.052	0.092	1.865	−0.622	5.850	979.535 *
FI	0.029	−0.047	1.459	−0.132	9.663	4504.348 *
RE	0.046	0.099	1.469	−0.943	9.145	4184.668 *

Note: * is significant at the confidence level of 1%.

It was found that skewness values of the TI, FI, and RE were less than 0, kurtosis values were greater than 3, and JB statistical values were far greater than the critical value of 9.210 based on observing Table 1. The distribution of indices presented the characteristics of peak and thick tails and non-normality, and fractal distribution better described the distribution of the indices. In addition, the median and mean of the TI, FI, and RE were all close to 0, which indicates that there were some extreme values in the three indices but that they still showed the characteristics of fluctuating around zero. The standard deviation of the TI was larger than that of the RE and FI, indicating that the TI had stronger volatility, possibly because the TI was more affected by noise.

In summary, the fluctuation-sequence charts and descriptive statistical results of the TI, FI, and RE show that the fluctuations of the TI, FI, and RE were relatively unstable. Large fluctuations were often accompanied by larger fluctuations, whereas small fluctuations were often accompanied by smaller fluctuations, presenting a relatively obvious volatility aggregation, which may have been due to the interference of noise information. If the study directly analyzes the original sequences and ignores the impact of exponential fluctuations, it may lead to a deviation in the research result. Therefore, in order to accurately analyze the fractal characteristics between the indices, it is necessary to first decrease the noise information.

4.3. Denoising Analysis

The time-series data in the financial market and economic market often have nonlinear characteristics, which may easily lead to the removal of much useful information in the process of denoising by traditional methods. Therefore, this paper used the wavelet-threshold denoising method by selecting different wavelet functions, decomposition layers, and threshold functions to denoise the indices according to the characteristics of the time series.

In the practical operation of wavelet-threshold denoising, the selection of threshold function is essential. This paper selected the $symN$ wavelet-basis function, which can deal with discrete wavelet transformation and has orthogonality and compact support. Although $symN$ and dbN wavelet-basis function are similar in terms of support length, continuity, and filter length, $symN$ has better symmetry—that is, to a certain extent, it can reduce the phase distortion during signal analysis and reconstruction. Generally speaking, an appropriate vanishing moment is crucial in the analysis of financial or economic time series, and the mutability of time series makes it necessary to smooth the higher-order part of the signal. After repeated experiments to compare the denoising effect, the $sym6$ wavelet-basis function was selected in this paper.

At the same time, in the wavelet-threshold denoising, it is also very important to choose the appropriate number of decomposition layers. When the number of decomposition layers is higher, the more real signals will be removed from the signals in the denoising process. Therefore, in the actual operation of wavelet-threshold denoising, this paper selected one-layer denoising, which can not only effectively remove the noise information but also retain more useful information. More importantly, this paper applied the soft- and hard-threshold compromise function. It not only overcomes the discontinuity problem in the hard-threshold function but also reduces the constant deviation in the soft-threshold function.

The denoising signals of TI, FI, and RE based on the selected wavelet function, the number of decomposition layers, and the threshold function are shown in Figure 3.

In Figure 3, the fluctuation-aggregation degree of the denoising indices was weakened and the indices showed a certain stability. The original signals of the TI, FI, and RE fluctuated sharply during the stock-market crash in 2015 and the COVID-19 pandemic that started in 2019, and there were a lot of effective signals as well as noises. After using the wavelet-threshold denoising method, the fluctuation amplitude of signals decreased. In particular, the fluctuations of the indices during the crisis periods were still more volatile than that in the stable periods, which is consistent with the crisis circumstance at that time.

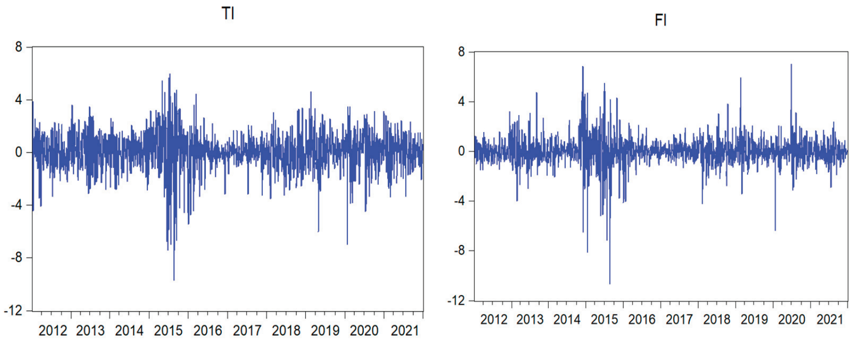

(**a**) (**b**)

Figure 3. *Cont.*

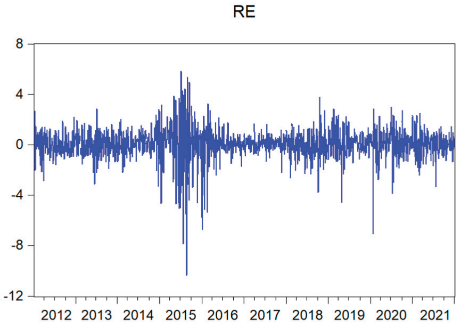

(**c**)

Figure 3. Wavelet-threshold denoising results of different indices. (**a**) TI. (**b**) FI. (**c**) RE.

4.4. Fractal-Characteristics Analysis of Interaction Relationship

The improved OSW-MF-DCCA method in this paper can further avoid the pseudo-fluctuation errors to improve the accuracy of the results. Based on this, this paper focused on the TI, FI, and RE after wavelet-threshold denoising and quantitatively estimated their nonlinear cross-correlation relationship and multifractal characteristics via the MF-DCCA method. Referring to previous studies of scholars [41], the fluctuation order q in this paper was set in the range of $[-10, 10]$ for practical applications. In addition, Peng and other scholars pointed out that $5 \leq s \leq N/4$ is more appropriate in practical applications [24], and this study referred to their recommended parameter-setting standard. In the calculation process, the fitting order of this study was set as the first order.

4.4.1. Multifractal Analysis

Fractal theory shows that the relationship between the Hurst value of the interaction between variables and the fluctuation order q can effectively determine whether the fractal characteristic is single or multiple. If the Hurst index of the interaction between the two variables changes significantly with the change in the fluctuation order q, it means that the fractal characteristic of the interaction between the two variables is multiple. Otherwise, the interaction between the two is simplex.

In order to observe the interaction among the TI, FI, and RE in a more comprehensive way, this paper traversed all fluctuation orders. Figure 4 plots the relationship between the generalized Hurst value of cross-correlation and the fluctuation order q. For the purpose of comparison, the results of the TI and RE, the FI and RE, and the TI and FI were all plotted in the same chart, which can be seen in Figure 4a.

It is also worthwhile to pay attention to whether the fractal characteristics change with time changes. This paper analyzed the time variance of fractal characteristics, specifically observing the cross-correlation fractal characteristics in different periods and exploring the dynamic evolution of cross-correlation fractal characteristics from a local perspective. Firstly, the index data were divided into 10 sub-samples, and then the MF-DCCA method with sliding window was applied to each sub-sample to explore the cross-correlation fractal characteristics. The results are shown in Figure 4b–d. More sample data sets will be more persuasive to explain the research results.

In the case of the total sample, Figure 4a shows the q-$H(q)$ results of the cross-correlation among the TI, FI, and RE. The Hurst value of cross-correlation changed with the volatility order q. This indicates that the cross-correlation presented multifractal characteristics rather than single-fractal characteristics. Specifically, with the increase in the fluctuation order q, the Hurst value of cross-correlation among the TI, FI, and RE monotonically decreased. In contrast, with the change in the fluctuation order q, the Hurst value of the interaction between the RE and FI was roughly the same as the Hurst value of the interaction between the FI and TI, and the change range in the Hurst value was almost the same. However, the Hurst value of the interaction between the TI and RE underwent a bigger change. This shows that the multifractal characteristics of the interaction between TI and RE were more significant than those of other two. Such results also imply that the interaction between the TI and RE was relatively unstable.

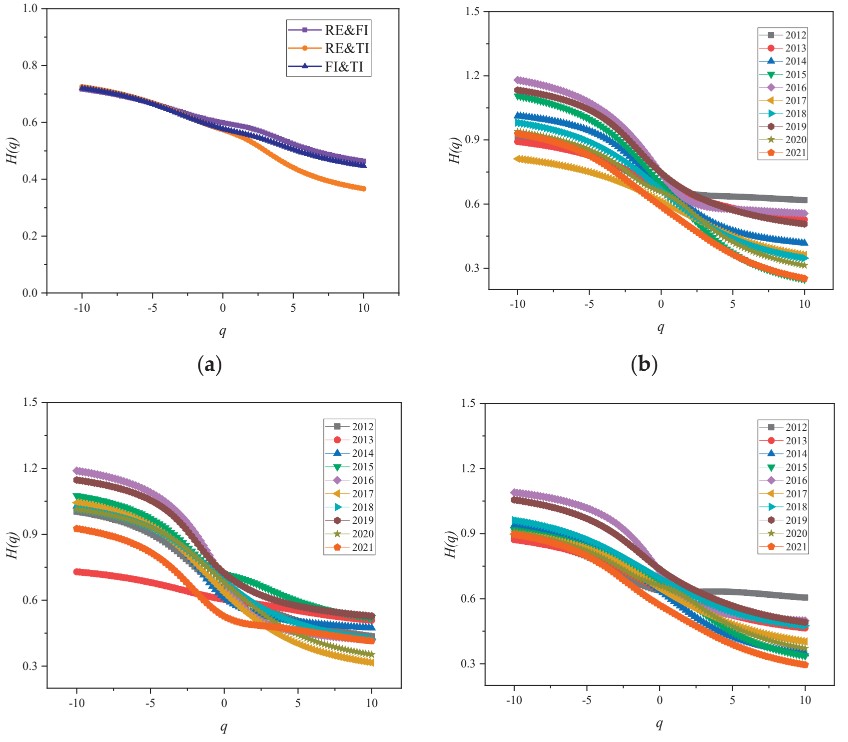

(**a**) (**b**) (**c**) (**d**)

Figure 4. The q-$H(q)$ results of the TI, FI, and RE. (**a**) Overall sample. (**b**) Subsample RE and FI. (**c**) Subsample RE and TI. (**d**) Subsample FI and TI.

In the sub-sample, Figure 4b–d clearly shows the dynamic evolution of the Hurst value of the interaction among the TI, FI, and RE in different periods. For the RE and TI, the Hurst value of cross-correlation between them decreased with an increase in the fluctuation order q in any period. This shows that the cross-correlation fractal characteristic between the RE and TI was multiple at any time. For the FI and the RE, the Hurst value of cross-correlation between them in different periods was also not constant, which also means that they presented significant cross-correlation multifractal characteristics. The same performance happened in the cross-correlation fractal characteristics between FI and TI.

4.4.2. Time-Varying Memory Analysis

Studies related to complex dynamics suggest that whether the sequence is autocorrelation or cross-correlation, there may be a long-memory phenomenon in the process of fluctuations, which can also be called persistence. Simply put, it is about how long the impact of past information on the future will last, which can generally be measured by the value of the Hurst index.

In order to better understand the long-term-memory phenomenon of the interaction among the TI, FI, and RE, this paper observed the Hurst values of cross-correlation among the three indices in different periods and different degrees of volatility. Specifically, this study separately calculated the mean values of the Hurst indices of the interaction among TI, FI, and RE with the cases of when the fluctuation order q was greater than 0 and when the fluctuation order q was less than 0. The specific results are shown in Figure 5.

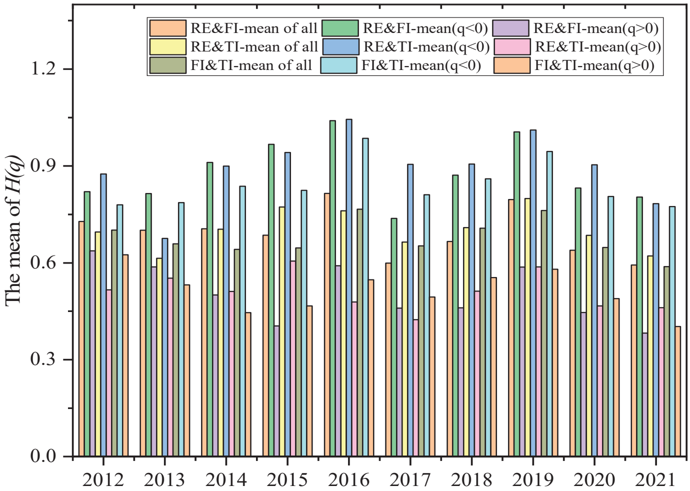

Figure 5. Tim-evarying memory analysis of $H(q)$ mean among TI, FI, and RE.

Figure 5 shows the Hurst values of cross-correlation among the TI, FI, and RE under different fluctuation degrees. Firstly, the mean values of the Hurst indices among the three indices were significantly higher than 0.5 when the fluctuation order q was considered in all cases, which indicates that the interaction among the three indices was characterized by long memory in the overall situation. Secondly, when the volatility order q was less than 0, the mean values of Hurst indices of cross-correlation among the three indices were also significantly higher than 0.5 under the fractal characteristics of small fluctuations. Moreover, the range of Hurst values above 0.5 in the case of small fluctuations was much larger than that of Hurst values above 0.5 in the overall case, which means that the interaction between the three indices in the period of small fluctuations had stronger long-term memory. Thirdly, when the fluctuation order q was greater than 0, that is, in the case of large-fluctuation fractal characteristics, the mean values of the Hurst indices among the three indices were significantly lower than 0.5. This indicates that the long-memory characteristics of the interaction among the three indices were not obvious in the period of big fluctuations and the interaction had the performance of anti-persistence. In summary, the interaction between the three had typical characteristics of long memory. However, in part, the long-term memory of the interaction among the three indices was more significant in the case of small fluctuations, whereas the interaction among the three indices may have shown anti-persistence in the case of large fluctuations.

As can be seen from the Hurst indices in the figure, the Hurst value of cross-correlation among the TI, FI, and RE deviated from 0.5 in 2015–2017 and 2019–2021 and was significantly higher than that of other periods. This phenomenon may have had something to do with the stock-market crash in 2015 and the COVID-19 pandemic that began in 2019. To be specific, various favorable policies in the early stage of 2015 resulted in irrational excessive growth of the market and a huge financial bubble. Furthermore, the overall financial market was depressed in 2015 and later. From another perspective, the change in Hurst value of the interaction among the TI, FI, and RE presented characteristics of time lag. Although the stock-market disaster occurred in 2015, the continuous influence of cross-correlation led to a significant deviation in the Hurst value from 0.5 in 2015 and the following years. The COVID-19 pandemic spread all over the world in 2019–2021, leading to a continuous downturn in all industries. During this period, the continuous and anti-continuous cross-correlation among the TI, FI, and RE alternated, which shows that the cross-correlation multifractal characteristics among the TI, FI, and RE during and after the crisis were significantly stronger than those in the stable periods.

4.4.3. Singularity Analysis of Fractal Spectrum

The fractal spectrum also contains much information about the correlation of time-series fluctuations, and the shape of the fractal spectrum indirectly reflects the singularity and complexity of the fluctuation relationship between different variables. Before describing the fractal spectrum of cross-correlation among the TI, FI, and RE, the results of scale index $\tau(q)$ on the fluctuation order q are shown in Figure 6. The scale index $\tau(q)$ was a convex function with a strict monotonical increase with respect to fluctuation order q, both for the total sample and for the subsample. This means that there was an obvious nonlinear relationship between $\tau(q)$ and fluctuation order q. These results again indicate that the cross-correlation among the TI, FI, and RE had multifractal characteristics.

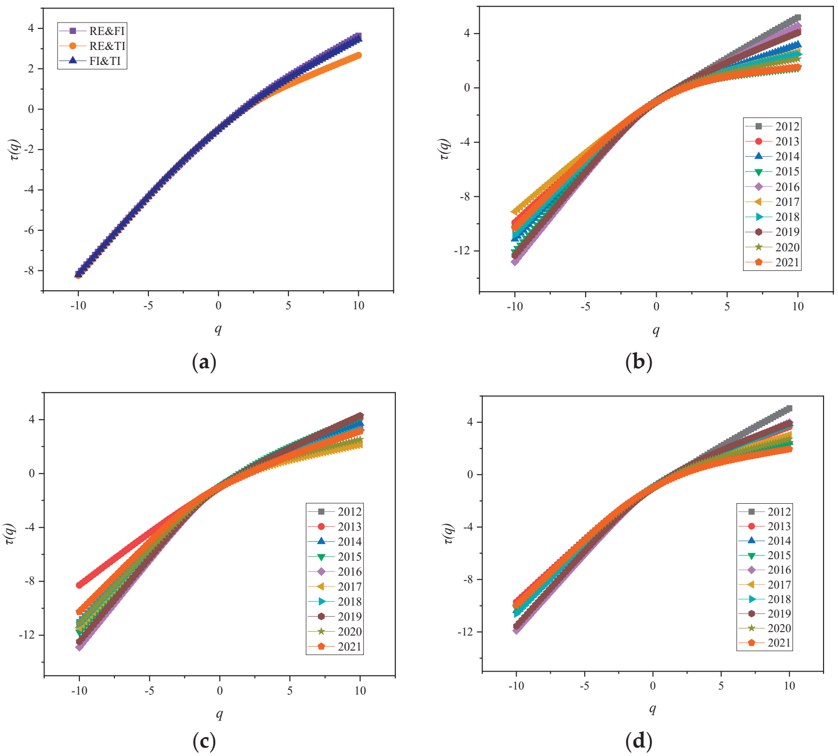

(**a**) (**b**) (**c**) (**d**)

Figure 6. The q-$\tau(q)$ results of the TI, FI, and RE. (**a**) Overall sample. (**b**) Subsample RE and FI. (**c**) Subsample RE and TI. (**d**) Subsample FI and TI.

The shape of the fractal spectrum can also reflect whether the fractal characteristics are multiple. When the fractal spectrum was expressed as a point, the time series of the financial market or the economic market was expressed as a single fractal. Otherwise, when the fractal spectrum did not exist in the form of points, the sequence was shown to be multifractal. Figure 7 shows the fractal spectrum of cross-correlation among the TI, FI, and RE. Obviously, no matter the total sample or sub-sample, the fractal spectrum of cross-correlation among the three indices showed a parabolic shape with a large opening, which did not exist in the form of points. This further confirms the existence and connection of multifractal characteristics among the TI, FI, and RE from the perspective of the fractal spectrum.

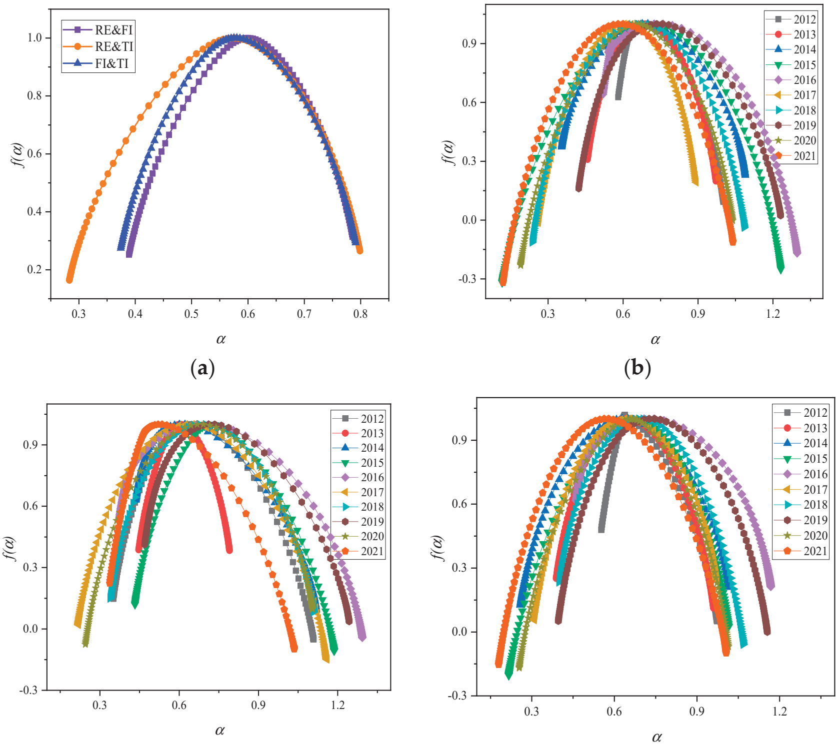

(**a**) (**b**)

(**c**) (**d**)

Figure 7. Multifractal spectrum among the TI, FI, and RE. (**a**) Overall sample. (**b**) Subsample RE and FI. (**c**) Subsample RE and TI. (**d**) Subsample FI and TI.

The parameters of the multifractal spectrum also convey information about local fluctuations in many markets, especially the width difference $\Delta\alpha$ and height difference $\Delta f(\alpha)$ of the multifractal spectrum. The fractal-spectrum analysis of cross-correlation was similar to that of the single time series. The $\Delta\alpha = \alpha_{max} - \alpha_{min}$ represents the dispersion of the distribution. The $\Delta\alpha = 0$ corresponds to a completely uniform distribution. The larger $\Delta\alpha$ indicates that the distribution of the time series was more uneven and the cross-correlation fluctuations between the indices were more intense. The $\Delta f(\alpha) = f(\alpha_{min}) - f(\alpha_{max})$ conveys the degree of local fluctuations of cross-correlation. Some studies have also pointed out that $\Delta f(\alpha)$ represents the number of occurrences of the singular index value, reflecting the proportion of the sequence signals at the peak and trough positions. The higher the $|\Delta f(\alpha)|$ is, the more chaotic the local fluctuations of the cross-correlation are.

Taking the overall sample as an example, the $\Delta\alpha$ and $|\Delta f(\alpha)|$ among the TI, FI, and RE were calculated and are listed in Table 2. The parameters of the multifractal spectrum among the TI, FI, and RE were constantly changing, and their corresponding function densities were inconsistent. In terms of $\Delta\alpha$, the $\Delta\alpha$ of TI-RE was the largest, followed by the $\Delta\alpha$ value of FI-TI, and the $\Delta\alpha$ value of FI-RE was the smallest. The values of $\Delta\alpha$ prove that the interactive relation between the RE and TI was more complex and the degree of multifractal was stronger. On the contrary, the multifractal degree between the RE and FI was relatively weaker.

Table 2. Parameters of multifractal spectrum.

Variable	α_{min}	α_{max}	$\Delta\alpha$	$f(\alpha_{min})$	$f(\alpha_{max})$	$\lvert\Delta f(\alpha)\rvert$
RE and FI	0.3890	0.7857	0.3967	0.2521	0.3137	0.0615
RE and TI	0.2830	0.7988	0.5157	0.1637	0.2651	0.1014
FI and TI	0.3744	0.7911	0.4167	0.2746	0.2936	0.0190

In terms of $|\Delta f(\alpha)|$, the $|\Delta f(\alpha)|$ value of RE-TI was the largest. This indicates that the local fluctuations of the cross-correlation between the RE and TI were more volatile, whereas the $|\Delta f(\alpha)|$ value of RE-FI and FI-TI were significantly smaller than that of TI-RE. This means that the local dislocations of the cross-correlation between the RE and FI as well as FI and TI were relatively simple.

The fractal-spectrum shape of the FI-RE was very similar to that of FI-TI. The difference between the value of $\Delta\alpha$ for FI-RE and that of FI-TI was 0.02, and the difference between the $|\Delta f(\alpha)|$ of FI-RE and that of FI-TI was 0.0425. From the perspective of fractal spectrum, the change trend of the interaction between the FI and RE was similar to that between the FI and TI. In comparison, the fractal-spectrum width of TI-RE was more 0.099 that of TI-FI and FI-RE, and the fractal-spectrum height was also more than 0.0399. These show that the cross-correlation between TI and RE was unstable and partially chaotic.

In addition, the changes in multifractal-spectrum parameters of cross-correlation among the TI, FI, and RE in different periods were also explored, including the $\Delta\alpha$ and $|\Delta f(\alpha)|$. The results are shown in Figure 8. Consistently, the multifractal spectrum of cross-correlation among the TI, FI, and RE also had time-varying characteristics. For the TI and RE, the value of $\Delta\alpha$ was higher in 2015–2018 and 2020, and the value of $|\Delta f(\alpha)|$ was higher in 2019, 2019, and 2021. For the FI-RE, the value of $\Delta\alpha$ was higher in 2015–2016 and 2020–2021, and the value of $|\Delta f(\alpha)|$ was higher in 2016 and 2020. For the FI-TI, the value of $\Delta\alpha$ was also higher in 2015–2016 and 2021, and the value of $|\Delta f(\alpha)|$ was higher in 2015–2016 and 2020. The parameter changes of the multifractal spectrum among the TI, FI, and RE were similar.

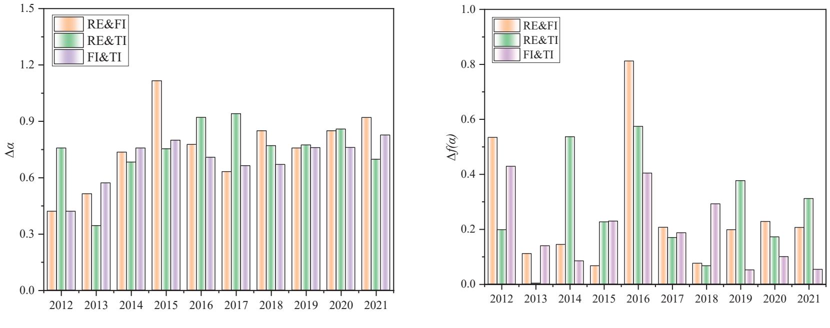

(**a**) (**b**)

Figure 8. Time-varying analysis of multifractal-spectral parameters. (**a**) Width difference of fractal spectrum. (**b**) Height difference of fractal spectrum.

It is worth noting that the parameter change of the multifractal spectrum also presented the characteristics of time delay. Although the stock-market crash occurred in 2015, the value of $\Delta\alpha$ and $|\Delta f(\alpha)|$ among the TI, FI, and RE remained at a higher level in the years following 2015. Similarly, the COVID-19 pandemic, which began at the end of 2019, kept the global economy in a sustained downturn, and the value of $|\Delta f(\alpha)|$ in 2019 and the following years also remained at a higher level. It can be concluded that the multifractal-spectrum parameters of the TI, FI, and RE changed significantly during the crisis periods and the subsequent periods.

5. Conclusions

The research results of the denoising analysis show that wavelet-threshold denoising can remove some noise information of technological-innovation, financial-market, and real-economy indices to improve the availability of effective information. Compared with the traditional denoising method, the effect of wavelet-threshold denoising is significantly more effective. After denoising, the volatility agglomeration of technological-innovation, financial-market, and real-economy indices was significantly reduced and the stability was improved. This was helpful for this study to observe a more authentic and reliable fluctuation relationship among technological-innovation, financial-market, and real-economy indices.

Several valuable findings were obtained from the study of the cross-correlation fractal between technological-innovation, financial-market, and real-economy indices, which were mainly manifested in the multiplicity, time-varying memory, and singularity of fractal characteristics. Firstly, the Hurst value of cross-correlation among technological-innovation, financial-market, and real-economy indices showed a decreasing trend with the increase in the fluctuation order. This means that the cross-correlation among them presented obvious multifractal characteristics rather than single-fractal characteristics. Secondly, the cross-correlation among technological-innovation, financial-market, and real-economy indices demonstrated the phenomenon of long memory, that is, the interaction between them had a long-term correlation in most periods. Locally, when the fluctuation was small, the cross-correlation among the three indices showed the characteristics of continuity. In the period of great fluctuation, the cross-correlation between them may have had the characteristics of anti-persistence, among which the cross-correlation between technological-innovation and real-economy indices had the strongest anti-persistence. Thirdly, the shape of the multifractal spectrum among the indices of technological innovation, the financial market, and the real economy were all parabola-like shapes with the opening facing down, which confirms the cross-correlation multifractal characteristics from the perspective of the fractal spectrum. In contrast, the width difference in the cross-correlation multifractal spectrum between the technological-innovation and real-economy indices was the largest, which indicates that the interaction between technological innovation and the real economy was more complex. Similarly, the height difference of the fractal spectrum between technological-innovation and real-economy indices was also the largest, which reflects the high degree of local chaos and instability of the interaction between the two.

In addition, it was found that the Hurst value and fractal spectrum of cross-correlation among the three indices were obviously different in different periods, but the change trend of the fractal characteristics among the three indices was roughly similar over time. The fractal characteristics of the crisis events during the period of occurrence and the following years were significantly strengthened, which indicates that the interaction between the three indices may have had a certain time delay and continuity.

Based on the study above, the research results are of great significance to investors and administrative departments. For investors, the conclusions will help them to realize the nonlinear dependence and potential dynamic mechanism between the three industries and have a deeper understanding of the linkage relationship and information transmission among the industries so as to provide investors with a decision-making basis. For economic policymakers, the fractal characteristics of interaction can help them understand the transmission and diffusion of market risks, deeply consider the important factors affecting the healthy growth of the real economy, and carry out policy regulation and management in a timely manner.

There are still many areas for in-depth discussion on the interaction between technological innovation, financial markets, and the real economy. For example, according to the different multifractal characteristics, how to control the risk diffusion in practice will be the focus of our future research, and the optimization of parameters also needs to be explored further.

Author Contributions: Conceptualization, J.K. and Y.D.; methodology, C.X.; software, Y.D.; validation, Y.Z. and C.X.; formal analysis, Y.D.; investigation, Y.Z.; resources, C.X.; data curation, Y.Z.; writing—original draft preparation, J.K., Y.D. and C.X.; writing—review and editing, Y.D. and J.K.; visualization, Y.Z.; supervision, J.K.; project administration, J.K.; funding acquisition, J.K. All authors have read and agreed to the published version of the manuscript.

Funding: This research was partially funding supported by the National Natural Science Foundation of China (No. 72101020) and the Beijing Municipal Commission of Science and Technology (No. z181100007218009).

Data Availability Statement: This research was conducted by using publicly available CSI stock-index data, and the data are available from the corresponding author upon request.

Acknowledgments: The author team thanks Wen Fang for conceptualization suggestion and partial financial support, and thanks are extended to the reviewers for their comments and suggestions.

Conflicts of Interest: The authors declare no conflict of interest.

References

1. Moshirian, F.; Tian, X.; Zhang, B.H.; Zhang, W.R. Stock market liberalization and innovation. *Financ. Econ.* **2021**, *139*, 985–1014. [CrossRef]
2. Liu, Y.; Failler, P.; Ding, Y. Enterprise financialization and technological innovation: Mechanism and heterogeneity. *PLoS ONE* **2022**, *17*, e0275461. [CrossRef] [PubMed]
3. Rounaghi, M.M.; Zadeh, F.N. Investigation of market efficiency and financial stability between S&P 500 and London stock exchange: Monthly and yearly forecasting of time series stock returns using ARMA model. *Physica A* **2016**, *456*, 10–21.
4. Mandelbrot, B.B. A multifractal walk down Wall Street. *Sci. Am.* **1999**, *280*, 70–73. [CrossRef]
5. Chorowski, M.; Kutner, R. Multifractal company market: An application to the stock market indices. *Entropy* **2022**, *24*, 130. [CrossRef] [PubMed]
6. Sangwan, V.; Prakash, P.; Singh, S. Financial technology: A review of extant literature. *Stud. Econ. Financ.* **2020**, *37*, 71–88. [CrossRef]
7. Chen, Y.; Bellavitis, C. Blockchain disruption and decentralized finance: The rise of decentralized business models. *J. Bus. Ventur.* **2020**, *13*, e00151. [CrossRef]
8. Vučinić, M. Fintech and financial stability potential influence of FinTech on financial stability, risks and benefits. *J. Cent. Bank Theor. Pr.* **2020**, *9*, 43–66. [CrossRef]
9. Pradhan, R.P.; Arvin, M.B.; Nair, M.; Bennett, S.E.; Bahmani, S.; Hall, J.H. Endogenous dynamics between innovation, finan-cial markets, venture capital and economic growth: Evidence from Europe. *J. Multinatl. Financ. Manag.* **2018**, *45*, 15–34. [CrossRef]
10. Chen, X.H.; Yan, D.; Chen, W. Can the digital economy promote fintech development? *Growth Chang.* **2021**, *53*, 221–247. [CrossRef]
11. Kihombo, S.; Ahmed, Z.; Chen, S.; Adebayo, T.; Kirikkaleli, D. Linking financial development, economic growth, and ecological footprint: What is the role of technological innovation? *Environ. Sci. Pollut. Res.* **2021**, *28*, 61235–61245. [CrossRef] [PubMed]
12. Lv, Y.; Fang, K. Research on the coupling relationship between China's regional economy, science and technology and finance-based on the comparative analysis of the greater bay area of Guangdong, Hong Kong and Macao. *Sci. Technol. Manag. Res.* **2020**, *40*, 149–156.
13. Dagar, V.; Khan, M.K.; Alvarado, R.; Rehman, A.; Irfan, M.; Adekoya, O.B.; Fahad, S. Impact of renewable energy consumption, financial development and natural resources on environmental degradation in OECD countries with dynamic panel data. *Environ. Sci. Pollut. Res.* **2022**, *29*, 18202–18212. [CrossRef] [PubMed]
14. Qi, J.; Li, L. On the impact of financial technology on the real economy—An analysis based on the stock data of listed companies. *Acad Exch.* **2021**, *328*, 107–118.
15. Peng, Z.; Ke, J. Spillover effect of the interaction between fintech and the real economy based on tail risk dependent structure analysis. *Sustainability* **2022**, *14*, 7818. [CrossRef]
16. Lai, X.B.; Yue, S.J.; Guo, C.; Zhang, X.H. Does FinTech reduce corporate excess leverage? Evidence from China. *Econ. Anal. Policy.* **2023**, *77*, 281–299. [CrossRef]
17. Bernier, M.; Plouffe, M. Financial innovation, economic growth, and the consequences of macroprudential policies. *Res. Econ.* **2019**, *73*, 162–173. [CrossRef]
18. Knight, E.; Wójcik, D. FinTech, economy and space: Introduction to the special issue. *Environ. Plan. A* **2020**, *52*, 1490–1497. [CrossRef]
19. Mandelbrot, B. New methods in statistical economics. *J. Polit. Econ.* **1963**, *71*, 421–440. [CrossRef]
20. Peters, E.E. *Fractal Market Analysis: Applying Chaos Theory to Investment and Economics*; John Wiley & Sons: New York, NY, USA, 1994.
21. Lo, A.W. Long-term memory in stock market prices. *Econometrica* **1991**, *59*, 1279–1313. [CrossRef]
22. Liaw, S.S.; Chiu, F.Y.; Wang, C.Y.; Shiau, Y.H. Fractal Analysis of Stock Index and Electrocardiograph. *Chin. J. Phys.* **2010**, *48*, 814–828.

23. Ogawa, H.; Sato, Y.; Tamai, T. Who gains from capital market integration? Tax competition between unionized and non-unionized countries. *Can. J. Econ. Rev. Can. Econ.* **2016**, *49*, 76–110. [CrossRef]
24. Peng, C.K.; Buldyrev, S.V.; Havlin, S.; Simons, M.; Stanley, H.E.; Goldberger, A.L. Mosaic organization of DNA nucleotides. *Phys. Rev. E* **1994**, *49*, 1685–1689. [CrossRef] [PubMed]
25. Kantelhardt, J.W.; Zschiegner, S.A.; Koscielny-Bunde, E.; Havlin, S.; Bunde, A.; Stanley, H.E. Multifractal detrended fluctua-tion analysis of nonstationary time series. *Physica A* **2002**, *316*, 87–114. [CrossRef]
26. Gulich, D.; Zunino, L.A. criterion for the determination of optimal scaling ranges in DFA and MF-DFA. *Physica A* **2014**, *397*, 17–30. [CrossRef]
27. Podobnik, B.; Stanley, H.E. Detrended cross-correlation analysis: A new method for analyzing two non-stationary time series. *Phys. Rev. Lett.* **2008**, *100*, 084102. [CrossRef]
28. Zhou, W. Multifractal detrended cross-correlation analysis for two nonstationary signals. *Phys. Rev. Lett.* **2008**, *77*, 066211. [CrossRef]
29. Fan, Q.J.; Li, D. Multifractal cross-correlation analysis in electricity spot market. *Physica A* **2015**, *429*, 17–27. [CrossRef]
30. Barzegar, R.; Aalami, M.T.; Adamowski, J. Coupling a hybrid CNN-LSTM deep learning model with a boundary corrected maximal overlap discrete wavelet transform for multiscale lake water level forecasting. *J. Hydrol.* **2021**, *598*, 126196. [CrossRef]
31. Zhang, Q.Y.; Wang, L.; Sun, W.C. Signal denoising with average sampling. *Digit. Signal Prog.* **2012**, *22*, 226–232. [CrossRef]
32. Sejdic, E.; Djurovic, I.; Stankovic, L. Fractional fourier transform as a signal processing tool: An overview of recent developments. *Signal Process.* **2011**, *91*, 1351–1369. [CrossRef]
33. Simon, C.; Ventosa, S.; Schimmel, M.; Heldring, A.; Danobeitia, J.J.; Gallart, J.; Manuel, A. The S-Transform and its inverses: Side effects of discretizing and filtering. *IEEE Trans. Signal Process.* **2007**, *55*, 4928–4937. [CrossRef]
34. Mallat, S.; Hwang, W.L. Singularity detection and processing with wavelets. *IEEE Trans. Inf. Theory* **1992**, *38*, 617–643. [CrossRef]
35. Donoho, D.L.; Johnstone, I.M. Ideal spatial adaptation by wavelet shrinkage. *Biometrika* **1994**, *81*, 425–455. [CrossRef]
36. Hu, H.P.; Zhang, L.M.; Yan, H.C.; Bai, Y.P.; Wang, P. Denoising and baseline drift removal method of MEMS hydrophone sig-nal based on VMD and wavelet threshold processing. *IEEE Access.* **2019**, *7*, 59913–59922. [CrossRef]
37. Donoho, D.L. De-noising by soft-thresholding. *IEEE Trans. Inf. Theory* **1995**, *41*, 613–627. [CrossRef]
38. Zhang, L.; Bao, P.; Pan, Q. Threshold analysis in wavelet-based denoising. *Electron. Lett.* **2001**, *37*, 1485–1486. [CrossRef]
39. Singh, B.N.; Tiwari, A.K. Optimal selection of wavelet basis function applied to ECG signal denoising. *Digit. Signal Prog.* **2006**, *16*, 275–287. [CrossRef]
40. Xu, C.; Ke, J.C.; Peng, Z.; Fang, W.; Duan, Y. Asymmetric fractal characteristics and market efficiency analysis of style stock indices. *Entropy* **2022**, *24*, 969. [CrossRef]
41. Huang, M.; Shao, W.; Wang, J. Correlations between the crude oil market and capital markets under the Russia–Ukraine conflict: A perspective of crude oil importing and exporting countries. *Resour. Policy* **2023**, *80*, 103233. [CrossRef]

fractal and fractional

Article

Stock Prediction Model Based on Mixed Fractional Brownian Motion and Improved Fractional-Order Particle Swarm Optimization Algorithm

Hongwen Hu, Chunna Zhao *, Jing Li and Yaqun Huang

School of Information Science and Engineering, Yunnan University, Kunming 615202, China
* Correspondence: zhaochunna@ynu.edu.cn

Abstract: As one of the main areas of value investing, the stock market attracts the attention of many investors. Among investors, market index movements are a focus of attention. In this paper, combining the efficient market hypothesis and the fractal market hypothesis, a stock prediction model based on mixed fractional Brownian motion (MFBM) and an improved fractional-order particle swarm optimization algorithm is proposed. First, the MFBM model is constructed by adjusting the parameters to mix geometric Brownian motion (GBM) and geometric fractional Brownian motion (GFBM). After that, an improved fractional-order particle swarm optimization algorithm is proposed. The position and velocity formulas of the fractional-order particle swarm optimization algorithm are improved using new fractional-order update formulas. The inertia weight in the update formula is set to be linearly decreasing. The improved fractional-order particle swarm optimization algorithm is used to optimize the coefficients of the MFBM model. Through experiments, the accuracy and validity of the prediction model are proven by combining the error analysis. The model with the improved fractional-order particle swarm optimization algorithm and MFBM is superior to GBM, GFBM, and MFBM models in stock price prediction.

Keywords: stock forecast; fractional-order particle swarm optimization algorithm; mixed fraction Brownian motion; Hurst

Citation: Hu, H.; Zhao, C.; Li, J.; Huang, Y. Stock Prediction Model Based on Mixed Fractional Brownian Motion and Improved Fractional-Order Particle Swarm Optimization Algorithm. *Fractal Fract.* **2022**, *6*, 560. https://doi.org/10.3390/fractalfract6100560

Academic Editor: Leung Lung Chan

Received: 13 August 2022
Accepted: 28 September 2022
Published: 2 October 2022

1. Introduction

Stock market investment, as one of the most profitable financial investments, is favored by many investors. The forecast of stock price movement has also been the focus of investors' attention [1,2]. From the establishment of the stock market to date, research on market forecasting has never stopped [3]. There are many forecasting methods [4]. From the mathematical finance perspective, there are two main categories. One is the approach based on the efficient market hypothesis (EMH) [5,6] and the other is based on the fractal market hypothesis (FMH) [7].

In the 1970s, Fama [8,9] proposed the famous EMH based on the random wandering model. In EMH, the stock price trend follows the geometric Brownian motion (GBM) model [10]. EMH argued that every investor in the market was rational. Every stock price movement in the market is a comprehensive response to asset information. With prices following a random walk model, it is hard for investors receive a "free lunch" from the market. However, the efficient market hypothesis is only an ideal state and does not correspond to reality. Not every investor in the market has a rational mind and the information that occurs at each point in time is not fully embodied in the price. Some investors make good profits from the market. Therefore, many investors are skeptical of the efficient market hypothesis [11]. From the GBM model, GBM also has three conceptual errors. (1) For the GBM model, future changes are independent of past changes, which is not consistent with the fundamental characteristics of financial market development [12,13]. (2) The GBM model depicts a normal distribution, but real share prices have a "spike and a thick tail" [14]. (3) In stock prices, time series correlation is common everywhere [15]. That is to say, large decreases are usually accompanied by increases in volatility, while large increases are usually accompanied by decreases in volatility. Therefore, GBM cannot correctly describe the phenomenon and the laws of stock prices.

With further research, Peters [16] proposed the FMH from a nonlinear perspective and integrated fractal theory into financial markets. In FMH, stock price changes follow fractional Brownian motion (FBM) and yield obeys a fractal distribution characterized by self-similarity and long memory. FMH believes that the structure of the stock market is fractal and that it has a long memory [17]. The long memory is characterized by the Hurst value. In 2001, Wu pointed out that capital market price movements were mostly the fractal time series [18] and they explored the fractal dimension of stock prices using fractal and chaotic methods. However, Rostek [19,20] thought that there would be arbitrage in applying fractional Brownian motion to simulate prices under the fractal market assumption.

A better solution is to mix geometric Brownian motion and fractional Brownian motion. Then, mixed fractional Brownian motion (MFBM) is constructed to describe the process of asset price change [21]. In terms of the Hurst characteristic index, the standard Brownian motion is just a particular state of price fluctuations. For example, when the Hurst value is equal to 1/2, the fractional Brownian motion is converted to standard Brownian motion [22]. For another view of modern financial theory, the EMH and FMH are internally consistent, and the former is a special case of the latter. The EMH and FMH depict the linear and non-linear natures of financial markets. The fractal market is the general form and steady state of the securities market, while the effective market is the special form and biased state of the securities market. Therefore, the two theories have intrinsic uniformity. EMH reveals the ideal and special state of financial markets. FMH describes the volatility of market prices and the laws of market operation, and it provides a higher level of abstraction and description of financial fields [23]. The combination of EMH and FMH, that is, the combination of geometric and fractional Brownian to form MFBM, is the best model to describe asset price changes [24]. The market under the MFBM model not only has no arbitrage opportunity, but also is complete. It is more suitable for describing the operation and development of the market.

A perfectly efficient market describes the ideal state of financial markets. The most mature U.S. financial market is only between a weakly efficient market and a semi-strongly efficient market. For the Chinese stock market, the limit on ups and downs will keep the stock market in a relatively flat state, which satisfies the semi-strong EMH. In addition, the Chinese stock market is highly cyclical (long memory) [25]. Given these facts, this paper combines EMH and FMH. The price trends of the U.S. and Chinese stock markets are predicted through mixed fractional Brownian motion to obtain better forecasting results.

In this paper, we analyze stock price forms under the EMH and FMH. Then, MFBM is constructed by adjusting the parameters to mix GBM with FBM. The drift and diffusion coefficients in the MFBM model are solved by the maximum likelihood estimation (MLE) method. Then, the fractional-order particle swarm optimization algorithm is improved. The drift and diffusion coefficients of the MFBM are optimized by the improved fractional-order particle swarm optimization algorithm. Finally, the Hurst values are solved by the rescaled range (R/S) analysis method. The solved Hurst values are optimized by the improved fractional-order particle swarm optimization algorithm to find the optimal parameters and analyze the stock price prediction. Three market indices are selected for the Hurst solution and all results show that the three markets have long memory. The accuracy and validity of the prediction model are proven by combining the error analysis. The model with the improved fractional-order particle swarm optimization algorithm and MFBM is superior to GBM, GFBM, and MFBM in stock price prediction.

The main contributions of this paper are summarized as follows. (1) The parameters are adjusted to hybridize geometric and fractional Brownian motions. The MFBM model is constructed and used for stock market forecasting. (2) The fractional-order particle swarm optimization algorithm is improved. The MFBM model coefficients are optimized by the improved fractional-order particle swarm optimization algorithm. New variables are added to reduce the dependence of the update formula on the order of the fractional order. Both velocity and position formulas are derived for fractional order at the same time to improve the convergence speed. (3) The inertia weight factor in the improved fractional-order particle swarm optimization algorithm sets the linear decreasing principle in this paper. This reduces oscillations and increases the randomness of the particles. Therefore, the probability of the population falling into a local optimum is reduced.

The rest of this paper is organized as follows. Section 2 briefly introduces the generalized form of Brownian motion and constructs a stock price prediction model based on mixed fraction Brownian motion. In Section 3, the improvement process of the fractional-order particle swarm optimization algorithm is described in detail. Then, the parameters in the model are solved and optimized separately. In Section 4, three actual stock indices are selected to verify the validity of the IFPSO-MFBM methodology. The conclusion is given in Section 5.

2. MFBM Model

The MFBM model is constructed based on FBM and GBM. Then, some Brownian motion forms are briefly described.

2.1. Geometric Brownian Motion

Geometric Brownian motion is a stochastic equation of motion in continuous time. Since its trajectory is similar to the stock price trajectory, it is continuous but not derivable, with independent increments [26]. Therefore, it is often combined with the Black–Scholes model for stock price simulation in the field of financial mathematics. The stochastic process of GBM is determined by

$$\frac{dS(t)}{S(t)} = \mu dt + \sigma dB(t), \tag{1}$$

where $S(t)$ represents the stock price. The $\frac{dS(t)}{S(t)}$ is the logarithmic return on the stock price and $B(t)$ is the standard Brownian motion (or Wiener process) obeying $N(0,t)$. The drift percentage μ and the volatility percentage σ are both constants. μ is the mathematical expectation of the asset price return. σ is the standard deviation of the asset price return.

From an economic point, Equation (1) can be interpreted using the Itô form stochastic equation, whose solution can be written as a geometric (economic) Brownian motion defined by

$$S_t = S_0 \exp\left\{\sigma B(t) + \left(\mu - \frac{\sigma^2}{2}\right)t\right\}, \tag{2}$$

where S_t is the stock price at time t and S_0 is the initial share price.

Although the B–S pricing model is based on the geometric Brownian motion, the geometric Brownian motion describes share prices that are only appropriate for strong efficient markets. No market currently has strong efficient market conditions, so the geometric Brownian motion does not describe real market share prices.

2.2. Fractional Brownian Motion

Fractional Brownian motion is a derivative form of Brownian motion in the fractal market. There are two main differences between fractional Brownian motion and Brownian motion. One is that increments in fractional Brownian motion are not independent, whereas increments in Brownian motion are independent. The other difference is the dimensional value [27]. Fractional Brownian motion (fractal noise) has a fractional dimensional value. The value is equal to $1/H$; here, H is the Hurst exponent [28]. Brownian motion (white noise) has a fractional dimensional value of 2. The above properties of fractional Brownian motion make it a suitable tool for mathematical finance. The formula for the covariance function of the FBM is determined by

$$E\Big[B^H(t)B^H(s)\Big] = \frac{1}{2}\Big(|t|^{2H} + |s|^{2H} - |t-s|^{2H}\Big), \tag{3}$$

The stochastic process of geometric FBM is as follows:

$$dS(t) = \mu(t)S(t)dt + \sigma S(t)dB^H(t), \tag{4}$$

where B^H is the fractional Brownian motion. The share price is based on (5) as follows:

$$S(t) = S_0 \exp\left(\sigma B^H(t) + \mu t - \frac{1}{2}\sigma^2 t^{2H}\right), \tag{5}$$

Fractional Brownian motion has long memory and is useful for financial market forecasting. Theoretically, there would be arbitrage in the model with FBM as the logarithmic price. In particular, it has been shown that arbitrage opportunities exist when trading in continuous or in discrete time [29,30].

2.3. Mixed Fractional Brownian Motion

Based on the intrinsic consistency of the EMH and FMH, a mixed fractional Brownian motion is constructed by adjusting the parameters to hybridize the geometric Brownian motion with the geometric fractional Brownian motion. The stochastic process of MFBM is determined by

$$dS(t) = \mu(t)S(t)dt + \sigma S(t)dW^H(t), \tag{6}$$

$$dW^H(t) = \rho dB^H(t) + (1-\rho)dB(t),\ \rho \in (0,1), \tag{7}$$

where ρ is the mixing factor to be adjusted. The drift percentage μ and the volatility percentage σ are both constants. The $B(t)\big(t \in R^+\big)$ is a standard Brownian motion. The $B^H(t)\big(t \in R^+\big)$ is a fractional Brownian motion with a Hurst value of H. These are independent of each other. The share price form is as follows:

$$S_t = S_0 \exp\{\ \mu t + \sigma W^H(t)\}, \tag{8}$$

which converts to Itô form as follows:

$$S_t = S_0 \exp\{\mu t + \sigma W^H(t) - \frac{1}{2}\sigma^2\rho^2 t^{2H} - \frac{1}{2}\sigma^2(1-\rho)^2 t\}, \tag{9}$$

In the MFBM model, the solution process of $B^H(t)$ is as follows:

$$B^H(t) = \int_t^0 K_H(t,s)dB(s), \tag{10}$$

$$K_H(t,s) = c(H)\frac{1}{s^{H-\frac{1}{2}}}\int_t^s \frac{u^{H-\frac{1}{2}}}{u - s^{\frac{3}{2}-H}}du, \tag{11}$$

$$c(H) = \sqrt{\frac{2H\Gamma\left(\frac{3}{2}-H\right)}{\Gamma\left(H+\frac{1}{2}\right)\Gamma(2-2H)}}(H - \frac{1}{2}), \tag{12}$$

In (12), $K_H(t,s)$ is a definite kernel, $c(H)$ is the normalization constant, and Γ is the Gamma function, which can be solved according to Euler's residue formula. The definition of the Gamma function over the real number field is defined by

$$\Gamma(x) = \int_0^{+\infty} t^{x-1}e^{-t}dt(x>0), \tag{13}$$

Then, the $B^H(t)$ value can be found here. The mixed fractional Brownian motion removes the arbitrage of fractional Brownian motion and retains its memorability [31]. It also combines the incremental and smooth characteristics of geometric Brownian motion.

3. IFPSO-MFBM

The MFBM model that is constructed in the previous section contains a large number of parameters. Therefore, this section focuses on solving and optimizing the model parameters. Firstly, the fractional-order particle swarm optimization algorithm is improved. Hurst values in the model are then solved using rescaled range (R/S) analysis. Finally, the maximum likelihood estimate (MLE) method is used to find the drift and diffusion coefficients and the coefficients are further optimized using the improved fractional-order particle swarm optimization algorithm (IFPSO). The flow chart of stock index forecasting, based on the MFBM model and IFPSO algorithm, is shown in Figure 1.

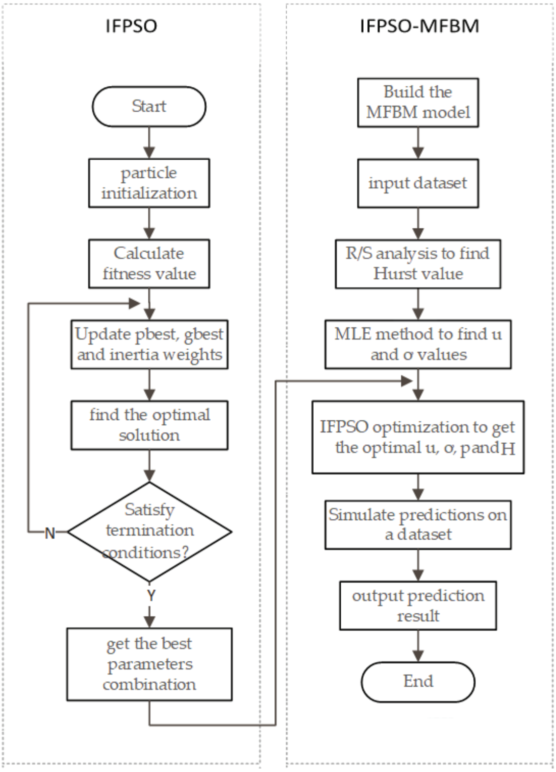

Figure 1. IFPSO-MFBM prediction model flow chart.

3.1. *Fractional-Particle Swarm Optimization Algorithm Improvement*

The particle swarm optimization (PSO) algorithm originated from the simulation of the foraging behavior of birds [32]. The PSO algorithm is conceptually simple. It is easy to implement and converges quickly [33]. It is widely used to solve multi-objective optimization problems [34]. The standard PSO algorithm velocity and position formula are defined by

$$V_{id}^{k+1} = w \times V_{id}^{k} + c_1 \times r_1 \times \left(P_{id}^{k} - X_{id}^{k}\right) + c_2 \times r_2 \times \left(P_{gd}^{k} - X_{id}^{k}\right), \tag{14}$$

$$X_{id}^{k+1} = X_{id}^{k} + V_{id}^{k+1}, \tag{15}$$

where k is the number of iterations. P_{id}^{k} is the particle position and V_{id}^{k} is the particle velocity. c_1 and c_2 are acceleration factors. r_1 and r_2 are random numbers distributed between (0, 1). w is the inertia weight factor. The weight update equation is computed by

$$w(k) = w_{max} - \frac{(w_{max} - w_{min}) * k}{k_{max}}, \tag{16}$$

In the standard PSO algorithm, the particles converge slowly. Therefore, Pires [35] introduced fractional order calculus into PSO and proposed the fractional order particle swarm optimization (FOPSO) algorithm. The convergence speed of the algorithm is improved by introducing fractional order integration in the particle swarm velocity equation. However, the FOPSO algorithm is susceptible to falling into local solutions. When dealing with complex multi-peaked problems, the FOPSO algorithm tends to the local optimum. The convergence performance is directly dependent on the fractional order α. When the value of α increases, the particles converge more slowly. When the value of α decreases, the population tends to fall into a local optimum. In this paper, we improve the fractional-order algorithm. The velocity and position equations are derived by fractional order calculus simultaneously. The inertia weight factor w is set to be linearly decreasing to avoid falling into a local optimum.

When improving the PSO algorithm, the fractional order Grunwald–Letnikov (G–L) definition is used. Its α(R) order derivative is approximated in discrete time as follows:

$$D^{\alpha} f(x) = \frac{1}{T^{a}} \sum\nolimits_{k=0}^{r} \frac{(-1)^{k} \Gamma(\alpha+1) f(x-kh)}{\Gamma(k+1)\Gamma(\alpha-k+1)}, \tag{17}$$

where T is the sampling period and Γ is the Gamma function.

The PSO fractional order improvement process is as follows:

Step 1: A left-right transformation of the standard particle swarm algorithm is made; then, there is the following equation

$$V_{id}^{k+1} - V_{id}^{k} = (w-1) \times V_{id}^{k} + c_1 \times r_1 \times \left(P_{id}^{k} - X_{id}^{k}\right) + c_2 \times r_2 \times \left(P_{gd}^{k} - X_{id}^{k}\right), \tag{18}$$

where $V_{id}^{k+1} - V_{id}^{k}$ is the derivative of the discrete state at fractional order α = 1;

Step 2: Assuming a sampling period T = 1, followed by a generalization of Equation (18) to fractional order differentiation:

$$D^{a}\left[V_{id}^{k+1}\right] = (w-1) \times V_{id}^{k} + c_1 \times r_1 \times \left(P_{id}^{k} - X_{id}^{k}\right) + c_2 \times r_2 \times \left(P_{gd}^{k} - X_{id}^{k}\right); \tag{19}$$

Step 3: Considering the decreasing relationship between the number of contemporary particles and the number of particles of previous generations, Equation (19) is kept for only the first four generations of vectors owing to the memory property of fractional order calculus. The velocity formulation of the particle swarm algorithm is extended from first order to arbitrary order through the fractional order G-L definition.

$$D^{a}\left[V_{id}^{k+1}\right] = V_{id}^{k+1} - aV_{id}^{k} - \frac{1}{2}a(1-a)V_{id}^{(k-1)} - \frac{1}{6}a(1-a)(2-a)V_{id}^{(k-2)} - \frac{1}{24}a(1-a)(2-a)(3-a)V_{id}^{(k-3)}; \tag{20}$$

Step 4: Combining (19) and (20), the final velocity equation of the fractional-order particle swarm algorithm with linearly decreasing weight coefficients is obtained

$$\begin{gathered} V_{id}^{k+1} = (w-1+a)V_{id}^{k} + \tfrac{1}{2}a(1-a)V_{id}^{(k-1)} - \tfrac{1}{6}a(1-a)(2-a)V_{id}^{(k-2)} + \\ \tfrac{1}{24}a(1-a)(2-a)(3-a)V_{id}^{(k-3)} + c_1 \times r_1 \times \left(P_{id}^{k} - X_{id}^{k}\right) + c_2 \times r_2 \times \left(P_{gd}^{k} - X_{id}^{k}\right), \end{gathered} \tag{21}$$

By introducing fractional order differential operators, the current particle swarm algorithm is made to relate to the particle velocities of previous stages. Therefore, the algorithm is made to have a memory function;

Step 5: Then, the same fractional-order improvement is performed for the position update. The position updating formula of the fractional order particle swarm algorithm with linearly decreasing weight coefficients is obtained:

$$\begin{gathered}X_{id}^{k+1} = (w - 1 + a)V_{id}^{k} + \tfrac{1}{2}a(1 - a)V_{id}^{(k-1)} - \tfrac{1}{6}a(1 - a)(2 - a)V_{id}^{(k-2)} + \\ \tfrac{1}{24}a(1 - a)(2 - a)(3 - a)V_{id}^{(k-3)} + c_1 \times r_1 \times \left(P_{id}^{k} - X_{id}^{k}\right) + \\ c_2 \times r_2 \times \left(P_{gd}^{k} - X_{id}^{k}\right) + \beta X_{id}^{k} + \tfrac{1}{2}\beta(1 - \beta)X_{id}^{k-1} + \tfrac{1}{6}\beta(1 - \beta)(2 - \beta)X_{id}^{k-2}\end{gathered} \tag{22}$$

The positions of the particles of the improved fractional-order particle swarm algorithm (IFPSO) are no longer only influenced by the fractional order α. The introduction of fractional order β allows the position update to be associated with the previous position.

The IFPSO offers significant improvements in convergence speed, stability, and accuracy, and further enhances the ability to find globally optimal solutions.

3.2. R/S Analysis for Hurst Index

When Hurst (the British hydrologist) studied the relationship between water flow and storage capacity in the Nile reservoir, he found that the relationship could be better described in terms of fractal Brownian motion [36]. He then proposed the Hurst index. There are several methods for solving the Hurst exponent [37]. The earliest method proposed by scholars in the time domain is the R/S estimation method. After that, wavelet analysis, the variance method, and the mean value method were gradually derived [38]. This paper focuses on solving Hurst values using R/S analysis. The process is as follows:

1. Let a time series $\{x_t\}_t^M = 1$, of length M, be divided into N adjacent subintervals of length $\mid \frac{M}{N} \mid$;
2. For the subintervals, let the sample mean be $e_u = \frac{1}{N}\sum_{i=1}^{N} x_i + (u - 1) \times N \left(u = 1, 2, \ldots, \mid \frac{M}{N} \mid\right)$;
3. For a subinterval u, take $y_{u,i} = x_i + (u - 1) \times N - e_u(i = 1,\ 2,\ \ldots,\ N)$ such that $z_{u,i} = \sum_{i=1}^{N} y_{u,i}$. The $z_{u,i}$ is the cumulative return. Here, u = 1, 2, ... ,$\mid \frac{M}{N} \mid$;
4. Calculate $R_u = \max_{1 \le N \le N} Z_{u,i} - \min_{1 \le i \le N} Z_{u,i}$ as the extreme deviation of the subinterval u. Let S_u be the standard deviation of the cumulative return for the interval;
5. Calculate the rescaled polar difference R_u/S_u for each interval; $\mid \frac{M}{N} \mid$ intervals can obtain $\mid \frac{M}{N} \mid$ values (u = 1, 2, ...). Take its mean value R_N/S_N as the rescaled polar deviation value for an interval of length N;
6. Taking the logarithm of both ends of the $R_N/S_N = bN^H$ equation yields: $\log(R_N/S_N) = H\log N + \log b y(n)$; b is a constant and H is the Hurst index;
7. Repeat Steps 1 to 6 for different interval lengths N to obtain different values of R_N/S_N. By regression analysis, the slope is the desired H value.

Given a time series X_i, $i = 1, 2, \ldots, N$, calculate the sum of the partial series as $y(n) = \sum_{i=1}^{n} X_i$ and define the sample variance as $S^2(n)$; then, one obtains the formula:

$$S^2(n) = \frac{1}{n}\sum_{i=1}^{n} X_i^2 - \frac{1}{n^2}y^2(n), \tag{23}$$

The final R/S is calculated by

$$\frac{R}{S}(n) = \frac{1}{S(n)}\left[\max_{0 \le t \le n}\left(y(t) - \frac{t}{n}y(t)\right) - \min_{0 \le t \le n}\left(y(t) - \frac{t}{n}y(t)\right)\right], \tag{24}$$

When $n \to \infty$, $E[R/S(n)] \sim C_H n^H$, C_H is a constant positive constant, taking the logarithm of the above Equation (24). A log–log plot is drawn and a straight line is fitted using least squares regression. The slope of this line is calculated as the Hurst index value for a given time series.

3.3. MLE Method for the Drift Coefficient μ and the Diffusion Coefficient σ

The MLE method [39] is chosen to estimate the parameters σ and μ in this paper. According to the solution of ordinary differential equations, take the logarithm of the left and right sides of Equation (9) to obtain:

$$\ln(S_t) - \ln(S_0) = \mu t + \sigma W_t^H, \tag{25}$$

Thus, the parameter estimate for Equation (25) is equivalent:

$$Y_t = \mu t + \sigma W_t^H,\ t \geq 0, \tag{26}$$

The time series observation interval is h. The vector $t = (h, 2h, \ldots, Nh)$ is used to represent the observation time point. The observation vectors $Y = (Y_h,\ Y_{2h}, \ldots,\ Y_{Nh})$ are obtained. The MFBM process is $W_t^H = \left(W_{(h)}^H,\ W_{(2h)}^H, \ldots,\ W_{(Nh)}^H\right)$. Then, the maximum likelihood estimates of the drift coefficient μ and the diffusion coefficient σ are derived from the following steps.

According to the joint density of the multidimensional normal distribution, the MFBM model has the properties of a Gaussian process. Therefore, the observation vector Y obeys a multivariate normal distribution. Substitute Y into Equation (26) and then derive the specific expression for each covariance σ_H^2 in the discrete covariance matrix $\sum_H$ based on (25) as follows:

$$\sigma_H^2 = \left[E\left[W_{(ih)}^H, W_{(jh)}^H\right]\right]_{i,j=1,2,\ldots N} = \frac{\sigma^2}{2} h^{2H}\left(i^{2H} + j^{2H} - \left|i-j\right|^{2H}\right)_{i,j=1,2,\ldots N}, \tag{27}$$

The joint probability density function of the multidimensional normal distribution of Y is defined by

$$g(Y) = \left(2\pi\sigma^2\right)^{-\frac{N}{2}} |\Gamma_H|^{-\frac{1}{2}} \exp\left(-\frac{1}{2\sigma^2}(Y-\mu t)'\Gamma_H^{-1}(Y-\mu t)\right), \tag{28}$$

where $\Gamma_H = \frac{1}{2}h^{2H}\left(i^{2H} + j^{2H} - \left|i-j\right|^{2H}\right)_{i,j=1,2,\ldots,N}$.

Find the log-likelihood function for the joint probability density function:

$$\ln g(Y) = -\frac{N}{2}\ln\left(2\pi\sigma^2\right) - \frac{1}{2}\ln|\Gamma_H| - \frac{1}{2\sigma^2}(Y-\mu t)'\Gamma_H^{-1}(Y-\mu t), \tag{29}$$

Find the partial derivatives for μ and σ^2 with respect to (26). Set the partial derivatives equal to 0.

The maximum likelihood estimate of the drift coefficient μ is obtained by taking the partial derivative of μ as:

$$\grave{\mu} = \frac{t'\Gamma_H^{-1}Y}{t'\Gamma_H^{-1}t'}, \tag{30}$$

Similarly, the maximum likelihood estimate for finding the partial derivative σ^2 is as follows:

$$\grave{\sigma}^2 = \frac{1}{N}\frac{\left(Y'\Gamma_H^{-1}Y\right)\left(t'\Gamma_H^{-1}t\right) - \left(t'\Gamma_H^{-1}Y\right)^2}{t'\Gamma_H^{-1}t}, \tag{31}$$

3.4. IFPOS Algorithm Optimizing σ, μ, ρ, and H

In this paper, σ, μ, ρ, and H are optimized by the improved fractional PSO algorithm in Section 3.1. The steps can be summarized as follows:

Step 1: The Hurst of the MFBM model is obtained from known stock market data and the unknown parameters are determined based on R/S analysis;

Step 2: Using the maximum likelihood estimation method, the drift coefficient σ and the diffusion coefficient μ are solved separately to obtain the original values of each parameter of the model;

Step 3: The IFPSO algorithm is used to continue the optimization of the model parameters. The individual extreme value of each particle is set to the current position. According to the weight update formula, the current inertia weight value is calculated and updated. The velocity and position of the particle are updated according to the improved particle velocity and position update formula;

Step 4: The updated fitness value of each particle is calculated according to the fitness function of the particle. The fitness value of each particle is compared with its individual extreme value. If the individual extreme value is better than the fitness value, the individual extreme value is updated. Otherwise, the original fitness value is kept;

Step 5: The updated individual polar values of each particle are compared with the global polar values. If the individual extreme value is better than the global polar value, the global polar value is updated. Otherwise, the original global polar value is kept;

Step 6: The optimization search process is broken based on the setting fitness function and iterations. Then, the final MFBM prediction model is established.

This section focuses on the solution and optimization of three parameters in the MFBM model. The Hurst value is solved using R/S analysis and the MLE method is used to solve the drift and diffusion coefficients. Finally, the fractional order particle swarm algorithm is improved and used to optimize each parameter in the MFBM model.

4. Experiments

Three market indices are selected for research and analysis in this section. They are the A-share SSE, the Hong Kong Hang Seng index, and the US Dow Jones index. Firstly, the Hurst values of the three market indices are solved to verify the existence of memory. Then, the parameters are solved and optimized by the above steps. Finally, the stock price forecasting results from IFPSO-MFBM, MFBM, FBM, and GBM are compared. The forecasting effect of the IFPSO-MFBM model is analyzed.

4.1. Model Evaluation Indicators

Three performance indicators are used to evaluate and compare the prediction effectiveness. They are mean absolute percentage error (MAPE), symmetric mean absolute percentage error (SMAPE), and coefficient of determination (R2).

MAPE is one of the most popular indicators that can be used to assess predictive performance. It is given by the following equation:

$$\mathrm{MAPE} = \frac{100\%}{n} \sum\nolimits_{i=1}^{n} \left| \frac{\grave{R}_i - R_i}{R_i} \right|, \tag{32}$$

where $\grave{R}_i$ is the predicted value and R_i is the true value.

SMAPE overcomes the asymmetry of MAPE. It is one of the commonly used indicators to assess predictive performance. Its equation is as follows:

$$\mathrm{SMAPE} = \frac{100\%}{n} \sum\nolimits_{i=1}^{n} \frac{\left|\grave{R}_i - R_i\right|}{\left(\grave{R}_i + R_i\right)/2}, \tag{33}$$

The benefit of the model is judged according to the value of R2, $\mathrm{R2} \in (0, 1)$. If R2 is closer to 1, it is better for the model fit.

$$\mathrm{R2} = 1 - \sum\nolimits_{i=1}^{n} \frac{\left(\grave{R}_i - R_i\right)^2}{\left(R_i - R_i\right)^2}, \tag{34}$$

Table 1 shows the interpretation of the results acquired with MAPE and SMAPE.

Table 1. Explanation of MAPE and SMAPE evaluation indicators.

MAPE Value	SMAPE Value	Predictive Performance Evaluation
<10%	<10%	Highly accurate forecasting
10–20%	10–20%	Good forecasting
20–50%	20–50%	Reasonable forecasting
>50%	>50%	Inaccurate forecasting

The physical significance, data units, and orders of magnitude of each attribute in the selected dataset are different.

4.2. Experimental Data

The required stock price data are obtained from Yahoo Finance's historical data for the past five years (https://www.yahoo.com/finance, access date: 6 July 2022.). Three market indicators are selected for model validation analysis. They are SSE, Hang Seng, and Dow Jones. The main index data are the opening price, closing price, high price, and low price of stock.

4.3. Experimental Verification and Analysis

Considering a long memory of fractional Brownian motion, this paper selected as a market cycle [40] (252 day,) as the observation data set; the prediction is the next ten trading days of the index trend, that is, 1 July 2019–15 July 2019, based on the past year's trading day data predicted from the same data after that. As shown in Figure 2, the experimental data uses a sliding window (windows = 252) to move backward and forward by 10 trading day lengths each time, so as to obtain the complete set of predicted data.

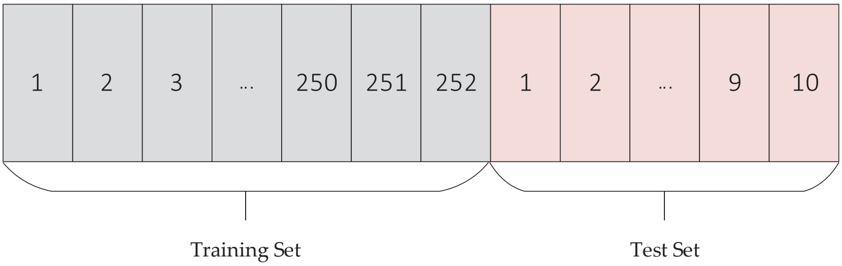

Figure 2. Comparison of SSE index results of algorithm optimization search.

Here, the prediction performance of the GBM, GFBM, MFBM, and IFPSO-MFBM models proposed in this paper are compared for stock price trends. The forecasting results of the four models are analyzed.

4.3.1. SSE Index Data Prediction Analysis

This experiment uses the Chinese A-share SSE index dataset to validate the model prediction effect. The main data is the daily closing price of the SSE index from 1 July 2019–1 July 2022.

1. Parameter solving and optimization

The parameters in the MFBM model are solved and optimized according to the steps in Section 3.

From Figure 3, it can be seen that improved fractional-order particle swarm algorithm (IFPSO) outperforms the particle swarm algorithm (PSO) in terms of both convergence speed and merit-seeking effect. The results are shown in Table 2.

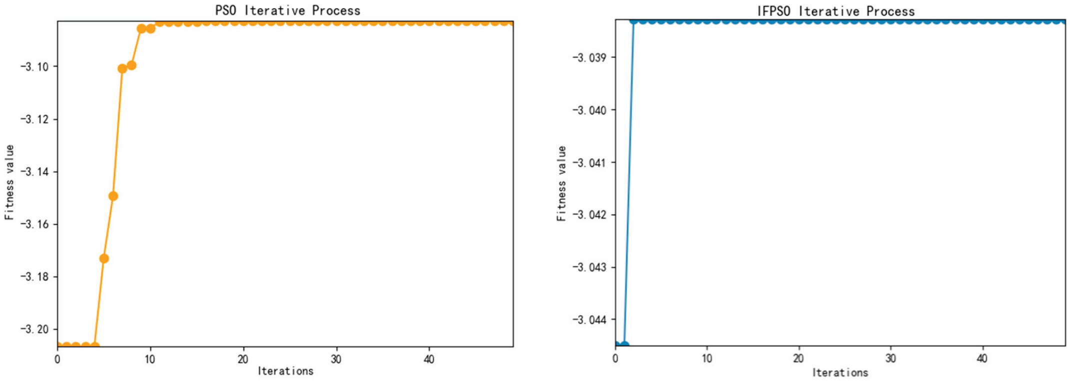

(**a**) (**b**)

Figure 3. Comparison of SSE index results of algorithm optimization search. (**a**) PSO, (**b**) IFPSO.

Table 2. MFBM model parameters and optimization results for the SSE index.

Index Set	Parameters	R/S	MLE	IFPSO
SSE	μ	-	0.0521	0.1209
	σ	-	0.1739	0.1221
	ρ	-	-	0.7893
	H	0.5214	-	0.5334

Based on the SSE index data, the mean Hurst value of 0.5214 is first obtained by R/S analysis. Then, we obtain $\grave{\mu} = 0.0521$ and $\grave{\sigma} = 0.1739$ by the MLE method. Since the value by the MLE method is not optimal, it is further optimized by the IFPSO algorithm in this paper to obtain $\mu = 0.1209$, $\sigma = 0.1221$, and $\rho = 0.789$. To reduce the influence of the initial value, the Hurst value is also optimized using the IFPSO, and H = 0.5334 is finally obtained. The change in optimization is evident in the data. The final optimization effect is judged by the magnitude of MAPE, SMAPE, and R2.

The seed is the random seed number of the random model. The experiment takes the best seed value in the seed (1~200).

2. Comparison of Simulation Results

The parameters of the four models (GBM, GFBM, MFBM, and IFPSO-MFBM) are set as in Table 3. The experimental comparison images are as follows:

Table 3. Parameters of the SSE in the four models.

Index Set	Model	Seed	μ	σ	ρ	Hurst
SSE	GBM	87	0.0521	0.1739	-	-
	GFBM	136	0.0521	0.1739	-	0.5214
	MFBM	143	0.0521	0.1739	0.5	0.5214
	IFPSO – MFBM	143	0.1209	0.1221	0.7893	0.5334

Figure 4a shows the result of the predictive simulation of the SSE in the GBM. The main parameters of the model are Seed = 87, u = 0.0521, and $\sigma = 0.1739$. Figure 4b is the result of the predictive simulation of the SSE in the FBM model. The main parameters have that Seed = 136, u = 0.0521, $\sigma = 0.1739$, and H = 0.5214. Figure 4c shows the result of the predictive simulation of the SSE in MFBM model, with Seed = 143, u = 0.0521, $\sigma = 0.1739$, $\rho = 0.5$, and H = 0.5214. Figure 4d shows the predictive simulation result of the SSE index in the optimized IFPSO-MFBM model. The main parameters are Seed = 143, u = 0.1209, σ = 0.1221, ρ = 0.7893, and H = 0.5334. The specific error magnitudes can be shown in Table 4.

(**a**) (**b**)

(**c**) (**d**)

Figure 4. Comparison of the true and predicted values of SSE under the four models. (**a**) GBM, (**b**) GFBM, (**c**) MFBM, (**d**) IFPSO-MFBM.

Table 4. Comparative error analysis of SSE index under four models.

Index Set	Model	MAPE%	SMAPE%	R2
SSE	GBM	4.3782	4.2857	0.6089
	GFBM	3.6379	3.6439	0.7163
	MFBM	4.3878	4.4227	0.6247
	IFPSO-MFBM	3.3442	3.3262	0.7019

As can be seen, the MFBM model has the largest error in prediction, with a MAPE of 4.3878%. The optimized IFPSO-MFBM has the smallest error, with a MAPE of 3.3342%. The IFPSO-MFBM model has a reduced MAPE of 1.0436% compared to the MFBM model. In addition, the forecasting errors of the SSE index in all four models are less than 10%. It can be proven that all four models achieve high precision forecasting results.

Based on the forecast results, considering an incremental increase of more than 2% per 10 trading days and a forecast error of less than 1% (i.e., the trend is the same and the error is less than 1%), the returns obtained are shown in Table 5.

The GBM model return of 17.14%, the GFBM model return of 14.41%, the MBM model return of 15.45% and the IFPSO-MFBM model return of 28.15% can be seen. All four models returned greater than 10%, and the MFBM model had the best return

Table 5. Comparative analysis of SSE index returns under four models.

Index Set	Model	Returns (1 July 2019–1 July 2022)
SSE	GBM	0.1714
	GFBM	0.1441
	MFBM	0.1545
	IFPSO-MFBM	0.2815

4.3.2. Hang Seng Index Data Prediction Analysis

This experiment uses the Hong Kong Hang Seng index dataset to validate the model prediction effect. The main data is the daily closing price of the Hang Seng index from 1 July 2019–1 July 2022.

1. Parameter solving and optimization

The parameters in the MFBM model are solved and optimized according to the steps in Section 3.

From Figure 5, it can be seen that IFPSO outperforms the PSO algorithm in terms of the merit-seeking effect. The results are shown in the table below.

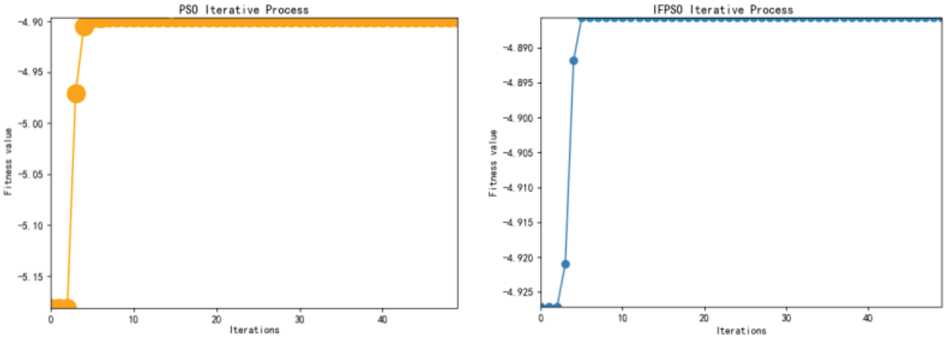

(**a**) (**b**)

Figure 5. Comparison of Hang Seng index results of algorithm optimization search. (**a**) PSO, (**b**) IFPSO.

As can be seen in Table 6, the mean Hurst value of 0.5651 is first obtained by R/S analysis. Then, we obtain $\hat{\mu} = -0.0677$, $\hat{\sigma} = 0.2318$ by the MLE method. This is further optimized by the IFPSO algorithm in this paper to obtain $\mu = 0.2631$, $\sigma = 0.5820$, and $\rho = 0.7496$. The Hurst is also optimized using IFPSO and Hurst = 0.6160 is finally obtained. The change in optimization is evident in the data. The final optimization effect is judged by the magnitude of MAPE, SMAPE, and R2.

The seed is the random seed number setting of the random model, this experiment takes the best seed value in the seed (1~200).

Table 6. MFBM model parameters and optimization results for the Hang Seng index.

Index Set	Parameters	R/S	MLE	IFPSO
Hang Seng	μ	-	-0.0677	0.2631
	σ	-	0.2318	0.5820
	ρ	-	-	0.7496
	H	0.5651	-	0.6160

2. Comparison of Simulation Results

The parameters of the four models (GBM, GFBM, MFBM, and IFPSO-MFBM) are set as in Table 7; the experimental comparison images are as follows.

Table 7. Parameters of the Hang Seng in the four models.

Index Set	Model	Seed	μ	σ	ρ	Hurst
Hang Seng	GBM	107	−0.0677	0.2318	-	-
	GFBM	121	−0.0677	0.2318	-	0.5651
	MFBM	89	−0.0677	0.2318	0.5	0.5651
	IFPSO − MFBM	89	0.2631	0.5820	0.7496	0.6160

Figure 6a shows a plot of the results of the predictive simulation of the Hang Seng in the GBM. Figure 6b shows a plot of the results of the predictive simulation of the Hang Seng in the FBM model. Figure 6c shows a plot of the results of the predictive simulation of the Hang Seng in the MFBM model. Figure 6d shows a plot of the predictive simulation results of the Hang Seng index in the IFPSO-MFBM model. For the specific error magnitudes, see the table below.

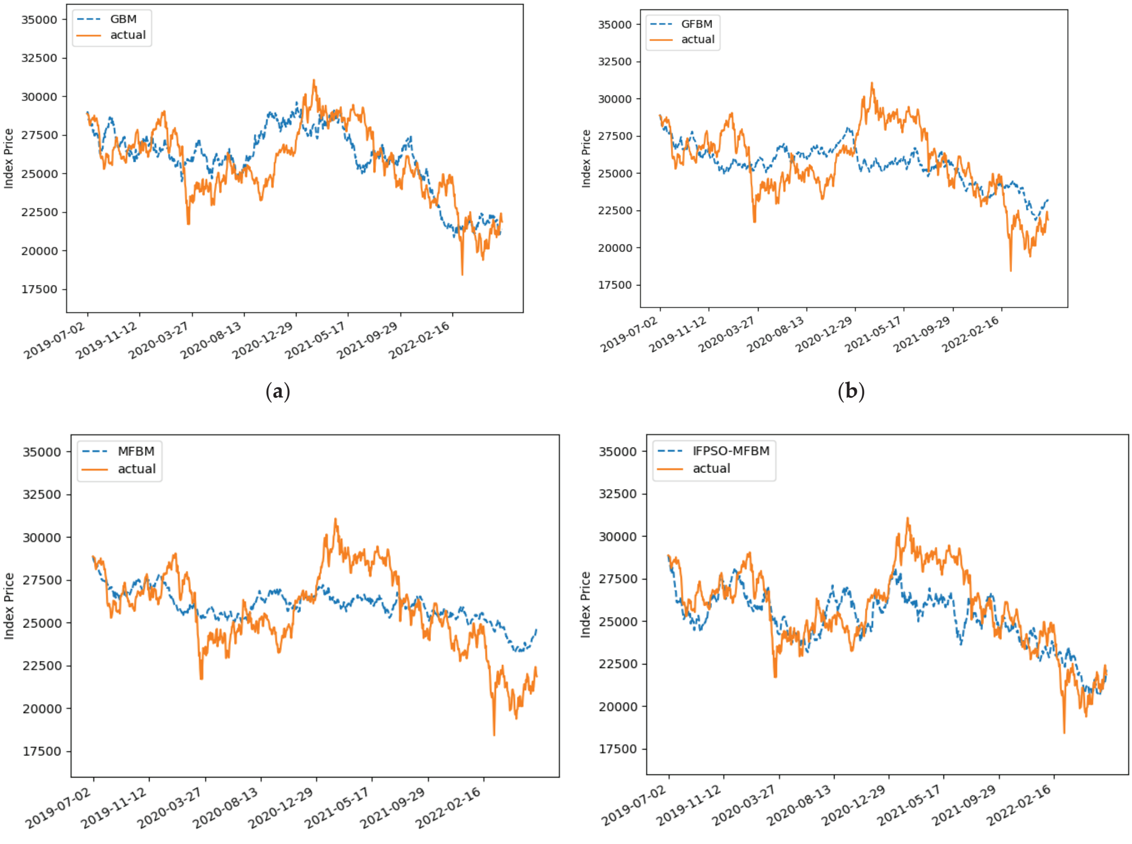

(**a**) (**b**) (**c**) (**d**)

Figure 6. Comparison of the true and predicted values of Hang Seng under the four models. (**a**) GBM, (**b**) GFBM, (**c**) MFBM, (**d**) IFPSO-MFBM.

As can be seen from Table 8, the GFBM model has the largest error in prediction, with a MAPE of 6.5526%. The IFPSO-MFBM has the smallest error, with a MAPE of 4.8857%. The IFPSO-MFBM model has a reduced MAPE of 1.3307% compared to the MFBM model. The IFPSO-MFBM after parameter optimization has been improved to a certain extent. In addition, the forecasting error of the Hang Seng index in all four models are less than 10%. This proves that all four models achieve high precision forecasting results and have a highly accurate forecasting effect.

Table 8. Comparative error analysis of Hang Seng index under four models.

Index Set	Model	MAPE%	SMAPE%	R2
Hang Seng	GBM	5.4472	5.3733	0.4893
	GFBM	6.5526	6.5584	0.2990
	MFBM	6.2164	6.1092	0.3836
	IFPSO-MFBM	4.8857	4.9752	0.5348

Based on the forecast results, the returns obtained are shown in Table 9.

Table 9. Comparative analysis of Hang Seng index returns under four models.

Index Set	Model	Returns (1 July 2019–1 July 2022)
Hang Seng	GBM	0.1474
	GFBM	0.1168
	MFBM	0.1173
	IFPSO-MFBM	0.2307

The GBM model return of 14.74%, GFBM model return of 11.68%, MBM model return of 11.73%, and the IFPSO-MFBM model return of 23.07% can be seen. All four models returned greater than 10%, and the MFBM model had the best return

4.3.3. Dow Jones Index Data Prediction Analysis

This experiment uses the US Dow Jones index dataset to validate the model prediction effect; the main data is the daily closing price of the Dow Jones index from 1 July 2019–1 July 2022.

1. Parameter solving and optimization

The parameters in the MFBM model were solved and optimized according to the parameter solving and optimization process in Part 3.

From Figure 7, it can be seen that IFPSO outperforms the PSO algorithm in terms of both convergence speed and merit-seeking effect. The results are shown in the table below.

As can be seen in Table 10, the Hurst value of 0.5939 is first obtained by R/S analysis; then, $\hat{\mu} = 0.0804$ and $\hat{\sigma} = 0.2436$ were obtained by the MLE method. Since the value obtained by the MLE method is not optimal. It is further optimized by the IFPSO algorithm in this paper to obtain $\mu = 0.0127$, $\sigma = 0.2790$, and $\rho = 0.3983$. To reduce the influence of the initial value, the Hurst is also optimized using IFPSO, and Hurst = 0.5480 is finally obtained. The change in optimization is evident in the data and the final optimization effect is judged by the magnitude of MAPE and SMAPE.

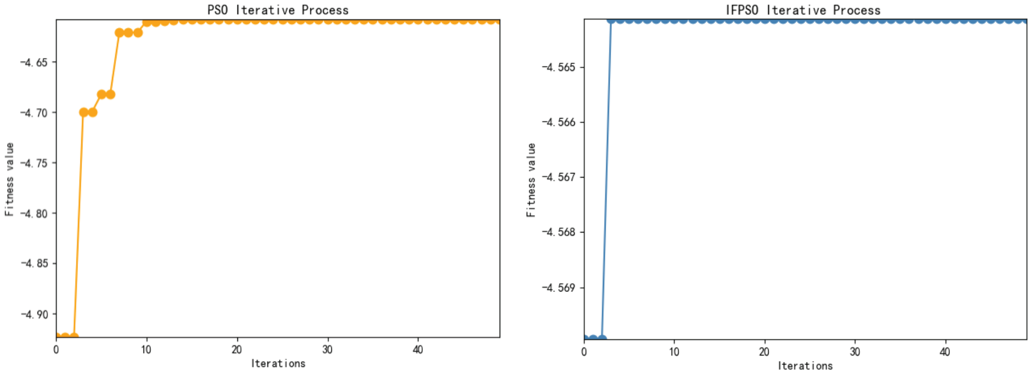

(**a**) (**b**)

Figure 7. Comparison of Dow Jones results of algorithm optimization search. (**a**) PSO, (**b**) IFPSO.

Table 10. MFBM model parameters and optimization results for the Dow Jones index.

Index Set	Parameters	R/S	MLE	IFPSO
Dow Jones	μ	-	0.0804	0.0127
	σ	-	0.2436	0.2790
	ρ	-	-	0.3983
	H	0.5939	-	0.5480

The seed is the random seed number setting of the random model, this experiment takes the best seed value in the seed (1~200).

2. Comparison of Simulation Results

The parameters of the four models (GBM, GFBM, MFBM, and IFPSO-MFBM) are set as in Table 11 and the experimental comparison images are as follows.

Table 11. Parameters of the Dow Jones in the four models.

Index Set	Model	Seed	μ	σ	ρ	Hurst
Dow Jones	GBM	170	0.0804	0.2436	-	-
	GFBM	188	0.0804	0.2436	-	0.5939
	MFBM	52	0.0804	0.2436	0.5	0.5939
	IFPSO − MFBM	52	0.0127	0.2790	0.3983	0.5480

Figure 8a shows the result of the predictive simulation of the Dow Jones in the GBM. Figure 8b shows the result of the predictive simulation of the Dow Jones in the FBM model. Figure 8c shows the result of the predictive simulation of the Dow Jones in the MFBM model. Figure 8d shows the predictive simulation result of the Dow Jones index in the IFPSO-MFBM model. For specific error magnitudes, see the table below.

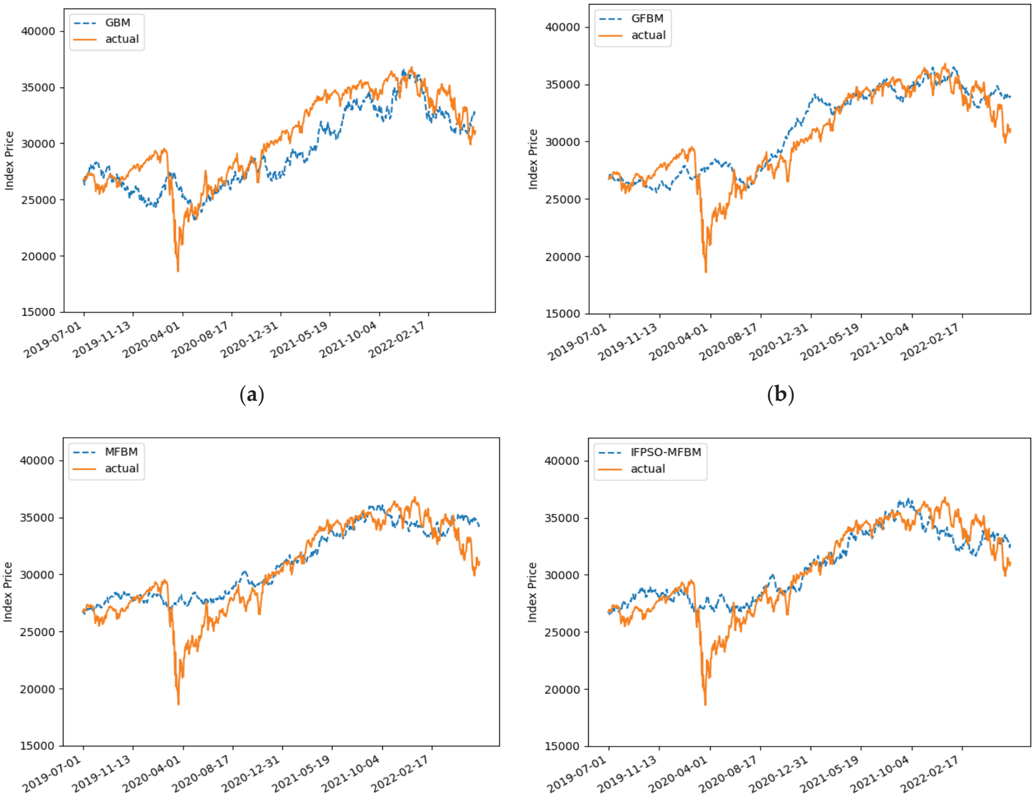

(**a**) (**b**) (**c**) (**d**)

Figure 8. True vs. predicted values of the Dow Jones index under the four models. (**a**) GBM, (**b**) GFBM, (**c**) MFBM, (**d**) IFPSO-MFBM.

As can be seen in Table 12, the GBM model has the largest error in prediction, with a MAPE of 6.0259%. The IFPSO-MFBM had the smallest error, with a MAPE of 4.4196%. The IFPSO-MFBM model has a reduced MAPE of 1.0939% compared to the MFBM model. The IFPSO-MFBM after parameter optimization was improved to a certain extent. In addition, the R2 of the Dow Jones index in all four models is larger than 0.6, which proves that all four models have a good forecasting effect.

Table 12. Comparative error analysis of Dow Jones index under four models.

Index Set	Model	MAPE%	SMAPE%	R2
Dow Jones	GBM	6.0259	6.1553	0.6816
	FBM	4.9502	4.7362	0.7591
	MFBM	5.5135	5.3750	0.7113
	IFPSO-MFBM	4.4196	4.1912	0.7662

Based on the forecast results, the returns obtained are shown in Table 13.

Table 13. Comparative analysis of the Dow Jones index returns under four models.

Index Set	Model	Returns (1 July 2019–1 July 2022)
Dow Jones	GBM	0.1426
	GFBM	0.2158
	MFBM	0.1033
	IFPSO-MFBM	0.3083

The GBM model return of 14.26%, GFBM model return of 21.58%, MBM model return of 10.33% and the IFPSO-MFBM model return of 30.83% can be seen. All four models returned greater than 10%, and the MFBM model had the best return

From three experiments, it can be shown that the IFPSO-MFBM has the best result of the four models. The MAPE is reduced by 0.9203% on average and the returns are greater than 20%. The IFPSO-MFBM has a more significant improvement.

5. Conclusions

The efficient market hypothesis and the fractal market hypothesis are combined in this paper to study the stock forecasting problem. Firstly, the shortcomings of geometric and fractional Brownian motion are analyzed and the MFBM model is constructed. Then the fractional-order particle swarm optimization algorithm is improved. Last but not least, the IFPSO-MFBM is proposed to forecast stock price.

For the GBM model, there is a clear error in the price prediction. The graph is normally distributed, but the real share price follows the “spike and thick tail”, which does not match the specific form of the share price. The fractional Brownian motion model has arbitrage and is not a sound mode. The MFBM has memory and eliminates arbitrage, and it enables better forecasting of stock prices. However, its parameters are not optimal.

Most stock price time series have a long memory in nature. The Hurst index is the most commonly characterized method. However, in practical applications, R/S analysis method has some obvious shortcomings for calculating long memory parameters and the obtained Hurst values are not optimal. Therefore, the Hurst values are further optimized by IFPSO. Other coefficients are optimized by the improved fractional-order particle swarm optimization algorithm. The final MFBM model with optimal parameters is obtained, which is the IFPSO-MFBM model. Through experimental analyses, it can be found that the IFPSO-MFBM model is superior to GBM, FBM, and MFBM models in stock price prediction.

Author Contributions: Conceptualization, H.H. and C.Z.; methodology, H.H., C.Z., and J.L.; software, H.H. and C.Z.; validation, H.H. and C.Z.; formal analysis, H.H. and C.Z.; investigation, H.H., C.Z. and Y.H.; resources, H.H. and C.Z.; data curation, H.H., C.Z. and Y.H.; writing—original draft preparation, H.H. and C.Z.; writing—review and editing, H.H. and C.Z.; visualization, H.H. and C.Z.; supervision, H.H. and C.Z.; project administration, C.Z.; funding acquisition, C.Z. All authors have read and agreed to the published version of the manuscript.

Funding: This research was funded by National Natural Science Foundation of China, grant numbers 61862062 and 61104035.

Data Availability Statement: Not applicable.

Acknowledgments: The authors would like to thank referees for their extraordinary comments, which help to enrich the content of this paper.

Conflicts of Interest: The authors declare no conflict of interest.

References

1. Thakkar, A.; Chaudhari, K. Fusion in stock market prediction: A decade survey on the necessity, recent developments, and potential future directions. *Inf. Fusion* **2020**, *65*, 95–107. [CrossRef] [PubMed]
2. Akhilesh Kumar, S.; Srivastava, A.; Singh, S.; Tripta, S.S.; Shubham, G. Design of Machine-Learning Classifier for Stock Market Prediction. *SN Comput. Sci.* **2021**, *3*, 88.

3. Khan, W.; Malik, U.; Ghazanfar, M.A.; Azam, M.A.; Alyoubi, K.H.; Alfakeeh, A.S. Predicting stock market trends using machine learning algorithms via public sentiment and political situation analysis. *Soft Comput.* **2020**, *24*, 11019–11043. [CrossRef]
4. Tarasov, V.E. On history of mathematical economics: Application of fractional calculus. *Mathematics* **2019**, *7*, 509. [CrossRef]
5. Salas-Molina, F.; Pla-Santamaria, D.; Mayor-Vitoria, F.; Vercher-Ferrandiz, M.L. A Multicriteria Extension of the Efficient Market Hypothesis. *Mathematics* **2021**, *9*, 649. [CrossRef]
6. Jovanovic, F. A comparison between qualitative and quantitative histories: The example of the efficient market hypothesis. *J. Econ. Methodol.* **2018**, *25*, 291–310. [CrossRef]
7. Karp, A.; Van Vuuren, G. Investment implications of the fractal market hypothesis. *Ann. Financ. Econ.* **2019**, *14*, 27. [CrossRef]
8. Fama, E.F. The behavior of stock market prices. *J. Bus.* **1965**, *38*, 34–105. [CrossRef]
9. Malkiel Burton GFama Eugene, F. Efficient Capital Markets: A Review of Theory And Empirical Work. *J. Financ.* **1970**, *25*, 383–417. [CrossRef]
10. Ibrahim, S.N.I.; Misiran, M.; Laham, M.F. Geometric fractional Brownian motion model for commodity market simulation. *Alex. Eng. J.* **2021**, *60*, 955–962. [CrossRef]
11. Delcey, T. Samuelson vs. Fama on the Efficient Market Hypothesis The Point of View of Expertise. *Œconomia. Hist. Methodol. Philos.* **2019**, *9*, 37–58. [CrossRef]
12. Gao, H.; Mei, S. Random variable assumption errors and correction in financial mathematics. *Times Financ.* **2021**, *20*, 92–95.
13. Gao, H. Theoretical Errors and Corrections of Geometric Brownian Motion Model of Stock Prices. *Times Financ.* **2019**, *11*, 50–51.
14. Antwi, O.; Bright, K.; Wereko, K.A. Jump diffusion modeling of stock prices on Ghana stock exchange. *J. Appl. Math. Phys.* **2020**, *8*, 1736–1754. [CrossRef]
15. Nielsen, A. *Practical Time Series Analysis: Prediction with Statistics and Machine Learning*; O'Reilly Media: Sebastopol, CA, USA, 2019.
16. Peters, E.E. *Chaos and Order in the Capital Market*, 2nd ed.; John Wiley & Sons, Inc.: New York, NY, USA, 1996.
17. Peters, E.E. *Fractal Market Analysis: Applying Chaos Theory to Investment and Economics*; John Wiley & Sons, Inc.: New York, NY, USA, 1994.
18. Wu, H.; Li, D.; Gao, R. On the Fractal and Chaos of the Securities Market. *World Econ.* **2001**, *7*, 32–37.
19. Rostek, S.; Schöbel, R. A note on the use of fractional Brownian motion for financial modeling. *Econ. Model.* **2013**, *30*, 30–35. [CrossRef]
20. Cheridito, P. Arbitrage in fractional Brownian motion models. *Financ. Stoch.* **2003**, *74*, 533–553. [CrossRef]
21. Cheridito, P. Mixed fractional Brownian motion. *Bernoulli* **2001**, *7*, 913–934. [CrossRef]
22. Zhang, H.; Mo, Z.; Wang, J.; Miao, Q. Nonlinear-drifted fractional Brownian motion with multiple hidden state variables for remaining useful life prediction of lithium-ion batteries. *IEEE Trans. Reliab.* **2019**, *69*, 768–780. [CrossRef]
23. Liu, G.; Yu, C.P.; Shiu, S.N.; Shih, I.T. The Efficient Market Hypothesis and the Fractal Market Hypothesis: Interfluves, Fusions, and Evolutions. *SAGE Open* **2022**, *12*, 21582440221082137. [CrossRef]
24. Brătian, V.; Acu, A.M.; Oprean-Stan, C.; Dinga, E.; Ionescu, G.M. Efficient or Fractal Market Hypothesis? A Stock Indexes Modelling Using Geometric Brownian Motion and Geometric Fractional Brownian Motion. *Mathematics* **2021**, *9*, 2983. [CrossRef]
25. Tan, Z.; Fu, Y.; Cheng, H.; Liu, J. Stock prices' long memory in China and the United States. *Int. J. Emerg. Mark.* **2020**, *17*, 1292–1314. [CrossRef]
26. Asiri, F.F. The Price of Stocks, Geometric Brownian Motion, and Black Scholes Formula. Master's Thesis, University of Windsor, Windsor, ON, Canada, 2018.
27. Xu, L.B. An Effective Method to Explore the Efficiency of Capital Markets: Fractal Market Analysis. *Financ. Econ. Res.* **1999**, *1*, 43–47.
28. Garcin, M. Hurst exponents and delampertized fractional Brownian motions. *Int. J. Theor. Appl. Financ.* **2019**, *22*, 1950024. [CrossRef]
29. Garcin, M. Forecasting with fractional Brownian motion: A financial perspective. *Quant. Financ.* **2021**, *22*, 1495–1512. [CrossRef]
30. Guasoni, P.; Nika, Z.; Rásonyi, M. Trading fractional Brownian motion. *SIAM J. Financ. Math.* **2019**, *10*, 769–789. [CrossRef]
31. Djeutcha, E.; Njomen DA, N.; Fono, L.A. Solving Arbitrage Problem on the Financial Market Under the Mixed Fractional Brownian Motion With Hurst Parameter H∈]1/2, 3/4[. *J. Math. Res.* **2019**, *11*, 76–92. [CrossRef]
32. Wang, D.; Tan, D.; Liu, L. Particle swarm optimization algorithm: An overview. *Soft Comput.* **2018**, *22*, 387–408. [CrossRef]
33. Tharwat, A.; Schenck, W. A conceptual and practical comparison of PSO-style optimization algorithms. *Expert Syst. Appl.* **2021**, *167*, 114430. [CrossRef]
34. Zhang, X.W.; Liu, H.; Tu, L.P. A modified particle swarm optimization for multimodal multi-objective optimization. *Eng. Appl. Artif. Intell.* **2020**, *95*, 103905. [CrossRef]
35. Solteiro Pires, E.J.; Tenreiro Machado, J.A.; de Moura Oliveira, P.B.; Boaventura Cunha, J.; Mendes, L. Particle swarm optimization with fractional-order velocity. *Nonlinear Dyn.* **2010**, *61*, 295–301. [CrossRef]
36. Davies, R.B.; Harte, D.S. Tests for Hurst effect. *Biometrika* **1987**, *74*, 95–101. [CrossRef]
37. García MN, L.; Requena JP, R. Different methodologies and uses of the Hurst exponent in econophysics. *Stud. Appl. Econ.* **2019**, *37*, 96–108. [CrossRef]

38. Millán, G.; Osorio-Comparán, R.; Lefranc, G. Preliminaries on the accurate estimation of the Hurst exponent using time series. In Proceedings of the 2021 IEEE International Conference on Automation/XXIV Congress of the Chilean Association of Automatic Control (ICA-ACCA), Valparaíso, Chile, 22–26 March 2021; pp. 1–8.
39. Xiao, W.L.; Zhang, W.G.; Zhang, X.L. Maximum-likelihood estimators in the mixed fractional Brownian motion. *Statistics* **2011**, *45*, 73–85. [CrossRef]
40. Avellaneda, M.; Lee, J.H. Statistical arbitrage in the US equities market. *Quant. Financ.* **2010**, *10*, 761–782. [CrossRef]

fractal and fractional

MDPI

Article

The Importance of Non-Systemically Important Banks—A Network-Based Analysis for China's Banking System

Yong Li

Business School, China University of Political Science and Law, Haidian, Beijing 100088, China; yongli@cupl.edu.cn

Abstract: There is important theoretical and practical significance to scientifically identifying the systemic importance of banks for effectively preventing and controlling systemic risks in the banking system. Prevalent identification methods are biased because they only pay attention to measuring the systemic risk contribution of individual banks to the whole system in order to determine that bank's systemic importance. Less attention is paid to the cascade effects of risk spillover among banks. This study proposes a novel method for measuring the cascade effects of risk spillover of banks and their contributions to systemic risks by building up a conditional tail risk network of China's banking system. Different from previous analyses of systemic risks based on the identification and risk measurement of systemically important banks (SIBs), this paper focuses on analyzing the risk spillover effects of non-SIBs and their contributions to systemic risks by building up a conditional tail risk network of China's banking system. Our empirical results show that some non-SIBs in China are more vulnerable to the shocks of systemic risk than SIBs, and that they are more likely to act as key intermediaries to transmit risk to SIBs, thereby triggering systemic risk. In view of this, we propose to identify key non-SIBs according to their risk spillover intensity because they are also systemically important. The market regulators not only need to pay attention to SIBs that are too big to fail, but also treat seriously the key intermediaries of "risk spillover too strong to fail" in the network in order to ensure the stability of the banking system.

Keywords: the generalized value at risk (GCoVaR); systemically important banks (SIBs); risk spillover

Citation: Li, Y. The Importance of Non-Systemically Important Banks—A Network-Based Analysis for China's Banking System. *Fractal Fract.* **2023**, *7*, 735. https://doi.org/10.3390/fractalfract7100735

Academic Editors: Carlo Cattani and Leung Lung Chan

Received: 25 July 2023
Revised: 9 August 2023
Accepted: 12 September 2023
Published: 6 October 2023

1. Introduction

After the 2008 financial crisis, strengthening the supervision of systemically important financial institutions (SIFIs) has become one of the core issues in the financial reform of various countries. The identification of SIFIs works under the premise of supervision and is also the focus of regulatory reform. A useful definition of SIFIs was advanced by Federal Reserve Governor Daniel Tarullo, who said that "Financial institutions are systemically important if the failure of the firm to meet its obligations to creditors and customers would have significant adverse consequences for the financial system and the broader economy." Although the definition of SIFIs is clear, the methods of identification are not consistent. International financial regulators and monetary authorities judge SIFIs mainly based on the indicator-based method. The Macroprudential Group (MPG) of the Basel Committee on Banking Supervision (BCBS) is responsible for developing indicators and methods for identifying SIFIs. MPG published a more detailed indicator system on 11 October 2010 [1], and improved it again in November 2022. The indicators usually focus on describing the scale, the correlation, and the negative externalities of SIFIs. Scholars often use the market-based method to determine the systemic importance of individual financial institutions. The existing market-based methods mainly include the marginal expected Shortfall (MES) [2,3], Shapley Value [4], CoVaR [5], and Extreme Value [6]. These methods are essentially based on the underlying theoretical position that the bigger a financial institution is, the greater the breadth of products it provides and the larger scale transactions it involves, the higher risk contribution to the financial system it has. These prevalent identification methods are biased because less attention is paid to the cascade effects of risk spillover among banks. With the development of the banking industry, the scale of interbank business has been expanding, and it can be argued that the linkages between banks are becoming stronger. Without taking into account the cascade effects of risk spillover between banks, the identification of such SIBs would be inaccurate.

In the case of China's banking system, the People's Bank of China (PBC) and the China Banking and Insurance Regulatory Commission (CBIRC) designated a total of 19 banks as systemically important banks (SIBs) in 2022, with a focus to deliver additional regulation to those banks. These 19 SIBs consist of six state-owned commercial banks (Industrial and Commercial Bank of China, Bank of China, China Construction Bank, Postal Savings Bank of China, Bank of Communications, and Agricultural Bank of China), nine joint-stock commercial banks (China Minsheng Bank, China Everbright Bank, Pingan Bank, Huaxia Bank, China Guangfa Bank, China CITIC Bank, and Shanghai Pudong Development Bank, China Merchants Bank, and Industrial Bank), and four city commercial banks (Bank of Ningbo, Bank of Jiangsu, Bank of Shanghai, and Bank of Beijing) (PBC press release, 9 September 2022). Each SIB's total assets exceed 1500 billion yuan. However, it is found that the expectation of SIBs being "too big to fail" actually reduces the probability of them causing systemic risks. Additionally, the non-SIBs, some small-sized banks, with total assets of about 500 billion yuan or less, often have a greater probability of failure, such as the recent bankruptcy of Baoshang Bank, Shantou Commercial Bank, Liaoyang Rural Commercial Bank, and Liaoning Taizihe Rural Bank, causing a considerable degree of public panic. Are the failures of non-SIBs or small-sized banks irrelevant? Are they really going to have no effect on systemic risk of the banking sector? This is a practical problem that urgently needs to be answered.

In this paper, we propose a novel method, which is the algorithm-based identification of the risk spillover effects of banks, in order to judge the systemic importance of banks by building up a conditional tail risk network of China's banking system. We conduct empirical analysis by using the data of stock prices of 54 listed banks in the Chinese securities market with a sample period from June 2021 to June 2023 and we adopt the method proposed in this paper to rank the systemic importance of these banks. Our empirical results shows that some non-SIBs in China are more vulnerable to the shocks of systemic risk than SIBs, and that they are more likely to act as key intermediaries for the transmission of risk to SIBs, in turn triggering systemic risk. In view of this, we propose to identify key non-SIBs according to their risk spillover intensity because they are also systemically important. The market regulators not only need to pay attention to SIBs that are too big to fail, but also seriously consider the key intermediaries of "risk spillover too strong to fail" in the network in order to ensure the stability of the banking system.

The remaining sections of this paper are as follows. In Section 2, we review the prevalent modeling methods of risk spillover effects among academia. In Section 3, we introduce all the technical methods used in this paper, including the GCoVaR method and the fitting technique. In Section 4, we present the empirical analysis of China's banking system and a robustness test for GCoVaR method. Section 5 concludes.

2. Literature Review

The financial system can be regarded as a financial network. The extreme risks of individual financial institutions would lead to the deterioration of the overall risk of the financial system through network links, which is the main manifestation of systemic financial risks. Network modeling is often used to explore such financial risk contagion. In these network model institutions are nodes, and the connecting edges represent the business relations between institutions. As an interdisciplinary technology, the complex network method provides a theoretical framework in order to help people better understand the internal structure and dynamic behavior of complex systems (Neveu, 2018). By constructing a network, researchers can not only analyze the network structure and characteristics from the perspective of the system, but also analyze the characteristics of important nodes in the system. The construction of a network requires a connection matrix used to express the risk contagion and information spillover among nodes. The data used for the calculation of connection matrix can be roughly divided into two categories. One is inter-institutions' offered credit or capital flow data. This is based on the specific business connections between institutions [7–10]. The other is market data, such as stock prices or credit default swap (CDS) prices of the institutions [11–13]. Based on the increasing availability of data, stock market data is being more and more widely used. The market data of financial institutions could reflect investors' sentiment and is real-time and forward-looking; it provides an immediate and transparent measure for studying systemic financial risks [14, 15].

The traditional methods used for the calculation of connection matrixes are mainly the correlation coefficient method [16], probabilistic analysis [17], and the error correction model [18]. Because these traditional methods are unable to describe the nonlinearity, dynamics, and asymmetry of risk spillovers, Conditional Value at Risk (CoVaR), introduced by Adrian and Brunnermeier [5], a method that quantifies the amount of tail risk an investment portfolio, has been widely used in recent years. Reboredo and Ugolini [19] analyzed the systemic risks of the European sovereign debt market by using CoVaR method and believed that this method could better identify the changes of risk spillovers before and after the Greek debt crisis. Reboredo and Rivera-Castro [20] verified the asymmetric risk spillover effect of the exchange rates between the Euro and the US Dollar on major global emerging stock markets by calculating their CoVaR. Warshaw [21] proved the effectiveness of CoVaR method by measuring the extreme risk spillover effect of the North American equity market and its changes before and after the subprime crisis.

However, Lopez-Espinosa et al. [22] found empirically that the original CoVaR model, based on the normal hypothesis, underestimated the systemic financial risks of the U.S. listed banks. In response, they introduced asymmetric terms to improve the quantile regression method of CoVaR. Girardi and Ergun [23] also pointed out that CoVaR would underestimate risks under extreme conditions by studying a network consisted of 74 listed banks in the United States, and then proposed an improved generalized conditional value at risk (GCoVaR) method. Their empirical analysis verified that GCoVaR could improve the stability of the measurements obtained. GCoVaR could consider more distress events within the tail region, which would more accurately reflect the characteristics of "volatility clustering, thick tail and nonlinear correlation" of financial markets. Torri et al. [24] believe that using GCoVaR to measure the risk spillover effect would not only help investors to manage portfolio risks, but also help market regulators to carry out dynamic monitoring of financial risks.

As for financial risk contagion, previous studies have mostly focused on the identification and risk measurement of systemically important financial institutions [14,15], and explore ways and tools for preventing and controlling the financial systemic risk based on systemically important financial institutions [25,26]. However, the financial system is made up of systemically important financial institutions and non-systemically important financial institutions, and they both have impacts on the formation and amplification of financial systemic risks. Mistrulli [27] stated that systemic risk can be characterized as a negative pecuniary externality exerted by financial institutions, and that any institution's risk exposure may evolve into a systemic risk through its interconnectedness within the financial system. Scholars engaged in correlation research believe that the stronger the correlation among institutions, the greater the effect of risk contagion, and more easily to induce systemic risks. However, some scholars suggest that correlation is an effective way to disperse systemic risks [28]. Georg [29]pointed out that the degree of connection between institutions and the level of risk contagion have a non-monotonic relationship. A higher degree of connection between institutions is conducive to risk diversification when the connection level is low, but when it exceeds a certain threshold, the risk of contagion would increase rapidly and could lead to large-scale collapse of institutions. Therefore, some scholars propose that it should pay attention not only to institutions that are "too big to fail", but also to banks that are "too connected to fail" in order to prevent and control systemic risk [30,31].

It can be seen above that most studies in this area are based on the systemically important financial institutions in order to explore ways to identify and mitigate systemic risks. Less research has been done specifically on non-systemically important financial institutions. The mechanism of risk transfer between SIBs and non-SIBs has not been well understood. In addition, compared with systemically important financial institutions, the number of non-systemically important financial institutions is large, which is difficult to focus on in the research process. In view of this, based on the perspective of risk contagion, this paper measures the risk spillover effect among listed banks in China using the GCoVaR method and Copula technology, and explores the role of non-SIBs in the formation and accumulation of systemic risks in the banking sector. Different from the conventional mode of analyzing systemic risks based on SIBs in previous studies, we focus on analyzing the role and influence of non-SIBs in China's banking system from two aspects–the risk contribution of non-SIBs to systemic risk and the risk impact of the whole banking system on non-SIBs–in order to test whether or not non-SIBs are unimportant.

3. Methodology

Risk spillover is the transmission of risk from one institution (industry or market) to another institution (industry or market). This is because financial data, in reality, is usually not normally distributed, and presents a "peak and thick tail" distribution. The traditional parametric regression method based on mean estimation cannot accurately reflect the relationship between different parts of the overall distribution. We consider using the tail dependence relationship of stock price of related banks to establish connection matrix of the network of China's banking system, and the GCoVaR approach to identify risks that are "extra" parts due to the presence of other banks in distress.

3.1. GCoVaR Model

The traditional method measuring the risk, value at risk (*VaR*), refers to the maximum possible loss of a certain bank in a certain period in the future under a certain confidence level. Let R^i represent the return rate of bank *i*, then the VaR^i of R^i at a significance level α can be expressed as:

$$P\left(R^i \leq VaR^i\right) = \alpha, \tag{1}$$

VaR can only measure the risk of a single bank. Based on this value, conditional value at risk (*CoVaR*) proposed by Adrian and Brunnermeier [5] can be used to measure the risk spillover between different banks. Let R^j represents the return rate of bank *j*, under the condition of R^i having an extreme loss VaR^i, at the confidence level of β, the extreme loss of R^j would be $CoVaR^{j|i}$, the mathematical expression is:

$$P\left(R^j \leq CoVaR^{j|i} \middle| R^i = VaR^i\right) = \beta, \tag{2}$$

According to Girardi and Ergun [23], the $GCoVaR^{j|i}$ is the VaR of bank *j* conditional on bank *i* being at most at its *VaR* ($R^i \leq VaR^i$) as opposed to being exactly at its *VaR* ($R^i = VaR^i$).

$$P\left(R^j \leq GCoVaR^{j|i} \middle| R^i \leq VaR^i\right) = \beta, \tag{3}$$

This change allows us to consider more severe distress events of bank *i* that are farther along the tail (below its *VaR*) so as to more accurately reflect the characteristics of financial time series: "volatility agglomeration, thick tail and nonlinear correlation". This change also improves the consistency of risk measurement with respect to the dependence parameter.

1. The risk spillover between bank *i* and *j*

We define the systemic risk contribution of a bank as the change from its *GCoVaR* in its benchmark state (defined as a one-standard deviation event) to its *GCoVaR* under financial distress, so we can get the risk spillover effect of bank *i* to bank *j* when bank *i* in extreme distress:

$$\Delta GCoVaR^{j|i} = GCoVaR^{j|i} - MCoVaR^{j|i}, \tag{4}$$

where $MCoVaR^{j|i}$ represent the financial distress in *GCoVaR* of bank *j* when bank *i* at a normal state (i.e., α = 0.5), it meets:

$$P\left(R^j \le MCoVaR^{j|i} \middle| R^i \le 0.5\right) = \beta, \tag{5}$$

Define risk spillover intensity γ, which is the change rate of *GCoVaR* with respect to *MCoVaR*:

$$\gamma^{j|i} = \frac{GCoVaR^{j|i} - MCoVaR^{j|i}}{MCoVaR^{j|i}}, \tag{6}$$

The risk spillover effect is usually bidirectional. Bank *i* may spill risks to bank *j*, and conversely, bank *j* may spill risks to bank *i*. In addition to effectively measuring the extreme risk spillover effect, another advantage of *GCoVaR* method is that it can measure the asymmetry of this effect. Let $\Delta GCoVaR^{i|j}$ represents the risk spillover of bank *j* on bank *i*, the calculation formula can be similarly derived.

2. The risk contribution of bank *i* to the financial system

Let $GCoVaR^{index\,|\,i}$ stands for the generalized conditional value at risk of the financial system suffering from the impact of bank *i* in distress. Using the same logic above, we have

$$P\left(R^{index} \le GCoVaR^{index|i} \middle| R^i \le VaR^i\right) = \beta, \tag{7}$$

$$\Delta GCoVaR^{index|i} = GCoVaR^{index|i} - MCoVaR^{index|i}, \tag{8}$$

$$\gamma^{index|i} = \frac{GCoVaR^{index|i} - MCoVaR^{index|i}}{MCoVaR^{index|i}}, \tag{9}$$

3. The risk spillover of bank *i* suffered from financial system

Let $GCoVaR^{i\,|\,index}$ stands for the generalized conditional value at risk of bank *i* when the whole financial system is in trouble. VaR^{index} is unconditional value at risk of the financial system. It represents the risk level of the financial system as a whole, we have:

$$P\left(R^j \le GCoVaR^{i|index} \middle| R_t^{index} \le VaR_{\alpha,t}^{index}\right) = \beta, \tag{10}$$

$$\Delta GCoVaR^{i|index} = GCoVaR^{i|index} - MCoVaR^{i|index}, \tag{11}$$

$$\gamma^{i|index} = \frac{GCoVaR^{i|index} - MCoVaR^{i|index}}{MCoVaR^{i|index}}, \tag{12}$$

3.2. To Measure GCoVaR Based on Copula Model

According to the definition of conditional probability, Equation (3) can be transformed into:

$$P\left(R^j \le CoVaR^{j|i},\, R^i \le VaR^i\right) = \beta \cdot P\left(R^i \le VaR^i\right) = \alpha\beta, \tag{13}$$

It can be seen from Equation (13) that the joint distribution of R^j and R^i need to be known in order to calculate *GCoVaR*. A convenient method is to use Copula function to construct joint distribution of multivariate random variables. Copula function is also known as link function, which can describe the tail correlation between random variables.

According to Sklar's theorem, we can construct the joint distribution of random variables by treating each one-dimensional distribution of multiple random variables as marginal distribution. Equation (13) can be written in the following Copula form:

$$c\left(F_j\left(GCoVaR^{j|i}\right),\ F_i\left(VaR^i\right)\right) = \alpha\beta, \tag{14}$$

where, $c(\cdot,\cdot)$ is the Copula function, and $F_i(\cdot)$ and $F_j(\cdot)$ are the edge distribution functions of R^i and R^j, respectively. According to the definition of VaR, Equation (1) means,

$$F_i\left(VaR^i\right) = \alpha, \tag{15}$$

According to Equations (3) and (14), given the marginal distribution, the form of Copula connect function, and the confidence level of α and β, the $GCoVaR^{j|i}$ can be solved. Setting the α to 0.5, the same two equations above can be used to solve for the $MCoVaR^{j|i}$; According to Equations (4)–(6), the $\Delta GCoVaR^{j|i}$ and $\gamma^{j|i}$ could be calculated to measure the risk spillover effect of bank i on j. Repeating the above process, we can obtain $\Delta GCoVaR^{i|j}$ and $\gamma^{i|j}$, the risk spillover effect of bank j on i. The marginal distribution, time-varying Copula function and its parameter estimation methods are shown in Appendix B.

4. Empirical Analysis

4.1. Sample Selection

In this paper, 54 listed banks are selected to construct the banking system of China. The selected banks and their total assets are shown in Appendix A. The sample period is from 1 June 2021 to 30 June 2023. The selection of sample periods is mainly based on the consideration that they have normal transaction data in the sample period, so as to make the calculation of value at risk meaningful. All sample data are collected from the Wind Database (https://www.wind.com.cn/portal/zh/WFT/index.html accessed on 30 June 2023). Additionally, R language software (R-4.0.2) is used for Copula function regression analysis, and Python 3.5.0 (Networkx 3.1) is used for mapping.

In Figure 1, the size of the nodes are measured by the weighted degree centrality of nodes. The larger the node's size is, the nearer to the center the node tends to be in the network.

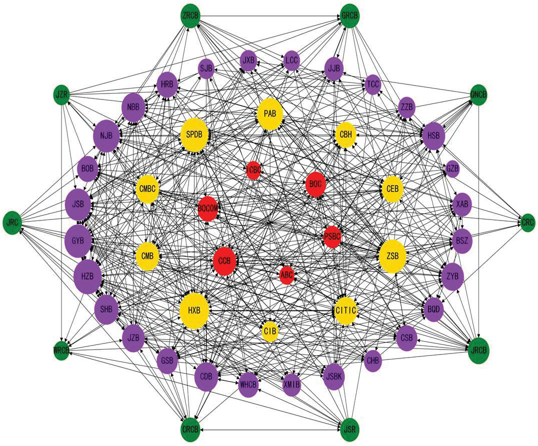

Figure 1. Visual representation of conditional tail risk networks for China's banking system computed on the periods June 2021–June 2023. Note: The nodes in the figure with background color red are state-owned banks, with background color yellow are joint-stock commercial banks, with background color purple are city commercial banks, and with background color green are rural commercial banks.

4.2. Risk Spillover Effect Analysis

4.2.1. The Risk Spillover Effect between Banks

The risk spillover effect of bank i on j can be calculated by Equations (3)–(6) when bank i is in distress. Considering that smaller quantile values are often used in risk management to capture the characteristics of the peak and fat tail of financial time series, here we choose $\beta = 0.025$. Since our research sample includes 54 banks, there should be 1431 different combinations of banks, and there are 1431 risk spillover intensity measures. Table 1 gives the results, which are listed in descending order of $\gamma^{j|i}$. Only the top 30 are listed in order to save space.

Table 1. The risk spillover from bank i to j (Top 30) and ranking by $\gamma^{j|i}$.

	Bank *i*		**Bank *j***					
	Bank Code	**Total Assets (Billion Yuan)**	**Bank Code**	**Total Assets (Billion Yuan)**	$MCoVaR^{j\|i}$	$GCoVaR^{j\|i}$	$\Delta GCoVaR^{j\|i}$	$\gamma^{j\|i}$ (%)
1	CDB	652.43	**CMBC**	6950.23	8.14	12.36	4.22	51.84
2	BSZ	388.07	NJB	1517.08	7.45	11.26	3.81	51.14
3	ZYB	757.48	ZZB	561.64	9.4	13.19	3.79	40.32
4	CRC	1135.93	CHB	547.81	7.73	10.66	2.93	37.90
5	NJB	1517.08	**CEB**	5368.11	8.13	11.04	2.91	35.79
6	CSB	704.24	**CIB**	7894.00	9.72	13.16	3.44	35.39
7	CRCB	208.69	HZB	1169.26	8.11	10.8	2.69	33.17
8	JZB	777.99	HRB	598.60	7.45	9.70	2.25	30.20
9	CHB	561.64	SJB	1037.96	7.48	9.66	2.18	29.14
10	JRCB	200.36	JZB	777.99	8.17	10.51	2.34	28.64
11	QRCB	406.81	BQD	459.83	8.2	10.52	2.32	28.29
12	**SPDB**	7950.22	GYB	590.68	8.73	11.18	2.45	28.06
13	SJB	1037.96	**PAB**	4468.51	8.87	11.26	2.39	26.94
14	ZRCB	143.82	**JSB**	2337.89	7.64	9.66	2.02	26.44
15	CRCB	208.69	JSR	139.44	9.26	11.59	2.33	25.16
16	JJB	415.79	JXB	458.69	8.51	10.54	2.03	23.85
17	**JSB**	2337.89	**ZSB**	2048.23	9.15	11.33	2.18	23.83
18	GZB	456.40	**HXB**	6950.23	8.87	10.95	2.08	23.45
19	HSB	1271.70	CBH	3399.82	9.26	11.39	2.13	23.00
20	GYB	590.68	**CITIC**	1393.52	9.86	12.11	2.25	22.82
21	ZRCB	143.82	NJB	7511.16	9.83	12.00	2.17	22.08
22	JRCB	142.77	WRCB	547.81	9.14	11.13	1.99	21.77
23	JZR	217.66	JJB	415.79	9.78	11.81	2.03	20.76
24	**CMBC**	6950.23	GSB	342.36	9.36	11.29	1.93	20.62
25	TCC	687.76	**BOB**	2900.00	9.81	11.83	2.02	20.59
26	**NBB**	1626.75	JSR	139.44	10.76	12.97	2.21	20.54
27	NJB	1517.08	BSZ	388.07	9.72	11.71	1.99	20.47
28	**CMBC**	6950.23	CDB	415,79	9.56	11.51	1.95	20.40
29	WRCB	547.81	JRCB	757.48	9.86	11.87	2.01	20.39
30	**ABC**	28,132.25	**CCB**	27,205.05	9.62	11.57	1.95	20.27

Note: SIBs are highlighted in bold black.

Table 1 shows that:

First, given bank i and j, the level of $\mathrm{GCoVaR}^{j|i}$ is larger than that of $\mathrm{MCoVaR}^{j|i}$. This suggests that when one bank gets into trouble, other banks are exposed to more than their own level of risk. As shown in line No. 1 of Table 1, $\mathrm{MCoVaR}^{\mathrm{CMBC}\,|\,\mathrm{CDB}} = 8.14$, $\mathrm{GCoVaR}^{\mathrm{CMBC}\,|\,\mathrm{CDB}} = 12.36$. Obviously, $\mathrm{MCoVaR}^{\mathrm{CMBC}\,|\,\mathrm{CDB}} < \mathrm{GCoVaR}^{\mathrm{CMBC}\,|\,\mathrm{CDB}}$.

Second, $\mathrm{GCoVaR}^{j|i} \neq \mathrm{GCoVaR}^{i|j}$. The reason is that for $\mathrm{GCoVaR}^{j|I}$, the conditional event is bank i in distress, while for $\mathrm{GCoVaR}^{i|j}$, the conditional event is bank j in distress. Different directions of risk shocks might have different effects. Take the Table 1 line No. 2 as an example: when BSZ is in distress, NJB would suffer risk impact of $\mathrm{GCoVaR}^{\mathrm{NJB}\,|\,\mathrm{BSZ}} = 11.26$; when NJB is in distress, as shown in line No. 27 of Table 1, BSZ would suffer risk impact of $\mathrm{GCoVaR}^{\mathrm{BSZ}\,|\,\mathrm{NJB}} = 11.71$; as such, apparently, $\mathrm{GCoVaR}^{\mathrm{BSZ}\,|\,\mathrm{NJB}} \neq \mathrm{GCoVaR}^{\mathrm{NJB}\,|\,\mathrm{BSZ}}$

Third, from Table 1 we can find that the non-SIBs' risk spillover should never be underestimated. For the first 30 strongest risk spillover effects, sixteen of them are from non-SIB to non-SIB, eight are from non-SIB to SIBs, two are from SIB to SIB, and four from SIB to non-SIB. The eight non-SIBs who transmit risk to SIBs should be paid special attention. We take CDB, a city commercial bank among the non-SIBs, as an example in order to analyze its risk spillover performance and determine who has the greatest risk impact on SIB. Table 2 shows the banks affected by the risk impact of CDB and the banks from which CDB receives risk spillover. As a relatively small sized city commercial bank with total assets of 652.43 billion yuan, its risk spillovers mainly transmit to other related city commercial banks (CHB, GZB, WHCB, BQD), joint-stock commercial banks (CMBC, CIB, CBH, PAB, HXB), and state-owned commercial banks (BOC, BOCOM), and it received risk spillover from other related city commercial banks (WHCB, SHB, CHB, JZB, JJB, JSB, HSB, SJB), rural commercial banks (CRC, JRC, JSR, JRCB, JZR), and joint-stock commercial banks (CMBC).

Table 2. CDB's risk spillover relations.

No.	CDB Transmits Risk Spillover to			No.	CDB Receives Risk Spillover from		
	Bank Code	**Total Assets (Billion Yuan)**	$\gamma^{i\,|\,CDB}$ **(%)**		**Bank Code**	**Total Assets (Billion Yuan)**	$\gamma^{CDB\,|\,i}$ **(%)**
1	**CMBC**	6950.23	51.84	1	**CMBC**	6950.23	20.40
2	**CIB**	7894.00	18.19	2	**SHB**	2462.14	19.91
3	CBH	1393.52	18.12	3	CRC	1135.93	18.79
4	**BOC**	24,402.66	14.49	4	**JSB**	143.82	13.69
5	**PAB**	4468.514	14.34	5	WHCB	267.602	11.45
6	CRC	1135.93	12.45	6	JSR	2337.89	8.28
7	**BOCOM**	10,697.62	12.05	7	CHB	561.64	7.64
8	**HXB**	3399.82	11.77	8	JZB	1169.26	7.32
9	CHB	561.64	7.57	9	JJB	2462.14	6.16
10	GZB	456.40	5.23	10	JRC	200.363	5.09
11	WHCB	267.60	1.56	11	HSB	1271.70	3.37
12	BQD	459.83	1.32	12	SJB	1037.96	1.57
				13	JZR	139.44	0.44
				14	JRCB	142.77	0.23

Note: SIBs are highlighted in bold black.

For the rural commercial banks among non-SIBs, we take CRC as an example to analyze its risk spillover performance. As a rural commercial bank, CRC has the highest risk spillover on other banks. Table 3 shows the banks impacted by CRC's risk spillover and the banks from which CRC receives risk spillover. We can see that its risk spillover mainly affects related city commercial banks (CHB, WHCB, CDB, JZB, JSB, GSB, NBB) and rural commercial banks (JSR, ZRCB, JZR, GRCB), while it mainly receives risks from other rural commercial banks (JSR, GRCB, JZR, JRC).

Table 3. CRC's risk spillover relations.

No.	CRC Transmits Risk Spillover to			No.	CRC Receives Risk Spillover from		
	Bank Code	**Total Assets (Billion Yuan)**	$\gamma^{i\mid CRC}$ **(%)**		**Bank Code**	**Total Assets (Billion Yuan)**	$\gamma^{CRC\mid i}$ **(%)**
1	CHB	561.64	40.32	1	JSR	139.44	18.79
2	CDB	652.43	19.91	2	GRCB	1027.87	15.22
3	JSR	217.66	13.69	3	JZR	217.66	12.16
4	ZRCB	143.82	7.32	4	JRC	142.77	12.04
5	WHCB	267.60	19.91	5	CHB	561.64	9.25
6	JZB	777.99	4.49	6	CDB	652.43	8.12
7	JZR	217.66	4.34				
8	**JSB**	2337.89	2.45				
9	GSB	342.36	1.77				
10	GRCB	1027.87	1.52				
11	**NBB**	1626.75	0.22				

Note: SIBs are highlighted in bold black.

Fourth, SIBs mainly are state-owned commercial banks and joint-stock commercial banks. For the state-owned commercial banks among the SIBs, we take CCB as an example. Table 4 shows the banks affected by CCB's risk spillover when it is in distress and the banks impacting CCB by risk spillover. All of them are joint-stock commercial banks and city commercial banks, except ABC, which ranks No. 1 in risk outflow column and ranks No. 12 in risk inflow column. It should be noted that the same is true for other state-owned commercial banks' spillover relations, indicating that the six state-owned commercial banks are relatively independent from each other and the risk spillover intensity between them is generally small.

Table 4. CCB's risk spillover relations.

No.	CCB Transmits Risk Spillover to			No.	CCB Receives Risk Spillover from		
	Bank Code	**Total Assets (Billion Yuan)**	$\gamma^{i\mid ABC}$ **(%)**		**Bank Code**	**Total Assets (Billion Yuan)**	$\gamma^{ABC\mid i}$ **(%)**
1	**ABC**	28,132.25	20.27	1	**BOB**	2900.01	18.86
2	**HXB**	3399.82	9.98	2	**JSB**	2337.89	8.04
3	**CIB**	7894.00	4.27	3	SJB	1037.96	7.80
4	**SHB**	2462.14	3.72	4	JJB	415.79	5.99
5	**CMBC**	6950.23	1.11	5	CHB	561.64	5.45
6	HRB	598.60	0.95	6	**SHB**	2462.14	5.00
7	CBH	1393.52	0.92	7	JZB	777.99	1.52
8	**BOB**	2900.01	0.83	8	WHCB	267.60	1.16
9	**JSB**	2337.89	0.44	9	JSBK	270.94	0.46
10	SJB	1037.96	0.27	10	ZYB	757.48	0.33
				11	BSZ	388.07	0.21
				12	**ABC**	28,132.25	0.18
				13	HSB	1271.70	0.15
				14	XMIB	285.15	0.14
				15	XAB	306.39	0.11

Note: SIBs are highlighted in bold black.

For the joint-stock commercial bank among the SIBs, we take CMBC as an example. Table 5 shows the banks affected by CMBC's risk spillover when it is in distress and the banks impacting CMBC by risk spillover. We can see that its risk spillover mainly affects the related city commercial banks (GSB, CDB, SHB, NJB) and joint-stock and state-owned commercial banks (ZSB, CBH, CIB, CCB, ABC), while it mainly receives risks from other joint-stock commercial banks (SPDB, CIB) and city commercial banks (CDB, JSB, SHB, XAB,

CHB, GYB, JSBK, ZYB, BSZ, HRB, HSB, XMIB, CSB). It should be noted that the same is true for other joint-stock commercial banks' spillover relations.

Table 5. CMBC's risk spillover relations.

No.	CMBC Transmits Risk Spillover to			No.	CMBC Receives Risk Spillover from		
	Bank Code	Total Assets (Billion Yuan)	$\gamma^{i\,\vert\,CMBC}$ (%)		Bank Code	Total Assets (Billion Yuan)	$\gamma^{CMBC\,\vert\,i}$ (%)
1	GSB	342.36	20.62	1	**CDB**	415,79	51.84
2	CDB	415.79	20.40	2	**JSB**	2337.89	18.04
3	**ZSB**	2048.23	14.27	3	SHB	1037.96	17.80
4	**SHB**	2462.14	3.72	4	XAB	415.79	15.29
5	NJB	1517.08	2.44	5	CHB	561.64	11.45
6	CBH	1393.52	0.95	6	**SPDB**	7950.22	9.20
7	**CIB**	7894.00	0.92	7	GYB	590.68	7.52
8	**CCB**	28,132.25	0.83	8	JSBK	270.94	3.16
9	**ABC**	27,205.05	0.55	9	ZYB	757.48	1.46
				10	BSZ	388.07	1.33
				11	HRB	598.60	1.18
				12	HSB	1271.70	1.15
				13	**CIB**	7894.00	0.78
				14	XMIB	285.15	0.51
				15	CSB	7042.35	0.48

Note: SIBs are highlighted in bold black.

The above analysis shows that the risk spillover of China's banking system not only has characteristics of contagious diffusion within the same level regional or local banks, but also has a characteristic of hierarchical diffusion, that is, the diffusion from rural commercial banks to city commercial banks to joint-stock commercial banks and state-owned commercial banks. The coordination and cooperation between national banks' branches and local banks often play a key role in such hierarchical diffusion. Non-SIBs are intended to act as risk transmission intermediaries and transmit risks to SIBs, further inducing systemic risks of the whole banking sector.

4.2.2. The Risk Spillover Effect from Bank to Banking System

Based on Formulas (7)–(9), the individual bank's risk contribution to the entire banking system $\gamma^{index\,\vert\,i}$ are calculated when the individual bank is in distress. The calculated results are shown in Figure 2.

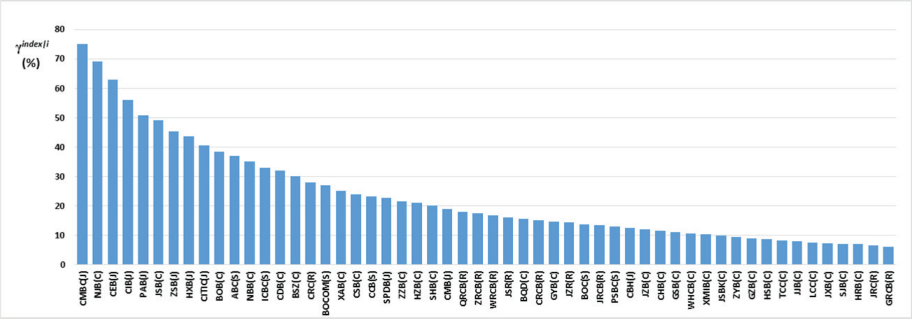

Figure 2. Single bank's contribution to systemic risk $\gamma^{index\,\vert\,i}$. Notes: The last digit in parentheses of the bank code is the bank types, S stands for state-owned bank, J for joint-stock bank, C for city commercial bank, and R for rural commercial bank.

As it can be seen from Figure 2, the contributions of banks to systemic risk do not fully positively correspond to their total assets. e.g., the top three biggest China's banks based on total assets in 2022 (ICBC (with total assets 33,345.10 billion yuan), CCB (28,132.25 billion yuan) and ABC (27,205.05 billion yuan)) have $\gamma^{index\,|\,i}$ 45.88%, 34.7%, 56%, respectively, which are 6th, 17th, and 4th in the ranking of 54 banks' contribution to systemic risk, respectively. While the banks with the top three highest values of $\gamma^{index\,|\,i}$ (CMBC ($\gamma^{\mathrm{index}\,|\,\mathrm{CMBC}}$ = 75%), NJB (69%) and CEB (63%)) have only 6950.23, 1517.08, and 5368.11 billion yuan in total assets, respectively, which rank 11th, 20th, and 13th among total assets, respectively.

4.2.3. The Risk Spillover Effect from Banking System to Individual Banks

Figure 3 shows the calculated results of $\gamma^{i\,|\,index}$ based on Equations (10)–(12). It can be seen that the strongest shocks from the banking system hit non-SIBs rather than SIBs. Non-SIBs are subject to relatively strong impact by the systematic risks. We find CDB, ranking second, is not only subject to significant systemic risk impact, but also transmits a strong risk spillover to SIBs (see Table 2). If a non-SIB is more vulnerable to the shocks of systemic risk, and it is more likely to transmit risk to SIBs, it will be systemically important because its risk transmission could increases the accumulation of systemic risk greatly. We call it a key intermediary or a key non-SIB.

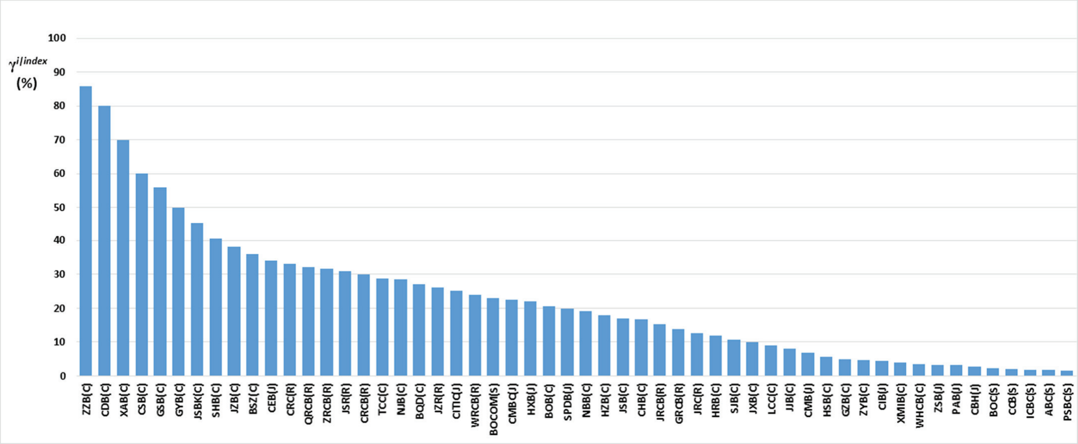

Figure 3. The individual banks' $\gamma^{i\,|\,index}$. Notes: The last digit in parentheses of the bank code is the bank types, S stands for state-owned bank, J for joint-stock bank, C for city commercial bank, and R for rural commercial bank.

As is shown in Figure 3, there is only one SIB -SHB, its $\gamma^{i\,|\,index}$ is at the upstream level, ranks the eighth; nine SIBs' $\gamma^{i\,|\,index}$ are at the middle level, $\gamma^{CEB\,|\,index}$ ranks the 11th, $\gamma^{CITIC\,|\,index}$, $\gamma^{BOCOM\,|\,index}$, $\gamma^{CMBC\,|\,index}$, $\gamma^{HXB\,|\,index}$, $\gamma^{BOB\,|\,index}$, $\gamma^{SPDB\,|\,index}$, $\gamma^{NBB\,|\,index}$ and $\gamma^{JSB\,|\,index}$ ranks the 21th, 23th to 28th, and 30th; other nine SIBs' $\gamma^{i\,|\,index}$ are at the lower level; the six state-owned commercial banks are almost unaffected by systemic risks. That indicates that although the transaction scale and scope of banks are the basic determining factors of systemic importance, the inter-bank correlation and its risk spillover characteristics in the network have a more structural influence on their systemic importance ranking in the financial system.

4.3. A Robustness Test

In order to test the reliability of the GCoVaR method used in this paper, a robustness test is conducted by using the adjacency information entropy method. This method is also a network analysis approach and works well for investigating the direct and indirect connection effects in the network, which helps to reflect the full view of systemic importance of financial institutions in the financial system (Jamil and Yukongdi, 2020; Allen and Gale, 2000 [32,33]). The basic idea of the adjacency information entropy method is that it regards each bank as a node in the banking network and computes the adjacency information entropy of every node by calculating its degree of adjacency. Subsequently, the importance of each node in the banking network is identified in line with the size of adjacency information entropy. We calculate the adjacency information entropy H of each bank for the 54 public offered banks by referring to Equations (A8)–(A13) in Appendix C (For simplicity, we assume $\lambda = 0.5$, means pay equal attention to the in-degree and out-degree). Then, rankings of banks are obtained and demonstrated in Figure 4. Please refer to Appendix C for specific calculation procedures.

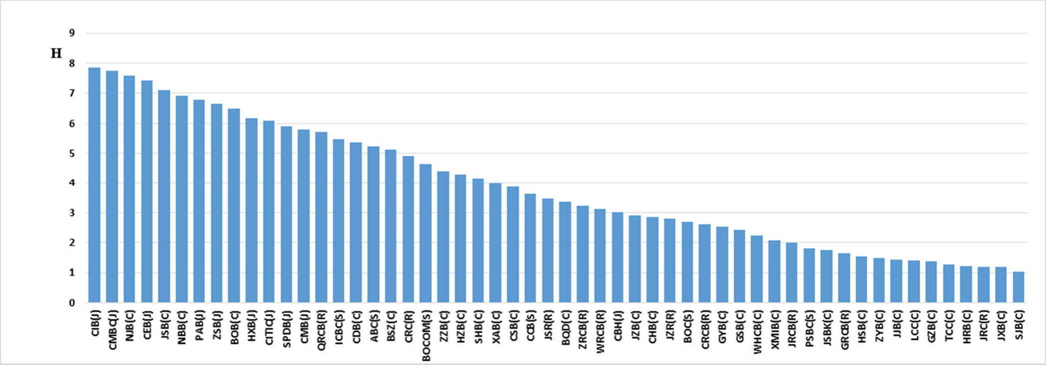

Figure 4. The individual banks' the adjacency information entropy. Notes: The last digit in parentheses of the bank code is the bank types, S stands for state-owned bank, J for joint-stock bank, C for city commercial bank, and R for rural commercial bank.

The ranking of banks in Figure 4 are basically consistent with that in Figure 2 in terms of the bank types. For some small and medium-sized city commercial banks e.g., NJB, JSB, NBB, their risk features are much higher than those of SIBs. It shows that the GCoVaR method used in this paper is robust and can provide useful measurement of the non-SIBs' risk spillover effects and rankings of systemically risky banks.

5. Conclusions

In the banking system, banks are closely connected and interact with each other, thus forming a financial network. Since the individual extreme risks of banks could be reflected by tail risks, it is necessary to scientifically reveal the correlation mechanism of banks' tail risks and its heterogeneous characteristics. There is important theoretical and practical significance to scientifically identifying the systemic importance of banks for effectively preventing and controlling systemic risks of banking system.

In this paper, the GCoVaR method is used to measure the risk spillover intensity between any two banks of China's banking system. The results show that:

1. Compared with SIBs, the non-SIBs are weaker to resist systemic risk impact. Figure 3 ranks the individual banks based on the intensity of systemic risk impact in descending order. Most of the SIBs have a stronger ability to withstand the impact of systemic risks in the banking sector, especially the state-owned SIBs are almost unaffected by systemic risk in terms of $\gamma^{i\,|\,index}$. On the contrary, non-SIBs are mostly severely affected by systemic risks.
2. China's banking risk spillover has characteristics of hierarchical diffusion from rural commercial banks to city commercial banks to joint-stock commercial banks and

state-owned commercial banks. It is mainly from non- SIBs that SIBs receive large risk impacts. It can be seen that in China's banking system, some non-SIBs, especially some city commercial banks, are more vulnerable to the shocks of systemic risk than SIBs, and they are more likely to act as key intermediaries to transmit risk to SIBs, in turn to trigger systemic risk. So, if the risk prevention and control efforts for the key intermediary are insufficient, the seemingly small risk shocks are likely to be transmitted from non-SIBs to SIBs, thus generating the 'butterfly effect' of risk shocks and inducing systemic risks in the banking sector.

In view of this, we propose that the supervisory authority should not only pay close attention to the SIBs, but also needs to strengthen the identification and regulation of the key intermediaries in the process of preventing and controlling systemic risks. Taking CDB (with a total asset of 652.43 billion yuan) as an example, its contribution to the systemic risk of China's banking sector is much higher than that of other banks with larger total assets (see Appendix A). The reason is that total asset size and risk spillover are two dimensions to determine the importance of banks. That is, in addition to SIBs officially being designated, it should be based on different perspectives, e.g., risk spillover intensity to identify and pay attention to the key intermediaries. For these kinds of banks, a dynamic management scheme should be established for real-time supervision of their transaction scale and frequency of business operations, and focusing on reducing the possibility and scope of risk spillover, so as to reduce the systemic risk accumulation. The use of risk spillover intensity to distinguish key intermediaries will help regulators not only pay attention to banks that are too big to fail, but also treat seriously the key intermediaries of "risk spillover too strong to fail" in the financial network, so as to avoid missing real SIBs and ensure the stability of the banking system.

Funding: This research was funded by the Fundamental research Funds for the Central University, The scientific research and innovation project of China University of Political Science and Law, grant number CUPL 10822501.

Informed Consent Statement: This research article describing a study do not involve humans.

Data Availability Statement: The China's listed banks data is at https://www.wind.com.cn/ accessed on 30 June 2023.

Conflicts of Interest: The author declares no conflict of interest.

Appendix A.

Table A1. Sample of China listed banks in June 2022–June 2023 (total assets for the quarter ending, 30 June 2023).

	Institution Code	Short Name	Total Assets (Billion Yuan)	Attributes of Banks
1	Bank of China	BOC	24,402.66	Six state-owned banks
2	Industrial and Commercial Bank of China	ICBC	33,345.06	
3	Bank of Communications	BOCOM	10,697.62	
4	China Construction Bank	CCB	28,132.25	
5	Agricultural Bank of China	ABC	27,205.05	
6	Postal Savings Bank of China	PSBC	11,353.26	
7	Ping An Bank	PAB	4468.51	Ten joint-stock commercial banks
8	Shanghai Pudong Development Bank	SPDB	7950.22	
9	China Minsheng Banking	CMBC	6950.23	
10	China Merchants Bank	CMB	8361.45	
11	Hua Xia Bank	HXB	3399.82	
12	Industrial Bank	CIB	7894.00	
13	China CITIC Bank	CITIC	7511.16	
14	China Zheshang Bank	ZSB	2048.23	
15	China Everbright Bank	CEB	5368.11	
16	China Bohai Bank Co., Ltd.	CBH	1393.52	

Table A1. *Cont.*

Institution Code		Short Name	Total Assets (Billion Yuan)	Attributes of Banks
17	Bank of Ningbo	NBN	1626.75	Twenty-eight city commercial banks
18	Bank of Nanjing	NJB	1517.08	
19	Bank of Beijing	BOB	2900.01	
20	Bank of Jiangsu	JSB	2337.89	
21	Bank of Guiyang	GYB	590.68	
22	Bank of Hangzhou	HZB	1169.26	
23	Bank of Shanghai	SHB	2462.14	
24	Bank of Jinzhou	JZB	777.99	
25	Bank of Gansu	GSB	342.36	
26	Bank of Chendu	CDB	652.43	
27	Weihai City Commercial Bank	WHCB	267.60	
28	Xiamen International Bank	XMIB	285.15	
29	Jin Shang Bank	JSBk	270.94	
30	Bank of Chongqing	CHB	561.64	
31	Bank of Changsha	CSB	704.24	
32	Bank of Qingdao	BQD	459.83	
33	Zhongyuan Bank	ZYB	757.48	
34	Bank of Suzhou	BSZ	388.07	
35	Bank of Xi'an	XAB	306.39	
36	Bank of Guizhou	GZB	456.40	
37	Huishang Bank	HSB	1271.70	
38	Bank of Zhengzhou	ZZB	547.81	
39	Tianjin City CommercialBank	TCC	687.76	
40	Bank of Jiujiang	JJB	415.79	
41	Luzhou City Commercial Bank	LCC	118.89	
42	Jiangxi Bank	JXB	458.69	
43	Shengjing Bank	SJB	1037.96	
44	Harbin Bank	HRB	598.60	
45	Jiangyin Rural Commercial Bank	JRC	142.77	Ten rural commercial banks
46	Wuxi Rural Commercial Bank	WRCB	180.02	
47	Changshu Rural Commercial Bank	CRCB	208.69	
48	Jiangsu Suzhou Rural Commercial Bank	JSR	139.44	
49	Jiutai Rural Commercial Bank	JRCB	200.36	
50	Chongqing Rural Commercial Bank	CRC	1135.93	
51	Qingdao Rural Commercial Bank	QRCB	406.81	
52	Guangzhou Rural commercial Bank	GRCB	1027.87	
53	Rural Commercial Bank of Zhangjiagang	ZRCB	143.82	
54	Jiangsu Zijin Rural Commercial Bank	JZR	217.66	

Appendix B. Edge Distribution, Time Varying Copula Model and Its Parameter Estimation

Since financial return series often have empirical stylized facts, such as volatility clustering, price reversals, asymmetric distributions, fat tails, GARCH model can effectively model time series with conditional heteroscedasticity. Therefore, ARMA(p, q)-GARCH(1, 1) model driven by a generalized error distribution (GED) is chose to fit return series R_t^i of bank i and R_t^j of bank j, respectively. The mean value equation of this model can be described by the following ARMA(p, q) process:

$$\mathrm{R}_\mathrm{t}^\tau = \varphi_0 + \sum_{\rho=1}^{p} \varphi_\mathrm{j} \mathrm{R}_{\mathrm{t}-\rho}^\tau + \varepsilon_t^\tau + \sum_{\rho=1}^{q} \theta_\rho \varepsilon_{t-\rho}^\tau = \mu_t^\tau + \varepsilon_t^\tau,\ \tau = i, j, \tag{A1}$$

Here, p and q are non-negative integers. $\varepsilon_t^\tau = \sigma_t^\tau z_t^\tau$, z_t^τ follows the GED distribution with the mean of 0 and degrees of freedom of υ, and σ_t^τ is the conditional standard deviation, satisfying the variance equation as follows:

$$\sigma_t^{\tau 2} = \omega + \alpha_1 \varepsilon_{t-1}^\tau + \beta_1 {\sigma_{t-1}^\tau}^2, \tag{A2}$$

Here, ω, α_1, and β_1 are the parameters to be estimated. In order to ensure the stationality of the series, α_1 and β_1 must satisfy $\alpha_1 + \beta_1 < 1$. After estimating all model parameters with maximum likelihood estimation method, the marginal distribution function of the return series of bank *i* and bank *j* can be obtained:

$$F^{\tau}(\mathrm{R}_{\mathrm{t}}^{\tau}) = P(\varepsilon_t^{\tau} \le \mathrm{R}_{\mathrm{t}}^{\tau} - \mu_t^{\tau}) = P\left(z_t^{\tau} \le \frac{\mathrm{R}_{\mathrm{t}}^{\tau} - \mu_t^{\tau}}{\sigma_t^{\tau}}\right) = GED_{\upsilon}\left(\frac{\mathrm{R}_{\mathrm{t}}^{\tau} - \mu_t^{\tau}}{\sigma_t^{\tau}}\right), \tag{A3}$$

Here, $GED_{\upsilon}(\cdot)$ is the distribution function of the generalized error distribution, and its expression is:

$$GED_{\upsilon}(x) = \int_{-\infty}^{x} \Gamma\left(\frac{3}{\upsilon}\right)^{\frac{1}{2}} \Gamma\left(\frac{1}{\upsilon}\right)^{\frac{-1}{2}} \exp\left\{-|x|^{\upsilon}\left[\frac{\Gamma\left(\frac{3}{\upsilon}\right)}{\Gamma\left(\frac{1}{\upsilon}\right)}\right]^{\frac{\upsilon}{2}}\right\} dx, \tag{A4}$$

Copula is a function that connects edge distributions to construct joint distributions. It can capture the nonlinear and asymmetric relations between variables. There are many forms of Copula function. In order to accurately describe the dependent structure between bank *i* and bank *j*, Gaussian Copula, t-Copula, Clayton Copula and SJC Copula with different tail characteristics are selected for modeling respectively. By using AIC values of different models, the Copula function type with the best fitting effect is selected to further measure generalized CoVaR (GCoVaR).

We use two-stage stepwise estimation method to estimate its parameters, and the specific steps are as follows:

First, all parameters θ in the margin distribution function of the return series of bank *i* and *j* fitted by ARMA(*p*, *q*)-GARCH(1, 1) model are estimated. The estimated values of the parameters are:

$$\hat{\theta}^{\tau} = argmax \sum_{t=1}^{T} lnf_t^{\tau}(\mathrm{R}_{\mathrm{t}}^{\tau}; \theta^{\tau}),\ \tau = i,\ j, \tag{A5}$$

Here, *T* is the sample size, and $f_t^{\tau}(\cdot)$ is the density function of the edge distribution.

Second, put the marginal distribution estimated in the first step into the time-varying Copula model. The maximum likelihood method is also used to estimate all parameters θ_C in the time-varying Copula model, the estimated values are:

$$\hat{\theta}_c = argmax \sum_{t=1}^{T} lnc_t(F_j\ (\mathrm{R}_{\mathrm{t}}^{j}; \hat{\theta}^{j}),\ F_i\left(R_t^{i}; \hat{\theta}^{i}\right);\ \theta_c), \tag{A6}$$

where, $c_t(\cdot,\cdot)$ is the time-varying Copula density function.

To estimate the parameters for different time-varying Copula models respectively, and calculate *AIC* values of different models. *AIC* values are calculated as follows:

$$AIC = 2k - 2\sum_{t=1}^{T} lnc_t(F_j\ (\mathrm{R}_{\mathrm{t}}^{j}; \hat{\theta}^{j}),\ F_i\left(R_t^{i}; \hat{\theta}^{i}\right);\ \theta_c), \tag{A7}$$

Here, *k* is the number of model parameters. The smaller *AIC* value is, the higher fitting degree model is. Therefore, the time-varying Copula model with the minimum *AIC* value is selected as the optimal model, and the GCoVaR between bank *i* and *j* is measured on that.

The following R program are used to give probability density functions of Gaussian Copula, t-Copula, Clayton Copula, and Gumbel Copula functions respectively, and the four copula functions are used to synthesize the joint distribution for any distribution, and their simulated data.

```
library(copula)
library(psych)
library(VineCopula)

X_1 <- runif(100, 0, 100)
X_2 <-X_1+ runif(100, 0, 50)

plot(X_1,X_2)
abline(lm(X_2~X_1),col=‘red’,lwd=1)
cor(X_1,X_2,method=‘spearman’)

#u <- pobs(as.matrix(cbind(X_1,X_2)))[,1]
#v <- pobs(as.matrix(cbind(X_1,X_2)))[,2]
#selectedCopula <- BiCopSelect(u,v,familyset=NA)
#selectedCopula

gaussian.cop <- normalCopula(dim=2)
set.seed(500)

m <- pobs(as.matrix(cbind(X_1,X_2)))
fit <- fitCopula(gaussian.cop,m,method=‘ml’)
coef(fit)
rho <- coef(fit)[1]

cor(u,method=‘spearman’)
X_1_mu <- mean(X_1)
X_1_sd <- sd(X_1)
X_2_mu <- mean(X_2)
X_2_sd <- sd(X_2)
copula_dist <- mvdc(copula=normalCopula(rho,dim=2), margins=c(“norm”,”norm”),
paramMargins=list(list(mean=X_1_mu, sd=X_1_sd),
list(mean=X_2_mu, sd=X_2_sd)))
sim <- rMvdc(3965,copula_dist)
plot(X_1,X_2,main=‘relation’)
points(sim[,1],sim[,2],col=‘red’,pch=‘.’)
legend(‘bottomright’,c(‘Observed’,’Simulated’),col=c(‘black’,’red’),pch=21)
################################################
t.cop <- tCopula(dim=2)
set.seed(500)
m <- pobs(as.matrix(cbind(X_1,X_2)))
fit <- fitCopula(t.cop,m,method=‘ml’)
coef(fit)
rho <- coef(fit)[1]
df <- coef(fit)[2]
persp(tCopula(dim=2,rho,df=df),dCopula)

u <- rCopula(3965,tCopula(dim=2,rho,df=df))
plot(u[,1],u[,2],pch=‘.’,col=‘blue’)
cor(u,method=‘spearman’)
X_1_mu <- mean(X_1)
X_1_sd <- sd(X_1)
X_2_mu <- mean(X_2)
X_2_sd <- sd(X_2)

copula_dist <- mvdc(copula=tCopula(rho,dim=2,df=df), margins=c(“norm”,”norm”),
paramMargins=list(list(mean=X_1_mu, sd=X_1_sd),
list(mean=X_2_mu, sd=X_2_sd)))
sim <- rMvdc(3965,copula_dist)
plot(X_1,X_2,main=‘relation’)
points(sim[,1],sim[,2],col=‘red’,pch=‘.’)
legend(‘bottomright’,c(‘Observed’,’Simulated’),col=c(‘black’,’red’),pch=21)
#############################################################
clayton.cop <- claytonCopula(dim=2)
set.seed(500)
m <- pobs(as.matrix(cbind(X_1,X_2)))
fit <- fitCopula(clayton.cop,m,method=‘ml’)
coef(fit)
alpha <- coef(fit)[1]

persp(claytonCopula(dim=2,alpha),dCopula)

u <- rCopula(3965,claytonCopula(dim=2,alpha))
plot(u[,1],u[,2],pch=‘.’,col=‘blue’)
cor(u,method=‘spearman’)
X_1_mu <- mean(X_1)
X_1_sd <- sd(X_1)
X_2_mu <- mean(X_2)
X_2_sd <- sd(X_2)
```

```
copula_dist <- mvdc(copula=claytonCopula(dim=2,alpha), margins=c("norm","norm"),
paramMargins=list(list(mean=X_1_mu, sd=X_1_sd),
list(mean=X_2_mu, sd=X_2_sd)))
sim <- rMvdc(3965,copula_dist)
plot(X_1,X_2,main='relation')
points(sim[,1],sim[,2],col='red',pch='.')
legend('bottomright',c('Observed','Simulated'),col=c('black','red'),pch=21)
############################################################
gumbel.cop <- gumbelCopula(dim=2)
set.seed(500)
m <- pobs(as.matrix(cbind(X_1,X_2)))
fit <- fitCopula(gumbel.cop,m,method='ml')
coef(fit)
alpha <- coef(fit)[1]

persp(gumbelCopula(dim=2,alpha),dCopula)

u <- rCopula(3965,gumbelCopula(dim=2,alpha))
plot(u[,1],u[,2],pch='.',col='blue')
cor(u,method='spearman')
X_1_mu <- mean(X_1)
X_1_sd <- sd(X_1)
X_2_mu <- mean(X_2)
X_2_sd <- sd(X_2)

copula_dist <- mvdc(copula=gumbelCopula(dim=2,alpha), margins=c("norm","norm"),
paramMargins=list(list(mean=X_1_mu, sd=X_1_sd),
list(mean=X_2_mu, sd=X_2_sd)))
sim <- rMvdc(3965,copula_dist)
plot(X_1,X_2,main='relation')
points(sim[,1],sim[,2],col='red',pch='.')
legend('bottomright',c('Observed','Simulated'),col=c('black','red'),pch=21)
```

Appendix C. Algorithm for the Adjacency Information Entropy of the Bank

Following Hu et al. [34] and Zhao et al. [35], the calculation steps for the adjacency information entropy of bank j are as follows:

1. calculate the weight (E_{ji}) of effect on bank *j* by bank *i*.

$$E_{ji} = \frac{e_{ji}}{\sum_i e_{ji}}, \tag{A8}$$

   where e_{ji} denotes the extent of the risk connection effect by bank *i* on bank *j*, can be obtained by Granger causality test between the return rate offered by banks' stocks.

2. calculate the in-degree of bank *j* (s_j^{in}), which denotes the risk spillover received by bank *j*,

$$s_j^{in} = \sum_{i \in_j} E_{ji}, \tag{A9}$$

   where $_j$ is the set of banks connected with bank *j*.

3. calculate the out-degree of bank *j* (s_j^{out}), which denotes the risk spillover transmitted by bank *j*,

$$s_j^{out} = \sum_{i \in_j} E_{ij}, \tag{A10}$$

4. calculate the total risk spillover of bank *j* (s_j),

$$s_j = \lambda s_j^{in} + (1-\lambda) s_j^{out}, \tag{A11}$$

   where λ is the relative importance effect coefficient.

5. calculate the adjacency degree (Q_i),

$$Q_i = \lambda \sum_{k \in_i} s_{ik} + (1-\lambda) \sum_{k \in_i} s_{ki} \tag{A12}$$

6. calculate the adjacency information entropy of bank j (H_j),

$$H_j = \sum_{i \in j} \left| \left(-\frac{s_j}{Q_i} log \frac{s_j}{Q_i} \right) \right|, \tag{A13}$$

References

1. BCBS. *Global Systemically Important Banks, Assessment Methodology and the Additional Loss Absorbency Requirement*; BCBS: Basel, Switzerland, 2011.
2. Acharya, V.; Santos, J.; Yorulmazer, T. Systemic Risk and Deposit Insurance Premiums. *Econ. Policy Rev. Fed. Reserve Bank N. Y.* **2010**, *16*, 89–99. [CrossRef]
3. Brownlees, C.; Engle, R. *Volatility, Correlation and Tails for Systemic Risk Measurement*; Working Paper; New York University: New York, NY, USA, 2011.
4. Drehmann, M.; Tarashev, N. Systemic importance, some simple indicators. *BIS Q. Rev.* **2011**, 25–37.
5. Adrian, T.; Brunnermeier, M.K. CoVaR. *Am. Econ. Rev.* **2016**, *106*, 1705–1741. [CrossRef]
6. Zhou, C. Are Banks Too Big to Fail? Measuring Systemic Importance of Financial Institutions. *Int. J. Cent. Bank.* **2010**, *6*, 205–250.
7. Aldasoro, I.; Alves, I. Multiplex interbank networks and systemic importance—An application to European data. *J. Financ. Stab.* **2018**, *35*, 17–37. [CrossRef]
8. Corsi, F.; Lillo, F.; Pirino, D.; Trapin, L. Measuring the propagation of financial distress with Granger-causality tail risk networks. *J. Financ. Stab.* **2018**, *38*, 18–36. [CrossRef]
9. Poledna, S.; Hinteregger, A.; Thurner, S. Identifying Systemically Important Companies by Using the Credit Network of an Entire Nation. *Entropy* **2018**, *20*, 792. [CrossRef] [PubMed]
10. Pablo, R.K.; Alessandro, S. Identifying systemically important financial institutions, a network approach. *Comput. Manag. Sci.* **2019**, *16*, 155–185.
11. Diebold, F.X.; Yilmaz, K. On the network topology of variance decompositions, Measuring the connectedness of financial firms. *J. Econom.* **2014**, *182*, 119–134. [CrossRef]
12. Demirer, M.; Diebold, F.X.; Liu, L.; Yilmaz, K. Estimating global bank network connectedness. *J. Appl. Econom.* **2018**, *33*, 1–15. [CrossRef]
13. Baumöhl, E.; Bouri, E.; Hoang, T.-H.-V.; Shahzad, S.J.H.; Výrost, T. *From Physical to Financial Contagion, the COVID-19 Pandemic and Increasing Systemic Risk among Banks*; ZBW—Leibniz Information Centre for Economics: Hamburg, Germany, 2020.
14. Guo, Y.; Li, P.; Li, A. Tail risk contagion between international financial markets during COVID-19 pandemic. *Int. Rev. Financ. Anal.* **2021**, *73*, 101649. [CrossRef]
15. Naifar, N.; Shahzad, S.J.H. Tail event-based sovereign credit risk transmission network during COVID-19 pandemic. *Financ. Res. Lett.* **2022**, *45*, 102182. [CrossRef]
16. King, M.; Wadhwani, S. Transmission of Volatility between Stock Markets. *Rev. Financ. Stud.* **1990**, *3*, 5–33. [CrossRef]
17. Eichengreen, B.; Rose, A.; Wyplosz, C. Contagious Currency Crises, First Tests. *Scand. J. Econ.* **1996**, *98*, 463–484. [CrossRef]
18. Arize, A. Foreign trade and exchange-rate risk in the G-7 countries, co-integration and error—Correction models. *Rev. Finan. Econ.* **1997**, *6*, 95–112. [CrossRef]
19. Reboredo, J.C.; Ugolini, A. Systemic risk in European sovereign debt markets, A CoVaR—Copula approach. *J. Int. Money Financ.* **2015**, *51*, 214–244. [CrossRef]
20. Reboredo, J.C.; Rivera-Castro, M.A.; Ugolini, A. *Downside and Upside Risk* Spillovers Between Exchange Rates and Stock Prices. *J. Bank. Financ.* **2016**, *62*, 76–96.
21. Warshaw, E. Extreme dependence and risk spillovers across North American equity markets. *N. Am. J. Econ. Financ.* **2019**, *47*, 237–251. [CrossRef]
22. Lopez-Espinosa, G.; Moreno, A.; Rubia, A.; Valderrama, L.; Moreno, A. Systemic risk and asymmetric responses in the financial industry. *IMF Work. Pap.* **2012**, *58*, 471–485. [CrossRef]
23. Girardi, G.; Erguen, A.T. Systemic risk measurement, Multivariate GARCH estimation of CoVaR. *J. Bank. Financ.* **2013**, *37*, 3169–3180. [CrossRef]
24. Torri, G.; Giacometti, R.; Tichý, T. Network tail risk estimation in the European banking system. *J. Econ. Dyn. Control.* **2021**, *127*, 104125. [CrossRef]
25. Lai, Y.; Hu, Y. A study of systemic risk of global stock markets under COVID-19 based on complex financial networks. Phys. *A Stat. Mech. Its Appl.* **2021**, *566*, 125613. [CrossRef]
26. Barigozzi, M.; Hallin, M.; Soccorsi, S.; von Sachs, R. Time-varying feneral dynamic factor models and the measurement of financial connectedness. *J. Econom.* **2021**, *222*, 324–343. [CrossRef]
27. Mistrulli, P.E. Assessing Financial Contagion in the Interbank Market, Maximum Entropy versus Observed Interbank Lending Patterns. *J. Bank. Financ.* **2011**, *35*, 1114–1127. [CrossRef]
28. Peltonen, T.A.; Scheicher, M.; Vuillemey, G. The Network Structure of the CDS Market and its Determinants. *J. Financ. Stab.* **2014**, *13*, 118–133. [CrossRef]

29. Georg, C.P. The Effect of the Interbank Network Structure on Contagion and Common Shocks. *J. Bank. Financ.* **2013**, *37*, 2216–2228. [CrossRef]
30. Yang, G.A.; Yl, A.; Yw, B. Risk spillover and network connectedness analysis of China's green bond and financial markets, Evidence from financial events of 2015–2020. *N. Am. J. Econ. Financ.* **2021**, *57*, 101386.
31. Berger, A.N.; Cai, J.; Roman, R.A.; Sedunov, J. Supervisory enforcement actions against banks and systemic risk. *J. Bank. Financ.* **2022**, *140*, 106222. [CrossRef]
32. Jamil, S.; Yukongdi, V. Information Systems Workforce and Innovative Work Behavior, The Role of Participatory Management, Affective Trust and Guanxi. *Int. J. Semant. Web Inf. Syst.* **2020**, *16*, 146–165. [CrossRef]
33. Allen, F.; Gale, D. Financial Contagion. *J. Political Econ.* **2000**, *108*, 1–33. [CrossRef]
34. Hu, G.; Xu, X.; Gao, H.; Guo, X. Node importance recognition algorithm based on adjacency information entropy in networks. *Syst. Eng.—Theory Pract.* **2020**, *40*, 714–725.
35. Zhao, L.; Li, Y.; Wu, Y.J. An Identification Algorithm of Systemically Important Financial Institutions Based on Adjacency Information Entropy. *Comput. Econ.* **2022**, *59*, 1735–1753. [CrossRef]

fractal and fractional

Article

Uncertain Currency Option Pricing Based on the Fractional Differential Equation in the Caputo Sense

Qinyu Liu [1], Ting Jin [1,*], Min Zhu [1,*], Chenlei Tian [1] , Fuzhen Li [1] and Depeng Jiang [2]

[1] School of Science, Nanjing Forestry University, Nanjing 210037, China; liuqinyu@njfu.edu.cn (Q.L.); targaryentcl@njfu.edu.cn (C.T.); pandajun@njfu.edu.cn (F.L.)
[2] Department of Community Health Sciences, University of Manitoba, S113-750 Bannatyne Ave, Winnipeg, MB R3E 0W3, Canada; depeng.jiang@umanitoba.ca
* Correspondence: tingjin@njfu.edu.cn (T.J.); zhumin@njfu.edu.cn (M.Z.)

Abstract: The foreign exchange market comprises the largest global volume, so the pricing of foreign exchange options has always been a hot issue in the foreign exchange market. This paper treats the exchange rate as an uncertain process that is described by an uncertain fractional differential equation, and establishes a new uncertain fractional currency model. The uncertain process is driven by Liu process, and, with the application of the Mittag-Leffler function, the solution of the fractional differential equation in a Caputo sense is presented. Then, according to the uncertain fractional currency model, the pricing formulas of European and American currency options are given. Lastly, the two numerical examples of European and American currency options are given; the price of the currency option increased when p changed from 1.0 to 1.1, and prices with different p were all decreasing functions of exercise price K.

Keywords: fractional differential equation; uncertainty theory; currency model; currency option pricing

Citation: Liu, Q.; Jin, T.; Zhu, M.; Tian, C.; Li, F.; Jiang, D. Uncertain Currency Option Pricing Based on the Fractional Differential Equation in the Caputo Sense. *Fractal Fract.* **2022**, *6*, 407. https://doi.org/10.3390/fractalfract6080407

Academic Editor: Leung Lung Chan

Received: 20 June 2022
Accepted: 21 July 2022
Published: 24 July 2022

1. Introduction

Options originated from the earliest stock trading. Until the 1980s, due to the increasingly fierce exchange rate fluctuations in the international financial market and the development of international trade, foreign exchange options gradually developed. The first foreign exchange options were sterling and deutschemark options undertaken by the Philadelphia Stock Exchange in 1982. From the perspective of trading volume, the foreign exchange options market has become the deepest and largest global option market with strong liquidity [1]. Therefore, establishing mathematical models for foreign exchange options is significant in modern mathematical finance [2].

With the development of foreign exchange options, pricing has become a hot issue in the financial market. Scholars first use probability theory to solve the pricing problem of financial markets. However, many real and reliable data are needed in the application of probability theory, and there are certain obstacles during data collection in real life and regarding the reliability of data, which means that probability theory may cause loopholes in practical applications. To solve the above problems, scholars replace probability with the belief degree of experts in the respective professional field. However, subsequent studies found that the degree of belief is also not accurate and can be easily influenced by personal perspectives [3], which can lead to huge deviations in the results.

It was not until 2007 that Liu [4] first put forward the uncertainty theory that the problem of the irrationality of expert belief degree was solved. Uncertainty theory is a new branch of mathematics based on four axioms: normalization, duality, subadditivity, and product axiom. Due to its ability to deal with imprecise information such as subjective judgment, uncertainty theory boasts a series of major achievements. For more information, please refer to [5,6]. Liu [5,7] optimized uncertainty theory by using an uncertainty measure, and gave the definition of uncertain process. In order to study the uncertain calculus of uncertain processes, Liu proposed the Liu process [6] in 2009, which is an uncertain process with stationary independent increment that can more accurately simulate the uncertain dynamic system.

On this basis, Liu [7] established a differential equation that is driven by an uncertain process in 2008. Subsequently, many studies have been conducted. Chen and Liu [8] put forward the existence and uniqueness theorem of solutions under the global Lipschitz condition. Gao [9] proved that the theorem also holds under the local Lipschitz condition. Chen and Liu [8] obtained the analytic solutions of linear uncertain differential equations. Yao and Chen [10] proposed a numerical method to solve uncertain differential equations.

Since stock prices follow the Liu process, Liu [7] introduced the uncertainty theory into a financial field for the first time and proposed an uncertain stock model. Soon after that, the European option price formula was derived from Liu's work. Then, Chen [11] further derived the American option pricing formula. Peng and Yao [12] proposed another uncertain stock model and studied the pricing formula of the option. Gao [13] gave the price formulas of the American barrier option. Chang and Sun [14] proposed a nonlinear multiperiod portfolio selection model based on uncertainty theory to solve an uncertain multiperiod portfolio selection problem. Furthermore, in addition to the stock market, scholars applied the uncertainty model to the other financial fields. Chen and Gao [15] inserted the uncertainty model into the interest rate market and proposed a pricing formula for zero coupon bonds. Liu [16] introduced the uncertainty model into the insurance market field.

Scholars from different countries have performed many studies on using uncertain differential equations to solve financial problems. However, because the volatility of financial market is continuous, an uncertain differential equation cannot precisely reflect this property. Therefore, an uncertain fractional differential equation is more suitable for financial markets due to its continuity and memory.

Because the assumptions of fractional differential equations are more consistent with the facts and more reasonable to solve practical problems, many scholars have studied fractional differential equations. Lakshmikantham et al. [17] expounded the basic theory of fractional differential equations. Lakshmikantham and Vasundhara Devi [18] elaborated the details of the theory of fractional differential equations in Banach space. On the basis of the above theories, Belmekki et al. [19] studied the existence of periodic solutions for nonlinear fractional differential equations. Kosmatov [20] studied the integral equations and initial value problems of nonlinear fractional differential equations. Zhang [21] explored the monotone iterative method for the initial value problem of fractional derivatives. In 2013, Zhu [22] introduced uncertainty into fractional differential equations for the first time and gave two forms of UFDEs. Then, Zhu [23] gave the Lipschitz condition and linear growth conditions, and obtained the existence and uniqueness of UFDE's solution. Jin et al. [24] studied the extremal problem of uncertain fractional differential equations. On the basis of the expected and optimistic values, Lu [25] gave the pricing formulas of the Asian options, which are driven by an uncertain fractional differential equation.

Foreign exchange options are becoming increasingly important, but there are few scholars using uncertain fractional differential equations to price foreign exchange options. Therefore, this paper introduces an uncertain fractional option model and deduces its pricing formula.

2. Preliminary

2.1. Numerical Methods of the Solution of UFDEs

In this part, we introduce some basic knowledge regarding uncertainty theory and the results obtained by some scholars. These results include general methods for obtaining the numerical solutions of UFDEs. This section is a preparation for the later discussion on option pricing, so it is relatively simple. For more detailed and more comprehensive knowledge about uncertainty and UDEs, please refer to [5–7].

Suppose there are two variables, p and C_t. p is a variable with an independent stationary property that satisfies the following conditions: $0 \leq n-1 < p \leq n$. C_t is a Liu normative process [6] that satisfies the following conditions: (i) If $t = 0$, then $C_0 = 0$, and the sampling paths are always Lipschitz-continuous; (ii) the Liu normative process has a stable and independent increment; (iii) each increment $C_{s+t} - C_s$ corresponds to a normal uncertain distribution: $\Phi_t(x) = \left(1 + \exp\left(-\frac{\pi x}{\sqrt{3}t}\right)\right)^{-1}, x \in \Re$. The expected value of this normal uncertain distribution is 0, and the variance is t^2. In addition, there are two functions, F and H, which are continuous on $[0, T] \times \mathcal{R}$.

Zhu [22] presented two forms of UFDEs: the Riemann–Liouville and Caputo types. For this article, we just focus on UFDEs of the Caputo type, that is,

$$\begin{cases} {}^cD^pX_t = F(t, X_t) + H(t, X_t)\frac{dC_t}{dt} \\ X_t^{(k)} \mid_{t=0} = x_k, k = 0, 1, \ldots, n-1. \end{cases} \tag{1}$$

Lu [26] obtained the result of (1) that satisfies the following integral equation:

$$\begin{aligned} X_t &= \sum_{k=0}^{n-1} \frac{x_k t^k}{\Gamma(k+1)} + \frac{1}{\Gamma(p)} \int_0^t (t-s)^{p-1} F(s, X_s) ds \\ &\quad + \frac{1}{\Gamma(p)} \int_0^t H(s, X_s)(t-s)^{p-1} dC_s, \end{aligned} \tag{2}$$

where $\Gamma(p) = \int_0^\infty t^{p-1} \exp(-t) dt$ is the gamma function.

In addition, if $F(t, X_t) = AX_t + B(t)$, $H(t, X_t) = \sigma(t)$, we obtain a special type of UFDE:

$$\begin{cases} {}^cD^pX_t = AX_t + B(t) + \sigma(t)\frac{dC_t}{dt} \\ X_t^{(k)} \mid_{t=0} = x_k, k = 0, 1, \ldots, n-1. \end{cases} \tag{3}$$

The Mittag-Leffler function was applied to the solution of (3), and Lu [26] obtained

$$\begin{aligned} X_t &= \sum_{k=0}^{n-1} x_k t^k E_{p,(k+1)}(At^p) + \int_0^t (t-s)^{p-1} E_{p,q}(A(t-s)^p) B(s) ds \\ &\quad + \int_0^t (t-s)^{p-1} Ep, q(A(t-s)^p) \sigma(s) dC_s. \end{aligned} \tag{4}$$

where $E_{p,(k+1)}(At^p)$ satisfies the Mittag-Leffler function:

$$E_{\alpha,\beta}(z) = \sum_{k=0}^{\infty} \frac{z^k}{\Gamma(\alpha k + \beta)}$$

In terms of the properties of the solutions, Zhu [23] reported that the coefficients $F(t, x)$ and $H(t, x)$ satisfied

1. Lipschitz condition:

   $$|F(t, x) - F(t, y)| + |H(t, x) - H(t, y)| \leq L|x - y|, \ \forall x, y \in R^n, t \in [0, +\infty),$$

2. linear growth condition:

   $$|F(t, x)| + |H(t, x)| \leq L(1 + |x|), \ \forall x \in R^n, t \in [0, +\infty),$$

   where L is a positive constant, and X_t is sample-continuous. Then, we can find the X_t, the solution of UFDE (1), which should exist and be unique.

In order to obtain the numerical solutions of UFDEs, an α-path is introduced into the solution process. The α-path is a solution to the following equation:

$$\begin{cases} {}^{c}D^{p}X_t^{\alpha} = F(t, X_t^{\alpha}) + \mid H(t, X_t^{\alpha}) \mid \Phi^{-1}(\alpha) \\ X_t^{(k)} \mid_{t=0} = x_t, k = 0, 1, \ldots, n-1, \end{cases} \tag{5}$$

where $0 < \alpha < 1, \Phi^{-1}(\alpha) = \frac{\sqrt{3}}{\pi} \ln \frac{\alpha}{1-\alpha}$. Equation (5) is the relevant FDE of UFDE (1).

Lu [27] then gave the definition of α-path, which was used to build the relationship between UFDEs and FDE. Suppose that X_t is the unique solution of (1), and X_t^{α} is the α-path of the (1). Then,

$$\begin{cases} \mathcal{M}\{X_t \leq X_t^{\alpha}, \forall t \in [0, T]\} = \alpha \\ \mathcal{M}\{X_t > X_t^{\alpha}, \forall t \in [0, T]\} = 1 - \alpha \end{cases} \tag{6}$$

and the IUD of solution X_t is

$$\Psi_s^{-1}(\alpha) = X_t^{\alpha}, \tag{7}$$

which can be seen in [27].

2.2. Extreme Values for the Solution to UFDE

This section introduces the research on the extremum of uncertain fractional differential equations. Scholars have carried out relevant studies. Jin and Zhu et al. [24] studied the extreme value problem for solutions of a class of uncertain fractional differential equations. On the basis of the definition of α-path, the inverse theorem of uncertain distribution of extremum is given. The corresponding numerical algorithm was designed, and the validity of the algorithm is verified by an example.

According to Jin's work [24], the definition of the extreme value of the uncertain fractional differential equation is as follows:

Let X_t and X_t^{α} be the unique solution, and the α-path for the following UFDE:

$$\begin{cases} {}^{c}D^{p}X_t = F(t, X_t) + H(t, X_t)\frac{dC_t}{dt} \\ X_t^{(k)} \mid_{t=0} = x_k, k = 0, 1, \ldots, n-1 \end{cases}$$

respectively.

There exists an IUD of supremum $\sup\limits_{0 \leq t \leq s} J(X_t)$,

$$\Upsilon_s^{-1}(\alpha) = \sup_{0 \leq t \leq s} J(X_t^{\alpha}), \tag{8}$$

where $J(x)$ strictly increases. Comparably,

$$\Upsilon_s^{-1}(\alpha) = \sup_{0 \leq t \leq s} J(X_t^{1-\alpha}),$$

where $J(x)$ strictly decreases.

Simultaneously, there exists an IUD of infimum $\inf\limits_{0 \leq t \leq s} J(X_t)$,

$$\overline{\Upsilon}_s^{-1}(\alpha) = \inf_{0 \leq t \leq s} J(X_t^{\alpha}),$$

where $J(x)$ strictly increases. Comparably,

$$\overline{\Upsilon}_s^{-1}(\alpha) = \inf_{0 \leq t \leq s} J(X_t^{1-\alpha}),$$

where $J(x)$ strictly decreases.

For the specific proof process, please refer to Jin et al. [24].

2.3. Uncertain Currency Model

As a result of trade, inflation, and other factors, the exchange rate is always changing. Assuming that the exchange rate follows the geometric Liu process is acceptable. For the above reasons, Liu [28] introduced the uncertain differential equation into the currency option pricing model. Assume that X_t is the domestic risk-free currency, Y_t is the foreign risk-free currency, and Z_t is the exchange rate, and they are defined as follows:

$$\begin{cases} X_t = X_0 e^{ut} \\ Y_t = Y_0 e^{vt} \\ Z_t = Z_0 e^{et+\sigma C_t}, \end{cases} \tag{9}$$

where u represents the domestic interest rate, and v represents the foreign interest rate. Here, Z_t follows a geometric Liu process with log-drift e and log-diffusion σ.

On the basis of the above assumptions and uncertainty theory, an uncertain currency model with uncertain exchange rate is given as follows:

$$\begin{cases} dX_t = uX_t dt \\ dY_t = vY_t dt \\ dZ_t = eZ_t dt + \sigma Z_t dC_t. \end{cases} \tag{10}$$

Exchange rate Z_t has the following inverse uncertainty distribution:

$$\Phi_t^{-1}(\alpha) = Z_0 \exp(et + \frac{\sqrt{3}\sigma t}{\pi} \ln \frac{\alpha}{1-\alpha}).$$

2.4. Uncertain Fractional Stock Model

In existing studies [16,24,29], scholars attempted to apply the uncertain fractional differential equation to the stock pricing model. Assume that A_t represents the bond price, B_t is the stock price, and r is the constant interest rate. On the basis of the UFDE of the Caputo type, the stock model with geometric canonical process can be given as follows:

$$\begin{cases} dA_t = rA_t dt \\ {}^cD^p B_t = eB_t + \sigma B_t \frac{dC_t}{dt} \\ B^{(k)}(0) = b_k, k = 0, 1, \ldots, n-1, \end{cases} \tag{11}$$

where e is the stock drift, and σ is the stock diffusion.

According to Equation (4), the UFDE (11) has an α-path:

$$B_t^\alpha = \sum_{k=0}^{n-1} b_k t^k E_{p,(k+1)}\Big((e+ \mid \sigma \mid \Phi^{-1}(\alpha))t^p\Big). \tag{12}$$

Jin et al. [24] performed a detailed study on the pricing of call and put options of American stocks by using uncertain differential equations; for more details, see Jin et al. [24].

3. European Currency Option Pricing

Since foreign exchange options are a variant of stock options, we discuss the pricing of European currency options on the basis of the previous stock model. In this section, we use the uncertain fractional differential equation to obtain the European currency option pricing formula.

3.1. Uncertain Fractional Currency Model

On the basis of the hypothesis and conclusions of the uncertain monetary model in the preliminary data, a novel uncertain fractional currency model with uncertain exchange rate is defined as follows:

$$\begin{cases} dX_t = uX_t dt \\ dY_t = vY_t dt \\ {}^cD^pZ_t = eZ_t + \sigma Z_t \frac{dC_t}{dt} \\ Z^{(k)}(0) = z_k, k = 0, 1, \dots, n-1. \end{cases} \tag{13}$$

Exchange rate Z_t has the following inverse uncertainty distribution:

$$\Psi_s^{-1}(\alpha) = Z_t^\alpha = \sum_{k=0}^{n-1} z_k t^k E_{p,(k+1)}\Big((e+ \mid \sigma \mid \Phi^{-1}(\alpha))t^p\Big). \tag{14}$$

3.2. Option Pricing Model

In the process of option pricing, the most important link is to ensure the balance of profits between buyer and seller. Let us consider a European currency option with contract price f and exercise price K. In this section, K is a preagreed exchange rate. Suppose one is a buyer of the above European currency option who purchased the European currency option contract for f at time $t = 0$. Then, when the option is executed at T (the European option can only be executed at option expiry date T), one obtains $(Z_T - K)^+$ as the return. Thus, one can easily calculate their expected return as a buyer at time $t = 0$:

$$-f + \exp(-uT)E[(Z_T - K)^+], \tag{15}$$

which is equal to the present value of the return $E[(Z_T - K)^+]$ minus the option contract price f paid at time $t = 0$, where the value of return at present is influenced by domestic interest rate u because we use domestic risk-free currency as settlement currency. Hence, $\exp(-uT)$ can be viewed as the discount rate.

Now let us switch the identity, assuming one is the seller of the above European currency option who sold the European currency option contract for f at time $t = 0$. At this point, there is an income f. Then, when the contract is executed at time T (the European option only can be executed at option expiry date T), one pays $(1 - k/Z_T)^+$. As a result, one can easily calculate their expected return as a trader at T:

$$f - Z_0 \exp(-vT)E[(1 - K/Z_T)^+], \tag{16}$$

which is equal to the income obtained by the seller selling the option at time $t = 0$, the price of option f, minus the present value of potential loss $E[(1 - K/Z_T)^+]$ at time T, where the discount rate is written as $\exp(-vT)$ because, to a seller, the settlement currency is foreign risk-free currency. However, the calculating unit of f is domestic risk-free currency. Then, exchange rate Z_0 (at $t = 0$) is used to calculate the value that has the same unit of f.

To obtain a fair price for a currency option, the expected return of the buyer and seller should be equal. Thus, Equations (15) and (16) need to be equal, that is,

$$-f + \exp(-uT)E[(Z_T - K)^+] = f - Z_0 \exp(-vT)E[(1 - K/Z_T)^+].$$

On the basis of the above discussion, it can be concluded that the price of a European currency option with option expiry time T and strike price K is

$$f = \frac{1}{2}\big(\exp(-uT)E[(Z_T - K)^+] + Z_0 \exp(-vT)E[(1 - K/Z_T)^+]\big), \tag{17}$$

which was defined by Liu et al. [28] in 2015.

In order to obtain the option price of uncertain fractional differential equation monetary Model (13), we need to give the formula for value f. Assuming that the option in Model (13) is a European currency option with option expiry time T and strike price K, the price of the European currency option is then given in the following theorem.

Theorem 1. *Assume that a European currency option for uncertain fractional currency Model* (13) *has a strike price K and an option expiry date T. Then, the European currency option price is*

$$\begin{aligned} f =&\frac{1}{2}\exp(-uT)\int_0^1\left(\sum_{k=0}^{n-1} z_k T^k E_{p,(k+1)}\Big((e+\mid\sigma\mid\Phi^{-1}(\alpha))T^p\Big)-K\right)^+ d\alpha \\ &+\frac{1}{2}Z_0\exp(-vT)\int_0^1\left(1-K/\left(\sum_{k=0}^{n-1} z_k T^k E_{p,(k+1)}\Big((e+\mid\sigma\mid\Phi^{-1}(\alpha))T^p\Big)\right)\right)^+ d\alpha. \end{aligned}$$

where $E_{p,(k+1)}\big((e+\mid\sigma\mid\Phi^{-1}(\alpha))T^p\big)$ *satisfies the Mittag-Leffler function, and* $z_k = Z_t{}^{(k)}(0)$ *represent the derivatives of exchange rate at* $t=0$*.*

Proof. For European options, the execution date is a fixed time T. When Z_T increases, $(Z_T-K)^+$ and $(1-K/Z_T)^+$ also increase. In other words, $(Z_T-K)^+$ and $(1-K/Z_T)^+$ are increasing functions of Z_T. Thus, they all had inverse uncertainty distribution.

According to Equation (14), the inverse uncertainty distribution of $(Z_T-K)^+$ is

$$\Phi^{-1}(\alpha)=\left(\sum_{k=0}^{n-1} z_k T^k E_{p,(k+1)}\Big((e+\mid\sigma\mid\Phi^{-1}(\alpha))T^p\Big)-K\right)^+.$$

The inverse uncertainty distribution of $(1-K/Z_T)^+$ is

$$\Psi^{-1}(\alpha)=\left(1-K/\left(\sum_{k=0}^{n-1} z_k T^k E_{p,(k+1)}\Big((e+\mid\sigma\mid\Phi^{-1}(\alpha))T^p\Big)\right)\right)^+.$$

To sum up, since $f=f_1+f_2$, the European currency option pricing formula is proved. □

Remark 1. *If* $p=1$*, it is obvious that the inverse uncertainty distribution of* $(Z_T-K)^+$ *and* $(1-K/Z_T)^+$ *can be rewritten as*

$$\Phi^{-1}(\alpha)=\left(Z_0\exp\left(eT+\frac{\sqrt{3}\sigma T}{\pi}\ln\frac{\alpha}{1-\alpha}\right)-K\right)^+$$

and

$$\Psi^{-1}(\alpha)=\left(1-K\Big/Z_0\exp\left(eT+\frac{\sqrt{3}\sigma T}{\pi}\ln\frac{\alpha}{1-\alpha}\right)\right)^+,$$

respectively, which are consistent with the results in Liu et al. [28] for UDEs.

4. American Currency Option Pricing

The greatest difference between European and American currency options is the exercise time. Comparatively speaking, the American option is more flexible in time than the European option is. In Section 3, we discussed the pricing of European currency options. In this section, we use the uncertain fractional differential equation to obtain the pricing formula of American currency options.

Option Pricing Model

Let us consider an American currency option with contract price of f and exercise price K. Suppose that one is a buyer of the above American currency option who purchased the American currency option contract for f at time $t = 0$. Then, when the option is executed during its life (the American option can be executed at any time before option expiry date T), one obtains $\sup\limits_{0 \le s \le T} \exp(-rs)(Z_s - K)^+$ as return. Thus, one can easily calculate their expected return as a buyer at time $t = s$:

$$-f + E[\sup_{0 \le s \le T} \exp(-rs)(Z_s - K)^+], \tag{18}$$

which is equal to the present value of the return $\sup\limits_{0 \le s \le T} \exp(-us)(Z_s - K)^+$ minus the option contract price f paid at time $t = 0$. $\exp(-vs)$ can be viewed as a discount rate, whose reason is similar to that in European currency option pricing model.

Similarly, now let us switch the identity, assuming that one is the seller of the above American currency option who sold the American currency option contract for f at time t_0. At this point, there is an income f. Then, when the contract is executed during its life (the American option can be executed at any time before option expiry date T), one pays $\sup\limits_{0 \le s \le T} Z_0 \exp(-rs)(1 - K/Z_s)^+$. As a result, one can easily calculate their expected return at $t = s$:

$$f - E[\sup_{0 \le s \le T} Z_0 \exp(-vs)(1 - K/Z_s)^+], \tag{19}$$

which is equal to the income obtained by the bank selling the option at time t_0 minus the present value of potential loss $\sup\limits_{0 \le s \le T} Z_0 \exp(-rs)(1 - K/Z_s)^+$ at time $t = s$.

A fair option price needs to render the expected return of the buyer and the seller equal at time $t = 0$ (before the beginning of the option). Thus, Equations (18) and (19) need to be equal, that is,

$$-f + E[\sup_{0 \le s \le T} \exp(-us)(Z_s - K)^+] = f - E[\sup_{0 \le s \le T} Z_0 \exp(-vs)(1 - K/Z_s)^+].$$

On the basis of the above discussion, it can be concluded that the price of an American currency option, the option expiry date T (during the whole life of the currency option, the option can be executed) and the strike price K is

$$f = \frac{1}{2}(E[\sup_{0 \le s \le T} \exp(-us)(Z_s - K)^+] + E[\sup_{0 \le s \le T} Z_0 \exp(-vs)(1 - K/Z_s)^+]. \tag{20}$$

which was also defined by Liu et al. [28] in 2015.

In order to obtain the option price of uncertain fractional differential equation monetary Model (13), we need to give the formula for value f. Assuming that the option in Model (13) is an American currency option with option expiry date T and strike price K, the price of the American currency option is given in the following theorem.

Theorem 2. *Assume that an American currency option for uncertain fractional currency Model* (13) *has a strike price K and an option expiry date T. Then, the American currency option price is*

$$\begin{aligned} f =& \frac{1}{2}\int_0^1 \sup_{0 \le s \le T} \exp(-us)\left(\sum_{k=0}^{n-1} z_k s^k E_{p,(k+1)}\Big((e+ \mid \sigma \mid \Phi^{-1}(\alpha))s^p\Big) - K\right)^+ d\alpha \\ &+ \frac{1}{2}\int_0^1 \sup_{0 \le s \le T} Z_0 \exp(-vs)\left(1 - K/\left(\sum_{k=0}^{n-1} z_k s^k E_{p,(k+1)}\Big((e+ \mid \sigma \mid \Phi^{-1}(\alpha))s^p\Big)\right)\right)^+ d\alpha. \end{aligned}$$

Proof. When Z_s increases, $\sup\limits_{0\le s\le T}\exp(-us)(Z_s-K)^+$ and $\sup\limits_{0\le s\le T} Z_0\exp(-vs)(1-K/Z_s)^+$ also increase. In other words, $\sup\limits_{0\le s\le T}\exp(-us)(Z_s-K)^+$ and $\sup\limits_{0\le s\le T} Z_0\exp(-vs)(1-K/Z_s)^+$ are increasing functions of Z_s.

According to Equation (8), they all have inverse uncertainty distribution. The inverse uncertainty distribution of $\sup\limits_{0\le s\le T}\exp(-us)(Z_s-K)^+$ is

$$\Phi^{-1}(\alpha)=\sup_{0\le s\le T}\exp(-us)\left(\sum_{k=0}^{n-1} z_k s^k E_{p,(k+1)}\Big((e+\mid\sigma\mid\Phi^{-1}(\alpha))s^p\Big)-K\right)^+.$$

The inverse uncertainty distribution of $\sup\limits_{0\le s\le T} Z_0\exp(-vs)(1-K/Z_s)^+$ is

$$\Psi^{-1}(\alpha)=\sup_{0\le s\le T} Z_0\exp(-vs)\left(1-K\Big/\left(\sum_{k=0}^{n-1} z_k s^k E_{p,(k+1)}\Big((e+\mid\sigma\mid\Phi^{-1}(\alpha))s^p\Big)\right)\right)^+.$$

To sum up, since $f=f_1+f_2$, the American currency option pricing formula is proven. □

Remark 2. *If $p=1$, it is obvious that the inverse uncertainty distribution of $\sup\limits_{0\le s\le T}\exp(-us)$ $(Z_s-K)^+$ and $\sup\limits_{0\le s\le T} Z_0\exp(-vs)(1-K/Z_s)^+$ can be rewritten as*

$$\Phi^{-1}(\alpha)=\sup_{0\le s\le T}\exp(-us)\left(Z_0\exp\left(es+\frac{\sqrt{3}\sigma s}{\pi}\ln\frac{\alpha}{1-\alpha}\right)-K\right)^+$$

and

$$\Psi^{-1}(\alpha)=\sup_{0\le s\le T} Z_0\exp(-vs)\left(1-K\Big/Z_0\exp\left(es+\frac{\sqrt{3}\sigma s}{\pi}\ln\frac{\alpha}{1-\alpha}\right)\right)^+,$$

respectively, which are consistent with the results in Liu et al. [28] for UDEs.

5. Numerical Calculation

5.1. European Currency Option Pricing

Example 1. *Assume that uncertain fractional currency Model* (13) *has $u=6\%$, $v=3\%$, $e=0.05$, $\sigma=0.3$, and initial exchange rate $Z_0=4.2$, $p\in(0,2]$. Consider the European currency option with expiration date $T=2$ and a striking price $K=4.5$.*

In this numerical example, the two currencies are RMB and SGD, and the initial exchange rate Z_0 was changed a little. These two currencies and the financial markets in both countries were considered to be stable enough, so the parameters in the example are reasonable. In addition, $z_1=0.7861$ represents the derivative of exchange rate at $t=0$.

In order to simplify the calculation and reduce the computing time, a numerical calculation was adopted for the integral calculation in numerical examples. Numerical integration can solve most real-life problems, and its error acceptable. For this example, we used the compound trapezoid formula whose interval value was 0.001. Let $p=0.1,0.2,\dots,1.9,2.0$, and we obtained the following European currency option price f.

As shown in Table 1, the price of the European currency option increased with an increase in p in $(0,0.8]$, and decreased with an increase in p in $(0.8,1]$ and $(1.1,2]$. The price jumped when p changes from 1.0 to 1.1 because of the initial value of $Z'(0)$. Such a jump is similar to the results obtained by Lu [26]. Obviously, different initial values may cause different values of price f.

With the setting of $u = 6\%$, $v = 3\%$, $e = 0.05$, $\sigma = 0.3$, $Z_0 = 4.2$, $T = 2$, and $K = 4.5$, we obtained Table 1, which shows the variation in price f with different p, including its jump. The compound Simpson formula is another numerical method to calculate numerical integration, and its algebraic precision is better than that of the compound trapezoid formula. We then changed the numerical method, using the compound Simpson formula whose value was also 0.001. Then, we obtained the following European currency option price $\tilde{f}$ in Table 2.

Table 1. Price of the European option with different p (compound Trapezoid formula).

p	0.1	0.2	0.3	0.4	0.5	0.6	0.7	0.8	0.9	1.0
f	0.7090	0.8147	0.8900	0.9420	0.9765	0.9977	1.0086	1.0113	1.0075	0.9986
p	1.1	1.2	1.3	1.4	1.5	1.6	1.7	1.8	1.9	2.0
f	1.7737	1.7489	1.7223	1.6943	1.6654	1.6357	1.6055	1.5750	1.5444	1.5138

Table 2. Price of the European option with different p (compound Simpson formula).

p	0.1	0.2	0.3	0.4	0.5	0.6	0.7	0.8	0.9	1.0
$\tilde{f}$	0.7089	0.8146	0.8899	0.9419	0.9765	0.9977	1.0085	1.0112	1.0075	0.9985
p	1.1	1.2	1.3	1.4	1.5	1.6	1.7	1.8	1.9	2.0
$\tilde{f}$	1.7736	1.7488	1.7222	1.6943	1.6653	1.6357	1.6055	1.5750	1.5444	1.5138

With the change in the method of numerical integration, we obtained another series of price $\tilde{f}$. From Table 2, we can intuitively observe that the prices of option changed little, and some were the same in both tables. There existed a round-off error among computer calculations, the methodical errors of the two numerical methods were small enough to be ignored. Calculating $\left|\tilde{f} - f\right|$ then generated Figure 1.

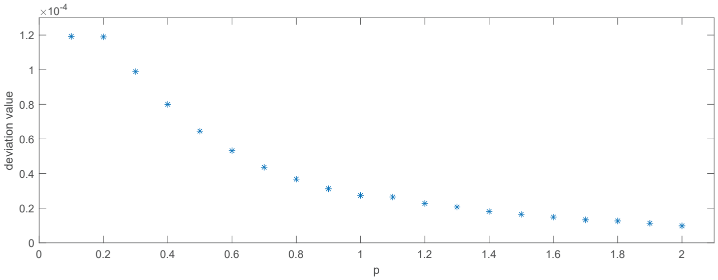

Figure 1. The deviation value of prices $\left|\tilde{f} - f\right|$ between two formulas with different p.

As is shown in Figure 1, most of the deviation values of prices were smaller than 10^{-4} and becoming smaller. The values of f in the table were saved as four-digit decimals, so the change in the numerical integration formula made little difference.

Remark 3. *Though the compound Simpson formula has better algebraic precision, the application of the compound trapezoid formula is more appropriate because of the shorter computing time and it being easy for code writing.*

Now, we discuss the European currency option price with a constant p and different K, considering that K in $[3.5, 5.5]$ and $p = 0.9, 1.1, 1.9$. With the comparison of the two numerical methods above, we used the compound trapezoid formula to calculate numerical integration and obtain f. Then, we could generate Figure 2.

As is illustrated in Figure 2, for different p, price f was a decreasing function of K, and its decrease was nonlinear. Such a conclusion could also be obtained by observing the structure of Function (17). While K increased, the values of $(Z_T - K)^+$ and $(1 - K/Z_T)^+$ decreased or were equal to 0.

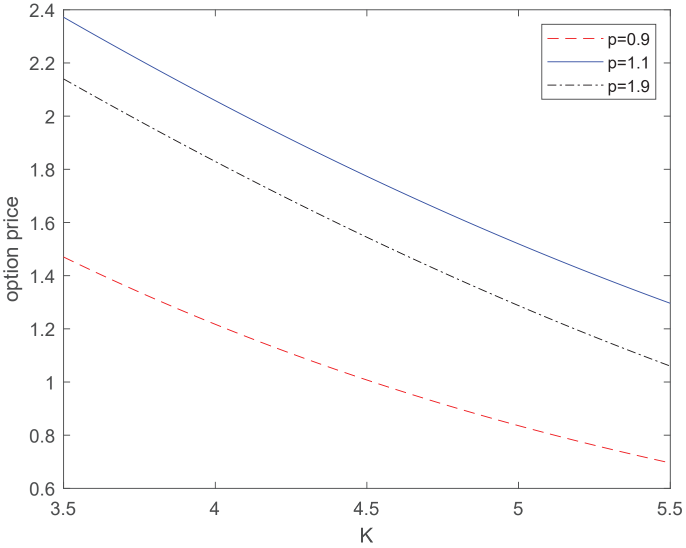

Figure 2. The price of the option with different K in $[3.5, 5.5]$ while p is constant.

Remark 4. *The price of European currency option f in this paper was a decreasing function of K, while other parameters were constant, which is similar to the result in Liu et al. [28] for UDEs.*

Now, we discuss the European currency option price with $p = 1.9$ and $K = 4.5$, considering the variation of the price while u and v changed in $[0.02, 0.07]$. With the comparison of the two numerical methods above, we used the compound trapezoid formula to calculate numerical integration and obtain f. Then, we could generate Figure 3.

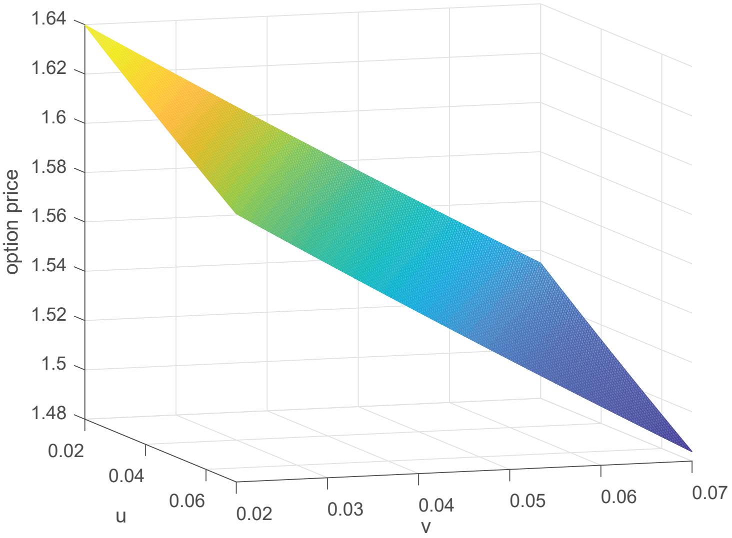

Figure 3. The price of the option with different u, v in $[3.5, 5.5]$ while $p = 1.9, K = 4.5$.

As is shown in Figure 3, price f was a decreasing function of both u and v. In Function (17), taking derivatives in u and v, the decrease was nonlinear. In addition, as u and v increased simultaneously, the value of price f decreased.

Remark 5. *The price of European currency option f in this paper was a decreasing function of both u and v, while other parameters were constant, which is similar to the result in Liu et al. [28] for UDEs.*

5.2. American Currency Option Pricing

Example 2. *We assumed that uncertain fractional currency Model* (13) *had $u = 6\%$, $v = 3\%$, $e = 0.05$, $\sigma = 0.3$, and the initial exchange rate $Z_0 = 4.2$, $p \in (0, 2)$, and considered the American currency option with expiration date $T = 2$ and striking price $K = 4.5$.*

In this numerical example, similar to the previous example, the two currencies were RMB and SGD, and the initial exchange rate Z_0 was changed a little. These two currencies and the financial markets in both countries were considered to be stable enough, so the parameters in the example were reasonable. As in the previous example, $z_1 = 0.7861$ represents the derivative of the exchange rate at $t = 0$.

Due to the particularity of the American currency option whose price is influenced by the maximal $Z_s, s \in [0, T]$, we viewed Z_s as a discrete instead of a continuous case. It could also be reasonable to set the interval to be small enough and reduce the computing time. To solve the problem in this example, we divided the whole time T into 100 equal intervals. Hence, our work turned to calculating the maximum of these 100 values to obtain American currency option price f.

Similar to the previous example, we used the compound trapezoid and Simpson formulas whose interval values were both 0.001 to compute the integral of α over $(0, 1)$. We first used the compound trapezoid formula to calculate American currency option price f; results are shown in Table 3.

Table 3. Price of the American option with different p (compound trapezoid formula).

p	0.1	0.2	0.3	0.4	0.5	0.6	0.7	0.8	0.9	1.0
f	0.7090	0.8147	0.8900	0.9420	0.9765	0.9977	1.0086	1.0113	1.0075	0.9986
p	1.1	1.2	1.3	1.4	1.5	1.6	1.7	1.8	1.9	2.0
f	1.7737	1.7489	1.7223	1.6947	1.6665	1.6380	1.6094	1.5810	1.5529	1.5253

As is shown in Table 3, the price of the American currency option increased with the increase in p in $(0, 0.8]$, and decreased with the increase in p in $(0.8, 1]$ and $(1.1, 2]$. The price jumped when p changed from 1.0 to 1.1 because of the initial value of $Z'(0)$, similar to the price function of the European currency option. Such a jump is similar to that in the results obtained by Lu [26]. Obviously, different initial values may cause different values of price f.

Meanwhile, the value of prices were the same as that of the European currency option when $p \leq 1$. That is to say, with the setting of $u = 6\%$, $v = 3\%$, $e = 0.05$, $\sigma = 0.3$, $p \leq 1$, and initial exchange rate $Z_0 = 4.2$, American currency option price f was an increasing function of time s.

Now, we change the method of numerical integration. With the use of the compound Simpson formula, we obtained the American currency option price f in Table 4.

Table 4. Price of the American option with different p (compound Simpson formula).

p	0.1	0.2	0.3	0.4	0.5	0.6	0.7	0.8	0.9	1.0
f	0.7089	0.8146	0.8899	0.9419	0.9765	0.9977	1.0085	1.0112	1.0075	0.9985
p	1.1	1.2	1.3	1.4	1.5	1.6	1.7	1.8	1.9	2.0
f	1.7736	1.7488	1.7223	1.6947	1.6665	1.6379	1.6094	1.5810	1.5529	1.5253

With the change in the method of numerical integration, we obtain another series of price $\tilde{f}$. From Table 4, we can intuitively observe that the prices of option changed little, and some were the same in the two tables. Similar to the previous part, we calculated $|\tilde{f} - f|$ and generated Figure 4.

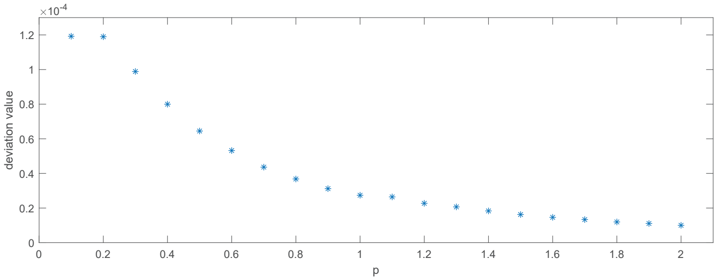

Figure 4. The deviation value of prices $|\tilde{f} - f|$ between two formulas with different p.

As is shown in Figure 4, most of the deviation values of prices were smaller than 10^{-4} and becoming smaller. For the same reason, we still chose the compound trapezoid formula instead of the compound Simpson formula.

Remark 6. *Similar to Remark 3, though the compound Simpson formula has better algebraic precision, the application of the compound trapezoid formula is more appropriate because of the shorter computing time and it being easy for code writing.*

Now, we discuss the American currency option price with a constant p and different K, considering that K was $[3.5, 5.5]$ and $p = 0.9, 1.1, 1.9$. With the comparison of two numerical methods above, we used the compound trapezoid formula to calculate the numerical integration and obtain f. Then, we could generate Figure 5.

As is illustrated in Figure 5, for the different p, price f was a decreasing function of K, and its decrease was nonlinear. Such a conclusion could also be obtained by observing the structure of Function (20). While K increased, the values of $\sup_{0 \le s \le T} \exp(-us)(Z_s - K)^+$ and $\sup_{0 \le s \le T} Z_0 \exp(-vs)(1 - K/Z_s)^+$ decreased or were equal to 0.

Remark 7. *Similar to Remark 4, the price of American currency option f in this paper was a decreasing function of K, while other parameters were constant, which is similar to the result in Liu et al. [28] for UDEs.*

Now, we discuss the American currency option price with $p = 1.9$ and $K = 4.5$, considering variation in the price while u and v were changed in $[0.02, 0.07]$. With the comparison of the two numerical methods above, we used the compound trapezoid formula to calculate the numerical integration and obtain f. Then, we could generate Figure 6.

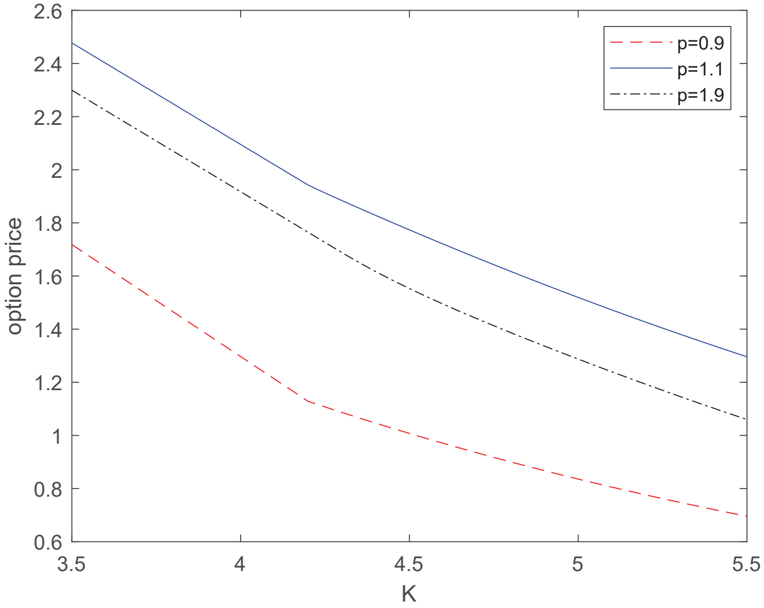

Figure 5. Price of the option with different K in $[3.5, 5.5]$ while p is constant.

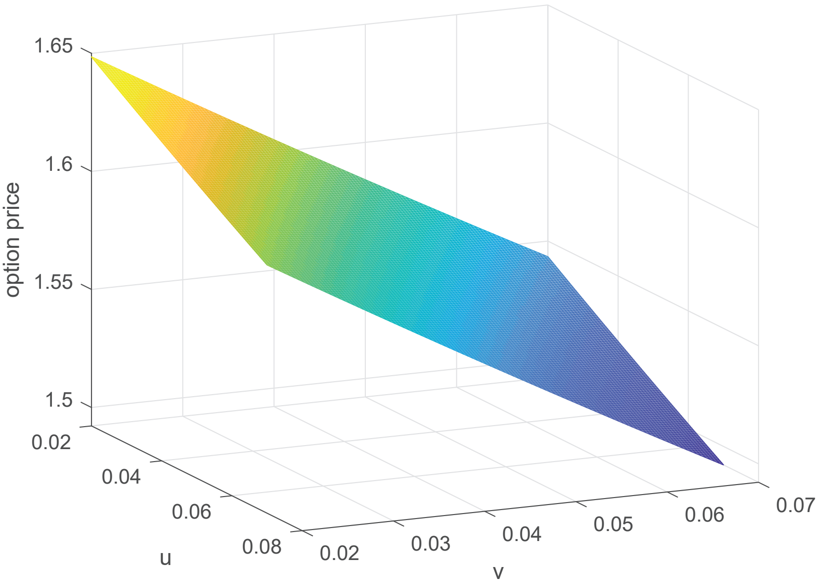

Figure 6. The price of the option with different u, v in $[3.5, 5.5]$ while $p = 1.9, K = 4.5$.

As is shown in Figure 6, price f was a decreasing function of both u and v. In Function (20), taking derivatives in u and v, the decrease was nonlinear. In addition, as u and v increased simultaneously, the value of price f decreased.

Remark 8. *The price of American currency option f in this paper was a decreasing function of both u and v, while other parameters were constant, which is similar to the result in Liu et al. [28] for UDEs.*

6. Conclusions

In this paper, two option pricing formulas were given that use the Mittag-Leffler function to solve fractional differential equations in the Caputo sense. Moreover, the exchange rate of two currencies Z_t is driven by geometric Liu process. An uncertain fractional currency model was presented, and the option pricing formulas were proposed. Both option prices (European and American currency options) of that model had the same monotonicity as that in previous works that price f (for both the European and American currency options) was a decreasing function of exercise price K and interest rates u and v. Lastly, two given numerical examples illustrated the prices of the currency options under different $p(p \in (0, 2])$. Future work could modify the price function with the parameters of log-drift e and log-diffusion σ, and examine the relationship between the price jump and its decrease while some parameters are constant. Moreover, the interpretations for the decrease in mathematical and practical meaning in real life can be another future direction.

Author Contributions: Conceptualization, T.J.; Data curation, Q.L.; Formal analysis, Q.L.; Funding acquisition, M.Z. and D.J.; Investigation, F.L.; and D.J.; Methodology, T.J.; Project administration, M.Z.; Resources, T.J., M.Z. and D.J.; Software, Q.L. and C.T.; Supervision, T.J.; Validation, C.T.; Writing—original draft, Q.L.; Writing—review & editing, F.L. All authors have read and agreed to the published version of the manuscript.

Funding: This research was funded by the National Natural Science Foundation of China grant number no.12071219 and the Natural Science Foundation of Jiangsu Province grant number no. BK20210605. This work is also supported by the Academic Program Development of Jiangsu Higher Education Institutions (PAPD), the General Research Projects of Philosophy and Social Sciences in Colleges and Universities (2022SJYB0140), the Jiangsu Province Student Innovation Training Program (202110298040Z and 202210298050Z), and Postgraduate Research & Practice Innovation Program of Jiangsu Province (SJCX22_0311).

Institutional Review Board Statement: Not applicable.

Informed Consent Statement: Not applicable.

Data Availability Statement: Data sharing is not applicable to this article as no datasets were generated or analyzed during the current study.

Conflicts of Interest: The authors declare no conflict of interest.

References

1. Soleymani, F.; Itkin, A. Pricing foreign exchange options under stochastic volatility and interest rates using an RBF–FD method. *J. Comput. Sci.* **2019**, *37*, 101028. [CrossRef]
2. Alvise, D.; Alessandro, G.; Martino, G. Smiles all around: FX joint calibration in a multi-Heston model. *J. Bank. Financ.* **2013**, *37*, 3799–3818. [CrossRef]
3. Tversky, K. Prospect Theory: An Analysis of Decision under Risk. *Econometrica* **1979**, *47*, 163–291.
4. Liu, B. *Uncertainty Theory*; Springer: Berlin/Heidelberg, Germany, 2007.
5. Liu, B. *Uncertainty Theory: A Branch of Mathmatics for Modeling Human Uncertainty*; Springer: Berlin/Heidelberg, Germany, 2011.
6. Liu, B. Some research problems in uncertainty theory. *J. Uncertain Syst.* **2009**, *3*, 3–10.
7. Liu, B. Fuzzy Process, Hybrid Process and Uncertain Process. *J. Uncertain Syst.* **2008**, *2*, 3–16.
8. Chen, X.; Liu, B. Existence and uniqueness theorem for uncertain differential equations. *Fuzzy Optim. Decis. Mak.* **2010**, *9*, 69–81. [CrossRef]
9. Gao, Y. Existence and Uniqueness Theorem on Uncertain Differential Equations with Local Lipschitz Condition. *J. Uncertain Syst.* **2012**, *6*, 223–232.
10. Yao, K.; Chen, X. A numerical method for solving uncertain differential equations. *J. Intell. Fuzzy Syst.* **2013**, *25*, 825–832. [CrossRef]
11. Chen, X. American option pricing formula for uncertain financial market. In Proceedings of the First International Conference on Uncertainty Theory, Berlin, Germany, 22–23 November 2010.
12. Peng, J.; Yao, K. A new option pricing model for stocks in uncertainty markets. *Int. J. Oper. Res.* **2010**, *7*, 213–224.

13. Gao, R.; Liu, K.; Li, Z.; Lv, R. American Barrier Option Pricing Formulas for Stock Model in Uncertain Environment. *IEEE Access* **2019**, *7*, 97846–97856. doi: [CrossRef]
14. Chang, J.; Sun, L.; Zhang, B.; Peng, J. Multi-period portfolio selection with mental accounts and realistic constraints based on uncertainty theory. *J. Comput. Appl. Math.* **2020**, *377*, 112892. doi: [CrossRef]
15. Chen, X.; Gao, J. Uncertain term structure model of interest rate. *Soft Comput.* **2013**, *17*, 597–604. [CrossRef]
16. Liu, B. Extreme value theorems of uncertain process with application to insurance risk models. *Soft Comput.* **2013**, *17*, 549–556. [CrossRef]
17. Lakshmikantham, V.; Vatsala, A. Theory of fractional differential equations. *Nonlinear Anal.* **2008**, *69*, 2677–2782. [CrossRef]
18. Lakshmikantham, V.; Devi, J. Theory of fractional differential equations in Banach space. *Nonlinear Anal.* **2008**, *1*, 38–45.
19. Belmekki, M.; Nieto, J.; Rodríguez-López, R. Existence of Periodic Solution for a Nonlinear Fractional Differential Equation. *Bound. Value Probl.* **2009**, *2009*, 324561. [CrossRef]
20. Kosmatov, N. Integral equations and initial value problems for nonlinear differential equations of fractional order. *Nonlinear Anal. Theory Methods Appl.* **2019**, *70*, 2521–2529. [CrossRef]
21. Zhang, S. Monotone iterative method for initial value problem involving Riemann–Liouville fractional derivatives. *Nonlinear Anal. Theory Methods Appl.* **2009**, *71*, 2087–2093. [CrossRef]
22. Zhu, Y. Uncertain fractional differential equations and an interest rate model. *Math. Methods Appl. Sci.* **2015**, *38*, 3359–3368. [CrossRef]
23. Zhu, Y. Existence and uniqueness of the solution to uncertain fractional differential equation. *Uncertain. Anal. Appl.* **2015**, *3*, 5. [CrossRef]
24. Jin, T.; Sun, Y.; Zhu, Y. Extreme values for solution to uncertain fractional differential equation and application to American option pricing model. *Phys. A Stat. Mech. Its Appl.* **2019**, *534*, 122357. [CrossRef]
25. Lu, Z.; Zhu, Y.; Li, B. Critical value-based Asian option pricing model for uncertain financial markets. *Phys. A Stat. Mech. Its Appl.* **2019**, *525*, 694–703. doi: [CrossRef]
26. Lu, Z.; Yan, H.; Zhu, Y. European option pricing model based on uncertain frational differential equation. *Fuzzy Optim. Decis. Mak.* **2019**, *18*, 199–217. [CrossRef]
27. Lu, Z.; Zhu, Y. Numerical approach for solution to an uncertain fractional differential equation. *Appl. Math. Comput.* **2019**, *343*, 137–148. [CrossRef]
28. Liu, Y.; Chen, X.; Ralescu, D. Uncertain Currency Model and Currency Option Pricing. *Int. J. Intell. Syst.* **2015**, *30*, 40–51. [CrossRef]
29. Diethelm, K.; Ford, N.; Freed, A. A Predictor-Corrector Approach for the Numerical Solution of Fractional Differential Equations. *Nonlinear Dyn.* **2002**, *29*, 3–22. [CrossRef]

fractal and fractional

MDPI

Article

A New Homotopy Transformation Method for Solving the Fuzzy Fractional Black–Scholes European Option Pricing Equations under the Concept of Granular Differentiability

Jianke Zhang [1,2,*], Yueyue Wang [2,3] and Sumei Zhang [1]

[1] School of Science, Xi'an University of Posts and Telecommunications, Xi'an 710121, China; zhanggsumei@163.com
[2] Shaanxi Key Laboratory of Network Data Analysis and Intelligent Processing, Xi'an University of Posts and Telecommunications, Xi'an 710121, China; wyy0480@163.com
[3] Industry School of Modern Post, Xi'an University of Posts and Telecommunications, Xi'an 710121, China
* Correspondence: jiankezhang@xupt.edu.cn

Abstract: The Black–Scholes option pricing model is one of the most significant achievements in modern investment science. However, many factors are constantly fluctuating in the actual financial market option pricing, such as risk-free interest rate, stock price, option underlying price, and security price volatility may be inaccurate in the real world. Therefore, it is of great practical significance to study the fractional fuzzy option pricing model. In this paper, we proposed a reliable approximation method, the Elzaki transform homotopy perturbation method (ETHPM) based on granular differentiability, to solve the fuzzy time-fractional Black–Scholes European option pricing equations. Firstly, the fuzzy function is converted to a real number function based on the horizontal membership function (HMF). Secondly, the specific steps of the ETHPM are given to solve the fuzzy time-fractional Black–Scholes European option pricing equations. Finally, some examples demonstrate that the new approach is simple, efficient, and accurate. In addition, the fuzzy approximation solutions have been visualized at the end of this paper.

Keywords: homotopy perturbation method; Elaki transform; fractional Black–Scholes equation; granular differentiability

Citation: Zhang, J.; Wang, Y.; Zhang, S. A New Homotopy Transformation Method for Solving the Fuzzy Fractional Black–Scholes European Option Pricing Equations under the Concept of Granular Differentiability. *Fractal Fract.* **2022**, *6*, 286. https://doi.org/10.3390/fractalfract6060286

Academic Editor: Leung Lung Chan

Received: 7 April 2022
Accepted: 24 May 2022
Published: 26 May 2022

1. Introduction

Option pricing is a major subject in financial investing and a significant component of contemporary financial theory research. Not only has the development of option pricing theory facilitated financial derivative innovation, but also the flow and growth of financial markets. How to reasonably price options is a serious problem facing investors during the forming and developing of international derivative financial markets. The Black–Scholes model [1] is one of the most influential mathematical models in the financial sector. In 1973, Fisher Black and Myron Scholes established an option pricing model by using non-arbitrage pricing theory. Soon after, the Chicago Board Options Exchange applied the Black–Scholes model into practical problems by programing it with computer. Their study results laid new foundation for option pricing theory and also gave significant instructions on the application and management of financial derivative instruments, for which they received th Nobel Memorial Prize in Economic Sciences in 1997. By using computers and advanced communication technology, it is possible to express complex option pricing equation in a function.

The Black–Scholes equation is a partial differential equation depicting options' price changes. However, this model needs to be improved due to the huge differences between its ideal hypothesis and the actual financial markets [2–4]. In the perspective of mathematics, a fractional Black–Scholes equation is more accurate than an integer order equation to reflect the middle process of price changes. In finance, some researchers believe that asset prices have long-term relativity [5], which indicates that the price of an item at a specific point is related to both the present price and the price from a long time ago. Decision makers can make decisions based on past market experiences [6]. A fractional Black–Scholes equation can depict the long-term relativity in behavioral finance [7,8]. In recent decades, fractional derivatives have drawn the attention of mathematicians and physicists [9]. Fractional derivatives have over 20 different kinds of definitions, including the most commonly used ones, such as Riemann–Liouville's, Caputo's, Jumare's, Conformable's, etc. The theories of fractional calculus have been widely studied and applied in many fields, including economics, sociology, computer science, biology, material science, etc. [10]. Many scholars applied the fractional calculus model to the modeling of natural phenomenon. Fractional calculus has its own characteristics, such as memorizing and inheriting. Therefore, fractional calculus equations are highly suitable for describing complex systems with heredity and memorization features. Examples include the anthrax disease model in animals [11], the mathematical model for COVID-19 transmission [12,13], the fractional-order epidemic model for childhood diseases [14] and hearing loss in children caused by the mumps virus model [15]. However, it is extremely difficult to find the accurate result of fractional differential equations (FDE). Thus, people turned to approximate analytical solutions for solving FDE. Therefore, some approximation methods have been applied to solve FDE.

The uncertain factors in the actual financial market are inevitable, while fuzzy analysis can draw the uncertain phenomenon into an algorithmic system. In reality, massive problems provide uncertainties from different angles. Integrating the fuzzy phenomenon into FDE can result in fuzzy FDE. This kind of mixed equation can describe option pricing models under the uncertain circumstances of financial markets. The following are the study results of solving fuzzy derivative equations: Puri and Ralescu introduced Hukuhara differentiability (H-differentiability) of fuzzy functions in 1983; Bede and Stefanini came up with general Hukuhara differentiability (gH-differentiability) of fuzzy functions in 2013. Moreover, FDE would lead to two different geometric-meaning types of solutions under this differentiability. Mazandarani and others [16–18] introduced how to gain fuzzy-number derivatives by using granular differentiability (gr-differentiability) and horizontal membership function and how to solve fuzzy differential equations in 2018. In the research of fuzzy differential equations, gr-differentiability has the following advantages [18]:

1. An FDE has only one solution so as to avoid the multiplicity of solutions drawback.
2. It avoids the doubling property problem for solving each FDE, which means solving just one individual differential equation.
3. This method does not lead to the unnatural behavior in modeling (UBM) phenomenon.

The Homotopy Perturbation Method (HPM) [19] is a new type of asymptotic numerical algorithm developed with the foundation of artificial parameter perturbation method in recent years. HPM, which combines homotopy theory and the perturbation method, is proposed by He [20]. Because homotopy perturbation is utilized to solve nonlinear differential equations and integral equations, it is considered to be very accurate and not overly difficult to calculate. Currently, HPM has been widely applied in solving all kinds of fractional partial differential equations and fractional integral equations [21–26]. The main character of fractional derivatives is their non-limitation. Relatively, the numerical simulation process of fractional equations has a massive amount of calculations. However, the computational efficiency of the option pricing model has an impact on the actual application effect, and a longer calculation time will lead to the deviation of option pricing results [27]. We added fractional Elzaki transformation, an advanced Laplace and Sumudu transform, into the HPM algorithm, then combined HPM and Elzaki transform together [28–30]. This approach makes the calculation more uncomplicated and more efficient.

Actual option pricing is affected by the following factors, such as the risk preference of investors, the market environment, and regional economic policies [31]. Due to the uncertainty of these factors, we describe these factors by using fuzzy information, while some use random information. The fuzzy options could better consider the above uncertain factors at a comprehensive level to improve option pricing accuracy. Thus, studying fuzzy option pricing is meaningful.

The remainder of this article is laid out as follows: In Section 2, some fundamental definitions involved in fractional derivatives and fuzzy differentiation are introduced. In Section 3, the ETHPM steps are presented. In Section 4, some examples are provided to illustrate the application results. In Section 5, the conclusion of our research is presented.

2. Preliminaries

This section presents some necessary definitions and theorems that will be used later. Throughout this paper, the set of all real numbers is denoted by $\mathbb{R}$, the set of complex numbers is denoted by $\mathbb{C}$, and the set of all the fuzzy numbers on $\mathbb{R}$ by $\mathbb{E}$.

Definition 1 ([32]). *A real function $f(x)$, $x > 0$, is said to be in the space C_μ, $\mu \in \mathbb{R}$ if there exists a real number $p > \mu$, such that $f(x) = x^p h(x)$, where $h(x) \in [0, \infty)$ and it is said to be in space C_μ^m if $f^{(m)} \in C_\mu$, $m \in N$.*

Definition 2 ([32]). *The Riemann–Liouville fractional integral operator of order $\alpha > 0$, of a function $f \in C_m$, is defined as*

$$J^\alpha f(t) = \begin{cases} \frac{1}{\Gamma(\alpha)} \int_0^t \frac{f(s)}{(t-s)^{1-\alpha}} ds = \frac{1}{\Gamma(\alpha)} t^{\alpha-1} * f(t) & \alpha > 0, t > 0, \\ f(t) & \alpha = 0, \end{cases} \tag{1}$$

where $t^{\alpha-1} * f(t)$ is the convolution product of $t^{\alpha-1}$ and $f(t)$.

For the Riemann–Liouville fractional integral, we have

1. $J^\alpha t^\beta = \frac{\Gamma(\beta+1)}{\Gamma(\beta+\alpha+1)} t^{\alpha+\beta}, \beta > -1,$
2. $J^\alpha(\lambda f(t) + \mu g(t)) = \lambda J^\alpha f(t) + \mu J^\alpha g(t),$

where λ and μ are real constants.

This paper utilizes the Caputo derivative condition, which is defined as follows.

Definition 3 ([33,34]). *Let $f(t) : [0, +\infty) \to \mathbb{R}$ be a function, and n be the upper positive integer of $\alpha(\alpha > 0)$. The Caputo fractional derivative is defined by*

$$D^\alpha f(t) = \frac{1}{\Gamma(n-\alpha)} \int_0^t \frac{f^{(n)}(s)}{(t-s)^{\alpha+1-n}} ds, \\ n-1 < \alpha \le n, n \in N. \tag{2}$$

For the Caputo derivative, we have

1. $D^\alpha J^\alpha f(t) = f(t),$
2. $J^\alpha D^\alpha f(t) = f(t) - \sum_{i=0}^{n-1} y^{(i)}(0) \frac{t^i}{i!},$
3. $D^\alpha t^\beta = \begin{cases} \frac{\Gamma(\beta+1)}{\Gamma(\beta+1-\alpha)} t^{\beta-\alpha} & \beta \ge \alpha \\ 0 & \beta < \alpha \end{cases},$
4. $D^\alpha c = 0,$
5. $D^\alpha(\lambda f(t) + \mu g(t)) = \lambda D^\alpha f(t) + \mu D^\alpha g(t),$

where λ, μ and c are real constants.

The derivative of conformable fractional derivative is defined as follows.

Definition 4 ([35])**.** *Given a function $f : [0, \infty) \to \mathbb{R}$. Then the conformable derivative of f order $\alpha \in (0, 1]$ is defined by*

$$
{}^{CF}D_*^{\alpha}(f)(t) = \lim_{\varepsilon \to 0} \frac{f\left(t + \varepsilon t^{1-\alpha}\right) - f(t)}{\varepsilon}, \tag{3}
$$

for all $t > 0$.

Definition 5 ([35,36])**.** *Let f be n-times differentiable at t. Then the conformable derivative of f order α is defined as*

$$
{}^{CF}D_*^{\alpha}(f(t)) = \lim_{\varepsilon \to 0} \frac{f^{(\lceil \alpha \rceil - 1)}\left(t + \varepsilon t^{(\lceil \alpha \rceil - \alpha)}\right) - f^{(\lceil \alpha \rceil - 1)}(t)}{\varepsilon}, \tag{4}
$$

for all $t > 0$, $\alpha \in (n, n+1]$. Here $\lceil \alpha \rceil$ is the smallest integer greater than or equal to α.

Theorem 1 ([35])**.** *Let f be n-times differentiable at t. Then*

$$
{}^{CF}D_*^{\alpha}(f(t)) = t^{\lceil \alpha \rceil - \alpha} f^{\lceil \alpha \rceil}(t), \tag{5}
$$

for all $t > 0, \alpha \in (n, n+1]$.

Definition 6 ([37])**.** *The single parameter and the two parameters variants of the Mittag–Leffler function are denoted by $E_\alpha(t)$ and $E_{\alpha,\beta}(t)$, respectively, which are relevant for their connection with fractional calculus, and are defined as*

$$
E_\alpha(t) = \sum_{j=0}^{\infty} \frac{t^j}{\Gamma(\alpha j + 1)}, \ \alpha > 0, \ t \in \mathbb{C}, \tag{6}
$$

$$
E_{\alpha,\beta}(t) = \sum_{j=0}^{\infty} \frac{t^j}{\Gamma(\alpha j + \beta)}, \ \alpha, \beta > 0, \ t \in \mathbb{C}. \tag{7}
$$

Based on the HMF, Mazandarani proposed the concepts of relative distance measure (RDM) and granular differentiability.

Definition 7 ([16,17])**.** *For a fuzzy number $\widetilde{u} : [a, b] \to [0, 1]$ with parametric form $[u]^\mu = [\underline{u}^\mu, \ \bar{u}^\mu]$, $\underline{u}^\mu$ is a bounded non-decreasing left continuous function in (0,1], and it is right continuous at $\mu = 0$, $\bar{u}^\mu$ is a bounded non-increasing left continuous function in (0,1], and it is right continuous at $\mu = 0$, $\underline{u}^\mu \leq \bar{u}^\mu$. The HMF $u^{\mathrm{gr}} : [0, 1] \times [0, 1] \to [a, b]$ with $x = u^{\mathrm{gr}}(\mu, \alpha_u) = \underline{u}^\mu + (\bar{u}^\mu - \underline{u}^\mu)\alpha_u$ stands for the granule of information included in $x \in [a, b]$, $\mu \in [0, 1]$ is the membership degree of x in $\widetilde{u}(x)$, $\alpha_u \in [0, 1]$ is called RDM.*

Note 1 [16,17]. We can also denote the HMF of $\widetilde{u} \in \mathbb{E}$ by $\mathcal{H}(\widetilde{u}) \triangleq u^{\mathrm{gr}}(\mu, \alpha_u)$, In particular, if $\widetilde{u} = (a, b, c)$, $a \leq b \leq c$ is a triangular fuzzy number, then the HMF of $\widetilde{u}$ is $\mathcal{H}(\widetilde{u}) = a + (b - a)\mu + (1 - \mu)(c - a)\alpha_u$.
Note 2 [16]. The μ -level sets of $\widetilde{u} \in \mathbb{E}$ which are the span of the information granule can be obtained by using

$$
\mathcal{H}^{-1}(u^{gr}(\mu, \alpha_u)) = [\widetilde{u}]^\mu = \left[\inf_{\beta \geq \mu} \min_{\alpha_u} u^{gr}(\beta, \alpha_u), \sup_{\beta \geq \mu} \max_{\alpha_u} u^{gr}(\beta, \alpha_u) \right]. \tag{8}
$$

In Figure 1, the picture shows the triangular fuzzy number $\widetilde{u} = (1, 2, 9)$.

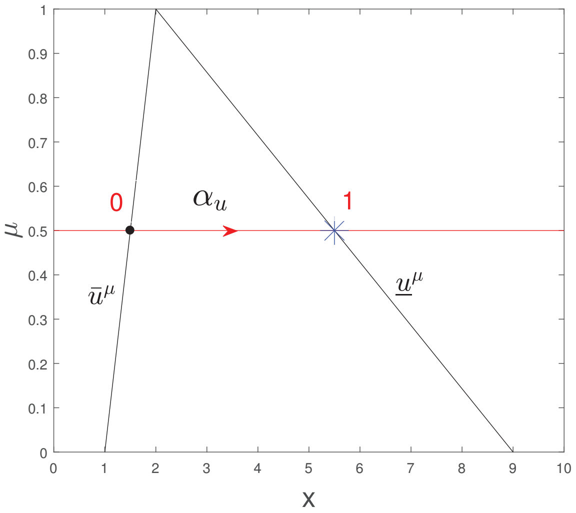

Figure 1. The fuzzy number $\widetilde{u} = (1, 2, 9)$.

Definition 8 ([16])**.** *The fuzzy-valued function* $\widetilde{f} : [a, b] \to \mathbb{E}$ *is said to be granular differentiable (gr-differentiable for short) at a point* $t_0 \in [a, b]$ *if there exists an element* $\frac{d^{gr}\widetilde{f}(t_0)}{dt} \in \mathbb{E}$ *such that the following limit*

$$\lim_{\Delta t \to 0} \frac{\widetilde{f}(t_0 + \Delta t) \ominus^{\mathrm{gr}} \widetilde{f}(t_0)}{\Delta t} = \frac{d^{gr}\widetilde{f}(t_0)}{dt}, \tag{9}$$

exists for Δt *sufficiently near 0.* $\frac{d^{gr}\widetilde{f}(t_0)}{dt}$ *is called gr-derivative of fuzzy-valued function* $\widetilde{f}$ *at the point* t_0*. If the gr-derivative exists for all points* $t \in [a, b] \subseteq \mathbb{R}$*, we say that* $\widetilde{f}$ *is gr-differentiable on* $[a, b] \subseteq \mathbb{R}$*. We use* $C^1(U, \mathbb{E})$ *to denote the space of all continuously gr-differentiable fuzzy-valued functions on* $U \subseteq \mathbb{R}$*.*

Theorem 2 ([16])**.** *The fuzzy function* $\widetilde{f} : [a, b] \subseteq \mathbb{R} \to \mathbb{E}$ *is gr-differentiable at the point* $t \in [a, b]$ *if and only if its HMF is differentiable with respect to* t *at that point. Moreover,*

$$\mathcal{H}\left(\frac{d\widetilde{f}(t)}{dt}\right) = \frac{\partial f^{gr}\left(t, \mu, \alpha_f\right)}{\partial t}. \tag{10}$$

The definition and properties of the Elzaki transform are as follows.

Definition 9 ([29])**.** *Elzaki transform, a new transform, defining for function of exponential order we consider functions in the set* A*, defined by*

$$A = f(t) : \exists M,\ k_1,\ k_2 > 0,\ |f(t)| < Me^{\frac{|t|}{k_j}},\ if\ t \in (-1)^j \times [0, \infty). \tag{11}$$

For a given function in the set, the constant G must be finite number, k_1, k_2 may be finite or infinite. The Elzaki transform which is defined by the integral equation.

$$E[f(t)] = T(v) = v \int_0^\infty f(t) e^{\frac{-t}{v}}\, dt,\ t \geq 0,\ k_1 \leq v \leq k_2. \tag{12}$$

The following results can be obtained from the definition and simple calculations.

1. $E[t^n] = n!v^{n+2}$,
2. $E[f'(t)] = \frac{T(v)}{v} - vf(0)$,
3. $E[f''(t)] = \frac{T(v)}{v^2} - f(0) - vf'(0)$,
4. $E[f^{(n)}(t)] = \frac{T(v)}{v^n} - \sum_{k=0}^{n-1} v^{2-n+k} f^{(k)}(0)$,
5. $E[t^\alpha] = \int_0^\infty e^{-vt} t^\alpha dt = v^{\alpha+1}\Gamma(\alpha+1),\ \mathbb{R}(\alpha) > 0$.

Theorem 3 ([30]). *If $T(v)$ is Elzaki transform of $f(t)$, one can consider the following Elzaki transform of the Riemann–Liouville derivative*

$$E[D^\alpha f(t)] = v^{-\alpha}[T(v) - \sum_{k=1}^{n} v^{\alpha-k+2}[D^{\alpha-k} f(0)]],\ -1 < n-1 \le \alpha < n. \tag{13}$$

Definition 10 ([30]). *The Elzaki transform of the Caputo fractional derivative by using Theorem 3 is defined as follows*

$$E[D^\alpha f(t)] = v^{-\alpha} E[f(t)] - \sum_{k=0}^{m-1} v^{2-\alpha+k} f^{(k)}(0), \tag{14}$$

where $m-1 < \alpha < m$.

3. Elzaki Transform Homotopy Perturbation Method (ETHPM)

Consider the following fractional differential equations to explain the core steps of this method

$$D_t^\alpha \widetilde{u}(x,t) = \mathcal{L}(\widetilde{u}(x,t)) + \mathcal{N}(\widetilde{u}(x,t)) + \widetilde{f}(x,t), \tag{15}$$

with initial condition

$$D_t^k \widetilde{u}(x,0) = \widetilde{g}_k, k = 0, \ldots, n-1, \tag{16}$$

where D_t^α is the fractional derivative, $\mathcal{L}$ is a linear operator, $\mathcal{N}$ is a nonlinear differential operator, and $\widetilde{f}$ is a known fuzzy function.

Step 1. By using the HMF for Equation (15), we get

$$D_t^\alpha \mathcal{H}[\widetilde{u}(x,t)] = \mathcal{L}[\mathcal{H}(\widetilde{u}(x,t))] + \mathcal{N}[\mathcal{H}(\widetilde{u}(x,t))] + \mathcal{H}[\widetilde{f}(x,t)], \tag{17}$$

with the initial condition

$$\mathcal{H}[\widetilde{u}(x,0)] = u^{gr}(\mu, \alpha_c, x, 0). \tag{18}$$

Step 2. After using the Elzaki transform of the Equation (17), we obtain

$$E[D_t^\alpha \mathcal{H}[\widetilde{u}(x,t)]] = E\Big[\mathcal{L}[\mathcal{H}(\widetilde{u}(x,t))] + \mathcal{N}[\mathcal{H}(\widetilde{u}(x,t))] + \mathcal{H}[\widetilde{f}(x,t)]\Big]. \tag{19}$$

Applying Equation (14), we obtain

$$E[\mathcal{H}[\widetilde{u}(x,t)]] = v^\alpha E[\mathcal{L}[\mathcal{H}[\widetilde{u}(x,t)]] + \mathcal{N}[\mathcal{H}[\widetilde{u}(x,t)]]] + \mathcal{H}[\widetilde{g}(x,t)]. \tag{20}$$

Step 3. By applying the inverse Elzaki transform for the Equation (20), we get

$$\mathcal{H}[\widetilde{u}(x,t)] = \mathcal{H}[\widetilde{G}(x,t)] + E^{-1}[v^\alpha E[\mathcal{L}[\mathcal{H}[\widetilde{u}(x,t)]] + \mathcal{N}[\mathcal{H}[\widetilde{u}(x,t)]]]], \tag{21}$$

where $\mathcal{H}[\widetilde{G}(x,t)]$ is the result of the integration of the initial condition and the known functions $\mathcal{H}[\widetilde{f}(x,t)]$.

Step 4. Now, we construct the following homotopy equation

$$\mathcal{H}[\widetilde{u}(x,t)] = \sum_{n=0}^{\infty} p^n \mathcal{H}[\widetilde{u}_n(x,t)]. \tag{22}$$

In order to make the calculation of the equation simple, we use the He polynomial

$$\mathcal{N}[\mathcal{H}[\widetilde{u}(x,t)]] = \sum_{n=0}^{\infty} p^n H_n[\mathcal{H}(\widetilde{u})], \tag{23}$$

where $H_n[\mathcal{H}(\widetilde{u})]$ stands for He's polynomial in nature,

$$H_n\mathcal{H}[(\widetilde{u}_0,\widetilde{u}_1,\widetilde{u}_2\ldots\widetilde{u}_n)] = \frac{1}{n!}\frac{\partial^n}{\partial p^n}\left[\mathcal{N}\left(\sum_{i=0}^{\infty} p^i \mathcal{H}[\widetilde{u}_i(x,t)]\right)\right]_{p=0}, n = 0,1,2,\cdots. \tag{24}$$

Equation (21) can be written as

$$\begin{aligned}\sum_{n=0}^{\infty} p^n \mathcal{H}[\widetilde{u}_n(x,t)] = \mathcal{H}[\widetilde{G}(x,t)] + p\left[E^{-1}\left[v^\alpha E\left[\mathcal{L}\left(\sum_{n=0}^{\infty} p^n \mathcal{H}[\widetilde{u}_n(x,t)]\right)\right]\right.\right.\\ \left.\left.+v^\alpha E\left[\mathcal{N}\left(\sum_{n=0}^{\infty} p^n H_n[\mathcal{H}(\widetilde{u})]\right)\right]\right]\right].\end{aligned} \tag{25}$$

Comparing the coefficient of like powers of p, we obtain

$$\begin{aligned}
p^0 &: \mathcal{H}[\widetilde{u}_0(x,t)] = \mathcal{H}[\widetilde{G}(x,t)],\\
p^1 &: \mathcal{H}[\widetilde{u}_1(x,t)] = E^{-1}[v^\alpha E[\mathcal{L}[\mathcal{H}[\widetilde{u}_0(x,t)]] + H_0(\mathcal{H}(\widetilde{u}))]],\\
p^2 &: \mathcal{H}[\widetilde{u}_2(x,t)] = E^{-1}[v^\alpha E[\mathcal{L}[\mathcal{H}[\widetilde{u}_1(x,t)]] + H_1(\mathcal{H}(\widetilde{u}))]],\\
p^3 &: \mathcal{H}[\widetilde{u}_3(x,t)] = E^{-1}[v^\alpha E[\mathcal{L}[\mathcal{H}[\widetilde{u}_2(x,t)]] + H_2(\mathcal{H}(\widetilde{u}))]],\\
&\vdots\\
p^n &: \mathcal{H}[\widetilde{u}_n(x,t)] = E^{-1}[v^\alpha E[\mathcal{L}[\mathcal{H}[\widetilde{u}_{n-1}(x,t)]] + H_{n-1}(\mathcal{H}(\widetilde{u}))]].
\end{aligned} \tag{26}$$

The result is as follows

$$\mathcal{H}[\widetilde{u}(x,t)] = \lim_{p\to 1}\mathcal{H}[\widetilde{u}_n(x,t)] = \mathcal{H}[\widetilde{u}_0(x,t)] + \mathcal{H}[\widetilde{u}_1(x,t)] + \mathcal{H}[\widetilde{u}_2(x,t)] + \cdots. \tag{27}$$

Remark 1. *The value of $|\widetilde{Res}(x,t)|$ describes the difference between the precise solution and approximate solution. Normally, the precise value of $|\widetilde{Res}(x,t)|$ is zero for any $\alpha \in (0,1]$. The definition of $|\widetilde{Res}(x,t)|$ is as follows*

$$\begin{aligned}max|\widetilde{Res}(x,t)| = \max_{\mu\in[0,1],\alpha_c\in[0,1]} |D_t^\alpha[u^{gr}(\mu,\alpha_c,x,t)] - \mathcal{L}[u^{gr}(\mu,\alpha_c,x,t)]\\ -\mathcal{N}[u^{gr}(\mu,\alpha_c,x,t)] - f^{gr}(\mu,\alpha_c,x,t)|.\end{aligned} \tag{28}$$

4. Illustrative Examples

We use the Elzaki transform homotopy perturbation method [38] (ETHPM), homotopy perturbation method [39] (HPM), residual power series method [40] (RPSM) and the conformable fractional Adomian decomposition method [41] (CFADM) respectively to calculate the following three examples. Literature [38–41] mainly studied the problems of the deterministic fractional Black–Scholes equations. We use these methods to recalculate the fuzzy fractional Black–Scholes equation under the concept of granular differentiability.

Example 1. *Consider the fractional Black–Scholes equation*

$$\frac{\partial^{\alpha}\widetilde{u}}{\partial t^{\alpha}}=\frac{\partial^{2}\widetilde{u}}{\partial x^{2}}+(k-1)\frac{\partial\widetilde{u}}{\partial x}-k\widetilde{u}, \tag{29}$$

with the initial condition

$$\widetilde{u}(x,0)=\widetilde{c}\max(e^{x}-1,0), \tag{30}$$

$$\widetilde{c}=(0,1,2). \tag{31}$$

By using the HMF, we have

$$\frac{\partial^{\alpha}\mathcal{H}[\widetilde{u}(x,t)]}{\partial t^{\alpha}}=\frac{\partial^{2}\mathcal{H}[\widetilde{u}(x,t)]}{\partial x^{2}}+(k-1)\frac{\partial\mathcal{H}[\widetilde{u}(x,t)]}{\partial x}-k\mathcal{H}[\widetilde{u}(x,t)], \tag{32}$$

$$\mathcal{H}[\widetilde{u}(x,0)]=[\mu+2(1-\mu)\alpha_{c}]\max(e^{x}-1,0), \tag{33}$$

for each $\mu,\alpha_c\in[0,1]$ and

$$\mathcal{H}[\widetilde{u}(x,t)]=u^{gr}(\mu,\alpha_{c},x,t). \tag{34}$$

Firstly, the ETHPM is used to solving the Example 1.

After using the Elzaki transform for the Equation (30), we get

$$E[\frac{\partial^{\alpha}\mathcal{H}[\widetilde{u}(x,t)]}{\partial t^{\alpha}}]=E[\frac{\partial^{2}\mathcal{H}[\widetilde{u}(x,t)]}{\partial x^{2}}+(k-1)\frac{\partial\mathcal{H}[\widetilde{u}(x,t)]}{\partial x}-k\mathcal{H}[\widetilde{u}(x,t)]]. \tag{35}$$

By using the Elzaki transform's differential property, we obtain

$$\begin{aligned}v^{-\alpha}[E[\mathcal{H}[\widetilde{u}(x,t)]]-v^{2}\mathcal{H}[\widetilde{u}(x,0)]]=E[&\frac{\partial^{2}\mathcal{H}[\widetilde{u}(x,t)]}{\partial x^{2}}\\&+(k-1)\frac{\partial\mathcal{H}[\widetilde{u}(x,t)]}{\partial x}-k\mathcal{H}[\widetilde{u}(x,t)]],\end{aligned} \tag{36}$$

and,

$$\begin{aligned}E[\mathcal{H}[\widetilde{u}(x,t)]]=v^{\alpha}[E[&\frac{\partial^{2}\mathcal{H}[\widetilde{u}(x,t)]}{\partial x^{2}}+(k-1)\frac{\partial\mathcal{H}[\widetilde{u}(x,t)]}{\partial x}\\&-k\mathcal{H}[\widetilde{u}(x,t)]]]+v^{2}\mathcal{H}[\widetilde{u}(x,0)].\end{aligned} \tag{37}$$

By applying the inverse Elzaki transform for the Equation (35), we get

$$\begin{aligned}\mathcal{H}[\widetilde{u}(x,t)]=E^{-1}[v^{\alpha}[E[&\frac{\partial^{2}\mathcal{H}[\widetilde{u}(x,t)]}{\partial x^{2}}+(k-1)\frac{\partial\mathcal{H}[\widetilde{u}(x,t)]}{\partial x}\\&-k\mathcal{H}[\widetilde{u}(x,t)]]]]+\mathcal{H}[\widetilde{u}(x,0)],\end{aligned} \tag{38}$$

$$\sum_{n=0}^{\infty}p^{n}\mathcal{H}[\widetilde{u}_{n}(x,t)]=\mathcal{H}[\widetilde{u}(x,0)]+pE^{-1}\left[v^{\alpha}E[\sum_{n=0}^{\infty}p^{n}\mathcal{H}[\widetilde{\Psi}_{n}(x,t)]]\right], \tag{39}$$

where

$$\mathcal{H}[\widetilde{\Psi}_{n}(x,t)]=\mathcal{H}[\frac{\partial^{2}\widetilde{u}_{n}(x,t)}{\partial x^{2}}+(k-1)\frac{\partial\widetilde{u}_{n}(x,t)}{\partial x}-k\widetilde{u}_{n}(x,t)]. \tag{40}$$

After comparing the similar power coefficients of p, the following results can be obtained

$$\begin{aligned}
p^0 &: \mathcal{H}[\widetilde{u}_0(x,t)] = [\mu + 2(1-\mu)\alpha_c]\max(\mathrm{e}^x - 1, 0),\\
p^1 &: \mathcal{H}[\widetilde{u}_1(x,t)] = E^{-1}\left[v^\alpha E\left[\mathcal{H}\left[\widetilde{\Psi}_0(x,t)\right]\right]\right]\\
&= [\mu + 2(1-\mu)\alpha_c][-\frac{(-kt^\alpha)}{\Gamma(\alpha+1)}\max(\mathrm{e}^x, 0)\\
&+ \frac{(-kt^\alpha)}{\Gamma(\alpha+1)}\max(\mathrm{e}^x - 1, 0)],\\
p^2 &: \mathcal{H}[\widetilde{u}_2(x,t)] = E^{-1}\left[v^\alpha E\left[\mathcal{H}\left[\widetilde{\Psi}_1(x,t)\right]\right]\right]\\
&= [\mu + 2(1-\mu)\alpha_c][-\frac{(-kt^\alpha)^2}{\Gamma(2\alpha+1)}\max(\mathrm{e}^x, 0)\\
&+ \frac{(-kt^\alpha)^2}{\Gamma(2\alpha+1)}\max(\mathrm{e}^x - 1, 0)],\\
&\vdots\\
p^n &: \mathcal{H}[\widetilde{u}_n(x,t)] = E^{-1}\left[v^\alpha E\left[\mathcal{H}\left[\widetilde{\Psi}_{n-1}(x,t)\right]\right]\right]\\
&= [\mu + 2(1-\mu)\alpha_c][-\frac{(-kt^\alpha)^n}{\Gamma(n\alpha+1)}\max(\mathrm{e}^x, 0)\\
&+ \frac{(-kt^\alpha)^n}{\Gamma(n\alpha+1)}\max(\mathrm{e}^x - 1, 0)].
\end{aligned} \tag{41}$$

As a result, the exact solution $\mathcal{H}[\widetilde{u}(x,t)]$ is given by

$$\begin{aligned}
u^{gr}(\mu, \alpha_c, x, t) &= \mathcal{H}[\widetilde{u}(x,t)]\\
&= \sum_{n=0}^{\infty} p^n \mathcal{H}[\widetilde{u}_n(x,t)]\\
&= [\mu + 2(1-\mu)\alpha_c][\max(\mathrm{e}^x, 0)(1 - E_\alpha(-kt^\alpha))\\
&+ \max(\mathrm{e}^x - 1, 0)E_\alpha(-kt^\alpha)],
\end{aligned} \tag{42}$$

$$\begin{aligned}
\mathcal{H}^{-1}[u^{gr}(\mu, \alpha_c, x, t)] &= [\mu, 2-\mu][\max(\mathrm{e}^x, 0)(1 - E_\alpha(-kt^\alpha))\\
&+ \max(\mathrm{e}^x - 1, 0)E_\alpha(-kt^\alpha)].
\end{aligned} \tag{43}$$

The trigonometric fuzzy number form of the exact solution is as follow

$$\begin{aligned}
\widetilde{u}(x,t) &= \underset{\mu}{\cup}[\mu, 2-\mu][\max(\mathrm{e}^x, 0)(1 - E_\alpha(-kt^\alpha))\\
&+ \max(\mathrm{e}^x - 1, 0)E_\alpha(-kt^\alpha)]\\
&= (0, 1, 2)[\max(\mathrm{e}^x, 0)(1 - E_\alpha(-kt^\alpha))\\
&+ \max(\mathrm{e}^x - 1, 0)E_\alpha(-kt^\alpha)].
\end{aligned} \tag{44}$$

Secondly, the HPM is used to solving the Example 1.

$$D_t^{\alpha}\left[\sum_{n=0}^{\infty} p^n \mathcal{H}[\widetilde{u}_n(x,t)]\right] = p\left[\sum_{n=0}^{\infty} p^n \mathcal{H}[\widetilde{\Psi}_n(x,t)]\right], \tag{45}$$

where

$$\mathcal{H}[\widetilde{\Psi}_n(x,t)] = \mathcal{H}[\frac{\partial^2 \widetilde{u}_n(x,t)}{\partial x^2} + (k-1)\frac{\partial \widetilde{u}_n(x,t)}{\partial x} - k\widetilde{u}_n(x,t)], \tag{46}$$

$$\sum_{n=0}^{\infty} p^n \mathcal{H}[\widetilde{u}_n(x,t)] = \mathcal{H}[\widetilde{u}(x,0)] + J^{\alpha}\left[p\left[\sum_{n=0}^{\infty} p^n \mathcal{H}[\widetilde{\Psi}_n(x,t)]\right]\right]. \tag{47}$$

After comparing the similar power coefficients of p, the following results can be obtained

$$\begin{aligned}
p^0 : \mathcal{H}[\widetilde{u}_0(x,t)] &= [\mu + 2(1-\mu)\alpha_c]\max(\mathrm{e}^x - 1, 0),\\
p^1 : \mathcal{H}[\widetilde{u}_1(x,t)] &= J^{\alpha}\left[\mathcal{H}\left[\widetilde{\Psi}_0(x,t)\right]\right]\\
&= [\mu + 2(1-\mu)\alpha_c][-\frac{(-kt^{\alpha})}{\Gamma(\alpha+1)}\max(\mathrm{e}^x, 0)\\
&+ \frac{(-kt^{\alpha})}{\Gamma(\alpha+1)}\max(\mathrm{e}^x - 1, 0)],\\
p^2 : \mathcal{H}[\widetilde{u}_2(x,t)] &= J^{\alpha}\left[\mathcal{H}\left[\widetilde{\Psi}_1(x,t)\right]\right]\\
&= [\mu + 2(1-\mu)\alpha_c][-\frac{(-kt^{\alpha})^2}{\Gamma(2\alpha+1)}\max(\mathrm{e}^x, 0)\\
&+ \frac{(-kt^{\alpha})^2}{\Gamma(2\alpha+1)}\max(\mathrm{e}^x - 1, 0)],\\
&\vdots\\
p^n : \mathcal{H}[\widetilde{u}_n(x,t)] &= J^{\alpha}\left[\mathcal{H}\left[\widetilde{\Psi}_{n-1}(x,t)\right]\right]\\
&= [\mu + 2(1-\mu)\alpha_c][-\frac{(-kt^{\alpha})^n}{\Gamma(n\alpha+1)}\max(\mathrm{e}^x, 0)\\
&+ \frac{(-kt^{\alpha})^n}{\Gamma(n\alpha+1)}\max(\mathrm{e}^x - 1, 0)].
\end{aligned} \tag{48}$$

So, we have

$$\begin{aligned}
\widetilde{u}(x,t) &= \bigcup_{\mu}[\mu, 2-\mu][\max(\mathrm{e}^x, 0)(1 - E_{\alpha}(-kt^{\alpha}))\\
&+ \max(\mathrm{e}^x - 1, 0)E_{\alpha}(-kt^{\alpha})]\\
&= (0,1,2)[\max(\mathrm{e}^x, 0)(1 - E_{\alpha}(-kt^{\alpha}))\\
&+ \max(\mathrm{e}^x - 1, 0)E_{\alpha}(-kt^{\alpha})].
\end{aligned} \tag{49}$$

Thirdly, the RPSM is used to solving the Example 1.

$$\mathcal{H}[\widetilde{u}(x,t)] = \sum_{n=0}^{\infty} \mathcal{H}[\widetilde{f}_n(x)]\frac{t^{\alpha n}}{\Gamma(1+n\alpha)}, \tag{50}$$

$$\mathcal{H}[\widetilde{u}_i(x,t)] = \sum_{n=0}^{i} \mathcal{H}[\widetilde{f}_n(x)]\frac{t^{n\alpha}}{\Gamma(1+n\alpha)}, \tag{51}$$

$$\mathcal{H}[\widetilde{f}_0(x)] = \mathcal{H}[\widetilde{u}_0(x,t)] = [\mu + 2(1-\mu)\alpha_c]\max(\mathrm{e}^x - 1, 0). \tag{52}$$

The *i*th residual function as follows

$$Res_i^{gr}(x,t,\mu,\alpha_c) = \frac{\partial^\alpha \mathcal{H}[\widetilde{u}_i(x,t)]}{\partial t^\alpha} - \frac{\partial^2 \mathcal{H}[\widetilde{u}_i(x,t)]}{\partial x^2} - (k-1)\frac{\partial \mathcal{H}[\widetilde{u}_i(x,t)]}{\partial x} + k\mathcal{H}[\widetilde{u}_i(x,t)], \tag{53}$$

$$D_t^{(i-1)\alpha} Res_i^{gr}(x,0,\mu,\alpha_c) = 0. \tag{54}$$

Then, we obtain

$$\begin{aligned} Res_1^{gr}(x,t,\mu,\alpha_c) &= \frac{\partial^\alpha \mathcal{H}[\widetilde{u}_1(x,t)]}{\partial t^\alpha} - \frac{\partial^2 \mathcal{H}[\widetilde{u}_1(x,t)]}{\partial x^2} - (k-1)\frac{\partial \mathcal{H}[\widetilde{u}_1(x,t)]}{\partial x} + k\mathcal{H}[\widetilde{u}_1(x,t)] \\ &= f_1^{gr}(x,\mu,\alpha_c) - D_x^2[f_0^{gr}(x,\mu,\alpha_c)] - D_x^2[f_1^{gr}(x,\mu,\alpha_c)]\frac{t^\alpha}{\Gamma(\alpha+1)} \\ &\quad - (k-1)\left(D_x[f_0^{gr}(x,\mu,\alpha_c)] + D_x[f_1^{gr}(x,\mu,\alpha_c)]\frac{t^\alpha}{\Gamma(\alpha+1)}\right) \\ &\quad + k\left(f_0^{gr}(x,\mu,\alpha_c) + f_1^{gr}(x,\mu,\alpha_c)\frac{t^\alpha}{\Gamma(\alpha+1)}\right). \end{aligned} \tag{55}$$

Thereby, from $Res_1^{gr}(x,0,\mu,\alpha_c) = 0$, we obtain

$$f_1^{gr}(x,\mu,\alpha_c) = [\mu + 2(1-\mu)\alpha_c][k\max(\mathrm{e}^x, 0) - k\max(\mathrm{e}^x - 1, 0)], \tag{56}$$

$$\mathcal{H}[\widetilde{u}_1(x,t)] = [\mu + 2(1-\mu)\alpha_c]\left[\max(\mathrm{e}^x - 1, 0) + [\max(\mathrm{e}^x - 1, 0) - \max(\mathrm{e}^x, 0)]\frac{(-kt^\alpha)}{\Gamma(\alpha+1)}\right]. \tag{57}$$

$$\begin{aligned} Res_2^{gr}(x,t,\mu,\alpha_c) &= \frac{\partial^\alpha \mathcal{H}[\widetilde{u}_2(x,t)]}{\partial t^\alpha} - \frac{\partial^2 \mathcal{H}[\widetilde{u}_2(x,t)]}{\partial x^2} - (k-1)\frac{\partial \mathcal{H}[\widetilde{u}_2(x,t)]}{\partial x} + k\mathcal{H}[\widetilde{u}_2(x,t)] \\ &= f_1^{gr}(x,\mu,\alpha_c) + f_2^{gr}(x,\mu,\alpha_c)\frac{t^\alpha}{\Gamma(\alpha+1)} \\ &\quad - D_x^2[f_0^{gr}(x,\mu,\alpha_c)] - D_x^2[f_1^{gr}(x,\mu,\alpha_c)]\frac{t^\alpha}{\Gamma(\alpha+1)} - D_x^2[f_2^{gr}(x,\mu,\alpha_c)]\frac{t^{2\alpha}}{\Gamma(2\alpha+1)} \\ &\quad - (k-1)\left[D_x[f_0^{gr}(x,\mu,\alpha_c)] + D_x[f_1^{gr}(x,\mu,\alpha_c)]\frac{t^\alpha}{\Gamma(\alpha+1)} + D_x[f_2^{gr}(x,\mu,\alpha_c)]\frac{t^{2\alpha}}{\Gamma(2\alpha+1)}\right] \\ &\quad + k\left(f_0^{gr}(x,\mu,\alpha_c) + f_1^{gr}(x,\mu,\alpha_c)\frac{t^\alpha}{\Gamma(\alpha+1)} + f_2^{gr}(x,\mu,\alpha_c)\frac{t^{2\alpha}}{\Gamma(2\alpha+1)}\right). \end{aligned} \tag{58}$$

And, from $D_x^\alpha Res_2^{gr}(x,0,\mu,\alpha_c) = 0$, we get

$$f_2^{gr}(x,\mu,\alpha_c) = [\mu + 2(1-\mu)\alpha_c][-k^2\max(\mathrm{e}^x, 0) + k^2\max(\mathrm{e}^x - 1, 0)], \tag{59}$$

$$\mathcal{H}[\widetilde{u}_2(x,t)] = [\mu + 2(1-\mu)\alpha_c]\left[\max(\mathrm{e}^x - 1, 0) + [\max(\mathrm{e}^x - 1, 0) - \max(\mathrm{e}^x, 0)][\frac{(-kt^\alpha)}{\Gamma(\alpha+1)} + \frac{(-kt^\alpha)^2}{\Gamma(2\alpha+1)}]\right]. \tag{60}$$

Continuing this way, we can get the exact solution

$$\begin{aligned}\widetilde{u}(x,t) &= \underset{\mu}{\cup}[\mu, 2-\mu][\max(\mathrm{e}^x, 0)(1-E_\alpha(-kt^\alpha)) \\ &+ \max(\mathrm{e}^x - 1, 0)E_\alpha(-kt^\alpha)] \\ &= (0,1,2)[\max(\mathrm{e}^x, 0)(1-E_\alpha(-kt^\alpha)) \\ &+ \max(\mathrm{e}^x - 1, 0)E_\alpha(-kt^\alpha)].\end{aligned} \tag{61}$$

Finally, the CFADM is used to solving the Example 1.

Assume that $L_\alpha = {}^{CF}D_*^\alpha = \frac{\partial^\alpha}{\partial t^\alpha}$ is a linear operator

$${}^{CF}D_*^\alpha \mathcal{H}[\widetilde{u}(x,t)] = \frac{\partial^2 \mathcal{H}[\widetilde{u}(x,t)]}{\partial x^2} + (k-1)\frac{\partial \mathcal{H}[\widetilde{u}(x,t)]}{\partial x} - k\mathcal{H}[\widetilde{u}(x,t)], \tag{62}$$

$$t^{1-\alpha}\partial_t \mathcal{H}[\widetilde{u}(x,t)] = \frac{\partial^2 \mathcal{H}[\widetilde{u}(x,t)]}{\partial x^2} + (k-1)\frac{\partial \mathcal{H}[\widetilde{u}(x,t)]}{\partial x} - k\mathcal{H}[\widetilde{u}(x,t)]. \tag{63}$$

From $L_\alpha^{-1} = \int_0^t \frac{1}{\zeta^{1-\alpha}}(.)d\zeta$, we get

$$\mathcal{H}[\widetilde{u}(x,t)] = \mathcal{H}[\widetilde{u}(x,0)] + L_\alpha^{-1}\left[\frac{\partial^2 \mathcal{H}[\widetilde{u}(x,t)]}{\partial x^2} + (k-1)\frac{\partial \mathcal{H}[\widetilde{u}(x,t)]}{\partial x} - k\mathcal{H}, [\widetilde{u}(x,t)]\right], \tag{64}$$

$$\mathcal{H}[\widetilde{u}(x,t)] = \sum_{n=0}^{\infty} \mathcal{H}[\widetilde{u}_n(x,t)]. \tag{65}$$

In the Adomian decomposition method, we assume that the nonlinear operator may be decomposed into an infinite polynomial series, then

$$\mathcal{N}[\mathcal{H}[\widetilde{u}(x,t)]] = \sum_{n=0}^{\infty} A_n, \tag{66}$$

where $A_n[\mathcal{H}(\widetilde{u})]$ are Adomian polynomials, which are defined as

$$A_n\mathcal{H}[(\widetilde{u}_0, \widetilde{u}_1, \widetilde{u}_2 \ldots \widetilde{u}_n)] = \frac{1}{n!}\frac{d^n}{d\lambda^n}\left[\mathcal{N}\left(\sum_{i=0}^{n} \lambda^i \mathcal{H}[\widetilde{u}_i(x,t)]\right)\right]_{\lambda=0}, n = 0, 1, 2, \cdots. \tag{67}$$

So, from $A_n[\mathcal{H}(\widetilde{u})]$, we get

$$\begin{aligned}\mathcal{H}[\widetilde{u}_0(x,t)] &= [\mu + 2(1-\mu)\alpha_c]\max(\mathrm{e}^x - 1, 0), \\ \mathcal{H}[\widetilde{u}_1(x,t)] &= L_\alpha^{-1}\left[\frac{\partial^2 \mathcal{H}[\widetilde{u}_0(x,t)]}{\partial x^2} + (k-1)\frac{\partial \mathcal{H}[\widetilde{u}_0(x,t)]}{\partial x} - k\mathcal{H}[\widetilde{u}_0(x,t)]\right] \\ &= [\mu + 2(1-\mu)\alpha_c][\max(\mathrm{e}^x - 1, 0) - \max(\mathrm{e}^x, 0)]\frac{-kt^\alpha}{\alpha}, \\ \mathcal{H}[\widetilde{u}_2(x,t)] &= L_\alpha^{-1}\left[\frac{\partial^2 \mathcal{H}[\widetilde{u}_1(x,t)]}{\partial x^2} + (k-1)\frac{\partial \mathcal{H}[\widetilde{u}_1(x,t)]}{\partial x} - k\mathcal{H}[\widetilde{u}_1(x,t)]\right] \\ &= [\mu + 2(1-\mu)\alpha_c][\max(\mathrm{e}^x - 1, 0) - \max(\mathrm{e}^x, 0)]\frac{(-kt^\alpha)^2}{2!\alpha^2}, \\ \mathcal{H}[\widetilde{u}_3(x,t)] &= L_\alpha^{-1}\left[\frac{\partial^2 \mathcal{H}[\widetilde{u}_2(x,t)]}{\partial x^2} + (k-1)\frac{\partial \mathcal{H}[\widetilde{u}_2(x,t)]}{\partial x} - k\mathcal{H}[\widetilde{u}_2(x,t)]\right] \\ &= [\mu + 2(1-\mu)\alpha_c][\max(\mathrm{e}^x - 1, 0) - \max(\mathrm{e}^x, 0)]\frac{(-kt^\alpha)^3}{3!\alpha^3}, \\ &\vdots\end{aligned}$$

$$
\begin{aligned}
\mathcal{H}[\widetilde{u}_n(x,t)] &= L_\alpha^{-1}\left[\frac{\partial^2\mathcal{H}[\widetilde{u}_{n-1}(x,t)]}{\partial x^2}+(k-1)\frac{\partial\mathcal{H}[\widetilde{u}_{n-1}(x,t)]}{\partial x}-k\mathcal{H}[\widetilde{u}_{n-1}(x,t)]\right]\\
&= [\mu+2(1-\mu)\alpha_c][\max(\mathrm{e}^x-1,0)-\max(\mathrm{e}^x,0)]\frac{(-kt^\alpha)^n}{n!\alpha^n},\\
\widetilde{u}(x,t) &= \underset{\mu}{\cup}[\mu,2-\mu][\max(\mathrm{e}^x,0)(1-e^{-\frac{kt}{\alpha}})\\
&+\max(\mathrm{e}^x-1,0)e^{-\frac{kt}{\alpha}})]\\
&= (0,1,2)[\max(\mathrm{e}^x,0)(1-e^{-\frac{kt}{\alpha}})\\
&+\max(\mathrm{e}^x-1,0)e^{-\frac{kt}{\alpha}})].
\end{aligned}
\tag{68}
$$

In Tables 1–3, we show the $\mathcal{H}[\widetilde{u}(x,t)]$ and $max|\widetilde{Res}(x,t)|$ of ETHPM, HPM, RPSM, and CFADM between different values of x and t when the fractions $\alpha = 0.5,\ 0.75,\ 1$, parameter $k = 2$, respectively. Although the approximate solutions for ETHPM, HPM, and RPSM are the same, HPM requires fractional integration and RPSM requires fractional differentiation, which are computationally more complex. In contrast, the ETHPM doesn't require fractional integration or differentiation and the ETHPM has a smaller $max|\widetilde{Res}(x,t)|$ than the CFADM.

Remark 2. *In Example 1, the value of* $max|\widetilde{Res}(x,t)|$ *doesn't vary with* x *because when* $x > 0$,

$$
\begin{aligned}
\mathcal{H}[\widetilde{u}(x,t)] &= \sum_{n=0}^{\infty}\mathcal{H}[\widetilde{u}_n(x,t)]\\
&= [\mu+2(1-\mu)\alpha_c]\Big[\mathrm{e}^x-1-(\frac{(-kt^\alpha)}{\Gamma(\alpha+1)}+\frac{(-kt^\alpha)^2}{\Gamma(2\alpha+1)}+\ldots+\frac{(-kt^\alpha)^n}{\Gamma(n\alpha+1)})\Big],
\end{aligned}
$$

$$
\begin{aligned}
max|\widetilde{Res}(x,t)| &= \underset{\mu\in[0,1],\alpha_c\in[0,1]}{max}\left|\frac{\partial^\alpha\mathcal{H}[\widetilde{u}(x,t)]}{\partial t^\alpha}-\frac{\partial^2\mathcal{H}[\widetilde{u}(x,t)]}{\partial x^2}-(k-1)\frac{\partial\mathcal{H}[\widetilde{u}(x,t)]}{\partial x}+k\mathcal{H}[\widetilde{u}(x,t)]\right|\\
&= \underset{\mu\in[0,1],\alpha_c\in[0,1]}{max}\Big|[\mu+2(1-\mu)\alpha_c]\Big[\frac{1}{\Gamma(1-\alpha)}\sum_{n=1}^{\infty}\Big[-\frac{(-k)^n}{\Gamma(n\alpha+1)}\int_0^t\frac{s^{n\alpha}}{(t-s)^\alpha}\mathrm{d}s\Big]\\
&-\mathrm{e}^x-(k-1)\mathrm{e}^x+k[\mathrm{e}^x-1-\sum_{n=1}^{\infty}(\frac{(-kt^\alpha)^n}{\Gamma(n\alpha+1)})]\Big]\Big|\\
&= \underset{\mu\in[0,1],\alpha_c\in[0,1]}{max}\Big|[\mu+2(1-\mu)\alpha_c]\Big[\frac{1}{\Gamma(1-\alpha)}\sum_{n=1}^{\infty}\Big[-\frac{(-k)^n}{\Gamma(n\alpha+1)}\int_0^t\frac{s^{n\alpha}}{(t-s)^\alpha}\mathrm{d}s\Big]\\
&-k[1+\sum_{n=1}^{\infty}(\frac{(-kt^\alpha)^n}{\Gamma(n\alpha+1)})]\Big]\Big|,
\end{aligned}
$$

where the x *terms are cancelled out.*

Remark 3. *The advantages of the ETHPM are as follows*

1. *Compared with the HPM*

HPM requires fractional integration operations. The numerical integration operated by fractional integration needs linearization and discretization. Thus, this operation causes errors, and its higher complexity requires a giant storage cell in a computer. The results of ETHPM and HPM are the same, but after the Elzaki transform, fractional integration is not necessary. ETHPM is more suitable to be achieved by computer programming.

2. *Compared with the RPSM*

RPSM needs to operate the residuals through fractional differentiation. However, computers have insufficient processing power to operate the fractional differentiation due to its massive calculation requirement and high complexity. ETHPM doesn't need a fractional differentiation operation, which reduces the complexity and the amount of computation.

3. *Compared with the CFADM*

It is most intuitive that the value of $max|\widetilde{Res}(x,t)|$ *of ETHPM is smaller, while CFADM also requires fractional integration operation.*

Table 1. $\mathcal{H}[\widetilde{u}(x,t)]$ and $max|\widetilde{Res}(x,t)|$ by ETHPM, HPM, RPSM, CFADM for $\alpha = 0.5, k = 2$.

		ETHPM		**HPM**		**RPSM**		**CFADM**	
x	t	$\mathcal{H}[\widetilde{u}(x,t)]$	$max\|\widetilde{Res}(x,t)\|$	$\mathcal{H}[\widetilde{u}(x,t)]$	$max\|\widetilde{Res}(x,t)\|$	$\mathcal{H}[\widetilde{u}(x,t)]$	$max\|\widetilde{Res}(x,t)\|$	$\mathcal{H}[\widetilde{u}(x,t)]$	$max\|\widetilde{Res}(x,t)\|$
0.2	0.1	$[\mu+2(1-\mu)\alpha_c]0.72536$	1.69448	$[\mu+2(1-\mu)\alpha_c]0.72536$	1.69448	$[\mu+2(1-\mu)\alpha_c]0.72536$	1.69448	$[\mu+2(1-\mu)\alpha_c]1.02362$	1.34924
	0.2	$[\mu+2(1-\mu)\alpha_c]0.96892$	0.42818	$[\mu+2(1-\mu)\alpha_c]0.96892$	0.42818	$[\mu+2(1-\mu)\alpha_c]0.96892$	0.42818	$[\mu+2(1-\mu)\alpha_c]1.36431$	3.81622
	0.3	$[\mu+2(1-\mu)\alpha_c]1.24634$	1.03090	$[\mu+2(1-\mu)\alpha_c]1.24634$	1.03090	$[\mu+2(1-\mu)\alpha_c]1.24634$	1.03090	$[\mu+2(1-\mu)\alpha_c]1.76501$	7.01085
	0.4	$[\mu+2(1-\mu)\alpha_c]1.57115$	2.75655	$[\mu+2(1-\mu)\alpha_c]1.57115$	2.75655	$[\mu+2(1-\mu)\alpha_c]1.57115$	2.75655	$[\mu+2(1-\mu)\alpha_c]2.24970$	10.79391
	0.5	$[\mu+2(1-\mu)\alpha_c]1.94486$	4.76615	$[\mu+2(1-\mu)\alpha_c]1.94486$	4.76615	$[\mu+2(1-\mu)\alpha_c]1.94486$	4.76615	$[\mu+2(1-\mu)\alpha_c]2.82107$	15.08494
0.4	0.1	$[\mu+2(1-\mu)\alpha_c]0.99578$	1.69448	$[\mu+2(1-\mu)\alpha_c]0.99578$	1.69448	$[\mu+2(1-\mu)\alpha_c]0.99578$	1.69448	$[\mu+2(1-\mu)\alpha_c]1.29405$	1.34924
	0.2	$[\mu+2(1-\mu)\alpha_c]1.23935$	0.42818	$[\mu+2(1-\mu)\alpha_c]1.23935$	0.42818	$[\mu+2(1-\mu)\alpha_c]1.23935$	0.42818	$[\mu+2(1-\mu)\alpha_c]1.63473$	3.81622
	0.3	$[\mu+2(1-\mu)\alpha_c]1.51676$	1.03090	$[\mu+2(1-\mu)\alpha_c]1.51676$	1.03090	$[\mu+2(1-\mu)\alpha_c]1.51676$	1.03090	$[\mu+2(1-\mu)\alpha_c]2.03543$	7.01085
	0.4	$[\mu+2(1-\mu)\alpha_c]1.84158$	2.75655	$[\mu+2(1-\mu)\alpha_c]1.84158$	2.75655	$[\mu+2(1-\mu)\alpha_c]1.84158$	2.75655	$[\mu+2(1-\mu)\alpha_c]2.52012$	10.79391
	0.5	$[\mu+2(1-\mu)\alpha_c]2.21529$	4.76615	$[\mu+2(1-\mu)\alpha_c]2.21529$	4.76615	$[\mu+2(1-\mu)\alpha_c]2.21529$	4.76615	$[\mu+2(1-\mu)\alpha_c]3.09149$	15.08494
0.6	0.1	$[\mu+2(1-\mu)\alpha_c]1.32608$	1.69448	$[\mu+2(1-\mu)\alpha_c]1.32608$	1.69448	$[\mu+2(1-\mu)\alpha_c]1.32608$	1.69448	$[\mu+2(1-\mu)\alpha_c]1.62434$	1.34924
	0.2	$[\mu+2(1-\mu)\alpha_c]1.56964$	0.42818	$[\mu+2(1-\mu)\alpha_c]1.56964$	0.42818	$[\mu+2(1-\mu)\alpha_c]1.56964$	0.42818	$[\mu+2(1-\mu)\alpha_c]1.96503$	3.81622
	0.3	$[\mu+2(1-\mu)\alpha_c]1.84706$	1.03090	$[\mu+2(1-\mu)\alpha_c]1.84706$	1.03090	$[\mu+2(1-\mu)\alpha_c]1.84706$	1.03090	$[\mu+2(1-\mu)\alpha_c]2.36572$	7.01085
	0.4	$[\mu+2(1-\mu)\alpha_c]2.17187$	2.75655	$[\mu+2(1-\mu)\alpha_c]2.17187$	2.75655	$[\mu+2(1-\mu)\alpha_c]2.17187$	2.75655	$[\mu+2(1-\mu)\alpha_c]2.85042$	10.79391
	0.5	$[\mu+2(1-\mu)\alpha_c]2.54558$	4.76615	$[\mu+2(1-\mu)\alpha_c]2.54558$	4.76615	$[\mu+2(1-\mu)\alpha_c]2.54558$	4.76615	$[\mu+2(1-\mu)\alpha_c]3.42178$	15.08494

Table 2. $\mathcal{H}[\widetilde{u}(x,t)]$ and $max|\widetilde{Res}(x,t)|$ by ETHPM, HPM, RPSM, CFADM for $\alpha = 0.75, k = 2$.

		ETHPM		**HPM**		**RPSM**		**CFADM**	
x	t	$\mathcal{H}[\widetilde{u}(x,t)]$	$max\|\widetilde{Res}(x,t)\|$	$\mathcal{H}[\widetilde{u}(x,t)]$	$max\|\widetilde{Res}(x,t)\|$	$\mathcal{H}[\widetilde{u}(x,t)]$	$max\|\widetilde{Res}(x,t)\|$	$\mathcal{H}[\widetilde{u}(x,t)]$	$max\|\widetilde{Res}(x,t)\|$
0.2	0.1	$[\mu+2(1-\mu)\alpha_c]0.53087$	2.43534	$[\mu+2(1-\mu)\alpha_c]0.53087$	2.43534	$[\mu+2(1-\mu)\alpha_c]0.53087$	2.43534	$[\mu+2(1-\mu)\alpha_c]0.60095$	0.07109
	0.2	$[\mu+2(1-\mu)\alpha_c]0.68703$	1.54889	$[\mu+2(1-\mu)\alpha_c]0.68703$	1.54889	$[\mu+2(1-\mu)\alpha_c]0.68703$	1.54889	$[\mu+2(1-\mu)\alpha_c]0.78545$	0.33817
	0.3	$[\mu+2(1-\mu)\alpha_c]0.81811$	0.78071	$[\mu+2(1-\mu)\alpha_c]0.81811$	0.78071	$[\mu+2(1-\mu)\alpha_c]0.81811$	0.78071	$[\mu+2(1-\mu)\alpha_c]0.9286$	0.84205
	0.4	$[\mu+2(1-\mu)\alpha_c]0.95402$	0.01695	$[\mu+2(1-\mu)\alpha_c]0.95402$	0.01695	$[\mu+2(1-\mu)\alpha_c]0.95402$	0.01695	$[\mu+2(1-\mu)\alpha_c]1.06532$	1.60861
	0.5	$[\mu+2(1-\mu)\alpha_c]1.11121$	0.93152	$[\mu+2(1-\mu)\alpha_c]1.11121$	0.93152	$[\mu+2(1-\mu)\alpha_c]1.11121$	0.93152	$[\mu+2(1-\mu)\alpha_c]1.21435$	2.65765
0.4	0.1	$[\mu+2(1-\mu)\alpha_c]0.80130$	2.43534	$[\mu+2(1-\mu)\alpha_c]0.80130$	2.43534	$[\mu+2(1-\mu)\alpha_c]0.80130$	2.43534	$[\mu+2(1-\mu)\alpha_c]0.87137$	0.07109
	0.2	$[\mu+2(1-\mu)\alpha_c]0.95745$	1.54889	$[\mu+2(1-\mu)\alpha_c]0.95745$	1.54889	$[\mu+2(1-\mu)\alpha_c]0.95745$	1.54889	$[\mu+2(1-\mu)\alpha_c]1.05587$	0.33817
	0.3	$[\mu+2(1-\mu)\alpha_c]1.08854$	0.78071	$[\mu+2(1-\mu)\alpha_c]1.08854$	0.78071	$[\mu+2(1-\mu)\alpha_c]1.08854$	0.78071	$[\mu+2(1-\mu)\alpha_c]1.19906$	0.84205
	0.4	$[\mu+2(1-\mu)\alpha_c]1.22445$	0.01695	$[\mu+2(1-\mu)\alpha_c]1.22445$	0.01695	$[\mu+2(1-\mu)\alpha_c]1.22445$	0.01695	$[\mu+2(1-\mu)\alpha_c]1.33575$	1.60861
	0.5	$[\mu+2(1-\mu)\alpha_c]1.38163$	0.93152	$[\mu+2(1-\mu)\alpha_c]1.38163$	0.93152	$[\mu+2(1-\mu)\alpha_c]1.38163$	0.93152	$[\mu+2(1-\mu)\alpha_c]1.48477$	2.65765
0.6	0.1	$[\mu+2(1-\mu)\alpha_c]1.13159$	2.43534	$[\mu+2(1-\mu)\alpha_c]1.13159$	2.43534	$[\mu+2(1-\mu)\alpha_c]1.13159$	2.43534	$[\mu+2(1-\mu)\alpha_c]1.20166$	0.07109
	0.2	$[\mu+2(1-\mu)\alpha_c]1.28774$	1.54889	$[\mu+2(1-\mu)\alpha_c]1.28774$	1.54889	$[\mu+2(1-\mu)\alpha_c]1.28774$	1.54889	$[\mu+2(1-\mu)\alpha_c]1.38616$	0.33817
	0.3	$[\mu+2(1-\mu)\alpha_c]1.41883$	0.78071	$[\mu+2(1-\mu)\alpha_c]1.41883$	0.78071	$[\mu+2(1-\mu)\alpha_c]1.41883$	0.78071	$[\mu+2(1-\mu)\alpha_c]1.52935$	0.84205
	0.4	$[\mu+2(1-\mu)\alpha_c]1.55474$	0.01695	$[\mu+2(1-\mu)\alpha_c]1.55474$	0.01695	$[\mu+2(1-\mu)\alpha_c]1.55474$	0.01695	$[\mu+2(1-\mu)\alpha_c]1.66604$	1.60861
	0.5	$[\mu+2(1-\mu)\alpha_c]1.71193$	0.93152	$[\mu+2(1-\mu)\alpha_c]1.71193$	0.93152	$[\mu+2(1-\mu)\alpha_c]1.71193$	0.93152	$[\mu+2(1-\mu)\alpha_c]1.81506$	2.65765

Remark 4. *In Tables 1–3, $\mathcal{H}[\widetilde{u}(x,t)]$ is converted into trigonometric fuzzy number form as follows*

$$\begin{aligned}\mathcal{H}[\widetilde{u}(x,t)] &= u^{gr}(\mu,\alpha_c,x,t),\\ \mathcal{H}^{-1}[u^{gr}(\mu,\alpha_c,x,t)] &= \left[\inf_{\beta\geq\mu}\min_{\alpha_c} u^{gr}(\beta,\alpha_c,x,t), \sup_{\beta\geq\mu}\max_{\alpha_c} u^{gr}(\beta,\alpha_c,x,t)\right]\\ &= [\mu, 2-\mu][\max(\mathrm{e}^x,0)(1-E_\alpha(-kt^\alpha))\\ &\quad+\max(\mathrm{e}^x-1,0)E_\alpha(-kt^\alpha)],\end{aligned} \tag{69}$$

when $k = 2$, by using the μ-level sets representation theorem, we have

$$\begin{aligned} \widetilde{u}(0.2,0.1) &= \underset{\mu}{\cup}[\mu, 2-\mu][\max(\mathrm{e}^x,0)(1-E_\alpha(-kt^\alpha)) \\ &\quad + \max(\mathrm{e}^x-1,0)E_\alpha(-kt^\alpha)] \\ &= (0,1,2)0.40274. \end{aligned} \tag{70}$$

Table 3. $\mathcal{H}[\widetilde{u}(x,t)]$ and $max|\widetilde{Res}(x,t)|$ by ETHPM, HPM, RPSM, CFADM for $\alpha = 1, k = 2$.

		ETHPM		**HPM**		**RPSM**		**CFADM**	
x	t	$\mathcal{H}[\widetilde{u}(x,t)]$	$max\lvert\widetilde{Res}(x,t)\rvert$	$\mathcal{H}[\widetilde{u}(x,t)]$	$max\lvert\widetilde{Res}(x,t)\rvert$	$\mathcal{H}[\widetilde{u}(x,t)]$	$max\lvert\widetilde{Res}(x,t)\rvert$	$\mathcal{H}[\widetilde{u}(x,t)]$	$max\lvert\widetilde{Res}(x,t)\rvert$
0.2	0.1	$[\mu+2(1-\mu)\alpha_c]0.40274$	0.00534	$[\mu+2(1-\mu)\alpha_c]0.40274$	0.00534	$[\mu+2(1-\mu)\alpha_c]0.40274$	0.00534	$[\mu+2(1-\mu)\alpha_c]0.40274$	0.00534
	0.2	$[\mu+2(1-\mu)\alpha_c]0.55207$	0.04267	$[\mu+2(1-\mu)\alpha_c]0.55207$	0.04267	$[\mu+2(1-\mu)\alpha_c]0.55207$	0.04267	$[\mu+2(1-\mu)\alpha_c]0.55207$	0.04267
	0.3	$[\mu+2(1-\mu)\alpha_c]0.67740$	0.14400	$[\mu+2(1-\mu)\alpha_c]0.67740$	0.14400	$[\mu+2(1-\mu)\alpha_c]0.67740$	0.14400	$[\mu+2(1-\mu)\alpha_c]0.67740$	0.14400
	0.4	$[\mu+2(1-\mu)\alpha_c]0.78674$	0.34133	$[\mu+2(1-\mu)\alpha_c]0.78674$	0.34133	$[\mu+2(1-\mu)\alpha_c]0.78674$	0.34133	$[\mu+2(1-\mu)\alpha_c]0.78674$	0.34133
	0.5	$[\mu+2(1-\mu)\alpha_c]0.88807$	0.66667	$[\mu+2(1-\mu)\alpha_c]0.88807$	0.66667	$[\mu+2(1-\mu)\alpha_c]0.88807$	0.66667	$[\mu+2(1-\mu)\alpha_c]0.88807$	0.66667
0.4	0.1	$[\mu+2(1-\mu)\alpha_c]0.67316$	0.00534	$[\mu+2(1-\mu)\alpha_c]0.67316$	0.00534	$[\mu+2(1-\mu)\alpha_c]0.67316$	0.00534	$[\mu+2(1-\mu)\alpha_c]0.67316$	0.00534
	0.2	$[\mu+2(1-\mu)\alpha_c]0.82249$	0.04267	$[\mu+2(1-\mu)\alpha_c]0.82249$	0.04267	$[\mu+2(1-\mu)\alpha_c]0.82249$	0.04267	$[\mu+2(1-\mu)\alpha_c]0.82249$	0.04267
	0.3	$[\mu+2(1-\mu)\alpha_c]0.94782$	0.14400	$[\mu+2(1-\mu)\alpha_c]0.94782$	0.14400	$[\mu+2(1-\mu)\alpha_c]0.94782$	0.14400	$[\mu+2(1-\mu)\alpha_c]0.94782$	0.14400
	0.4	$[\mu+2(1-\mu)\alpha_c]1.05716$	0.34133	$[\mu+2(1-\mu)\alpha_c]1.05716$	0.34133	$[\mu+2(1-\mu)\alpha_c]1.05716$	0.34133	$[\mu+2(1-\mu)\alpha_c]1.05716$	0.34133
	0.5	$[\mu+2(1-\mu)\alpha_c]1.15849$	0.66667	$[\mu+2(1-\mu)\alpha_c]1.15849$	0.66667	$[\mu+2(1-\mu)\alpha_c]1.15849$	0.66667	$[\mu+2(1-\mu)\alpha_c]1.15849$	0.66667
0.6	0.1	$[\mu+2(1-\mu)\alpha_c]1.00345$	0.00534	$[\mu+2(1-\mu)\alpha_c]1.00345$	0.00534	$[\mu+2(1-\mu)\alpha_c]1.00345$	0.00534	$[\mu+2(1-\mu)\alpha_c]1.00345$	0.00534
	0.2	$[\mu+2(1-\mu)\alpha_c]1.15279$	0.04267	$[\mu+2(1-\mu)\alpha_c]1.15279$	0.04267	$[\mu+2(1-\mu)\alpha_c]1.15279$	0.04267	$[\mu+2(1-\mu)\alpha_c]1.15279$	0.04267
	0.3	$[\mu+2(1-\mu)\alpha_c]1.27812$	0.14400	$[\mu+2(1-\mu)\alpha_c]1.27812$	0.14400	$[\mu+2(1-\mu)\alpha_c]1.27812$	0.14400	$[\mu+2(1-\mu)\alpha_c]1.27812$	0.14400
	0.4	$[\mu+2(1-\mu)\alpha_c]1.38745$	0.34133	$[\mu+2(1-\mu)\alpha_c]1.38745$	0.34133	$[\mu+2(1-\mu)\alpha_c]1.38745$	0.34133	$[\mu+2(1-\mu)\alpha_c]1.38745$	0.34133
	0.5	$[\mu+2(1-\mu)\alpha_c]1.48879$	0.66667	$[\mu+2(1-\mu)\alpha_c]1.48879$	0.66667	$[\mu+2(1-\mu)\alpha_c]1.48879$	0.66667	$[\mu+2(1-\mu)\alpha_c]1.48879$	0.66667

In Figure 2, the picture shows the fuzzy approximate solution $\widetilde{u}(x,t)$ of the Black–Scholes equation at the fractional parameter $\alpha = 1$ and the auxiliary parameters $k = 2$, $\mu = 0.5$.

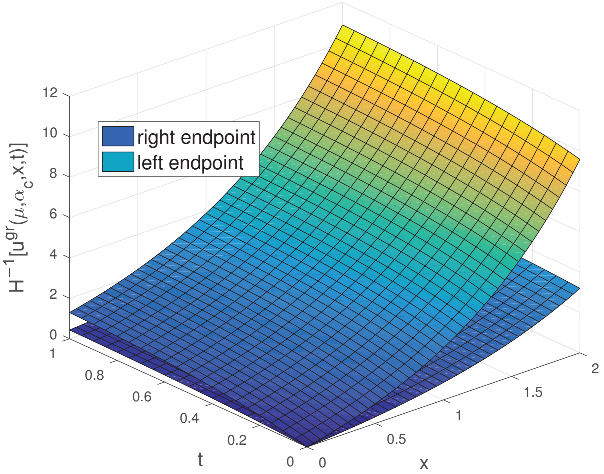

Figure 2. The fuzzy approximate solution $\widetilde{u}(x,t)$ of Example 1.

Example 2. *Consider the generalized Black–Scholes equation*

$$\frac{\partial^\alpha \widetilde{u}}{\partial t^\alpha} + 0.08(2+\sin x)^2 x^2 \frac{\partial^2 \widetilde{u}}{\partial x^2} + 0.06x\frac{\partial \widetilde{u}}{\partial x} - 0.06\widetilde{u} = 0, \tag{71}$$

with the initial condition

$$\widetilde{u}(x,0) = \widetilde{c}\max\Big(x - 25e^{-0.06}, 0\Big), \tag{72}$$

$$\widetilde{c} = (0,1,2). \tag{73}$$

From Definitions 7 and 8, we have

$$\begin{aligned}\frac{\partial^\alpha \mathcal{H}[\widetilde{u}(x,t)]}{\partial t^\alpha} &= -0.08(2+\sin x)^2 x^2 \frac{\partial^2 \mathcal{H}[\widetilde{u}(x,t)]}{\partial x^2} \\ &\quad - 0.06x\frac{\partial \mathcal{H}[\widetilde{u}(x,t)]}{\partial x} + 0.06\mathcal{H}[\widetilde{u}(x,t)],\end{aligned} \tag{74}$$

and,

$$\mathcal{H}[\widetilde{u}(x,0)] = [\mu + 2(1-\mu)\alpha_c]\max\Big(x - 25e^{-0.06}, 0\Big), \tag{75}$$

for each $\mu, \alpha_c \in [0,1]$ and

$$\mathcal{H}[\widetilde{u}(x,t)] = u^{gr}(\mu,\alpha_c,x,t). \tag{76}$$

Firstly, the ETHPM is used to solving the Example 2.

After using the Elzaki transform for the Equation (74), we get

$$\begin{aligned}E\left[\frac{\partial^\alpha \mathcal{H}[\widetilde{u}(x,t)]}{\partial t^\alpha}\right] &= E[-0.08(2+\sin x)^2 x^2 \frac{\partial^2 \mathcal{H}[\widetilde{u}(x,t)]}{\partial x^2} \\ &\quad - 0.06x\frac{\partial \mathcal{H}[\widetilde{u}(x,t)]}{\partial x} + 0.06\mathcal{H}[\widetilde{u}(x,t)]].\end{aligned} \tag{77}$$

Using the properties of the Elzaki transform, we get

$$v^{-\alpha}[E[\mathcal{H}[\widetilde{u}(x,t)] - v^2\mathcal{H}[\widetilde{u}(x,0)]]] \\ = E[-0.08(2+\sin x)^2x^2\frac{\partial^2\mathcal{H}[\widetilde{u}(x,t)]}{\partial x^2} \\ - 0.06x\frac{\partial\mathcal{H}[\widetilde{u}(x,t)]}{\partial x} + 0.06\mathcal{H}[\widetilde{u}(x,t)]], \tag{78}$$

$$E[\mathcal{H}[\widetilde{u}(x,t)]] = v^{\alpha}[E[-0.08(2+\sin x)^2x^2\frac{\partial^2\mathcal{H}[\widetilde{u}(x,t)]}{\partial x^2} \\ - 0.06x\frac{\partial\mathcal{H}[\widetilde{u}(x,t)]}{\partial x} + 0.06\mathcal{H}[\widetilde{u}(x,t)]]] + v^2\mathcal{H}[\widetilde{u}(x,0)]. \tag{79}$$

By applying the inverse Elzaki transform for the Equation (79), we get

$$\mathcal{H}[\widetilde{u}(x,t)] = E^{-1}[v^{\alpha}[E[-0.08(2+\sin x)^2x^2\frac{\partial^2\mathcal{H}[\widetilde{u}(x,t)]}{\partial x^2} \\ - 0.06x\frac{\partial\mathcal{H}[\widetilde{u}(x,t)]}{\partial x} + 0.06\mathcal{H}[\widetilde{u}(x,t)]]]] + \mathcal{H}[\widetilde{u}(x,0)], \tag{80}$$

$$\sum_{n=0}^{\infty} p^n\mathcal{H}[\widetilde{u}_n(x,t)] = \mathcal{H}[\widetilde{u}(x,0)] + pE^{-1}\left[v^{\alpha}E[\sum_{n=0}^{\infty} p^n\mathcal{H}[\widetilde{\Psi}_n(x,t)]]\right], \tag{81}$$

where

$$\mathcal{H}[\widetilde{\Psi}_n(x,t)] = \mathcal{H}[-0.08(2+\sin x)^2x^2\frac{\partial^2\widetilde{u}_n(x,t)}{\partial x^2} \\ - 0.06x\frac{\partial\widetilde{u}_n(x,t)}{\partial x} + 0.06\widetilde{u}_n(x,t)]. \tag{82}$$

After comparing the similar power coefficients of p, the following results can be obtained

$$p^0 : \mathcal{H}[\widetilde{u}_0(x,t)] = [\mu + 2(1-\mu)\alpha_c]\max\left(x - 25e^{-0.06}, 0\right),$$

$$p^1 : \mathcal{H}[\widetilde{u}_1(x,t)] = E^{-1}\left[v^{\alpha}E\left[\mathcal{H}\left[\widetilde{\Psi}_0(x,t)\right]\right]\right] \\ = [\mu + 2(1-\mu)\alpha_c][-x\frac{0.06t^{\alpha}}{\Gamma(\alpha+1)} \\ + \frac{0.06t^{\alpha}}{\Gamma(\alpha+1)}\max\left(x - 25e^{-0.06}, 0\right)],$$

$$p^2 : \mathcal{H}[\widetilde{u}_2(x,t)] = E^{-1}\left[v^{\alpha}E\left[\mathcal{H}\left[\widetilde{\Psi}_1(x,t)\right]\right]\right] \\ = [\mu + 2(1-\mu)\alpha_c][-x\frac{(0.06t^{\alpha})^2}{\Gamma(2\alpha+1)} \\ + \frac{(0.06t^{\alpha})^2}{\Gamma(2\alpha+1)}\max\left(x - 25e^{-0.06}, 0\right)],$$

$$\vdots$$

$$p^n : \mathcal{H}[\widetilde{u}_n(x,t)] = E^{-1}\left[v^{\alpha}E\left[\mathcal{H}\left[\widetilde{\Psi}_{n-1}(x,t)\right]\right]\right] \\ = [\mu + 2(1-\mu)\alpha_c][-x\frac{(0.06t^{\alpha})^n}{\Gamma(n\alpha+1)} \\ + \frac{(0.06t^{\alpha})^n}{\Gamma(n\alpha+1)}\max\left(x - 25e^{-0.06}, 0\right)]. \tag{83}$$

So that the solution $\mathcal{H}[\widetilde{u}(x,t)]$ of the problem is given by

$$\begin{aligned} u^{gr}(\mu,\alpha_c,x,t) &= \mathcal{H}[\widetilde{u}(x,t)] \\ &= \sum_{n=0}^{\infty} p^n \mathcal{H}[\widetilde{u}_n(x,t)] \\ &= [\mu+2(1-\mu)\alpha_c][x(1-E_\alpha(0.06t^\alpha)) \\ &+ \max\Big(x-25e^{-0.06},0\Big)E_\alpha(0.06t^\alpha)], \end{aligned} \tag{84}$$

$$\begin{aligned} \mathcal{H}^{-1}[u^{gr}(\mu,\alpha_c,x,t)] = [\mu,2-\mu][x(1-E_\alpha(0.06t^\alpha)) \\ + \max\Big(x-25e^{-0.06},0\Big)E_\alpha(0.06t^\alpha)]. \end{aligned} \tag{85}$$

By using the μ-level sets representation theorem, we have

$$\begin{aligned} \widetilde{u}(x,t) &= \bigcup_{\mu}[\mu,2-\mu][x(1-E_\alpha(0.06t^\alpha)) \\ &+ \max\Big(x-25e^{-0.06},0\Big)E_\alpha(0.06t^\alpha)] \\ &= (0,1,2)[x(1-E_\alpha(0.06t^\alpha)) \\ &+ \max\Big(x-25e^{-0.06},0\Big)E_\alpha(0.06t^\alpha)]. \end{aligned} \tag{86}$$

Secondly, the HPM is used to solving the Example 2.

$$D_t^\alpha\left[\sum_{n=0}^{\infty} p^n \mathcal{H}[\widetilde{u}_n(x,t)]\right] = p\left[\sum_{n=0}^{\infty} p^n \mathcal{H}[\widetilde{\Psi}_n(x,t)]\right], \tag{87}$$

where

$$\begin{aligned} \mathcal{H}[\widetilde{\Psi}_n(x,t)] = \mathcal{H}[-0.08(2+\sin x)^2 x^2 \frac{\partial^2 \mathcal{H}[\widetilde{u}(x,t)]}{\partial x^2} \\ - 0.06x\frac{\partial \mathcal{H}[\widetilde{u}(x,t)]}{\partial x} + 0.06\mathcal{H}[\widetilde{u}(x,t)], \end{aligned} \tag{88}$$

$$\sum_{n=0}^{\infty} p^n \mathcal{H}[\widetilde{u}_n(x,t)] = \mathcal{H}[\widetilde{u}(x,0)] + J^\alpha\left[p\left[\sum_{n=0}^{\infty} p^n \mathcal{H}[\widetilde{\Psi}_n(x,t)]\right]\right]. \tag{89}$$

After comparing the similar power coefficients of p, the following results can be obtained

$$p^0 : \mathcal{H}[\widetilde{u}_0(x,t)] = [\mu+2(1-\mu)\alpha_c]\max\Big(x-25e^{-0.06},0\Big),$$

$$\begin{aligned} p^1 : \mathcal{H}[\widetilde{u}_1(x,t)] &= J^\alpha\Big[\mathcal{H}\Big[\widetilde{\Psi}_0(x,t)\Big]\Big] \\ &= [\mu+2(1-\mu)\alpha_c][-x\frac{0.06t^\alpha}{\Gamma(\alpha+1)} \\ &+ \frac{0.06t^\alpha}{\Gamma(\alpha+1)}\max\Big(x-25e^{-0.06},0\Big)], \end{aligned}$$

$$\begin{aligned} p^2 : \mathcal{H}[\widetilde{u}_2(x,t)] &= J^\alpha\Big[\mathcal{H}\Big[\widetilde{\Psi}_1(x,t)\Big]\Big] \\ &= [\mu+2(1-\mu)\alpha_c][-x\frac{(0.06t^\alpha)^2}{\Gamma(2\alpha+1)} \\ &+ \frac{(0.06t^\alpha)^2}{\Gamma(2\alpha+1)}\max\Big(x-25e^{-0.06},0\Big)], \\ &\vdots \\ p^n : \mathcal{H}[\widetilde{u}_n(x,t)] &= J^\alpha\Big[\mathcal{H}\Big[\widetilde{\Psi}_{n-1}(x,t)\Big]\Big] \\ &= [\mu+2(1-\mu)\alpha_c][-x\frac{(0.06t^\alpha)^n}{\Gamma(n\alpha+1)} \\ &+ \frac{(0.06t^\alpha)^n}{\Gamma(n\alpha+1)}\max\Big(x-25e^{-0.06},0\Big)]. \end{aligned} \tag{90}$$

So,we have

$$\begin{aligned} \widetilde{u}(x,t) &= \underset{\mu}{\cup}[\mu,2-\mu][x(1-E_\alpha(0.06t^\alpha)) \\ &+ \max\Big(x-25e^{-0.06},0\Big)E_\alpha(0.06t^\alpha)] \\ &= (0,1,2)[x(1-E_\alpha(0.06t^\alpha)) \\ &+ \max\Big(x-25e^{-0.06},0\Big)E_\alpha(0.06t^\alpha)]. \end{aligned} \tag{91}$$

Thirdly, the RPSM is used to solving the Example 2.

$$\mathcal{H}[\widetilde{u}(x,t)] = \sum_{n=0}^{\infty}\mathcal{H}[\widetilde{f}_n(x)]\frac{t^{\alpha n}}{\Gamma(1+n\alpha)}, \tag{92}$$

$$\mathcal{H}[\widetilde{u}_i(x,t)] = \sum_{n=0}^{i}\mathcal{H}[\widetilde{f}_n(x)]\frac{t^{n\alpha}}{\Gamma(1+n\alpha)}, \tag{93}$$

$$\mathcal{H}[\widetilde{f}_0(x)] = \mathcal{H}[\widetilde{u}_0(x,t)] = [\mu+2(1-\mu)\alpha_c]\max\Big(x-25\mathrm{e}^{-0.06},0\Big). \tag{94}$$

The ith residual function can be written as

$$Res_i^{gr}(x,t,\mu,\alpha_c) = \frac{\partial^\alpha\mathcal{H}[\widetilde{u}_i(x,t)]}{\partial t^\alpha} + 0.08(2+\sin x)^2x^2\frac{\partial^2\mathcal{H}[\widetilde{u}_i(x,t)]}{\partial x^2} + 0.06x\frac{\partial\mathcal{H}[\widetilde{u}_i(x,t)]}{\partial x} - 0.06\mathcal{H}[\widetilde{u}_i(x,t)], \tag{95}$$

$$D_t^{(i-1)\alpha}Res_i^{gr}(x,0,\mu,\alpha_c) = 0. \tag{96}$$

Then, we obtain

$$\begin{aligned} Res_1^{gr}(x,t,\mu,\alpha_c) &= \frac{\partial^\alpha\mathcal{H}[\widetilde{u}_1(x,t)]}{\partial t^\alpha} + 0.08(2+\sin x)^2x^2\frac{\partial^2\mathcal{H}[\widetilde{u}_1(x,t)]}{\partial x^2} + 0.06x\frac{\partial\mathcal{H}[\widetilde{u}_1(x,t)]}{\partial x} - 0.06\mathcal{H}[\widetilde{u}_1(x,t)] \\ &= f_1^{gr}(x,\mu,\alpha_c) + 0.08(2+\sin x)^2x^2\Big[D_x^2[f_0^{gr}(x,\mu,\alpha_c)] + D_x^2[f_1^{gr}(x,\mu,\alpha_c)]\frac{t^\alpha}{\Gamma(\alpha+1)}\Big] \\ &+ 0.06x\Big(D_x[f_0^{gr}(x,\mu,\alpha_c)] + D_x[f_1^{gr}(x,\mu,\alpha_c)]\frac{t^\alpha}{\Gamma(\alpha+1)}\Big) \\ &- 0.06\Big(f_0^{gr}(x,\mu,\alpha_c) + f_1^{gr}(x,\mu,\alpha_c)\frac{t^\alpha}{\Gamma(\alpha+1)}\Big). \end{aligned} \tag{97}$$

By calculating $Res_1^{gr}(x,0,\mu,\alpha_c) = 0$, we obtain

$$f_1^{gr}(x,\mu,\alpha_c) = [\mu+2(1-\mu)\alpha_c]\Big[0.06\max\Big(x-25\mathrm{e}^{-0.06},0\Big)-0.06x\Big], \tag{98}$$

$$\mathcal{H}[\widetilde{u}_1(x,t)] = [\mu+2(1-\mu)\alpha_c]\Big[\max\Big(x-25\mathrm{e}^{-0.06},0\Big)+[0.06\max\Big(x-25\mathrm{e}^{-0.06},0\Big)-0.06x]\frac{t^\alpha}{\Gamma(\alpha+1)}\Big]. \tag{99}$$

$$\begin{aligned}
Res_2^{gr}(x,t,\mu,\alpha_c) &= \frac{\partial^\alpha\mathcal{H}[\widetilde{u}_2(x,t)]}{\partial t^\alpha}+0.08(2+\sin x)^2x^2\frac{\partial^2\mathcal{H}[\widetilde{u}_2(x,t)]}{\partial x^2}+0.06x\frac{\partial\mathcal{H}[\widetilde{u}_2(x,t)]}{\partial x}-0.06\mathcal{H}[\widetilde{u}_2(x,t)]\\
&= f_1^{gr}(x,\mu,\alpha_c)+f_2^{gr}(x,\mu,\alpha_c)\frac{t^\alpha}{\Gamma(\alpha+1)}\\
&+0.08(2+\sin x)^2x^2\Big[D_x^2[f_0^{gr}(x,\mu,\alpha_c)]+D_x^2[f_1^{gr}(x,\mu,\alpha_c)]\frac{t^\alpha}{\Gamma(\alpha+1)}+D_x^2[f_2^{gr}(x,\mu,\alpha_c)]\frac{t^{2\alpha}}{\Gamma(2\alpha+1)}\Big]\\
&+0.06x\Big[D_x[f_0^{gr}(x,\mu,\alpha_c)]+D_x[f_1^{gr}(x,\mu,\alpha_c)]\frac{t^\alpha}{\Gamma(\alpha+1)}+D_x[f_2^{gr}(x,\mu,\alpha_c)]\frac{t^{2\alpha}}{\Gamma(2\alpha+1)}\Big]\\
&-0.06\Big(f_0^{gr}(x,\mu,\alpha_c)+f_1^{gr}(x,\mu,\alpha_c)\frac{t^\alpha}{\Gamma(\alpha+1)}+f_2^{gr}(x,\mu,\alpha_c)\frac{t^{2\alpha}}{\Gamma(2\alpha+1)}\Big).
\end{aligned} \tag{100}$$

By calculating $D_x^\alpha Res_2^{gr}(x,0,\mu,\alpha_c)=0$, we obtain

$$f_2^{gr}(x,\mu,\alpha_c) = [\mu+2(1-\mu)\alpha_c]0.06^2\Big[\max\Big(x-25\mathrm{e}^{-0.06},0\Big)-x\Big], \tag{101}$$

$$\mathcal{H}[\widetilde{u}_2(x,t)] = [\mu+2(1-\mu)\alpha_c]\Big[\max\Big(x-25\mathrm{e}^{-0.06},0\Big)+[\max\Big(x-25\mathrm{e}^{-0.06},0\Big)-x][\frac{(0.06t^\alpha)}{\Gamma(\alpha+1)}+\frac{(0.06t^\alpha)^2}{\Gamma(2\alpha+1)}]\Big]. \tag{102}$$

Continuing this way, one may find the values of $f_3^{gr}(x,\mu,\alpha_c), f_4^{gr}(x,\mu,\alpha_c),\ldots$, we obtain

$$\begin{aligned}
\widetilde{u}(x,t) &= \bigcup_\mu[\mu,2-\mu][x(1-E_\alpha(0.06t^\alpha))\\
&+\max\Big(x-25e^{-0.06},0\Big)E_\alpha(0.06t^\alpha)]\\
&=(0,1,2)[x(1-E_\alpha(0.06t^\alpha))\\
&+\max\Big(x-25e^{-0.06},0\Big)E_\alpha(0.06t^\alpha)].
\end{aligned} \tag{103}$$

Finally, the CFADM is used to solving the Example 2.

Let $L_\alpha = {}^{CF}D_*^\alpha = \frac{\partial^\alpha}{\partial t^\alpha}$ be a linear operator

$${}^{CF}D_*^\alpha\mathcal{H}[\widetilde{u}(x,t)] = -0.08(2+\sin x)^2x^2\frac{\partial^2\mathcal{H}[\widetilde{u}(x,t)]}{\partial x^2}-0.06x\frac{\partial\mathcal{H}[\widetilde{u}(x,t)]}{\partial x}+0.06\mathcal{H}[\widetilde{u}(x,t)], \tag{104}$$

$$t^{1-\alpha}\partial_t\mathcal{H}[\widetilde{u}(x,t)] = -0.08(2+\sin x)^2x^2\frac{\partial^2\mathcal{H}[\widetilde{u}(x,t)]}{\partial x^2}-0.06x\frac{\partial\mathcal{H}[\widetilde{u}(x,t)]}{\partial x}+0.06\mathcal{H}[\widetilde{u}(x,t)]. \tag{105}$$

By the inverse of operator L_α which is $L_\alpha^{-1}=\int_0^t\frac{1}{\zeta^{1-\alpha}}(.)d\zeta$, we get

$$\mathcal{H}[\widetilde{u}(x,t)] = \mathcal{H}[\widetilde{u}(x,0)]-L_\alpha^{-1}\Big[0.08(2+\sin x)^2x^2\frac{\partial^2\mathcal{H}[\widetilde{u}(x,t)]}{\partial x^2}+0.06x\frac{\partial\mathcal{H}[\widetilde{u}(x,t)]}{\partial x}-0.06\mathcal{H}[\widetilde{u}(x,t)]\Big], \tag{106}$$

$$\mathcal{H}[\widetilde{u}(x,t)] = \sum_{n=0}^{\infty}\mathcal{H}[\widetilde{u}_n(x,t)]. \tag{107}$$

The nonlinear operator can also be decomposed into an infinite polynomial series using the Adomian decomposition method

$$\mathcal{N}[\mathcal{H}[\widetilde{u}(x,t)]] = \sum_{n=0}^{\infty} A_n, \tag{108}$$

where $A_n[\mathcal{H}(\widetilde{u})]$ are Adomian polynomials, which are defined as

$$A_n\mathcal{H}[(\widetilde{u}_0, \widetilde{u}_1, \widetilde{u}_2 \ldots \widetilde{u}_n)] = \frac{1}{n!}\frac{d^n}{d\lambda^n}\left[\mathcal{N}\left(\sum_{i=0}^{n} \lambda^i \mathcal{H}[\widetilde{u}_i(x,t)]\right)\right]_{\lambda=0}, n = 0, 1, 2, \cdots. \tag{109}$$

So, by using the Adomian decomposition method in conformable sense, we get

$$\begin{aligned}
\mathcal{H}[\widetilde{u}_0(x,t)] &= [\mu + 2(1-\mu)\alpha_c] \max\Big(x - 25\mathrm{e}^{-0.06}, 0\Big), \\
\mathcal{H}[\widetilde{u}_1(x,t)] &= -L_\alpha^{-1}\left[0.08(2+\sin x)^2 x^2 \frac{\partial^2 \mathcal{H}[\widetilde{u}_0(x,t)]}{\partial x^2} + 0.06x \frac{\partial \mathcal{H}[\widetilde{u}_0(x,t)]}{\partial x} - 0.06\mathcal{H}[\widetilde{u}_0(x,t)]\right] \\
&= [\mu + 2(1-\mu)\alpha_c]\Big[\max\Big(x - 25\mathrm{e}^{-0.06}, 0\Big) - x\Big]\frac{0.06t^\alpha}{\alpha}, \\
\mathcal{H}[\widetilde{u}_2(x,t)] &= -L_\alpha^{-1}\left[0.08(2+\sin x)^2 x^2 \frac{\partial^2 \mathcal{H}[\widetilde{u}_1(x,t)]}{\partial x^2} + 0.06x \frac{\partial \mathcal{H}[\widetilde{u}_1(x,t)]}{\partial x} - 0.06\mathcal{H}[\widetilde{u}_1(x,t)]\right] \\
&= [\mu + 2(1-\mu)\alpha_c]\Big[\max\Big(x - 25\mathrm{e}^{-0.06}, 0\Big) - x\Big]\frac{(0.06t^\alpha)^2}{2!\alpha^2}, \\
\mathcal{H}[\widetilde{u}_3(x,t)] &= -L_\alpha^{-1}\left[0.08(2+\sin x)^2 x^2 \frac{\partial^2 \mathcal{H}[\widetilde{u}_2(x,t)]}{\partial x^2} + 0.06x \frac{\partial \mathcal{H}[\widetilde{u}_2(x,t)]}{\partial x} - 0.06\mathcal{H}[\widetilde{u}_2(x,t)]\right] \\
&= [\mu + 2(1-\mu)\alpha_c]\Big[\max\Big(x - 25\mathrm{e}^{-0.06}, 0\Big) - x\Big]\frac{(0.06t^\alpha)^3}{3!\alpha^3}, \\
&\vdots \\
\mathcal{H}[\widetilde{u}_n(x,t)] &= -L_\alpha^{-1}\left[0.08(2+\sin x)^2 x^2 \frac{\partial^2 \mathcal{H}[\widetilde{u}_{n-1}(x,t)]}{\partial x^2} + 0.06x \frac{\partial \mathcal{H}[\widetilde{u}_{n-1}(x,t)]}{\partial x} - 0.06\mathcal{H}[\widetilde{u}_{n-1}(x,t)]\right] \\
&= [\mu + 2(1-\mu)\alpha_c]\Big[\max\Big(x - 25\mathrm{e}^{-0.06}, 0\Big) - x\Big]\frac{(0.06t^\alpha)^n}{n!\alpha^n}.
\end{aligned}$$

$$\begin{aligned}
\widetilde{u}(x,t) &= \bigcup_\mu [\mu, 2-\mu][x(1 - e^{\frac{0.06t}{\alpha}})) + \max\Big(x - 25\mathrm{e}^{-0.06}, 0\Big)e^{\frac{0.06t}{\alpha}})] \\
&= (0, 1, 2)[x(1 - e^{\frac{0.06t}{\alpha}})) + \max\Big(x - 25\mathrm{e}^{-0.06}, 0\Big)e^{\frac{0.06t}{\alpha}})].
\end{aligned} \tag{110}$$

In Tables 4–6, we show the $\mathcal{H}[\widetilde{u}(x,t)]$ and $max|\widetilde{Res}(x,t)|$ of ETHPM, HPM, RPSM, and CFADM between different values of x and t when the fractions $\alpha = 0.5, 0.75, 1$, respectively. It is easy to see in the table that the value of $max|\widetilde{Res}(x,t)|$ increases with t when α, x is fixed and the value of $max|\widetilde{Res}(x,t)|$ increases with x when α, t is fixed.

In Figure 3, the picture shows the fuzzy approximate solution $\widetilde{u}(x,t)$ of the Black–Scholes equation at the fractional parameter $\alpha = 1$ and the auxiliary parameter $\mu = 0.5$.

Table 4. $\mathcal{H}[\widetilde{u}(x,t)]$ and $max|\widetilde{Res}(x,t)|$ by ETHPM, HPM, RPSM, CFADM for $\alpha = 0.5$.

		ETHPM		**HPM**		**RPSM**		**CFADM**	
x	t	$\mathcal{H}[\widetilde{u}(x,t)]$	$max\lvert\widetilde{Res}(x,t)\rvert$	$\mathcal{H}[\widetilde{u}(x,t)]$	$max\lvert\widetilde{Res}(x,t)\rvert$	$\mathcal{H}[\widetilde{u}(x,t)]$	$max\lvert\widetilde{Res}(x,t)\rvert$	$\mathcal{H}[\widetilde{u}(x,t)]$	$max\lvert\widetilde{Res}(x,t)\rvert$
0.2	0.1	$-[\mu+2(1-\mu)\alpha_c]0.00435$	0.00243	$-[\mu+2(1-\mu)\alpha_c]0.00435$	0.00243	$-[\mu+2(1-\mu)\alpha_c]0.00435$	0.00243	$-[\mu+2(1-\mu)\alpha_c]0.00774$	0.02493
	0.2	$-[\mu+2(1-\mu)\alpha_c]0.00620$	0.00490	$-[\mu+2(1-\mu)\alpha_c]0.00620$	0.00490	$-[\mu+2(1-\mu)\alpha_c]0.00620$	0.00490	$-[\mu+2(1-\mu)\alpha_c]0.01103$	0.02532
	0.3	$-[\mu+2(1-\mu)\alpha_c]0.00764$	0.00738	$-[\mu+2(1-\mu)\alpha_c]0.00764$	0.00738	$-[\mu+2(1-\mu)\alpha_c]0.00764$	0.00738	$-[\mu+2(1-\mu)\alpha_c]0.01359$	0.02563
	0.4	$-[\mu+2(1-\mu)\alpha_c]0.00886$	0.00988	$-[\mu+2(1-\mu)\alpha_c]0.00886$	0.00988	$-[\mu+2(1-\mu)\alpha_c]0.00886$	0.00988	$-[\mu+2(1-\mu)\alpha_c]0.01577$	0.02589
	0.5	$-[\mu+2(1-\mu)\alpha_c]0.00995$	0.01240	$-[\mu+2(1-\mu)\alpha_c]0.00995$	0.01240	$-[\mu+2(1-\mu)\alpha_c]0.00995$	0.01240	$-[\mu+2(1-\mu)\alpha_c]0.01771$	0.02612
0.4	0.1	$-[\mu+2(1-\mu)\alpha_c]0.00871$	0.00486	$-[\mu+2(1-\mu)\alpha_c]0.00871$	0.00486	$-[\mu+2(1-\mu)\alpha_c]0.00871$	0.00486	$-[\mu+2(1-\mu)\alpha_c]0.01547$	0.04986
	0.2	$-[\mu+2(1-\mu)\alpha_c]0.01240$	0.00980	$-[\mu+2(1-\mu)\alpha_c]0.01240$	0.00980	$-[\mu+2(1-\mu)\alpha_c]0.01240$	0.00980	$-[\mu+2(1-\mu)\alpha_c]0.02205$	0.05065
	0.3	$-[\mu+2(1-\mu)\alpha_c]0.01528$	0.01476	$-[\mu+2(1-\mu)\alpha_c]0.01528$	0.01476	$-[\mu+2(1-\mu)\alpha_c]0.01528$	0.01476	$-[\mu+2(1-\mu)\alpha_c]0.02717$	0.05126
	0.4	$-[\mu+2(1-\mu)\alpha_c]0.01772$	0.01976	$-[\mu+2(1-\mu)\alpha_c]0.01772$	0.01976	$-[\mu+2(1-\mu)\alpha_c]0.01772$	0.01976	$-[\mu+2(1-\mu)\alpha_c]0.03154$	0.05178
	0.5	$-[\mu+2(1-\mu)\alpha_c]0.01989$	0.02478	$-[\mu+2(1-\mu)\alpha_c]0.01989$	0.02478	$-[\mu+2(1-\mu)\alpha_c]0.01989$	0.02478	$-[\mu+2(1-\mu)\alpha_c]0.03542$	0.05225
0.6	0.1	$-[\mu+2(1-\mu)\alpha_c]0.01306$	0.00730	$-[\mu+2(1-\mu)\alpha_c]0.01306$	0.00730	$-[\mu+2(1-\mu)\alpha_c]0.01306$	0.00730	$-[\mu+2(1-\mu)\alpha_c]0.02321$	0.07478
	0.2	$-[\mu+2(1-\mu)\alpha_c]0.01861$	0.01470	$-[\mu+2(1-\mu)\alpha_c]0.01861$	0.01470	$-[\mu+2(1-\mu)\alpha_c]0.01861$	0.01470	$-[\mu+2(1-\mu)\alpha_c]0.03308$	0.07597
	0.3	$-[\mu+2(1-\mu)\alpha_c]0.02291$	0.02214	$-[\mu+2(1-\mu)\alpha_c]0.02291$	0.02214	$-[\mu+2(1-\mu)\alpha_c]0.02291$	0.02214	$-[\mu+2(1-\mu)\alpha_c]0.04076$	0.07689
	0.4	$-[\mu+2(1-\mu)\alpha_c]0.02658$	0.02964	$-[\mu+2(1-\mu)\alpha_c]0.02658$	0.02964	$-[\mu+2(1-\mu)\alpha_c]0.02658$	0.02964	$-[\mu+2(1-\mu)\alpha_c]0.04731$	0.07767
	0.5	$-[\mu+2(1-\mu)\alpha_c]0.02984$	0.03718	$-[\mu+2(1-\mu)\alpha_c]0.02984$	0.03718	$-[\mu+2(1-\mu)\alpha_c]0.02984$	0.03718	$-[\mu+2(1-\mu)\alpha_c]0.05313$	0.07837

Table 5. $\mathcal{H}[\widetilde{u}(x,t)]$ and $max|\widetilde{Res}(x,t)|$ by ETHPM, HPM, RPSM, CFADM for $\alpha = 0.75$.

		ETHPM		**HPM**		**RPSM**		**CFADM**	
x	t	$\mathcal{H}[\widetilde{u}(x,t)]$	$max\lvert\widetilde{Res}(x,t)\rvert$	$\mathcal{H}[\widetilde{u}(x,t)]$	$max\lvert\widetilde{Res}(x,t)\rvert$	$\mathcal{H}[\widetilde{u}(x,t)]$	$max\lvert\widetilde{Res}(x,t)\rvert$	$\mathcal{H}[\widetilde{u}(x,t)]$	$max\lvert\widetilde{Res}(x,t)\rvert$
0.2	0.1	$-[\mu+2(1-\mu)\alpha_c]0.00234$	0.00242	$-[\mu+2(1-\mu)\alpha_c]0.00234$	0.00242	$-[\mu+2(1-\mu)\alpha_c]0.00234$	0.00242	$-[\mu+2(1-\mu)\alpha_c]0.00287$	0.02434
	0.2	$-[\mu+2(1-\mu)\alpha_c]0.00395$	0.00486	$-[\mu+2(1-\mu)\alpha_c]0.00395$	0.00486	$-[\mu+2(1-\mu)\alpha_c]0.00395$	0.00486	$-[\mu+2(1-\mu)\alpha_c]0.00484$	0.02458

Table 5. *Cont.*

		ETHPM		HPM		RPSM		CFADM	
	0.3	$-[\mu+2(1-\mu)\alpha_c]0.00538$	0.00732	$-[\mu+2(1-\mu)\alpha_c]0.00538$	0.00732	$-[\mu+2(1-\mu)\alpha_c]0.00538$	0.00732	$-[\mu+2(1-\mu)\alpha_c]0.00659$	0.02479
	0.4	$-[\mu+2(1-\mu)\alpha_c]0.00671$	0.00978	$-[\mu+2(1-\mu)\alpha_c]0.00671$	0.00978	$-[\mu+2(1-\mu)\alpha_c]0.00671$	0.00978	$-[\mu+2(1-\mu)\alpha_c]0.00821$	0.02499
	0.5	$-[\mu+2(1-\mu)\alpha_c]0.00796$	0.01226	$-[\mu+2(1-\mu)\alpha_c]0.00796$	0.01226	$-[\mu+2(1-\mu)\alpha_c]0.00796$	0.01226	$-[\mu+2(1-\mu)\alpha_c]0.00974$	0.02517
0.4	0.1	$-[\mu+2(1-\mu)\alpha_c]0.00468$	0.00484	$-[\mu+2(1-\mu)\alpha_c]0.00468$	0.00484	$-[\mu+2(1-\mu)\alpha_c]0.00468$	0.00484	$-[\mu+2(1-\mu)\alpha_c]0.00573$	0.04869
	0.2	$-[\mu+2(1-\mu)\alpha_c]0.00791$	0.00970	$-[\mu+2(1-\mu)\alpha_c]0.00791$	0.00970	$-[\mu+2(1-\mu)\alpha_c]0.00791$	0.00970	$-[\mu+2(1-\mu)\alpha_c]0.00964$	0.04916
	0.3	$-[\mu+2(1-\mu)\alpha_c]0.01077$	0.01462	$-[\mu+2(1-\mu)\alpha_c]0.01077$	0.01462	$-[\mu+2(1-\mu)\alpha_c]0.01077$	0.01462	$-[\mu+2(1-\mu)\alpha_c]0.01318$	0.04958
	0.4	$-[\mu+2(1-\mu)\alpha_c]0.01341$	0.01956	$-[\mu+2(1-\mu)\alpha_c]0.01341$	0.01956	$-[\mu+2(1-\mu)\alpha_c]0.01341$	0.01956	$-[\mu+2(1-\mu)\alpha_c]0.01642$	0.04997
	0.5	$-[\mu+2(1-\mu)\alpha_c]0.01592$	0.02454	$-[\mu+2(1-\mu)\alpha_c]0.01592$	0.02454	$-[\mu+2(1-\mu)\alpha_c]0.01592$	0.02454	$-[\mu+2(1-\mu)\alpha_c]0.01949$	0.05034
0.6	0.1	$-[\mu+2(1-\mu)\alpha_c]0.00702$	0.00724	$-[\mu+2(1-\mu)\alpha_c]0.00702$	0.00724	$-[\mu+2(1-\mu)\alpha_c]0.00702$	0.00724	$-[\mu+2(1-\mu)\alpha_c]0.00860$	0.07303
	0.2	$-[\mu+2(1-\mu)\alpha_c]0.01186$	0.01456	$-[\mu+2(1-\mu)\alpha_c]0.01186$	0.01456	$-[\mu+2(1-\mu)\alpha_c]0.01186$	0.01456	$-[\mu+2(1-\mu)\alpha_c]0.01453$	0.07374
	0.3	$-[\mu+2(1-\mu)\alpha_c]0.01615$	0.02194	$-[\mu+2(1-\mu)\alpha_c]0.01615$	0.02194	$-[\mu+2(1-\mu)\alpha_c]0.01615$	0.02194	$-[\mu+2(1-\mu)\alpha_c]0.01978$	0.07437
	0.4	$-[\mu+2(1-\mu)\alpha_c]0.02012$	0.02934	$-[\mu+2(1-\mu)\alpha_c]0.02012$	0.02934	$-[\mu+2(1-\mu)\alpha_c]0.02012$	0.02934	$-[\mu+2(1-\mu)\alpha_c]0.02463$	0.07496
	0.5	$-[\mu+2(1-\mu)\alpha_c]0.02388$	0.03682	$-[\mu+2(1-\mu)\alpha_c]0.02388$	0.03682	$-[\mu+2(1-\mu)\alpha_c]0.02388$	0.03682	$-[\mu+2(1-\mu)\alpha_c]0.02923$	0.07551

Table 6. $\mathcal{H}[\widetilde{u}(x,t)]$ and $max|\widetilde{Res}(x,t)|$ by ETHPM, HPM, RPSM, CFADM for $\alpha = 1$.

		ETHPM		HPM		RPSM		CFADM	
x	t	$\mathcal{H}[\widetilde{u}(x,t)]$	$max\lvert\widetilde{Res}(x,t)\rvert$	$\mathcal{H}[\widetilde{u}(x,t)]$	$max\lvert\widetilde{Res}(x,t)\rvert$	$\mathcal{H}[\widetilde{u}(x,t)]$	$max\lvert\widetilde{Res}(x,t)\rvert$	$\mathcal{H}[\widetilde{u}(x,t)]$	$max\lvert\widetilde{Res}(x,t)\rvert$
0.2	0.1	$-[\mu+2(1-\mu)\alpha_c]0.00120$	0.02414	$-[\mu+2(1-\mu)\alpha_c]0.00120$	0.02414	$-[\mu+2(1-\mu)\alpha_c]0.00120$	0.02414	$-[\mu+2(1-\mu)\alpha_c]0.00120$	0.02414
	0.2	$-[\mu+2(1-\mu)\alpha_c]0.00241$	0.02429	$-[\mu+2(1-\mu)\alpha_c]0.00241$	0.02429	$-[\mu+2(1-\mu)\alpha_c]0.00241$	0.02429	$-[\mu+2(1-\mu)\alpha_c]0.00241$	0.02429
	0.3	$-[\mu+2(1-\mu)\alpha_c]0.00363$	0.02444	$-[\mu+2(1-\mu)\alpha_c]0.00363$	0.02444	$-[\mu+2(1-\mu)\alpha_c]0.00363$	0.02444	$-[\mu+2(1-\mu)\alpha_c]0.00363$	0.02444
	0.4	$-[\mu+2(1-\mu)\alpha_c]0.00486$	0.02458	$-[\mu+2(1-\mu)\alpha_c]0.00486$	0.02458	$-[\mu+2(1-\mu)\alpha_c]0.00486$	0.02458	$-[\mu+2(1-\mu)\alpha_c]0.00486$	0.02458
	0.5	$-[\mu+2(1-\mu)\alpha_c]0.00609$	0.02473	$-[\mu+2(1-\mu)\alpha_c]0.00609$	0.02473	$-[\mu+2(1-\mu)\alpha_c]0.00609$	0.02473	$-[\mu+2(1-\mu)\alpha_c]0.00609$	0.02473

Table 6. *Cont.*

		ETHPM		HPM		RPSM		CFADM	
0.4	0.1	$-[\mu+2(1-\mu)\alpha_c]0.00241$	0.04829	$-[\mu+2(1-\mu)\alpha_c]0.00241$	0.04829	$-[\mu+2(1-\mu)\alpha_c]0.00241$	0.04829	$-[\mu+2(1-\mu)\alpha_c]0.00241$	0.04829
	0.2	$-[\mu+2(1-\mu)\alpha_c]0.00483$	0.04858	$-[\mu+2(1-\mu)\alpha_c]0.00483$	0.04858	$-[\mu+2(1-\mu)\alpha_c]0.00483$	0.04858	$-[\mu+2(1-\mu)\alpha_c]0.00483$	0.04858
	0.3	$-[\mu+2(1-\mu)\alpha_c]0.00727$	0.04887	$-[\mu+2(1-\mu)\alpha_c]0.00727$	0.04887	$-[\mu+2(1-\mu)\alpha_c]0.00727$	0.04887	$-[\mu+2(1-\mu)\alpha_c]0.00727$	0.04887
	0.4	$-[\mu+2(1-\mu)\alpha_c]0.00972$	0.04917	$-[\mu+2(1-\mu)\alpha_c]0.00972$	0.04917	$-[\mu+2(1-\mu)\alpha_c]0.00972$	0.04917	$-[\mu+2(1-\mu)\alpha_c]0.00972$	0.04917
	0.5	$-[\mu+2(1-\mu)\alpha_c]0.01218$	0.04946	$-[\mu+2(1-\mu)\alpha_c]0.01218$	0.04946	$-[\mu+2(1-\mu)\alpha_c]0.01218$	0.04946	$-[\mu+2(1-\mu)\alpha_c]0.01218$	0.04946
0.6	0.1	$-[\mu+2(1-\mu)\alpha_c]0.00361$	0.07243	$-[\mu+2(1-\mu)\alpha_c]0.00361$	0.07243	$-[\mu+2(1-\mu)\alpha_c]0.00361$	0.07243	$-[\mu+2(1-\mu)\alpha_c]0.00361$	0.07243
	0.2	$-[\mu+2(1-\mu)\alpha_c]0.00724$	0.07287	$-[\mu+2(1-\mu)\alpha_c]0.00724$	0.07287	$-[\mu+2(1-\mu)\alpha_c]0.00724$	0.07287	$-[\mu+2(1-\mu)\alpha_c]0.00724$	0.07287
	0.3	$-[\mu+2(1-\mu)\alpha_c]0.01090$	0.07331	$-[\mu+2(1-\mu)\alpha_c]0.01090$	0.07331	$-[\mu+2(1-\mu)\alpha_c]0.01090$	0.07331	$-[\mu+2(1-\mu)\alpha_c]0.01090$	0.07331
	0.4	$-[\mu+2(1-\mu)\alpha_c]0.01457$	0.07375	$-[\mu+2(1-\mu)\alpha_c]0.01457$	0.07375	$-[\mu+2(1-\mu)\alpha_c]0.01457$	0.07375	$-[\mu+2(1-\mu)\alpha_c]0.01457$	0.07375
	0.5	$-[\mu+2(1-\mu)\alpha_c]0.01827$	0.07419	$-[\mu+2(1-\mu)\alpha_c]0.01827$	0.07419	$-[\mu+2(1-\mu)\alpha_c]0.01827$	0.07419	$-[\mu+2(1-\mu)\alpha_c]0.01827$	0.07419

Example 3. *Consider the following fractional Black–Scholes option pricing equation*

$$\frac{\partial^\alpha \widetilde{u}}{\partial t^\alpha} + \frac{\sigma^2}{2}x^2\frac{\partial^2 \widetilde{u}}{\partial x^2} + (r-\tau)x\frac{\partial \widetilde{u}}{\partial x} - r\widetilde{u} = 0, \tag{111}$$

with the initial condition

$$\widetilde{u}(x,0) = \widetilde{c}\max(Ax-B,0), \tag{112}$$

$$\widetilde{c} = (0,1,2), \tag{113}$$

From Definitions 7 and 8, we have

$$\begin{aligned}\frac{\partial^\alpha \mathcal{H}[\widetilde{u}(x,t)]}{\partial t^\alpha} &= -\frac{\sigma^2}{2}x^2\frac{\partial^2 \mathcal{H}[\widetilde{u}(x,t)]}{\partial x^2} \\ &\quad -(r-\tau)x\frac{\partial \mathcal{H}[\widetilde{u}(x,t)]}{\partial x} + r\mathcal{H}[\widetilde{u}(x,t)],\end{aligned} \tag{114}$$

and,

$$\mathcal{H}[\widetilde{u}(x,0)] = [\mu + 2(1-\mu)\alpha_c]\max(Ax-B,0), \tag{115}$$

for each $\mu, \alpha_c \in [0,1]$ and

$$\mathcal{H}[\widetilde{u}(x,t)] = u^{gr}(\mu,\alpha_c,x,t). \tag{116}$$

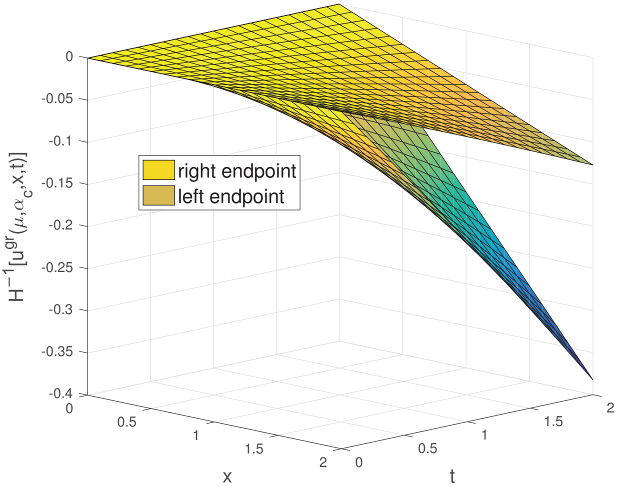

Figure 3. The fuzzy approximate solution $\widetilde{u}(x,t)$ of Example 2.

Firstly, the ETHPM is used to solving the Example 3.

After using the Elzaki transform for the Equation (114), we get

$$E\left[\frac{\partial^{\alpha}\mathcal{H}[\widetilde{u}(x,t)]}{\partial t^{\alpha}}\right] = E[-\frac{\sigma^2}{2}x^2\frac{\partial^2\mathcal{H}[\widetilde{u}(x,t)]}{\partial x^2} - (r-\tau)x\frac{\partial\mathcal{H}[\widetilde{u}(x,t)]}{\partial x} + r\mathcal{H}[\widetilde{u}(x,t)]]. \tag{117}$$

Using the properties of the Elzaki transform, we get

$$v^{-\alpha}[E[\mathcal{H}[\widetilde{u}(x,t)] - v^2\mathcal{H}[\widetilde{u}(x,0)]]] = E[-\frac{\sigma^2}{2}x^2\frac{\partial^2\mathcal{H}[\widetilde{u}(x,t)]}{\partial x^2} - (r-\tau)x\frac{\partial\mathcal{H}[\widetilde{u}(x,t)]}{\partial x} + r\mathcal{H}[\widetilde{u}(x,t)]], \tag{118}$$

$$E[\mathcal{H}[\widetilde{u}(x,t)]] = v^{\alpha}[E[-\frac{\sigma^2}{2}x^2\frac{\partial^2\mathcal{H}[\widetilde{u}(x,t)]}{\partial x^2} - (r-\tau)x\frac{\partial\mathcal{H}[\widetilde{u}(x,t)]}{\partial x} + r\mathcal{H}[\widetilde{u}(x,t)]]] + v^2\mathcal{H}[\widetilde{u}(x,0)]. \tag{119}$$

By applying the inverse Elzaki transform for the Equation (119), we get

$$\mathcal{H}[\widetilde{u}(x,t)] = E^{-1}[v^{\alpha}[E[-\frac{\sigma^2}{2}x^2\frac{\partial^2\mathcal{H}[\widetilde{u}(x,t)]}{\partial x^2} - (r-\tau)x\frac{\partial\mathcal{H}[\widetilde{u}(x,t)]}{\partial x} + r\mathcal{H}[\widetilde{u}(x,t)]]]] + \mathcal{H}[\widetilde{u}(x,0)], \tag{120}$$

$$\sum_{n=0}^{\infty} p^n\mathcal{H}[\widetilde{u}_n(x,t)] = \mathcal{H}[\widetilde{u}(x,0)] + pE^{-1}\left[v^{\alpha}E[\sum_{n=0}^{\infty} p^n\mathcal{H}[\widetilde{\Psi}_n(x,t)]]\right], \tag{121}$$

where

$$\mathcal{H}[\widetilde{\Psi}_n(x,t)] = \mathcal{H}[-\frac{\sigma^2}{2}x^2\frac{\partial^2\widetilde{u}_n(x,t)}{\partial x^2} \\ - (r-\tau)x\frac{\partial\widetilde{u}_n(x,t)}{\partial x} + r\widetilde{u}_n(x,t)]. \tag{122}$$

After comparing the similar power coefficients of p, the following results can be obtained

$$p^0 : \mathcal{H}[\widetilde{u}_0(x,t)] = [\mu + 2(1-\mu)\alpha_c]\max(Ax - B, 0),$$

$$\begin{aligned} p^1 : \mathcal{H}[\widetilde{u}_1(x,t)] &= E^{-1}\Big[v^\alpha E\Big[\mathcal{H}\Big[\widetilde{\Psi}_0(x,t)\Big]\Big]\Big] \\ &= [\mu + 2(1-\mu)\alpha_c][-x\max(A,0)\frac{(r-\tau)t^\alpha}{\Gamma(\alpha+1)} \\ &+ \frac{(rt^\alpha)}{\Gamma(\alpha+1)}\max(Ax-B,0)], \end{aligned}$$

$$\begin{aligned} p^2 : \mathcal{H}[\widetilde{u}_2(x,t)] &= E^{-1}\Big[v^\alpha E\Big[\mathcal{H}\Big[\widetilde{\Psi}_1(x,t)\Big]\Big]\Big] \\ &= [\mu + 2(1-\mu)\alpha_c][-x\max(A,0)\frac{(r^2-\tau^2)(t^\alpha)^2}{\Gamma(2\alpha+1)} \\ &+ \frac{(rt^\alpha)^2}{\Gamma(2\alpha+1)}\max(Ax-B,0)], \\ &\vdots \\ p^n : \mathcal{H}[\widetilde{u}_n(x,t)] &= E^{-1}\Big[v^\alpha E\Big[\mathcal{H}\Big[\widetilde{\Psi}_{n-1}(x,t)\Big]\Big]\Big] \\ &= [\mu + 2(1-\mu)\alpha_c][-x\max(A,0)\frac{(r^n-\tau^n)(t^\alpha)^n}{\Gamma(n\alpha+1)} \\ &+ \frac{(rt^\alpha)^n}{\Gamma(n\alpha+1)}\max(Ax-B,0)]. \end{aligned} \tag{123}$$

So that the solution $\mathcal{H}[\widetilde{u}(x,t)]$ of the problem is given by

$$\begin{aligned} u^{gr}(\mu,\alpha_c,x,t) &= \mathcal{H}[\widetilde{u}(x,t)] \\ &= \sum_{n=0}^{\infty} p^n\mathcal{H}[\widetilde{u}_n(x,t)] \\ &= [\mu + 2(1-\mu)\alpha_c][\max(Ax-B,0)E_\alpha(rt^\alpha) \\ &- \max(A,0)[E_\alpha(rt^\alpha) - E_\alpha(\tau t^\alpha)]], \end{aligned} \tag{124}$$

$$\begin{aligned} \mathcal{H}^{-1}[u^{gr}(\mu,\alpha_c,x,t)] = [\mu, 2-\mu][\max(Ax-B,0)E_\alpha(rt^\alpha) \\ - \max(A,0)[E_\alpha(rt^\alpha) - E_\alpha(\tau t^\alpha)]]. \end{aligned} \tag{125}$$

By using the μ-level sets representation theorem, we have

$$\begin{aligned} \widetilde{u}(x,t) &= \underset{\mu}{\cup}[\mu, 2-\mu][\max(Ax-B,0)E_\alpha(rt^\alpha) \\ &- \max(A,0)[E_\alpha(rt^\alpha) - E_\alpha(\tau t^\alpha)]] \\ &= (0,1,2)[\max(Ax-B,0)E_\alpha(rt^\alpha) \\ &- \max(A,0)[E_\alpha(rt^\alpha) - E_\alpha(\tau t^\alpha)]]. \end{aligned} \tag{126}$$

Secondly, the HPM is used to solving the Example 3.

$$D_t^{\alpha}\left[\sum_{n=0}^{\infty} p^n \mathcal{H}[\widetilde{u}_n(x,t)]\right] = p\left[\sum_{n=0}^{\infty} p^n \mathcal{H}[\widetilde{\Psi}_n(x,t)]\right], \tag{127}$$

where

$$\begin{aligned}\mathcal{H}[\widetilde{\Psi}_n(x,t)] = \mathcal{H}[&-\frac{\sigma^2}{2}x^2\frac{\partial^2\mathcal{H}[\widetilde{u}(x,t)]}{\partial x^2} \\ &-(r-\tau)x\frac{\partial\mathcal{H}[\widetilde{u}(x,t)]}{\partial x} + r\mathcal{H}[\widetilde{u}(x,t)],\end{aligned} \tag{128}$$

$$\sum_{n=0}^{\infty} p^n \mathcal{H}[\widetilde{u}_n(x,t)] = \mathcal{H}[\widetilde{u}(x,0)] + J^{\alpha}\left[p\left[\sum_{n=0}^{\infty} p^n \mathcal{H}[\widetilde{\Psi}_n(x,t)]\right]\right]. \tag{129}$$

After comparing the similar power coefficients of p, the following results can be obtained

$$\begin{aligned}
p^0 : \mathcal{H}[\widetilde{u}_0(x,t)] &= [\mu + 2(1-\mu)\alpha_c]\max(Ax-B,0),\\
p^1 : \mathcal{H}[\widetilde{u}_1(x,t)] &= J^{\alpha}\left[\mathcal{H}\left[\widetilde{\Psi}_0(x,t)\right]\right]\\
&= [\mu + 2(1-\mu)\alpha_c][-x\max(A,0)\frac{(r-\tau)t^{\alpha}}{\Gamma(\alpha+1)}\\
&+ \frac{(rt^{\alpha})}{\Gamma(\alpha+1)}\max(Ax-B,0)],\\
p^2 : \mathcal{H}[\widetilde{u}_2(x,t)] &= J^{\alpha}\left[\mathcal{H}\left[\widetilde{\Psi}_1(x,t)\right]\right]\\
&= [\mu + 2(1-\mu)\alpha_c][-x\max(A,0)\frac{(r^2-\tau^2)(t^{\alpha})^2}{\Gamma(2\alpha+1)}\\
&+ \frac{(rt^{\alpha})^2}{\Gamma(2\alpha+1)}\max(Ax-B,0)],\\
&\vdots\\
p^n : \mathcal{H}[\widetilde{u}_n(x,t)] &= J^{\alpha}\left[\mathcal{H}\left[\widetilde{\Psi}_{n-1}(x,t)\right]\right]\\
&= [\mu + 2(1-\mu)\alpha_c][-x\max(A,0)\frac{(r^n-\tau^n)(t^{\alpha})^n}{\Gamma(n\alpha+1)}\\
&+ \frac{(rt^{\alpha})^n}{\Gamma(n\alpha+1)}\max(Ax-B,0)].
\end{aligned} \tag{130}$$

So, we have

$$\begin{aligned}
\widetilde{u}(x,t) &= \bigcup_{\mu}[\mu, 2-\mu][\max(Ax-B,0)E_{\alpha}(rt^{\alpha})\\
&- \max(A,0)[E_{\alpha}(rt^{\alpha}) - E_{\alpha}(\tau t^{\alpha})]]\\
&= (0,1,2)[\max(Ax-B,0)E_{\alpha}(rt^{\alpha})\\
&- \max(A,0)[E_{\alpha}(rt^{\alpha}) - E_{\alpha}(\tau t^{\alpha})]].
\end{aligned} \tag{131}$$

Thirdly, the RPSM is used to solving the Example 3.

$$\mathcal{H}[\widetilde{u}(x,t)] = \sum_{n=0}^{\infty}\mathcal{H}[\widetilde{f}_n(x)]\frac{t^{\alpha n}}{\Gamma(1+n\alpha)}, \tag{132}$$

$$\mathcal{H}[\widetilde{u}_i(x,t)] = \sum_{n=0}^{i} \mathcal{H}[\widetilde{f}_n(x)]\frac{t^{n\alpha}}{\Gamma(1+n\alpha)}, \tag{133}$$

$$\mathcal{H}[\widetilde{f}_0(x)] = \mathcal{H}[\widetilde{u}_0(x,t)] = [\mu + 2(1-\mu)\alpha_c]\max(Ax-B,0). \tag{134}$$

The ith residual function as follows,

$$Res_i^{gr}(x,t,\mu,\alpha_c) = \frac{\partial^{\alpha}\mathcal{H}[\widetilde{u}_i(x,t)]}{\partial t^{\alpha}} + \frac{\sigma^2}{2}x^2\frac{\partial^2\mathcal{H}[\widetilde{u}_i(x,t)]}{\partial x^2} + (r-\tau)x\frac{\partial\mathcal{H}[\widetilde{u}_i(x,t)]}{\partial x} - r\mathcal{H}[\widetilde{u}_i(x,t)], \tag{135}$$

$$D_t^{(i-1)\alpha}Res_i^{gr}(x,0,\mu,\alpha_c) = 0. \tag{136}$$

Then, we obtain

$$\begin{aligned} Res_1^{gr}(x,t,\mu,\alpha_c) &= \frac{\partial^{\alpha}\mathcal{H}[\widetilde{u}_1(x,t)]}{\partial t^{\alpha}} + \frac{\sigma^2}{2}x^2\frac{\partial^2\mathcal{H}[\widetilde{u}_1(x,t)]}{\partial x^2} + (r-\tau)x\frac{\partial\mathcal{H}[\widetilde{u}_1(x,t)]}{\partial x} - r\mathcal{H}[\widetilde{u}_1(x,t)] \\ &= f_1^{gr}(x,\mu,\alpha_c) + \frac{\sigma^2}{2}x^2\left[D_x^2[f_0^{gr}(x,\mu,\alpha_c)] + D_x^2[f_1^{gr}(x,\mu,\alpha_c)]\frac{t^{\alpha}}{\Gamma(\alpha+1)}\right] \\ &+ (r-\tau)x\left(D_x[f_0^{gr}(x,\mu,\alpha_c)] + D_x[f_1^{gr}(x,\mu,\alpha_c)]\frac{t^{\alpha}}{\Gamma(\alpha+1)}\right) \\ &- r\left(f_0^{gr}(x,\mu,\alpha_c) + f_1^{gr}(x,\mu,\alpha_c)\frac{t^{\alpha}}{\Gamma(\alpha+1)}\right). \end{aligned} \tag{137}$$

By calculating $Res_1^{gr}(x,0,\mu,\alpha_c) = 0$, we obtain

$$f_1^{gr}(x,\mu,\alpha_c) = [\mu + 2(1-\mu)\alpha_c][r\max(Ax-B,0) - (r-\tau)x\max(A,0)], \tag{138}$$

$$\mathcal{H}[\widetilde{u}_1(x,t)] = [\mu + 2(1-\mu)\alpha_c]\left[\max(Ax-B,0) + [r\max(Ax-B,0) - (r-\tau)x\max(A,0)]\frac{t^{\alpha}}{\Gamma(\alpha+1)}\right]. \tag{139}$$

$$\begin{aligned} Res_2^{gr}(x,t,\mu,\alpha_c) &= \frac{\partial^{\alpha}\mathcal{H}[\widetilde{u}_2(x,t)]}{\partial t^{\alpha}} + \frac{\sigma^2}{2}x^2\frac{\partial^2\mathcal{H}[\widetilde{u}_2(x,t)]}{\partial x^2} + (r-\tau)x\frac{\partial\mathcal{H}[\widetilde{u}_2(x,t)]}{\partial x} - r\mathcal{H}[\widetilde{u}_2(x,t)] \\ &= f_1^{gr}(x,\mu,\alpha_c) + f_2^{gr}(x,\mu,\alpha_c)\frac{t^{\alpha}}{\Gamma(\alpha+1)} \\ &+ \frac{\sigma^2}{2}x^2\left[D_x^2[f_0^{gr}(x,\mu,\alpha_c)] + D_x^2[f_1^{gr}(x,\mu,\alpha_c)]\frac{t^{\alpha}}{\Gamma(\alpha+1)} + D_x^2[f_2^{gr}(x,\mu,\alpha_c)]\frac{t^{2\alpha}}{\Gamma(2\alpha+1)}\right] \\ &+ (r-\tau)x\left[D_x[f_0^{gr}(x,\mu,\alpha_c)] + D_x[f_1^{gr}(x,\mu,\alpha_c)]\frac{t^{\alpha}}{\Gamma(\alpha+1)} + D_x[f_2^{gr}(x,\mu,\alpha_c)]\frac{t^{2\alpha}}{\Gamma(2\alpha+1)}\right] \\ &- r\left(f_0^{gr}(x,\mu,\alpha_c) + f_1^{gr}(x,\mu,\alpha_c)\frac{t^{\alpha}}{\Gamma(\alpha+1)} + f_2^{gr}(x,\mu,\alpha_c)\frac{t^{2\alpha}}{\Gamma(2\alpha+1)}\right). \end{aligned} \tag{140}$$

By calculating $D_x^{\alpha}Res_2^{gr}(x,0,\mu,\alpha_c) = 0$, we obtain

$$f_2^{gr}(x,\mu,\alpha_c) = [\mu + 2(1-\mu)\alpha_c]\left[r^2\max(Ax-B,0) - (r^2-\tau^2)x\max(A,0)\right], \tag{141}$$

$$\begin{aligned} \mathcal{H}[\widetilde{u}_2(x,t)] &= [\mu + 2(1-\mu)\alpha_c][\max(Ax-B,0) + [r\max(Ax-B,0) - (r-\tau)x\max(A,0)]\frac{t^{\alpha}}{\Gamma(\alpha+1)} \\ &+ [r^2\max(Ax-B,0) - (r^2-\tau^2)x\max(A,0)]\frac{t^{2\alpha}}{\Gamma(2\alpha+1)}]. \end{aligned} \tag{142}$$

Continuing this way, one may find the values of $f_3^{gr}(x,\mu,\alpha_c), f_4^{gr}(x,\mu,\alpha_c),\ldots$, we obtain

$$\begin{aligned}\widetilde{u}(x,t) &= \underset{\mu}{\cup}[\mu,2-\mu][\max(Ax-B,0)E_\alpha(rt^\alpha)\\ &- \max(A,0)[E_\alpha(rt^\alpha)-E_\alpha(\tau t^\alpha)]]\\ &= (0,1,2)[\max(Ax-B,0)E_\alpha(rt^\alpha)\\ &- \max(A,0)[E_\alpha(rt^\alpha)-E_\alpha(\tau t^\alpha)]].\end{aligned} \tag{143}$$

Finally, the CFADM is used to solving the Example 3.

Let $L_\alpha = {}^{CF}D_*^\alpha = \frac{\partial^\alpha}{\partial t^\alpha}$ be a linear operator

$${}^{CF}D_*^\alpha\mathcal{H}[\widetilde{u}(x,t)] = -\frac{\sigma^2}{2}x^2\frac{\partial^2\mathcal{H}[\widetilde{u}(x,t)]}{\partial x^2} - (r-\tau)x\frac{\partial\mathcal{H}[\widetilde{u}(x,t)]}{\partial x} + r\mathcal{H}[\widetilde{u}(x,t)], \tag{144}$$

$$t^{1-\alpha}\partial_t\mathcal{H}[\widetilde{u}(x,t)] = -\frac{\sigma^2}{2}x^2\frac{\partial^2\mathcal{H}[\widetilde{u}(x,t)]}{\partial x^2} - (r-\tau)x\frac{\partial\mathcal{H}[\widetilde{u}(x,t)]}{\partial x} + r\mathcal{H}[\widetilde{u}(x,t)]. \tag{145}$$

By the inverse of operator L_α which is $L_\alpha^{-1} = \int_0^t \frac{1}{\zeta^{1-\alpha}}(.)d\zeta$, we get

$$\mathcal{H}[\widetilde{u}(x,t)] = \mathcal{H}[\widetilde{u}(x,0)] - L_\alpha^{-1}\left[\frac{\sigma^2}{2}x^2\frac{\partial^2\mathcal{H}[\widetilde{u}(x,t)]}{\partial x^2} + (r-\tau)x\frac{\partial\mathcal{H}[\widetilde{u}(x,t)]}{\partial x} - r\mathcal{H}[\widetilde{u}(x,t)]\right], \tag{146}$$

$$\mathcal{H}[\widetilde{u}(x,t)] = \sum_{n=0}^{\infty}\mathcal{H}[\widetilde{u}_n(x,t)]. \tag{147}$$

Also assumed in the Adomian decomposition method is that the nonlinear operator may be decomposed into an infinite polynomial series

$$\mathcal{N}[\mathcal{H}[\widetilde{u}(x,t)]] = \sum_{n=0}^{\infty}A_n, \tag{148}$$

where $A_n[\mathcal{H}(\widetilde{u})]$ are Adomian polynomials, which are defined as

$$A_n\mathcal{H}[(\widetilde{u}_0,\widetilde{u}_1,\widetilde{u}_2\ldots\widetilde{u}_n)] = \frac{1}{n!}\frac{d^n}{d\lambda^n}\left[\mathcal{N}\left(\sum_{i=0}^{n}\lambda^i\mathcal{H}[\widetilde{u}_i(x,t)]\right)\right]_{\lambda=0}, n=0,1,2,\cdots. \tag{149}$$

So, by using the Adomian decomposition method in conformable sense, we get

$$\begin{aligned}\mathcal{H}[\widetilde{u}_0(x,t)] &= [\mu+2(1-\mu)\alpha_c]\max(Ax-B,0),\\ \mathcal{H}[\widetilde{u}_1(x,t)] &= -L_\alpha^{-1}\left[\frac{\sigma^2}{2}x^2\frac{\partial^2\mathcal{H}[\widetilde{u}_0(x,t)]}{\partial x^2} + (r-\tau)x\frac{\partial\mathcal{H}[\widetilde{u}_0(x,t)]}{\partial x} - r\mathcal{H}[\widetilde{u}_0(x,t)]\right]\\ &= [\mu+2(1-\mu)\alpha_c][r\max(Ax-B,0)-(r-\tau)x\max(A,0)]\frac{t^\alpha}{\alpha},\\ \mathcal{H}[\widetilde{u}_2(x,t)] &= -L_\alpha^{-1}\left[\frac{\sigma^2}{2}x^2\frac{\partial^2\mathcal{H}[\widetilde{u}_1(x,t)]}{\partial x^2} + (r-\tau)x\frac{\partial\mathcal{H}[\widetilde{u}_1(x,t)]}{\partial x} - r\mathcal{H}[\widetilde{u}_1(x,t)]\right]\\ &= [\mu+2(1-\mu)\alpha_c][r^2\max(Ax-B,0)-(r^2-\tau^2)x\max(A,0)]\frac{(t^\alpha)^2}{2!\alpha^2},\end{aligned}$$

$$\mathcal{H}[\widetilde{u}_3(x,t)] = -L_\alpha^{-1}\left[\frac{\sigma^2}{2}x^2\frac{\partial^2\mathcal{H}[\widetilde{u}_2(x,t)]}{\partial x^2} + (r-\tau)x\frac{\partial\mathcal{H}[\widetilde{u}_2(x,t)]}{\partial x} - r\mathcal{H}[\widetilde{u}_2(x,t)]\right]$$

$$= [\mu + 2(1-\mu)\alpha_c][r^3\max(Ax-B,0) - (r^3-\tau^3)x\max(A,0)]\frac{(t^\alpha)^3}{3!\alpha^3},$$

$$\vdots$$

$$\mathcal{H}[\widetilde{u}_n(x,t)] = -L_\alpha^{-1}\left[\frac{\sigma^2}{2}x^2\frac{\partial^2\mathcal{H}[\widetilde{u}_{n-1}(x,t)]}{\partial x^2} + (r-\tau)x\frac{\partial\mathcal{H}[\widetilde{u}_{n-1}(x,t)]}{\partial x} - r\mathcal{H}[\widetilde{u}_{n-1}(x,t)]\right]$$

$$= [\mu + 2(1-\mu)\alpha_c][r^n\max(Ax-B,0) - (r^n-\tau^n)x\max(A,0)]\frac{(t^\alpha)^n}{n!\alpha^n}.$$

$$\begin{aligned}\widetilde{u}(x,t) &= \bigcup_\mu[\mu, 2-\mu][\max(Ax-B,0)e^{\frac{rt}{\alpha}} \\ &\quad - \max(A,0)(e^{\frac{rt}{\alpha}} - e^{\frac{\tau t}{\alpha}})] \\ &= (0,1,2)[\max(Ax-B,0)e^{\frac{rt}{\alpha}} \\ &\quad - \max(A,0)(e^{\frac{rt}{\alpha}} - e^{\frac{\tau t}{\alpha}})].\end{aligned} \tag{150}$$

In Tables 7–9, we show the $\mathcal{H}[\widetilde{u}(x,t)]$ and $max|\widetilde{Res}(x,t)|$ of ETHPM, HPM, RPSM, and CFADM between different values of x and t when the fractions $\alpha = 0.5,\ 0.75,\ 1$ and the parameters $\tau = 0.2,\ r = 0.25,\ A = 1, B = 10$, respectively. It is easy to see in the table that the value of $max|\widetilde{Res}(x,t)|$ increases with t when α, x is fixed, the value of $max|\widetilde{Res}(x,t)|$ increases with x when α, t is fixed and the value of $max|\widetilde{Res}(x,t)|$ increases with α when x, t is fixed.

In Figure 4, the picture shows the fuzzy approximate solution $\widetilde{u}(x,t)$ of the Black–Scholes equation at the fractional parameter $\alpha = 1$ and the auxiliary parameters $\mu = 0.5$, $\tau = 0.2, r = 0.25, A = 1, B = 10$.

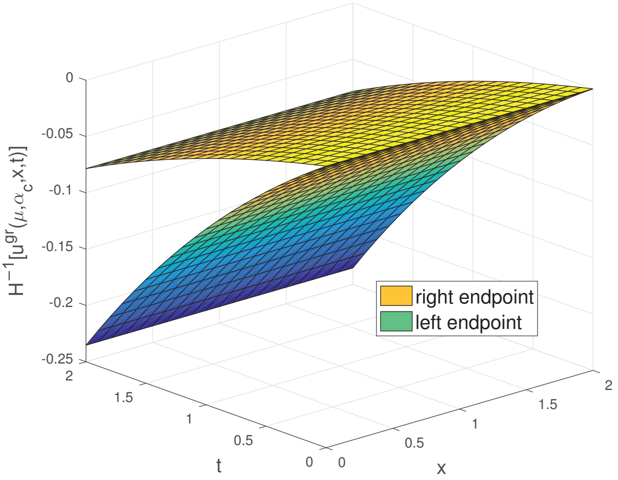

Figure 4. The fuzzy approximate solution $\widetilde{u}(x,t)$ of Example 3.

Table 7. $\mathcal{H}[\widetilde{u}(x,t)]$ and $max|\widetilde{Res}(x,t)|$ by ETHPM, HPM, RPSM, CFADM for $\alpha = 0.5, \tau = 0.2$, $r = 0.25, A = 1, B = 10$.

		ETHPM		**HPM**		**RPSM**		**CFADM**	
x	t	$\mathcal{H}[\widetilde{u}(x,t)]$	$max\|\widetilde{Res}(x,t)\|$	$\mathcal{H}[\widetilde{u}(x,t)]$	$max\|\widetilde{Res}(x,t)\|$	$\mathcal{H}[\widetilde{u}(x,t)]$	$max\|\widetilde{Res}(x,t)\|$	$\mathcal{H}[\widetilde{u}(x,t)]$	$max\|\widetilde{Res}(x,t)\|$
0.2	0.1	$-[\mu+2(1-\mu)\alpha_c]0.00405$	0.00061	$-[\mu+2(1-\mu)\alpha_c]0.00405$	0.00061	$-[\mu+2(1-\mu)\alpha_c]0.00405$	0.00061	$-[\mu+2(1-\mu)\alpha_c]0.00729$	0.02339
	0.2	$-[\mu+2(1-\mu)\alpha_c]0.00605$	0.00225	$-[\mu+2(1-\mu)\alpha_c]0.00605$	0.00225	$-[\mu+2(1-\mu)\alpha_c]0.00605$	0.00225	$-[\mu+2(1-\mu)\alpha_c]0.01093$	0.02490
	0.3	$-[\mu+2(1-\mu)\alpha_c]0.00772$	0.00416	$-[\mu+2(1-\mu)\alpha_c]0.00772$	0.00416	$-[\mu+2(1-\mu)\alpha_c]0.00772$	0.00416	$-[\mu+2(1-\mu)\alpha_c]0.01399$	0.02609
	0.4	$-[\mu+2(1-\mu)\alpha_c]0.00923$	0.00627	$-[\mu+2(1-\mu)\alpha_c]0.00923$	0.00627	$-[\mu+2(1-\mu)\alpha_c]0.00923$	0.00627	$-[\mu+2(1-\mu)\alpha_c]0.01676$	0.02712
	0.5	$-[\mu+2(1-\mu)\alpha_c]0.01063$	0.00852	$-[\mu+2(1-\mu)\alpha_c]0.01063$	0.00852	$-[\mu+2(1-\mu)\alpha_c]0.01063$	0.00852	$-[\mu+2(1-\mu)\alpha_c]0.01936$	0.02803
0.4	0.1	$-[\mu+2(1-\mu)\alpha_c]0.00811$	0.00122	$-[\mu+2(1-\mu)\alpha_c]0.00811$	0.00122	$-[\mu+2(1-\mu)\alpha_c]0.00811$	0.00122	$-[\mu+2(1-\mu)\alpha_c]0.01458$	0.04677
	0.2	$-[\mu+2(1-\mu)\alpha_c]0.01210$	0.00449	$-[\mu+2(1-\mu)\alpha_c]0.01210$	0.00449	$-[\mu+2(1-\mu)\alpha_c]0.01210$	0.00449	$-[\mu+2(1-\mu)\alpha_c]0.02185$	0.04980
	0.3	$-[\mu+2(1-\mu)\alpha_c]0.01544$	0.00832	$-[\mu+2(1-\mu)\alpha_c]0.01544$	0.00832	$-[\mu+2(1-\mu)\alpha_c]0.01544$	0.00832	$-[\mu+2(1-\mu)\alpha_c]0.02798$	0.05219
	0.4	$-[\mu+2(1-\mu)\alpha_c]0.01845$	0.01253	$-[\mu+2(1-\mu)\alpha_c]0.01845$	0.01253	$-[\mu+2(1-\mu)\alpha_c]0.01845$	0.01253	$-[\mu+2(1-\mu)\alpha_c]0.03353$	0.05424
	0.5	$-[\mu+2(1-\mu)\alpha_c]0.02127$	0.01704	$-[\mu+2(1-\mu)\alpha_c]0.02127$	0.01704	$-[\mu+2(1-\mu)\alpha_c]0.02127$	0.01704	$-[\mu+2(1-\mu)\alpha_c]0.04191$	0.06780
0.6	0.1	$-[\mu+2(1-\mu)\alpha_c]0.01216$	0.00182	$-[\mu+2(1-\mu)\alpha_c]0.01216$	0.00182	$-[\mu+2(1-\mu)\alpha_c]0.01216$	0.00182	$-[\mu+2(1-\mu)\alpha_c]0.02187$	0.07016
	0.2	$-[\mu+2(1-\mu)\alpha_c]0.01815$	0.00674	$-[\mu+2(1-\mu)\alpha_c]0.01815$	0.00674	$-[\mu+2(1-\mu)\alpha_c]0.01815$	0.00674	$-[\mu+2(1-\mu)\alpha_c]0.03278$	0.07470
	0.3	$-[\mu+2(1-\mu)\alpha_c]0.02316$	0.01249	$-[\mu+2(1-\mu)\alpha_c]0.02316$	0.01249	$-[\mu+2(1-\mu)\alpha_c]0.02316$	0.01249	$-[\mu+2(1-\mu)\alpha_c]0.04197$	0.07828
	0.4	$-[\mu+2(1-\mu)\alpha_c]0.02768$	0.01880	$-[\mu+2(1-\mu)\alpha_c]0.02768$	0.01880	$-[\mu+2(1-\mu)\alpha_c]0.02768$	0.01880	$-[\mu+2(1-\mu)\alpha_c]0.05029$	0.08136
	0.5	$-[\mu+2(1-\mu)\alpha_c]0.03190$	0.02556	$-[\mu+2(1-\mu)\alpha_c]0.03190$	0.02556	$-[\mu+2(1-\mu)\alpha_c]0.03190$	0.02556	$-[\mu+2(1-\mu)\alpha_c]0.05808$	0.08410

Table 8. $\mathcal{H}[\widetilde{u}(x,t)]$ and $max|\widetilde{Res}(x,t)|$ by ETHPM, HPM, RPSM, CFADM for $\alpha = 0.75, \tau = 0.2$, $r = 0.25, A = 1, B = 10$.

		ETHPM		**HPM**		**RPSM**		**CFADM**	
x	t	$\mathcal{H}[\widetilde{u}(x,t)]$	$max\|\widetilde{Res}(x,t)\|$	$\mathcal{H}[\widetilde{u}(x,t)]$	$max\|\widetilde{Res}(x,t)\|$	$\mathcal{H}[\widetilde{u}(x,t)]$	$max\|\widetilde{Res}(x,t)\|$	$\mathcal{H}[\widetilde{u}(x,t)]$	$max\|\widetilde{Res}(x,t)\|$
0.2	0.1	$-[\mu+2(1-\mu)\alpha_c]0.00205$	0.00128	$-[\mu+2(1-\mu)\alpha_c]0.00205$	0.00128	$-[\mu+2(1-\mu)\alpha_c]0.00205$	0.00128	$-[\mu+2(1-\mu)\alpha_c]0.00250$	0.02122

Table 8. *Cont.*

		ETHPM		HPM		RPSM		CFADM	
	0.2	$-[\mu+2(1-\mu)\alpha_c]0.00357$	0.00292	$-[\mu+2(1-\mu)\alpha_c]0.00357$	0.00292	$-[\mu+2(1-\mu)\alpha_c]0.00357$	0.00292	$-[\mu+2(1-\mu)\alpha_c]0.00436$	0.02209
	0.3	$-[\mu+2(1-\mu)\alpha_c]0.00501$	0.00472	$-[\mu+2(1-\mu)\alpha_c]0.00501$	0.00472	$-[\mu+2(1-\mu)\alpha_c]0.00501$	0.00472	$-[\mu+2(1-\mu)\alpha_c]0.00610$	0.02287
	0.4	$-[\mu+2(1-\mu)\alpha_c]0.00641$	0.00666	$-[\mu+2(1-\mu)\alpha_c]0.00641$	0.00666	$-[\mu+2(1-\mu)\alpha_c]0.00641$	0.00666	$-[\mu+2(1-\mu)\alpha_c]0.00779$	0.02360
	0.5	$-[\mu+2(1-\mu)\alpha_c]0.00779$	0.00871	$-[\mu+2(1-\mu)\alpha_c]0.00779$	0.00871	$-[\mu+2(1-\mu)\alpha_c]0.00779$	0.00871	$-[\mu+2(1-\mu)\alpha_c]0.00947$	0.02431
0.4	0.1	$-[\mu+2(1-\mu)\alpha_c]0.00409$	0.00257	$-[\mu+2(1-\mu)\alpha_c]0.00409$	0.00257	$-[\mu+2(1-\mu)\alpha_c]0.00409$	0.00257	$-[\mu+2(1-\mu)\alpha_c]0.00500$	0.04244
	0.2	$-[\mu+2(1-\mu)\alpha_c]0.00715$	0.00584	$-[\mu+2(1-\mu)\alpha_c]0.00715$	0.00584	$-[\mu+2(1-\mu)\alpha_c]0.00715$	0.00584	$-[\mu+2(1-\mu)\alpha_c]0.00872$	0.04417
	0.3	$-[\mu+2(1-\mu)\alpha_c]0.01001$	0.00945	$-[\mu+2(1-\mu)\alpha_c]0.01001$	0.00945	$-[\mu+2(1-\mu)\alpha_c]0.01001$	0.00945	$-[\mu+2(1-\mu)\alpha_c]0.01220$	0.04574
	0.4	$-[\mu+2(1-\mu)\alpha_c]0.01281$	0.01331	$-[\mu+2(1-\mu)\alpha_c]0.01281$	0.01331	$-[\mu+2(1-\mu)\alpha_c]0.01281$	0.01331	$-[\mu+2(1-\mu)\alpha_c]0.01559$	0.04721
	0.5	$-[\mu+2(1-\mu)\alpha_c]0.01558$	0.01742	$-[\mu+2(1-\mu)\alpha_c]0.01558$	0.01742	$-[\mu+2(1-\mu)\alpha_c]0.01558$	0.01742	$-[\mu+2(1-\mu)\alpha_c]0.01894$	0.04861
0.6	0.1	$-[\mu+2(1-\mu)\alpha_c]0.00614$	0.00385	$-[\mu+2(1-\mu)\alpha_c]0.00614$	0.00385	$-[\mu+2(1-\mu)\alpha_c]0.00614$	0.00385	$-[\mu+2(1-\mu)\alpha_c]0.00750$	0.06366
	0.2	$-[\mu+2(1-\mu)\alpha_c]0.01072$	0.00877	$-[\mu+2(1-\mu)\alpha_c]0.01072$	0.00877	$-[\mu+2(1-\mu)\alpha_c]0.01072$	0.00877	$-[\mu+2(1-\mu)\alpha_c]0.01308$	0.06626
	0.3	$-[\mu+2(1-\mu)\alpha_c]0.01502$	0.01417	$-[\mu+2(1-\mu)\alpha_c]0.01502$	0.01417	$-[\mu+2(1-\mu)\alpha_c]0.01502$	0.01417	$-[\mu+2(1-\mu)\alpha_c]0.01831$	0.06861
	0.4	$-[\mu+2(1-\mu)\alpha_c]0.01922$	0.01997	$-[\mu+2(1-\mu)\alpha_c]0.01922$	0.01997	$-[\mu+2(1-\mu)\alpha_c]0.01922$	0.01997	$-[\mu+2(1-\mu)\alpha_c]0.02338$	0.07081
	0.5	$-[\mu+2(1-\mu)\alpha_c]0.02338$	0.02613	$-[\mu+2(1-\mu)\alpha_c]0.02338$	0.02613	$-[\mu+2(1-\mu)\alpha_c]0.02338$	0.02613	$-[\mu+2(1-\mu)\alpha_c]0.02841$	0.07292

Table 9. $\mathcal{H}[\tilde{u}(x,t)]$ and $max|\widetilde{Res}(x,t)|$ by ETHPM, HPM, RPSM, CFADM for $\alpha = 1, \tau = 0.2$, $r = 0.25, A = 1, B = 10$.

		ETHPM		HPM		RPSM		CFADM	
x	t	$\mathcal{H}[\tilde{u}(x,t)]$	$max\|\widetilde{Res}(x,t)\|$	$\mathcal{H}[\tilde{u}(x,t)]$	$max\|\widetilde{Res}(x,t)\|$	$\mathcal{H}[\tilde{u}(x,t)]$	$max\|\widetilde{Res}(x,t)\|$	$\mathcal{H}[\tilde{u}(x,t)]$	$max\|\widetilde{Res}(x,t)\|$
0.2	0.1	$-[\mu+2(1-\mu)\alpha_c]0.00102$	0.02051	$-[\mu+2(1-\mu)\alpha_c]0.00102$	0.02051	$-[\mu+2(1-\mu)\alpha_c]0.00102$	0.02051	$-[\mu+2(1-\mu)\alpha_c]0.00102$	0.02051
	0.2	$-[\mu+2(1-\mu)\alpha_c]0.00209$	0.02102	$-[\mu+2(1-\mu)\alpha_c]0.00209$	0.02102	$-[\mu+2(1-\mu)\alpha_c]0.00209$	0.02102	$-[\mu+2(1-\mu)\alpha_c]0.00209$	0.02102
	0.3	$-[\mu+2(1-\mu)\alpha_c]0.00321$	0.02155	$-[\mu+2(1-\mu)\alpha_c]0.00321$	0.02155	$-[\mu+2(1-\mu)\alpha_c]0.00321$	0.02155	$-[\mu+2(1-\mu)\alpha_c]0.00321$	0.02155

Table 9. *Cont.*

		ETHPM		**HPM**		**RPSM**		**CFADM**	
	0.4	$-[\mu+2(1-\mu)\alpha_c]0.00438$	0.02209	$-[\mu+2(1-\mu)\alpha_c]0.00438$	0.02209	$-[\mu+2(1-\mu)\alpha_c]0.00438$	0.02209	$-[\mu+2(1-\mu)\alpha_c]0.00438$	0.02209
	0.5	$-[\mu+2(1-\mu)\alpha_c]0.00559$	0.02264	$-[\mu+2(1-\mu)\alpha_c]0.00559$	0.02264	$-[\mu+2(1-\mu)\alpha_c]0.00559$	0.02264	$-[\mu+2(1-\mu)\alpha_c]0.00559$	0.02264
0.4	0.1	$-[\mu+2(1-\mu)\alpha_c]0.00205$	0.04101	$-[\mu+2(1-\mu)\alpha_c]0.00205$	0.04101	$-[\mu+2(1-\mu)\alpha_c]0.00205$	0.04101	$-[\mu+2(1-\mu)\alpha_c]0.00205$	0.04101
	0.2	$-[\mu+2(1-\mu)\alpha_c]0.00418$	0.04205	$-[\mu+2(1-\mu)\alpha_c]0.00418$	0.04205	$-[\mu+2(1-\mu)\alpha_c]0.00418$	0.04205	$-[\mu+2(1-\mu)\alpha_c]0.00418$	0.04205
	0.3	$-[\mu+2(1-\mu)\alpha_c]0.00642$	0.04311	$-[\mu+2(1-\mu)\alpha_c]0.00642$	0.04311	$-[\mu+2(1-\mu)\alpha_c]0.00642$	0.04311	$-[\mu+2(1-\mu)\alpha_c]0.00642$	0.04311
	0.4	$-[\mu+2(1-\mu)\alpha_c]0.00875$	0.04419	$-[\mu+2(1-\mu)\alpha_c]0.00875$	0.04419	$-[\mu+2(1-\mu)\alpha_c]0.00875$	0.04419	$-[\mu+2(1-\mu)\alpha_c]0.00875$	0.04419
	0.5	$-[\mu+2(1-\mu)\alpha_c]0.01119$	0.04529	$-[\mu+2(1-\mu)\alpha_c]0.01119$	0.04529	$-[\mu+2(1-\mu)\alpha_c]0.01119$	0.04529	$-[\mu+2(1-\mu)\alpha_c]0.01894$	0.04861
0.6	0.1	$-[\mu+2(1-\mu)\alpha_c]0.00307$	0.06152	$-[\mu+2(1-\mu)\alpha_c]0.00307$	0.06152	$-[\mu+2(1-\mu)\alpha_c]0.00307$	0.06152	$-[\mu+2(1-\mu)\alpha_c]0.00307$	0.06152
	0.2	$-[\mu+2(1-\mu)\alpha_c]0.00628$	0.06307	$-[\mu+2(1-\mu)\alpha_c]0.00628$	0.06307	$-[\mu+2(1-\mu)\alpha_c]0.00628$	0.06307	$-[\mu+2(1-\mu)\alpha_c]0.00628$	0.06307
	0.3	$-[\mu+2(1-\mu)\alpha_c]0.00963$	0.06466	$-[\mu+2(1-\mu)\alpha_c]0.00963$	0.06466	$-[\mu+2(1-\mu)\alpha_c]0.00963$	0.06466	$-[\mu+2(1-\mu)\alpha_c]0.00963$	0.06466
	0.4	$-[\mu+2(1-\mu)\alpha_c]0.01313$	0.06628	$-[\mu+2(1-\mu)\alpha_c]0.01313$	0.06628	$-[\mu+2(1-\mu)\alpha_c]0.01313$	0.06628	$-[\mu+2(1-\mu)\alpha_c]0.01313$	0.06628
	0.5	$-[\mu+2(1-\mu)\alpha_c]0.01678$	0.06793	$-[\mu+2(1-\mu)\alpha_c]0.01678$	0.06793	$-[\mu+2(1-\mu)\alpha_c]0.01678$	0.06793	$-[\mu+2(1-\mu)\alpha_c]0.01678$	0.06793

5. Conclusions

In this research, we handled the approximate solution of the fuzzy time-fractional Black–Scholes' European option pricing equation by using the homotopy transforming method under gr-differentiability circumstances. According to the comparative analysis of the four methods, it can be seen that ETHPM doesn't require fractional differentiation or integration operations, which reduces the complexity and the amount of computation. Our method is better suited to computer programming implementations.

Author Contributions: Conceptualization, J.Z. and Y.W.; methodology, J.Z. and Y.W.; Analysis, J.Z. and S.Z.; Writing—original draft preparation, J.Z. and Y.W.; Discussion, J.Z., S.Z. and Y.W. All authors have read and agreed to the published version of the manuscript.

Funding: This research was funded by Shaanxi Provincial Key Research and Development Program (Nos. 2021SF-480).

Institutional Review Board Statement: Not applicable.

Informed Consent Statement: Not applicable.

Data Availability Statement: Not applicable.

Acknowledgments: The authors would like to thank the editors and anonymous reviewers for their detailed and valuable suggestions and comments, which improved the quality of the original manuscript.

Conflicts of Interest: The authors declare no conflict of interest.

References

1. Black, F.; Scholes, M. The pricing of options and corporate liabilities. *J. Political Econ.* **1973**, *81*, 637–654. [CrossRef]
2. Zhang, S.M.; Wang, L.H. A fast Fourier transform technique for pricing European options with stochastic volatility and jump risk. *Math. Probl. Eng.* **2012**, *2012*, 291–300. [CrossRef]
3. Zhang, S.M.; Wang, L.H. A fast numerical approach to option pricing with stochastic interest rate, stochastic volatility and double jumps. *Commun. Nonlinear Sci. Numer. Simul.* **2013**, *18*, 1832–1839. [CrossRef]
4. Zhang, S.M.; Wang, L.H. Fast Fourier transform option pricing with stochastic interest rate, stochastic volatility and double jumps. *Appl. Math. Comput.* **2013**, *219*, 10928–10933. [CrossRef]
5. Rezaei, M.; Yazdanian, A.R.; Ashrafi, A.; Mahmoudi, S.M. Numerical pricing based on fractional Black–Scholes equation with time-dependent parameters under the CEV model: Double barrier options. *Comput. Math. Appl.* **2021**, *90*, 104–111. [CrossRef]
6. Hussain, J.; Khan, S. On numerical pricing of put-call parities for Asian options driven by new time-fractional Black–Scholes evolution equation. *Filomat* **2021**, *35*, 4427–4450. [CrossRef]
7. Cheridito, P. Arbitrage in fractional Brownian motion models. *Appl. Math. Comput.* **2003**, *7*, 533–553. [CrossRef]
8. Guo, C.; Fang, S.; He, Y. Derivation and Application of Some Fractional Black–Scholes Equations Driven by Fractional G-Brownian Motion. *Comput. Econ.* **2022**, 1–25. [CrossRef]
9. Oldham, K.B.; Spanier, J. The fractional calculus. *Tmath. Gaz.* **1974**, *56*, 396–400.
10. Machado, J.T. Numerical calculation of the left and right fractional derivatives. *J. Comput. Phys.* **2015**, *293*, 96–103. [CrossRef]
11. Rezapour, S.; Etemad, S.; Mohammadi, H. A mathematical analysis of a system of Caputo–Fabrizio fractional differential equations for the anthrax disease model in animals. *Adv. Differ. Equ.* **2020**, *2020*, 1–30. [CrossRef]
12. Tuan, N.H.; Mohammadi, H.; Rezapour, S. A mathematical model for COVID-19 transmission by using the Caputo fractional derivative. *Chaos Solitons Fractals* **2020**, *140*, 110107. [CrossRef]
13. Mohammadi, H.; Rezapour, S.; Jajarmi, A. On the fractional SIRD mathematical model and control for the transmission of COVID-19: The first and the second waves of the disease in Iran and Japan. *ISA Trans.* **2021**, *124*, 103–114. [CrossRef]
14. Baleanu, D.; Aydogn, S.M.; Mohammadi, H.; Rezapour, S. On modelling of epidemic childhood diseases with the Caputo-Fabrizio derivative by using the Laplace Adomian decomposition method. *Alex. Eng. J.* **2020**, *59*, 3029–3039. [CrossRef]
15. Mohammadi, H.; Kumar, S.; Rezapour, S.; Etemad, S. A theoretical study of the Caputo–Fabrizio fractional modeling for hearing loss due to Mumps virus with optimal control. *Chaos Solitons Fractals* **2021**, *144*, 110668. [CrossRef]
16. Mazandarani, M.; Pariz, N.; Kamyad, A.V. Granular differentiability of fuzzy-number-valued functions. *IEEE Trans. Fuzzy Syst.* **2018**, *26*, 310–323. [CrossRef]
17. Mazandarani, M.; Pariz, N. Sub-optimal control of fuzzy linear dynamical systems under granular differentiability concept. *ISA Trans.* **2018**, *76*, 1–17. [CrossRef]
18. Mazandarani, M.; Zhao, Y. Fuzzy Bang-Bang control problem under granular differentiability. *J. Frankl. Inst.* **2018**, *355*, 4931–4951. [CrossRef]
19. He, J.H. Homotopy perturbation technique. *Comput. Methods Appl. Mech. Eng.* **1999**, *178*, 257–262. [CrossRef]
20. He, J.H. A coupling method of a homotopy technique and a perturbation technique for non-linear problems. *Int. J. Non-Linear Mech.* **2000**, *35*, 37–43. [CrossRef]
21. Gavurin, M.K. Nonlinear functional equations and continuous analogues of iteration methods. *Izv. Vyss. Uchebnykh Zaved. Mat.* **1958**, *5*, 18–31.
22. He, J.H. Application of homotopy perturbation method to nonlinear wave equations. *Chaos Solitons Fractals* **2005**, *26*, 695–700. [CrossRef]
23. Das, S.; Gupta, P.K. An approximate analytical solution of the fractional diffusion equation with absorbent term and external force by homotopy perturbation method. *Z. Naturforschung A* **2010**, *65*, 182–190. [CrossRef]
24. Liao, S.J.; Tan, Y.A. A general approach to obtain series solutions of nonlinear differential equations. *Stud. Appl. Math.* **2007**, *119*, 297–354. [CrossRef]
25. Biazar, J.; Eslami, M. A new homotopy perturbation method for solving systems of partial differential equations. *Comput. Math. Appl.* **2011**, *62*, 225–234. [CrossRef]
26. Filobello-Nino, U.; Vazquez-Leal, H.; Khan, Y. Laplace transform-homotopy perturbation method as a powerful tool to solve nonlinear problems with boundary conditions defined on finite intervals. *Comput. Appl. Math.* **2015**, *34*, 1–16. [CrossRef]
27. Chen, W.; Wang, S. A 2nd-order ADI finite difference method for a 2D fractional Black–Scholes equation governing European two asset option pricing. *Math. Comput. Simul.* **2020**, *171*, 279–293. [CrossRef]
28. Elzaki, T.M.; Hilal, E.M. Solution of linear and nonlinear partial differential equations using mixture of Elzaki transform and the projected differential transform method. *Math. Theory Model.* **2012**, *2*, 50–59.
29. Elzaki, T.M. The new integral transform Elzaki transform. *Glob. J. Pure Appl. Math.* **2011**, *7*, 57–64.

30. Sedeeg, A.K.H. A coupling Elzaki transform and homotopy perturbation method for solving nonlinear fractional Heat-Like equations. *Am. J. Math. Comput. Model.* **2016**, *1*, 15–20.
31. Zhang, W.G.; Li, Z.; Liu, Y.J.; Zhang, Y. Pricing European option under fuzzy mixed fractional Brownian motion model with jumps. *Comput. Econ.* **2021**, *58*, 483–515. [CrossRef]
32. Baleanu, D.; Diethelm, K.; Scalas, E.; Trujillo, J. *Fractional Calculus: Models and Numerical Methods*; World Scientific: Singapore, 2012; Volume 3.
33. Keshavarz, E.; Ordokhani, Y.; Razzaghi, M. Bernoulli wavelet operational matrix of fractional order integration and its applications in solving the fractional order differential equations. *Appl. Math. Model.* **2014**, *38*, 6038–6051. [CrossRef]
34. Rahimkhani, P.; Ordokhani, Y.; Babolian, E. Numerical solution of fractional pantograph differential equations by using generalized fractional-order Bernoulli wavelet. *J. Comput. Appl. Math.* **2016**, *309*, 493–510. [CrossRef]
35. Khalil, R.; Al Horani, M.; Yousef, A.; Sababheh, M. A new definition of fractional derivative. *J. Comput. Appl. Math.* **2014**, *264*, 65–70. [CrossRef]
36. Abdeljawad, T. On conformable fractional calculus. *J. Comput. Appl. Math.* **2015**, *279*, 57–66. [CrossRef]
37. Haubold, H.J.; Mathai, A.M.; Saxena, R.K. Mittag-Leffler functions and their applications. *J. Appl. Math.* **2011**, *2011*, 298628. [CrossRef]
38. Bhadane, P.; Ghadle, K.P.; Hamoud, A.A. Approximate solution of fractional Black-Schole's European option pricing equation by using ETHPM. *Nonlinear Funct. Anal. Appl.* **2020**, *25*, 331–344. [CrossRef]
39. Kumar, S.; Kumar, D.; Singh, J. Numerical computation of fractional Black–Scholes equation arising in financial market. *Egypt. J. Basic Appl. Sci.* **2014**, *1*, 177–183. [CrossRef]
40. Jena, R.M.; Chakraverty, S. A new iterative method based solution for fractional Black–Scholes option pricing equations (BSOPE). *SN Appl. Sci.* **2019**, *1*, 1–11. [CrossRef]
41. Yavuz, M.; Özdemir, N. A different approach to the European option pricing model with new fractional operator. *Math. Model. Nat. Phenom.* **2018**, *13*, 12. [CrossRef]

fractal and fractional

Article

Numerical Investigation of Fractional Step-Down ELS Option

Xinpei Wu [1], Shuai Wen [2], Wei Shao [3] and Jian Wang [4,5,*,†]

[1] Department of Mathematics and Applied Mathematics, Reading Academy, Nanjing University of Information Science and Technology, Nanjing 210044, China
[2] School of Mathematics, Harbin Institute of Technology, Harbin 150001, China
[3] School of Economics, Nanjing University of Finance and Economics, Nanjing 210023, China
[4] Center for Applied Mathematics of Jiangsu Province, Nanjing University of Information Science and Technology, Nanjing 210044, China
[5] Jiangsu International Joint Laboratory on System Modeling and Data Analysis, Nanjing University of Information Science and Technology, Nanjing 210044, China
* Correspondence: 003328@nuist.edu.cn
† Current address: School of Mathematics and Statistics, Nanjing University of Information Science and Technology, Nanjing 210044, China.

Abstract: In this paper, we use the finite difference methods to explore step-down Equity Linked Securities (ELS) options under the fractional Black-Scholes model. We establish Crank-Nicolson scheme under one asset and study the impact of Hurst exponent (H) on return of repayment under fixed stock price. We also explore the impact of stock price on return of repayment under different H. Through numerical experiments, it is found that the return of repayment of options is related to H, and the result of difference scheme will increase with the increase of H. In the case of two assets, we establish implicit scheme, and in the case of three assets, we use operator splitting method (OSM) method to establish semi-implicit scheme. We get the result that the H also influences the return of repayment in two and three assets. We also conduct Greeks analysis. Through Greeks analysis, we find that the long-term correlation of stocks has a huge impact on investment gains or losses. Therefore, we take historical volatility (fractal exponents) into account which can significantly reduce risk and increase revenue for investors.

Keywords: fractional Black-Scholes model; ELS; finite difference scheme

Citation: Wu, X.; Wen, S.; Shao, W.; Wang, J. Numerical Investigation of Fractional Step-Down ELS Option. *Fractal Fract.* **2023**, *7*, 126. https://doi.org/10.3390/fractalfract7020126

Academic Editor: Leung Lung Chan

Received: 16 December 2022
Revised: 17 January 2023
Accepted: 18 January 2023
Published: 30 January 2023

1. Introduction

Options originated in the United States and European markets in the late 18th century, but it was not until the 1970s that options trading developed rapidly with the unification and standardization of the trading of options contracts. In recent decades, with the repaid development of economy, the investment risk of financial market is also increasing, and investors are gradually keen to invest in options with hedging, management and analysis function. Therefore, more and more new options have emerged, which not only enrich the financial market, but also meet the needs of a large number of investors to avoid risks. Equity Linked Securities (ELS) is a kind of hybrid debt securities. As one of the most popular derivatives in structured financial instrument, its annual issuance scale exceeds 5 trillion US dollars. Step-down ELS option contains knocks-in and knock-out and the option price will gradually decrease with time. In addition, ELS option products can be based on an underlying asset, such as the Shanghai 50 index. It can also be based on two or three basic assets at the same time, such as Shanghai 50 index, Kospi 200 index, Hang Seng index, etc. Chen and Kensinger [1] studied the pricing of American ELS options and found that the variable interest paid by ELS is related to the performance of S & P 500 stock market index. Baubonis et al. [2] used numerical algorithm to price ELS options. After that, Kim et al. [3] used a new finite difference method to solve the three assets pricing problem based on the operator splitting method which is used by Jeong et al. [4].

Bachelier [5] established many bond price motion models under Brown motion to describe the price return of stock. Because of the negative value of the results obtained from the Brownian motion, Sumuelson [6] proposed a geometric Brownian motion model. Since the 1970s, Black and Scholes [7] gave European call option pricing formula, the research results of options have been increasing, but the results of option pricing research are mainly obtained under the geometric Brownian motion. But in reality, the changes of the target asset price described by the traditional geometric Brownian motion are not necessarily satisfied with the normal, independent increment and continuous path. Mandelbrot and Ness [8] proved that the distribution of capital market income is not symmetrical and does not obey normal distribution. Therefore, some scholars have focused on the study of options under fractional Brownian motion [9,10] or improve reaserch methods [11]. Peter [12] considered that the characteristics of fractional Brownian motion, such as long memory, thick tail and self similarity, can describe the changes of asset prices in financial markets, and puts forward the fractal market hypothesis. Seidler [13] had proved in his paper that the logarithmic return of financial assets has the characteristics of asymmetry, peak and thick tail, capital market mutation or reversal, deviation and so on. But compared with the traditional Brownian motion, the fractional Brownian motion can well describe these characteristics. At the same time, many financial products in financial market have fractal structure [14–17]. Necula [18] studied European option under fractional Brownian motion and gave the corresponding pricing formula. Liu and Yang [19] studied the European option on dividend-paying stock under fractional Brownian motion which is a new option form. Murwaningtyas et al. [20] studied the European option pricing problem under mixed fractional Brownian motion which includes fractional and geometric, and took the method based on Fourier transformation and quasi conditional expectation to solve the problem. Finally, them gave a formula to calculate the European call option. Jian Wang et al. [21] used Monte Carlo method to study ELS options under fractional Brownian motion and compared the results with those of ELS options and actual results under traditional geometric Brownian motion. Ali et al. [22] developed new group iterative schemes for the numerical solution of two-dimensional anomalous fractional sub-diffusion equation subject to specific initial and Dirichlet boundary conditions. Oderinu et al. [23] considered the nature of these time-fractional differential equations are in sense of Caputo. Nikan et al. [24] addressed the solution of the Rayleigh–Stokes problem for an edge in a generalized Oldroyd-B fluid using fractional derivatives and the radial basis function-generated finite difference (RBF-FD) method. Golbabai et al. [25] considered a partial integro-differential equation (PIDE) problem with a free boundary. Golbabai et al. [26] provided methods for accurate modeling of anomalous diffusion and transport dynamics in determined multifaceted systems. Golbabai et al. [27] investigated the pricing of double barrier options when the price change of the underlying is considered as a fractal transmission system. Golbabai et al. [28] managed to determine the numerical solution of the time fractional Black–Scholes model (TFBSM) by using a truly mesh-free scheme. Nikan et al. [29] proposed an efficient and modified local mesh-less method for the numerical simulation of the TFBSE.

The results of fractional Brownian motion are more close to the actual results. It also shows that the asymmetry, peak thick tail and bias of fractional Brownian motion are more in line with the actual situation. Therefore, we consider the finite difference method to study ELS option under fractional Brownian motion. In order to better observe the financial market, issues must be considered in actual operations. At present, under the environment of the rapid economic development, various financial markets gradually become active, and the demand for investment continues to increase. The resource allocation has become very important. According to the efficiency and risk characteristics of the markets, investors can better price assets, optimize the risk control and perfect their investment portfolios more reasonably with the model we proposed. The efficiency of the market can be used in the pricing of assets and the allocation of resources. Its importance is self-evident in the financial market. Notice that the financial market is not simple linear, it has a complex structure inside, and the fractal market hypothesis can describe the nonlinear structure inside the market. Therefore our model can identify the market much more accurately and can benefit investors profoundly.

The structure and content of this paper are as follows. In Section 2, we give the definition of fractional Brownian motion and establish the mathematical model of fractional step-down ELS. In Section 3, we establish a finite difference scheme for the mathematical model, and carry out numerical experiments in Section 4. Finally, we give the experimental conclusion in Section 5.

2. Fractional Step-Down ELS Model

ELS is a structured product which includes two processes of knock-in and knock-out. Its trading principle is based on financial assets. The return of ELS depends on three forms: early redemption, final redemption and maturity redemption. For one asset, if the price date of the asset at the first exercise is higher than the predetermined exercise price, ELS will give the specified exercise price for early redemption, and the contract will be terminated. Otherwise, the contract will continue to be judged until the next expiration date. If the contract fails to be redeemed in advance when it matures, the return on investment depends on whether the contract meets the knock-in-barrier. When the underlying asset does not reach the knock-in-barrier, ELS gives a fixed value return determined by the fictitious interest rate as the maturity redemption. Otherwise, the final redemption will be made at the asset price on the maturity date.

The trading mechanism of fractional step-down ELS is the same as ELS, only in the holding stage, it meets the conditions of fractional Black-Scholes model. Step-down ELS option means option price gradually decreases with time. Next, we introduce fractional Brownian motion and establish fractional step-down ELS model under different assets, and give the corresponding parameters.

2.1. Fractional Brownian Motion

We suppose that the random process $\{B(t), t \geq 0\}$ is Brownian motion, then fractional Brownian motion is to modify $B(t)$ in Brownian motion to $B^H(t)$ with parameter Hurst exponent (H). H is the earliest statistical measure proposed by Hu and Oksendal [30] applied to fractal analysis. In time series analysis, using H as a measure, we can see how a time series has a long memory and moves irregularly. In fractional Brownian motion, a larger H value indicates a stronger fluctuation trend. Now we define the following: let (Ω, F, P) be a probability space and H be a constant on $(0,1)$. If the one dimensional Gaussian process satisfies:

- $B_0^H = E\left[B_t^H\right]$, for any $t > 0$.
- $E\left(B_t^H B_s^H\right) = \frac{1}{2}\left\{t^{2H} + s^{2H} - |t-s|^{2H}\right\}$, for any $t, s > 0$.

The Gaussian process B_t^H is called fractional Brownian motion with H. E is the mathematical expectation of probability measure p. The function of B_t^H is:

$$p\left(B_t^H - B_0^H \leq x\right) = \frac{1}{\sqrt{2\pi t^{2H}}} \int_{-\infty}^{S} exp\left(-\frac{S^2}{2t^{2H}}\right) dS, \forall t \geq 0. \tag{1}$$

At the same time, there are two important properties of fractional Brownian motion.

1. Fractional Brownian motion has self-similarity. For any $H \in (0,1)$ and $\alpha > 0$, $B_{\alpha t}^H$ and αB_t^H have the same finite-dimensional distribution.
2. When $H = 0.5$, it is the standard Brownian motion. When $H > 0.5$, B_t^H has a long-term dependence. When $0 < H < 0.5$, B_t^H has anti persistence.

If the underlying asset price $S(t)$ satisfies:

$$dS(t) = \mu(t)S(t) + \sigma(t)S(t)dB_t^H. \tag{2}$$

Then $S(t)$ is said to obey geometric fractional Brownian motion. $\mu(t)$ and $\sigma(t)$ represent the forecast return and volatility of the risk asset price respectively. Under the risk neutral measure, μ replaces with risk-free rate r. Equation (2) can be changed to Equation (3):

$$dS(t) = r(t)S(t) + \sigma(t)S(t)dB_t^H. \tag{3}$$

If $r(t) = r$ and $\sigma(t) = \sigma$ are constants, then Equation (3) can be changed to Equation (4):

$$dS(t) = rS(t) + \sigma S(t)dB_t^H. \tag{4}$$

We call the underlying asset price $S(t)$ is an $It\hat{o}$ type fractional Black-Scholes market when it satisfies the usual Black-Scholes model conditions and obeys geometric fractional Brownian motion. Hu and Oksendal [30] proved that the market is complete and there is no arbitrage.

2.2. Fractional Step-Down ELS Model of One Asset

We first give the main parameters of fractional step-down ELS option under one asset through Table 1.

Table 1. Parasmeters of fractional step-down ELS.

Hurst Exponent	**Strike Price**	**Underlying Asset Price**
H	K	S
Maturity	**Knock-in-barrier**	**Dummy**
T	D	d
Numer of observation dates	**Face value**	**Strike date**
n	F	δ
Volatility	**Risk-free rate**	**Coupon rate**
σ	r	β

In the holding stage, the asset satisfies the fractional Black-Scholes model, therefore, the change of asset satisfies the fractional Black-Scholes partial differential equation (PDE). Through establishing hedge techniques and $It\hat{o}$ fractional formula, we can get the fractional Black-Schoels PDE.

$$\frac{\partial V}{\partial t} + H\Delta t^{2H-1} S^2 \sigma^2 \frac{\partial^2 V}{\partial S^2} + rS\frac{\partial V}{\partial S} - rV = 0. \tag{5}$$

In Equation (5), $V = V(S,t)$ represents the return of repayment and Δt represents time step of T. $\phi(S)$ represents V when $t = T$. To transform the backward-in-time in PDE into forward-in-time, we take $\tau = T - t$ and obtain the PDE with initial value problem.

$$\begin{cases} \frac{\partial V}{\partial \tau} = H\Delta t^{2H-1} S^2 \sigma^2 \frac{\partial^2 V}{\partial S^2} + rS\frac{\partial V}{\partial S} - rV, \quad \tau \in (0,T), S \in [0,+\infty), \\ V(S,0) = \phi(S). \end{cases} \tag{6}$$

In the exercise stage, its judging form is the same as that of ELS. We assume that there are n strike prices, n coupon rates and n strike dates. At the same time, we set $S(t)$ to represent the value of the underlying asset at time t, $S(0)$ is the price at the initial time, and the above corresponding symbols are:

$$K_1 \geq K_2 \geq \ldots \geq K_n, \beta_1 \leq \beta_2 \leq \ldots \leq \beta_n, \delta_1 \leq \delta_2 \leq \ldots \leq \delta_n.$$

It is worth noting that when comparing with the execution price, we use the ratio of the underlying asset price to the initial price. Therefore, judgment conditions of exercise stage can be expressed as follows.

$$V(S,t)=\begin{cases} F(1+\beta_1), & if\ S(t_1)\geq K_1,\\ F(1+\beta_2), & if\ K_2\leq S(t_2)\leq K_1, D\leq S(t_1)\leq K_1,\\ \dots & \dots\\ F(1+\beta_n), & if\ K_n\leq S(t_n)\leq\dots\leq K_1,\dots D\leq S(t_{n-1})\leq K_{n-1},\\ F(1+d), & otherwise.\end{cases}$$

2.3. Fractional Step-Down ELS Model of Two Assets

In two assets, we let x and y denote the price of two underlying assets and H in x direction and y direction are expressed as H_x and H_y. The symbols of other parameters remain unchanged. In the holding stage, for $(x,y)\in\Phi$, $t\in[0,T]$, the return of repayment $V(x,y,t)$ follows fraction Black-Scholes partial differential equation (PDE):

$$V_t+rxV_x+ryV_y+H_x\Delta t^{2H_x-1}\sigma_x^2x^2V_{xx}$$

$$+H_y\Delta t^{2H_y-1}\sigma_y^2y^2V_{yy}+\big(H_x+H_y\big)\Delta t^{H_x+H_y-1}\rho_{xy}\sigma_x\sigma_yV_{xy}-rV=0.$$

In this equation, σ_x, σ_y represent the volatility of x and y respectively and ρ_{xy} represents the correlation value between x and y. We also take $\tau=T-t$ and $\vartheta(x,y)$ represents V when $t=T$. We obtain the PDE with initial value problem.

$$\begin{cases} V_\tau=rxV_x+ryV_y+H_x\Delta t^{2H_x-1}\sigma_x^2x^2V_{xx}\\ +H_y\Delta t^{2H_y-1}\sigma_y^2y^2V_{yy}+\\ \big(H_x+H_y\big)\Delta t^{H_x+H_y-1}\rho_{xy}\sigma_x\sigma_yxyV_{xy}-rV, \quad (x,y,\tau)\in\Phi \text{ times } [0,T],\\ V(x,y,0)=\vartheta(x,y).\end{cases} \tag{7}$$

In the exercise stage, the fractional step-down ELS of two assets is different from that of one asset. The base price of two assets' fractional step-down ELS is expressed by the minimum value of two underlying assets. If the minimum value is larger than or equal to the strike price at the strike date, the contract will be terminated. If the early redemption fails on the maturity date, the return depends on whether the minimum value of the two underlying assets reaches the knock-in-barrier. Therefore, We take $u_i=min\{x(t_i),y(t_i),i=1,2,\dots,n\}$ and judgment conditions of exercise stage can be expressed as follows.

$$V(x,y,t)=\begin{cases} F(1+\beta_1), & if\ u_1\geq K_1,\\ F(1+\beta_2), & if\ K_2\leq u_2\leq K_1, D\leq u_1\leq K_1,\\ \dots & \dots\\ F(1+\beta_n), & if\ K_n\leq u_n\leq K_{n-1}\leq\dots\leq K_1,\dots, D\leq u_{n-1}\leq K_{n-1},\\ F(1+d), & otherwise.\end{cases}$$

2.4. Fractional Step-Down ELS Model of Three Assets

In three assets, we let x, y and z denote the price of three underlying assets and H in direction of x, y and z are expressed as H_x, H_y and H_z. The symbols of other parameters remain unchanged. In the holding stage, for $(x,y,z)\in\Psi$, $t\in[0,T]$, the return of repayment $V(x,y,z,t)$ follows fractional Black-Scholes PDE:

$$V_t+rxV_x+ryV_y+rzV_z$$

$$+H_x\Delta t^{2H_x-1}\sigma_x^2x^2V_{xx}+H_y\Delta t^{2H_y-1}\sigma_y^2y^2V_{yy}$$

$$+H_z\Delta t^{2H_z-1}\sigma_z^2 z^2 V_{zz} + \left(H_x + H_y\right)\Delta t^{H_x+H_y-1}\rho_{xy}\sigma_x\sigma_y xyV_{xy}$$

$$+\left(H_y + H_z\right)\Delta t^{H_y+H_z-1}\rho_{yz}\sigma_y\sigma_z yzV_{yz}$$

$$+(H_x + H_z)\Delta t^{H_x+H_z-1}\rho_{xz}\sigma_x\sigma_z xzV_{xz} - rV = 0.$$

In this equation, σ_x, σ_y, σ_z represent the volatility of x, y and z respectively. ρ_{xy}, ρ_{yz}, ρ_{zx} represent the correlation value between two subscript assets variables. We also take $\tau = T - t$ and $\psi(x,y,z)$ represents V when $t = T$. We obtain the PDE with initial value problem.

$$\begin{cases} V_\tau = rxV_x + ryV_y + rzV_z \\ +H_x\Delta t^{2H_x-1}\sigma_x^2 x^2 V_{xx} + H_y\Delta t^{2H_y-1}\sigma_y^2 y^2 V_{yy} \\ +H_z\Delta t^{2H_z-1}\sigma_z^2 z^2 V_{zz} + \left(H_x + H_y\right)\Delta t^{H_x+H_y-1}\rho_{xy}\sigma_x\sigma_y xyV_{xy} \\ +\left(H_y + H_z\right)\Delta t^{H_y+H_z-1}\rho_{yz}\sigma_y\sigma_z yzV_{yz} \\ +(H_x + H_z)\Delta t^{H_x+H_z-1}\rho_{xz}\sigma_x\sigma_z xzV_{xz} - rV = 0, \\ (x,y,z,\tau) \in \Psi \text{ times } [0,T], \\ V(x,y,z,0) = \psi(x,y,z). \end{cases} \tag{8}$$

In the exercise stage, the fractional step-down ELS of three assets is similar to that of two assets. The base price of two assets' fractional step-down ELS is expressed by the minimum value of three underlying assets. Therefore, judgment conditions of exercise stage can be expressed as follows.

$$V(x,y,z,t) = \begin{cases} F(1+\beta_1), & if\ l_1 \geq K_1, \\ F(1+\beta_2), & if\ K_2 \leq l_2 \leq K_1, D \leq l_1 \leq K_1, \\ \ldots & \ldots \\ F(1+\beta_n), & if\ K_n \leq l_1 \leq K_{n-1} \leq \ldots \leq K_1,\ldots,D \leq l_1 \leq K_{n-1}, \\ F(1+d), & otherwise, \end{cases}$$

where, $l_i = min\{x(t_i), y(t_i), z(t_i), i = 1,2,\ldots,n\}$.

3. Numerical Method

In the holding stage of fractional step-down ELS option. The chang of its return satisfies the fractional Black-Scholes equation. We consider using the finite difference method to solve the initial problem. We establish Crank-Nicolson scheme under one asset and establish implicit scheme under two assets, and in the case of three assets, we use operator splitting method (OSM) method to establish semi-implicit scheme. We also take the judgment condition of the exercise stage and Dirichlet zero boundary as its boundary conditions. On the one asset and two assets, Crank-Nicolson scheme and implicit scheme are unconditionally stable and convergent [31]. On the three asset, OSM method is also proved to be convergent and stable by reference [3,4,32].

3.1. One Underlying Asset

We grid on area $\Sigma : \{0 \leq S \leq S_{max}, 0 \leq t \leq T\}$. From $t = 0$ to $t = T$, we divide the option price into several equal intervals. We take $\Delta t = \frac{T}{N_t}$, $\Delta S = \frac{S_{max}-S_{min}}{N_S}$, Δt represents the time step of T, ΔS represents the price step of S.

There are $N_t + 1$ time periods and $N_s + 1$ option price: 0, Δt, $2\Delta t \ldots T$ and 0, $\Delta S, \ldots, S_{max}$. In this grid, $V(i,j)$denotes the corresponding time $i\Delta t$ and option price: $j\Delta S = S_j$, where $i = 0,\ldots,N_t$, $j = 0,\ldots,N_S$. We take $V_j^i = V(i,j)$ to express the return at point S_j. For Equation (6), we consider the Crank-Nicolson scheme.

$$\frac{V_j^{i+1}-V_j^i}{\Delta t} = \frac{1}{2}(H\Delta t^{2H-1}\sigma^2 S_j^2 \frac{V_{j+1}^i - 2V_j^i + V_{j-1}^i}{\Delta S^2}$$

$$+rS_j\tfrac{V_{j+1}^i-V_{j-1}^i}{2\Delta S}-rV_j^i)+\tfrac{1}{2}(H\Delta t^{2H-1}\sigma^2 S_j^2\tfrac{V_{j+1}^{i+1}-2V_j^{i+1}+V_{j-1}^{i+1}}{\Delta S^2}$$

$$+rS_j\tfrac{V_{j+1}^{i+1}-V_{j-1}^{i+1}}{2\Delta S}-rV_j^{i+1}).$$

After sorting out the above difference scheme and adding zero Dirichilet boundary condition at $S=0$ and nonlinear boundary condition at $t=T$, we can observe the equation as follows:

$$\begin{cases}\alpha_j V_{j-1}^{i+1}+B_j V_j^{i+1}+\gamma_j V_{j+1}^{i+1}=\frac{V_j^i}{\Delta t}+H\Delta t^{2H-1}\sigma^2 S_j^2\frac{V_{j+1}^{i+1}-2V_j^{i+1}+V_{j-1}^{i+1}}{2\Delta S^2}\\ +rS_j\frac{V_{j+1}^{i+1}-V_{j-1}^{i+1}}{4\Delta S}-\frac{r}{2}V_j^{i+1}, 1\le j\le N_S-1, 0\le i\le N_t-1,\\ V_j^T=\phi(S_j), 0\le j\le N_S,\\ V_{S_{max}}^i=V_0^i=V_j^0=0, 0\le i\le N_t, 0\le j\le N_s.\end{cases} \tag{9}$$

and

$$\alpha_j=\frac{rS_j}{4\Delta S}-\frac{H\Delta t^{2H-1}\sigma^2 S_j^2}{2\Delta S^2},$$

$$B_j=\frac{1}{\triangle t}+H\Delta t^{2H-1}\sigma^2\frac{S_j^2}{\Delta S^2}+\frac{r}{2},$$

$$\gamma_j=-\frac{rS_j}{4\Delta S}-\frac{H\Delta t^{2H-1}\sigma^2 S_j^2}{2\Delta S^2}.$$

In the system of Equation (9), like ELS option, fractional ELS option has different returns whether the underlying asset occurs knock-in-barrier event. And the boundary conditions at $V_j^T=\phi(S_j)$ are also different.

When knock-in-barrier event occurs, $\phi(S_j)$ can be expressed as:

$$\phi(S_j)=\begin{cases}S_j, & if\ S_j\le D,\\ F(1+d), & if\ D\le S_j\le K_1,\\ F(1+\beta_1), & if\ K_1\le S_j.\end{cases}$$

When knock-in-barrier event doesn't occur, $\phi(S_j)$ can be expressed as:

$$\phi(S_j)=\begin{cases}S_j, & if\ S_j\le D,\\ S_j, & if\ D\le S_j\le K_1,\\ F(1+d), & otherwise.\end{cases}$$

3.2. Two Underlying Assets

For region Φ times $[0,T]=\{0\le y\le y_{max}, 0\le x\le x_{max}, 0\le t\le T\}$, we grid it. From $t=0$ to $t=T$, we divide the option price into several equal intervals. We take $\Delta t=\frac{T}{N_t}$, $\Delta x=\frac{x_{max}}{N_x}$, $\Delta y=\frac{y_{max}}{N_y}$, Δt represents the time step of T, Δx, Δy represent the price step of x and y. There are N_t+1 time periods, N_x+1 option price of x and N_y+1 option price of y. These are expressed as:

$$0, \Delta t, 2\Delta t\ldots T; 0, \Delta x, \ldots, x_{max} \text{ and } 0, \Delta y, \ldots, y_{max}.$$

In this grid, $V(i,j,k)$ denotes the corresponding time $i\Delta t$ and option price of x and y: $j\Delta x=x_j, k\Delta y=y_k$, where $i=0,\ldots,N_t$; $j=0,\ldots,N_x$; $k=0,\ldots,N_y$. We take $V_{j,k}^i=V(i,j,k)$ to express the return of repayment at point (j,k). For Equation (7), we consider the following difference scheme to establish implicit scheme. We also use zero Dirichilet boundary conditions at $x = 0, y = 0$ and nonlinear boundary condition at $t = T$.

$$V_t = \frac{V^{i+1} - V^i}{\Delta t}, V_x = \frac{V_{j+1} - V_{j-1}}{2\Delta x}, V_{xx} = \frac{V_{j+1} - 2V_j + V_{j-1}}{\Delta x^2},$$

$$V_{xy} = \frac{1}{4\Delta x \Delta y}\Big(V_{j+1,k+1} - V_{j-1,k+1} - V_{j+1,k-1} + V_{j-1,k+1}\Big),$$

$$\begin{aligned}\frac{V^{i+1}_{jk} - V^i_{jk}}{\Delta t} &= r x_j \frac{V^{i+1}_{j+1,k} - V^{i+1}_{j-1,k}}{2\Delta x} + r y_k \frac{V^{i+1}_{j,k+1} - V^{i+1}_{j,k-1}}{2\Delta y} \\ &+ H_x \Delta t^{2H_x - 1} \sigma_x^2 x_j^2 \frac{V^{i+1}_{j+1,k} - 2V^{i+1}_{j,k} + V^{i+1}_{j-1,k}}{\Delta x^2} \\ &+ H_y \Delta t^{2H_y - 1} \sigma_y^2 y_k^2 \frac{V^{i+1}_{j,k+1} - 2V^{i+1}_{j,k} + V^{i+1}_{j,k-1}}{\Delta y^2} \\ &+ (H_x + H_y)\Delta t^{H_x + H_y - 1} \rho_{xy} \sigma_x \sigma_y x_j y_k \frac{V^{i+1}_{j+1,k+1} - V^{i+1}_{j-1,k+1} - V^{i+1}_{j+1,k-1} + V^{i+1}_{j-1,k-1}}{4\Delta x \Delta y} \\ &- r V^{i+1}_{j,k}.\end{aligned}$$

After sorting out the above difference scheme and adding zero Dirichilet boundary condition at point $(x, y) = (0, 0)$ and nonlinear boundary condition at $t = T$, we can observe the equation as follows:

$$\begin{cases} g^x_j V^{i+1}_{j-1,k} + q^x_j V^{i+1}_{j,k} + w^x_j V^{i+1}_{j+1,k} \\ + g^y_k V^{i+1}_{j,k-1} + q^y_k V^{i+1}_{j,k} + w^y_k V^{i+1}_{j,k+1} = \frac{V^i_{j,k}}{\Delta t} + \varsigma^{i+1}_{j,k}, \\ 1 \le j \le N_x - 1, 0 \le i \le N_t - 1, 1 \le k \le N_y - 1, \\ V^T_{j,k} = \vartheta(x_j, y_k, 0), 0 \le j \le N_x, 0 \le k \le N_y, \\ V^i_{x_{max},k} = V^i_{j,y_{max}} = V^i_0 = V^0_{j,k} = 0, \\ 0 \le i \le N_t, 0 \le j \le N_x, 0 \le k \le N_y, \end{cases} \tag{10}$$

where,

$$g^x_j = \frac{r x_j}{4\Delta x} - \frac{H_x \Delta t^{2H_x - 1} \sigma_x^2 x_j^2}{2\Delta x^2}, g^y_k = \frac{r y_k}{4\Delta y} - \frac{H_y \Delta t^{2H_y - 1} \sigma_y^2 y_k^2}{2\Delta y^2},$$

$$q^x_j = \frac{1}{\Delta t} + H_x \Delta t^{2H_x - 1} \sigma_x^2 \frac{x_j^2}{\Delta x^2} + \frac{r}{2}, q^y_k = \frac{1}{\Delta t} + H_y \Delta t^{2H_y - 1} \sigma_y^2 \frac{y_k^2}{\Delta y^2} + \frac{r}{2},$$

$$w^x_j = -\frac{r x_j}{4\Delta x} - \frac{H_x \Delta t^{2H_x - 1} \sigma_x^2 x_j^2}{2\Delta x^2}, w^y_k = -\frac{r y_k}{4\Delta y} - \frac{H_y \Delta t^{2H_y - 1} \sigma_y^2 y_k^2}{2\Delta y^2},$$

$$\varsigma^{i+1}_{j,k} = \frac{(H_x + H_y)\Delta t^{H_x + H_y - 1} \rho_{xy} x y \sigma_x \sigma_y \Big(V^{i+1}_{j+1,k+1} - V^{i+1}_{j-1,k+1} - V^{i+1}_{j+1,k-1} + V^{i+1}_{j-1,k-1}\Big)}{4\Delta x \Delta y}.$$

It is similar to one asset, $V^T_{j,k} = \vartheta(x_j, y_k, T)$ can also be divided into two situations. When knock-in-barrier event occurs, $V^T_{j,k} = \vartheta(x_j, y_k, T)$ can be expressed as:

$$\vartheta(x_j, y_k, T) = \begin{cases} min\{x_j, y_k\}, & if\ min\{x_j, y_k\} \le D, \\ F(1 + d), & if\ D \le min\{x_j, y_k\} \le K_1, \\ F(1 + \beta 1), & if\ K_1 \le min\{x_j, y_k\}. \end{cases}$$

When knock-in-barrier event doesn't occur, $V^T_{jk} = \vartheta(x_j, y_k, 0)$ can be expressed as:

$$\vartheta(x_j, y_k, T) = \begin{cases} min\{x_j, y_k\}, & if\ min\{x_j, y_k\} \le D, \\ min\{x_j, y_k\}, & if\ D \le min\{x_j, y_k\} \le K_1, \\ F(1+d), & otherwise. \end{cases}$$

3.3. Three Underlying Assets

We grid region Ψ times $[0, T] = \{0 \le x \le x_{max}, 0 \le y \le y_{max}, 0 \le z \le z_{max}, 0 \le t \le T\}$ uniformly. From $t = 0$ to $t = T$, we divide the option price into several equal intervals. We take $\Delta t = \frac{T}{N_t}$, $\Delta x = \frac{x_{max}}{N_x}$, $\Delta y = \frac{y_{max}}{N_y}$, $\Delta z = \frac{z_{max}}{N_z}$, Δt represents the time step of T, Δx, Δy and Δz represent the price step of x, y and z. There are $N_t + 1$ time periods, $N_x + 1$ option price of x, $N_y + 1$ option price of y and $N_z + 1$ option price of z. These are expressed as:

$$0, \Delta t, 2\Delta t \ldots T; 0, \Delta x, \ldots, x_{max}; 0, \Delta y, \ldots, y_{max} \text{ and } 0, \Delta z, 2\Delta z, \ldots, z_{max}.$$

In this grid, $V(i, j, k, m)$ denotes the corresponding time $i\Delta t$ and option price of x, y and z: $j\Delta x = x_j$, $k\Delta y = y_k$ and $m\Delta z = z_m$, where $i = 0, \ldots, N_t$; $j = 0, \ldots, N_x$; $k = 0, \ldots, N_y$; $m = 0, \ldots, N_z$. We take $V^i_{j,k,m} = V(i, j, k, m)$ to express the return of repayment at point (j, k, m). We also consider using zero Dirichilet boundary conditions at $x = 0$, $y = 0$ and $z = 0$. As for $t = T$, we employ nonlinear boundary condition. We also use OSM method [4,31,32] which is the most extensive to establish semi-implicit scheme. And the reference [3,4,32] have proved that this method is convergent.

$$\frac{V^{i+1}_{j,k,m} - V^i_{j,k,m}}{\Delta t} = (\gamma^x V)^{i+\frac{1}{3}}_{j,k,m} + (\gamma^y V)^{i+\frac{2}{3}}_{j,k,m} + (\gamma^z V)^{i+1}_{j,k,m}. \tag{11}$$

In Equation (11), we define difference operators γ^x, γ^y and γ^z as follows:

$$\begin{aligned}(\gamma^x V)^{i+\frac{1}{3}}_{j,k,m} = {} & H_x t^{2H_x-1} U_{xx} V^{i+\frac{1}{3}}_{j,k,m} + r x_j U_x V^{i+\frac{1}{3}}_{j,k,m} + \frac{1}{3}\Big((H_x + H_y)\Delta t^{H_x+H_y-1} \sigma_x \sigma_y x_j y_k U_{xy} V^i_{j,k,m} \\ & + (H_z + H_y)\Delta t^{H_z+H_y-1} \sigma_y \sigma_z y_k z_m U_{yz} V^i_{j,k,m} \\ & + (H_x + H_z)\Delta t^{H_x+H_z-1} \sigma_z \sigma_x z_m x_j U_{zx} V^i_{j,k,m}) - r V^{i+\frac{1}{3}}_{j,k,m} \Big), \\ (\gamma^y V)^{i+\frac{2}{3}}_{j,k,m} = {} & H_y t^{2H_y-1} U_{yy} V^{i+\frac{2}{3}}_{j,k,m} + r y_k U_y V^{i+\frac{2}{3}}_{j,k,m} + \frac{1}{3}\Big((H_x + H_y)\Delta t^{H_x+H_y-1} \sigma_x \sigma_y x_j y_k U_{xy} V^{i+\frac{1}{3}}_{j,k,m} \\ & + (H_z + H_y)\Delta t^{H_z+H_y-1} \sigma_y \sigma_z y_k z_m U_{yz} V^{i+\frac{1}{3}}_{j,k,m} \\ & + (H_x + H_z)\Delta t^{H_x+H_z-1} \sigma_z \sigma_x z_m x_j U_{zx} V^{i+\frac{1}{3}}_{j,k,m}) - r V^{i+\frac{2}{3}}_{j,k,m} \Big), \\ (\gamma^z V)^{i+1}_{j,k,m} = {} & H_z \Delta t^{2H_z-1} U_{zz} V^{i+1}_{j,k,m} + r z_m U_z V^{i+1}_{j,k,m} + \frac{1}{3}\Big((H_x + H_y)\Delta t^{H_x+H_y-1} \sigma_x \sigma_y x_j y_k U_{xy} V^{i+\frac{2}{3}}_{j,k,m} \\ & + (H_z + H_y)\Delta t^{H_z+H_y-1} \sigma_y \sigma_z y_k z_m U_{yz} V^{i+\frac{2}{3}}_{j,k,m} \\ & + (H_x + H_z)\Delta t^{H_x+H_z-1} \sigma_z \sigma_x z_m x_j U_{zx} V^{i+\frac{2}{3}}_{j,k,m}) - r V^{i+1}_{j,k,m} \Big).\end{aligned}$$

We take the following difference scheme for Equation (11),

$$U_x V_{j,k,m} = \tfrac{1}{2\Delta x}\Big(V_{j+1,k,m} - V_{j-1,k,m}\Big),$$

$$U_{xx} V_{j,k,m} = \tfrac{1}{\Delta x^2}\Big(V_{j-1,k,m} - 2V_{j,k,m} + V_{j+1,k,m}\Big),$$

$$U_{xy} V_{j,k,m} = \tfrac{1}{4\Delta x \Delta y}\Big(V_{j+1,k+1,m} - V_{j-1,k+1,m} - V_{j+1,k-1,m} + V_{j-1,k-1,m}\Big).$$

$$\frac{V_{j,k,m}^{i+\frac{1}{3}} - V_{j,k,m}^{i}}{\Delta t} = (\gamma^x V)_{j,k,m}^{i+\frac{1}{3}}, \tag{12}$$

$$\frac{V_{j,k,m}^{i+\frac{2}{3}} - V_{j,k,m}^{i+\frac{1}{3}}}{\Delta t} = (\gamma^y V)_{j,k,m}^{i+\frac{2}{3}}, \tag{13}$$

$$\frac{V_{j,k,m}^{i+1} - V_{j,k,m}^{i+\frac{2}{3}}}{\Delta t} = (\gamma^z V)_{j,k,m}^{i+1}. \tag{14}$$

We give V_{jkm}^{i} and rewrite the Equation (12) as follows:

$$a_j V_{j-1,k,m}^{i+\frac{1}{3}} + b_j V_{j,k,m}^{i+\frac{1}{3}} + c_j V_{j+1,k,m}^{i+\frac{1}{3}} = f_{j,k,m}, \text{ for j} = 1, \dots, N_x,$$

where,

$$\begin{aligned} a_j &= -\frac{2H_x \Delta t^{2H_x - 1} \sigma_x^2 x_j^2 + r x_j \Delta x \Delta t}{2\Delta x^2}, \\ \beta_j &= \frac{2H_x \Delta t^{2H_x - 1} \sigma_x^2 x_j^2}{\Delta x^2} + \frac{1}{\Delta t}, \\ c_j &= \frac{-2H_x t^{2H_x - 1} \sigma_x^2 x_j^2 - r x_j \Delta x}{2\Delta x^2}, \\ f_{j,k,m} &= \frac{1}{3}(H_x + H_y) t^{H_x + H_y - 1} \rho_{xy} \sigma_x \sigma_y x_j y_k U_{xy} V_{j,k,m}^{i} \\ &+ \frac{1}{3}(H_z + H_y) t^{H_z + H_y - 1} \rho_{yz} \sigma_z \sigma_y z_m y_k U_{yz} V_{j,k,m}^{i} \\ &+ \frac{1}{3}(H_x + H_z) t^{H_x + H_z - 1} \rho_{xz} \sigma_x \sigma_z x_j z_m U_{xz} V_{j,k,m}^{i}) - \frac{1}{\Delta t} V_{j,k,m}^{i}. \end{aligned}$$

It is similar to the direction of y and z. By the reference of Kim et al. [3], we can get the solution method for the finite difference scheme.

Similar to two assets and one asset, $V_{j,k,m}^{T} = \psi(x_j, y_k, z_m, T)$ can also be divided into two situations.

When knock-in-barrier event occurs, $V_{j,k,m}^{T} = \psi(x_j, y_k, z_m, T)$ can be expressed as:

$$\psi(x_j, y_k, z_m, T) = \begin{cases} min\{x_j, y_k, z_m\}, & if\ min\{x_j, y_k, z_m\} \le D, \\ F(1+d), & if\ D \le min\{x_j, y_k, z_m\} \le K_1, \\ F(1+\beta_1), & otherwise. \end{cases}$$

When knock-in-barrier event doesn't occur, $V_{j,k,m}^{T} = \psi(x_j, y_k, z_m, T)$ can be expressed as:

$$\psi(x_j, y_k, z_m, T) = \begin{cases} min\{x_j, y_k, z_m\}, & if\ min\{x_j, y_k, z_m\} \le D, \\ min\{x_j, y_k, z_m\}, & if\ D \le min\{x_j, y_k, z_m\} \le K_1, \\ F(1+d), & otherwise. \end{cases}$$

4. Numerical Experiments

All the computations are processed by using Matlab R2022a on an Rog Strix Intel(R) Core(TM) i9-12950HX CPU constructed in Chongqing, China 2.30 GHz processor.

In Section 3, we establish different finite difference schemes for one, two and three assets. We let kv be the return of repayment without knock-in-barrier, v be the return of repayment with knock-in-barrier and error represents $|kv - v|$. Now we assign values to parameters and then take numerical experiments.

4.1. One Underlying Asset

First, we research the relationship between H and v as well as kv at a fixed point S under different values of H. We take values of H at equal intervals from 0.1 to 0.9 for 20 groups. We take $n = 4$ and take S from 0 to 200 for 21 groups. For other parameters, our values are as follows:

$$\sigma = 0.3, r = 0.03, N_S = 20, T = 1, N_t = 100, \Delta t = \frac{T}{N_t} = 0.01,$$
$$\delta_1 = \frac{N_t}{4}, \delta_2 = \frac{N_t}{2}, \delta_3 = \frac{3N_t}{4}, \delta_4 = N_t + 2,$$

$$K_1 = 90, K_2 = 85, K_3 = 80, K_4 = 75,$$
$$\beta_1 = 0.055, \beta_2 = 0.11, \beta_3 = 0.165, \beta_4 = 0.22, D = 50, d = 0.16.$$

K_1 to K_4, β_1 to β_4 and $\delta_1$to δ_4 represent the strike price in strike date and the corresponding coupon rate. We can get the corresponding figures at point S = 70 as follows.

In Figure 1, we can obtain that whether the knock-in-barrier is triggered or not, the change of H value will affect the return of repayment. Therefore, we explore the relationship between the option price S and the return of repayment v and kv and the error between each other under a specific H value. Next, we take the specific H values of 0.3, 0.5, 0.7 and don't change the values of other parameters. We get the figures of S and v, S and kv and figures of error between S and $|kv - v|$. These figures are as shown below.

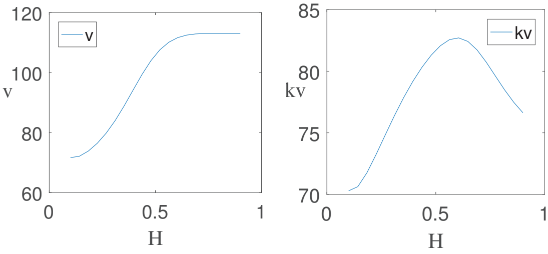

Figure 1. The effect of different H on v and kv when $S = 70$.

In Figures 2–4, (a), (b), (c) in turn represent the result figures obtained when H values are 0.3, 0.5 and 0.7. In Figures 2 and 3, we obtained that the change of v and kv with H is mainly in the range of S value from 50 to 100, which includes strike price and knock-in-barrier. With the increase of H value, the value of v and kv corresponding to S value on 50 to 100 will also increase. It can also be confirmed from Figure 4 that with the increase of H value, the maximum value of the error between v and kv also increases, and the range of the changed wave is about 50 to 100. Next, we explore whether the change of H value in different dimensions will also affect v and kv.

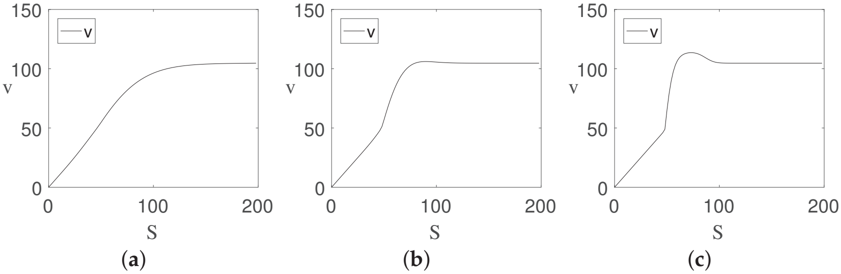

Figure 2. (**a**) denotes v for different S when $H = 0.3$, (**b**) denotes v for different S when $H = 0.5$ and (**c**) denotes v for different S when $H = 0.7$.

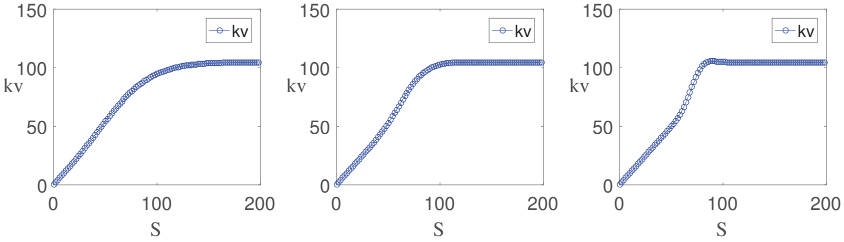

(**a**) (**b**) (**c**)

Figure 3. (**a**) denotes kv for different S when $H = 0.3$, (**b**) denotes kv for different S when $H = 0.5$ and (**c**) denotes kv for different S when $H = 0.7$.

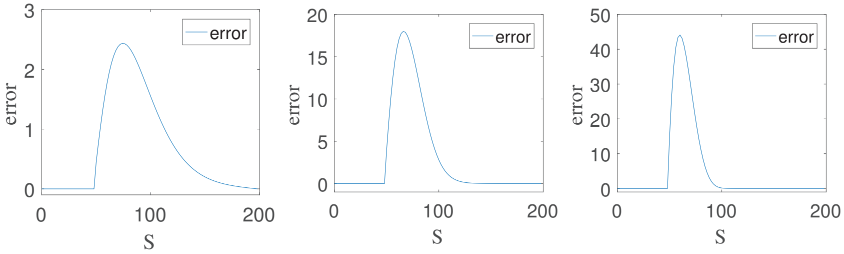

(**a**) (**b**) (**c**)

Figure 4. (**a**) denotes $|kv - v|$ for different S when $H = 0.3$, (**b**) denotes $|kv - v|$ for different S when $H = 0.5$ and (**c**) denotes $|kv - v|$ for different S when $H = 0.7$.

4.2. Two Underlying Assets

The same as one underlying asset, we first research the relationship between H_x, H_y and v as well as kv at a fixed point (x, y) under different values of H_x and H_y. We take values of H_x and H_y at equal intervals from 0.1 to 0.9 for 20 groups. We take $n = 4$ and take x and y from 0 to 300 for 31 groups. For other parameters, our values are as follow:

$$\sigma_x = \sigma_y = 0.3,\, r = 0.03,\, N_x = N_y = 30,\, \Delta x = \Delta y = 10,\, T = 1,\, N_t = 100,\, \Delta t = \frac{T}{N_t} = 0.01,$$

$$\delta_1 = \frac{N_t}{4},\, \delta_2 = \frac{N_t}{2},\, \delta_3 = \frac{3N_t}{4},\, \delta_4 = N_t + 2,\, \rho_{xy} = 0.5,\, K_1 = 90,\, K_2 = 85,\, K_3 = 80,\, K_4 = 75,$$

$$\beta_1 = 0.055,\, \beta_2 = 0.11,\, \beta_3 = 0.165,\, \beta_4 = 0.22,\, D = 50,\, d = 0.16.$$

K_1 to K_4, β_1 to β_4 and δ_1 to δ_4 represent the strike price in strike date and the corresponding coupon rate. We can get the corresponding figures at a fixed point $(x, y) = (100, 100)$ as follows.

In Figure 5, we can observe that the change of H_x, H_y will also affect v and kv in the case of fixed point (x, y). With the increase of H_x and H_y, the values of v and kv are also increasing. Therefore, we explore the relationship of x, y and v, x, y and kv. Next, we take the specific H_x, H_y values of 0.3, 0.5, 0.7 at the same time, and change $N_x = N_y = 150$, $\Delta x = \Delta y = 2$. We take x and y from 0 to 300 for 151 groups. Then, we don't change the values of other parameters. We get the figures of x, y and v, x, y and kv. At the same time, we obtain the error figures of x, y and $|kv - v|$. These figures are as shown in the Figures 6–8 below.

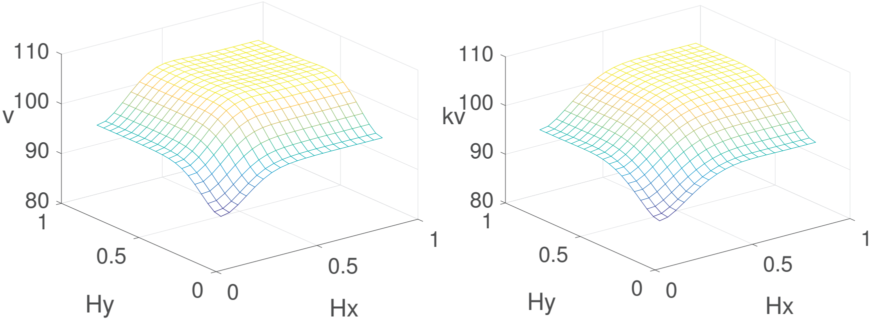

Figure 5. The effect of different H_x and H_y on v and kv when $(x, y) = (100, 100)$.

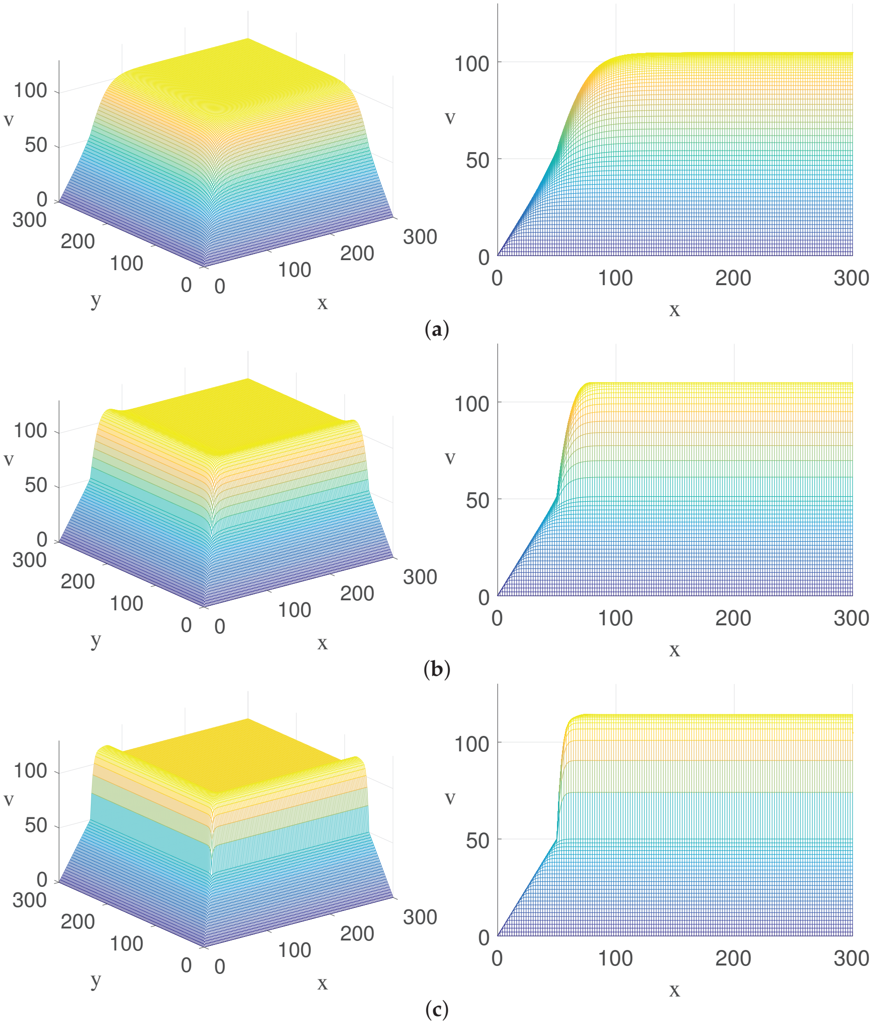

(**a**)

(**b**)

(**c**)

Figure 6. (**a**) denotes v for different x, y when $H_x = H_y = 0.3$, (**b**) denotes v for different x, y when $H_x = H_y = 0.5$ and (**c**) denotes v for different x, y when $H_x = H_y = 0.7$.

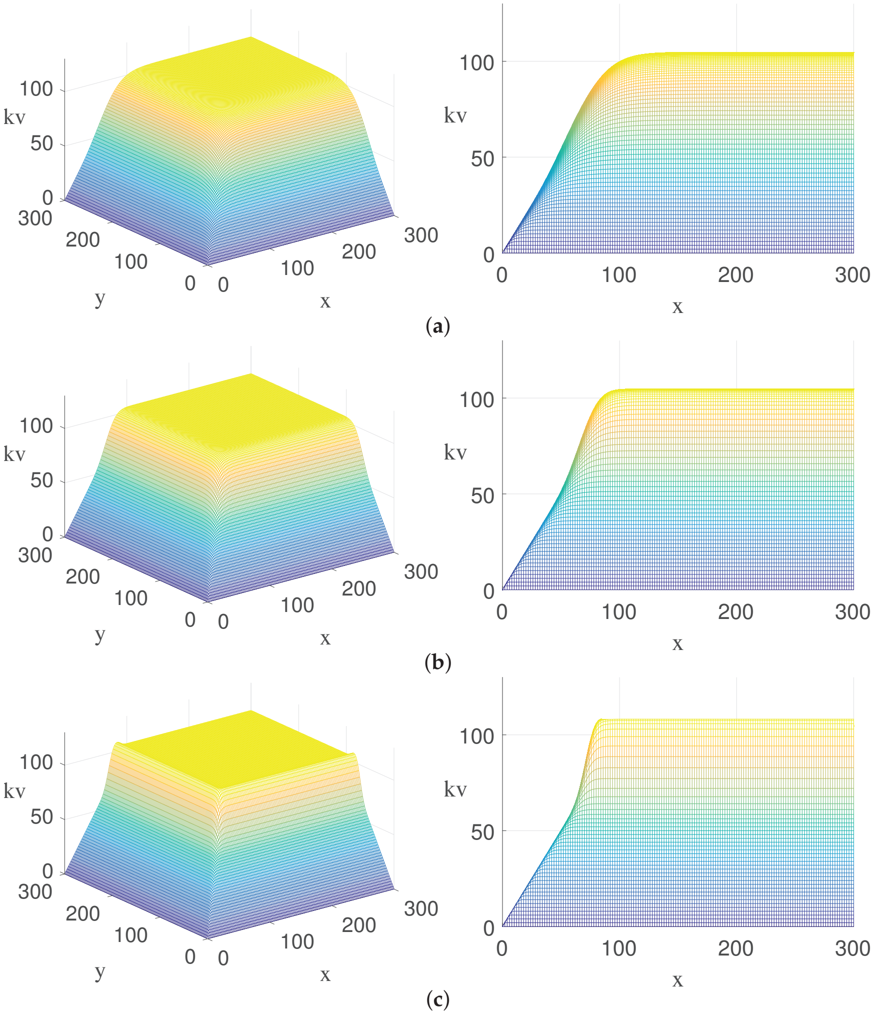

(**a**)

(**b**)

(**c**)

Figure 7. (**a**) denotes kv for different x, y when $H_x = H_y = 0.3$, (**b**) denotes kv for different x, y when $H_x = H_y = 0.5$ and (c) denotes kv for different x, y when $H_x = H_y = 0.7$.

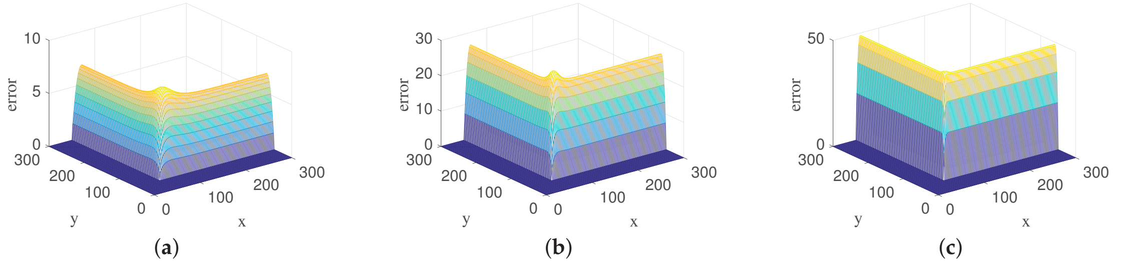

(**a**) (**b**) (**c**)

Figure 8. (**a**) denotes $|kv - v|$ for different x, y when $H_x = H_y = 0.3$, (**b**) denotes $|kv - v|$ for different x, y when $H_x = H_y = 0.5$ and (**c**) denotes $|kv - v|$ for different x, y when $H_x = H_y = 0.7$.

In Figures 6–8, (a), (b), (c) in turn represent the result figures obtained when $H_x = H_y = 0.3, 0.5, 0.7$. In Figures 6 and 7, similar to the case of one asset, the change of H_x

and H_y values will also affect the results of v and kv. The variation of v and kv values is mainly in the range of S value from 50 to 100, and this range just includes strike price and knock-in-barrier. If the influence of H_x and H_y on v and kv values is not considered in practical application, there will be a great error in calculating the return of repayment in the exercise stage, and even the result of wrong judgment. On the other hand, it can also be confirmed from Figure 8 that with the increase of H_x and H_y values, the maximum value of the error between v and kv also increases.

4.3. Three Underlying Assets

In three underlying assets, we also explore the relationship between H_x, H_y, H_z and v as well as kv at a fixed point (x, y, z) and fixed value H_z under different values of H_x, H_y. We take values of H_x and H_y at equal intervals from 0.1 to 0.9 for 20 groups. We take $n = 4$ and take x and y from 0 to 200 for 21 groups. For other parameters, our values are as follow:

$$\sigma_x = \sigma_y = \sigma_z = 0.3, r = 0.03, N_x = N_y = N_z = 20, T = 3, N_t = 90, \Delta t = \frac{T}{N_t} = \frac{1}{30},$$

$$\rho_{xy} = \rho_{yz} = \rho_{xz} = 0.5, \delta_1 = \frac{N_t}{6}, \delta_2 = \frac{N_t}{3}, \delta_3 = \frac{N_t}{2}, \delta_4 = \frac{4N_t}{6}, \delta_5 = \frac{5}{6}N_t, \delta_6 = \frac{7}{6}N_t,$$

$$K_1 = 95, K_2 = 95, K_3 = 90, K_4 = 90, K_5 = 85, K_6 = 85,$$

$$\beta_1 = 0.05, \beta_2 = 0.1, \beta_3 = 0.15, \beta_4 = 0.2, \beta_5 = 0.25, \beta_6 = 0.30, D = 50, d = 0.3.$$

K_1 to K_4, β_1 to β_4 and δ_1 to δ_4 represent the strike price in strike date and the corresponding coupon rate. We can get the corresponding figure at point $(x, y, z) = (100, 100, 100)$ as follows.

In Figure 9, (a) represents the figure of H_x, H_y and v at fixed point $(x, y, z) = (100, 100, 100)$ when $H_z = 0.5$. (b) represents the figure of H_x, H_y and kv at fixed point $(x, y, z) = (100, 100, 100)$ when $H_z = 0.5$. In two assets, we get the conclusion that the change of H_x and H_y will affect the results of v and kv. In three assets, this conclusion is still true, and with the increase of H_x, H_y values, the results of v and kv also increase. Next, we take the specific H_x, H_y, H_z values of 0.3, 0.5, 0.7 at the same time, and change $N_x = N_y = N_z = 100$, $\Delta x = \Delta y = \Delta z = 2$. Therefore, we take x, y and z from 0 to 200 for 101 groups. And then we don't change the values of other parameters. Therefore, we can get the figures of x, y and v, the figures of x, y and kv when $z = 100$. At the same time, we also give the figures of x, y and $|kv - v|$ when $z = 100$. These are as shown in Figures 10–12 below.

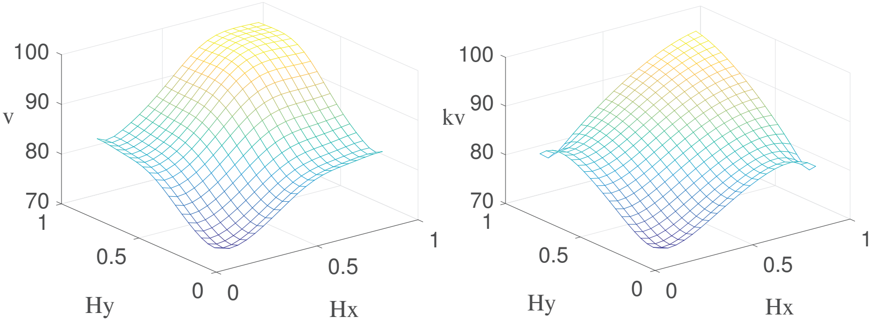

(**a**) (**b**)

Figure 9. The effect of different H_x, H_y on v and kv when $(x, y, z) = (100, 100, 100)$ and $H_z = 0.5$.

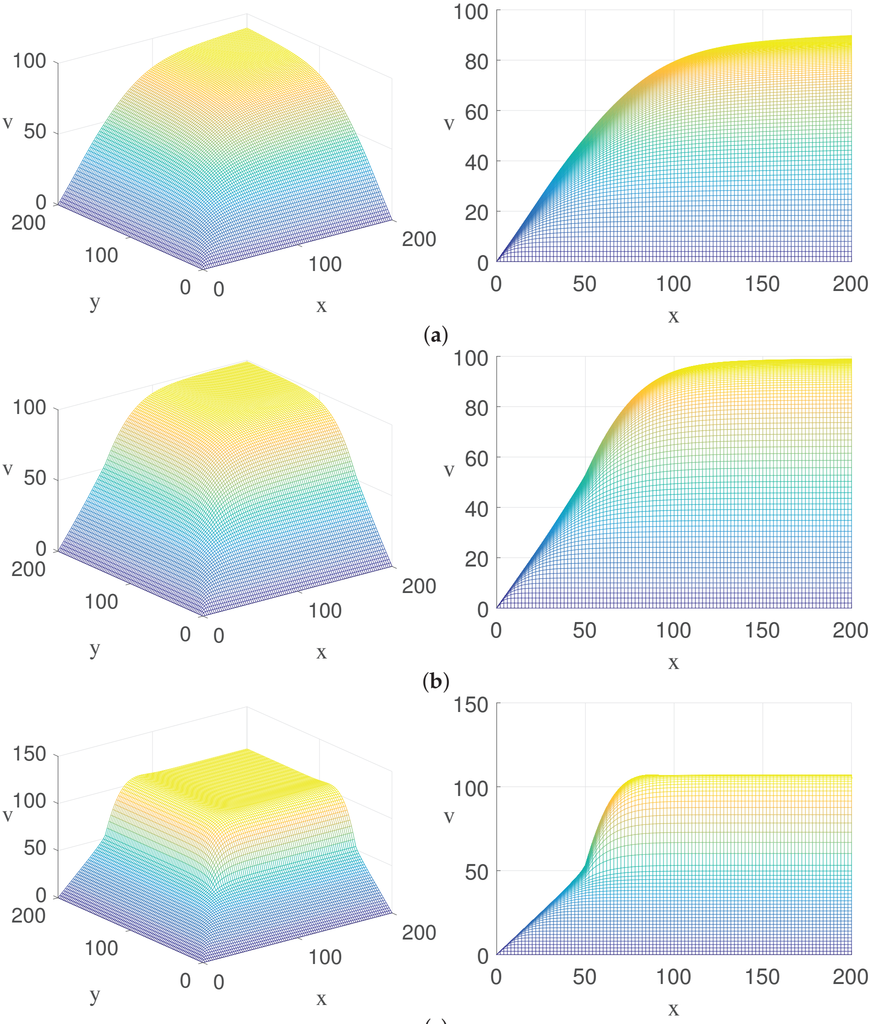

(**a**)

(**b**)

(**c**)

Figure 10. (**a**) denotes v for different x, y when $H_x = H_y = H_z = 0.3$ and $z = 100$, (**b**) denotes v for different x, y when $H_x = H_y = H_z = 0.5$ and $z = 100$ and (**c**) denotes v for different x, y when $H_x = H_y = H_z = 0.7$ and $z = 100$.

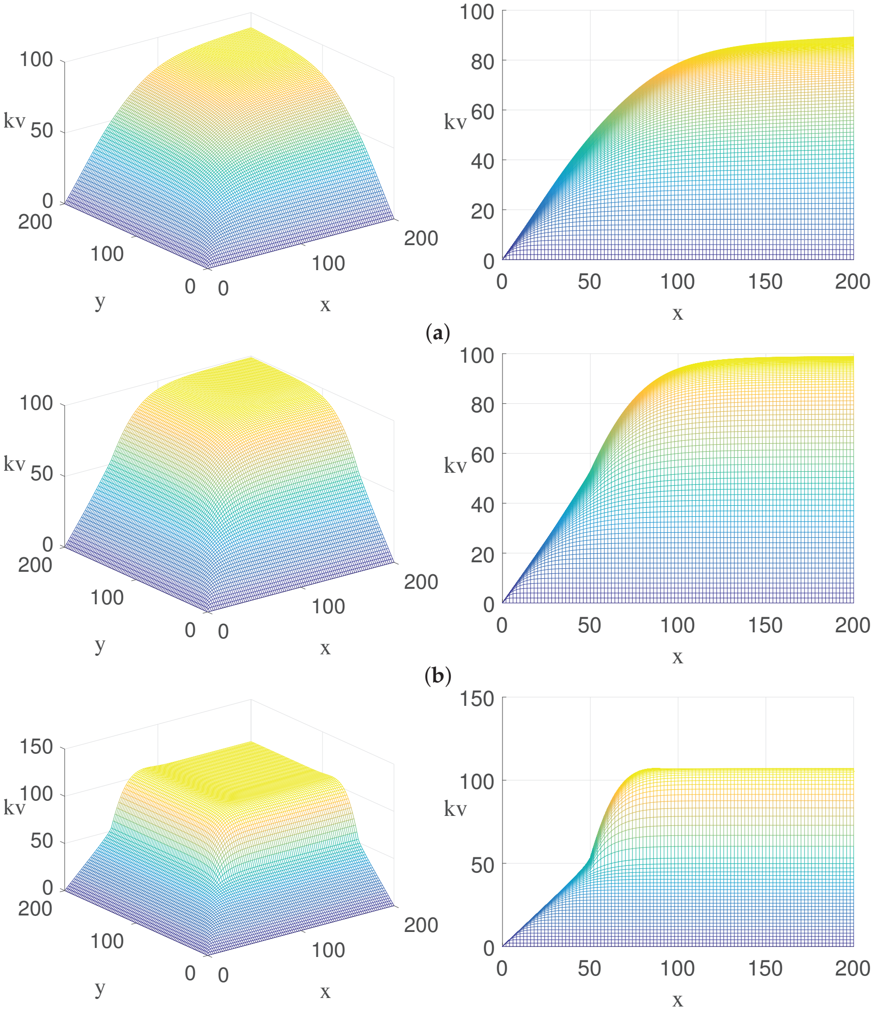

(**a**)

(**b**)

(**c**)

Figure 11. (**a**) denotes kv for different x, y when $H_x = H_y = H_z = 0.3$ and $z = 100$, (**b**) denotes kv for different x, y when $H_x = H_y = H_z = 0.5$ and $z = 100$ and (**c**) denotes kv for different x, y when $H_x = H_y = H_z = 0.7$ and $z = 100$.

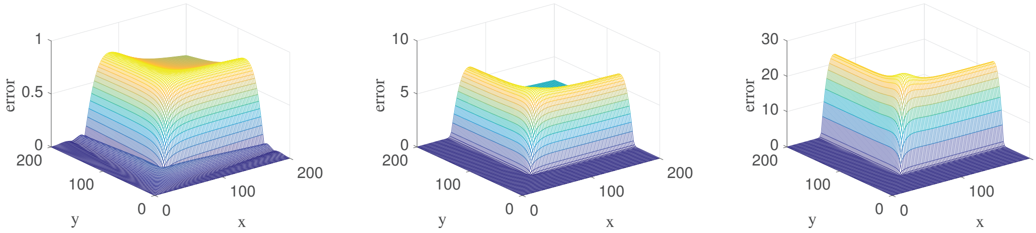

(**a**) (**b**) (**c**)

Figure 12. (**a**) denotes $|kv - v|$ for different x, y when $H_x = H_y = H_z = 0.3$ and $z = 100$, (**b**) denotes $|kv - v|$ for different x, y when $H_x = H_y = H_z = 0.5$ and $z = 100$ and (**c**) denotes $|kv - v|$ for different x, y when $H_x = H_y = H_z = 0.7$ and $z = 100$.

In Figures 10–12, (a), (b) and (c) respectively represent the corresponding figures when $H_x = H_y = H_z = 0.3$, 0.5 and 0.7. In Figures 10 and 11, we can observe the conclusion that the change of H value will still affect v and kv values, and the main change occurs in a reign containing strike price and knock-in-barrier. At the same time, we also calculate that v and kv at a fixed point $(x, y, z) = (100, 100, 100)$, when $H_x = H_y = H_z = 0.3$, the corresponding values of v and kv are 71.5396 and 89.7243 respectively. When $H_x = H_y = H_z = 0.5$, the corresponding values of v and kv at this point are 89.7243 and 84.2065. When $H_x = H_y = H_z = 0.7$, the corresponding values of v and kv at this point are 106.3668 and 95.9271. We can obtain that the value of v and kv increase with the increase of H_x, H_y and H_z. In Figure 12, the error value increases with increase of H_x, H_y and H_z values, which indicates that with the increase of H_x, H_y and H_z values, the difference between v and kv value becomes significant. In practice, H value is not directly obtainable. Nowadays, the value of H is estimated mainly based on historical data. Barunik and Kristoufek [33] point out that it is most effective to estimate H by using the GHE method suitable for multifractal measurement of time series. But if the influence of H value is ignored, there may be a big error between the calculated result and the actual result, which will affect the final decision.

4.4. Empirical Evidence for Well-Posed of the Model and Validation of the Solution

In this section, we select an actual three-asset ELS product to price three-asset step-down ELS with Monte Carlo simulation)(MCs). The three-asset ELS product consists of three underlying assets such as KOSPI200, EU- ROSTOXX50, and S&P500 whose details can be accessed on 12 December 2020 and can be referred to website "http://www.miraeassetdaewoo.com".

According to the investment statement of the selected ELS, we observe the following parameters as: the face value $F = 10000$, the expiration time $T = 3$, the volatilizes $\sigma_1 = 0.2414$ (KOSPI200), $\sigma_2 = 0.2871$ (EUROSTOXX50), $\sigma_3 = 0.3509$ (S&P500), the correlations of two underlying assets $\rho_{12} = 0.5474$, $\rho_{13} = 0.3357$, $\rho_{23} = 0.7172$, the dummy rate $d = 0.135$, the initial prices of three-asset are $315.89pt$, $3160.95pt$, $3281.06pt$, which correspond to KOSPI200, EUROSTOXX50, and S&P500, respectively. Here for convenience, we set the benchmark prices of three underlying assets $S(0) = S_1(0) = S_2(0) = S_3(0) = 100$, then all the knock-in-barrier levels of three assets are $D = 0.45 \times S(0)$. Besides, the free risk interest rate is chosen by the current London InterBank Offered Rate $r = 0.023631$.

The next step is to determine the long-memory characteristics of each asset, namely, the values of Hurst exponent. There have been many methods proposed for estimating the Hurst exponent, we here adopt generalized Hurst exponent (GHE) approach to calculate the Hvalue of each asset. GHE is a suitable method for measuring the multifractality of time series. For instance, a time series $S(t)$ with length N, where $t = (1, 2, \cdots, \delta t)$, calculate the $H(q)$ based on the scaling of qth order moments defined by the distribution as $K_q(\tau) = \frac{\sum_{t=0}^{N-\tau} |X(t+\tau)-X(t)|^q}{N-\tau+1}$, where $1 < \tau < t_{max}$, and τ_{max} always varies between 5 and 19, we choose $\tau_{max} = 15$ in this paper. We obtain the statistic scales by the power-law $K_q(\tau) \propto c\tau^{qH(q)}$. When $q = 2$, the $K_2(\tau)$ represents the scaling of the auto-correlation function of the increments. We estimate the $K_2(\tau) \propto c\tau^{2H(2)}$ in this study, and we can easily estimate $2H(2)$ by the least squares regression on logarithms of $logK_2(\tau)$ and $log\tau$, then we obtain the Hurst exponents for three-asset step-down ELS in the following table.

We observe from Table 2 that the classic ELS model calculates a price that is obviously higher than the reference price, whereas the proposed model almost exactly corresponds to the reference price. As a result, ELS models should take into consideration long-range correlations of underlying assets. Buyers or sellers will suffer significant losses when selling an ELS contract with large amounts, if not considering Hurst exponent. Besides, we average the 20 prices and obtain the ELS prices of the classical ELS model and the ELS-MCs model are 9109.8, and 8948.6 while the reference price is given by 8931.2.

Table 2. Hurst exponents for three-asset step-down ELS calculated by GHE approach.

KOSPI200	EUROSTOXX50	S&P500
H_1 0.4946	H_2 0.4941	H_3 0.4870

4.5. Greeks

In one asset, we explore Greeks and obtain the conclusion that the change of H will affect the numerical solution of Greeks. Therefore, we also explore whether the change of H will also affect the numerical solution of three dimensional Greeks. We remain the value of parameters unchanged and use semi-implicit to obtain solution of Greeks in x direction. But in Rho, the value of r is selected in $[0.02985, 0.03015]$. In Vega, the value of σ is selected in $[0.3, 0.4]$. In x direction, we give the finite difference scheme of calculating Greeks.

Finite difference scheme of Greeks:

$$Delta = V_x(x,T) \approx \frac{V(x+h,y,z,T) - V(x-h,y,z,T)}{2h},$$

$$Gamma = V_{xx}(x,T) \approx \frac{V(x-h,y,z,T) - 2V(x,y,z,T) + V(x+h,y,z,T)}{h^2},$$

$$Theta = V_t(x,T) \approx \frac{V(x,y,z,T) - V(x,y,z,T-\Delta t)}{\Delta t},$$

$$Rho = V_r(x,T)|_{r=0.03} \approx \frac{V(x,y,z,T)|_{r=0.03015} - V(x,y,z,T)|_{r=0.02985}}{0.0003},$$

$$Vega = V_{\sigma_x}(x,T)|_{\sigma_x=0.35} \approx \frac{V(x,y,z,T)|_{\sigma_x=0.4} - V(x,y,z,T)|_{\sigma_x=0.3}}{0.1}.$$

We also change the value of H_x, H_y, H_z and we observe the numerical figures under different values of H_x, H_y, H_z.

Delta is the rate of change of the option price with respect to the price of the underlying asset. With the increase of H_x, H_y, H_z, the peak value of the figure increases gradually and the figure becomes steeper. Gamma is the change in the Delta of an option relative to the change in the underlying assets. With the increase of H_x, H_y, H_z, the peak value of the figure also increases gradually and the figure also becomes steeper. Theta represents the speed of option yield decay with time. With the increase of H_x, H_y, H_z, the value range of the curve in the figure fluctuates obviously. When $H_x = H_y = H_z = 0.7$, there are obvious fluctuations in this figure. Rho is the partial differential of option yield to risk-free interest rate. With the increase of H_x, H_y, H_z, the peak value of the figure decline gradually. Vega is the ratio between the change of option price and the change of underlying asset volatility. With the increase of H_x, H_y, H_z, the figure becomes smoother and wider. But the peak value of the figure hardly changed.

In Figures 13–15, the black curve represents option price without knock-in-barrier and the blue curve stands for option price with knock-in-barrier. From the results of figures, we can obtain that the change of H will also affect the final result in the Greeks of three assets. In the fractional Black-Scholes model, there is a big error between the result and the actual result if we don't consider the effect of H.

Our proposed model incorporates the concept of fractals on the basis of efficient market theory. Since the concept of fractal is added, there will be some changes in the price of options, which will lead to changes in Greeks. Considering that fractals add the historical volatility of stock prices into the calculation, this is consistent with the long-term memory, auto-correlation and persistence of stocks. More importantly, in the process of financial investment, considering the fractal exponents or not will have a considerable impact on investment Greeks risk hedging. When we consider the long-term correlation of stock prices, the fractal exponents helps us reduce the volatility of stock expectations which can effectively guide investment institutions or investors to reduce losses and increase revenue.

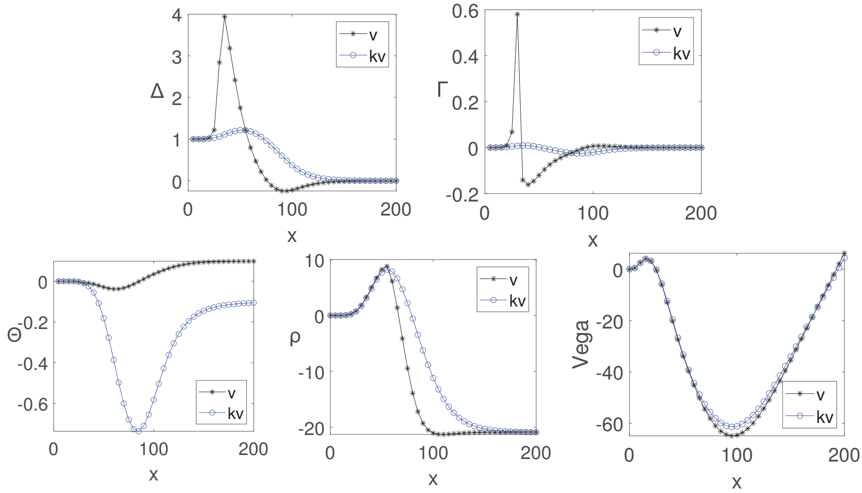

Figure 13. $H_x = H_y = H_z = 0.3$, figures represent in turn are Delta, Gamma, Theta, Rho and Vega. The blue curve stands for option price with knock-in-barrier while the black curve represents option price without knock-in-barrier. For interpretation of the references to color in the figure, the reader is referred to the web version of the article.

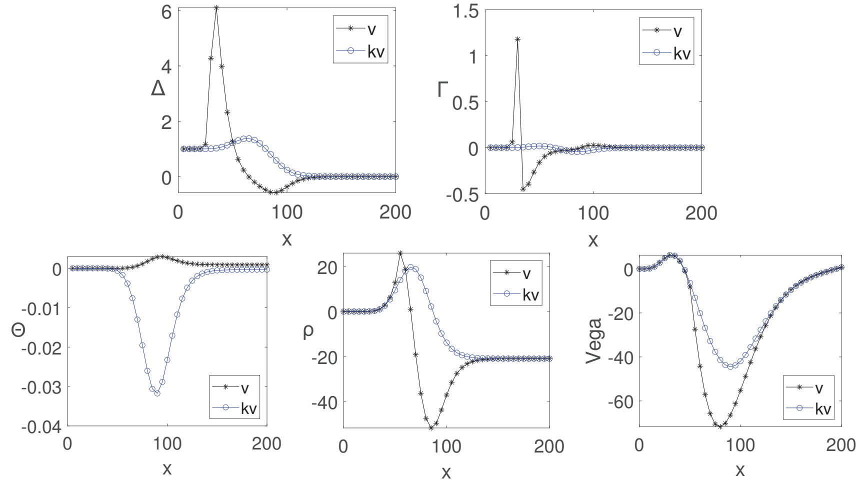

Figure 14. $H_x = H_y = H_z = 0.5$, figures represent in turn are Delta, Gamma, Theta, Rho and Vega. The blue curve stands for option price with knock-in-barrier while the black curve represents option price without knock-in-barrier. For interpretation of the references to color in the figure, the reader is referred to the web version of the article.

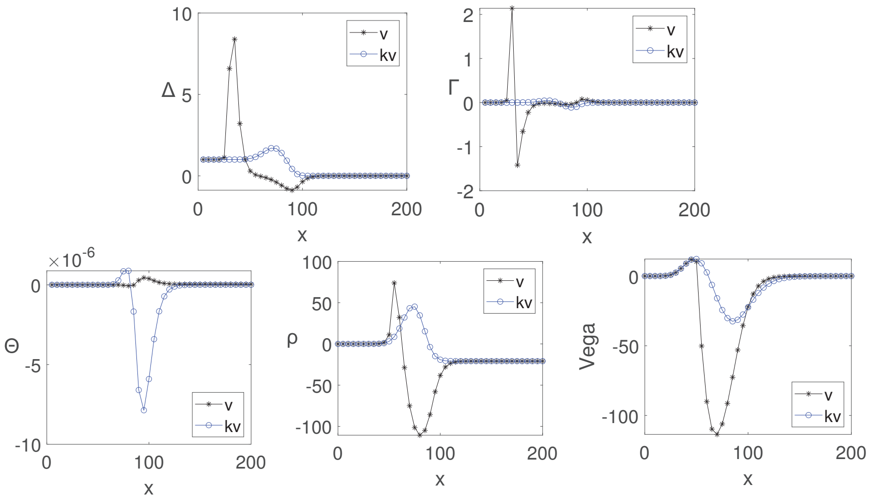

Figure 15. $H_x = H_y = H_z = 0.7$, figures represent in turn are Delta, Gamma, Theta, Rho and Vega. The blue curve stands for option price with knock-in-barrier while the black curve represents option price without knock-in-barrier. For interpretation of the references to color in the figure, the reader is referred to the web version of the article.

5. Conclusions

We established finite difference scheme for the step-down ELS option of one, two and three assets under the fractional Black-Scholes model. In the case of one asset, we established the Crank-Nicolson scheme, in the case of two assets, we established implicit scheme and in the case of three assets, we also used OSM method to establish semi-implicit scheme. Numerical experiments were performed after meshing at equal intervals, and the results were obtained. Regardless of whether the knock-in-barrier is triggered, the return of repayment will be affected by H. As the value of H increases, the return of repayment will also increase. The gap between the result v obtained when the knock-in-barrier is occurred and the result kv obtained when the knock-in-barrier is not occurred is also increasing. Under different assets forms, we also had explored the relationship between H and v and kv when option price is fixed. It can be confirmed that the conclusion that the values of v and kv increase with the increases of the value of H. We also conducted Greeks analysis and discovered that the values of Delta, Gamma, Theta, Rho and Vega are all different under the fractal exponents of 0.3, 0.5 and 0.7, which implies the stock price series of the investment market all have obvious long-term correlation and memory characteristics. In our model, during the process of hedging, different fractal exponents can provide investors or investment companies with constructive advice in the calculation process of Greeks hedging, and can help reduce losses in time before losses damage. Moreover, the option price can be more accurately described.

Author Contributions: Conceptualization, Software, Methodology X.W.; Writing-original draft, S.W.; Data curation, Validation, Visualization, W.S.; Writing—review & editing, Supervision, J.W. All authors have read and agreed to the published version of the manuscript.

Funding: This research was funded by the Natural Science Foundation of the Jiangsu Higher Education Institutions of China (Grant No. 22KJB110020).

Institutional Review Board Statement: Not applicable.

Informed Consent Statement: Not applicable.

Data Availability Statement: The data that support the findings of this study are available on request from the corresponding author upon reasonable request.

Acknowledgments: The corresponding author Jian Wang expresses thanks for the Natural Science Foundation of the Jiangsu Higher Education Institutions of China (Grant Nos. 22KJB110020). The authors are grateful to the reviewers for their valuable suggestions and comments, which significantly improved the quality of this article.

Conflicts of Interest: The authors declare no conflict of interest.

References

1. Chen, A.H.; Kensinger, J.W. An analysis of market-index certificates of deposit. *J. Financ. Serv. Res.* **1990**, *4*, 93–110. [CrossRef]
2. Baubonis, C.; Gastineau, G.L.; Purcell, D. The Banker's Guide to Equity-Linked Certificates of Deposit. *J. Deriv.* **1993**, *1*, 87–95. [CrossRef]
3. Kim, J.; Kim, T.; Jo, J.; Choi, Y.; Lee, S.; Hwang, H.; Yoo, M.; Jeong, D. A practical finite difference method for the three-dimensional Black-Scholes equation. *Eur. J. Oper. Res.* **2016**, *252*, 183–190. [CrossRef]
4. Jeong, D.; Kim, J. A comparison study of ADI and operator splitting methods on option pricing models. *J. Comput. Appl. Math.* **2013**, *247*, 162–171. [CrossRef]
5. Bachelier, L. Theoryofspeculation. In *The Random Characterof Stock Market*; Ksotner, P., Ed.; MIT Press: Cambridge, NA, USA, 1900.
6. Sumuelson, P.A. Rational theory of warrant pricing. *Ind. Manag. Rev.* **1965**, *6*, 13–31.
7. Black, F.; Scholes, M. The Pricing of Options and Corporate Liabilities. *J. Political Econ.* **1973**, *81*, 637–654. [CrossRef]
8. Mandelbrot, B.B.; Van Ness, J.W. Fractional Brownian motion, fractional noises and applications. *SIAM Rev.* **1968**, *10*, 422–436. [CrossRef]
9. Hazhir, A.; Mahsan, T.K.; Hamid, K. Option pricing under finite moment log stable process in a regulated market: A generalized fractional path integral formulation and Monte Carlo based simulation. *Commun. Nonlinear Sci. Numer. Simul.* **2020**, *90*, 105345.
10. Lin, S.; He, J.X. A regime switching fractional Black–Scholes model and European option pricing. *Commun. Nonlinear Sci. Numer. Simul.* **2020**, *85*, 105222. [CrossRef]
11. Grzegorz, K.; Marcin, M. A computational weighted finite difference method for American and barrier options in subdiffusive Black–Scholes model. *Commun. Nonlinear Sci. Numer. Simul.* **2021**, *95*, 105676.
12. Peter, E.E. Fractal Structure in the Captial Market. *Financ. Anal. J.* **1989**, *45*, 32–37. [CrossRef]
13. Karatzas, I.; Shreve, S.E. Brownian motion and stochastic calculus. *Acta Appl. Math.* **1991**, *24*, 197–200.
14. Radu, V. Analysis of the Romanian Capital Market Using the Fractal Dimension. *Fractal Fract.* **2022**, *6*, 564. [CrossRef]
15. Li, Y. Multifractal Characteristics of China's Stock Market and Slump's Fractal Prediction. *Fractal Fract.* **2022**, *6*, 499. [CrossRef]
16. Zhang, J.; Wang, Y.; Zhang, S. A New Homotopy Transformation Method for Solving the Fuzzy Fractional Black–Scholes European Option Pricing Equations under the Concept of Granular Differentiability. *Fractal Fract.* **2020**, *6*, 286. [CrossRef]
17. Sarraj, M.; Ben Mabrouk, A. The Systematic Risk at the Crisis—A Multifractal Non-Uniform Wavelet Systematic Risk Estimation. *Fractal Fract.* **2021**, *5*, 135. [CrossRef]
18. Necula, C. Option Pricing in a Fractional Brownina Motion Environment. *Math. Rep.* **2002**, *2*, 259–273.
19. Liu, S.Y.; Yang, X.Q. Pricing of european option on dividend-paying stock in a fractional Brownian motion environment. *Math. Econ.* **2002**, *19*, 35–39.
20. Murwaningtyas, C.E.; Kartiko, S.H.; Gunardi Suryawan, P.H. European option pricing by using a mixed fractional brownian motion. *J. Phys. Conf. Ser.* **2019**, *1180*, 012081. [CrossRef]
21. Wang, J.; Yan, Y.; Chen, W.B.; Shao, W.; Tang, W.W. Equitylinked securities option pricing by fractional brownian motion. *Chaos Solitons Fractals* **2021**, *144*, 110716. [CrossRef]
22. Ali, A.; Abbas, M.; Akram, T. New group iterative schemes for solving the two-dimensional anomalous fractional sub-diffusion equation. *J. Math. Comp. Sci.* **2021**, *22*, 119–127. [CrossRef]
23. Oderinu, R.A.; Owolabi, J.A.; Taiwo, M. Approximate solutions of linear time-fractional differential equations. *J. Math. Comput. Sci.* **2023**, *29*, 60–72. [CrossRef]
24. Nikan, O.; Golbabai, A.; Machado, J.A.; Nikazad, T. Numerical solution of the fractional Rayleigh–Stokes model arising in a heated generalized second-grade fluid. *Eng. Comput.* **2021**, *37*, 1751–1764. [CrossRef]
25. Golbabai, A.; Ahmadian, D.; Milev, M. Radial basis functions with application to finance: American put option under jump diffusion. *Math. Comput. Model.* **2012**, *55*, 1354–1362. [CrossRef]
26. Golbabai, A.; Nikan, O.; Nikazad, T. Numerical investigation of the time fractional mobile-immobile advection-dispersion model arising from solute transport in porous media. *Int. J. Appl. Comput. Math.* **2019**, *5*, 1–22. [CrossRef]
27. Golbabai, A.; Nikan, O. A computational method based on the moving least-squares approach for pricing double barrier options in a time-fractional Black–Scholes model. *Comput. Econ.* **2020**, *55*, 119–141. [CrossRef]
28. Golbabai, A.; Nikan, O.; Nikazad, T. Numerical analysis of time fractional Black–Scholes European option pricing model arising in financial market. *Comput. Appl. Math.* **2019**, *38*, 1–24. [CrossRef]
29. Nikan, O.; Avazzadeh, Z.; Tenreiro Machado, J.A. Localized kernel-based meshless method for pricing financial options underlying fractal transmission system. Mathematical Methods in the Applied Sciences. *Math. Methods Appl. Sci.* **2021**. [CrossRef]

30. Hu, Y.; Oksendal, B. Fractional white noise calculus and applications to finance. In *Infinite Dimensional Analysis Quantum Probability and Related Topics*; World Scientific: Singapore, 2003; Volume 6(01), pp. 1–32.
31. Duffy, D.J. *Finite Difference Methods in Financial Engineering: A Partial Differential Equation Approach*, 2nd ed.; John Wiley and Sons: New York, NY, USA, 2006.
32. Jeong, D.; Wee, I.S.; Kim, J. An operator splitting method for pricing the ELS option. *J. Korean Soc. Ind. Appl. Math.* **2010**, *14*, 175–187.
33. Barunik, J.; Kristoufek, L. On Hurst exponent estimation under heavy-tailed distributions. *Phys. A* **2010**, *389*, 3844–3855. [CrossRef]

fractal and fractional

Article

An Analysis of the Fractional-Order Option Pricing Problem for Two Assets by the Generalized Laplace Variational Iteration Approach

Sivaporn Ampun [1], Panumart Sawangtong [1,2,*] and Wannika Sawangtong [2,3]

[1] Department of Mathematics, Faculty of Applied Science, King Mongkut's University of Technology North Bangkok, Bangkok 10800, Thailand
[2] Center of Excellence in Mathematics, Commission on Higher Education, Bangkok 10400, Thailand
[3] Department of Mathematics, Faculty of Science, Mahidol University, Bangkok 10400, Thailand
* Correspondence: panumart.s@sci.kmutnb.ac.th

Abstract: An option is the right to buy or sell a good at a predetermined price in the future. For customers or financial companies, knowing an option's pricing is crucial. It is well recognized that the Black–Scholes model is an effective tool for estimating the cost of an option. The Black–Scholes equation has an explicit analytical solution known as the Black–Scholes formula. In some cases, such as the fractional-order Black–Scholes equation, there is no closed form expression for the modified Black–Scholes equation. This article shows how to find the approximate analytic solutions for the two-dimensional fractional-order Black–Scholes equation based on the generalized Riemann–Liouville fractional derivative. The generalized Laplace variational iteration method, which incorporates the generalized Laplace transform with the variational iteration method, is the methodology used to discover the approximate analytic solutions to such an equation. The expression of the two-parameter Mittag–Leffler function represents the problem's approximate analytical solution. Numerical investigations demonstrate that the proposed scheme is accurate and extremely effective for the two-dimensional fractional-order Black–Scholes Equation in the perspective of the generalized Riemann–Liouville fractional derivative. This guarantees that the generalized Laplace variational iteration method is one of the effective approaches for discovering approximate analytic solutions to fractional-order differential equations.

Keywords: fractional Black–Scholes equation; variational iteration method; generalized fractional derivative; generalized Laplace tranform; generalized Mittag–Leffler function

Citation: Ampun, S.; Sawangtong, P.; Sawangtong, W. An Analysis of the Fractional-Order Option Pricing Problem for Two Assets by the Generalized Laplace Variational Iteration Approach. *Fractal Fract.* **2022**, *6*, 667. https://doi.org/10.3390/fractalfract6110667

Academic Editor: Leung Lung Chan

Received: 15 October 2022
Accepted: 6 November 2022
Published: 11 November 2022

1. Introduction

The right to purchase or sell a basic product at a specific price in the future is known as an option. Options have a significant presence on marketplaces and exchanges. Determining the prices of an option is important for customers or financial companies. The valuation of options is one of the most important challenges in the field of financial investing. It is well known that the Black–Scholes model [1,2] is an effective instrument for figuring out an option's cost. There are analytical and numerical approaches used by researchers to solve the Black–Scholes Equations [3–10].

We observe that the Black–Scholes Equations (1)–(3) are partial differential equations with integer-order derivatives. Further study [11–14] demonstrates that the globalized financial markets are fractal in nature. This illustrates that the traditional Black–Scholes model does not adequately reflect the actual financial market. Studies confirmed the applicability of fractional differential equations many years ago, demonstrating their usefulness for researching aspects linked to fractal geometry and fractal dynamics. Secondly, fractional differential equations provide several benefits in describing significant phenomena in a variety of disciplines, including electromagnetics, fluid flow, acoustics, electrochemistry, as well as material science [15–18]. Is it reasonable to use the fractional differential equation in the financial market? The answer to the question is “yes”. Fractional derivatives can be used in the financial market because they have a property called “self-similarity”. Further, fractional derivatives respond better to long-term repositories than integer order derivatives. The fractional derivative’s remarkable abilities are employed to solve the fractal complexity in the financial market. At the present, there is an increase in the number of publications that discuss the use of fractional calculus in financial theory [19].

The Black–Scholes equation with two assets of a European call option is defined by:

$$\frac{\partial u}{\partial \tau} + \frac{1}{2}\sigma_1^2 S_1^2 \frac{\partial^2 u}{\partial S_1^2} + \frac{1}{2}\sigma_1^2 S_2^2 \frac{\partial^2 u}{\partial S_2^2} + \omega\sigma_1\sigma_2 \frac{\partial^2 u}{\partial S_1 \partial S_2} + r\left(S_1 \frac{\partial u}{\partial S_1} + S_2 \frac{\partial u}{\partial S_2}\right) - ru = 0, \qquad (1)$$

for $(S_1,S_2,\tau) \in [0,\infty) \times [0,\infty) \times [0,T]$, with the terminal condition:

$$u(S_1, S_2, T) = \max\{\beta_1 S_1 + \beta_2 S_2 - K, 0\} \text{ for } (S_1, S_2) \in [0,\infty) \times [0,\infty), \qquad (2)$$

where u is the call option depending on the underlying asset prices S_1, S_2 at time τ;
S_1, S_2 are the asset price variables;
σ_1, σ_2 are the volatility function of underlying assets;
β_1, β_2 are coefficients so that all risky asset price are at the same level;
ω is the volatility of S_1 and S_2;
r is the risk-free interest rate;
T is the expiration date;
$K = \max\{K_1, K_2\}$ where K_i is strike price of the ith underlying asset.

K. Trachoo, W. Sawangtong, and P. Sawangtong [20] researched the two-dimensional Black–Scholes equation with European call option (1) and (2) in 2017. Using the Laplace transform homotopy perturbation approach, they demonstrated that the explicit solution to this issue is represented as a Mellin–Ross function.

P. Sawangtong, K. Trachoo, W. Sawangtong, and B. Wiwattanapataphee [21] investigated the modified Black–Scholes model of (1) and (2) with two assets based on the Liouville–Caputo fractional derivative in 2018. They established, using the Laplace transform homotopy perturbation technique, that the explicit solution to this problem is represented as the Generalized Mittag–Leffler function.

2. The Modified Black–Scholes Equation

The modified Black–Scholes equation in fractional-order derivative form is presented in this section. Let $x = \ln(S_1) - \left(r - \frac{1}{2}\sigma_1^2\right)\tau$, $y = \ln(S_2) - \left(r - \frac{1}{2}\sigma_2^2\right)\tau$, $t = T - \tau$ and $u(S_1, S_2, \tau) = e^{-r(T-\tau)}v(x, y, t)$. Readers may find out more information for transformation in [21]. Without loss of generality, we consider the variables x and y by $x \in [0, x_{\max}]$ and $y \in [0, y_{\max}]$ where $x_{\max}$ and $y_{\max}$ are positive constants. In the end, the Black–Scholes partial differential equation with two assets of the European call option Equations (1) and (2) is capable of being converted into the following form:

$$v_t = \frac{1}{2}\sigma_1^2 \frac{\partial^2 v}{\partial x^2} + \frac{1}{2}\sigma_2^2 \frac{\partial^2 v}{\partial y^2} + \omega\sigma_1\sigma_2 \frac{\partial^2 v}{\partial x \partial y}, \text{ for } (x, y, t) \in [0, x_{\max}] \times [0, y_{\max}] \times [0, T], \qquad (3)$$

with the initial condition:

$$v(x, y, 0) = \max\{c_1 e^x + c_2 e^y - K, 0\}, \text{ for } (x, y) \in [0, x_{\max}] \times [0, y_{\max}], \qquad (4)$$

where c_1 and c_2 are constants defined by

$$c_1 = \beta_1 e^{(r - \frac{1}{2}\sigma_1^2)T} \text{ and } c_2 = \beta_2 e^{(r - \frac{1}{2}\sigma_2^2)T}. \qquad (5)$$

In this study, we extend the previous work [20] and analyze the general form of the Black–Scholes equation in Equations (3) and (4) by replacing the integer-order time derivative with the fractional-order time derivative. The fractional-order Black–Scholes equation based on the generalized Riemann–Liouville fractional derivative with $\alpha \in (0,1)$ is considered in the form:

$$D_t^{\alpha,\rho} u(x,y,t;\rho,\alpha) = \frac{1}{2}\sigma_1^2 \frac{\partial^2 u}{\partial x^2} + \frac{1}{2}\sigma_2^2 \frac{\partial^2 u}{\partial y^2} + \omega\sigma_1\sigma_2 \frac{\partial^2 u}{\partial x \partial y}, \text{ for } (x,y,t) \in [0, x_{\max}] \times [0, y_{\max}] \times [0,T], \tag{6}$$

with the fractional integral initial condition:

$$I_t^{1-\alpha,\rho} u(x,y,0;\rho,\alpha) = \max\{c_1 e^x + c_2 e^y - K, 0\}, \text{ for } (x,y) \in [0, x_{\max}] \times [0, y_{\max}]. \tag{7}$$

where $\rho > 0$, $D_t^{\alpha,\rho}$ and $I_t^{1-\alpha,\rho}$ denote the generalized Riemann–Liouville fractional-order derivative with order α and the generalized fractional-order integral with order $1-\alpha$, respectively.

The generalized Laplace variational iteration method is a methodology combining the variational iteration approach with the generalized Laplace transform. Analytical solutions are more complex to obtain than numerical solutions, particularly for fractional partial differential equations. Consequently, the analytical solution offers a valuable instrument for analyzing financial behavior. The generalized Laplace variational iteration approach is used in this research to provide the approximate analytic solution of the time fractional-order Black–Scholes model with two assets for the European call option (6) and (7). In addition, the closed-form analytic solution of the fractional-order Black–Scholes model (6) and (7) is investigated under certain requirements.

The structure of the article is as follows. The definitions of the generalized fractional-order derivative and integral are presented in Section 3. Section 4 discusses the generalized Laplace variational iteration technique's application and convergence analysis. The explicit solution of the fractional-order Black–Scholes equation is provided in Section 5. In Section 6, numerical results with various parameter values can be seen. This work's conclusion is provided into Section 7.

3. Basic Definitions

In this section, the generalized Riemann–Liouville fractional integral, the generalized Riemann–Liouville fractional derivative, and the generalized Laplace transform with their some properties have been discussed. For more details, readers can see [22,23]. Throughout this article, we assume that α and ρ are constants with $0 < \alpha \le 1$ and $\rho > 0$, and we denote the gamma function by Γ.

Definition 1. *The generalized fractional-order integral α of a continuous function $f : [0,\infty) \to R$ is expressed as*

$$I_t^{\alpha,\rho} f(t) = \frac{1}{\Gamma(\alpha)} \int_0^t \left(\frac{t^\rho - \tau^\rho}{\rho}\right)^{\alpha-1} \frac{f(\tau)}{\tau^{1-\rho}} d\tau.$$

Definition 2. *The generalized Riemann–Liouville fractional-order derivative of α of a continuous function $f : [0,\infty) \to R$ is given as*

$$D_t^{\alpha,\rho} f(t) = \frac{1}{\Gamma(1-\alpha)} \left(t^{1-\rho}\frac{d}{dt}\right) \int_0^t \left(\frac{t^\rho - \tau^\rho}{\rho}\right)^{-\alpha} \frac{f(\tau)}{\tau^{1-\rho}} d\tau.$$

We next give some properties that deal with the generalized Riemann–Liouville fractional derivative.

Lemma 1. *Let $f : [0,\infty) \to R$ be a continuous function and c be a constant. Then,*

1. $I_t^{\alpha,\rho}\left(\frac{t^\rho}{\rho}\right)^c = \frac{\Gamma(c+1)}{\Gamma(c+\alpha+1)}\left(\frac{t^\rho}{\rho}\right)^{c+\alpha}$,
2. $D_t^{\alpha,\rho} I_t^{\alpha,\rho} f(t) = f(t)$,
3. $D_t^{\alpha,\rho} c = \frac{\rho^{\alpha-1}}{\Gamma(1-\alpha)} t^{-\alpha\rho}$.

The following part discusses the generalized Laplace transform and some of its properties.

Definition 3. *The generalized Laplace transform of a continuous function* $f : [0,\infty) \to R$ *is defined as*

$$\mathcal{L}_\rho\{f(t)\}(s) = \int_0^\infty e^{-s\frac{t^\rho}{\rho}} \frac{f(t)}{t^{1-\rho}} dt,$$

where s is the Laplace transform parameter.

It is important to note that the generalized Laplace transform can be reduced to the Laplace transform when $\rho = 1$.

Lemma 2. *Let* $f : [0,\infty) \to R$ *be a continuous function and c be a constant. Then,*

1. $\mathcal{L}_\rho\left\{\left(\frac{t^\rho}{\rho}\right)^c\right\} = \frac{\Gamma(c)}{s^{c+1}}$,
2. $\mathcal{L}_\rho\left\{D_t^{\alpha,\rho} f(t)\right\} = s^\alpha \mathcal{L}_\rho\{f(t)\}(s) - I_t^{1-\alpha,\rho} f(0)$.

Definition 4. *Let* $f : [0,\infty) \to R$ *and* $g : [0,\infty) \to R$ *be continuous functions. The generalized convolution of f and g is defined by*

$$f(t) *_\rho g(t) = \int_0^t f\left((t^\rho - \tau^\rho)^{\frac{1}{\rho}}\right) g(\tau) \frac{d\tau}{\tau^{1-\rho}},$$

if the integral exists.

Lemma 3. *Let* $f : [0,\infty) \to R$ *and* $g : [0,\infty) \to R$ *be continuous functions. If* $\mathcal{L}_\rho\{f(t)\}(s)$ *and* $\mathcal{L}_\rho\{g(t)\}(s)$ *exist, then*

$$\mathcal{L}_\rho\{f(t) *_\rho g(t)\}(s) = \mathcal{L}_\rho\{f(t)\}(s)\mathcal{L}_\rho\{g(t)\}(s).$$

In the last part of this section, we will introduce a special function that helps us rewrite complex expressions in a simple form.

Definition 5. *The two-parameter Mittag–Leffler function is defined as follows:*

$$E_{\alpha,\beta}(z) = \sum_{k=0}^\infty \frac{z^k}{\Gamma(\alpha k + \beta)},$$

where Γ *denotes the Gamma function,* $\alpha > 0$, $\beta \in R$ *and* $z \in C$.

It is important to note that, $E_{1,2}(z) = \frac{e^z - 1}{z}$.

4. The General Methodology of the Generalized Laplace Variational Iteration Method

In this section, we apply the generalized variational iteration method to the nonlinear partial differential equation. Assume that Ω is the bounded domain. Let us consider the following general fractional differential equation in the generalized Riemann–Liouville fractional derivative

$$D_t^{\alpha,\rho} u(x,y,t) + R[u(x,y,t)] + N[u(x,y,t)] = f(x,y,t) \text{ for } (x,y,t) \in \Omega \times [0,T], \quad (8)$$

and the generalized Riemann–Liouville fractional initial condition

$$I_t^{1-\alpha,\rho}u(x,y,0) = g(x,y) \text{ for } (x,y) \in \overline{\Omega} \tag{9}$$

where $D_t^{\alpha,\rho}$ and $I_t^{\alpha,\rho}$ are the generalized Riemann–Liouville fractional derivative and integral of order $0 < \alpha \leq 1$, respectively, $R[u]$ is a linear term, $N[u]$ is a nonlinear term and f and g are given functions.

In the first step of the process, we find the suitable Lagrange multiplier λ that will be found by using properties of the generalized Riemann–Liouville fractional derivative and integral.

Based on the generalized Riemann–Liouville integration, the correction functional for the nonlinear problem (8) and (9) is defined by

$$u_{n+1}(x,y,t) = u_n(x,y,t) + I_t^{\alpha,\rho}\lambda\left((t^\rho - \tau^\rho)^{\frac{1}{\rho}}\right)[D_t^{\alpha,\rho}u_n(x,y,\tau) + R[u_n] + N[u_n] - f(x,y,t)]. \tag{10}$$

4.1. Lagrange Multipliers

Theorem 1. *The Lagrange multiplier λ for the fractional-order nonlinear partial differential Equations (8) and (9) can be determined by $\lambda\left((t^\rho - \tau^\rho)^{\frac{1}{\rho}}\right) = -1$.*

Proof. Let us consider the correction functional (10) for the nonlinear problem (8) and (9):

$$\begin{aligned}
u_{n+1}(x,y,t) &= u_n(x,y,t) + I_t^{\alpha,\rho}\lambda\left((t^\rho - \tau^\rho)^{\frac{1}{\rho}}\right)\Big[D_\tau^{\alpha,\rho}u_n(x,y,t) + R[u_n(x,y,t)] \\
&\quad - N[u_n(x,y,t)] - f(x,y,t)\Big] \\
u_{n+1}(x,y,t) &= u_n(x,y,t) + \frac{1}{\Gamma(\alpha)}\int_0^t \left(\frac{t^\rho - \tau^\rho}{\rho}\right)^{\alpha-1}\lambda\left((t^\rho - \tau^\rho)^{\frac{1}{\rho}}\right)D_\tau^{\alpha,\rho}u_n(x,y,\tau)\frac{d\tau}{\tau^{1-\rho}} \\
&\quad + \frac{1}{\Gamma(\alpha)}\int_0^t \left(\frac{t^\rho - \tau^\rho}{\rho}\right)^{\alpha-1}\lambda\left((t^\rho - \tau^\rho)^{\frac{1}{\rho}}\right)[R[u_n] - N[u_n] - f(x,y,\tau)]\frac{d\tau}{\tau^{1-\rho}}.
\end{aligned}$$

Let $a(t) = t^{\rho(\alpha-1)}\lambda(t)$. Thus,

$$\begin{aligned}
u_{n+1}(x,y,t) &= u_n(x,y,t) + \frac{\rho^{1-\alpha}}{\Gamma(\alpha)}a(t) *_\rho D_t^{\alpha,\rho}u_n(x,y,t) \\
&\quad + \frac{1}{\Gamma(\alpha)}\int_0^t \left(\frac{t^\rho - \tau^\rho}{\rho}\right)^{\alpha-1}\lambda\left((t^\rho - \tau^\rho)^{\frac{1}{\rho}}\right)\Big[R[u_n] - N[u_n] \\
&\quad - f(x,y,\tau)\Big]\frac{d\tau}{\tau^{1-\rho}},
\end{aligned}$$

where $a(t) *_\rho D_t^{\alpha,\rho}u_n(x,y,t)$ is the generalized convolution of a and $D_t^{\alpha,\rho}u_n$. The generalized Laplace variational iteration correction functional will be defined in the following manner:

$$\begin{aligned}
\mathcal{L}_\rho\{u_{n+1}(x,y,t)\}(s) &= \mathcal{L}_\rho\{u_n(x,y,t)\}(s) + \frac{\rho^{1-\alpha}}{\Gamma(\alpha)}\mathcal{L}_\rho\Big\{a(t) *_\rho D_\tau^{\alpha,\rho}u_n(x,y,t)\Big\}(s) \\
&\quad + \frac{1}{\Gamma(\alpha)}\mathcal{L}_\rho\Big\{\int_0^t \left(\frac{t^\rho - \tau^\rho}{\rho}\right)^{\alpha-1}\lambda\left((t^\rho - \tau^\rho)^{\frac{1}{\rho}}\right)\Big[R[u_n] - N[u_n] \\
&\quad - f(x,y,\tau)\Big]\frac{d\tau}{\tau^{1-\rho}}\Big\}(s)
\end{aligned}$$

or equivalenty, upon applying the properties of the Laplace transform, we have

$$\begin{aligned}\mathcal{L}_\rho\{u_{n+1}(x,y,t)\}(s) &= \mathcal{L}_\rho\{u_n(x,y,t)\}(s) + \frac{\rho^{1-\alpha}}{\Gamma(\alpha)}\mathcal{L}_\rho\{a(t)\}(s)\{s^\alpha\mathcal{L}_\rho\{u_n(x,y,t)\}(s) - g(x,y)\} \\ &\quad + \frac{1}{\Gamma(\alpha))}\mathcal{L}_\rho\Big\{\int_0^t \left(\frac{t^\rho - \tau^\rho}{\rho}\right)^{\alpha-1}\lambda\left((t^\rho - \tau^\rho)^{\frac{1}{\rho}}\right)\Big[R[u_n] - N[u_n] \\ &\quad - f(x,y,\tau)\Big]\frac{d\tau}{\tau^{1-\rho}}\Big\}(s)\end{aligned}$$

Taking the variation with respect to u_n of both side of the latter equation, leads to

$$\begin{aligned}\frac{\delta}{\delta u_n}\mathcal{L}_\rho\{u_{n+1}(x,y,t)\}(s) &= \frac{\delta}{\delta u_n}\mathcal{L}_\rho\{u_n(x,y,t)\}(s) \\ &\quad + \frac{\delta}{\delta u_n}\frac{\rho^{1-\alpha}}{\Gamma(\alpha)}\mathcal{L}_\rho\{a(t)\}(s)\{s^\alpha\mathcal{L}_\rho\{u_n(x,y,t)\}(s) - g(x,y)\} \\ &\quad + \frac{\delta}{\delta u_n}\frac{1}{\Gamma(\alpha))}\mathcal{L}_\rho\Big\{\int_0^t \left(\frac{t^\rho - \tau^\rho}{\rho}\right)^{\alpha-1}\lambda\left((t^\rho - \tau^\rho)^{\frac{1}{\rho}}\right)\Big[R[u_n] - N[u_n] \\ &\quad - f(x,y,\tau)\Big]\frac{d\tau}{\tau^{1-\rho}}\Big\}(s)\end{aligned}$$

and upopn simplification we obtain

$$\begin{aligned}\mathcal{L}_\rho\left\{\frac{\delta}{\delta u_n}u_{n+1}(x,y,t)\right\}(s) &= \mathcal{L}_\rho\left\{\frac{\delta}{\delta u_n}u_n(x,y,t)\right\}(s) \\ &\quad + \frac{\rho^{1-\alpha}}{\Gamma(\alpha)}\mathcal{L}_\rho\{a(t)\}(s)\frac{\delta}{\delta u_n}\{s^\alpha\mathcal{L}_\rho\{u_n(x,y,t)\}(s) - g(x,y)\} \\ &\quad + \frac{1}{\Gamma(\alpha)}\mathcal{L}_\rho\Big\{\int_0^t (t-\tau)^{\alpha-1}\lambda\left((t^\rho - \tau^\rho)^{\frac{1}{\rho}}\right)\frac{\delta}{\delta u_n}\Big[R[u_n] - N[u_n] \\ &\quad - f(x,y,\tau)\Big]\frac{d\tau}{\tau^{1-\rho}}\Big\}(s)\end{aligned}$$

Furthermore, the extra condition of u_{n+1} requires that $\frac{\delta}{\delta u_n}u_{n+1}(x,y,t) = 0$. Moreover, the terms $R[u_n]$ and $N[u_n]$ are considered as restricted variations, which implies $\frac{\delta}{\delta u_n}R[u_n] = 0$ and $\frac{\delta}{\delta u_n}N[u_n] = 0$. We then obtain $1 + \frac{\rho^{1-\alpha}s^\alpha}{\Gamma(\alpha)}\mathcal{L}_\rho\{a(t)\}(s) = 0$ or

$$\mathcal{L}_\rho\{a(t)\}(s) = -\frac{\Gamma(\alpha)}{\rho^{1-\alpha}s^\alpha}.$$

The inverse generalized Laplace transform implies that

$$a(t) = -\frac{1}{\rho^{1-\alpha}}\left(\frac{t^\rho}{\rho}\right)^{\alpha-1} = -t^{\rho(\alpha-1)}.$$

By the definition of a, the Lagrange multipliers is $\lambda(t) = -1$. □

Note that it follows form Theorem 1 that the correction functional (10) associated with (8) and (9), is formed as:

$$u_{n+1}(x,y,t) = u_n(x,y,t) - I_t^{\alpha,\rho}[D_t^{\alpha,\rho}u_n(x,y,\tau) + R[u_n] + N[u_n] - f(x,y,t)].$$

4.2. Convergence Analysis of the Proposed Method

In this section, we study the convergence of the generalized Laplace variational iteration method, when applied to the nonlinear partial differential Equations (8) and (9). The sufficient conditions for convergence of the method and the error estimate are presented. The main results are proposed in the below theorems.

We next define the operator $A : D(A) \subseteq H \to H$, where $D(A)$ is the domain of the operator A and $(H, \|\cdot\|_H)$ is a Banach space, by:

$$A[u(x,y,t)] = -I_t^{\alpha,\rho}\Big[D_t^{\alpha,\rho}u(x,y,t) + R[u(x,y,t)] + N[u(x,y,t)] - f(x,y,t)\Big], \tag{11}$$

and define the sequence $\{v_n\}_{n=0}^{\infty}$ by:

$$\left.\begin{aligned} v_0(x,y,t) &= u_0(x,y,t)\\ v_1(x,y,t) &= A[v_0]\\ v_2(x,y,t) &= A[v_0(x,y,t) + v_1(x,y,t)]\\ v_3(x,y,t) &= A[v_0(x,y,t) + v_1(x,y,t) + v_2(x,y,t)]\\ &\vdots\\ v_n(x,y,t) &= A[v_0(x,y,t) + v_1(x,y,t) + \ldots + v_{n-1}(x,y,t)]. \end{aligned}\right\} \tag{12}$$

The relationship between the sequences $\{u_n\}_{n=0}^{\infty}$ and $\{v_n\}_{n=0}^{\infty}$ given by (10) and (12), respectively, is shown in the following lemma.

Lemma 4. *Let $\{u_n\}_{n=0}^{\infty}$ and $\{v_n\}_{n=0}^{\infty}$ be the sequences constructed by (10) and (12), respectively. Then, $u_n = \sum\limits_{k=0}^{n} v_k$ for any $n = 0, 1, 2, \ldots$.*

Proof. We can deduce from (10) and (12) that $v_1 = A[v_0]$ and $u_1 = u_0 + A[u_0]$. This implies that

$$u_1 = u_0 + v_1. \tag{13}$$

We also know that from (10) and (12), $v_2 = A[v_0 + v_1]$ and $u_2 = u_1 + A[u_1]$. By (13), we then get

$$u_2 = u_1 + v_2. \tag{14}$$

Once again, we find that $v_3 = A[v_0 + v_1 + v_2]$ and $u_3 = u_2 + A[u_2]$. This yields, by (13) and (14), that $u_3 = u_2 + v_3$. Throughout this procedure, we finally discover that that $u_n = u_{n-1} + v_n$ for any $n \geq 1$. This will lead to the desired results. □

It is important to note that, if the limit exists, Lemma 4 enables us to get that $\lim_{n\to\infty} u_n(x,y,t) = \sum\limits_{n=0}^{\infty} v_n(x,y,t)$.

The next lemma shows the convergence of the infinite series $\sum\limits_{n=0}^{\infty} v_n(x,y,t)$.

Lemma 5. *Assume that there exists a positive real number γ with $\gamma < 1$ such that $\|v_{n+1}\|_H \leq \gamma \|v_n\|_H$ for any $n = 0, 1, 2, 3, \ldots$. Then, the infinite series $\sum\limits_{n=0}^{\infty} v_n(x,y,t)$ given by (12) converges.*

Proof. Let S_n denote the partial sum of the infinite series $\sum\limits_{n=0}^{\infty} v_n(x,y,t)$. We would like to show that the sequence $\{S_n\}_{n=0}^{\infty}$ is a Cauchy sequence in the Banach space H. It follows from the assumption of the theorem that we have:

$$\|S_{n+1} - S_n\|_H = \|v_{n+1}\|_H \leq \gamma\|v_n\|_H \leq \gamma^2\|v_{n-1}\|_H \leq \cdots \leq \gamma^{n+1}\|v_0\|_H. \tag{15}$$

Let n and m be any natural numbers with $n \geq m$. We consider that by (15):

$$\begin{aligned} \|S_n - S_m\|_H &= \|(S_n - S_{n-1}) + (S_{n-1} - S_{n-2}) + \ldots + (S_{m+1} - S_m)\|_H \\ &\leq \|S_n - S_{n-1}\|_H + \|S_{n-1} - S_{n-2}\|_H + \ldots + \|S_{m+1} - S_m\|_H \\ &\leq \gamma^n \|v_0\|_H + \gamma^{n-1}\|v_0\|_H + \ldots + \gamma^{m+1}\|v_0\|_H \\ &= \frac{1-\gamma^{n-m}}{1-\gamma}\gamma^{m+1}\|v_0\|_H. \end{aligned}$$

We can deduce from the fact that $0 < \gamma < 1$ that:

$$\lim_{m\to\infty} \|S_n - S_m\|_H = 0.$$

Therefore, $\{S_n\}_{n=0}^{\infty}$ is a Cauchy sequence in the Banach space H. This information indicates that the infinite series $\sum\limits_{n=0}^{\infty} v_n(x,y,t)$ determined by (12) converges in the Banach space H. Hence, Lemma 1 is proved completely.

The below theorem demonstrates that the convergent series $\sum\limits_{n=0}^{\infty} v_n(x,y,t)$ is the solution of the nonlinear Equations (8) and (9). □

Lemma 6. *Let $\phi(x,y,t)$ be the function such that the infinite series $\sum\limits_{n=0}^{\infty} v_n(x,y,t)$, determined by (12), converges to $\phi(x,y,t)$. Then, the function $\phi(x,y,t)$ is the solution of the nonlinear partial differential Equations (8) and (9) for any $(x,y,t) \in \overline{\Omega} \times [0,T]$.*

Proof. By the property of the convergent series $\sum\limits_{n=0}^{\infty} v_n(x,y,t)$, we get that $\lim_{n\to\infty} v_n(x,y,t) = 0$. Let us consider the following:

$$\sum_{n=0}^{k}[v_{n+1}(x,y,t) - v_n(x,y,t)] = v_{k+1}(x,y,t) - v_0(x,y,t)$$

and

$$\begin{aligned} &\sum_{n=0}^{\infty}[v_{n+1}(x,y,t) - v_n(x,y,t)] \\ =\ & \lim_{k\to\infty}\sum_{n=0}^{k}[v_{n+1}(x,y,t) - v_n(x,y,t)] \\ =\ & \lim_{k\to\infty} v_{k+1}(x,y,t) - v_0(x,y,t) \\ =\ & -v_0(x,y,t). \end{aligned} \tag{16}$$

Taking the generalized Riemann–Liouville fractional derivative on both sides of (17), we find that:

$$D_t^{\alpha,\rho}\sum_{n=0}^{\infty}[v_{n+1}(x,y,t) - v_n(x,y,t)] = \sum_{n=0}^{\infty} D_t^{\alpha,\rho}[v_{n+1}(x,y,t) - v_n(x,y,t)] = -D_t^{\alpha,\rho}v_0(x,y,t). \tag{17}$$

It follows from (11) and (12) and the linearity property of operators that we obtain:

$$\begin{aligned} & D_t^{\alpha,\rho}[v_{n+1}(x,y,t) - v_n(x,y,t)] \\ =\ & D_t^{\alpha,\rho}A[v_0(x,y,t) + v_1(x,y,t) + \ldots + v_n(x,y,t)] \\ & -D_t^{\alpha,\rho}A[v_0(x,y,t) + v_1(x,y,t) + \ldots + v_{n-1}(x,y,t)] \\ =\ & -D_t^{\alpha,\rho}v_n(x,y,t) - R[v_n] - N[v_0 + v_1 + \ldots + v_n] + N[v_0 + v_1 + \ldots + v_{n-1}] \end{aligned} \tag{18}$$

for all $n \geq 1$. As a result of (19), we now have that:

$$\begin{aligned}
&\sum_{n=0}^{k} D_t^{\alpha,\rho}[v_{n+1}(x,y,t) - v_n(x,y,t)] \\
= \; & D_t^{\alpha,\rho}[v_1(x,y,t) - v_0(x,y,t)] + \sum_{n=1}^{k} D_t^{\alpha,\rho}[v_{n+1}(x,y,t) - v_n(x,y,t)] \\
= \; & D_t^{\alpha,\rho} v_1(x,y,t) - D_t^{\alpha,\rho} v_0(x,y,t) \qquad (19)\\
& -D_t^{\alpha,\rho} v_1(x,y,t) - R[v_1(x,y,t)] - N[v_0(x,y,t) + v_1(x,y,t)] + N[v_0(x,y,t)] \\
& -D_t^{\alpha,\rho} v_2(x,y,t) - R[v_2(x,y,t)] - N[v_0(x,y,t) + v_1(x,y,t) + v_2(x,y,t)] + N[v_0 + v_1] \\
& \vdots \\
& -D_t^{\alpha,\rho} v_k(x,y,t) - R[v_k(x,y,t)] - N[v_0 + v_1 + \ldots + v_k] + N[v_0 + v_1 + \ldots + v_{k-1}].
\end{aligned}$$

The fact that $D_t^{\alpha,\rho} v_1(x,y,t) = D_t^{\alpha,\rho} A[v_0] = -D_t^{\alpha,\rho} v_0(x,y,t) - R[v_0(x,y,t)] - N[v_0(x,y,t)] + f(x,y,t)$, yields that the Equation (19) becomes:

$$\begin{aligned}
&\sum_{n=0}^{k} D_t^{\alpha,\rho}[v_{n+1}(x,y,t) - v_n(x,y,t)] \\
= \; & -D_t^{\alpha,\rho} v_0(x,y,t) - D_t^{\alpha,\rho}\left[\sum_{n=0}^{k} v_n(x,y,t)\right] - R\left[\sum_{n=0}^{k} v_n(x,y,t)\right] \qquad (20)\\
& -N\left[\sum_{n=0}^{k} v_n(x,y,t)\right] + f(x,y,t).
\end{aligned}$$

From (17) and (20), we obtain that as $k \to \infty$,

$$D_t^{\alpha,\rho}\left[\sum_{n=0}^{\infty} v_n(x,y,t)\right] + R\left[\sum_{n=0}^{\infty} v_n(x,y,t)\right] + N\left[\sum_{n=0}^{\infty} v_n(x,y,t)\right] = f(x,y,t),$$

or

$$D_t^{\alpha,\rho} \phi(x,y,t) + R[\phi(x,y,t)] + N[\phi(x,y,t)] = f(x,y,t).$$

This information implies $\sum\limits_{n=0}^{\infty} v_n(x,y,t)$ is the infinite series solution of the nonlinear partial differential Equations (8) and (9). □

Lemma 7. *Assume that the infinite series* $\sum\limits_{n=0}^{\infty} v_n(x,y,t)$, *where* v_n *is defined by (12), converges to the solution* u *of the nonlinear partial differential Equations (8) and (9). If the approximate analytic solution* u_{approx} *is the truncated series constructed by* $u_{approx} = u_M(x,y,t) = \sum\limits_{n=0}^{M} v_n(x,y,t)$ *for any* $(x,y,t) \in \overline{\Omega} \times [0,T]$, *then the maximum error norm can be evaluated as*

$$\|u - u_M\|_H \leq \frac{1}{1-\gamma}\gamma^{M+1}\|v_0\|_H$$

where γ *is the real number given in Lemma 5.*

Proof. Let n and M be any natural numbers with $n \geq M$. As discussed in Theorem 1, we obtain that:

$$\|S_n - S_M\|_H \leq \frac{1-\gamma^{n-M}}{1-\gamma}\gamma^{M+1}\|v_0\|_H$$

where S_n is the partial sum of the infinite series $\sum_{n=0}^{\infty} v_n(x,y,t)$. As we let n approach to infinity, we obtain that:

$$\left\| u - \sum_{n=0}^{M} v_n \right\|_H \le \frac{1-\gamma^{n-M}}{1-\gamma} \gamma^{M+1} \|v_0\|_H.$$

The definition of real number γ implies that $1-\gamma^{n-M} < 1$ and

$$\left\| u - \sum_{n=0}^{M} v_n \right\|_H \le \frac{1}{1-\gamma} \gamma^{M+1} \|v_0\|_H.$$

The proof of Lemma 7 is therefore complete. □

The following main theorem is the result from Lemmas 5 and 6.

Theorem 2. *By using the generalized Laplace variational iteration approach, the approximate analytic solution u_{approx} for the general fractional differential Equation (8) with the integral initial condition (9) can be obtained by the following iteration:*

$$\begin{aligned} &u_0(x,y,t) \text{ is an arbitrary function,} \\ &u_{n+1}(x,y,t) = u_n(x,y,t) - I_t^{\alpha,\rho}\left[D_\tau^{\alpha,\rho} u_n(x,y,t) + R[u_n(x,y,t)] + N[u_n(x,y,t)] - f(x,y,t)\right]. \end{aligned}$$

for any $(x,y,t) \in \overline{\Omega} \times [0,T]$ and for all $n \ge 1$. Moreover, if $\lim_{n\to\infty} u_n(x,y,t)$ exists, then the analytic solution u for the general fractional differential Equation (8) with the integral initial condition (9) can be found by

$$u(x,y,t) = \lim_{n\to\infty} u_n(x,y,t) \text{ for any } (x,y,t) \in \overline{\Omega} \times [0,T].$$

5. An Application of the Generalized Laplace Variational Iteration Method

In this part, we will apply the generalized Laplace variational iteration method to the fractional-order Black–Scholes equation based on the generalized Riemann–Liouville fractional derivative with the fractional integral initial condition (6) and (7). By (8) and (9), we set that $R[u_n] = -\left(\frac{1}{2}\sigma_1^2 \frac{\partial^2 u_n}{\partial x^2} + \frac{1}{2}\sigma_2^2 \frac{\partial^2 u_n}{\partial y^2} + \omega\sigma_1\sigma_2 \frac{\partial^2 u_n}{\partial x \partial y}\right)$, $N[u_n] = 0$, $f(x,y,t) = 0$ and $g(x,y) = \max\{c_1 e^x + c_2 e^y - K, 0\}$. By Theorem 2 and by choosing

$$u_0(x,y,t) = \frac{1}{\Gamma(\alpha)} \max\{c_1 e^x + c_2 e^y - K, 0\} \left(\frac{t^\rho}{\rho}\right)^{\alpha-1} + \frac{1}{\Gamma(\alpha+1)} \omega e^{x+y} \left(\frac{t^\rho}{\rho}\right)^{\alpha},$$

We obtain that:

$$\begin{aligned} u_0(x,y,t) &= \tfrac{1}{\Gamma(\alpha)} \max\{c_1 e^x + c_2 e^y - K, 0\} \left(\tfrac{t^\rho}{\rho}\right)^{\alpha-1} + \tfrac{1}{\Gamma(\alpha+1)} \omega e^{x+y} \left(\tfrac{t^\rho}{\rho}\right)^{\alpha}, \\ u_{n+1}(x,y,t) &= u_n(x,y,t) - \tfrac{1}{\Gamma(\alpha)} \int_0^t \left(\tfrac{t^\rho - \tau^\rho}{\rho}\right)^{\alpha-1} \Big(D_\tau^{\alpha,\rho} u_n - \tfrac{1}{2}\sigma_1^2 \tfrac{\partial^2 u_n}{\partial x^2} - \tfrac{1}{2}\sigma_2^2 \tfrac{\partial^2 u_n}{\partial y^2} \\ &\quad - \omega\sigma_1\sigma_2 \tfrac{\partial^2 u_n}{\partial x \partial y} \Big) \tfrac{d\tau}{\tau^{1-\rho}}, \ n \ge 0. \end{aligned}$$

Note that $I_t^{1-\alpha,\rho}u_0(x,y,0)=\max\{c_1e^x+c_2e^y-K,0\}$. The generalized Laplace transform is then used to aid us discover the terms u_n for $n\geq 1$. Let us consider the following:

$$\begin{aligned}
u_{n+1}(x,y,t) &= u_n(x,y,t)-\frac{1}{\Gamma(\alpha)}\int_0^t\left(\frac{t^\rho-\tau^\rho}{\rho}\right)^{\alpha-1}D_\tau^{\alpha,\rho}u_n(x,y,\tau)\frac{d\tau}{\tau^{1-\rho}}\\
&\quad+\frac{1}{\Gamma(\alpha)}\int_0^t\left(\frac{t^\rho-\tau^\rho}{\rho}\right)^{\alpha-1}\left(\frac{1}{2}\sigma_1^2\frac{\partial^2u_n}{\partial x^2}+\frac{1}{2}\sigma_2^2\frac{\partial^2u_n}{\partial y^2}+\omega\sigma_1\sigma_2\frac{\partial^2u_n}{\partial x\partial y}\right)\frac{d\tau}{\tau^{1-\rho}}\\
&= u_n(x,y,t)-\frac{\rho^{1-\alpha}}{\Gamma(\alpha)}t^{\rho(\alpha-1)}*_\rho D_t^{\alpha,\rho}u_n(x,y,t)\\
&\quad+\frac{\rho^{1-\alpha}}{\Gamma(\alpha)}t^{\rho(\alpha-1)}*_\rho\left(\frac{1}{2}\sigma_1^2\frac{\partial^2u_n}{\partial x^2}+\frac{1}{2}\sigma_2^2\frac{\partial^2u_n}{\partial y^2}+\omega\sigma_1\sigma_2\frac{\partial^2u_n}{\partial x\partial y}\right).
\end{aligned}$$

Taking the generalized Laplace transform on both sides of the above equation:

$$\begin{aligned}
\mathcal{L}_\rho\{u_{n+1}\}(s) &= \mathcal{L}_\rho\{u_n\}(s)-\frac{1}{\Gamma(\alpha)}\mathcal{L}_\rho\left\{\left(\frac{t^\rho}{\rho}\right)^{\alpha-1}\right\}(s)\mathcal{L}_\rho\left\{D_t^{\alpha,\rho}u_n(x,y,t)\right\}(s)\\
&\quad+\frac{1}{\Gamma(\alpha)}\mathcal{L}_\rho\left\{\left(\frac{t^\rho}{\rho}\right)^{\alpha-1}\right\}(s)\mathcal{L}_\rho\left\{\frac{1}{2}\sigma_1^2\frac{\partial^2u_n}{\partial x^2}+\frac{1}{2}\sigma_2^2\frac{\partial^2u_n}{\partial y^2}+\omega\sigma_1\sigma_2\frac{\partial^2u_n}{\partial x\partial y}\right\}(s)\\
&= \mathcal{L}_\rho\{u_n\}(s)-\frac{1}{s^\alpha}\left(s^\alpha\mathcal{L}_\rho\{u_n\}(s)-I_t^{1-\alpha,\rho}u_n(x,y,0)\right)\\
&\quad+\frac{1}{s^\alpha}\mathcal{L}_\rho\left\{\frac{1}{2}\sigma_1^2\frac{\partial^2u_n}{\partial x^2}+\frac{1}{2}\sigma_2^2\frac{\partial^2u_n}{\partial y^2}+\omega\sigma_1\sigma_2\frac{\partial^2u_n}{\partial x\partial y}\right\}(s).
\end{aligned}$$

The inverse generalized Laplace transform yields that

$$\begin{aligned}
u_{n+1}(x,y,t) &= \mathcal{L}_\rho^{-1}\left\{\frac{1}{s^\alpha}I_t^{1-\alpha,\rho}u_n(x,y,0)\right\}\\
&\quad+\mathcal{L}_\rho^{-1}\left\{\frac{1}{s^\alpha}\mathcal{L}_\rho\left\{\frac{1}{2}\sigma_1^2\frac{\partial^2u_n}{\partial x^2}+\frac{1}{2}\sigma_2^2\frac{\partial^2u_n}{\partial y^2}+\omega\sigma_1\sigma_2\frac{\partial^2u_n}{\partial x\partial y}\right\}(s)\right\}(t)
\end{aligned}\tag{21}$$

for $n\geq 1$. Thus, the generalized Laplace variational iteration method for finding the approximate analytic solution of the fractional-order Black–Scholes Equation (6) with the fractional integral condition (7) is defined by:

$$\begin{aligned}
&u_0(x,y,t)=\tfrac{1}{\Gamma(\alpha)}\max\{c_1e^x+c_2e^y-K,0\}\left(\tfrac{t^\rho}{\rho}\right)^{\alpha-1}+\tfrac{1}{\Gamma(\alpha+1)}\omega e^{x+y}\left(\tfrac{t^\rho}{\rho}\right)^{\alpha}\\
&u_{n+1}(x,y,t)=\mathcal{L}_\rho^{-1}\left\{\tfrac{1}{s^\alpha}I_t^{1-\alpha,\rho}u_n(x,y,0)\right\}+\mathcal{L}_\rho^{-1}\left\{\tfrac{1}{s^\alpha}\mathcal{L}_\rho\left\{\tfrac{1}{2}\sigma_1^2\tfrac{\partial^2u_n}{\partial x^2}+\tfrac{1}{2}\sigma_2^2\tfrac{\partial^2u_n}{\partial y^2}\right.\right.\\
&\qquad\left.\left.+\,\omega\sigma_1\sigma_2\tfrac{\partial^2u_n}{\partial x\partial y}\right\}(s)\right\}(t)\text{ for }n\geq 0,
\end{aligned}$$

with $I_t^{1-\alpha,\rho}u_n(x,y,0)=\max\{c_1e^x+c_2e^y-K,0\}$ for all $n\geq 0$.

Theorem 3. *The approximate analytic solution for the two dimensional fractional-order Black–Scholes Equation (6) with the fractional integral condition (7) can be defined by the following iteration:*

$$\begin{aligned} u_n(x,y,t) \;&=\; \frac{1}{\Gamma(\alpha)}\max\{c_1e^x+c_2e^y-K,0\}\left(\frac{t^\rho}{\rho}\right)^{\alpha-1} \\ &\quad+\sum_{k=0}^{n-1}\left(\frac{1}{2^{k+1}}\sigma_1^{2(k+1)}\max\{c_1e^x,0\}+\frac{1}{2^{k+1}}\sigma_2^{2(k+1)}\max\{c_2e^y,0\}\right) \\ &\quad\times\frac{1}{\Gamma((k+2)\alpha)}\left(\frac{t^\rho}{\rho}\right)^{(k+2)\alpha-1} \\ &\quad+\frac{1}{\Gamma((n+1)\alpha+1)}\left[\frac{1}{2}\sigma_1^2+\frac{1}{2}\sigma_2^2+\omega\sigma_1\sigma_2\right]^n\left(\frac{t^\rho}{\rho}\right)^{n\alpha} \end{aligned} \tag{22}$$

for any $(x,y,t)\in[0,x_{\max}]\times[0,y_{\max}]\times[0,T]$ *and for all* $n\geq 1$*. Furthermore, if*

$$\frac{1}{\Gamma((n+1)\alpha+1)}\left[\frac{1}{2}\sigma_1^2+\frac{1}{2}\sigma_2^2+\omega\sigma_1\sigma_2\right]^n\left(\frac{t^\rho}{\rho}\right)^{n\alpha}$$

approaches zero when n *goes to infinity for any fixed* $t\in[0,T]$*, then the analytic solution* u *for the fractional-order Black–Scholes Equations (6) and (7) is in the form:*

$$\begin{aligned} u(x,y,t) \;&=\; \max\{c_1e^x+c_2e^y-K,0\}\frac{1}{\Gamma(\alpha)}\left(\frac{t^\rho}{\rho}\right)^{\alpha-1} \\ &\quad+\frac{\sigma_1^2\max\{c_1e^x,0\}}{2}\left(\frac{t^\rho}{\rho}\right)^{2\alpha-1}E_{\alpha,2\alpha}\left(\frac{\sigma_1^2}{2}\left(\frac{t^\rho}{\rho}\right)^{\alpha}\right) \\ &\quad+\frac{\sigma_2^2\max\{c_2e^y,0\}}{2}\left(\frac{t^\rho}{\rho}\right)^{2\alpha-1}E_{\alpha,2\alpha}\left(\frac{\sigma_2^2}{2}\left(\frac{t^\rho}{\rho}\right)^{\alpha}\right) \end{aligned} \tag{23}$$

where $E_{\alpha,\beta}$ *denotes the two-parameter Mittag–Leffler function.*

Proof. Let $u_0(x,y,t)=\frac{1}{\Gamma(\alpha)}\max\{c_1e^x+c_2e^y-K,0\}\left(\frac{t^\rho}{\rho}\right)^{\alpha-1}+\frac{1}{\Gamma(\alpha+1)}\omega e^{x+y}\left(\frac{t^\rho}{\rho}\right)^{\alpha}$. The generalized Laplace variational iteration procedure is then started by computing the term u_1. By (22), we obtain:

$$\begin{aligned} u_1 \;&=\; \mathcal{L}_\rho^{-1}\left\{\frac{1}{s^\alpha}I_t^{1-\alpha,\rho}u_0(x,y,0)\right\}(t)+\mathcal{L}_\rho^{-1}\left\{\frac{1}{s^\alpha}\mathcal{L}_\rho\left\{\frac{1}{2}\sigma_1^2\frac{\partial^2u_0}{\partial x^2}+\frac{1}{2}\sigma_2^2\frac{\partial^2u_0}{\partial y^2}+\omega\sigma_1\sigma_2\frac{\partial^2u_0}{\partial x\partial y}\right\}(s)\right\}(t) \\ &=\; \max\{c_1e^x+\tilde{\beta}_2e^y-K,0\}\mathcal{L}_\rho^{-1}\left\{\frac{1}{s^\alpha}\right\}(t) \\ &\quad+\mathcal{L}_\rho^{-1}\left\{\frac{1}{s^\alpha}\mathcal{L}_\rho\left\{\frac{1}{2}\sigma_1^2\frac{\partial^2u_0}{\partial x^2}+\frac{1}{2}\sigma_2^2\frac{\partial^2u_0}{\partial y^2}+\omega\sigma_1\sigma_2\frac{\partial^2u_0}{\partial x\partial y}\right\}(s)\right\}(t) \\ &=\; \frac{1}{\Gamma(\alpha)}\max\{c_1e^x+c_2e^y-K,0\}\left(\frac{t^\rho}{\rho}\right)^{\alpha-1} \\ &\quad+\frac{1}{2}\sigma_1^2\max\{c_1e^x,0\}\frac{1}{\Gamma(2\alpha)}\left(\frac{t^\rho}{\rho}\right)^{2\alpha-1}+\frac{1}{2}\sigma_2^2\max\{c_2e^y,0\}\frac{1}{\Gamma(2\alpha)}\left(\frac{t^\rho}{\rho}\right)^{2\alpha-1} \\ &\quad+\frac{1}{2}\sigma_1^2\omega e^{x+y}\frac{1}{\Gamma(2\alpha+1)}\left(\frac{t^\rho}{\rho}\right)^{2\alpha}+\frac{1}{2}\sigma_2^2\omega e^{x+y}\frac{1}{\Gamma(2\alpha+1)}\left(\frac{t^\rho}{\rho}\right)^{2\alpha} \\ &\quad+\omega\sigma_1\sigma_2\omega e^{x+y}\frac{1}{\Gamma(2\alpha+1)}\left(\frac{t^\rho}{\rho}\right)^{2\alpha}. \end{aligned}$$

Then, the function u_1 is

$$\begin{aligned} u_1(x,y,t) &= \max\{c_1e^x + c_2e^y - K, 0\}\frac{1}{\Gamma(\alpha)}\left(\frac{t^\rho}{\rho}\right)^{\alpha-1} \\ &\quad + \left[\frac{1}{2}\sigma_1^2\max\{c_1e^x,0\} + \frac{1}{2}\sigma_2^2\max\{c_2e^y,0\}\right]\frac{1}{\Gamma(2\alpha)}\left(\frac{t^\rho}{\rho}\right)^{2\alpha-1} \\ &\quad + \left[\frac{1}{2}\sigma_1^2 + \frac{1}{2}\sigma_2^2 + \omega\sigma_1\sigma_2\right]\omega e^{x+y}\frac{1}{\Gamma(2\alpha+1)}\left(\frac{t^\rho}{\rho}\right)^{2\alpha}. \end{aligned}$$

Note that the function u_1 satisfies that $I_t^{1-\alpha,\rho}u_1(x,y,0) = \max\{c_1e^x + c_2e^y - K, 0\}$. We next find the function u_2. By (22), we get:

$$u_2 = \mathcal{L}_\rho^{-1}\left\{\frac{1}{s^\alpha}I_t^{1-\alpha,\rho}u_1(x,y,0)\right\}(t) + \mathcal{L}_\rho^{-1}\left\{\frac{1}{s^\alpha}\mathcal{L}_\rho\left\{\frac{1}{2}\sigma_1^2\frac{\partial^2 u_1}{\partial x^2} + \frac{1}{2}\sigma_2^2\frac{\partial^2 u_1}{\partial y^2} + \omega\sigma_1\sigma_2\frac{\partial^2 u_1}{\partial x\partial y}\right\}(s)\right\}(t)$$

Consider $\mathcal{L}_\rho\left\{\frac{1}{2}\sigma_1^2\frac{\partial^2 u_1}{\partial x^2} + \frac{1}{2}\sigma_2^2\frac{\partial^2 u_1}{\partial y^2} + \omega\sigma_1\sigma_2\frac{\partial^2 u_1}{\partial x\partial y}\right\}(s)$.

$$\begin{aligned} &\mathcal{L}_\rho\left\{\frac{1}{2}\sigma_1^2\frac{\partial^2 u_1}{\partial x^2} + \frac{1}{2}\sigma_2^2\frac{\partial^2 u_1}{\partial y^2} + \omega\sigma_1\sigma_2\frac{\partial^2 u_1}{\partial x\partial y}\right\}(s) \\ = \;& \frac{1}{2}\sigma_1^2\max\{c_1e^x,0\}\mathcal{L}_\rho\left\{\frac{1}{\Gamma(\alpha)}\left(\frac{t^\rho}{\rho}\right)^{\alpha-1}\right\}(s) + \frac{1}{2}\sigma_2^2\max\{c_2e^y,0\}\mathcal{L}_\rho\left\{\frac{1}{\Gamma(\alpha)}\left(\frac{t^\rho}{\rho}\right)^{\alpha-1}\right\}(s) \\ &+\frac{1}{2^2}\sigma_1^4\max\{c_1e^x,0\}\mathcal{L}_\rho\left\{\frac{1}{\Gamma(2\alpha)}\left(\frac{t^\rho}{\rho}\right)^{2\alpha-1}\right\}(s) + \frac{1}{2^2}\sigma_2^4\max\{c_2e^y,0\}\mathcal{L}_\rho\left\{\frac{1}{\Gamma(2\alpha)}\left(\frac{t^\rho}{\rho}\right)^{2\alpha-1}\right\}(s) \\ &+\frac{1}{2}\sigma_1^2\left[\frac{1}{2}\sigma_1^2 + \frac{1}{2}\sigma_2^2 + \omega\sigma_1\sigma_2\right]\omega e^{x+y}\mathcal{L}_\rho\left\{\frac{1}{\Gamma(2\alpha+1)}\left(\frac{t^\rho}{\rho}\right)^{2\alpha}\right\}(s) \\ &+\frac{1}{2}\sigma_2^2\left[\frac{1}{2}\sigma_1^2 + \frac{1}{2}\sigma_2^2 + \omega\sigma_1\sigma_2\right]\omega e^{x+y}\mathcal{L}_\rho\left\{\frac{1}{\Gamma(2\alpha+1)}\left(\frac{t^\rho}{\rho}\right)^{2\alpha}\right\}(s) \\ &+\omega\sigma_1\sigma_2\left[\frac{1}{2}\sigma_1^2 + \frac{1}{2}\sigma_2^2 + \omega\sigma_1\sigma_2\right]\omega e^{x+y}\mathcal{L}_\rho\left\{\frac{1}{\Gamma(2\alpha+1)}\left(\frac{t^\rho}{\rho}\right)^{2\alpha}\right\}(s) \\ = \;& \frac{1}{2}\sigma_1^2\max\{c_1e^x,0\}\frac{1}{s^\alpha} + \frac{1}{2}\sigma_2^2\max\{c_2e^y,0\}\frac{1}{s^\alpha} \\ &+\frac{1}{2^2}\sigma_1^4\max\{c_1e^x,0\}\frac{1}{s^{2\alpha}} + \frac{1}{2^2}\sigma_2^4\max\{c_2e^y,0\}\frac{1}{s^{2\alpha}} \\ &+\frac{1}{2}\sigma_1^2\left[\frac{1}{2}\sigma_1^2 + \frac{1}{2}\sigma_2^2 + \omega\sigma_1\sigma_2\right]\omega e^{x+y}\frac{1}{s^{2\alpha+1}} \\ &+\frac{1}{2}\sigma_2^2\left[\frac{1}{2}\sigma_1^2 + \frac{1}{2}\sigma_2^2 + \omega\sigma_1\sigma_2\right]\omega e^{x+y}\frac{1}{s^{2\alpha+1}} \\ &+\omega\sigma_1\sigma_2\left[\frac{1}{2}\sigma_1^2 + \frac{1}{2}\sigma_2^2 + \omega\sigma_1\sigma_2\right]\omega e^{x+y}\frac{1}{s^{2\alpha+1}}. \end{aligned}$$

Then, the term u_2 is determined by

$$\begin{aligned}
u_2(x,y,t) &= \frac{1}{\Gamma(\alpha)}\max\{c_1e^x+c_2e^y-K,0\}\left(\frac{t^\rho}{\rho}\right)^{\alpha-1} \\
&\quad +\frac{1}{2}\sigma_1^2\max\{c_1e^x,0\}\mathcal{L}_\rho^{-1}\left\{\frac{1}{s^{2\alpha}}\right\}(t)+\frac{1}{2}\sigma_2^2\max\{c_2e^y,0\}\mathcal{L}_\rho^{-1}\left\{\frac{1}{s^{2\alpha}}\right\}(t) \\
&\quad +\frac{1}{2^2}\sigma_1^4\max\{c_1e^x,0\}\mathcal{L}_\rho^{-1}\left\{\frac{1}{s^{3\alpha}}\right\}(t)+\frac{1}{2^2}\sigma_2^4\max\{c_2e^y,0\}\mathcal{L}_\rho^{-1}\left\{\frac{1}{s^{3\alpha}}\right\}(t) \\
&\quad +\frac{1}{2}\sigma_1^2\omega e^{x+y}\mathcal{L}_\rho^{-1}\left\{\frac{1}{s^{3\alpha+1}}\right\}(t)+\frac{1}{2}\sigma_2^2\omega e^{x+y}\mathcal{L}_\rho^{-1}\left\{\frac{1}{s^{3\alpha+1}}\right\}(t) \\
&\quad +\omega\sigma_1\sigma_2\omega e^{x+y}\mathcal{L}_\rho^{-1}\left\{\frac{1}{s^{3\alpha+1}}\right\}(t) \\
&= \frac{1}{\Gamma(\alpha)}\max\{c_1e^x+c_2e^y-K,0\}\left(\frac{t^\rho}{\rho}\right)^{\alpha-1} \\
&\quad +\left[\frac{1}{2}\sigma_1^2\max\{c_1e^x,0\}+\frac{1}{2}\sigma_2^2\max\{c_2e^y,0\}\right]\frac{1}{\Gamma(2\alpha)}\left(\frac{t^\rho}{\rho}\right)^{2\alpha-1} \\
&\quad +\left[\frac{1}{2^2}\sigma_1^4\max\{c_1e^x,0\}+\frac{1}{2^2}\sigma_2^4\max\{c_2e^y,0\}\right]\frac{1}{\Gamma(3\alpha)}\left(\frac{t^\rho}{\rho}\right)^{3\alpha-1} \\
&\quad +\left[\frac{1}{2}\sigma_1^2+\frac{1}{2}\sigma_2^2+\omega\sigma_1\sigma_2\right]^2\omega e^{x+y}\frac{1}{\Gamma(3\alpha+1)}\left(\frac{t^\rho}{\rho}\right)^{3\alpha}.
\end{aligned}$$

Note that the function u_2 satisfies that $I_t^{1-\alpha,\rho}u_2(x,y,0)=\max\{c_1e^x+c_2e^y-K,0\}$. As a result of the preceding explanation, we now have term u_3 as follows:

$$\begin{aligned}
u_3(x,y,t) &= \frac{1}{\Gamma(\alpha)}\max\{c_1e^x+c_2e^y-K,0\}\left(\frac{t^\rho}{\rho}\right)^{\alpha-1} \\
&\quad +\left[\frac{1}{2}\sigma_1^2\max\{c_1e^x,0\}+\frac{1}{2}\sigma_2^2\max\{c_2e^y,0\}\right]\frac{1}{\Gamma(2\alpha)}\left(\frac{t^\rho}{\rho}\right)^{2\alpha-1} \\
&\quad +\left[\frac{1}{2^2}\sigma_1^4\max\{c_1e^x,0\}+\frac{1}{2^2}\sigma_2^4\max\{c_2e^y,0\}\right]\frac{1}{\Gamma(3\alpha)}\left(\frac{t^\rho}{\rho}\right)^{3\alpha-1} \\
&\quad +\left[\frac{1}{2^3}\sigma_1^6\max\{c_1e^x,0\}+\frac{1}{2^3}\sigma_2^6\max\{c_2e^y,0\}\right]\frac{1}{\Gamma(4\alpha)}\left(\frac{t^\rho}{\rho}\right)^{4\alpha-1} \\
&\quad +\left[\frac{1}{2}\sigma_1^2+\frac{1}{2}\sigma_2^2+\omega\sigma_1\sigma_2\right]^3\omega e^{x+y}\frac{1}{\Gamma(4\alpha+1)}\left(\frac{t^\rho}{\rho}\right)^{4\alpha}.
\end{aligned}$$

Note that the function u_3 satisfies that $I_t^{1-\alpha,\rho}u_3(x,y,0)=\max\{c_1e^x+c_2e^y-K,0\}$. Using the same manner, we can find the expression of u_n in the following form:

$$\begin{aligned}
u_n(x,y,t) &= \frac{1}{\Gamma(\alpha)}\max\{c_1e^x+c_2e^y-K,0\}\left(\frac{t^\rho}{\rho}\right)^{\alpha-1} \\
&\quad +\sum_{k=0}^{n-1}\left(\frac{1}{2^{k+1}}\sigma_1^{2(k+1)}\max\{c_1e^x,0\}+\frac{1}{2^{k+1}}\sigma_2^{2(k+1)}\max\{c_2e^y,0\}\right) \qquad (24) \\
&\quad \times\frac{1}{\Gamma((k+2)\alpha)}\left(\frac{t^\rho}{\rho}\right)^{(k+2)\alpha-1} \\
&\quad +\frac{1}{\Gamma((n+1)\alpha+1)}\left[\frac{1}{2}\sigma_1^2+\frac{1}{2}\sigma_2^2+\omega\sigma_1\sigma_2\right]^n\left(\frac{t^\rho}{\rho}\right)^{n\alpha},
\end{aligned}$$

and $I_t^{1-\alpha,\rho}u_n(x,y,0) = \max\{c_1e^x + c_2e^y - K, 0\}$ for all $n \geq 1$. As a consequence of the generalized Laplace variational iteration process, we derive that, under the assumption of the theorem, the analytic solution for the fractional Black–Scholes equation is as follows:

$$\begin{aligned}
u(x,y,t) &= \lim_{n\to\infty} u_n(x,y,t) \\
&= \max\{c_1e^x + c_2e^y - K, 0\}\frac{1}{\Gamma(\alpha)}\left(\frac{t^\rho}{\rho}\right)^{\alpha-1} \\
&\quad + \sum_{k=0}^{\infty}\left(\frac{1}{2^{k+1}}\sigma_1^{2(k+1)}\max\{c_1e^x, 0\} + \frac{1}{2^{k+1}}\sigma_2^{2(k+1)}\max\{c_2e^y, 0\}\right) \\
&\quad \times \frac{1}{\Gamma((k+2)\alpha)}\left(\frac{t^\rho}{\rho}\right)^{(k+2)\alpha-1} \\
&= \max\{c_1e^x + c_2e^y - K, 0\}\frac{1}{\Gamma(\alpha)}\left(\frac{t^\rho}{\rho}\right)^{\alpha-1} \\
&\quad + \frac{\sigma_1^2\max\{c_1e^x, 0\}}{2}\left(\frac{t^\rho}{\rho}\right)^{2\alpha-1}\sum_{k=0}^{\infty}\frac{1}{\Gamma(\alpha k + 2\alpha)}\left[\frac{\sigma_1^2}{2}\left(\frac{t^\rho}{\rho}\right)^{\alpha}\right]^k \\
&\quad + \frac{\sigma_2^2\max\{c_2e^y, 0\}}{2}\left(\frac{t^\rho}{\rho}\right)^{2\alpha-1}\sum_{k=0}^{\infty}\frac{1}{\Gamma(\alpha k + 2\alpha)}\left[\frac{\sigma_2^2}{2}\left(\frac{t^\rho}{\rho}\right)^{\alpha}\right]^k \\
&= \max\{c_1e^x + c_2e^y - K, 0\}\frac{1}{\Gamma(\alpha)}\left(\frac{t^\rho}{\rho}\right)^{\alpha-1} \\
&\quad + \frac{\sigma_1^2\max\{c_1e^x, 0\}}{2}\left(\frac{t^\rho}{\rho}\right)^{2\alpha-1}E_{\alpha,2\alpha}\left(\frac{\sigma_1^2}{2}\left(\frac{t^\rho}{\rho}\right)^{\alpha}\right) \\
&\quad + \frac{\sigma_2^2\max\{c_2e^y, 0\}}{2}\left(\frac{t^\rho}{\rho}\right)^{2\alpha-1}E_{\alpha,2\alpha}\left(\frac{\sigma_2^2}{2}\left(\frac{t^\rho}{\rho}\right)^{\alpha}\right).
\end{aligned}$$

Therefore, the Theorem 3 is proved completely. □

Corollary 1. *The analytic solution for the two-dimensional fractional-order Black–Scholes equation based on the Riemann–Liouville fractional derivative with the Riemann–Liouville fractional integral condition is given in the following:*

$$\begin{aligned}
u(x,y,t) &= \max\{c_1e^x + c_2e^y - K, 0\}\frac{t^{\alpha-1}}{\Gamma(\alpha)} + \frac{\sigma_1^2\max\{c_1e^x, 0\}}{2}t^{2\alpha-1}E_{\alpha,2\alpha}\left(\frac{\sigma_1^2}{2}t^\alpha\right) \\
&\quad + \frac{\sigma_2^2\max\{c_2e^y, 0\}}{2}t^{2\alpha-1}E_{\alpha,2\alpha}\left(\frac{\sigma_2^2}{2}t^\alpha\right),
\end{aligned} \tag{25}$$

for any $(x,y,t) \in [0, x_{\max}] \times [0, y_{\max}] \times [0, T]$.

Proof. By setting $\rho = 1$, this corollary can be obtained immediately from Theorem 3. □

Corollary 2. *The analytic solution of the classical two-dimensional Black–Scholes equation with the European call option is:*

$$u(x,y,t) = \max\{c_1e^x + c_2e^y - K, 0\} + \max\{c_1e^x, 0\}\left(e^{\frac{\sigma_1^2}{2}t} - 1\right) + \max\{c_2e^y, 0\}\left(e^{\frac{\sigma_2^2}{2}t} - 1\right), \tag{26}$$

for any $(x,y,t) \in [0, x_{\max}] \times [0, y_{\max}] \times [0, T]$.

Proof. By Theorem 3, we have that

$$\begin{aligned} u(x,y,t) &= \max\{c_1e^x+c_2e^y-K,0\}\frac{1}{\Gamma(\alpha)}\left(\frac{t^\rho}{\rho}\right)^{\alpha-1}+\frac{\sigma_1^2\max\{c_1e^x,0\}}{2}\left(\frac{t^\rho}{\rho}\right)^{2\alpha-1} \\ &\quad \times E_{\alpha,2\alpha}\left(\frac{\sigma_1^2}{2}\left(\frac{t^\rho}{\rho}\right)^{\alpha}\right)+\frac{\sigma_2^2\max\{c_2e^y,0\}}{2}\left(\frac{t^\rho}{\rho}\right)^{2\alpha-1}E_{\alpha,2\alpha}\left(\frac{\sigma_2^2}{2}\left(\frac{t^\rho}{\rho}\right)^{\alpha}\right). \end{aligned}$$

Since the generalized Riemann–Liouville fractional derivative can be reduced to the usual derivative when $\rho=\alpha=1$, we obtain:

$$\begin{aligned} u(x,y,t) &= \max\{c_1e^x+c_2e^y-K,0\} \\ &\quad +\frac{\sigma_1^2\max\{c_1e^x,0\}}{2}tE_{1,2}\left(\frac{\sigma_1^2}{2}t\right)+\frac{\sigma_2^2\max\{c_2e^y,0\}}{2}tE_{1,2}\left(\frac{\sigma_2^2}{2}t\right), \end{aligned}$$

for any $(x,y,t)\in[0,x_{\max}]\times[0,y_{\max}]\times[0,T]$. □

6. Numerical Results

We will assume throughout this section that the strike price K is 70. The risk-free annual interest rate is 5%, thus $r=0.05$; the maturity time is $T=1$ year; and the volatilities of the underlying assets $x\in[0,5]$ and $y\in[0,5]$ are $\sigma_1=5\%$ and $\sigma_2=10\%$, respectively. In the following, we will demonstrate the European option prices computed from the previously described analytic solutions. Figure 1 shows the European call-option pricing with various values of the parameter α obtained by (24) with the asset pricing $y=5$ and $\rho=1$.

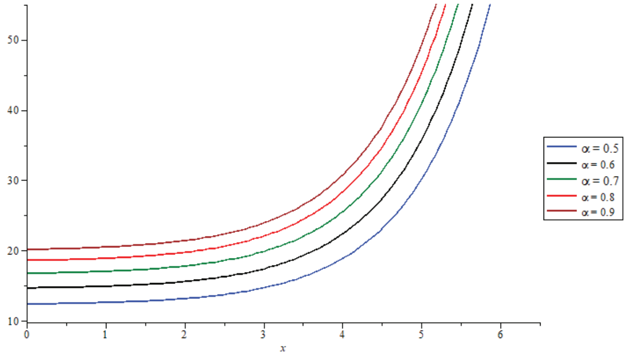

Figure 1. European call-option prices with various fractional-order α values.

Figure 2 demonstrates the European call-option pricing with various values of the parameter ρ given by (24) with the asset pricing $y=5$ and $\alpha=0.5$.

In case $\rho=1$, the graphs of the option pricing by (24) with four different values for fractional order $\alpha=0.3, 0.5, 0.7$, and 0.9 are shown in Figure 3.

It is well known that in the classical Black–Scholes model, the option price depends on five variables. These are volatility, the price of the underlying asset, the strike price of the option, the time until expiration of the option, and the risk-free interest rate. With these variables, sellers of options could, in theory, set prices for the options they sell that make sense. However, in the fractional-order Black–Scholes equation proposed here, there are two parameters added: α and ρ. In each of the figures, it is shown that the value of call options will increase according to the values of two parameters. Therefore, if we can figure out the right values for these two factors, the modified Black–Scholes equation will give us option prices that are close to what they are worth on the market.

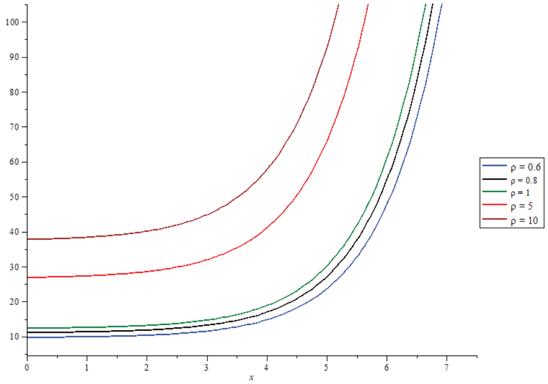

Figure 2. European call-option prices with various fractional-order ρ values.

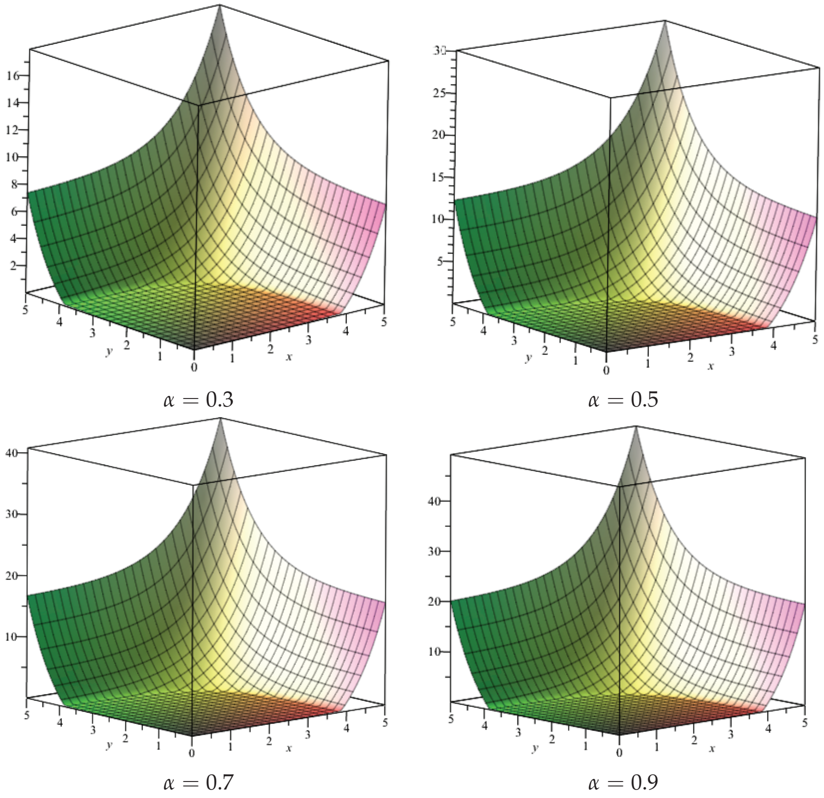

$\alpha = 0.3$ $\alpha = 0.5$

$\alpha = 0.7$ $\alpha = 0.9$

Figure 3. The graphs of the option pricing with different fractional-order α.

7. Conclusions

It is well known that in option pricing theory, the Black–Scholes equation is one of the most significant models for option pricing. In this manuscript, we developed the classical Black–Scholes equation in the form of the fractional-order Black–Scholes equation based on the generalized Riemann–Liouville derivative. This article provides the approximate analytic solution to the fractional-order Black–Scholes equation via the generalized Laplace variational iteration method. Moreover, we show that the solution to the classical Black–Scholes equation is achieved as a special case of the proposed approximate analytic solution.

This demonstrates that the generalized Laplace variational iteration method is one of the effective approaches for discovering approximate analytic solutions to fractional-order differential equations. The advantage of the modified Black–Scholes equation is that it has two parameters occurring in the definition of the fractional derivative, that is α and ρ. If we can correctly estimate the values of these two factors, the option prices produced from the modified form will be close to the market value of option prices. We may utilize the genetic algorithm and the actual value of the option to determine the proper values for two parameters. Option pricing may be determined by the solution to the modified Black–Scholes equation after the proper values for these two parameters are already known.

Author Contributions: Conceptualization, P.S.; Formal analysis, S.A., P.S. and W.S.; Investigation, P.S.; Methodology, S.A. and W.S.; Software, S.A., P.S. and W.S.; Supervision, P.S.; Writing—original draft, S.A.; Writing—review & editing, P.S. and W.S. All authors have read and agreed to the published version of the manuscript.

Funding: This research was funded by King Mongkut's University of Technology North Bangkok, contract no. KMUTNB-FF-65-58.

Data Availability Statement: Not applicable.

Conflicts of Interest: The authors declare no conflict of interest.

References

1. Stampái, J.; Victor, G. *The Mathematics of Finance: Modeling and Hedging*; Books/Cole Series in Advanced Mathematics; Books/Cole: Pacific Grove, CA, USA, 2001.
2. Wilmott, P.; Howison, S.; Dewynne, J. *The Mathematics of Financial Derivatives*; Cambridge University Press: Cambridge, UK, 1997.
3. Topper, J. *Financial Engineering with Finite Elements*; John Wiley & Sons: Hoboken, NJ, USA, 2008.
4. Wilmott, P.; Dewynneand, J.; Howisson, S. *Option Pricing: Mathematical Models and Computation*; Oxford Press: Oxford, UK, 1993.
5. Seydel, R. *Tools for Computational Finance*; Springer: Berlin/Heidelberg, Germany, 2003.
6. Achdou, Y.; Olivier, P. *Computational Methods for Option Pricing*; Society for Industrial and Applied Mathematics: Philadelphia, PA, USA, 2005.
7. Mrazek, M.; Pospisil, J.; Sobotka, T. On calibration of stochastic and fractional stochastic volatility models. *Eur. J. Oper. Res.* **2016**, *254*, 1036–1046. [CrossRef]
8. Alghalith, M. Pricing the American options using the Black-Scholes pricing formula. *Physica A* **2018**, *507*, 443–445. [CrossRef]
9. Laskin, N. Valuing options in shot noise market. *Physica A* **2018**, *502*, 518–533. [CrossRef]
10. Lin, L.; Li, Y.; Wu, J. The pricing of European options on two underlying assets with delays. *Physica A* **2018**, *495*, 143–151. [CrossRef]
11. Mandelbrot, B. The variation of certain speculative prices. *J. Bus.* **1963**, *36*, 394–413. [CrossRef]
12. Peters, E.E. Fractal structure in the capital markets. *Financ. Anal. J.* **1989**, *45*, 32–37. [CrossRef]
13. Li, H.Q.; Ma, C.Q. An empirical study of long-term memory of return and volatility in Chinese stock market. *J. Financ. Econ.* **2005**, *31*, 29–37.
14. Huang, T.F.; Li, B.Y.; Xiong, J.X. Test on the chaotic characteristic of Chinese futures market. *Syst. Eng.* **2012**, *30*, 43–53.
15. Debnath, L. Recent applications of fractional calculus to science and engineering. *Int. J. Math. Math. Sci* **2003**, *2003*, 753601. [CrossRef]
16. He, J.H.; El-Dib, Y.O. Periodic property of the time-fractional Kundu–Mukherjee–Naskar equation. *Results Phys.* **2020**, *19*, 103345. [CrossRef]
17. Noeiaghdam, S.; Dreglea, A.; He, J.; Avazzadeh, Z.; Suleman, M.; Fariborzi Araghi, M.A.; Sidorov, D.N.; Sidorov, N. Error Estimation of the Homotopy Perturbation Method to Solve Second Kind Volterra Integral Equations with Piecewise Smooth Kernels: Application of the CADNA Library. *Symmetry* **2003**, 12, 1730. [CrossRef]
18. Anjum, N.; He, J.H. Higher-order homotopy perturbation method for conservative nonlinear oscillators generally and microelectromechanical systems' oscillators particularly. *Int. J. Mod. Phys. B* **2020**, *34*, 2050313. [CrossRef]
19. Song, L. A semianalytical solution of the fractional derivative model and its application in financial market. *Complexity* **2018**, *2018*, 1872409. [CrossRef]
20. Trachoo, K.; Sawangtong, W.; Sawangtong, P. Laplace transform homotopy perturbation method for the two dimensional Black Scholes model with European call option. *Math. Comput. Appl.* **2017**, *22*, 23. [CrossRef]
21. Sawangtong, P.; Trachoo, K.; Sawangtong, W.; Wiwattanapataphee, B. The analytical solution for the Black-Scholes equation with two assets in the Liouville-Caputo fractional derivative sense. *Mathematics* **2018**, *6*, 129. [CrossRef]
22. Udita, N.K. A new approach to generalized fractional derivatives. *Bull. Math. Anal. Appl.* **2014**, *6*, 1–15.
23. Jarad, F.; Abdeljawad, T. A modifi ed Laplace transform for certain generalized fractional operators. *Results Nonlinear Anal.* **2018**, *1*, 88–98.

fractal and fractional

Article

An Efficient Numerical Method for Pricing Double-Barrier Options on an Underlying Stock Governed by a Fractal Stochastic Process

Samuel Megameno Nuugulu [1,2,*], Frednard Gideon [1] and Kailash C. Patidar [2]

[1] Department of Computing, Mathematical & Statistical Sciences, University of Namibia, Windhoek 13301, Namibia
[2] Department of Mathematics and Applied Mathematics, University of the Western Cape, Bellville 7535, South Africa
* Correspondence: snuugulu@unam.na

Abstract: After the discovery of the fractal structures of financial markets, enormous effort has been dedicated to finding accurate and stable numerical schemes to solve fractional Black-Scholes partial differential equations. This work, therefore, proposes a numerical scheme for pricing double-barrier options, written on an underlying stock whose dynamics are governed by a non-standard fractal stochastic process. The resultant model is time-fractional and is herein referred to as a time-fractional Black-Scholes model. The presence of the time-fractional derivative helps to capture the time-decaying effects of the underlying stock while capturing the globalized change in underlying prices and barriers. In this paper, we present the construction of the proposed scheme, analyse it in terms of its stability and convergence, and present two numerical examples of pricing double knock-in barrier-option problems. The results suggest that the proposed scheme is unconditionally stable and convergent with order $\mathcal{O}(h^2 + k^2)$.

Keywords: time-fractional Black-Scholes PDEs; double barriers options; numerical methods

MSC: 91B24; 91G20; 91G60

Citation: Nuugulu, S.M.; Gideon, F.; Patidar, K.C. An Efficient Numerical Method for Pricing Double-Barrier Options on an Underlying Stock Governed by a Fractal Stochastic Process. *Fractal Fract.* **2023**, *7*, 389. https://doi.org/10.3390/fractalfract7050389

Academic Editor: Leung Lung Chan

Received: 31 January 2023
Revised: 27 March 2023
Accepted: 28 March 2023
Published: 8 May 2023

1. Introduction

Over the years, exotic options have become very popular. Today, a wide variety of exotic options are readily available to investors as they are cheaper, and many offer specific tailor-made protections that have been formulated; see [1–4] and references therein. Several factors can explain the wide popularity of exotic options, one is their almost unlimited flexibility in addressing investors' specific needs, which may not be possible with standard options for which initial formulations are attributed to Black & Scholes [5] the early 70s. Therefore, with exotic options, an investor who would like to hedge against a large drop in an underlying asset price, for example, can sell a down-and-in put option with the barrier set at a lower level as the cheapest way to purchase the underlying asset.

On the other hand, exotic options play a significant hedging role in meeting investors' needs in very cost-effective ways; see for example [1,6,7] and references therein. Rational investors are moving away from buying general protections, and rather focus on designing complex strategies that serve to address their specific exposures at any given point in time. Most of these complex strategies are based on exotic options.

The oldest type of exotic option is the barrier option. Barrier options in general come in two forms—knock-out option (disappearing) or knock-in (appearing), when the underlying asset price triggers some pre-set price levels [8]. Barrier options are thus conditional options, and depend on whether the barrier(s) have been breached during the lifetime of the option.

Barrier options are also part of a class of option called path-dependent. According to Buchen and Konstandatos [1], barrier options are usually cheaper than their vanilla counterparts. This is due to the fact that a buyer of a barrier option has a more specific view of the underlying asset price dynamics within the time to maturity of the option as compared to its vanilla counterpart. Another hybrid barrier option is the so-called partial-time barrier options [1]. Here, the barrier is monitored (or active) for a time period that is shorter than the expiry time. These options are also called window-barrier options. Another refinement of these kinds of barrier options are those options where barrier(s) are monitored discretely in time. Comprehensive coverage of these kinds of options can be found for example in [8–10] to mention a few.

Another style of barrier options is a double-barrier option, some references to which can be found in [11–14], among others. Under the double-barrier case, there is an upper and a lower barrier. The upper barrier is set above and the lower barrier is below the current underlying asset price. Double knock-in options come to life, and double knock-out options terminate if either of the barriers is hit. It is worth noting that, under double-barrier options, investors can enjoy a greater leverage potential, e.g., under a knock-out option, the barriers can be set too close for comfort, and for knock-ins, the odds of knocking in can also be reduced without much discount [13].

Fractional calculus, and specifically fractional differential equations, are useful mathematical tools for modelling the dynamics of systems and phenomena in very diverse fields in the applied sciences. Some applications can be found in [7,15–20] among others. The discovery of the fractal nature of financial markets, and the subsequent development of fractal-based asset-pricing models, has intensified the search for accurate and stable numerical methods for solving these somewhat involved yet useful asset-pricing models.

Though numerical methods for classical asset-pricing models are abundant, numerical methods for fractional calculus-based models are very much limited. Since fractional models are, to some extent, a generalisation of classical models, several already existing numerical techniques for classical models can be extended to solving fractional ones.

In terms of the Black-Scholes model, there exists a very distinct difference between fractional Black-Scholes and classical Black-Scholes models, in the sense that the derivatives involved in fractional Black-Scholes models are globally defined, while classical models can only capture localized information about a function in a point-wise manner. As such, the non-locality nature of fractional derivatives-based models, among other things, contributes greatly to the complexity of the design, analysis, and implementation of the solution methods for fractional models.

At present, several numerical methods for fractional Black-Scholes models have been suggested. The existing methods can be categorised into three classes: methods based on finite difference [16,19–25], finite elements [26–28] and those based on the spectral approach [29–31]. Compared to the other two classes, the finite difference-based methods are proven to be more robust, efficient and tractable in solving fractional Black-Scholes equations.

In the current work, we extend the concept of double-barrier-option pricing into a time-fractional Black-Scholes framework. Pricing of double-barrier options via the time-fractional Black-Scholes framework is justified by evidence of “long memory” in the time direction observed in many asset time series; see, for example, [32–37]. It is imperative to note that, this desired long decay in the underlying asset in the time direction does not deteriorate the no-arbitrage constraint of asset-pricing theory. For more scientific evidence, see, [19,38,39] and references therein.

The combination of time-fractional Black-Scholes and double-barrier conditions adds additional degrees of complexity in designing solutions to the proposed model. Given the complexity involved, we designed a new robust numerical scheme for solving a time-fractional Black-Scholes model for pricing discrete-monitored double-barrier European options. This paper, therefore, serves to suggest an efficient numerical scheme for solving a time-fractional Black-Scholes model for pricing a discrete double-barrier-option problem.

The rest of this paper is organised as follows. Section 2 presents preliminary concepts and definitions while specifying the model under consideration. Section 3 presents the detailed construction of the numerical scheme. A comprehensive theoretical analysis of the method in terms of convergence and stability is presented in Section 4. Two practical examples of the use of the approach for pricing double knock-in European put stock options can be found in Section 5. Lastly, Section 6 presents some concluding remarks and sets the scope for future research.

2. Model

This section presents an overview of the preliminary knowledge of the subject of fractional differentiation while specifying the involved tfBS model and its brief derivation background.

2.1. Preliminaries

The most commonly used fractional derivative definitions in modelling financial data are the Caputo, Riemann–Liouville and the Jumarie-revised Riemann–Liouville definition. Though there exist numerous other definitions, these three possess specific properties that make them more appropriate for modelling financial data.

To develop the basis of our model, as well as touch base with the concept of fractional calculus in application to financial modelling and analysis, we will briefly revisit the above three definitions in terms of their mathematical formulations, merits, and demerits.

Definition 1. ***Caputo Derivative***

Let $f : \mathbb{R} \to \mathbb{R}$ be a continuous, but not necessarily a differentiable function. The Caputo fractional derivative of order α is defined as

$$D_t^\alpha f(t) = \frac{1}{\Gamma(\eta - \alpha)} \int_0^t \frac{1}{(t-\tau)^{\alpha-\eta+1}} \frac{d^\eta f(\tau)}{dt^\eta} d\tau, \quad \eta - 1 < \alpha \leq \eta. \tag{1}$$

Though the Caputo fractional derivative of a non-differentiable function may have a kernel at the origin, and that Caputo derivative of a constant function is not zero, according to [19], the Caputo definition allows for the incorporation of traditional initial and boundary conditions into the formulation of the problem, which provides a framework that is consistent with the classical definition.

Definition 2. ***Riemann–Liouville Derivative***

Let $f : \mathbb{R} \to \mathbb{R}$ be a continuous function, but not necessarily differentiable. Then, the Riemann–Liouville fractional derivative of order α is given by

$$D^\alpha f(t) = \frac{1}{\Gamma(\eta - \alpha)} \frac{d^\eta}{dt^\eta} \int_0^t \frac{f(\tau)}{(t-\tau)^{\alpha-\eta+1}} d\tau, \quad \eta - 1 < \alpha \leq \eta. \tag{2}$$

Just as with the Caputo derivative, the Riemann–Liouville derivative of a constant is non-zero, and the derivative of any function that is constant at the origin, for example, the exponential or Mittag–Leffler function, have singularities at the origins. Due to shortcomings in the Caputo and Riemann–Liouville definitions, their applications to modelling several non-linear real-life problems are limited [40].

A modified definition by Jumarie [41] with aid from the definition based on the Generalised Taylor series found in [19,41,42] addresses issues of singularities regarding the origin as well the non-zero constraint of constant functions.

Definition 3. ***Jumarie Derivative***

Let $f : \mathbb{R} \to \mathbb{R}$ be a continuous function, but not necessarily a differentiable, and suppose that $f(t)$ is

(i) a constant K, then its Jumarie fractional derivative of order α is defined by

$$D_t^\alpha f(t) = \begin{cases} \frac{K}{\Gamma(\eta-\alpha)} t^{-\alpha+1-\eta}, & \alpha \leq \eta - 1, \\ 0, & \alpha > \eta - 1, \end{cases} \tag{3}$$

(ii) not a constant, then

$$D_t^{\alpha} f(t) = \frac{1}{\Gamma(\eta - \alpha)} \frac{d^{\eta}}{dt^{\eta}} \int_0^t \frac{\{f(\tau) - f(0)\}}{(t - \tau)^{\alpha}} d\tau, \;\; \eta - 1 < \alpha < \eta, \tag{4}$$

$$D_t^{\alpha} f(t) = \frac{\partial^{\eta} f(t)}{\partial t^{\eta}}, \; \alpha = \eta \tag{5}$$

The Jumarie [37,41,43,44] definition above takes into account the existence of a fractional derivative at the origin, and the existence of a fractional derivative of a constant, therefore aligning the definition consistently well with local derivative-based differential calculus.

2.2. Model Specification

Let S be the stock price that follows the following non-random fractional stochastic process

$$dS = (r - \delta) S dt + \sigma S \omega(t) (dt)^{\alpha/2}, \; 0 < \alpha \leq 1, \tag{6}$$

which is driven by a fractal process $\beta_{\alpha}(t)$ governed by Gaussian white noise $\omega(t)$ such that

$$d\beta_{\alpha}(t) = \omega(t)(dt)^{\alpha/2}. \tag{7}$$

In (6), σ^2 represents the underlying stock volatility and r and δ represents the risk-free interest rate and the continuous dividend yield, respectively.

We note that in the fractional stochastic process (6), the standard Brownian motion is generalised by $\beta_{\alpha}(t)$ defined in (7). Furthermore, when $\alpha = 1$, Equation (6) is equivalent to a geometric Brownian motion.

Unlike in the standard Brownian motion, the non-Gaussian fractional process (6) does not make any prior assumptions about the underlying distribution of the stock price (S); see, for example, [20] and references therein. However, (6) does give insights on how the market is scaling with respect to time.

Using (6), we arrive at the time-fractional Black-Scholes (tfBS)-PDE (8) for pricing double-barrier put options, where the fractional derivative is defined in the Caputo sense. Detailed derivations of similar models for pricing standard options can be found in, among others, [19,41,43,44] and references therein.

$$\begin{cases} \frac{\partial^{\alpha} v}{\partial t^{\alpha}} = \left(rv - (r - \delta) \frac{S \partial v}{\partial S} \right) \frac{t^{1-\alpha}}{\Gamma(2-\alpha)} - \frac{\sigma^2 \Gamma(1+\alpha)}{2} \frac{S^2 \partial^2 v}{\partial S^2}, \; 0 < \alpha \leq 1, \\ B_l \leq S \leq B_u, t \in (0, T) \\ v(B_l, t) = R_l, \; V(B_u, t) = R_u. \end{cases} \tag{8}$$

In the above model, (8) B_l and B_u represent the lower and upper knock-in barriers, with R_l and R_u denoting the respective rebates paid when the corresponding barriers are hit. Moreover, r represents the risk-free interest rate and δ the dividend yield paid by the underlying dividend-paying stock.

To the best of our knowledge, there is a limited amount of literature on the subject of high-order solution schemes for barrier-option pricing time-fractional Black-Scholes PDEs, as the topic is still relatively new and limited to vanilla option problems.

Using variable transform ($\tau = T - t$) time to maturity, (8) can be transformed into the following initial value problem (IVP)

$$\tau^{\alpha-1}(T - \tau)^{1-\alpha} \frac{\partial^{\alpha} v}{\partial \tau^{\alpha}} - \left(\frac{rv}{\Gamma(2 - \alpha)} - (r - \delta) S^{\alpha} \frac{\partial^{\alpha} v}{\partial S^{\alpha}} \right) (T - \tau)^{1-\alpha} + \frac{\Gamma(1 + \alpha) \sigma^2 S^2}{2} \frac{\partial^2 v}{\partial S^2} = 0,$$

which simplifies to

$$\frac{\partial^\alpha v}{\partial \tau^\alpha} - \left(\frac{rv}{\Gamma(2-\alpha)} - (r-\delta)S\frac{\partial v}{\Gamma(2-\alpha)\partial S}\right)\tau^{1-\alpha} + \frac{\Gamma(1+\alpha)\sigma^2 S^2}{2}\frac{\partial^2 v}{\partial S^2} = 0, \quad 0 < \alpha \leq 1, \tag{9}$$

with initial and boundary conditions

$$\left.\begin{array}{l} S \in (B_l, B_u), \\ \tau \in (T, 0), \\ v(B_l, \tau) = R_l,\ v(B_u, \tau) = R_u. \end{array}\right\} \tag{10}$$

Considering the following change in variables $x = ln(S)$ and $v(x,\tau) = e^{r\tau}v(S,\tau)$ and without loss of notations, after simplification, we obtain

$$\frac{\partial^\alpha v(x,\tau)}{\partial \tau^\alpha} = \left(\frac{rv(x,\tau)}{\Gamma(2-\alpha)} - (r-\delta)x\frac{\partial v(x,\tau)}{\Gamma(2-\alpha)\partial x}\right)\tau^{1-\alpha} - \frac{\Gamma(1+\alpha)\sigma^2 x^2}{2}\frac{\partial^2 v}{\partial S^2}, \quad 0 < \alpha \leq 1, \tag{11}$$

with the following initial and barrier conditions

$$\left.\begin{array}{l} v(x,0) = \max(K - e^x, 0),\ 0 < \tau < T, \\ v(b_l, \tau) = r_l,\ v(b_u, \tau) = r_u,\ \ b_l < x < b_u. \end{array}\right\} \tag{12}$$

3. Numerical Scheme

This section presents the construction of the involved numerical scheme in solving (11), subject to initial and barrier conditions (12).

3.1. Model Discretization

Let L and N be positive integers and define $h = (b_u - b_l)/L$ and $k = T/N$ the space and time step-sizes, respectively. We denote $x_l = b_l + lh;$ for $l = 0, 1, 2, \ldots, L$ and $\tau_n = nk;\ n = 0, 1, 2, \ldots, N$, such that $x_l \in [b_l, b_u]$ and $\tau_n \in [0, T]$. Furthermore, we define $v_l^n = v(x_l, \tau_n)$ as the solution at the grid point $(x_l, \tau_n) = (b_l + lh, nk)$.

3.1.1. Temporal Discretization

Let us define

$$\Delta_t v_l^n = \Delta_t v(x_l, \tau_n) = \frac{v(x_l,\tau_n) - v(x_l, \tau_{n-1})}{k^\alpha} = \frac{v_l^n - v_l^{n-1}}{k^\alpha}, \tag{13}$$

and discretize the time-fractional derivative in (11) at the grid point (x_l, τ_{n+1}) by the following quadrature formula

$$\begin{aligned} \frac{\partial^\alpha v(x_l, \tau_{n+1})}{\partial \tau^\alpha} &= \frac{k^{-\alpha}}{\Gamma(2-\alpha)}\sum_{j=0}^{n}\sigma_j\big(v(x_l,\tau_{n-j+1}) - v(x_l, \tau_{n-j})\big) + \frac{\tau_n^{1-\alpha}}{\Gamma(2-\alpha)}k, \\ &= \frac{1}{\Gamma(2-\alpha)}\sum_{j=0}^{n}\sigma_j \Delta_t v(x_l, t_{n-j+1}) + \mathcal{O}(k^2), \end{aligned} \tag{14}$$

where

$$\sigma_j = (j+1)^{1-\alpha} - j^{1-\alpha},\ j = 0, 1, 2, \cdots, n, \tag{15}$$

such that $1 = \sigma_0 > \sigma_1 > \sigma_2 > \cdots > \to 0$ as $j \to n$.

3.1.2. Spatial Discretization

Let us define

$$\Delta_x v_l^n = \Delta_x v(x_l, \tau_n) = \frac{v(x_{l+1},\tau_n) - v(x_{l-1}, \tau_n)}{h^2} = \frac{v_{l+1}^n - v_{l-1}^n}{h^2}, \tag{16}$$

$$\Delta_{xx}v_l^n = \Delta_x v(x_l, \tau_n) = \frac{v(x_{l+1}, \tau_n) - 2v(x_l, \tau_n) + v(x_{l-1}, \tau_n)}{h^2} = \frac{v_{l+1}^n - 2v_l^n + v_{l-1}^n}{h^2}. \tag{17}$$

We approximate the spatial derivatives in (11), as follows:

$$\frac{\partial v(x_l, \tau_{n+1})}{\partial x} = \frac{v(x_{l+1}, \tau_{n+1}) - v(x_{l-1}, \tau_{n+1})}{2h} - \frac{h^2}{6}\frac{\partial^3 v(x_l, \tau_{n+1})}{\partial x^3} + \mathcal{O}(h^4), \tag{18}$$

and

$$\frac{\partial^2 v(x_l, \tau_{n+1})}{\partial x^2} = \frac{v(x_{l+1}, \tau_{n+1}) - 2v(x_l, \tau_{n+1}) + v(x_{l-1}, \tau_{n+1})}{h^2} - \frac{h^2}{12}\frac{\partial^4 v(x_l, \tau_{n+1})}{\partial x^4} + \mathcal{O}(h^2). \tag{19}$$

3.2. The Full Scheme

To obtain the full numerical scheme, we substitute (14), (18) and (19) into (11) and we obtain the following scheme

$$\frac{1}{\Gamma(2-\alpha)}\sum_{j=0}^{n}\sigma_j \Delta_t v_l^{n-j+1} = \left(r v_l^{n+1} - q\Delta_x v_l^{n+1}\right)\frac{\tau^{1-\alpha}}{\Gamma(2-\alpha)} - \omega(\alpha)\Delta_{xx}v_l^{n+1} - R_l^{n+1} \tag{20}$$

$$q = r - \delta,\ n \geq 0,\ \omega(\alpha) = \frac{\Gamma(1+\alpha)\sigma^2 x^2}{2}.$$

which, after some algebraic manipulations, can be simplified into

$$\sum_{j=1}^{n+1}\varphi_{j-1}v_l^{n-j+1} = a v_{l-1}^{n+1} + b v_l^{n+1} + c v_{l+1}^{n+1} + R_l^{n+1} \tag{21}$$

where by

$$a = -k^\alpha q \tfrac{\tau^{1-\alpha} - \omega'}{h^2},\ \ b = k^\alpha \tfrac{\tau^{1-\alpha} r + 2\omega'}{h^2},\ \ c = -k^\alpha q \tfrac{\tau^{1-\alpha} - \omega'}{h^2} - 1,$$
$$\omega' = k^\alpha \Gamma(2-\alpha)\omega(\alpha),\ \ \varphi_j = \sigma_j - \sigma_{j+1}.$$

The final scheme is explicitly given by

$$\varphi_0 v_l^n + \cdots + \varphi_{n-1}v_l^1 + \varphi_n v_l^0 = a v_{l-1}^{n+1} + b v_l^{n+1} + c v_{l+1}^{n+1}, \tag{22}$$

whereby the left-hand side of the scheme (22) captures the memory effects.

Furthermore, R_l^{n+1} in (21) represents the remainder after truncation, which is given by

$$R_l^{n+1} = \frac{h^2}{12}\left(\frac{\tau^{1-\alpha}}{\Gamma(2-\alpha)}\frac{\partial^3 v_l^{n+1}}{\partial x^3} + \omega(\alpha)\frac{\partial^4 v_l^{n+1}}{\partial x^4}\right) + \mathcal{O}\left(h^2 + k^2\right), \tag{23}$$

which implies that,

$$\left|R_l^{n+1}\right| = C\left(h^2, k^2\right), \tag{24}$$

for some constant C independent of h and k. The proof to this result follows in the next section.

4. Theoretical Analysis of the Scheme

In this section, we present the stability and convergence properties of the proposed difference scheme (22).

4.1. Stability Analysis

The stability properties of the proposed scheme (22) will be discussed using the concept of Fourier analysis. Suppose $\hat{v}_l^n$ is an approximate solution to the scheme (22) such that $v_l^n - \hat{v}_l^n = \epsilon_l^n$ for $l = 0, 1, \cdots, L$, then the following theorem holds.

Theorem 1. *The difference scheme in* (22) *is unconditional stable.*

To prove the above theorem, we substitute the roundoff error ϵ_l^n into (22), we obtain

$$\sum_{j=1}^{n+1} \varphi_{j-1}\epsilon_l^{n-j+1} \quad = \quad a\epsilon_{l-1}^{n+1} + b\epsilon_l^{n+1} + c\epsilon_{l+1}^{n+1}, \tag{25}$$

such that $\epsilon_0^n = \epsilon_L^n = 0$.

Let us define the grid function as follows,

$$\epsilon^n(x) = \begin{cases} \epsilon_l^n, & \text{when } \ x_l - \frac{h}{2} < x \le x_l + \frac{h}{2}, \ l = 1,2,\dots,L-1, \\ \\ 0, & \text{when } \ b_l \le x \le b_l + \frac{h}{2} \ \text{ or } \ b_u - \frac{h}{2} < x \le b_u + \frac{h}{2}, \end{cases} \tag{26}$$

which can be expanded in terms of the following Fourier series representation

$$\epsilon^n(x) = \sum_{j=1}^{\infty} \varrho_n(j) e^{i2\pi jx/b_u - b_l}, \quad n = 1,2,\dots,N, \tag{27}$$

where

$$\varrho_n(j) = \frac{1}{b_u - b_l}\int_0^{b_u - b_l} \epsilon^n(x) e^{-i2\pi jx/b_u - b_l} dx, \quad n = 1,2,\dots,N, \tag{28}$$

and $i = \sqrt{-1}$.

Let $\epsilon^n = (\epsilon_1^n, \epsilon_2^n, \cdots, \epsilon_{L-1}^n)^T$ and, define its norm

$$\|\epsilon^n\|_2 = \left(\sum_{l=1}^{L-1} h \mid \epsilon_l^n \mid^2\right)^{1/2} = \left(\int_0^{b_u - b_l} \mid \epsilon^n(x) \mid^2 dx\right)^{1/2}, \tag{29}$$

and apply the Parseval equality to obtain

$$\int_0^{b_u - b_l} \mid \epsilon^n(x)^2 \mid dx = \sum_{j=-\infty}^{\infty} \mid \varrho_n(j) \mid^2, \tag{30}$$

to obtain

$$\|\epsilon^n\|_2^2 = \int_0^{b_u - b_l} \mid \epsilon^n(x) \mid^2 dx = \sum_{j=-\infty}^{\infty} \mid \varrho_n(j) \mid^2 . \tag{31}$$

Therefore, the solution to (25) takes the following form

$$\epsilon_l^n = \varrho_n e^{i\beta lh}, \tag{32}$$

for $\beta := 2\pi j / b_u - b_l$ and $i = \sqrt{-1}$. Substituting the expression for ϵ^n into (25) we obtain

$$\varphi_0 \varrho_n e^{i\beta lh} + \cdots + \varphi_{n-1}\varrho_1 e^{i\beta lh} + \varphi_n \varrho_0 e^{i\beta lh} \quad = \quad a\varrho_{n+1} e^{i\beta(l-1)h} + b\varrho_{n+1} e^{i\beta lh} + c\varrho_{n+1} e^{i\beta(l+1)h}, \tag{33}$$

Which, after simplifications, leads to

$$(\varphi_0\varrho_n + \cdots + \varphi_{n-1}\varrho_1 + \varphi_n\varrho_0) e^{i\beta lh} \quad = \quad e^{i\beta lh}\varrho_{n+1}\Big(a e^{-i\beta h} + c e^{i\beta h} + b\Big), \tag{34}$$

$$\varphi_0\varrho_n + \cdots + \varphi_{n-1}\varrho_1 + \varphi_n\varrho_0 \quad = \quad \varrho_{n+1}\Big(a\Big(e^{-i\beta h} + e^{i\beta h}\Big) + b - 1\Big), \tag{35}$$

since $\beta_0 = 1$ and $a = c - \beta_0$.

From the Fourier series representation of $\cos \beta h$, we obtain

$$\varphi_0\varrho_n + \cdots + \varphi_{n-1}\varrho_1 + \varphi_n\varrho_0 \quad = \quad \varrho_{n+1}(a\cos\beta h + b - 1). \tag{36}$$

Proposition 1. *Suppose ϱ_{n+1} satisfies* (36)*, then $|\varrho_{n+1}| \le |\varrho_0|$, for all $n = 0,1,2,\cdots,N$.*

Let $n = 0$, then from (36) we have

$$|\varrho_1(a\cos\beta h + b - 1)| = |\varphi_0\varrho_0|, \tag{37}$$

which imply that

$$\begin{aligned} |\varrho_1| &= \left|\frac{\varphi_0\varrho_0}{a\cos\beta h + b - 1}\right|, \\ &\le \frac{\varphi_0}{|a\cos\beta h + b - 1|}|\varrho_0|, \\ &\le \frac{1-\beta_1}{|a\cos\beta h + b - 1|}|\varrho_0|, \\ &< \frac{1}{|a\cos\beta h + b - 1|}|\varrho_0|, \ (\because 1-\beta_1 < 1), \\ &< |\varrho_0|, \ \left(\because \frac{1}{|a\cos\beta h + b - 1|} < 1\right). \end{aligned} \tag{38}$$

This implies that,

$$|\varrho_1| \le |\varrho_0|.$$

For $n = 1$, we suppose $|\varrho_n| \le |\varrho_0|$ for all $n = 1, 2, \cdots, N$, and show that the same is true for $|\varrho_{n+1}| \le |\varrho_0|$ for all n.

Proof.

$$\begin{aligned} |\varrho_{n+1}| &= \left|\frac{\sum_{j=1}^{n+1}\varphi_{j-1}\varrho_{n-j+1}}{a\cos\beta h + b - 1}\right|, \\ &\le \frac{1}{|a\cos\beta h + b - 1|}\sum_{j=1}^{n+1}|\varphi_{j-1}\varrho_{n-j+1}|, \\ &\le \sum_{j=1}^{n+1}|\varphi_{j-1}\varrho_{n-j+1}|, \left(\because \frac{1}{|a\cos\beta h + b - 1|}\right) < 1, \\ &= \varphi_0|\varrho_n| + \varphi_1|\varrho_{n-1}| + \cdots + \varphi_{n-1}|\varrho_1| + \varphi_n|\varrho_0|, \\ &\le \varphi_0|\varrho_0| + \varphi_1|\varrho_0| + \cdots + \varphi_{n-1}|\varrho_0| + \varphi_n|\varrho_0|, \\ &= (\varphi_0 + \varphi_1 + \cdots + \varphi_{n-1} + \varphi_n)|\varrho_0|, \\ &= \sum_{j=1}^{n+1}\varphi_{j-1}|\varrho_0|, \\ &= |\varrho_0|, \ \left(\because \sum_{j=1}^{n+1}\varphi_{j-1} = 1\right). \end{aligned} \tag{39}$$

Therefore, $\left\|\epsilon_l^{n+1}\right\|_2 \le \left\|\epsilon_l^0\right\|_2$, which concludes the proof for Theorem 1. □

4.2. Convergence of the Numerical Scheme

In this subsection, we prove that the proposed scheme (22) converges with temporal order of two and is spatially accurate with fourth order. The analysis will follow the concept of Fourier analysis. Let R_l^{n+1} denote the truncation error involved in the approximation at grid point (x_l, τ_{n+1}), then, from (23), we obtain the following theorem:

Theorem 2. *The difference scheme* (22) *is convergent and converges with order* $\mathcal{O}(k^2 + h^4)$.

Let $\xi_l^n = v(x_l, t_n) - v_l^n$ denote the approximation error at grid point (t_n, x_l), such that $\xi_L^n = 0$, for $n = 1, 2, \cdots, N$ and $\xi_l^0 = 0$, for $l = 0, 1, \cdots, L$. By substituting ξ_l^n into the scheme (22) we obtain

$$\sum_{j=1}^{n+1} \varphi_{j-1}\xi_l^{n-j+1} + R_l^{n+1} \quad = \quad a\xi_{l-1}^{n+1} + b\xi_l^{n+1} + c\xi_{l+1}^{n+1}, \tag{40}$$

Similar to stability analysis, we define the following grid functions

$$\xi^n(S) = \begin{cases} \xi_l^n, & \text{when} \quad x_l - \frac{h}{2} < x \le S_l + \frac{h}{2}, \quad l = 1,2,\dots,L-1, \\ 0, & \text{when} \quad 0 \le x < \frac{h}{2} \quad \text{or} \quad x_{max} - \frac{h}{2} < S \le x_{max} + \frac{h}{2}, \end{cases} \tag{41}$$

$$R^n(x) = \begin{cases} C_l^n, & \text{when} \quad x_l - \frac{h}{2} < x \le x_l + \frac{h}{2}, \quad l = 1,2,\dots,L-1, \\ 0, & \text{when} \quad 0 \le x < \frac{h}{2} \quad \text{or} \quad x_{max} - \frac{h}{2} < x \le x_{max} + \frac{h}{2}, \end{cases} \tag{42}$$

which implies $\xi^n(x)$ and C_l^n have the following Fourier series representations

$$\xi^n(x) = \sum_{j=1}^{\infty} \tau_n(j) e^{i2\pi jx/x_{max}}; \quad n = 1,2,\dots,N, \tag{43}$$

$$R^n(x) = \sum_{j=1}^{\infty} \nu_n(j) e^{i2\pi jx/x_{max}}; \quad n = 1,2,\dots,N, \tag{44}$$

where

$$\tau_n(j) = \frac{1}{x_{max}} \int_0^{xmax} \xi^n(x) e^{-i2\pi jx/x_{max}} dx; \quad n = 1,2,\dots,N. \tag{45}$$

$$\nu_n(j) = \frac{1}{x_{max}} \int_0^{xmax} R^n(x) e^{-i2\pi jx/x_{max}} dx; \quad n = 1,2,\dots,N. \tag{46}$$

Let $\xi^n = (\xi_1^n, \xi_2^n, \cdots, \xi_{L-1}^n)^T$ and $R^n = (R_1^n, R_2^n, \cdots, R_{L-1}^n)^T$, and let us define their norms as follows:

$$\left\|\xi^n\right\|_2 = \left(\sum_{l=1}^{L-1} h|\ \xi_l^n\ |^2\right)^{1/2} = \left(\int_0^{x_{max}} |\ \xi^n(x)\ |^2 dx\right)^{1/2}, \tag{47}$$

$$\left\|R^n\right\|_2 = \left(\sum_{l=1}^{L-1} h|\ R_l^n\ |^2\right)^{1/2} = \left(\int_0^{x_{max}} |\ R^n(x)\ |^2 dx\right)^{1/2}, \tag{48}$$

and, apply the following Parseval equalities

$$\int_0^{S_{max}} |\ \xi^n(S)^2\ |\ dS = \sum_{j=-\infty}^{\infty} |\ \tau_n(j)\ |^2; \quad n = 1,2,\dots,N \tag{49}$$

$$\int_0^{S_{max}} |\ R^n(S)^2\ |\ dS = \sum_{j=-\infty}^{\infty} |\ \nu_n(j)\ |^2; \quad n = 1,2,\dots,N \tag{50}$$

to obtain

$$\left\|\xi^n\right\|_2^2 = \sum_{j=-\infty}^{\infty} |\ \tau_n(j)\ |^2; \quad n = 1,2,\dots,N. \tag{51}$$

$$\left\|R^n\right\|_2^2 = \sum_{j=-\infty}^{\infty} |\ \nu_n(j)\ |^2; \quad n = 1,2,\dots,N. \tag{52}$$

Based on this analysis, we can therefore propose that

$$\xi^n = \tau_n e^{i\beta lh} \quad \text{and} \quad R^n = \nu_n e^{i\beta lh}, \tag{53}$$

where $\beta = 2\pi j/S_{max}$ and $i = \sqrt{-1}$. Substituting the expressions in (53) into (40) we obtain

$$\sum_{j=1}^{n+1} \varphi_{j-1}\tau_{n-j+1}e^{i\beta lh} \quad = \quad a\tau_{n+1}e^{i\beta(l-1)h} + b\tau_{n+1}e^{i\beta lh} + c\tau_{n+1}e^{i\beta(l+1)h} - \nu_{n+1}e^{i\beta lh}, \quad (54)$$

which implies

$$\left(\sum_{j=1}^{n+1} \varphi_{j-1}\tau_{n-j+1}\right)e^{i\beta lh} \quad = \quad e^{i\beta lh}\tau_{n+1}\Big(\Big(ae^{-i\beta h} + ce^{i\beta h} + b\Big) - \nu_{n+1}\Big) \qquad (55)$$

which simplify into

$$\sum_{j=1}^{n+1} \varphi_{j-1}\tau_{n+1-j} \quad = \quad \tau_{n+1}(a\cos\beta h + b - 1) - \nu_{n+1}. \qquad (56)$$

Therefore

$$\tau_{n+1} \quad = \quad \frac{\sum_{j=1}^{n+1}\varphi_{j-1}\tau_{n+1-j} + \nu_{n+1}}{(a\cos\beta h + b - 1)}. \qquad (57)$$

Proposition 2. *Suppose τ_n for $n = 0, 1, \cdots, N$ is a solution to* (57)*; then, there exists some positive constant C such that $|\tau_n| \leq C|\nu_1|$ for all n.*

Proof. It is trivial to show that for $n = 0$, from (57), we have

$$|\tau_1| \quad = \quad \left|\frac{\varphi_0\tau_0 + \nu_1}{(a\cos\beta h + b - 1)}\right| \leq \nu_1. \qquad (58)$$

Suppose $|\tau_n| \leq C_0|\nu_1|$, for $n = 1, 2, \cdots, N$, for some constant C independent of h and k. Then,

$$\begin{aligned}
|\tau_{n+1}| \quad &\leq \quad \left|\frac{\sum_{j=1}^{n+1}\varphi_{j-1}\tau_{n+1-j} + \nu_{n+1}}{(a\cos\beta h + b - 1)}\right|, \\
&\leq \quad \sum_{j=1}^{n+1}\frac{1}{|(a\cos\beta h + b - 1)|}(\sigma_{j-1}|\tau_{n-j+1}| + |\nu_{n+1}|), \\
&\leq \quad \sum_{j=1}^{n+1} C_{j-1}(\sigma_{j-1}|\tau_{n-j+1}| + |\nu_{n+1}|), \\
&\leq \quad \sum_{j=1}^{n+1}\sigma_{j-1}C_{j-1}|\tau_{n-j+1}| + C_{n+1}|\nu_1|, \qquad (59) \\
&\leq \quad \sum_{j=1}^{n+1}\sigma_{j-1}C_{j-1}|\nu_1| + C_{n+1}|\nu_1|, \\
&= \quad \sigma_0C_0|\nu_1| + \sigma_1C_1|\nu_1| + \sigma_2C_2|\nu_1| + \cdots + \sigma_nC_n|\nu_1| + C_{n+1}|\nu_1|, \\
&\leq \quad \hat{C}(\sum_{j=1}^{n+1}\sigma_{j-1}|\nu_1| + \nu_1), (\hat{C} = \max_{0\leq j\leq n+1}\{C_j\}) \\
&= \quad \hat{C}(\sum_{j=0}^{n+1}\sigma_j)|\nu_1| \\
&= \quad C|\nu_1|.
\end{aligned}$$

We can therefore conclude that the scheme (22) is convergent, and this completes the proof to Theorem 2. □

5. Numerical Results and Discussions

In this section, we present two numerical examples of the pricing of double-barrier knock-in put-option problems.

Example 1. *Consider Equation* (8)*, subject to conditions* (12) *for pricing a double knock-in put option with the following parameters:* $K = 80,\ r = 0.05,\ \sigma = 0.01,\ T = 1,\ S_{\max} = 120,\ L = 100,\ N = 50, \delta = 0.025,$ *and* $0.075, \alpha = (0.5,\ 0.7,\ 0.9,\ 1.0),$ *with lower barrier located at* $B_l = 6$ *and upper barrier located at* $B_u = 110$.

To asses the effects of change in some key option parameters on the effectiveness of the approach, as well as, the numerical method herein, we considered a second example with two different sets of dividend yields δ, two different sets of barriers, the same interest rate r, the same strike price K, the same maturity time T and the same set of α values.

Example 2. *Consider Equation* (8)*, subject to conditions* (12) *for pricing double knock-in put options with the following parameters:* $K = 80,\ r = 0.05,\ \sigma = 0.015,\ T = 1,\ S_{\max} = 120,\ L = 100,\ N = 100, \delta = 0.045$ *and* $0.10, \alpha = (0.5,\ 0.7,\ 0.9,\ 1.0),$ *with lower barrier located at* $B_l = 10$ *and upper barrier located at* $B_u = 130$.

Option maturity payoff curves for the two considered examples (Examples 1 and 2, above) are presented in Figures 1 and 2 below.

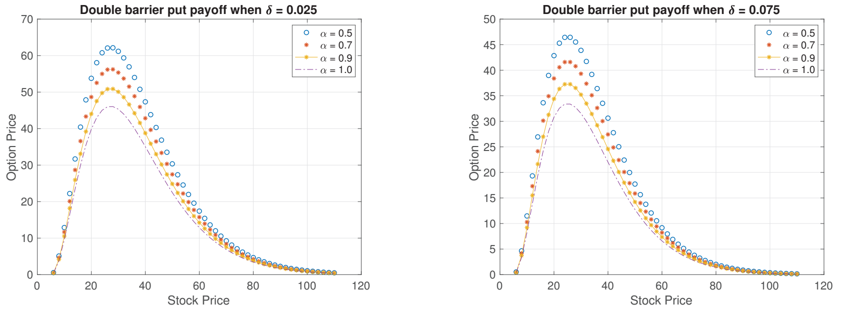

Figure 1. Double-barrier put-option payoffs for $\delta = 0.025,$ and 0.075, with $\alpha = (0.5,\ 0.7,\ 0.9,\ 1.0)$, and $B_l = 6,\ \ B_u = 110$ at $t = T$.

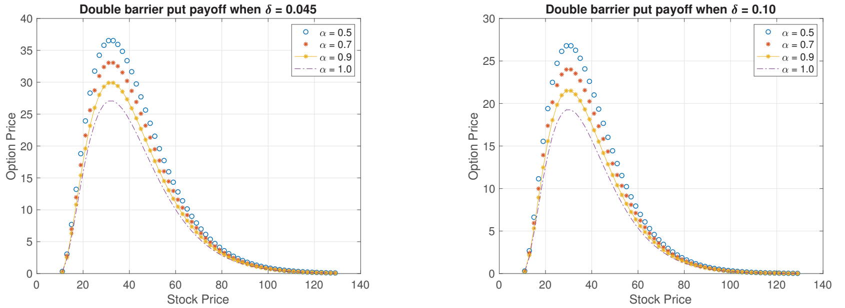

Figure 2. Double-barrier put-option payoffs for $\delta = 0.045,$ and 0.10, with $\alpha = (0.5,\ 0.7,\ 0.9,\ 1.0)$, and $B_l = 10,\ \ B_u = 130$ at $t = T$.

The results in Figures 1 and 2 are consistent with those obtained in [45] which are formulated using a call option. Figures 1 and 2 indicates that, change in dividend yield has an effect on the option price (premium). A higher dividend yield (δ) yields a lower option premium. This is not strange because, the holder of an option with a higher dividend yield is compensated more through dividends as compared to the one with a lower dividend yield.

Moreover, the considered tfBS in Equation (8) gives high option prices both for the in-the-money option and for when the underlying asset price (S) is close to the strike price (K) as compared to the classical BS model ($\alpha = 1$) case. This indicates that, the tfBS model in (8) is of a *power-law* nature as compared to the classical Black-Scholes model.

Tabular results for the two considered examples (Examples 1 and 2, above) are presented in Tables 1–4, below.

Table 1. Approximation errors for Example 1 with $r = 0.05$ and $\delta = 0.025$.

α	$N = 50$	$N = 100$	$N = 200$	$N = 400$	$N = 800$
0.1	7.1212×10^3	1.7901×10^3	4.4561×10^4	1.1525×10^4	2.9154×10^5
0.2	7.1336×10^3	1.8180×10^3	4.4711×10^4	1.1563×10^4	2.9250×10^5
0.3	7.3465×10^3	1.8383×10^3	4.5753×10^4	1.1827×10^4	2.9717×10^5
0.4	7.4609×10^3	1.9326×10^3	4.8371×10^4	1.2239×10^4	3.0759×10^5
0.5	8.1315×10^3	2.0213×10^3	5.1493×10^4	1.3000×10^4	3.2785×10^5
0.6	8.4515×10^3	2.1032×10^3	5.4620×10^4	1.3842×10^4	3.4915×10^5
0.7	9.5333×10^3	2.3909×10^3	6.1088×10^4	1.5478×10^4	3.7153×10^5
0.8	1.1062×10^2	2.5616×10^3	6.4925×10^4	1.6449×10^4	4.1409×10^5
0.9	1.2494×10^2	3.1452×10^3	7.8208×10^4	2.0062×10^4	5.0548×10^5
1.0	1.3815×10^2	3.4591×10^3	8.7754×10^4	2.2198×10^4	5.5953×10^5

Table 2. Rate of convergence for Example 1 with $r = 0.05$ and $\delta = 0.025$.

α	$N = 100$	$N = 200$	$N = 400$	$N = 800$
0.1	1.91	1.95	1.98	1.99
0.2	1.92	1.96	1.98	1.99
0.3	1.93	1.96	1.98	1.99
0.4	1.93	1.96	1.98	1.99
0.5	1.93	1.97	1.98	1.99
0.6	1.94	1.97	1.98	1.99
0.7	1.94	1.97	1.98	1.99
0.8	1.94	1.97	1.98	1.99
0.9	1.94	1.97	1.98	1.99
1.0	1.94	1.97	1.98	1.99

Table 3. Approximation errors for Example 2 with $r = 0.05$ and $\delta = 0.045$.

α	$N = 100$	$N = 200$	$N = 400$	$N = 800$	$N = 1600$
0.1	6.5512×10^2	1.6492×10^2	4.1892×10^3	1.0597×10^3	2.5953×10^4
0.2	5.7988×10^3	1.4694×10^2	3.7170×10^3	9.4025×10^4	2.3784×10^4
0.3	5.2147×10^2	1.3191×10^2	3.3368×10^3	8.4408×10^4	2.1352×10^4
0.4	4.7443×10^2	1.2001×10^2	3.0358×10^3	7.6794×10^4	1.9426×10^4
0.5	4.3746×10^2	1.1066×10^2	2.7993×10^3	7.0810×10^4	1.7912×10^4
0.6	4.0893×10^2	1.0344×10^2	2.6167×10^3	6.6192×10^4	1.6544×10^4
0.7	3.8773×10^2	9.8080×10^3	2.4898×10^3	6.2752×10^4	1.5688×10^4
0.8	3.7318×10^2	9.4300×10^3	2.3779×10^3	6.0305×10^4	1.4980×10^4
0.9	3.6499×10^2	9.3328×10^3	2.4355×10^3	5.9979×10^4	1.5745×10^4
1.0	3.7328×10^2	9.2895×10^3	2.4246×10^3	5.9803×10^4	1.5670×10^4

Table 4. Rate of convergence for Example 2 with $r = 0.05$ and $\delta = 0.045$.

α	$N = 200$	$N = 400$	$N = 800$	$N = 1600$
0.1	1.95	1.98	1.99	1.99
0.2	1.96	1.98	1.99	1.99
0.3	1.96	1.98	1.99	1.99
0.4	1.96	1.98	1.99	2.00
0.5	1.97	1.98	1.99	2.00
0.6	1.97	1.98	1.99	2.00
0.7	1.97	1.98	1.99	2.00
0.8	1.97	1.98	1.99	2.00
0.9	1.97	1.98	1.99	2.00
1.0	1.97	1.98	1.99	2.00

The numerical results herein confirm our theoretical deductions on the stability and convergence properties of the scheme as presented in Sections 4.1 and 4.2, respectively. The results indicates that, the proposed scheme is unconditionally stable (see Section 4.1) and converges with order $\mathcal{O}(h^2, k^2)$, i.e., the scheme converges with order two in both time and asset directions under all possible orders of the fractional derivative (α).

6. Concluding Remarks and Scope for Future Direction

In this paper we considered a double-barrier-option pricing problem under the time-fractional Black-Scholes setup. We propose a robust second-order numerical scheme for solving a discretely monitored double-barrier time-fractional Black-Scholes PDE. Two numerical examples are presented. Results indicates that, adding to the already established scientific evidence, the fractional Black-Scholes approach is a very efficient valuation technique for barrier option problems as compared to the usual/classical Black-Scholes approach. The double barrier-option tfBS model in Equation (8) is sensitive to dividend payouts, and allocates lower put premiums to higher dividend yield options. These results are well in line with the theory of no-arbitrage, where investors who are compensated well in dividends would receive prices lower than those of investors with lower dividend yield options. Moreover, the numerical scheme herein proves to be efficient at solving the involved time-fractional Black-Scholes model, though the approach using the general signal produces some asymmetric performances when $0 < \alpha < 0.5$. The approach is only effective when $0.5 \leq \alpha < 1$, and it is for this reason that we only presented results for when $\alpha = (0.5,\ 0.7,\ 0.9,\ 1.0)$. The calibration of the model to real-time market data remains the subject of future research.

Author Contributions: Conceptualization, K.C.P. and S.M.N.; methodology, K.C.P. and S.M.N.; software, K.C.P. and S.M.N.; validation, K.C.P. and S.M.N. and F.G.; formal analysis, S.M.N.; investigation, S.M.N. and K.C.P.; resources, K.C.P. and F.G.; data curation, S.M.N.; writing—original draft preparation, S.M.N.; writing—review and editing, S.M.N., K.C.P., and F.G.; visualization, S.M.N.; supervision, K.C.P. and F.G; project administration, K.C.P.; funding acquisition, K.C.P. All authors have read and agreed to the published version of the manuscript.

Funding: The research of S. M. Nuugulu was supported by the University of Namibia (Staff Development Program) and DAAD (In-country scholarship). Research for K. C. Patidar is supported by South African National Research Foundation, and F. Gideon was supported by the South African National Research Foundation under NRF-KIC grant of K. C. Patidar.

Data Availability Statement: The data that support the findings of this study are available from the corresponding author, [SM Nuugulu], upon reasonable request.

Conflicts of Interest: The authors declare no conflict of interest.

References

1. Buchen, P.; Konstandatos, O. A new approach to pricing double barrier options with arbitrary payoffs and exponential boundaries. *Appl. Math. Financ.* **2009**, *6*, 497–515. [CrossRef]
2. Hull, J. *Options, Futures and Other Derivatives*; Pearson Prentice Hall: Upper Saddle River, NJ, USA, 2009.
3. Luca, V.B.; Graziella, P.; Davide, R. A very efficient approach for pricing barrier options on an underlying described by the mixed fractional Brownian motion. *Chaos Solitons Fractals* **2016**, *87*, 240–248.
4. Wilmott, P. *Derivatives: The Theory and Practice of Financial Engineering*; John Wiley & Sons: West Sussex, UK, 1998.
5. Black, F.; Scholes, M. The pricing of options and corporate liabilities. *J. Polit. Econ.* **1973**, *81*, 637–654. [CrossRef]
6. Ballerster, R.; Company, C.; Jodar, L. An efficient method for option pricing with discrete dividend payment. *Comput. Math. Appl.* **2008**, *56*, 822–835. [CrossRef]
7. Kleinert, H.; Korbel, J. Option pricing beyond Black-Scholes based on double-fractional diffusion. *Phys. A* **2016**, *449*, 200–214. [CrossRef]
8. Broadie, M.; Glasserman, P. A continuity correction for discrete barrier options. *Math. Financ.* **1997**, *4*, 325–348. [CrossRef]
9. Ahn, D.; Gao, B.; Figlewski, S. Pricing discrete barrier options with an adaptive mesh model. *Quant. Anal. Financ. Mark.* **2002**, *33*, 296–313.
10. Feng, L.; Linetsky, V. Pricing discretely monitored barrier options and defaultable bonds in levy process models: A fast Hilbert transform approach. *Math. Financ.* **2008**, *3*, 337–384. [CrossRef]
11. Hsiao, Y.L.; Shen, S.Y.; Wang, A.M.L. Hybrids finite difference method for pricing tow-asst double barrier options. *Math. Probl. Eng.* **2015**, *2015*, 692695. [CrossRef]

12. Jeon, J.; Kim, J.Y.; Park, C. An analytic expansion method for the valuation of double-barrier options under as stochastic volatility model. *Math. Anal. Appl.* **2016**, *449*, 207–227. [CrossRef]
13. Song, S.; Wang, Y. Pricing double barrier options under a volatility regime-switching model with psychological barriers. *Rev. Deriv. Res.* **2017**, *2*, 225–280. [CrossRef]
14. Bollersleva, T.; Gibson, M.; Zhoud, H. Dynamic estimation of volatility risk premia and investor risk aversion from option-implied and realized volatilities. *J. Econom.* **2011**, *160*, 235–245. [CrossRef]
15. Benson, D.A.; Wheatcraft, S.W.; Meershaert, M.M. Application of a fractional advection-dispersion equation. *J. Water Resour. Res.* **2000**, *35*, 1403–1412. [CrossRef]
16. Huang, G.; Huang, Q.; Zhan, H. Evidence of one-dimensional scale-dependent fractional advection-dispersion. *J. Contemp. Hydrol.* **2006**, *85*, 53–71. [CrossRef]
17. Cutland, N.J.; Kopp, P.E.; Willinger, W. Stock price returns and the Joseph effect: A fractional version of the Black-Scholes model. *Semin. Stoch. Anal. Random Fields Appl.* **1995**, *36*, 327–351.
18. Chang-Ming, C.; Fawang, L.; Kevin, B. Finite difference methods and a fourier analysis for the fractional reaction sub diffusion equation. *Appl. Math. Comput.* **2008**, *2*, 754–769.
19. Nuugulu, S.M.; Gideon, F.; Patidar, K.C. A robust numerical solution to a time-fractional Black-Scholes equation. *Adv. Differ. Equ.* **2021**, *2021*, 123. [CrossRef]
20. Nuugulu, S.M.; Gideon, F.; Patidar, K.C. A robust numerical scheme for a time-fractional Black-Scholes partial differential equation describing stock exchange dynamics. *Chaos Solitons Fractals* **2021**, *145*, 110753. [CrossRef]
21. Donny, C.; Song, W. An upwind finite difference method for a nonlinear Black-Scholes equation governing European option valuation under transaction costs. *Appl. Math. Comput.* **2013**, *219*, 8811–8828.
22. Liang, J.; Wang, J.; Zhang, W.; Qiu, W.; Ren, F. Option pricing of a bi-fractional Black-Scholes model with the Hurst exponent H in $[1/2, 1]$. *Appl. Math. Lett.* **2010**, *23*, 859–863. [CrossRef]
23. Meerschaert, M.M.; Tadjeran, C. Finite difference methods for two-dimensional fractional dispersion equation. *J. Comput. Phys.* **2006**, *211*, 249–261. [CrossRef]
24. Murio, D.A. Implicit finite difference approximation for time fractional diffusion equations. *Comput. Math. Appl.* **2008**, *56*, 1138–1145. [CrossRef]
25. Wang, H.; Wang, K.X.; Sircar, T. A direct $\mathcal{O}(N \log^2 N)$ finite difference method for fractional diffusion equations. *J. Comput. Phys.* **2009**, *229*, 8095–8104. [CrossRef]
26. Bu, W.P.; Tang, Y.F.; Yang, J.Y. Galerkin finite element method for two-dimensional Riez space fractional diffusion equations. *J. Comput. Phys.* **2014**, *267*, 26–38. [CrossRef]
27. Ford, N.J.; Xiao, J.Y.; Yan, Y.B. A finite element method for time fractional partial differential equations. *Fract. Calc. Appl. Anal.* **2011**, *14*, 454–474. [CrossRef]
28. Jiang, Y.J.; Ma, J.T. High-order finite element methods for time-fractional partial differential equations. *J. Comput. Math.* **2011**, *235*, 3285–3290. [CrossRef]
29. Canuto, C.; Hussaini, M.Y.; Quarteroni, A.; Zang, T.A. *Spectral Methods: Fundamentals in Single Domains*; Springer: Berlin/Heidelberg, Germany, 2006.
30. Xu, C.; Lin, Y. Finite difference/spactral approximations for the time-fractional diffusion equation. *J. Comput. Phys.* **2007**, *225*, 1533–1552.
31. Doha, E.H.; Bhrawy, A.H.; Ezz-Eldien, S.S. Effecient chebyshev spectral methods for solving multi-term fractional differential equations. *J. Appl. Math. Model.* **2011**, *35*, 5662–5672. [CrossRef]
32. Kristoufek, L.; Vosvrda, M. Measuring capital market efficiency: Long-term memory, fractal dimension and approximate entropy. *Eur. Phys. J. B* **2014**, *87*, 162. [CrossRef]
33. Sensoy, A.; Tabak, B.M. Time-varying long term memory in the European Union stock markets. *Phys. A* **2015**, *436*, 147–158. [CrossRef]
34. Lahmiri, S. Long memory in international financial markets trends and short movements during the 2008 financial crisis based on variational mode decomposition and detrended fluctuation analysis. *Phys. A* **2015**, *437*, 130–138. [CrossRef]
35. Panas, E. Long memory and chaotic models of prices on the London metal exchange. *Resour. Policy* **2001**, *4*, 485–490. [CrossRef]
36. Acharya, V.V.; Richardson, M. Causes of the financial crisis. *Crit. Rev. Found.* **2009**, *21*, 195–210. [CrossRef]
37. Jumarie, G. Merton's model of optimal portfolio in a Black and Scholes market driven by a fractional Brownian motion with short-range dependence. *Insur. Math. Econ.* **2005**, *37*, 585–598. [CrossRef]
38. Garzarelli, F.; Cristelli, M.; Pompa, G.; Zaccaria, A.; Pietronero, L. Memory effects in stock price dynamics: Evidence of technical trading. *Scint. Rep.* **2014**, *4*, 4487. [CrossRef]
39. Chen, W.; Xu, X.; Zhu, S. Analytically pricing double barrier options on a time-fractional Black-Scholes equation. *Comput. Math. Appl.* **2015**, *69*, 1407–1419. [CrossRef]
40. Atangana, A.; Secer, A. A note on fractional order derivatives and table of fractional derivatives of some special functions. *Abstr. Appl. Anal.* **2013**, *2*, 279681. [CrossRef]
41. Jumarie, G. Modified Reimann-Liouville derivative and fractional Taylor series for non-differentiable functions, further results. *Comput. Math. Appl.* **2006**, *51*, 1367–1376. [CrossRef]
42. Osler, T.J. Taylor's series generalized for fractional derivatives and applications. *SAIM-J. Math. Anal.* **1971**, *2*, 37–47. [CrossRef]

43. Jumarie, G. Stock exchange fractional dynamics defined as fractional exponential growth driven by (usual) Gaussian white noise. Application to fractional Black-Scholes equations. *Insur. Math. Econ.* **2008**, *42*, 271–287. [CrossRef]
44. Jumarie, G. Derivation and solutions of some fractional Black-Scholes equations in coarse-grained space and time. Application to Merton's optimal portfolio. *Comput. Math. Appl.* **2010**, *59*, 1142–1164. [CrossRef]
45. Zhang, H.; Liu, F.; Turner, I.; Yang, Q. Numerical solution of the time fractional Black-Scholes model governing European options. *Comput. Math. Appl.* **2016**, *71*, 1772–1783. [CrossRef]

fractal and fractional

Article

Convergence Rate of the High-Order Finite Difference Method for Option Pricing in a Markov Regime-Switching Jump-Diffusion Model

Jun Liu [1],* and Jingzhou Yan [2]

[1] Shanghai Technical Institute of Electronics & Information, Shanghai 201411, China
[2] School of Economics, Sichuan University, Chengdu 610065, China; yanjingzhou036@163.com
* Correspondence: junliu7903@126.com

Abstract: The high-order finite difference method for option pricing is one of the most popular numerical algorithms. Therefore, it is of great significance to study its convergence rate. Based on the relationship between this algorithm and the trinomial tree method, as well as the definition of local remainder estimation, a strict mathematical proof is derived for the convergence rate of the high-order finite difference method for option pricing in a Markov regime-switching jump-diffusion model. The theoretical result shows that the convergence rate of this algorithm is $O(\Delta\tau)$. Moreover, the results also hold in the case of Brownian motion and jump-diffusion models that are specialized forms of the given model.

Keywords: convergence rate; high-order finite difference method; Markov regime-switching jump-diffusion model; partial integro-differential equations

Citation: Liu, J.; Yan, J. Convergence Rate of the High-Order Finite Difference Method for Option Pricing in a Markov Regime-Switching Jump-Diffusion Model. *Fractal Fract.* **2022**, *6*, 409. https://doi.org/10.3390/fractalfract6080409

Academic Editor: Leung Lung Chan

Received: 1 July 2022
Accepted: 25 July 2022
Published: 26 July 2022

1. Introduction

1.1. Background

Partial integro-differential equations (PIDEs) in a Markov regime-switching jump-diffusion model are popular in financial engineering ([1–14]). The advantages of this model lie in two aspects: on the one hand, the Markov chain reflects the information of market environments; on the other hand, it accurately describes the behavior of the underlying asset. However, it is difficult to solve the PIDEs due to the close relation to the Markov chain.

Some numerical methods, such as the high-order finite difference scheme, have been widely used to solve the PIDEs. The principle of the high-order difference method is to obtain finite difference approximations for high-order derivatives in the truncation error by operating on the differential equations as an auxiliary relation. The high-order schemes in a central difference approximation increase the order of accuracy. During and Fournie ([15–17]) derived a high-order difference scheme under the Heston model in 2012 and extended this method to non-uniform grids in 2014 and to multiple space dimensions in 2015. In 2019, During and Pitkin [18] applied this approach to stochastic volatility jump models. Additionally, some other scholars have put forward an improved algorithm based on higher-order finite difference in their papers ([19–25]). Rambeerich and Pantelous [4] developed a high-order finite element scheme to approximate the spatial terms of PIDE using linear and quadratic basis polynomial approximations and solved the resulting initial value problem using exponential time integration. Patel [6] proposed a fourth-order compact finite difference scheme for the solution of PIDE under regime-switching jump-diffusion models. Tour et al. [7] developed a high-order radial basis function finite difference (RBF-FD) approximation on a five-point stencil under the regime-switching stochastic volatility models with log-normal and contemporaneous jumps. Ma et al. [26] presented the high-order equivalence between the finite difference method and trinomial trees method for regime-switching models and proved the convergence rates of trinomial trees for pricing options with state-dependent switching rates using the theory of the FDMs.

It is of great importance to investigate the convergence rate of algorithms based on the Markov chain with finite difference schemes. In 2010, Alfonsi [27] presented weak second and third-order schemes for the CIR process and gave a general recursive construction method for obtaining weak second-order schemes. In 2017, Altmayer and Neuenkirch [28] established a weak convergence rate of order one under mild assumptions regarding the smoothness of the payoff. Zheng [29] derived that the weak convergence rate of a time-discrete scheme for the Heston stochastic volatility model was 2 for all parameter regimes. In 2018, Bossy and Olivero [30] studied the rate of convergence of a symmetrized version of the Milstein scheme applied to the solution of the one-dimensional SDE. Briani et al. studied the rate of weak convergence of Markov chains to diffusion processes under suitable, but quite general, assumptions in [31] and developed stability properties of a hybrid approximation of the functional of the Bates jump model with the stochastic interest rate in [32]. Lesmana and Wang [33] presented the consistency, stability, convergence, and numerical simulations of American options with transaction cost under a jump-diffusion process.

However, these papers all show the efficiency of this algorithm via numerical examples. It is important to give strict mathematical proof to guarantee the correctness of the high-order difference method. The objective of this article is to investigate the convergence rate of the high-order difference scheme (5)–(15) for option pricing assuming a Markov regime-switching jump-diffusion model (1) followed by the underlying asset.

1.2. The PIDEs in a Markov Regime-Switching Jump-Diffusion Model

Under the risk-neutral measure, the underlying $x_t = \log S_t$ will be modelled by a Markov regime-switching jump-diffusion model.

$$dx_t = [r(\alpha_t) - \beta(\alpha_t)\lambda(\alpha_t)]dt + \sigma(\alpha_t)dW_t + [\eta(\alpha_t) - 1]dQ_t \tag{1}$$

where $\{W_t\}_{t\geq 0}$ is a standard Brownian motion, $\{\alpha_t\}$ is a continuous-time Markov chain with finite states $\{1, 2, \cdots, n\}$, $r(\alpha_t) = r_i$ is the risk-free rate, $\sigma(\alpha_t) = \sigma_i$ denotes the constant volatility, $\{Q_t\}$ represents the compound Poisson process with intensity $\lambda(\alpha_t) = \lambda_i$ at state i, $[\eta(\alpha_t) - 1] = \eta_i - 1$ denotes the function which jump from S_t to $S_t\eta_i$. The expectation of this function is then given by $\beta(\alpha_t) = \beta_i$ where $\beta_i = E(\eta_i - 1)$. We assume that the stochastic processes $\{W_t\}_{t\geq 0}$ and $\{Q_t\}_{t\geq 0}$ in (1) are mutually independent in this paper.

Let $A = (\rho_{il}), i, l = 1, 2, \cdots, n$, be the generator matrix of the Markov chain process whose elements are constants satisfying $\rho_{il} \geq 0$ for $i \neq l$ and $\sum_{l=1}^{n} \rho_{il} = 0$ for $i = 1, 2, \cdots, n$.

Let the underlying x_t satisfy (1). Then, the value of a European option $V^i(x, \tau)$ satisfies the following PIDE:

$$\begin{cases} \frac{\partial V^i(x,\tau)}{\partial \tau} = \mathcal{L}V^i(x,\tau) + \mathcal{I}V^i(x,\tau) + \sum\limits_{l=1}^{n}\rho_{il}V^l(x,\tau),\ i = 1,2,\cdots,n,\ (x,\tau) \in R \times [0,T], \\ V^i(x,\tau) = \begin{cases} 0,\ x \to -\infty, \\ Ke^x - Ke^{-r_i\tau},\ x \to +\infty. \end{cases} \end{cases} \tag{2}$$

where

$$\mathcal{L}V^i(x,\tau) = \left(r_i - \lambda_i\beta_i - \frac{1}{2}\sigma_i^2\right)\frac{\partial V^i(x,\tau)}{\partial x} + \frac{1}{2}\sigma_i^2\frac{\partial^2 V^i(x,\tau)}{\partial x^2} - (r_i + \lambda_i)\, V^i(x,\tau) \tag{3}$$

$$\mathcal{I}V^i(x,\tau) = \lambda_i \int_{-\infty}^{+\infty} V^i(x,\tau) f^i(z - x)dz \tag{4}$$

and the density function $f^i(z-x)$ is given by [34]

$$f^i(z-x) = \frac{1}{\sqrt{2\pi}\gamma_i} \exp\left[-\frac{(z-x-\alpha_i)^2}{2\gamma_i^2} \right].$$

1.3. High-Order Finite Difference Method

The high-order finite difference method has been developed for option pricing [15–24]. The idea of this method is to obtain finite difference approximations for high-order derivatives in the truncation error. The high-order schemes in a central difference approximation increase the order of accuracy.

We divide the domain $(-\infty, +\infty)$ into three parts: $(-\infty, x_{\min})$, $[x_{\min}, x_{\max})$, and $[x_{\max}, +\infty)$ and introduce uniform grids with $\Delta x = (x_{\max} - x_{\min})/M$ and $\Delta\tau = (T-t)/N$ where M and N denote the number of space and time intervals, respectively. T is the maturity date of the option. Furthermore, let the mesh points be $x_m = x_{\min} + m\Delta x$ for $m = 0, 1, \cdots, M$ and $\tau_j = j\,\Delta\tau$ for $j = 0, 1, 2, \cdots, N$.

For the integral term in Equation (2), by choosing the appropriate interval$[x_{\min}, x_{\max}]$, we can assure that the integral value beyond this range can be ignored, that is,

$$\lambda_i \int_{-\infty}^{x_{\min}} V^i(x,\tau) f^i(z-x)dz \approx \lambda_i \int_{-\infty}^{x_{\min}} \max(1-\exp(\xi), 0) f^i(\xi)d\xi = 0 \tag{5}$$

$$\lambda_i \int_{x_{\max}}^{+\infty} V^i(x,\tau) f^i(z-x)dz \approx \lambda_i \int_{x_{\max}}^{+\infty} \max(1-\exp(\xi), 0) f^i(\xi)d\xi = 0. \tag{6}$$

By using the composite Simpson's rule and Equations (5) and (6), we obtain

$$\begin{aligned} \mathcal{I}V^i(x,\tau) &= \lambda_i \textstyle\int_{-\infty}^{+\infty} V^i(x,\tau) f^i(z-x)dz \approx \lambda_i \int_{x_{\min}}^{x_{\max}} V^i(x,\tau) f^i(z-x)dz \\ &\approx \tfrac{\lambda_i \Delta x}{3} \sum_{m=1}^{m_x/2} [V^i(x_{2m-2},\tau) f^i(x_{2m-2}-x) + 4V^i(x_{2m-1},\tau) f^i(x_{2m-1}-x) \\ &\qquad + V^i(x_{2m},\tau) f^i(x_{2m}-x)] \end{aligned} \tag{7}$$

For the differential term in Equation (2), we define $V^i_{m,j} \equiv V^i(x_m, \tau_j), j = 1, 2, \cdots, N$. Then, the standard central difference approximation to Equation (3) at point (x_m, τ_j) for regime i is

$$\mathcal{L}V^i_{m,j} = (r_i - \lambda_i\beta_i - \frac{1}{2}\sigma_i^2)\delta_x V^i_{m,j} + \frac{1}{2}\sigma_i^2 \delta_x^2 V^i_{m,j} - (r_i + \lambda_i)V^i_{m,j} + \varepsilon_m^{(i)} \tag{8}$$

where δ_x and δ_x^2 are the first- and second-order central difference approximations with respect to x, respectively. The truncation error is given by

$$\varepsilon_m^{(i)} = \frac{(\Delta x)^2}{12}\left(2r_i - 2\lambda_i\beta_i - \sigma_i^2\right)\frac{\partial^3 V^i_{m,j}}{\partial x^3} + \frac{1}{24}(\Delta x)^2\sigma_i^2 \frac{\partial^4 V^i_{m,j}}{\partial x^4} + \mathcal{O}\left((\Delta x)^4\right) \tag{9}$$

Differentiating Equation (3) with respect to x, we have

$$\frac{\partial^3 V^i_{m,j}}{\partial x^3} = \frac{2}{\sigma_i^2}\frac{\partial \mathcal{L}V^i_{m,j}}{\partial x} - \frac{2r_i - 2\lambda_i\beta_i - \sigma_i^2}{\sigma_i^2}\frac{\partial^2 V^i_{m,j}}{\partial x^2} + \frac{2(r_i+\lambda_i)}{\sigma_i^2}\frac{\partial V^i_{m,j}}{\partial x} \tag{10}$$

$$\frac{\partial^4 V^i_{m,j}}{\partial x^4} = \frac{2}{\sigma_i^2}\frac{\partial^2 \mathcal{L}V^i_{m,j}}{\partial x^2} - \frac{2\left(2r_i - 2\lambda_i\beta_i - \sigma_i^2\right)}{\sigma_i^4}\frac{\partial \mathcal{L}V^i_{m,j}}{\partial x} + \frac{\left(2r_i - 2\lambda_i\beta_i - \sigma_i^2\right)^2}{\sigma_i^4}\frac{\partial^2 V^i_{m,j}}{\partial x^2} - \frac{4(r_i+\lambda_i)\left(r_i - \lambda_i\beta_i - \sigma_i^2\right)}{\sigma_i^4}\frac{\partial V^i_{m,j}}{\partial x} \tag{11}$$

We substitute Equations (10) and (11) into (9) to obtain a new expression of the error term $\varepsilon_l^{(i)}$ that only includes terms which are either $\mathcal{O}\left((\Delta x)^4\right)$ or $\mathcal{O}\left((\Delta x)^2\right)$ multiplied by derivatives of V, which can be approximated to $\mathcal{O}\left((\Delta x)^2\right)$ within the compact stencil. Inserting this new expression for the error term in (8), we obtain

$$\begin{aligned}&\left[r_i-\lambda_i\beta_i-\tfrac{\sigma_i^2}{2}+\tfrac{(r_i+\lambda_i)(r_i-\lambda_i\beta_i)(\Delta x)^2}{6\sigma_i^2}\right]\delta_x V_{m,j}^i+\left[\tfrac{\sigma_i^2}{2}-\tfrac{\left(2r_i-2\lambda_i\beta_i-\sigma_i^2\right)^2(\Delta x)^2}{24\sigma_i^2}\right]\delta_x^2 V_{m,j}^i-(r_i+\lambda_i)V_{m,j}^i\\&=\mathcal{L}V_{m,j}^i-\tfrac{\left(2r_i-2\lambda_i\beta_i-\sigma_i^2\right)(\Delta x)^2}{12\sigma_i^2}\delta_x\mathcal{L}V_{m,j}^i-\tfrac{(\Delta x)^2}{12}\delta_x^2\mathcal{L}V_{m,j}^i\end{aligned} \tag{12}$$

According to Equations (7) and (12), we obtain the discretization of PIDE (2) at point $\left(x_m,\tau_j\right)$ for regime i

$$V_{m,j}^i=a_iV_{m+1,j+1}^i+b_iV_{m,j+1}^i+c_iV_{m-1,j+1}^i$$

where

$$a_i=\frac{1}{1+(r_i+\lambda_i)\Delta\tau}\frac{(\Delta x)^2[(r_i+\lambda_i-\rho_{ii})\Delta\tau-1]-(\Delta\tau-1)\left[\sigma_i^2-\frac{\left(2r_i-2\lambda_i\beta_i-\sigma_i^2\right)^2(\Delta x)^2}{12\sigma_i^2}\right]}{(r_i+\lambda_i-\rho_{ii})\Delta\tau(\Delta x)^2-(\Delta x)^2+\left[\sigma_i^2-\frac{\left(2r_i-2\lambda_i\beta_i-\sigma_i^2\right)^2(\Delta x)^2}{12\sigma_i^2}\right]} \tag{13}$$

$$b_i=\frac{1}{1+(r_i+\lambda_i)\Delta\tau}\frac{\left[\frac{\sigma_i^2}{2}-\frac{\left(2r_i-2\lambda_i\beta_i-\sigma_i^2\right)^2(\Delta x)^2}{24\sigma_i^2}\right]\Delta\tau+\frac{1}{2}\left[r_i-\lambda_i\beta_i-\frac{\sigma_i^2}{2}+\frac{(r_i+\lambda_i)(r_i-\lambda_i\beta_i)(\Delta x)^2}{6\sigma_i^2}\right]\Delta\tau\Delta x}{(r_i+\lambda_i-\rho_{ii})\Delta\tau(\Delta x)^2-(\Delta x)^2+\left[\sigma_i^2-\frac{\left(2r_i-2\lambda_i\beta_i-\sigma_i^2\right)^2(\Delta x)^2}{12\sigma_i^2}\right]} \tag{14}$$

$$c_i=\frac{1}{1+(r_i+\lambda_i)\Delta\tau}\frac{\left[\frac{\sigma_i^2}{2}-\frac{\left(2n_i-2\lambda_i\beta_i-\sigma_i^2\right)^2(\Delta x)^2}{24\sigma_i^2}\right]\Delta\tau-\frac{1}{2}\left[n_i-\lambda_i\beta_i-\frac{\sigma_i^2}{2}+\frac{(r_i+\lambda_i)(r_i-\lambda_i\beta_i)(\Delta x)^2}{6\sigma_i^2}\right]\Delta\tau\Delta x}{(r_i+\lambda_i-\rho_{ii})\Delta\tau(\Delta x)^2-(\Delta x)^2+\left[\sigma_i^2-\frac{\left(2r_i-2\lambda_i\beta_i-\sigma_i^2\right)^2(\Delta x)^2}{12\sigma_i^2}\right]} \tag{15}$$

1.4. Outline of This Paper

The rest of this paper is organized as follows. In Section 2, the relationship between the high-order difference scheme and the trinomial tree algorithm is investigated, and then the convergence rate of the high-order difference algorithm for option pricing in a Markov regime-switching model is obtained. Section 3 summarizes the main conclusions.

2. Main Results

In this section, we investigate the relationship between the high-order difference method and the trinomial tree approach and propose the estimation of the local remainder of this algorithm. After this, we can obtain the convergence rate.

2.1. The Two Lemmas

Lemma 1. *If* $\Delta\tau\le\frac{1+\left(2r_i-2\lambda_i\beta_i-\sigma_i^2\right)^2}{r_i+\lambda_i-\rho_{ii}}$ *and* $\Delta x\le\sigma\sqrt{\frac{\Delta\tau}{1-(r_i+\lambda_i-\rho_{ii})\Delta\tau+\left(2r_i-2\lambda_i\beta_i-\sigma_i^2\right)^2}}$ *, the high-order finite difference method is equivalent to a trinomial tree approach, that is, for the defined high-order finite difference (13)–(15), the following result holds for regime* $i=1,2,\cdots,n$*.*

$$a_i+b_i+c_i=\frac{1}{1+(r_i+\lambda_i)\Delta\tau}\text{ and }a_i\ge 0,b_i\ge 0,c_i\ge 0$$

Proof. Equations (13)–(15) imply that

$$\begin{aligned}
a_i + b_i + c_i = {} & \frac{1}{1+(r_i+\lambda_i)\,\Delta\tau}\frac{(\Delta x)^2[(r_i+\lambda_i-\rho_{ii})\,\Delta\tau-1]-(\Delta\tau-1)\left[\sigma_i^2-\frac{\left(2r_i-2\lambda_i\beta_i-\sigma_i^2\right)^2(\Delta x)^2}{12\sigma_i^2}\right]}{(r_i+\lambda_i-\rho_{ii})\,\Delta\tau(\Delta x)^2-(\Delta x)^2+\left[\sigma_i^2-\frac{\left(2r_i-2\lambda_i\beta_i-\sigma_i^2\right)^2(\Delta x)^2]}{12\sigma_i^2}\right]} \\
& +\frac{1}{1+(r_i+\lambda_i)\,\Delta\tau}\frac{\left[\frac{\sigma_i^2}{2}-\frac{\left(2r_i-2\lambda_i\beta_i-\sigma_i^2\right)^2(\Delta x)^2}{24\sigma_i^2}\right]\Delta\tau+\frac{1}{2}\left[r_i-\lambda_i\beta_i-\frac{\sigma_i^2}{2}+\frac{(r_i+\lambda_i)\,(r_i-\lambda_i\beta_i)\,(\Delta x)^2}{6\sigma_i^2}\right]\Delta\tau\Delta x}{(r_i+\lambda_i-\rho_{ii})\,\Delta\tau(\Delta x)^2-(\Delta x)^2+\left[\sigma_i^2-\frac{\left(2r_i-2\lambda_i\beta_i-\sigma_i^2\right)^2(\Delta x)^2}{12\sigma_i^2}\right]} \\
& +\frac{1}{1+(r_i+\lambda_i)\,\Delta\tau}\frac{\left[\frac{\sigma_i^2}{2}-\frac{\left(2r_i-2\lambda_i\beta_i-\sigma_i^2\right)^2(\Delta x)^2}{24\sigma_i^2}\right]\Delta\tau-\frac{1}{2}\left[r_i-\lambda_i\beta_i-\frac{\sigma_i^2}{2}+\frac{(r_i+\lambda_i)\,(r_i-\lambda_i\beta_i)\,(\Delta x)^2}{6\sigma_i^2}\right]\Delta\tau\Delta x}{(r_i+\lambda_i-\rho_{ii})\,\Delta\tau(\Delta x)^2-(\Delta x)^2+\left[\sigma_i^2-\frac{\left(2r_i-2\lambda_i\beta_i-\sigma_i^2\right)^2(\Delta x)^2}{12\sigma_i^2}\right]} \\
= {} & \frac{1}{1+(r_i+\lambda_i)\,\Delta\tau}
\end{aligned}$$

Under the condition in Lemma 1, it is easy to show $a_i \geq 0, b_i \geq 0, c_i \geq 0$. Therefore, the expressions $a_i[1+(r_i+\lambda_i)\Delta\tau]$, $b_i[1+(r_i+\lambda_i)\Delta\tau]$, and $c_i[1+(r_i+\lambda_i)\Delta\tau]$ can be interpreted as the probabilities of moving from x_m to $x_m,\ x_{m+1}$ and x_{m-1}, respectively. □

Let $V\left(x_m,\tau_j,i\right)$ denote a high-order finite difference approximation value at the node $\left(x_m,\tau_j\right)$ for regime i. Then, from Lemma 1, $V\left(x_m,\tau_j,i\right)$ can be calculated by

$$V\left(x_m,\tau_j,i\right) = e^{-r_i\Delta\tau}\sum_{l=1}^{n}\left[P_{il}\left(a_iV\left(x_{m+1},\tau_{j+1},l\right)+b_iV\left(x_m,\tau_{j+1},l\right)+c_iV\left(x_{m-1},\tau_{j+1},l\right)\right)\right] \tag{16}$$

where P_{il} is the transition probability from regime i to l, satisfying the following equation

$$(P_{il})_{n\times n} = I + \sum_{l=1}^{\infty}\frac{(\Delta\tau)^l A^l}{l!} \tag{17}$$

in which I denotes the unit matrix and A is the generation matrix of the Markov chain.

Define the local remainder of $V^i(x,\tau)$ for regime i at $\left(x_m,\tau_j\right)$ by

$$\begin{aligned}
R_j^i = V^i\left(x_m,\tau_j\right) - e^{-r_i\Delta\tau}\sum_{l=1}^{n}[P_{il}(a_iV\left(x_{m+1},\tau_{j+1},l\right)+b_iV\left(x_m,\tau_{j+1},l\right) \\
+c_iV(x_{m-1},\tau_{j+1},l))]
\end{aligned} \tag{18}$$

where $V^i\left(x_m,\tau_j\right)$ denotes the exact European option value for regime i at $\left(x_m,\tau_j\right)$.

Lemma 2. *Let $V(x,\tau)$ be a function for which the partial derivatives $\frac{\partial V}{\partial x}$, $\frac{\partial^2 V}{\partial x^2}$ and $\frac{\partial^3 V}{\partial x^3}$ are defined and continuous. The estimation of the local remainder R_j^i in (18) is given by $R_j^i = \mathcal{O}\left((\Delta\tau)^2\right)$ for regime $i = 1, 2, \cdots, n$.*

Proof. By applying Taylor expansion to $V^i\left(x_m,\tau_j\right)$, $V^i\left(x_{m+1},\tau_{j+1}\right)$ and $V^i\left(x_{m-1},\tau_{j+1}\right)$, $i = 1, 2, \cdots, n$ at τ_{j+1}, we have

$$V^i\left(x_m,\tau_j\right) = V^i\left(x_m,\tau_{j+1}\right) - \frac{\partial V^i\left(x_m,\tau_{j+1}\right)}{\partial\tau}\Delta\tau + \mathcal{O}\left((\Delta\tau)^2\right) \tag{19}$$

$$\begin{aligned}
V^i\left(x_{m+1},\tau_{j+1}\right) = V^i\left(x_m,\tau_{j+1}\right) + \frac{\partial V^i\left(x_m,\tau_{j+1}\right)}{\partial x}\Delta x_m \\
+\frac{1}{2}\frac{\partial^2 V^i\left(x_m,\tau_{j+1}\right)}{\partial x^2}(\Delta x_m)^2 + \frac{1}{6}\frac{\partial^3 V^i\left(x_m,\tau_{j+1}\right)}{\partial x^3}(\Delta x_m)^3 + \mathcal{O}((\Delta x_m)^4)
\end{aligned} \tag{20}$$

and

$$\begin{aligned} V^i\left(x_{m-1}, \tau_{j+1}\right) = {} & V^i\left(x_m, \tau_{j+1}\right) + \frac{\partial V^i\left(x_m, \tau_{j+1}\right)}{\partial x}\left(-\Delta x_m\right) \\ & + \frac{1}{2}\frac{\partial^2 V^i\left(x_m, \tau_{j+1}\right)}{\partial x^2}\left(-\Delta x_m\right)^2 + \frac{1}{6}\frac{\partial^3 V^i\left(x_m, \tau_{j+1}\right)}{\partial x^3}\left(-\Delta x_m\right)^3 + \mathcal{O}\left(\left(-\Delta x_m\right)^4\right) \end{aligned} \tag{21}$$

Substituting (19)–(21) into (18), we have

$$\begin{aligned} R_j^i = {} & V^i\left(x_m, \tau_j\right) - e^{-r_i \Delta \tau}\sum_{l=1}^{n} P_{il}\left(a_i V^l\left(x_{m+1}, \tau_{j+1}\right) + b_i V^l\left(x_m, \tau_{j+1}\right) + c_i V^l\left(x_{m-1}, \tau_{j+1}\right)\right) \\ = {} & V^i\left(x_m, \tau_{j+1}\right) - \frac{\partial V^i\left(x_m, \tau_{j+1}\right)}{\partial \tau}\Delta \tau + \mathcal{O}\left((\Delta \tau)^2\right) \\ & - e^{-r_i \Delta \tau}\sum_{l=1}^{n} P_{il}\left\{ \begin{array}{c} a_i\left[\begin{array}{c} V^l\left(x_m, \tau_{j+1}\right) + \frac{\partial V^l\left(x_m, \tau_{j+1}\right)}{\partial x}\Delta x_m + \frac{1}{2}\frac{\partial^2 V^l\left(x_m, \tau_{j+1}\right)}{\partial x^2}\left(\Delta x_m\right)^2 \\ + \frac{1}{6}\frac{\partial^3 V^l\left(x_m, \tau_{j+1}\right)}{\partial x^3}\left(\Delta x_m\right)^3 + \mathcal{O}\left(\left(\Delta x_m\right)^4\right) \end{array} \right] + b_i V^l\left(x_m, \tau_{j+1}\right) \\ + c_i\left[\begin{array}{c} V^l\left(x_m, \tau_{j+1}\right) + \frac{\partial V^l\left(x_m, \tau_{j+1}\right)}{\partial x}\left(-\Delta x_m\right) + \frac{1}{2}\frac{\partial^2 V^l\left(x_m, \tau_{j+1}\right)}{\partial x^2}\left(-\Delta x_m\right)^2 \\ + \frac{1}{6}\frac{\partial^3 V^l\left(x_m, \tau_{j+1}\right)}{\partial x^3}\left(-\Delta x_m\right)^3 + \mathcal{O}\left(\left(-\Delta x_m\right)^4\right) \end{array} \right] \end{array} \right\} \\ = {} & V^i\left(x_m, \tau_{j+1}\right) - \frac{\partial V^i\left(x_m, \tau_{j+1}\right)}{\partial \tau}\Delta \tau + \mathcal{O}\left((\Delta \tau)^2\right) \\ & - e^{-r_i \Delta \tau}\sum_{l=1}^{n} P_{il}\left\{ \begin{array}{c} \left(a_i + b_i + c_i\right) V^l\left(x_m, \tau_{j+1}\right) + \left(a_i - c_i\right)\frac{\partial V^l\left(x_m, \tau_{j+1}\right)}{\partial x}\Delta x_m \\ + \frac{1}{2}\left(a_i + c_i\right)\frac{\partial^2 V^l\left(x_m, \tau_{j+1}\right)}{\partial x^2}\left(\Delta x_m\right)^2 + \frac{1}{6}\left(a_i - c_i\right)\frac{\partial^3 V^l\left(x_m, \tau_{j+1}\right)}{\partial x^3}\left(\Delta x_m\right)^3 + \left(a_i + c_i\right)\mathcal{O}\left(\left(\Delta x_m\right)^4\right)\right) \end{array} \right\} \end{aligned} \tag{22}$$

Using Lemma 1 and Equation (17), we obtain

$$\begin{aligned} R_j^i & = \mathcal{O}\left((\Delta \tau)^2\right)\left[\begin{array}{c} \frac{\partial V^i\left(x_m, \tau_{j+1}\right)}{\partial \tau} - \left(r_i - \beta_i - \frac{1}{2}\sigma_i^2\right)\frac{\partial V^i\left(x_m, \tau_{j+1}\right)}{\partial x} - \frac{1}{2}\sigma_i^2\frac{\partial^2 V^i\left(x_m, \tau_{j+1}\right)}{\partial x^2} \\ -\left(r_i + \lambda_i\right) V^i\left(x_m, \tau_{j+1}\right) - \sum\limits_{j=1}^{n} \rho_{ij} V^i\left(x_m, \tau_{j+1}\right) - \lambda_i \int_{-\infty}^{+\infty} V(z, \tau, i) f(z - x, i) dz \end{array} \right]\Delta \tau \\ & = \mathcal{O}\left((\Delta \tau)^2\right) \end{aligned}$$

□

Based on Lemmas 1 and 2, the convergence rate of the high-order finite difference algorithm is investigated as follows.

2.2. The Main Theorem

Theorem 1. (*Convergence rate of the high-order finite difference method*). *We define the error of high-order finite difference at the node* $\left(x_m, \tau_j\right)$ *by*

$$\varepsilon_i^j\left(x_m\right) = V^i\left(x_m, \tau_j\right) - V\left(x_m, \tau_j, i\right),\ i = 1, 2, \cdots, n \tag{23}$$

and the infinity norm by

$$\|\varepsilon_i^j\|_\infty = \max\left|\varepsilon_i^j\left(x_m\right)\right|, i = 1, 2, \cdots, n \tag{24}$$

Then, the convergence rate of the high-order finite difference is estimated by

$$\|\varepsilon_i^j\|_\infty = |\mathcal{O}(\Delta \tau)|, i = 1, 2, \cdots, n \tag{25}$$

Proof. According to Equation (18),

$$V^i\left(x_m, \tau_j\right) = R_j^i + e^{-r_i \Delta \tau}\sum_{l=1}^{n} P_{il}\left(a_i V^l\left(x_{m+1}, \tau_{j+1}\right) + b_i V^l\left(x_m, \tau_{j+1}\right) + c_i V^l\left(x_{m-1}, \tau_{j+1}\right)\right) \tag{26}$$

Then, we note from Equations (16) and (26) that

$$\varepsilon_i^j(x_m) = e^{-r_i\Delta\tau}\sum_{l=1}^{n} P_{il}\left(a_i\varepsilon_l^{j+1}(x_{m+1}) + b_i\varepsilon_l^{j+1}(x_m) + c_i\varepsilon_l^{j+1}(x_{m-1})\right) + R_j^i$$

Therefore, the following inequality holds:

$$\begin{aligned}\left|\varepsilon_i^j(x_m)\right| &\leq \left|R_j^i\right| + e^{-r_i\Delta\tau}\sum_{l=1}^{n} P_{il}(a_i|\varepsilon_i^{j+1}(x_{m+1})| + b_i|\varepsilon_i^{j+1}(x_m)| + c_i|\varepsilon_i^{j+1}(x_{m-1})|) \\ &\leq \left|R_j^i\right| + e^{-r_i\Delta\tau}\sum_{l=1}^{n} P_{il}\|\varepsilon_l^{j+1}\|_\infty \\ &= e^{-r_i\Delta\tau}\sum_{l=1}^{n} P_{il}\|\varepsilon_l^{k+1}\|_\infty + |\mathcal{O}((\Delta\tau)^2)|\end{aligned} \tag{27}$$

The last line of (27) is obtained from Lemma 2. Therefore, by using Equation (17), we have

$$\begin{aligned}\sum_{i=1}^{n}\|\varepsilon_i^j\|_\infty &\leq \sum_{i=1}^{n} e^{-r_i\Delta\tau}\sum_{l=1}^{2} P_{il}\|\varepsilon_l^{j+1}\|_\infty + |\mathcal{O}((\Delta\tau)^2)| \\ &\leq \sum_{i=1}^{n}\left[1 + \sum_{i=1}^{n} a_{il}\Delta\tau + |\mathcal{O}\left((\Delta\tau)^2\right)|\right]\|\varepsilon_i^{j+1}\|_\infty + |\mathcal{O}((\Delta\tau)^2)|\end{aligned} \tag{28}$$

The term $\sum_{i=1}^{n} a_{il}\Delta\tau + |\mathcal{O}((\Delta\tau)^2)| \geq 0$ in Equation (28) implies

$$\sum_{i=1}^{n}\|\varepsilon_i^j\|_\infty \leq \sum_{i=1}^{n}\|\varepsilon_i^{j+1}\|_\infty + \left\{\sum_{j=1}^{n}\left[\sum_{i=1}^{n} a_{ij}\Delta\tau + |\mathcal{O}((\Delta\tau)^2)|\right]\right\}\sum_{i=1}^{n}\|\varepsilon_i^{j+1}\|_\infty + |\mathcal{O}((\Delta\tau)^2)|$$

Since $\sum_{j=1}^{n} a_{ij} = 0, i = 1, 2, \cdots, n$, the following inequality can be obtained:

$$\sum_{i=1}^{n}\|\varepsilon_i^j\|_\infty \leq [1 + |\mathcal{O}((\Delta\tau)^2)|]\sum_{i=1}^{n}\|\varepsilon_i^{j+1}\|_\infty + |\mathcal{O}((\Delta\tau)^2)| \tag{29}$$

By iterating (29), we have

$$\sum_{i=1}^{n}\|\varepsilon_i^j\|_\infty \leq [1 + |\mathcal{O}((\Delta\tau)^2|]^{n-j}\left(\sum_{i=1}^{n}\|\varepsilon_i^n\|_\infty\right) - 1 + [1 + |\mathcal{O}((\Delta\tau)^2)|]^{n-j} \tag{30}$$

At the final step $\tau_n = 0$, the following expression holds:

$$\varepsilon_i^n = V^i(x_m, \tau_n) - V(x_m, \tau_n, i) = 0, i = 1, 2, \cdots, n$$

According to (30), we have

$$\begin{aligned}\sum_{i=1}^{n}\|\varepsilon_i^j\|_\infty &\leq -1 + [1 + |\mathcal{O}((\Delta\tau)^2)|]^{n-j} \\ &= -1 + \sum_{l=0}^{n-j} C_{n-j}^l|\mathcal{O}((\Delta\tau)^2)|^l \\ &= C_{n-j}^1\mathcal{O}((\Delta\tau)^2) + \sum_{l=2}^{n-j} C_{n-j}^l|\mathcal{O}((\Delta\tau)^2)|^l \\ &\leq n\mathcal{O}((\Delta\tau)^2) = \frac{T}{\Delta\tau}\mathcal{O}((\Delta\tau)^2) = \mathcal{O}(\Delta\tau)\end{aligned}$$

□

3. Conclusions

In this paper, we have investigated the convergence rate of the high-order finite difference method for option pricing in a Markov regime-switching jump-diffusion model by employing the relationship between this algorithm and the trinomial tree approach. The result shows that the convergence rate of this algorithm is $\mathcal{O}(\Delta\tau)$. This theoretical proof ensures the validation of the high-order finite difference method for option pricing.

For future research, it is worth investigating the convergence rate of the high-order finite difference method for options with stochastic volatility jump models in the case of infinite states for the Markov chain.

Author Contributions: Conceptualization, J.L.; Investigation, J.L.; Methodology, J.L.; Writing—Original draft, J.L. and J.Y.; Writing—review and editing, J.L. and J.Y. All authors have read and agreed to the published version of the manuscript.

Funding: This research received no external funding.

Data Availability Statement: The data used to support the findings of this study are included within the article.

Conflicts of Interest: The authors declare no conflict of interest.

References

1. Bastani. A.F.; Ahmadi, Z.; Damircheli, D. A radial basis collocation method for pricing American options under regime-switching jump-diffusion models. *Appl. Numer. Math.* **2013**, *65*, 79–90. [CrossRef]
2. Costabile, M.; Leccadito, A.; Massabó, I.; Russo, E. Option pricing under regime-switching jump-diffusion models. *J. Comput. Appl. Math.* **2014**, *256*, 152–167. [CrossRef]
3. Florescu, I.; Liu, R.; Mariani, M.C. Numerical schemes for option pricing in regime-switching jump diffusions models. *Int. J. Theor. Appl. Financ.* **2014**, *16*, 1350046. [CrossRef]
4. Rambeerich, N.; Pantelous, A. A high order finite element scheme for pricing options under regime switching jump diffusion processes. *J. Comput. Appl. Math.* **2016**, *300*, 83–96. [CrossRef]
5. Dang, D.; Nguyen, D.; Sewell, G. Numerical schemes for pricing Asian options under state- dependent regime-switching jump-diffusion models. *Comput. Math. Appl.* **2016**, *71*, 443–458. [CrossRef]
6. Patel, K.S.; Mehra, M. Fourth-order compact finite difference scheme for American option pricing under regime-switching jump-diffusion models. *Int. J. Appl. Comput. Math.* **2017**, *3*, 547–567. [CrossRef]
7. Tour, G.; Thakoor, N.; Tangman, D.Y.; Bhuruth, M. A high-order RBF-FD method for option pricing under regime-switching stochastic volatility models with jumps. *J. Comput. Sci.* **2019**, *35*, 25–43. [CrossRef]
8. Liang, X.; Wang, G.; Dong, Y. A Markov regime switching jump-diffusion model for the pricing of portfolio credit derivatives. *Stat. Probabil. Lett.* **2013**, *83*, 373–381. [CrossRef]
9. Jin, Z.; Yin, G.; Wu, F. Optimal reinsurance strategies in regime-switching jump diffusion models: Stochastic differential game formulation and numerical methods. *Insur. Math. Econ.* **2013**, *53*, 733–746. [CrossRef]
10. Siu, T.K. Bond pricing under a Markovian regime-switching jump-augmented Vasicek model via stochastic flows. *Appl. Math. Comput.* **2010**, *216*, 3184–3190.
11. Jin, Z.; Yang, H.; Yin, G.G. Numerical methods for optimal dividend payment and investment strategies of regime-switching jump diffusion models with capital Injections. *Automatica* **2013**, *49*, 2317–2329. [CrossRef]
12. Weron, R.; Bierbrauer, M.; Trück, S. Modeling electricity prices: Jump diffusion and regime switching. *Phys. A Stat. Mech. Its Appl.* **2004**, *336*, 39–48. [CrossRef]
13. Zhang, X.; Elliott, R.J.; Siu, T.K. A stochastic maximum principle for a Markov regime-switching jump-diffusion model and its application to finance. *SIAM J. Control Optim.* **2012**, *50*, 964–990. [CrossRef]
14. Savku, E.; Weber, G.W. A stochastic maximum principle for a Markov regime-switching jump-diffusion model with delay and an application to finance. *J. Optim. Theory Appl.* **2017**, *179*, 696–721. [CrossRef]
15. During, B.; Fournie, M. High-order compact finite difference scheme for option pricing in stochastic volatility models. *J. Comput. Appl. Math.* **2012**, *236*, 4462–4473. [CrossRef]
16. During, B.; Fournie, M.; Heuer, C. High-order compact finite difference scheme for option pricing in stochastic volatility models on non-uniform grids. *J. Comput. Appl. Math.* **2014**, *271*, 247–266. [CrossRef]
17. During, B.; Heuer, C. High-order compact schemes for parabolic problems with mixed derivatives in multiple space dimensions. *SIAM J. Numer. Anal* **2015**, *53*, 2113–2134. [CrossRef]
18. During, B.; Pitkin, A. High-order compact finite difference scheme for option pricing in stochastic volatility jump models. *J. Comput. Appl. Math.* **2019**, *355*, 201–217. [CrossRef]

19. Vong, S.; Wang. Z. A high order compact finite difference scheme for time fractional Fokker-Planck equations. *Appl. Math. Lett.* **2015**, *43*, 38–43. [CrossRef]
20. Thakoor, N.; Behera, D.K.; Tangman, D.Y.; Bhuruth, M. Howard's algorithm for high-order approximations of American options under jump-diffusion models. *Int. J. Data Sci. Anal.* **2020**, *10*, 193–203. [CrossRef]
21. Hendricks, C.; Heuer, C.; Ehrhardt, M.; Günther, M. High-order ADI finite difference schemes for parabolic equations in the combination technique with application in finance. *J. Comput. Appl. Math.* **2017**, *316*, 175–194. [CrossRef]
22. Patel, K.S.; Mehra, M. High-order compact finite difference scheme for pricing Asian option with moving boundary condition. *Differ. Equ. Dyn. Syst.* **2017**, *27*, 39–56. [CrossRef]
23. Düring, B.; Pitkin, A. High-order compact finite difference scheme for option pricing in stochastic volatility with contemporaneous jump models. *SSRN Electron. J.* **2019**, *30*, 365–371.
24. Yousuf, M. High-order time stepping scheme for pricing American option under Bates model. *Int. J. Comput. Math.* **2018**, *96*, 18–32. [CrossRef]
25. During, B.; Heuer, C. Time-Adaptive High-Order Compact Finite Difference Schemes for Option Pricing in a Family of Stochastic Volatility Models. Available online: https://ssrn.com/abstract=3890159 (accessed on 20 July 2021).
26. Ma, J.; Tang, H.; Zhu, S.P. Connection between trinomial trees and finite difference methods for option pricing with state-dependent switching rates. *Int. J. Comput. Math.* **2018**, *95*, 341–360. [CrossRef]
27. Alfonsi, A. High order discretization schemes for the CIR process: Application to affine term structure and Heston models. *Math. Comp.* **2010**, *79*, 209–237. [CrossRef]
28. Altmayer, M.; Neuenkirch, A. Discretising the Heston model: An analysis of the weak convergence rate. *IMA J. Numer. Anal.* **2017**, *37*, 1930–1960. [CrossRef]
29. Bossy, M.; Olivero, H. Strong convergence of the symmetrized Milstein scheme for some CEV-like SDEs. *Bernoulli* **2018**, *24*, 1995–2042. [CrossRef]
30. Zheng, C. Weak convergence rate of a time-discrete scheme for the Heston stochastic volatility model. *SIAM J. Numer. Anal.* **2017**, *55*, 1243–1263. [CrossRef]
31. Briani, M.; Caramellino, L.; Terenzi, G. Convergence rate of Markov chains and hybrid numerical schemes to jump-diffusions with application to the Bates model. *SIAM J. Numer. Anal* **2021**, *59*, 477–502. [CrossRef]
32. Briani, M.; Caramellino, L.; Terenzi, G.; Zanette, A. Numerical stability of a hybrid method for pricing options. *Int. J. Theor. Appl. Financ.* **2019**, *22*, 1950036. [CrossRef]
33. Lesmana, D.C.; Wang, S. A numerical scheme for pricing American options with transaction costs under a jump diffusion process. *J. Ind. Manag. Optim.* **2017**, *13*, 1793–1813. [CrossRef]
34. Merton, R.C. Theory of rational option pricing. *Bell J. Econ. Manag. Sci* **1973**, *4*, 141–183. [CrossRef]

MDPI
St. Alban-Anlage 66
4052 Basel
Switzerland
www.mdpi.com

Fractal and Fractional Editorial Office
E-mail: fractalfract@mdpi.com
www.mdpi.com/journal/fractalfract

Academic Open
Access Publishing

mdpi.com

ISBN 978-3-7258-1092-5